STUDY OF THE ANTI-COKING PROPERTIES OF A NEW CENTRIFUGALLY CAST ALLOY FOR ETHYLENE CRACKER FURNACES

ELLIOT ALEXANDER WALTERS

A THESIS SUBMITTED TO THE UNIVERSITY OF BIRMINGHAM FOR THE DEGREE OF

DOCTOR OF PHILOSOPHY

SURFACE ENGINEERING GROUP

DEPARTMENT OF METALLURGY AND MATERIALS

COLLEGE OF ENGINEERING AND PHYSICAL SCIENCES

UNIVERSITY OF BIRMINGHAM

SEPTEMBER 2019

Abstract

Plastic production relies on the formation of ethylene through steam cracking of hydrocarbons at high temperatures. Coking is one of the biggest issues in the ethylene cracking process, resulting in reduced production efficiency and lifespan of the pipes used. This work was undertaken to assess Optim-Al, a new, aluminium containing alloy, as an improvement over the currently used alloy.

The focus of the research was on the ability of Optim-Al to form a thin, protective aluminium oxide layer to inhibit catalytic coking, and specifically to provide greater protection than the alloy currently used. Optim-Al was found to form a continuous aluminium oxide layer after oxidation in air and demonstrated greater coverage and adhesion of the oxide even under more extreme conditions. Optim-Al was found to be an improvement over alloys currently used in the industry. Spalling of the surface oxide layer was found to concentrate around machining marks on the substrate surfaces, and a smoother surface to be oxidised should lead to improved coverage of oxide layer on both alloys in service, resulting in greater retardation of catalytic coking.

Acknowledgements

Firstly, I would like to convey many thanks to my academic supervisors Professor Hanshan Dong and Dr Xiaoying Li for all their help over the last five years. Their expert guidance has been vital, helping me develop significantly as a student and a researcher, and providing countless support and insight. Furthermore, their assistance in critical evaluation and analysis of my results and helping to further my understanding was invaluable.

Secondly, my industrial supervisors from Doncasters, Dr Dominique Flahaut and Dr Zhu Zhang. Zhu was extremely helpful in both aiding my research through access to top quality testing equipment, and in helping me to improve my own experimental technique. To Dominique I owe significant gratitude, as without her support, encouragement, advice and education, as well as honesty and harsh truths when needed, I can say I do not believe I would have completed my PhD. Her infectious passion meant every meeting with her gave me either renewed excitement and drive for my project, or she gave me the kick to work harder when needed! Thanks also to Naveen Manikanteswaran for his help with JMatPro modelling, as well as his enthusiasm for the project during all encounters. Furthermore, I would like to acknowledge EPSRC through the IMPaCT DTC, as well as Doncasters, for the support and funding of this project.

I would also like to give warm thanks to Dr Yu Lung Chiu for being so kind as to allow me access to his Tescan SEM. This offered significant improvement in results, and reduced process times, enabling the volume of microscopy required to be feasible. It also unlocked observations previously unobtained, granting me significantly better results and understanding. Furthermore, thanks go to Ubaid-Ur-Rehman Ghori for his training and Minshi Wang who on countless occasions aided me with both microscopy knowhow and technical knowledge and discussion.

Similarly, thanks to Dr Mary Taylor for her equipment and significant assistance in running the low partial pressure of oxygen oxidation tests. Furthermore, her significant knowledge of the oxidation

process helped me significantly in the early stages of my research, giving me much greater understanding of a topic which I was unfamiliar with.

Thanks also to the rest of the surface engineering group, particularly Yana Liang for her help with XRD, and Behnam Dashtbozorg for significant help with training on numerous pieces of equipment, as well as for friendship through my PhD. Similarly, many thanks to Tatiana Mukinay, Rachel Jennings and Stefano Cademartori for both help and friendship throughout the IMPaCT PhD DTC.

Huge thanks also to all my friends and teammates at both the Birmingham Lions and Tamworth Phoenix. During the low points of my PhD, American Football was my escape, keeping me happy, motivated and committed. The successes we enjoyed in the face of adversity helped me find resilience where I struggled. Without football, I would not have got to the point of my PhD where I get to write an acknowledgements section!

I would like to extend thanks to my friends, family, and particularly my parents, who have shown the upmost love and support throughout my PhD. Substantial gratitude goes to my mum, not only for her support but also her help in improving the grammar in this thesis! Similarly, my dad helped pick me up when I was down, always helping in any way he could, whilst he has also instilled in me an ability to work harder than I knew I was capable of when needed, which I have learned watching him throughout my life. Both of them are a significant factor in all my successes, past, present and future.

Finally, and most importantly, I need to thank my girlfriend, Rachel. My appreciation for her immeasurable support, love and care throughout my PhD, especially when I was struggling, can never be overstated. Thank you for standing by me and being a better girlfriend than I could ever have dreamt of having. You, above all else, are the reason I have reached where I am today. Thank you. I love you.

Table of Contents

List of Figures

List of Tables

1 Introduction

Plastic is one of the most vital and versatile materials in the world today, being used in a multitude of situations; from lightweight car parts to food packaging, wire insulation to water pipes, and many other applications in between. The variety of uses of plastics come from their uniquely beneficial range of properties; easy net shape forming without significant post production machining required, highly varied mechanical properties which different plastics are able to meet for many given conditions, the electrical and heat insulation properties, their durability, and ability to be recycled, to name but a few. These properties mean that plastic is the ideal material for use across a wide spectrum of applications.

Plastic production and use continue to grow, year on year, therefore the demand for plastic precursors continues to grow. Many forms of plastic are derived from one precursor: ethylene. Ethylene, or ethene, is the shortest unsaturated hydrocarbon molecule, made up of two carbon atoms joined by a double bond, with four hydrogen atoms. This molecule is the building block for many of the different plastics used. Ethylene is produced by the process of steam cracking of hydrocarbons. This process involves heating the longer chain hydrocarbons to temperatures in the range of 800°C with steam, which results in the splitting of the long chain hydrocarbons into much shorter chain hydrocarbons, such as ethylene.

The high temperature and creep properties required of the pipes in which the hydrocarbons are cracked mean that highly developed alloys are required to operate in such conditions. Despite decades of progress with the alloys and the optimization of the cracking process, a significant amount of coke is still created during cracking, which builds up on the pipe walls over time. This coke causes substantial limitations on the run lengths of the cracking process, requiring the furnaces to be shut down, and cleaned out to remove the build up. This cleaning process currently

occurs around every 40 days, and takes up to 48 hours, resulting in a significant reduction in production efficiency.

The alloys used for the pipes are necessarily rich in iron and nickel in order to withstand the high temperatures and conditions required. However, nickel and iron act as catalysts for the coking by carbon rich feedstock, therefore protection of the alloy from the gas stream is necessary to inhibit this coking from occurring. Currently, the alloys used in industry rely on the generation of a chromium oxide layer on the inner surface of the pipe to act as a barrier between the gas and the alloy matrix, however this does not provide perfect protection, as coking still readily occurs. Studies have shown an aluminium oxide layer to have better anti-coking properties than those of chromium oxide, however such aluminium containing alloys have not yet been made which effectively produce or maintain an oxide layer whilst also demonstrating the necessary properties for service conditions.

The aims of this research were to investigate the effects of aluminium content and other alloying elements on the microstructure of new alloys to be used in ethylene cracker furnace tubes. Furthermore, the oxidation behaviour of these alloys was investigated, and compared to those of an alloy currently used in industry, to assess the potential improvements that the new aluminium containing alloy could bring to the anti-coking properties of the pipes. The growth and adherence of the aluminium oxide layer onto the new alloy was compared to that of the chromium oxide layer generated on the alloy currently used.

2 Literature Review

2.1 Introduction

Hydrocarbons are vital in current society, both for fuels for transport and energy, and as precursors to plastic products, which make up a vast proportion of the worldwide manufacturing sector, with global plastic production over 400 million tons in 2015, per Geyer et al. (1). Crude oil is the main source of hydrocarbons, and around 4% of the world's crude oil is used for plastic production (2).

Ethylene, or ethene, is a key building block for numerous different forms of plastics, as illustrated in Figure 2.2.1-1. The global demand for ethylene is vast and rising, estimated at 112 million tons in 2009 (3), 130 million tons in 2013 (4), and increasing to greater than 150 million tons per year in 2016, and growing further still (5). Figure 2.2.1-2 demonstrates that between low-density and high-density polyethylene (LDPE and HDPE respectively), these two plastics make up in the region of one third of global plastic production. Sources suggest that 60% of produced ethylene is used as LDPE or HDPE precursors (3,6). This suggests that ethylene is the precursor for around 50% of all plastic production, worldwide, or over 200 million tons.

Crude oil, and natural gas, are made up of many different, long chain hydrocarbons, and are processed to form the short chain hydrocarbons required for plastic production by cracking. Cracking is the act of shortening long chain hydrocarbons by breaking the carbon-carbon bonds, yielding shorter hydrocarbons which are in a greater demand and generally perceived as more useful of a product than long chain hydrocarbons.

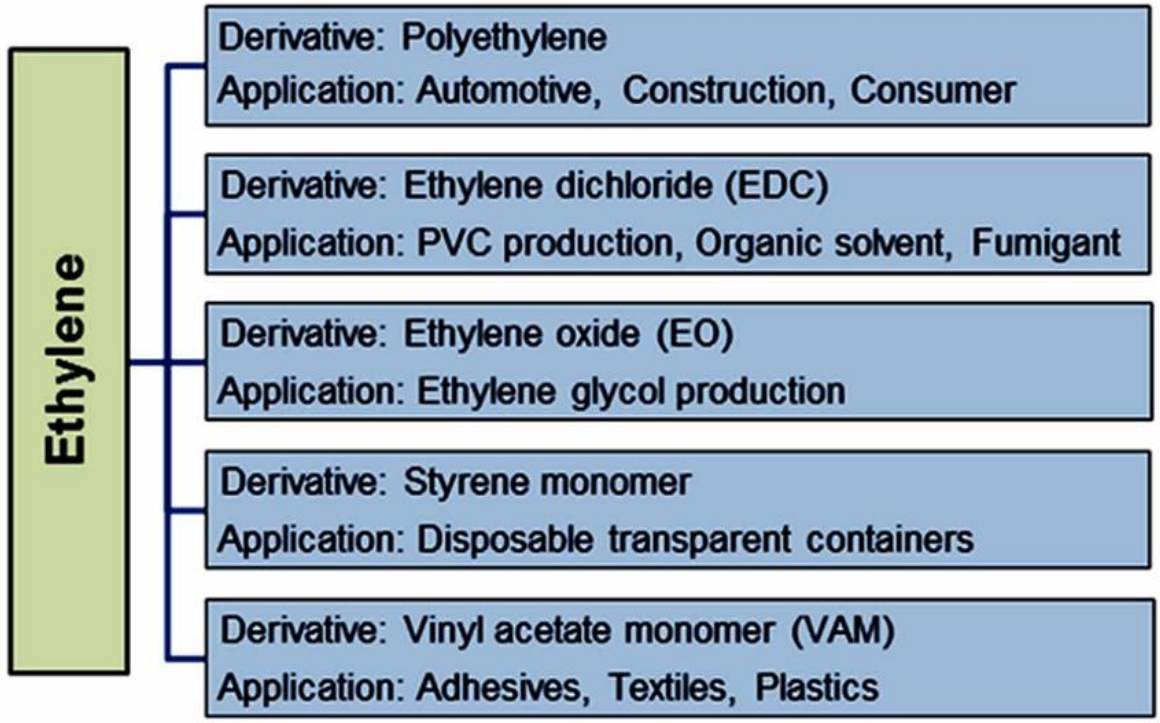

Figure 2.2.1-1: Illustration of chemicals derived from ethylene and their applications (7)

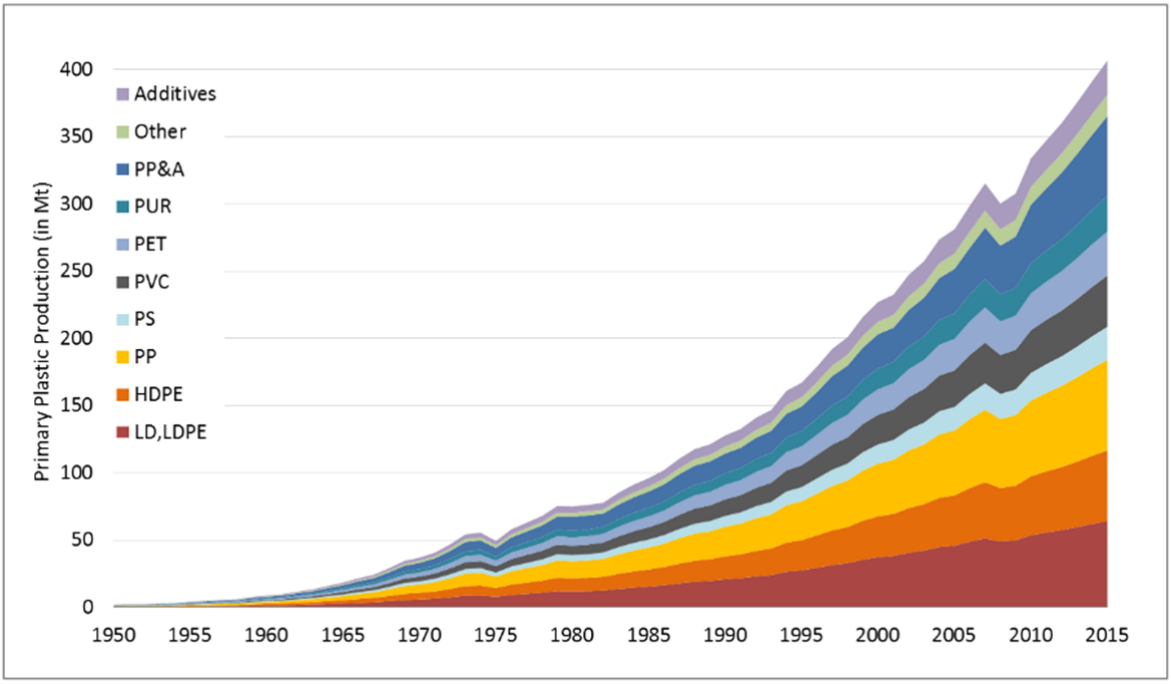

Figure 2.2.1-2: Global primary plastic production (in million metric tons) according to polymer type from 1950 to 2015 (8)

Steam cracking of hydrocarbons is employed as this process yields much greater volumes of unsaturated hydrocarbons compared to other cracking techniques such as catalytic cracking, due to the dilution of the hydrocarbon mix in the gas stream being preferential for olefin production

(9). Steam cracking occurs at high temperatures, over 850°C and higher, so the radiant coils must be able to withstand these relatively harsh conditions. Abghari found that the optimal operating temperature for ethylene cracking was 883°C, demonstrating the necessity for the alloy to cope at these high temperatures (10).

One of the major heat resistant alloys used in the petrochemical industry are high temperature steels, due to their excellent high temperature properties. These materials have much higher melting points, resistance to oxidation, and good creep resistance, all of which allow them to maintain their requisite properties during use in the steam cracking industry (11). Before the addition of nickel to steel, the mechanical properties were significantly poorer at high temperature, as nickel improved the creep resistance at high temperatures significantly. This allowed these nickel-containing high temperature steels to be employed and demonstrate significant improvement over previously used high temperature steels (12).

2.2 High temperature alloys for ethylene cracker furnaces

2.2.1 History of high temperature alloys

The requirement for high temperature materials occurred at the start of the 20th century, initially through the driving factors of the World Wars looking for high temperature materials for gun barrels, and later with the development of the jet engine, with other technologies emerging such as steam turbines and internal combustion engines prior to the wars. Since this period, development has been to push alloys to greater operating temperatures at which the materials can continue to maintain their beneficial properties. This is useful across a multitude of industries, such as ethylene cracking , fossil fuel power plants, and high temperature turbines, as the desire for greater efficiency in jet engines comes with ever increasing temperature (13–15).

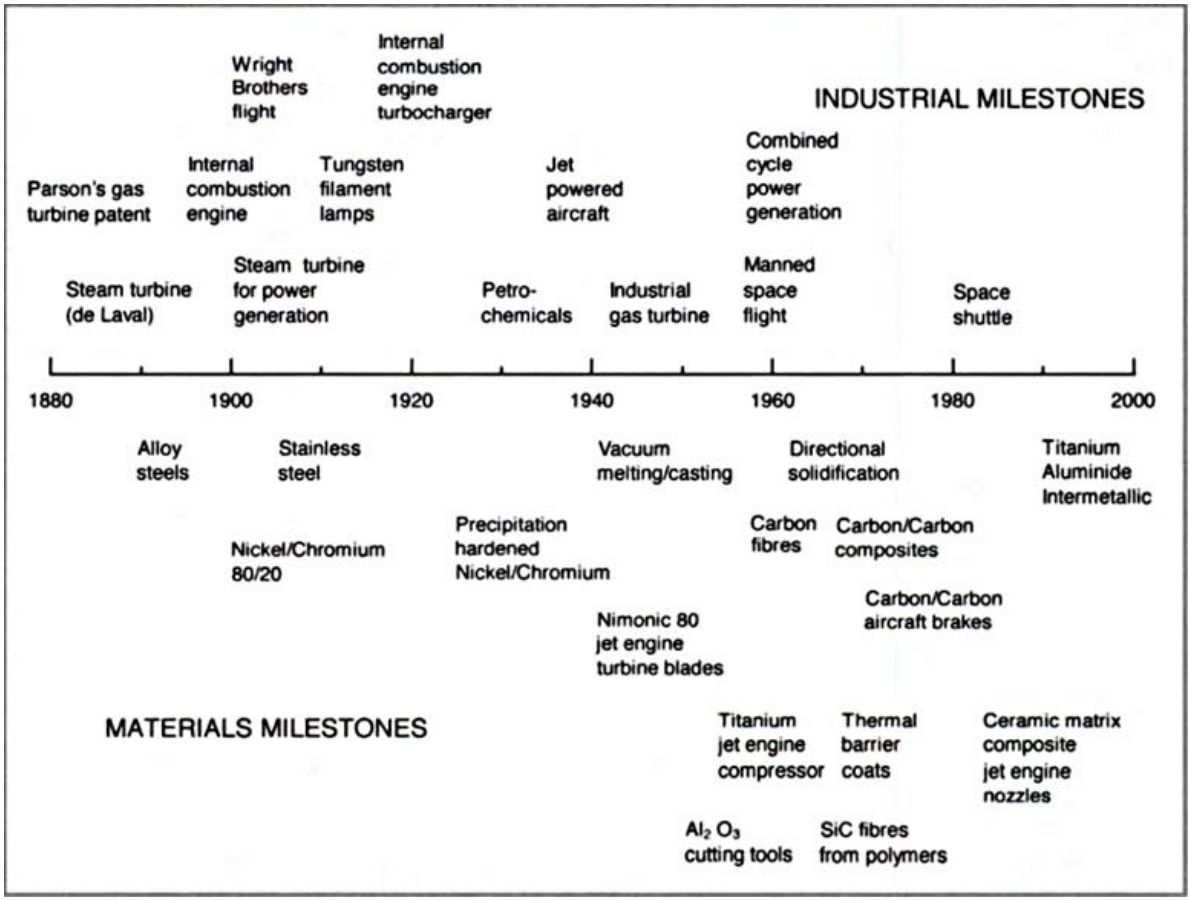

Figure 2.2.1-1: Major industrial milestones and associated material milestones (16)

The initial development was seen through advances in alloying in steels; the first chromium-containing steel was created in 1865, and the first nickel containing in 1888 (17). The first stainless steel was reportedly created in 1912 through the addition of chromium and molybdenum, resulting in a steel with good creep, oxidation and high temperature resistance properties (13). Following on from this discovery, chromium became an important alloying element, yielding the high temperature oxidation resistance required from the components.

The high melting point and relative abundance of nickel compared to similarly high melting point elements led to its use as an alloying addition, and then to becoming a base element for alloys, to be used in high temperature applications without costs being unfeasibly high. These high service temperature materials, the precursors to modern superalloys, were developed mainly for use in jet engines, first being developed in the 1930s (16).

In 1929 the alloying elements of aluminium and titanium were added to a nickel chromium alloy consisting of 80% nickel, and with this addition the creep strengths were seen to grow rapidly, forming the basis of the first 'superalloy'. Since the first ternary and quaternary alloys were developed, the development of superalloys has seen massive growth, with alloys containing over 10 elements being created for different applications across industry. All of these alloys consist of an FCC matrix with secondary phases present (14).

Whilst the petrochemical industry required high temperature resistance, carburisation resistance and good creep properties, the full benefit of superalloys was not realized in these applications, therefore Cr-Ni steels became commonplace in the early 1960s, benefiting from the desired properties but at a reduced cost, due to significantly lower nickel content compared to superalloys, in what has been termed the "second generation" of high temperature steels, following on from the carbon steels of the turn of the century (15,18,19). Through the mid to late 20th century the alloy composition evolved, increasing in nickel content, followed by additions of first niobium in small quantities, and then followed by other elements in even smaller volumes, forming the "third generation" of alloys (15,19). This included the addition of silicon to volume fractions in the region of 2%, which was found to greatly improve the carburisation resistance of the second generation alloys (15). The "fourth generation" alloys revolved around the nickel-chromium steel with added niobium and other elements such as titanium, but also included the addition of rare earth element in very small quantities, giving rise to the term "microalloys" to describe them. These additions were used to further enhance the service temperatures which they could withstand by further promoting creep strength (15). The latest developments in the alloy allows for operational temperatures to exceed 1150°C (20).

2.2.2 Metallurgy of current alloy

The high temperature steels widely used in industry today are termed “type 35/45”; typically a 35/45 Cr-Ni austenitic steel (21–24) with numerous further alloying additions. The high nickel content causes the austenitic nature of the alloy, with nickel being a strong austenite former, despite chromium and silicon acting as ferritic formers (25,26). Both nickel and chromium additions are well known for their improvement of creep strength, as well as corrosion resistance (27).

Carbon is present, as another austenite former and for the formation of the carbides within the alloy which are paramount for their inherent strength. The carbon content has been reported to need to be over 0.2% for adequate strength to be imparted (26). Niobium is also included, both as a precipitation hardener, and to reduce the potential for intergranular corrosion arising out of chromium depletion after oxidation (25,28,29).

Further alloying elements added as microalloying additions may include manganese, yttrium, titanium, vanadium, molybdenum, tungsten, tantalum, zirconium, cerium, neodymium, praseodymium and hafnium (19,30). These additions were added in an effort to further promote the high temperature strength of the alloys (31) whilst the transition elements can also form protective oxides (32). Yttrium has been shown to have an effect on the carbide distribution and the maintenance of oxide layer adhesion (33,34), whilst manganese aids in promotion of oxidation rate (35,36). Titanium, zirconium and hafnium act in a similar fashion to niobium as carbide formers to reduce the chromium carbide content (18,37) as well as aiding in carburisation resistance, as is the case with cerium (38). Molybdenum and tungsten are added to reduce the coarsening rate of carbides (39). Table 2.2.2-1 summarizes the roles of different elements as alloying additions.

The alloy currently used is made up of the austenitic matrix with $M_{23}C_6$, M_7C_3 and MC carbides. These carbides are typically $Cr_{23}C_6$ or Cr_7C_3, formed within the austenite matrix in the interdenritic region, with NbC (niobium carbides) formed at the grain boundaries (26,40,41). The carbide phases

act to inhibit grain movement, especially at high temperatures, therefore reducing creep in service conditions as well as adding strength properties (42,43). The NbC particles are more stable than the chromium carbides, therefore are formed preferentially and lead to greater chromium in solution in the matrix (33). Subsequent aging of the alloy either as a treatment or during service results in further precipitation of secondary carbides of $Cr_{23}C_6$ within the matrix phase (26,44,45), but this is not seen to greatly degrade the properties of the alloy (46).

Table 2.2.2-1: Summary of roles of alloying additions used in examined materials.

Alloying Addition	Role
C	Austenite former, carbide former
Al	Oxide former, solid solution strengthener
Si	Creep resistance, oxide adhesion, carburization resistance
Cr	Creep resistance, oxide former
Mn	Aids oxidation rate, reduce Cr evaporation
Ni	Austenite former, high temperature resistance, corrosion resistance
Nb	High temperature strengthener, intergranular corrosion resistance, carburization resistance
Ti	Intergranular corrosion resistance
Y	Oxide adhesion, microstructure refinement

2.2.3 Processing of nickel based high temperature alloys

2.2.3.1 Alloy production

Metallic alloys are generally produced through the induction heating of the raw elements, or more simple alloys (as they may be more stable than their elemental form), to a molten liquid form, and then combined with the other desired elements. The melting procedure and element addition schedule will vary between different alloys, usually predetermined through computer modelling as well as manufacturer experience. Slag removal may be required for alloys produced in furnaces open to the air, as oxidation products are common occurrence on the liquid alloy surface, along with additions to aid in desulfurization (47).

Heating methods are usually induction heating furnaces, or electric arc furnaces, as both have the ability to produce high heating rates and higher maximum heating temperatures than those achievable with traditional fuel-based furnaces.

Electric arc furnaces act by setting up an electrical arc between the feedstock material and an electrode, usually made from carbon to withstand the high temperatures without drastic denaturing of the electrode material itself. The molten alloy will undergo various processes to remove impurities from the feedstock material before being cast into either a final shape or an ingot for future processing.

Induction heating furnaces heat the material by inducing current into the feedstock material by induction coils. The induction coils are regularly made from copper and sit around the outside of the crucible which holds the feedstock material. A current is run through the induction coils, creating a magnetic field within the coils, which in turn induces a current into the feedstock material. This internal current is the source of the heating of the material and is maintained until complete melting of the feedstock material has occurred. This process is regularly completed under vacuum, resulting in much fewer compositional changes from the feedstock than those seen in electric arc melting which usually occurs in air (47).

2.2.3.2 Casting

Casting has been a technique used in metallurgy for millennia, in some form or another, and can be simplified to the melting of a metallic element, ore, or alloy, and pouring the molten material into a vessel - or die - to produce the desired new shape of the metal. Over time, the act of casting has become much more of an exact science, with precise, complex alloys being able to be created and very complex shapes able to be cast into, however the principles stay the same.

There are however many different casting techniques which are now used, such sand casting, die casting, investment casting, centrifugal casting and lost foam casting to name a few. These

processes generally differ in the die composition and layout, with some die materials being expendable, such as sand or foam casting. In other forms such as die casting the dies are permanent and continually reused. The major casting technique used in the production of ethylene cracker furnace tubes is centrifugal casting, and has been the case since the 1950s (15).

2.2.3.2.1 Centrifugal Casting

The ethylene cracker furnace tubes are formed by centrifugal casting of the alloy. The process of centrifugal casting is that of using the centrifugal force acting upon molten metal to form the shape of the die, forming a dense structure usually with a hollow centre, as shown in Figure 2.2.3-1. (48). This is used in the formation of pipes or other shapes which are symmetrical around the long axis and are hollow, without the requirement for a core to cast around. It is also a beneficial process due to its ability to cast thinner walled products than that of conventional casting, in part due to the reduced amount of cooling time before reaching the mould, and also in part due to the pressures applied to the molten material (49).

After creating the specific alloy and removing any slag forming upon the surface, the alloy is transferred to a ladle. From the ladle the alloy is poured into the mould which is already rotating at the required speed. The rotation speed can vary from 100rpm up to 3000rpm, depending upon the requirements for the part. If the rotation speed is too slow, full adherence to the mould walls will not be achieved, and so when material is at the top of the rotation some will ‘rain’ down upon the material below, creating what is known as a rain defect (48).

The die may be preheated to limit the effect of rapid cooling in the region in immediate contact with the die. The molten metal is poured into the rotating die at the specific casting temperature and it cools while the die continues to spin. As the material is constantly under pressure from the centrifugal force, and the material starts to cool at the surface of the die, this process does not

require a runner system as the molten material from the casting is always feeding the cooling process. Thus the products are dense and free from porosity and shrinkage (50).

The centrifugal force will also act upon the constituent elements in varying degrees, dependent upon their molecular weight. Lighter elements will migrate towards the inner walls of the solidifying metal tube, and similarly, any slag formed will usually be lighter and end up on the inner surface with slow enough solidification rates. Post processing is often undertaken to remove the inner surface to remove any impurities that have moved to this surface, and to obtain the exact required diameter for the finished product. In the case of the nickel rich high temperature steel pipes a cylindrical length of around 10 meters can be produced using horizontal centrifugal casting.

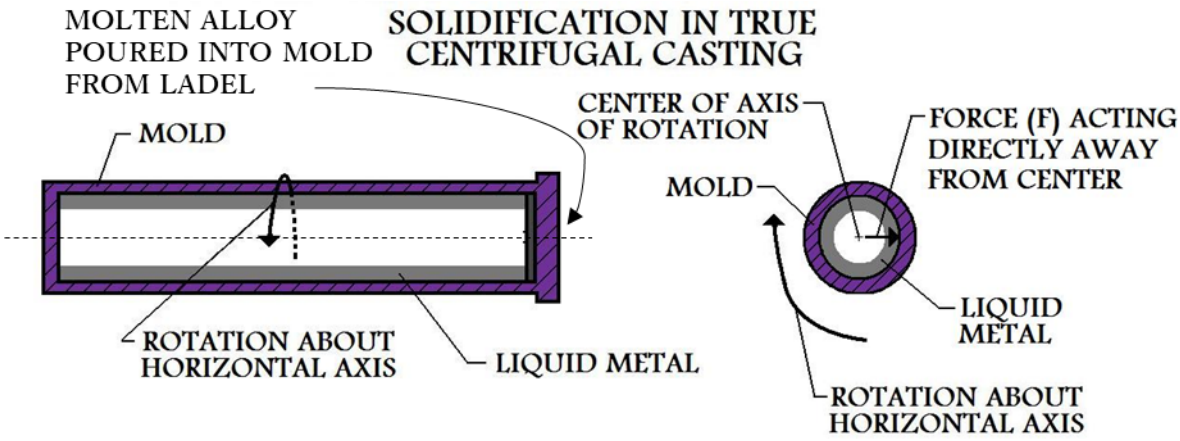

Figure 2.2.3-1: Schematic diagram of the centrifugal casting process adapted from (48) to show casting technique of molten alloy to form tube.

2.3 Ethylene cracking and coking

2.3.1 Ethylene cracking

In steam cracking, the hydrocarbon gas mixture is fed into the radiant coils, where they are heated to temperatures in the region of 800°C-1000°C whilst being mixed with steam. As the gases pass through the tubes with the steam the conditions cause the breakdown of the carbon-carbon bonds in the hydrocarbon backbone, splitting the hydrocarbon into smaller hydrocarbon molecules. Per Li and Yang, there are three cracking states, with the one utilized in ethylene cracking consisting of

a few dehydrogenation reactions, with most C-C bonds cracked, yielding the desired short chain hydrocarbons (21). The desired reaction for ethylene formation is shown, where a long chain alkane is cracked to form ethylene and a shorter chain alkane:

$$C_nH_{n+4} \rightarrow C_2H_4 + C_{n-2}H_n$$

When cracking purely ethane, the dehydrogenation of ethane to ethylene is the desired reaction:

$$C_2H_6 \leftrightarrow C_2H_4 + H_2$$

Low pressures are required in the tubes to promote ethylene as the thermodynamically favourable product of the reaction, whilst similarly the partial pressure of hydrogen is minimized to further promote the desired ethylene formation by increasing the favourability of H_2 formation, and forming ethylene, as shown in the reaction above (20). When cracking mixed hydrocarbon feedstock (naphtha), many reactions may occur, both as a direct ethylene forming reaction such as those shown previously, or one of many potential intermediate reactions which form precursors to ethylene formation, as described by Seifzadeh et al. (51).

2.3.2 Coking and de-coking

There is one major issue that does occur in the steam cracking process, despite the high temperature steels good thermal properties – coking. Coking, or the build-up of a high carbon content substance, on the inner surface of the radiant coils in ethylene cracking has been well documented by many studies, and the damage it can lead to (10,11,60–66,52–59). The deposited coke on the internal walls of the pipes also leads to increases in pressure and reduced heating of the feedstock, both of which act to negatively affect the yield of the cracking process (20,67). This coke must be removed from the internal walls of the pipe when it reaches a critical level, found by Sundaram et al. (60) to usually be reached after 20-60 days, depending on the feedstock and operating conditions.

The de-coking cycle takes in the range of 24-48 hours and causes a significant delay and cost to the production of ethylene. For de-coking to occur, high temperatures are required, with temperatures reaching 1100°C at points during the cleaning cycle, so the tubes employed for this role must be able to withstand these temperatures without undergoing degradation, melting, or significant creep processes. The cleaning process is the most thermally challenging part of service for the alloys, as it is undertaken at the fastest possible rate to reduce lost service time. This involves the gasification of the coke built up on the inner surface with steam through the following reactions:

$$C + H_2O \rightarrow CO + H_2$$

$$C + CO_2 \rightarrow 2CO + O_2$$

This process must avoid damage through carburisation and metal dusting of the inner diameter of the pipes (68). Avoiding metal dusting is achieved by maintenance of a protective oxide layer on the surface of the alloy (69).

Coking occurs in numerous different forms, with Albright et al. describing seven discrete forms of coke (70) and the exact nature of coke formation varies dependent on feedstock and operating conditions, thus the literature varies depending on conditions (10,65). However, the majority of coke initiates as a result of two major pathways; catalytic coke formation and pyrolytic coke formation (71).

2.3.2.1 Catalytic coke formation

Catalytic coke formation occurs mainly during the initial few hours of operation when the surface of the pipes are exposed. If not fully covered with a protective layer, this allows the metal surface to act as a catalyst for the coking reaction. The elements responsible for this are commonly nickel, iron and cobalt, therefore the high temperature steels required to cope with the temperature demands are equally problematic when considering coking resistance (72,73). Cr-Ni steel was found

to elicit coking rates two orders of magnitude greater than on the surface of a quartz or platinum pipe (56).

The coking initiates through the absorption of coke precursors from the hydrocarbon gas stream onto the surface of the exposed radiant coil pipes. The coke precursor forms a σ-π bond to the pipe surface material, leading to a weakening in the C=C bond, and subsequently promoting coke deposition (74).

Surface reactions follow to form coke from the hydrocarbon precursors, and this coke is able to diffuse into the surface of the pipes, accumulating at specific regions in the metal matrix (62,75). As the coke builds up in susceptible regions beneath the surface of the pipes the stress on the grain boundaries or dislocations of the alloy increases, until the yield stress is exceeded and failure occurs along the grain boundaries or dislocations, and a small particle of the metal pipe is removed from the pipe surface. This process is illustrated in Figure 2.3.2-1 (63). This particle of the pipe is found atop the tip of the now formed carbon deposit which protrudes from the pipe. The particle at the tip of the carbon protrusion has been found by both Baker et al and Rostrup-Nielsen & Trimm (58,75) to resemble a pear in shape, with the base of the shape facing the direction of the carbon growth away from the pipe surface.

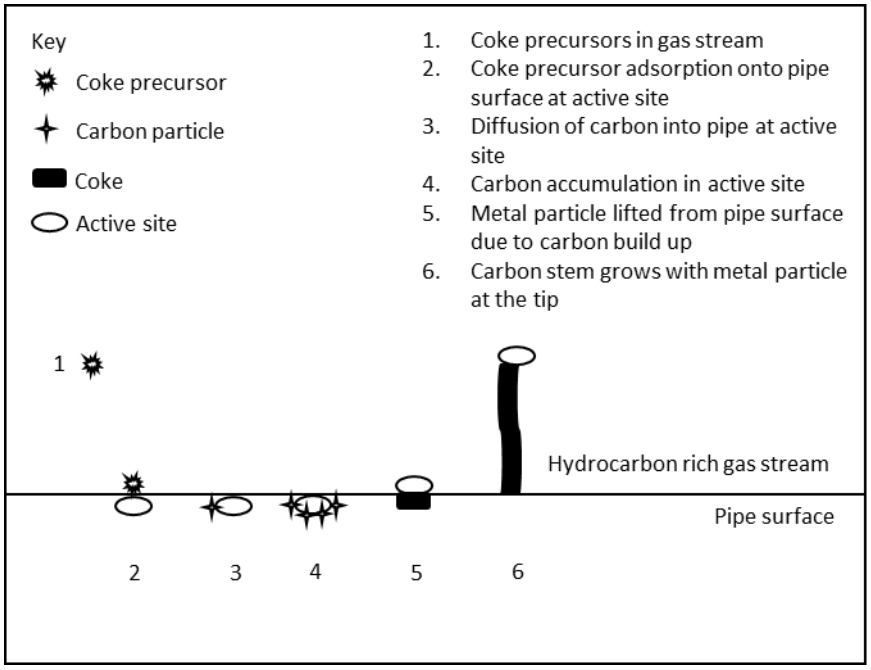

Figure 2.3.2-1: Diagram of catalytic coke formation mechanism, adapted figure from (63)*. Six phases of catalytic coking shown, from adsorption onto the pipe surface, accumulation, and to carbon filament growth.*

The coke that has been produced protrudes from the surface of the pipe filament and continues to lengthen as coking continues, forming the commonly identified filamentous coke (10,58,79,59,63,66,67,75–78). More coke is able to add to the filament as growth of the carbon filament occurs along with the formation of active centres in the carbon beneath the metal particle through the formation of structural deficiencies. These active sites react with susceptible molecules in the gas stream to provide the carbon to build the filament further. The filaments are found to be flocculent and hollow, and of an amorphous nature (63,75,79).

Catalytic coke formation is the fastest coking process affecting the radiant coils during their life; whilst it occurs mainly for a small period of time early in each cracking run, it creates significant volumes of coke. It has been found that coking rates are greatly reduced, if not halted entirely when the particle of metal at the tip of the filament is encased with carbon itself. This illustrates that the metal particle at the tip of the filament has a catalytic effect to drive forward the filamentous coke formation, and once this effect is inhibited the catalytic formation of coke is halted (79). Once this phase of coking has terminated, a porous coke layer of interwoven filaments is left coating the inner

surface of the radiant coils. These coke filaments further add to the accumulation of carbon by acting to catch pyrolytic carbon formed in the gas stream, and becoming a site for formation of pyrolytic carbon (65)(see Pyrolytic coke formation).

With carbon building up in the grain boundaries of the surface layer of the pipes, as well as being a precursor to catalytic carbon filaments, a continuous carbide network accumulates. These carbides in the pipes act as a path for crack propagation to occur due to the brittle nature of the carbides. Some pipes employ a deposited protective coating to inhibit the coke accumulation; however this is usually removed after the first cleaning process, and therefore carbides and catalytic coke are much more readily produced (80,81). As more carbon is absorbed and more carbides are formed, the internal stresses are also rising, making crack initiation more likely (52).

2.3.2.2 Pyrolytic coke formation

Pyrolytic coke formation is the second major coke forming pathway occurring in ethylene cracker radiant coils and is a process that occurs in the gas stream. This is sometimes known as radical coke formation. The high temperature of operation in cracking creates the conditions needed for some degradation of the hydrocarbons in the gas stream, as with radicals being generated from the hydrocarbons many different reactions are possible (65,82). Operating temperature plays a large part in the rate of coking via this method, as higher temperatures lead to greater radical numbers, which in turn boosts the coking rate as more of the coke molecules are formed via radical pathways. Wauters and Marin found an increased coking rate of 10 times for a 100°C temperature rise (83).

Glasier and Pacey found that pyrolytic carbon coking rate was a function of the concentration of benzene in the system, and that three acetylene molecules can readily react to form benzene (84). Abghari also stated that the highest rate of pyrolytic coke formation is coke generated from acetylene precursors which fits the same theory (10). Glasier and Pacey also found that while benzene molecules may decompose to coke themselves, they may also be a step in other routes of

coke formation, with addition reactions of the benzene forming large polycyclic aromatic hydrocarbons, which go on to dehydrogenate, forming coke which is then deposited. This suggests that a proportion of the pyrolytic carbon formed in the ethylene cracking process is via benzene which occurs in the gas stream as an intermediate reaction in the cracking reactions. Cai et al suggested that the aromatic molecule precursor route is only prominent above 700°C, suggesting this is a dominant pyrolytic carbon formation mechanism in ethylene cracking radiant coils which operate at temperatures in excess of 850°C (65).

The generation of larger molecules through radical addition in the gas stream, as mentioned previously, is also a potential coke forming pathway as the molecules can grow to form structures which condense in the gas stream as their boiling point is greater than the cracking conditions. The filamentous coke on the alloy surface formed by initial catalytic coking acts to trap pyrolytic or radical coke formed in the gas stream, along with other coke precursors such as tar condensation. These interwoven carbon structures and deposits subsequently dehydrogenate and cross link to form dense coke deposits on the surface of the radiant coils (63,65,68,85,86).

2.3.3 Failure mechanisms

Damage to the pipes can be avoided through careful operation practices, and regular maintenance. However, if emergency stoppages or rapid cooling occurs due to poor operating standards, the pipes can easily fracture. This is due to the difference in thermal expansion coefficient between the coke layer inside the pipe, and the pipe material itself, as there is an order of magnitude difference between the coke and the pipe, with the pipe having a larger change. This means that as the pipes cool, the coke restricts the metals contraction, and therefore increase the hoop stresses imparted upon the pipe. If a large enough coke build-up occurs such that the contracting stresses cannot cause the coke to be broken up; the generated hoop stresses can overcome the yield stress of the material. This causes fractures in the metal, and therefore ends the life of the pipes (11). As the

failure is in the direction of the hoop stresses, the cracks are characteristically large and longitudinal (52).

The second major failure mechanism is creep exhaustion of the pipes – this is the ductile mechanism of failure. As the pipes are cooled for the cleaning cycle, they compress upon the coke layer as previously discussed. If failure does not occur, the pipes experience a strain in order to remain with a greater diameter than would be present if the coke was not restricting contraction. This strain imparts a great stress upon the pipes. Once the plant is back up to high temperatures during decoking, these stresses relax through the action of creep. As this mechanism occurs repeatedly, the pipes experience creep every cycle to some degree, and this will at some point reach its creep limit. These failures are often characterised by bulges in the pipes, along with small cracks on the surface (52,81).

While creep exhaustion and brittle failure are the most common failures in ethylene cracker furnace tubes, other failure mechanisms can be present. Creep elongation is one such failure mechanism, caused by the weight of the pipes combined with the high operating temperatures, leading to the lengthening of the vertical pipes under the act of gravity. This can result in bowed and thinned coils, leading to elevated stresses and creep in these sections of pipe. Tube burnout is another issue, with overheating of the pipes due to the raised temperatures and the insulating effect of the carbon on the inner surface of the pipe, resulting in melting of parts of the pipe, destroying it (52). Furthermore, excessive temperatures have deleterious effects on the alloy microstructure, which can lead to significant declines in the mechanical properties. Subsequently a degradation of the creep and ductility properties can enable failure to occur more readily (87). Overheating can also be a function of poor furnace design and operation, which is controllable through more careful design and computational analysis of the conditions in the furnace (87).

One further mechanism leading to premature pipe failure is that of erosion. This occurs mainly in the bends of the pipes. It is thought that erosion occurs during the cleaning process; as larger coke particles are mechanically removed travel through the remainder of the pipe and impact the walls and bends in the pipes. This can be reduced by either ensuring the coke is gasified rather than spalled, or by reducing the gas flow velocity (52).

2.4 Attempts to reduce coking

Research into reducing and completely eradicating the coke build up inside the radiant coils of ethylene cracker furnaces has been mainly split across two main fields: alloy composition of the pipe material, and coatings on the inner surface of the pipes to protect them during service. Feedstock additions to chemically inhibit coking has also been researched.

2.4.1 Composition optimization

The alloys used in ethylene cracking necessarily use transition metal elements to cope with the service requirements placed upon them¸ however these are the elements which are also the catalysts for catalytic coking. To avoid exposure of these elements to the gas stream, the alloys are oxidised to form a physical barrier between the carbon in the gas stream and the reactive elements in the pipe. This drastically improves the resistance to catalytic coking of the transition elements (74). Shubo et al. found that excessive oxidation of the pipe inner surface can lead to a loose, porous oxide being formed after numerous cleaning cycles. This is negated by creation of a thinner, dense oxide which does not degrade during the cleaning cycles (74,88).

The 35/45 alloys currently used rely on the formation of a chromium oxide (Cr_2O_3) scale to form on the inner diameter of the tube, as uncoated alloys have regularly been shown to have significant growth of filamentous coke formation on the surface (88–90). Typical 35/45 alloys are known to produce this chromia layer after oxidation, with TiO_2, or rutile, often found atop the chromium oxide dependent on the alloying additions (91,92). The formation of the chromium oxide layer is

dependent on sufficient chromium availability in the alloy, and the ability of the chromium to diffuse to the alloy surface (93,94). This can be dependent on the chromium carbides, as Durham et al. found that coarser carbides did not allow sufficient chromium diffusion to the alloy surface, therefore resulting in a non-protective iron-rich oxide layer being formed (95).

This dependence on carbides for oxidation is due to the chromium depletion which occurs in the near surface region of the matrix after initial oxidation (96–98). Without further supply of chromium to the surface, oxidation rate of chromium is arrested, and alternative, undesired oxide products are capable of forming.

The addition of silicon to the alloy, which is commonplace due to its ability to improve carburisation resistance (15) also aids in altering the oxidation results of these alloys, by forming a dual oxide layer structure, with a silicon oxide layer forming beneath the surface chromium oxide scale which aids in the formation of the Cr_2O_3 oxide (94,95). Furthermore, the chromium oxide layer is commonly found to be topped with a $MnCr_2O_4$ spinel phase when manganese is included in the alloy. This has been found by many researchers to be more resistant to coking than chromium oxide (23,30,89,99–102).

The major issue facing protection with a chromium oxide layer is that of spallation, exposing the matrix and depleting the alloy of chromium and chromium carbides. Evans found that up to 40% loss of a chromium oxide layer can occur until sufficient relaxation of internal stresses occurs (103). Furthermore, as the oxide layer thickness increases, the temperature drop required to initiate spallation reduces. An oxide layer 4μm thick would be expected to initiate spallation with a temperature change of 300°C. As the changes in operating and cleaning temperatures are in this range, this demonstrates the readiness of a chromium oxide layer to spall.

The third oxide layer which is considered for effective protection of the alloy is that of aluminium oxide. However, there has been limited success in producing an alloy with adequate mechanical

properties and ability to form a protective layer. This is due to the formation of a highly brittle nickel aluminide phase which can render the alloy unsuitable for the service requirements, despite the inherent protective qualities that the aluminium oxide layer can provide (104), or the inability to produce an alloy with the necessary mechanical properties that can withstand the high temperatures required (105). In alloys which have been produced, the oxide layer is found to be either solely aluminium oxide, or a dual layer oxide made up of aluminium oxide topped by a spinel phase of nickel aluminate ($NiAl_2O_4$) (77,106–110).

An alumina layer has been found to exhibit greater adhesion and less spallation compared to chromia, therefore demonstrating the significant benefits of an alloy which is able to grow and maintain an aluminium oxide layer (111). Furthermore, Chyrkin et al. found repassivation of the oxide layer to occur with an aluminium oxide forming alloy via lateral diffusion of aluminium (111), whilst the reduction of coking created by an alumina surface has been regularly reported (23,112,113).

Currently there has not been an alloy which has been shown to provide a stable and adherent aluminium oxide layer, with equal mechanical properties to those used in industry which utilize the chromium oxide surface layer for protection. This research evaluates aluminium containing alloys ability to form, and maintain, a protective alumina layer, and compare this to an alloy currently used in industry, demonstrating the deficiencies of the current, chromia-forming alloy in comparison to an alumina-forming one.

2.4.2 Surface coatings

Coating the inner pipe surface is an obvious solution to protecting against the catalytic coke formation process. These coatings can either be a one off coating applied before service, or as an online process, recoating the surface after each decoking cycle is completed (114). This reapplication of the protective coating is generally more effective, especially across the life of the

pipe component, however inevitably it comes at a greater price and complexity than those solely pre-treated before service.

The main area of coating research has been in the area of SiO_2/S coatings, and these coatings combined with coking inhibitors in the gas flow. Zhou et al found a decrease in coking within the radiant coils of 69% with the coking inhibitor chemicals in the gas flow, and a decrease of 96% when the coking inhibitors were combined with an anti-coking coating of SiO_2/S. This study found that when the anti-coking coating and coke inhibitors were combined, the coke filaments characteristically seen as a result of catalytic coking were only found in the tests without the coating; that is that the SiO_2/S coating appeared to inhibit the formation of the filamental coke. Granular coke was instead found to be present on the inner surface of the radiant coils (22,76,115).

One potential disadvantage of the SiO_2/S coatings is the potential for the preferential creation of some olefins compared to others, with Zhou et al finding an increase in the C_2H_4 yield, and a drop in yield of C_4H_8 (116). Dependent on the desired yield products, this may lead to a reduction in profitability and therefore negate the positive effects seen as a result of the coatings.

Furthermore, coatings can lead to premature failure in the pipes, with Goswami and Kumar finding that a coating containing cerium used on a nickel based pipe saw failure occur within two years of service due to a preferential diffusion of the cerium to a defect, leading to catastrophic failure of the component (38).

Other coatings have involved chemical vapor deposition techniques, which may be multistage and considerably expensive, even if they do demonstrate improved coking resistance. The AlcroPlex treatment descried by Zychlinski et al. demonstrated such results, driving chromium and then aluminium into the pipes inner diameter (117). Whilst the results demonstrated improvements in coking resistance, if this surface layer could be formed through oxidation of the as cast alloy the costs would be lower and potential for repassivation would be significantly more beneficial.

It would appear that the research in coating technologies, whilst still in its infancy, has shown significant promise, and future development may well start to make coating of ethylene cracker furnace tubes commonplace. Currently the SiO_2 based coatings are those mainly being researched, with more complex glass coatings also having had some development (21). The economic viability and cost of these coatings along with their effectiveness can only be expected to improve in the coming years, with further research and development. They may well be the future for the industry, assuming they can be appropriately applied and can overcome the likely hurdles which will occur as progress continues, however their use appears significantly distant at the current moment.

2.4.3 Feedstock additions

Addition of coking inhibitors to the feedstock is another major avenue which has been explored to reduce coke formation. Towfighi et al. found additives to the feedstock were beneficial in three ways; replacing the carbon in adsorption onto the pipe inner surface, therefore impeding the ability of carbon-based particles to do so; interference with the chemical reactions occurring on the pipe surface leading to coke accumulation; and promotion of gasification of coke which has formed on the surface (32,63).

The addition of sulfur and phosphorous containing compounds have been the main source of success when evaluating the effectiveness of coking inhibition (88,118), however a H_2PtCl_6 additive has also been found to reduce surface coke formation, but in doing so it also appears to increase the activation energy of cracking (67).

A main issue with addition of sulfur comes in its effect on the alloy. Fedorova et al. found that addition of sulfur caused a decrease in adhesion of the surface oxide on the pipe alloy, therefore despite a potentially beneficial impact on coke production, the balance between coking rate and coking protection of the alloy may render the addition of sulfur deleterious to the anti-coking nature of the system (119).

2.5 Summary

The importance of ethylene cracking due to the global demand of plastics has been outlined. In industrial practice, the problem of coking of the ethylene cracker furnace pipes is well known and numerous studies have investigated the mechanisms of coking. Coking of the pipes causes significant costs in reduced efficiency of the cracking process, requirement for regular cleaning regimes to be undertaken, and can result in premature failure of the pipes.

The catalytic coking process occurs due to the contact of the hydrocarbon-rich gas stream with catalytic elements in the pipes, notably nickel and iron. Whilst both of these elements are required for the temperature and mechanical properties of the alloy, forming a continuous, dense oxide layer across the inner surface can isolate them from the gas, and stop the process of catalytic coking from occurring. Stopping or inhibiting the catalytic coking process would significantly improve the cracking process run time, as the catalytic coke acts as a trap for pyrolytic coke. Without the filamental coke formed on the surface of the alloy, the build up of coke would be significantly impaired.

Currently, the alloys in use form a chromium oxide layer as a protective barrier, however spallation and incomplete oxide coverage can allow the nickel- and iron-containing matrix to come into contact with the gas stream, promoting the catalytic coking action. Alumina has been shown to provide greater protection of the pipe from coking compared to chromia, however forming and maintaining an alumina layer on alloys which are viable and have the necessary mechanical and thermal properties required for use in industry has not been demonstrated.

This research will investigate three aluminium containing alloys and compare them to an alloy currently used in industry. The ability to form and retain a protective oxide layer will be the focus of the research, in doing so demonstrating the likely anti-coking abilities of these alloys and therefore improvement on currently used alloys.

3 Experimental Procedure

3.1 Material preparation

All the materials were created and provided by Doncasters Paralloy. The four alloys examined were all centrifugally cast alloys, the process of which was described in 2.2.3.2.1. The composition and description of the four alloys investigated are listed in Table 4.1.1-1 in section 4.1. The alloys were heated to a tapping temperature of 1730°C in the induction furnace before being poured into the die which was rotated at 100G. The alloys were supplied in the form of sections of cast tubes, either in the as cast form, or after processing. This processing involved the machining of the innermost region of the alloy through deep hole boring, removing the slag and potential shrinkage porosity, as well as any potential slag entrapped from within the inner diameter region of the tube.

Samples were cut from the pipe sections using Struers Accutom-5 and Accutom-50 cutting machines, using silicon carbide cutting discs spinning at 3000rpm, with a feed rate of 0.025mm/s. Figure 2.4.3-1 illustrates the sample location, shape and cross sectioning method employed after treatments. The cut samples were processed under the desired experimental regime (see Table 2.4.3-1), before being examined. In the case of oxidation treatment samples, the treated samples were first cross-sectioned (shown in Figure 2.4.3-1), then gold plated using an Emscope SC500 gold sputterer at 25mA for 3 minutes. This gold sputtered layer was followed by a nickel electroplating process using Frost Matt Nickel Plating Solution and a Skytronic 650.679 adjustable DC power supply, with current limited to 0.1A, plating for 6 minutes. The nickel-plated samples were then mounted in conductive bakelite using an ATM Opal 460 or Opal 400 bakelite press. After mounting, the samples were ground using grit paper incrementally decreasing in grit size from 120 grit to 1200 grit on a Struers LaboPol-5, followed by ultrasonic cleaning in acetone in an Ultrawave U2500H ultrasonic bath. The samples were then polished on the Struers LaboPol-5 using Dac polish cloth with 3μm diamond suspension, followed by 1μm diamond suspension with a Nap cloth to achieve

a mirror finish, free of all visible scratches. The samples were subsequently polished using a nap-less Chem cloth with activated alumina and once again cleaned ultrasonically in an acetone bath. Sample analysis was taken at different depths of the alloys, as illustrated in Figure 2.4.3-1.

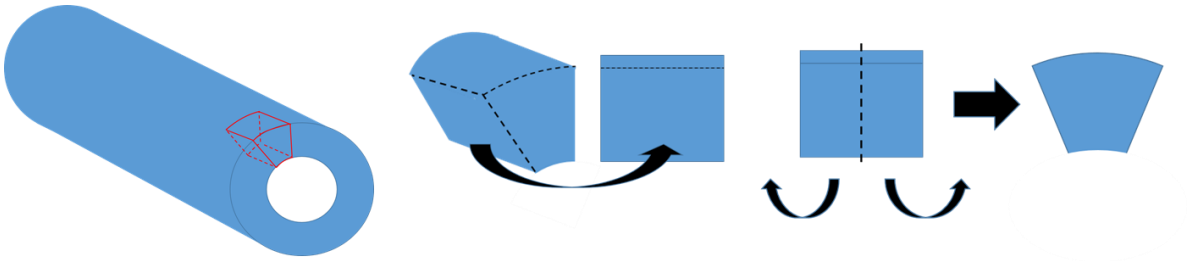

Figure 2.4.3-1: Diagram of sample cutting location and cross-sectioning of samples post oxidation.

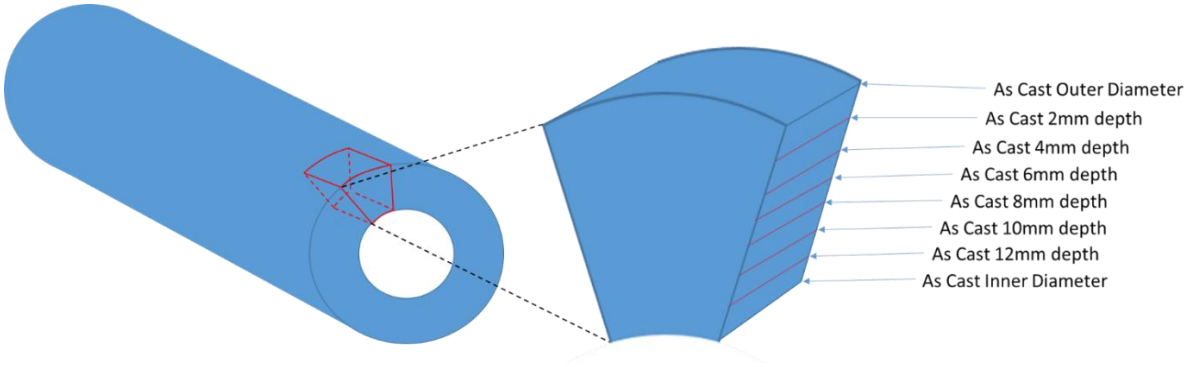

Figure 2.4.3-2: Schematic diagram of sample locations as investigated.

3.2 Heat treatments

Numerous oxidation heat treatments were completed, as shown in Table 2.4.3-1 The samples were cut as described previously, and cleaned using acetone, before being placed into the furnace. The air oxidation treatments were completed in Elite Thermal Systems BSF 12/10 full muffle kilns. Where the samples were furnace heated and cooled, the samples were put in at room temperature and heated at a rate of 5°C/minute until reaching target temperature. The samples were then held at temperature for the specified time before being furnace cooled. Where the samples were only furnace cooled, the furnace was heated to target temperature, and the samples put in once the furnace was at temperature. This was undertaken rapidly to avoid temperature fluctuations, however a dip in furnace temperature by up to 10°C was recorded during the sample insertion process. This temperature drop was recovered within 60 seconds.

The low partial pressure oxygen oxidation treatments were achieved using Carbolite CTF 12/65/550 tube furnaces with 5.1% hydrogen in argon gas at 35L/min flow rate. These treatments were either with or without titanium foil upstream, acting as an oxygen scavenger to further lower the partial pressure of oxygen. Titanium foil was used due to titanium's ability to oxidize at significantly lower partial pressures of oxygen than chromium as illustrated by the Ellingham diagram (Figure 4.2.4-1), but not as low as aluminium. The aim therefore was to inhibit chromium oxidation whilst allowing aluminium oxidation to occur. These low partial pressures of oxygen oxidation conditions were undertaken to evaluate the potential for a pre-treatment on the alloys before being placed into service conditions.

The gas was run through a first tube furnace to raise temperature and remove the oxygen with the titanium foil. The gas oxygen content was measured using a hygrometer to monitor the H_2O content of the gas stream, in ppm volume, comparing this to the hydrogen content of the gas to calculate the oxygen content. The samples were placed in an alumina boat, and moved into the tube furnace once at temperature, and removed after the 24-hour treatment time, without exposing the system to the external environment until returned to room temperature. This set up is illustrated in Figure 2.4.3-1.

For cyclic oxidation treatments, the samples were pre-oxidised at 875°C for 48 hours at $PO_2 = 10^{-27}$, before cyclic oxidation between 1150°C and 25°C, at 1150°C for 45 minutes and 25°C for 15 minutes, for 50 cycles.

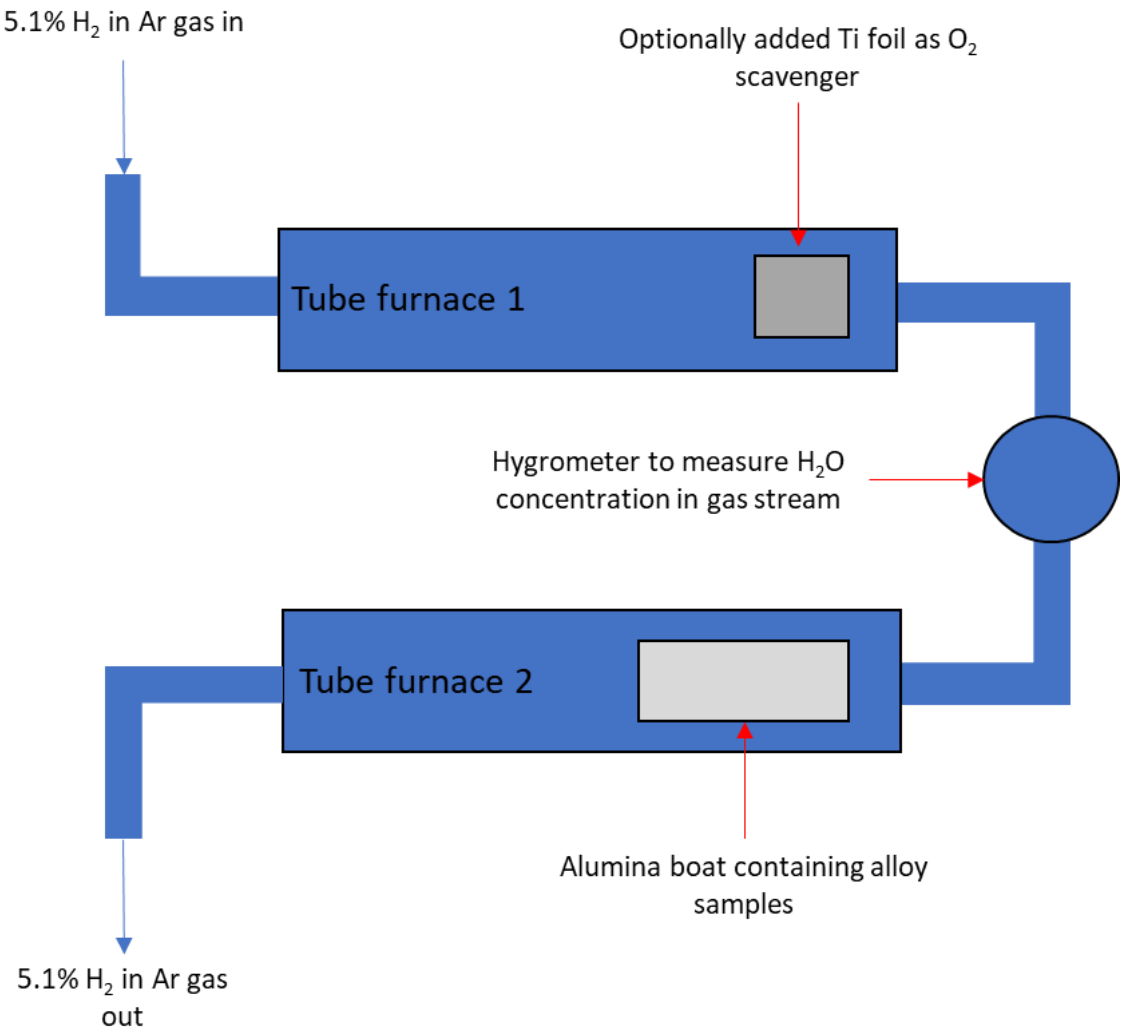

Figure 2.4.3-1: Schematic diagram of low partial pressure of oxygen oxidation furnace set up, using titanium foil as optional oxygen scavenger and hygrometer to monitor oxygen content via H_2O presence.

Table 2.4.3-1: Oxidation heat treatments

Treatment				Sample			
Temperature	Time	Environment	Regime	Base	Low-Al	High-Al	Optim-Al
1100°C	30 minutes	Air	Furnace Heated and Cooled	x	x	x	x
1100°C	8 hours	Air	Furnace Heated and Cooled	x	x	x	x
1100°C	24 hours	Air	Furnace Heated and Cooled	x	x	x	x
800°C	24 hours	$PO_2=10^{-25}$	Furnace Cooled	x	x	x	x
800°C	24 hours	$PO_2=10^{-25}$	Furnace Cooled	x	x	x	x
800°C	24 hours	$PO_2=10^{-25}$	Furnace Cooled	x	x	x	x
800°C	24 hours	$PO_2=10^{-25}$	Furnace Cooled	x	x	x	x
800°C	24 hours	$PO_2=10^{-23}$	Furnace Cooled	x	x	x	x
800°C	24 hours	$PO_2=10^{-23}$	Furnace Cooled	x	x	x	x
800°C	24 hours	$PO_2=10^{-23}$	Furnace Cooled	x	x	x	x
800°C	24 hours	$PO_2=10^{-23}$	Furnace Cooled	x	x	x	x
1100°C	1 hour	Air	Furnace Cooled	x			x
1100°C	2 hours	Air	Furnace Cooled	x			x
1100°C	4 hours	Air	Furnace Cooled	x			x
1100°C	8 hours	Air	Furnace Cooled	x			x
1100°C	16 hours	Air	Furnace Cooled	x			x
1100°C	24 hours	Air	Furnace Cooled	x			x
1100°C	36 hours	Air	Furnace Cooled	x			x
1100°C	48 hours	Air	Furnace Cooled	x			x
950°C	1 hour	Air	Furnace Cooled	x			x
950°C	2 hours	Air	Furnace Cooled	x			x
950°C	4 hours	Air	Furnace Cooled	x			x
950°C	8 hours	Air	Furnace Cooled	x			x
950°C	16 hours	Air	Furnace Cooled	x			x
950°C	24 hours	Air	Furnace Cooled	x			x
950°C	36 hours	Air	Furnace Cooled	x			x
950°C	48 hours	Air	Furnace Cooled	x			x
800°C	1 hour	Air	Furnace Cooled	x			x
800°C	2 hours	Air	Furnace Cooled	x			x
800°C	4 hours	Air	Furnace Cooled	x			x
800°C	8 hours	Air	Furnace Cooled	x			x
800°C	16 hours	Air	Furnace Cooled	x			x
800°C	24 hours	Air	Furnace Cooled	x			x
800°C	36 hours	Air	Furnace Cooled	x			x
800°C	48 hours	Air	Furnace Cooled	x			x

3.3 Metallurgical observations

Metallurgical observations were undertaken using a Tescan MIRA 3 XMU scanning electron microscope (SEM), utilizing the secondary electron imaging and the backscattered electron imaging processes. An accelerating voltage of 20keV was used. EDS (energy dispersive x-ray spectroscopy) analysis was achieved using a X-Max^N EDS detector on the Tescan SEM, using AZtec software for data capture manipulation, and presentation. Similarly, EBSD (electron back scatter diffraction) analysis was undertaken using the detector with the Tescan SEM, and utilizing AZtec software for data capture, and Channel5 Tango software for data manipulation and presentation.

3.4 Material Properties

Oxide layer thickness measurements and percentage oxide loss measurements were completed using the image processing software ImageJ. Thickness measurements were completed using the measurement feature, measuring the oxide thickness at a minimum of 100 measurements per sample and taking average values and standard deviations of these values. Oxide loss measurements were achieved using the particle analysis feature (120).

Differential scanning calorimetry (DSC) was undertaken with Netzsch STA 449 F3 thermal analyser. The heating regime for the samples is illustrated in Figure 2.4.3-1. The samples were heated to 1450°C, above their melting points, held, and cooled to 800°C. The heating was then repeated, to allow identification of any changes in properties. Thermogravimetric analysis (TGA) was also completed using the Netzsch STA 449 F3 thermal analyser. The samples were cut from the machined inner diameter region of the relevant alloys to have similar surface areas and a mass of 50mg. The samples were heated rapidly to 1100°C and held at temperature for 60 hours. This was undertaken to assess mass changes and compare with observed oxide growth of the alloys.

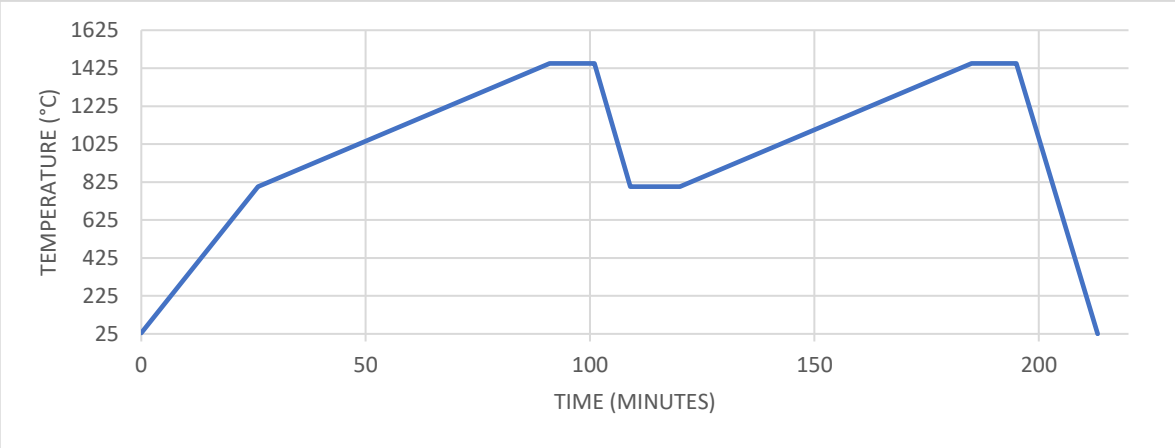

Figure 2.4.3-1: Heating profile of DSC measurements

Microhardness measurements were taken using a Mitutoya MVK-H1 hardness testing machine, taking three measurements of each indent at each applied load to acquire an accurate reading. Loads applied were 100g, 200g and 500g. Movement of the sample was controlled by integrated x-axis and y-axis micrometers to ensure accurate spacing of measurements. Hardness measurements allowed evaluation of the alloys properties, and changes through the depth of the alloys to be related to the observed microstructure changes.

X-ray diffraction (XRD) was undertaken to identify the crystallographic structure and phase composition of the as cast and oxidised samples. This was achieved using a Bruker D8 Advance X-ray diffractometer with CuKa (1.5405A) radiation. An X-ray beam was projected on the surface of the sample at incident two theta angles from 30° to 70°. After scanning, the results obtained were analysed and indexed using X'pert High Score Plus V.2 analytical software with database the PDF2004.

For the scratch tests, the four different alloys were cut, ground and polished as described previously. The different alloys were then oxidised under conditions to elicit the most consistent oxide layer for each of the four alloys. A force was applied by a diamond tip at a defined increasing rate; in this case a linear increase in force over time, from 0N to 60N as 1N per second for 60 seconds. Friction and acoustic emission of the test were measured, and the scratch tracks were

examined after the test using electron microscopy. The European Standard EN 1071-3 describes the scratch test procedure (121). Scratch tests allowed the adherence of surface oxides to the bulk alloy of each sample to be observed.

Phase composition and solidification modelling was completed using JMatPro (Java-based materials properties) modelling software. The software was used to model the predicted phases present at equilibrium during solidification from a liquid state in the four alloys. NiFe based superalloys was chosen as the material type, and the composition of the four alloys was input in weight percentage. The desired phases and properties to be modelled were selected, followed by temperature range (1500°C-800°C) and step rate, which was chosen as 5°C. Cooling rate was set to 1°C/s. The desired properties were then selected, and calculated volume fraction values were exported.

Glow-discharge optical emission spectroscopy (GDOES) analysis was undertaken using a Spectruma Analytik GMBH GDA 650HR analyser, using the software WinGDOES Professional to acquire the data. This was used to analyse the composition of the alloy surface layer from the external surface and moving in to the bulk material after oxidation treatments.

Thin foils for Transmission Electron Microscopy (TEM) were prepared using a FEI Quanta 3D FEG FIB-SEM microscope via Focused Ion Beam (FIB) milling. A platinum layer was deposited onto the site to protect the surface oxide layer during the FIB milling process, and then cut with the gallium ion beam with accelerating voltage of 30kV. This formed a thin film from the top of the oxide surface and down into the alloy matrix (Figure 2.4.3-2). The extracted section was thinned to <100nm using successively smaller ion beam milling currents once attached to a copper grid. The produced samples were examined under TEM, using a Jeol 2100 LaB6 TEM at a beam accelerating voltage of 200kV, and a FEI Tecnai F20 with STEM and Oxford Isis EDS instrument at 200kV. This was undertaken to assess crystallographic details and layer structures of the sample. Bright-Field (BF)

TEM images, Dark-Field (DF) TEM images and Selected Area Diffraction (SAD) patterns were taken from the sample areas. TEM analysis was undertaken for confirmation of XRD and EDS analysis.

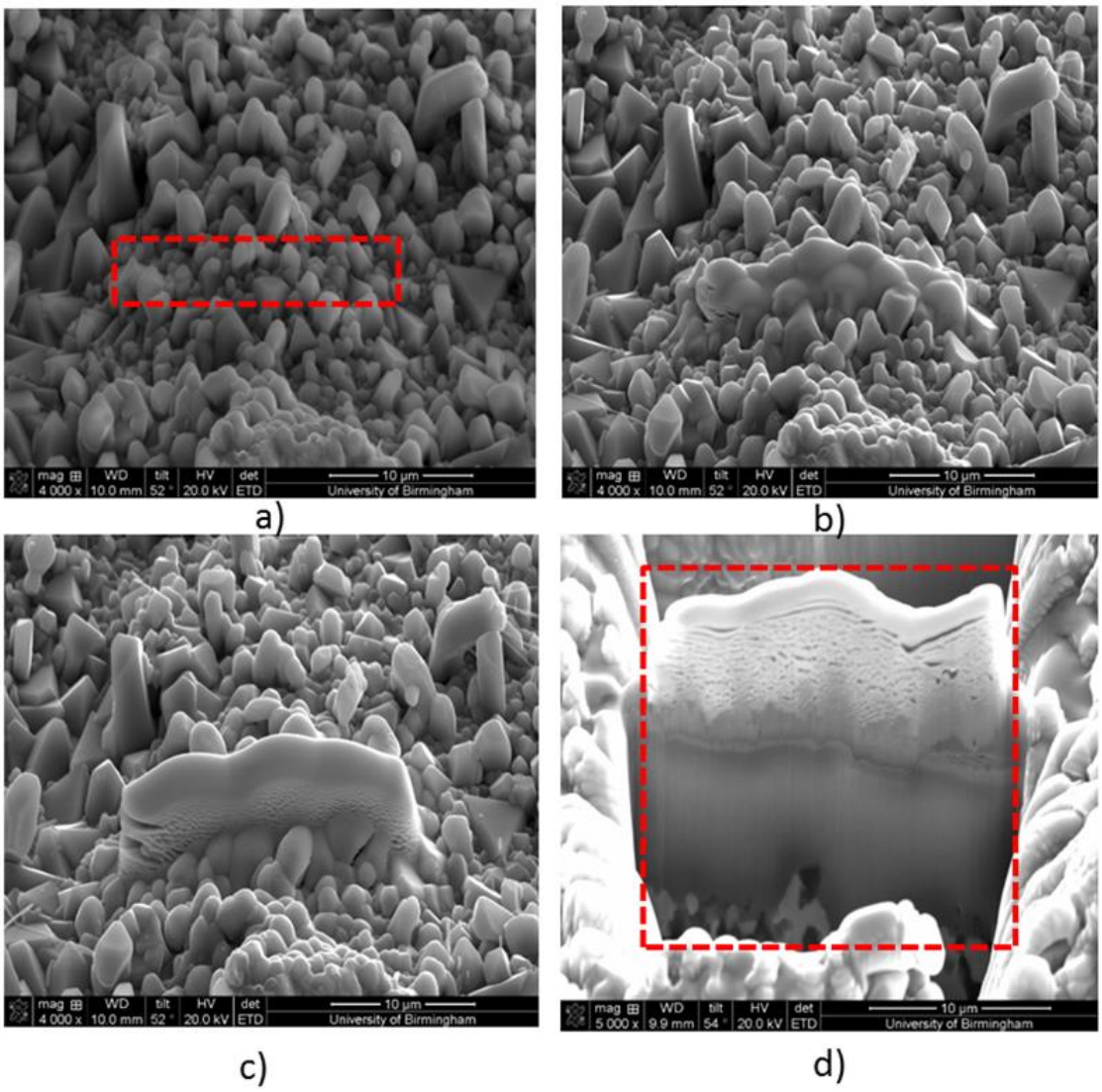

Figure 2.4.3-2: FIB/SEM images showing TEM sample preparation for a 1100°C, 8 hour oxidised Base alloy sample, showing selected area, platinum coating, and FIB milling to form sample.

For the surface roughness oxidation tests, the machined tube sections were prepared to give three different surface roughness conditions. One sample was left as machined, one was ground with just 120grit silicon carbide paper, and a third was ground from 120grit incrementally down to 1200grit silicon carbide paper. Surface roughness measurements were taken using a Surfcorder SE1700

surface roughness measuring instrument. Each sample was measured 3 times in both the x- and y-axis to get an average Ra measurement.

4 Results

4.1 Comparison of the microstructure of the alloys

The microstructural properties of the alloys being examined were analysed to investigate the differences in microstructure, caused by the differences in composition. The microstructure of the alloys in the as-cast state affects the mechanical properties and the oxidation behaviour of the alloys, and hence the potential protective surface.

All the samples were taken from cut sections of the as-cast pipes. Analysis was undertaken looking through the full diameter of the pipe, between the outer diameter surface of the tube, through to the inner diameter. This was done incrementally at 2mm intervals, allowing the changing nature of the microstructure to be observed. The nature of the centrifugal casting process used to form the pipes means differences between the microstructure of the pipe throughout its thickness are to be expected. Figure 2.4.3-2 demonstrates the regions of the samples that were analysed.

4.1.1 Chemical composition of the alloys

Four different alloys were investigated with slight differences in their composition. One alloy – Base – was an austenitic 35/45 Cr-Ni alloy which is currently used in industry (Paralloy trade name H46M) did not contain aluminium and therefore acted as the control alloy for comparison to the experimental addition of aluminium in the other three.

4.1.1.1 Chemical Analysis of the alloys

The four alloys investigated were analysed by spectrometer to assess their bulk composition. Their compositions are shown in Table 4.1.1-1.

Table 4.1.1-1: Composition of all four alloys investigated, as measured by mass spectrometry

Wt %	C	Al	Si	Cr	Mn	Fe	Ni	Nb	Ti	Y
Base	0.39	0.00	1.36	33.05	0.92	19.47	43.70	0.85	0.03	0.00
Low-Al	0.49	3.79	0.62	29.25	0.47	20.50	43.90	0.76	0.16	0.02
High-Al	0.48	5.56	0.61	30.35	0.67	17.94	43.15	0.81	0.36	0.07
Optim-Al	0.26	4.49	0.62	29.50	0.76	21.01	42.40	0.82	0.15	0.01

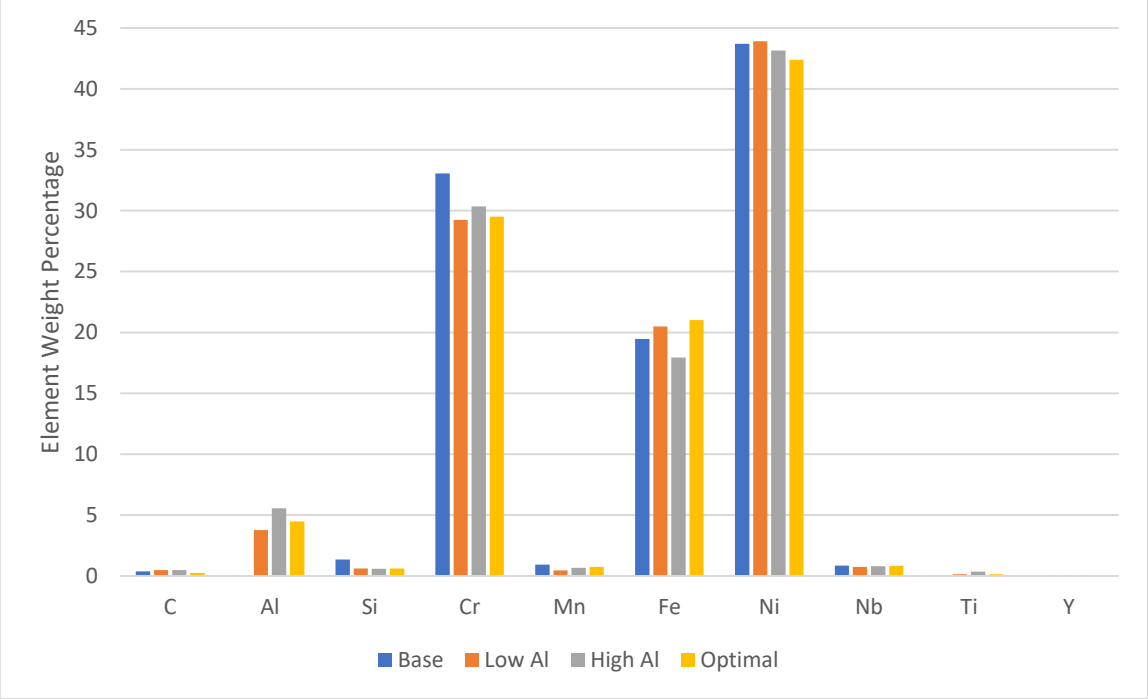

Figure 4.1.1-1 Composition differences between the four different alloys

The main differences between the Base alloy and the aluminium containing alloys came from the differing contents of oxide formers; the Base alloy contained a greater volume of silicon, chromium and manganese, which were replaced by the aluminium additions in the Low-, High- and Optim-Al alloys. The aluminium content in the three aluminium containing alloys naturally varied between the Low-Al alloy containing 3.78% Al, the High-Al alloy containing 5.55% aluminium, and the Optim-Al alloy containing 4.49% aluminium. This difference in aluminium content created the variation of the nickel and iron content between the three Al-containing alloys as balancing elements.

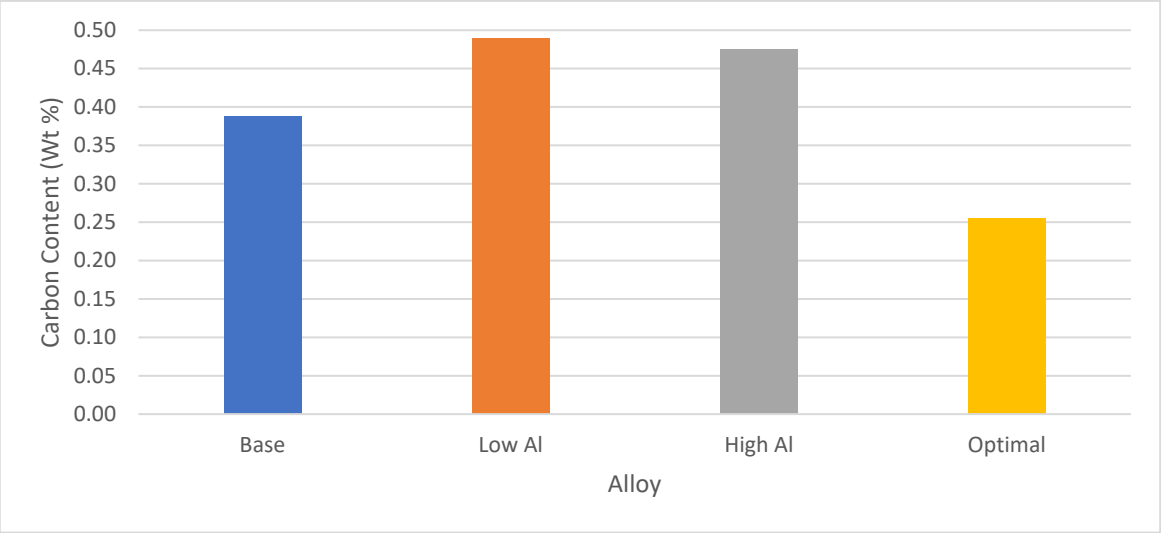

Figure 4.1.1-2: Graph showing carbon content of all four alloys.

Figure 4.1.1-2 shows the significant reduction in carbon content in the Optim-Al alloy compared to the other Al containing alloys and the Base alloy. This reduction in carbon was the major compositional difference between the Low-Al alloy and the Optim-Al alloy.

Glow discharge optical emission spectroscopy (GDOES) allows the composition of a conductive material to be measured by plasma sputtering of the top layer of the material and recording the resultant photons. When using GDOES to analyse the variation in alloy composition between the near outer and near inner diameter regions, as shown in Figure 4.1.1-3 and Figure 4.1.1-4, the Low-Al alloy was inconsistent with the other three alloys with regards to the nickel and chromium content changes. It showed a rise in chromium nearer the inner diameter compared to a fall seen with the other alloys. Correspondingly, the nickel content showed the inverse trend.

The largest variation in aluminium presence was observed in the Optim-Al alloy, with a significant increase of aluminium closer to the inner diameter. This is potentially beneficial, as more aluminium present at the inner surface of the pipe means the availability of aluminium to be oxidised to create an aluminium oxide layer is increased.

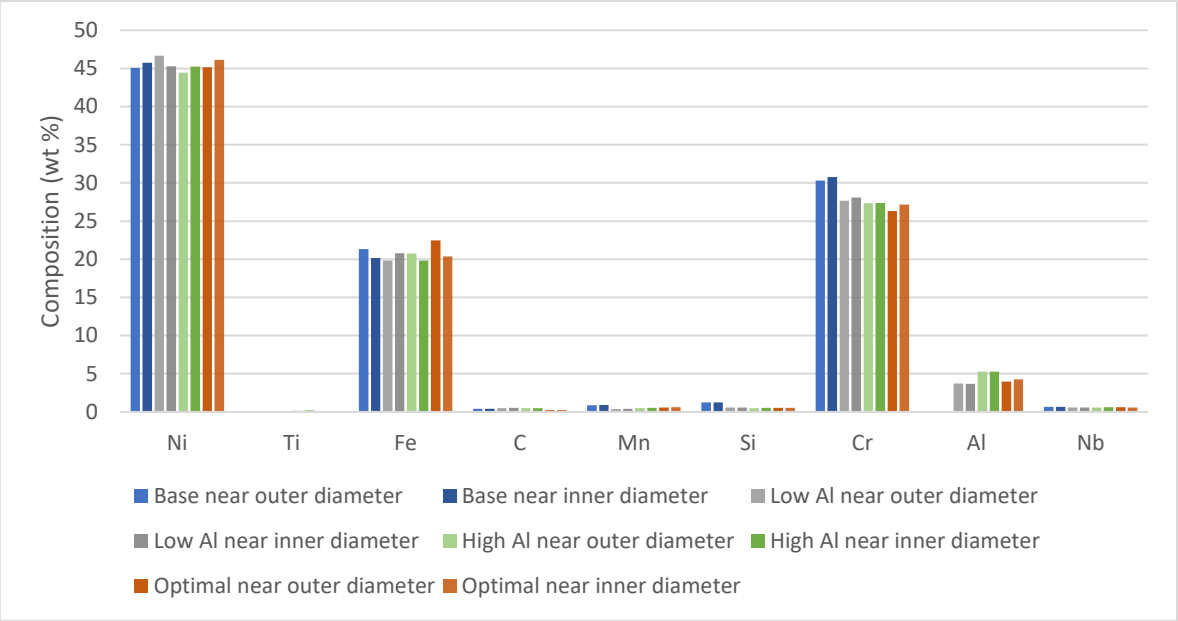

Figure 4.1.1-3: GDOES bulk composition analysis of all four alloys near both the inner and outer diameter of each alloy.

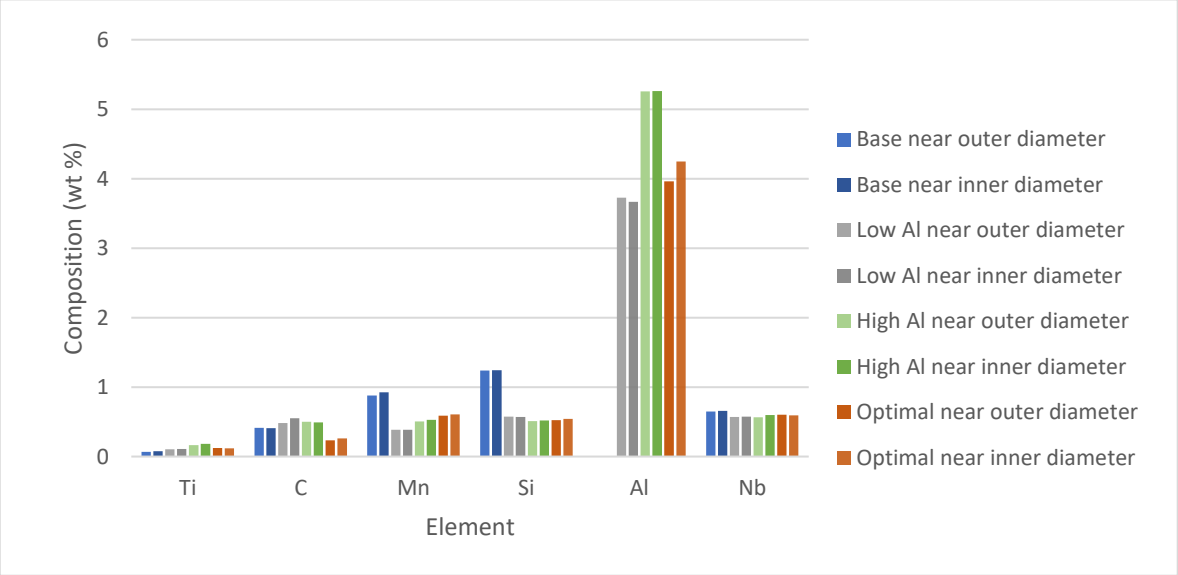

Figure 4.1.1-4: GDOES bulk composition analysis of low volume elements of all four examined alloys at ID and OD.

4.1.1.2 Compositional evolution of the matrix phase through the cross section of the alloys

These alloys are known to be made up of two distinct phases; the matrix, the austenitic phase of steel, resultant from the high nickel content, which makes up the bulk of the alloy; and the carbides, usually chromium or niobium based, which are found dispersed throughout the alloy. These two distinct phases are indicated in Figure 4.1.1-5. When analysing the composition of solely the matrix phase of all four alloys some further differences become evident. These measurements were taken

as the average composition of the matrix of the alloys generated by EDS point analysis, therefore excluding carbides and any other secondary phases generated during solidification of the alloy.

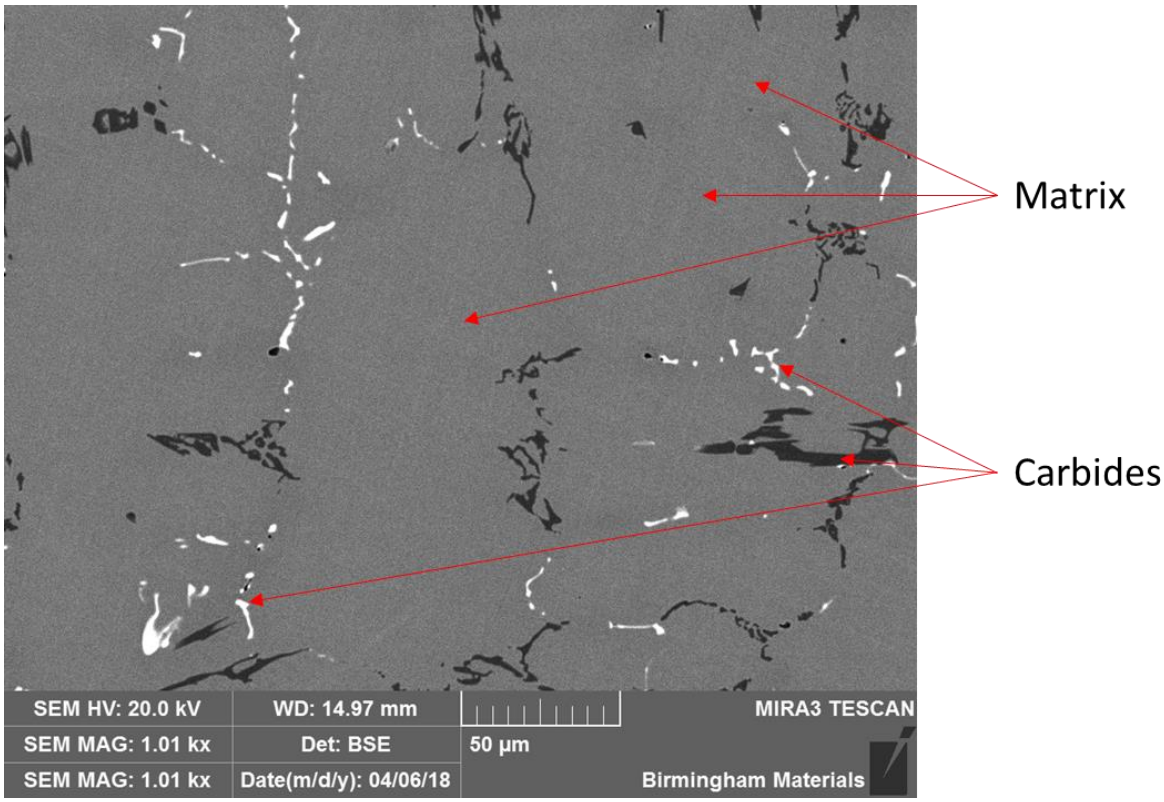

Figure 4.1.1-5: Indication of appearance of matrix and carbide phases within the alloys in backscattered electron imaging

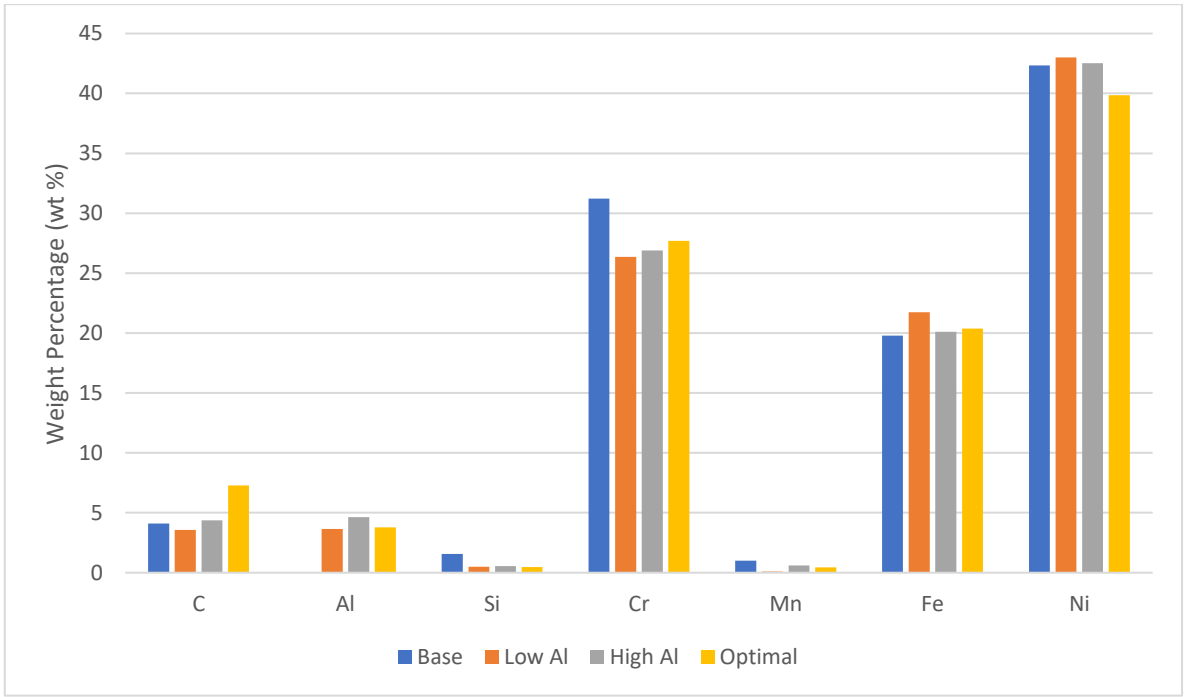

Figure 4.1.1-6 Variation in average matrix content of constituent elements in all four alloys

The content of chromium and silicon was higher in the Base alloy. This was due to the absence of aluminium when compared with the alloys containing aluminium. Within these aluminium containing alloys, a greater iron content was observed in the High-Al alloy compared to the other alloys' compositions. Similarly, there was an apparent relative increase in chromium retention in the matrix with the Optim-Al alloy compared to the other aluminium containing alloys. These differences will be discussed in detail later. The apparent high carbon concentrations in the matrix was due to the differing experimental techniques used to acquire the compositional data. The matrix composition data was gathered using EDS analysis, a technique which has limitations in low atomic number elements, with sources suggesting elements lighter than beryllium are indistinguishable through this technique (122). Carbon readings are known to be inflated above true values when using this technique due to the inaccuracies whilst sample and equipment contamination also leads to the increased presence of carbon.

When analysing the chemical composition of the four alloys, some variance between the compositions was seen – most notably reduced carbon content in the Optim-Al alloy, and varying levels of oxide formers in all of the alloys.

4.1.2 Modelling of solidification and phase formation of the alloys

Modelling software JMatPro (Java-based Materials Properties) was used to predict the phase formation and solidification properties of the four alloys. This powerful modelling software is used for the accurate prediction of multicomponent alloy properties, with numerous metallic alloy systems able to be evaluated. JMatPro can calculate phase equilibria, solidification calculations, mechanical properties, phase transformations, physical properties and other properties. The models are widely used in both industry and research and the software is widely accepted throughout industry, as it uses physical principles rather than databases for the basis of the models, and extensive validation of the models have been completed to ensure accuracy (123,124).

The software was used to model the predicted phases present at equilibrium during solidification from a liquid state of multiphase alloys. The compositions used for the models were those displayed previously in Table 4.1.1-1.

Table 4.1.2-1 displays the calculated liquidus and solidus temperatures, as shown in Figure 4.1.2-1- Figure 4.1.2-4 . The Base alloy displayed the highest liquidus and solidus temperature, whilst all three aluminium containing alloys demonstrated a wider solidification temperature range. This is potentially due to the decrease in silicon content from the Base alloy to the Al containing alloys, as Han et al. (125) showed that solidus and liquidus temperatures increased with silicon content in Fe-Cr-Al stainless steels. However Cieslak et al. (126) suggested addition of silicon and carbon to a nickel based alloy caused a reduction in solidus and liquidus temperature. The large difference in carbon content between the Optim-Al alloy and the Low-Al and High-Al alloys is likely the cause of the widened solidification range.

Figure 4.1.2-1 displays the predicted solidification of the Base alloy under equilibrium, demonstrating $Cr_{23}C_6$ and NbC carbides precipitating expected to be observed in the SEM imaging.

Table 4.1.2-1: Calculated solidus and liquidus temperatures for all four alloys as calculated by JMatPro

Alloy	Base	Low-Al	High-Al	Optim-Al
Liquidus (°C)	1348	1345	1321	1339
Solidus (°C)	1250	1240	1195	1200
Difference (°C)	98	105	126	139

Table 4.1.2-2: Solid fraction (by weight) of phases at 800°C predicted by JMatPro model

Phase	Base	Low-Al	High-Al	Optim-Al
M_7C_3		0.0333	0.0242	
$M_{23}C_6$	0.0566	0.0245	0.0448	0.0397
M_7C_3+$M_{23}C_6$	0.0566	0.0578	0.0690	0.0397
MC (NbC)	0.00667	0.0054	0.00147	0.00353
Ni_3Al		0.0399	0.17	0.091

The predicted volume fractions of all phases are shown in Table 4.1.2-2. Addition of aluminium resulted in the formation of the nickel aluminide phase, as predicted by the model in all three Al containing alloys. The onset of precipitation of the Ni_3Al phase in the solidification range seen in the High-Al alloy in Figure 4.1.2-3 is in contrast to the much lower temperature onset of this phase seen in the Low-Al and Optim-Al alloys, as shown in Figure 4.1.2-2 and Figure 4.1.2-4. This suggests the Ni_3Al phase will precipitate early during solidification in the High-Al alloy when compared to the other aluminium containing alloys, and therefore also results in a much greater volume fraction, compared to the other two aluminium containing alloys.

The higher carbon content and aluminium presence in the Low-Al and High-Al brings in the potential formation of Cr_7C_3 carbides as well as the $Cr_{23}C_6$ carbides seen in the Base alloy, whilst the reduced carbon content in Optim-Al supresses this, allowing only the primary chromium carbide to precipitate. Furthermore, the onset of carbide precipitation at temperatures above the liquidus temperature of particularly the High-Al alloy is in line with the widespread carbide precipitation between the dendrites of solidifying matrix.

The correlations and trends of the modelled alloys when compared to the observed microstructure is further explored in 5.1.

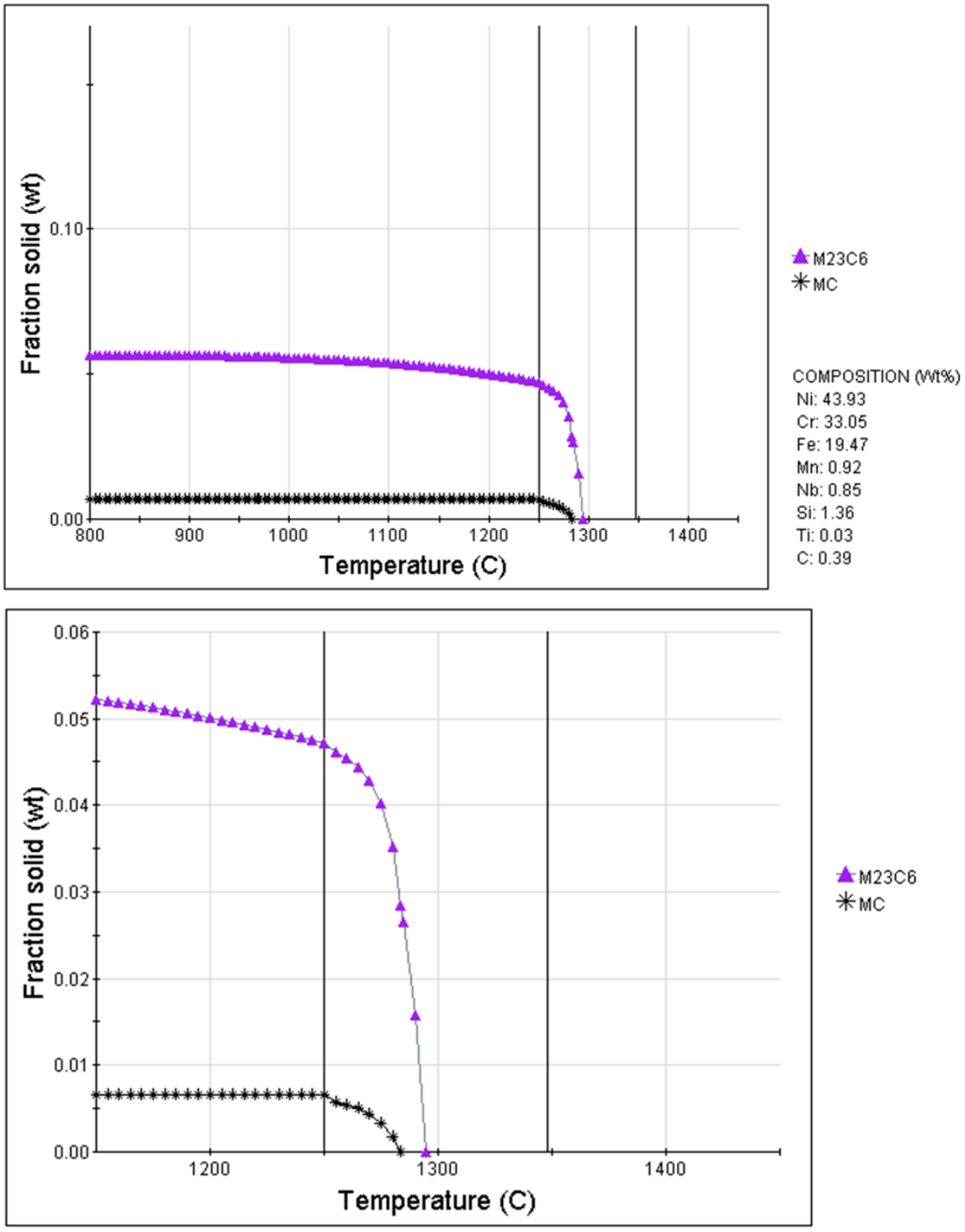

Figure 4.1.2-1: JMatPro model of Base alloy solidification phases solid fractions predicting the two carbide phases.

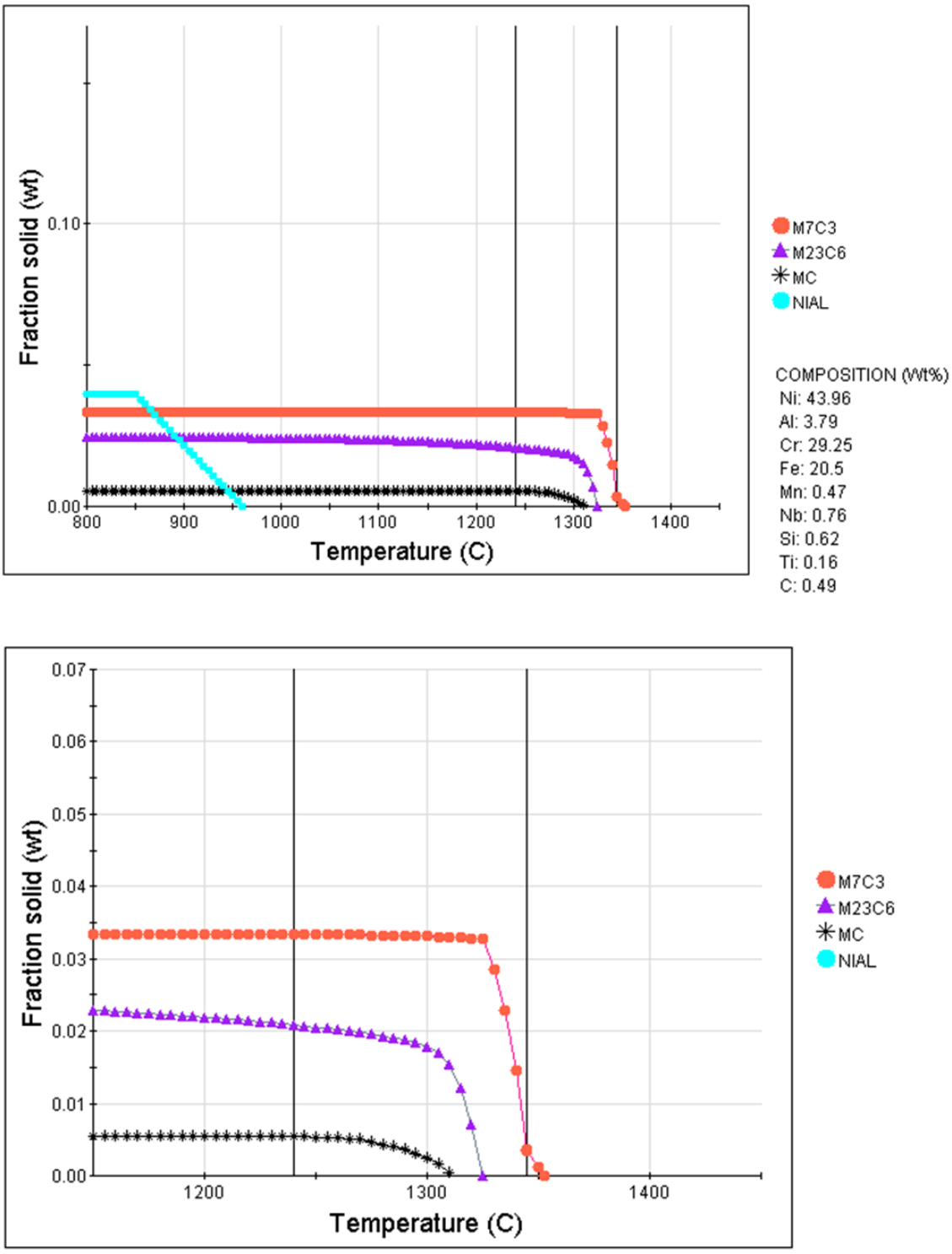

Figure 4.1.2-2: JMatPro model of Low-Al alloy solidification phases solid fraction predicting formation of three carbide phases, and a nickel and aluminium rich phase.

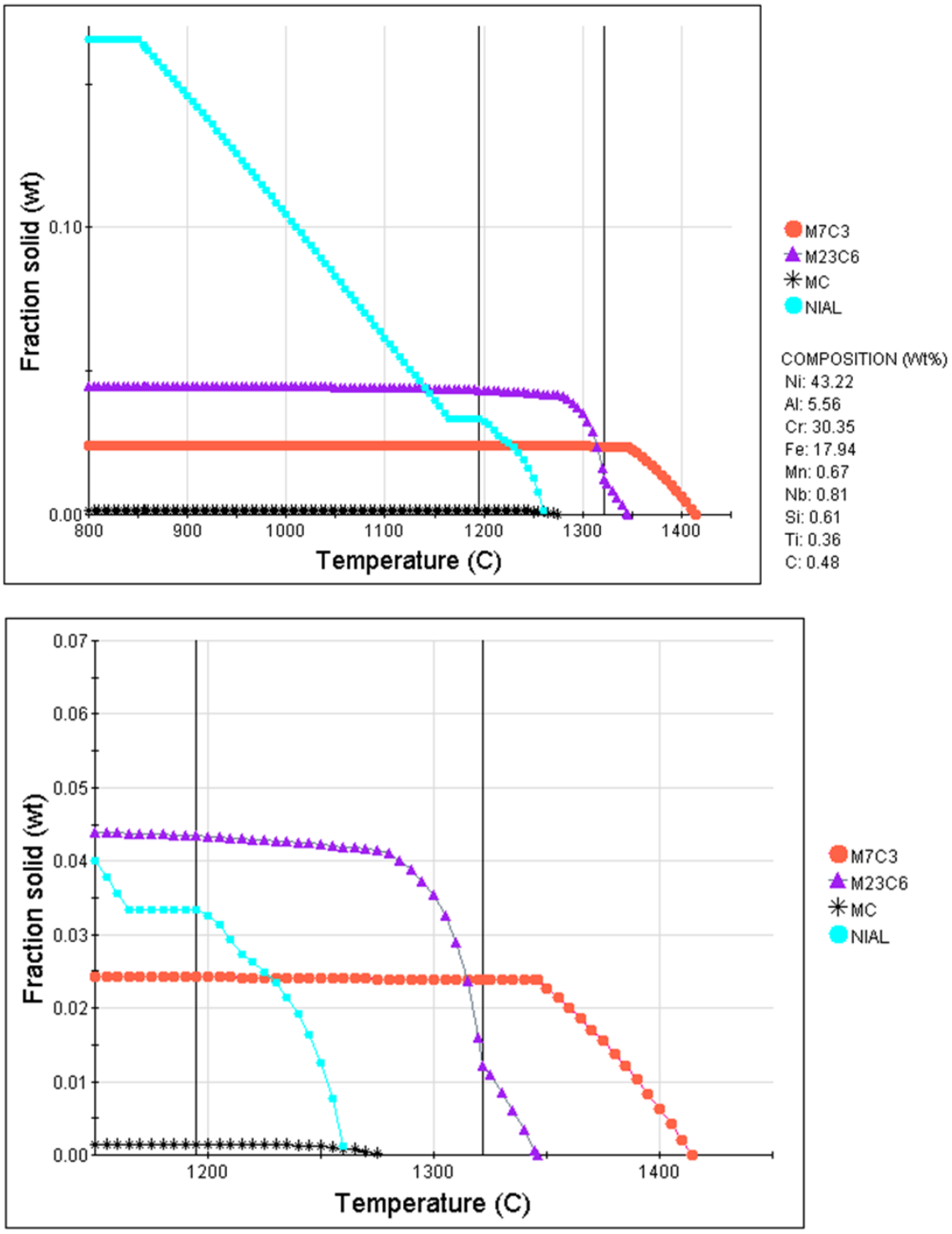

Figure 4.1.2-3: JMatPro model of High-Al alloy solidification phases solid fractions predicting similar phases to the Low-Al alloy, however with much greater presence of the nickel and aluminium rich phase.

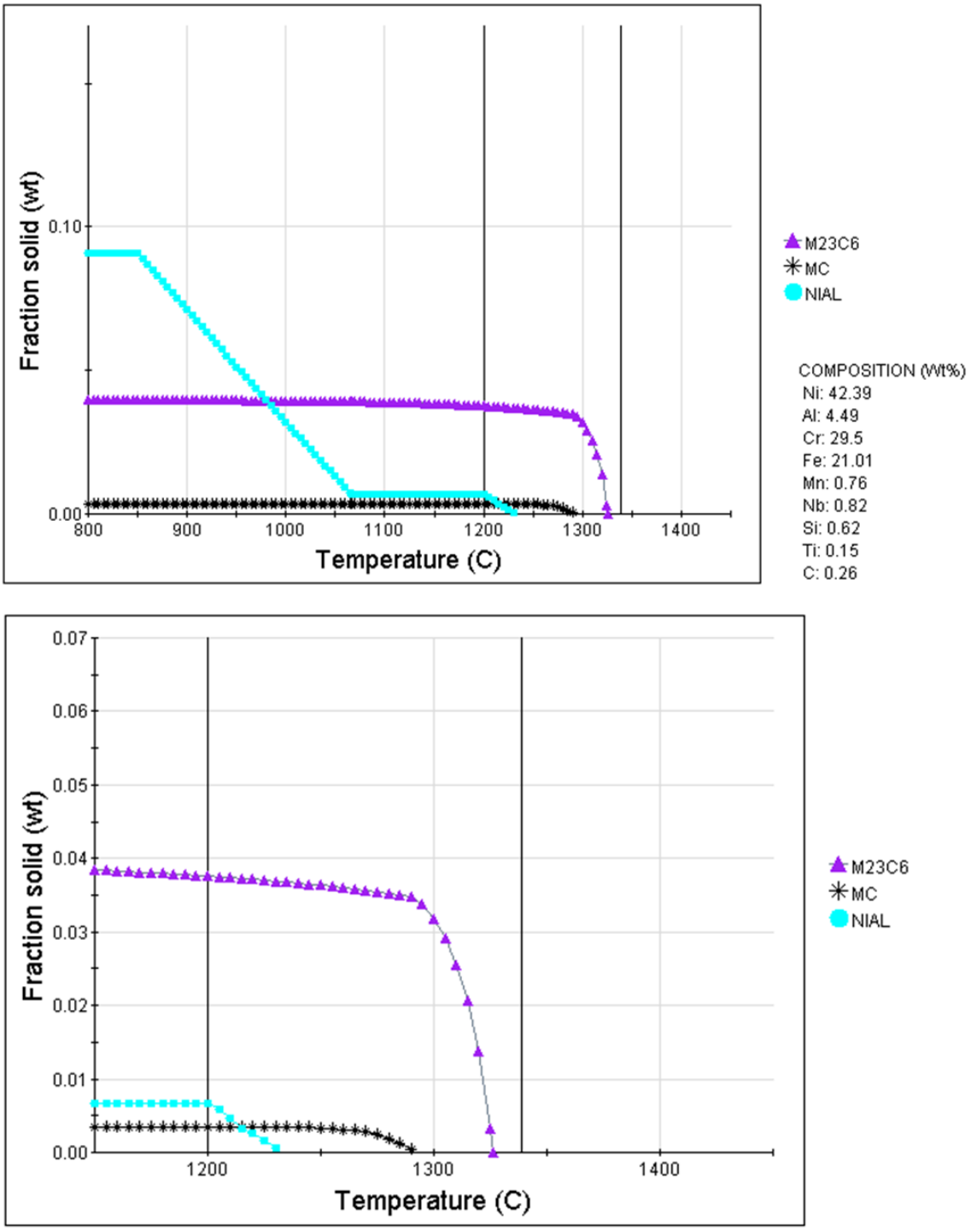

Figure 4.1.2-4: JMatPro model of Optim-Al alloy solidification phases solid fractions predicting the same carbide phases as Base, with the addition of the nickel and aluminium phase.

4.1.3 Changes of microstructure through the cross-section of the alloys

Imaging of the different alloys was undertaken at regions between the inner and outer diameters of the pipes to allow for the changing microstructure to be observed. A differing microstructure

throughout the samples was to be expected due to the nature of the centrifugal casting process by which all samples were produced. The microstructure of all four alloys showed three distinct regions, as illustrated in Figure 4.1.3-1. These regions varied in depth and size amongst the alloys but allowed each alloys' microstructure to be analysed in the three separate regions.

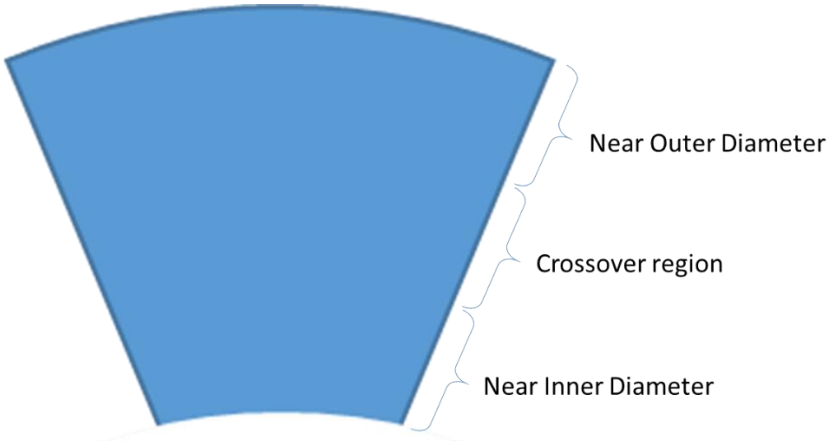

Figure 4.1.3-1: Three regions of microstructure seen in the alloys

4.1.3.1 Base alloy

The images in Figure 4.1.3-2 display the three distinct regions of the alloy microstructure; the near outer diameter region as seen in the outer diameter, 4mm and 6mm images (a, b and c), which display clear dendrites and interdendritic growth of a precipitated secondary phase; the crossover region at 8mm to 10mm depth (d and e) where both dendritic growth and equiaxed grains appear evident; and the near inner diameter region, characterized by the presence of almost entirely equiaxed grains, as seen at 12mm and the inner diameter (f and g). Steadily increasing grain size was observed moving from the outer diameter through the sample towards the inner diameter, as a result of the greater solidification times closer to the inner diameter due to the nature of the centrifugal casting process. The grain size shows progressive coarsening through the alloy; finer nearer the outer diameter and at its most coarse near the inner diameter. This was a function of the cooling rates being fastest at the pipe outer diameter as the cooling effect of the mould caused more rapid nucleation at the pipe outer surface. Furthermore, the centrifugal casting process

causes the inner diameter of the pipe to be the final region to solidify, as the lower density of the liquid material is forced towards the inside of the casting.

The increased solidification time also leads to changes in the nature of the carbide precipitation. The more rapid solidification experienced at the outer diameter region leads to finer carbide production, whereas slower cooling rates towards the inner diameter results in larger carbides which sit around the larger grains, therefore their distribution is less evenly spaced through the alloy compared to the outer diameter region. Comparing Figure 4.1.3-2 a and f demonstrates these observations.

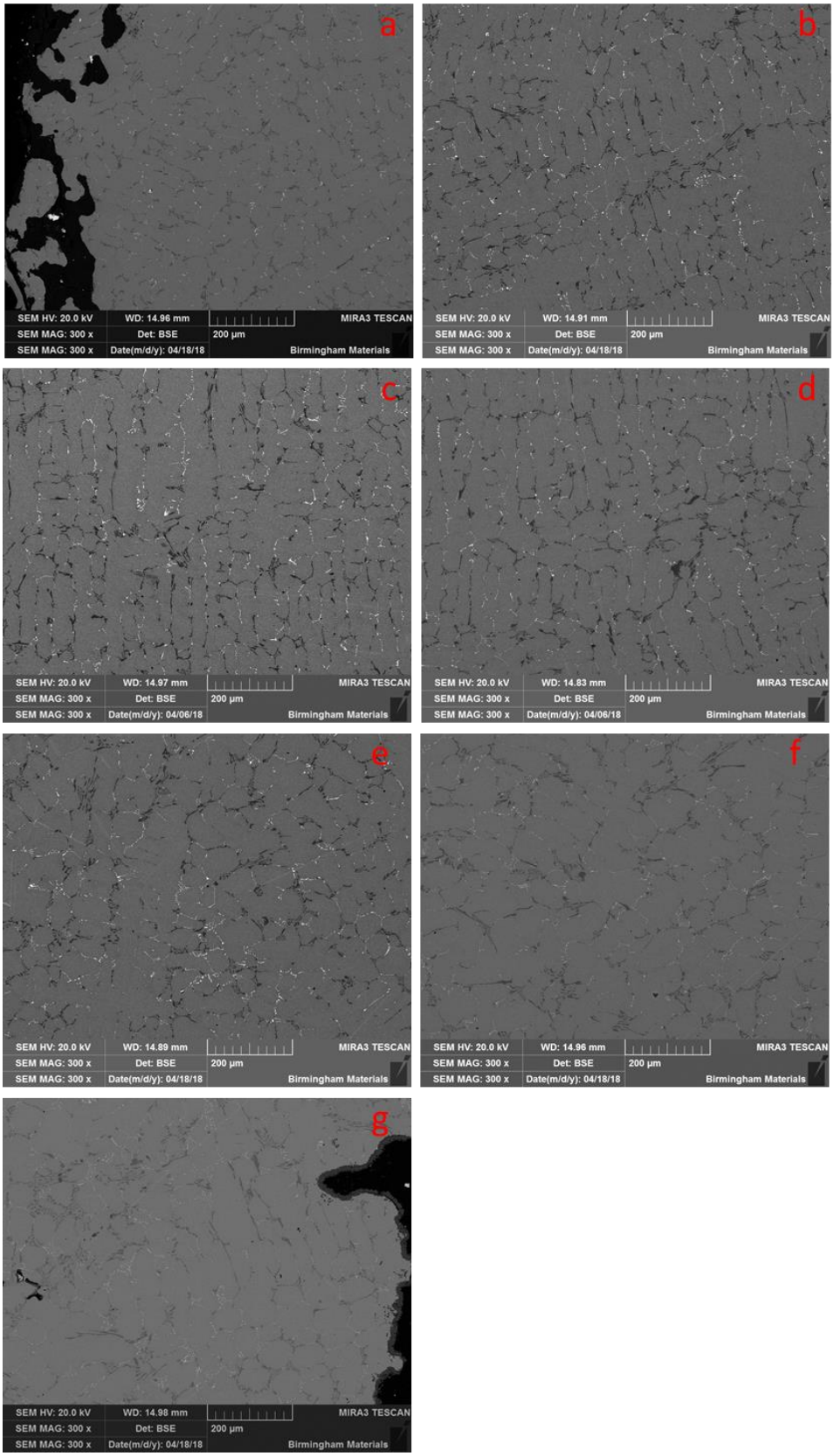

Figure 4.1.3-2: SEM backscattered images of Base alloy in the as cast state: Outer diameter (a); 4mm depth (b); 6mm depth (c); 8mm depth (d); 10mm depth (e); 12mm depth (f); Inner diameter (g). Images show the changing nature of the carbides and grains through the alloys depth.

4.1.3.1.1 Near Outer Diameter Region

The near outer diameter region is characterized by the dendritic growth of the matrix into columnar grains, growing away from the outer surface. This is a result of the temperature gradient introduced by the cold mould surface on the molten alloys. Subsequent growth of a secondary phase between the dendrites in these grains was observed. These secondary phases were identified as chromium carbides and niobium carbides by EDS elemental mapping, as shown in Figure 4.1.3-4. The backscattered image appearance of the chromium carbide is a darker feature than the matrix, demonstrating a lower mass phase, whilst the niobium carbide appears much brighter, due to it being a much heavier phase. This contrast in the backscattered images allowed for easy identification of the phases.

The formation of these carbides occurred due to carbide formers being ejected from the solidifying grain matrix and concentrating between the dendrites, creating a local concentration high enough to form the secondary phases.

The dendrites also showed some effect of the Coriolis force from the centrifugal casting technique, causing the grains to grow at an angle to the outer surface, rather than directly down the temperature gradient towards the inner surface of the pipe.

The EDS elemental map (Figure 4.1.3-4) shows the chromium carbides and the niobium carbides which were formed throughout the alloy. The chromium carbides appear to form with the primary dendrites shown by their acicular appearance as the darkest phase in the backscattered images. This showed them to run along the sides of a large vein of matrix – the primary dendrite. The niobium carbides however appeared to be present at secondary dendrites of the matrix, appearing between the primary dendrites and running at 90 degrees to them. This growth was expected, as carbide formation occurs primarily where there was significantly greater chromium in the alloy relative to niobium.

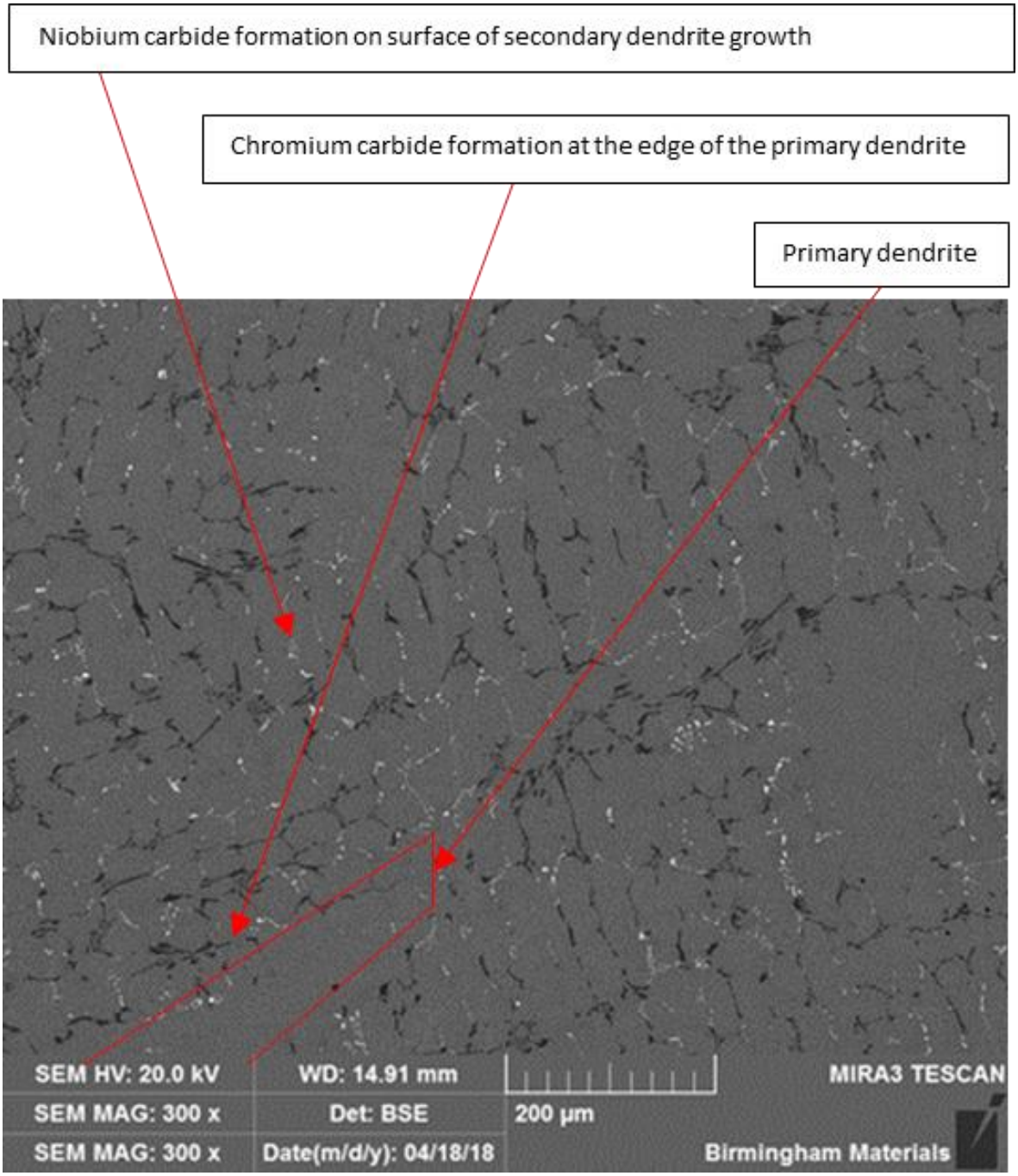

Figure 4.1.3-3 SEM backscattered image of 4mm region of Base alloy, representing the near outer diameter region of the alloy, showing dendrites and carbide growth.

In some cases, the formation of niobium carbides in contact with chromium carbides was also observed (Figure 4.1.3-5). This was caused by the niobium carbides acting as nucleation sites for the chromium carbide. This is due to the niobium carbides solidifying in the molten alloy, and these particles being trapped in the interdendritic regions of the solidifying matrix. The chromium was ejected into these regions as the matrix solidified, and the chromium carbides form. The niobium

carbides formed before the solidification of the matrix are identifiable by their triangular morphology, as seen in Figure 4.1.3-5. Slower cooling rates allow these carbides to move with the solidification front, whereas more rapid cooling, as seen near the outer diameter of the pipe, freezes the carbides within the solidifying alloy. These particles act as nucleation points for the matrix grains, aiding the formation of finer matrix grains in the outer diameter region.

Silicon ejection to the grain boundaries was also evident, with raised silicon concentrations apparent in Figure 4.1.3-4.

The apparent presence of manganese in the carbides is misleading, due to the overlapping energy intensities of chromium and manganese. These carbides are confirmed to be chromium carbides, demonstrated in Figure 4.1.3-5, and do not contain significant quantities of manganese as the elemental mappings would suggest. This occurs throughout the elemental mappings of the alloys; therefore true manganese presence is identified accordingly.

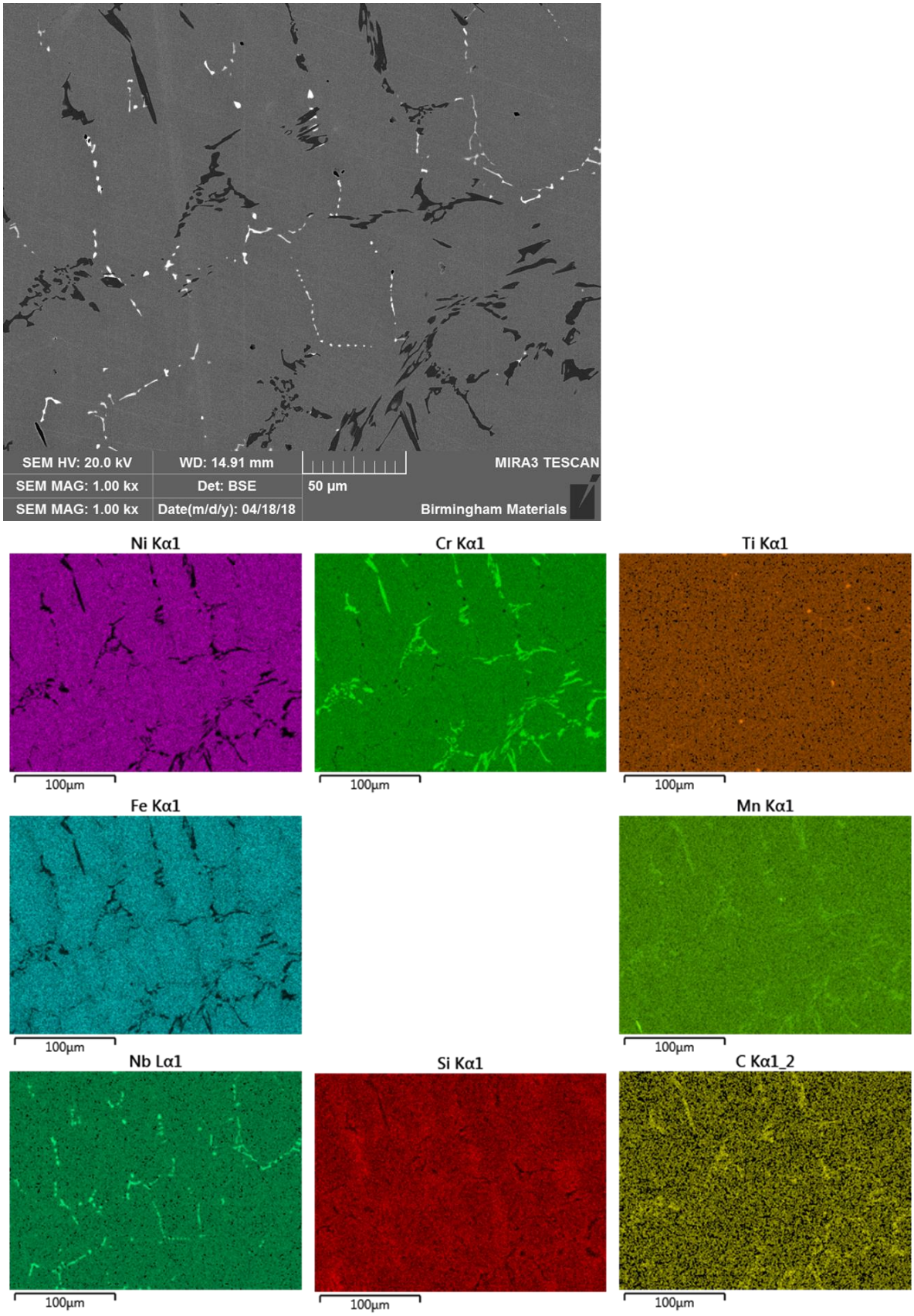

Figure 4.1.3-4 Elemental mapping of the near outer diameter region of the Base alloy, highlighting chromium and niobium carbide phases.

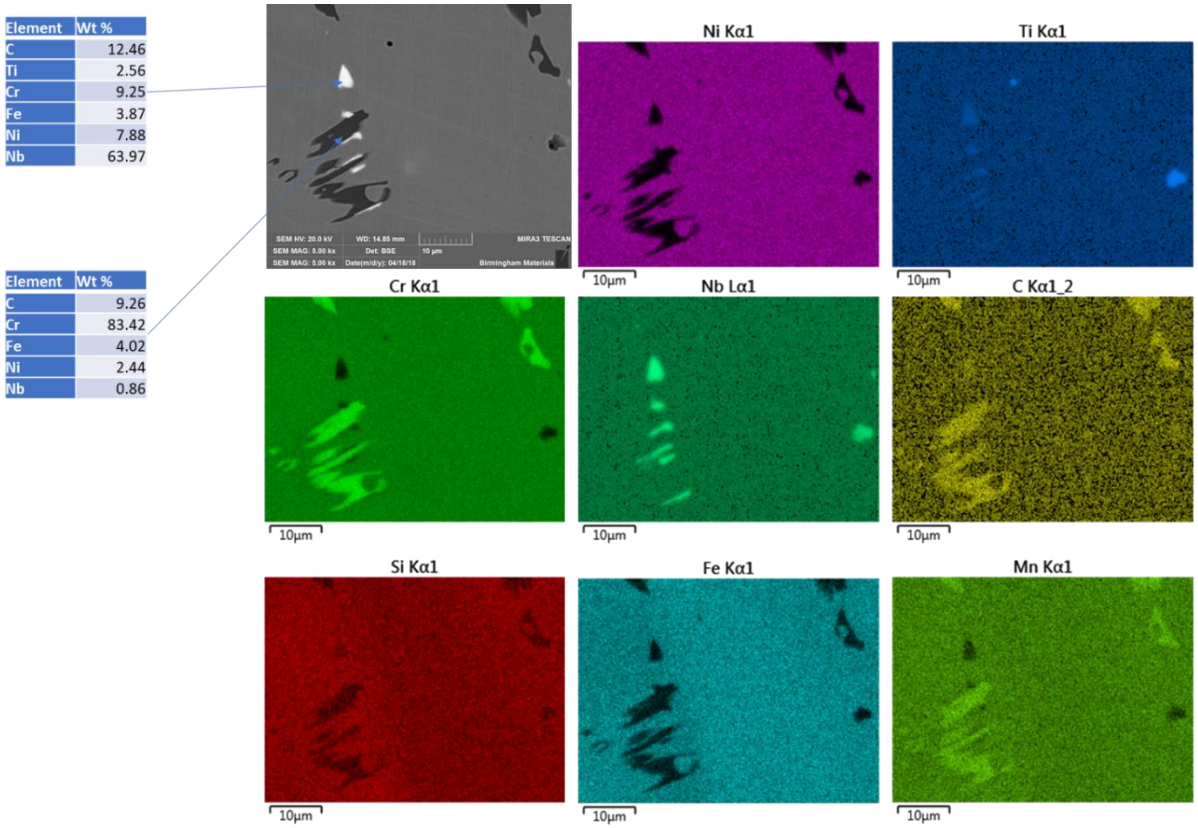

Figure 4.1.3-5 Elemental mapping and EDS quantitative analysis of Base alloy in the near outer diameter region, identifying chromium carbides and niobium carbides.

4.1.3.1.2 Crossover Region

In the cross over region there was evidence of both columnar grain growth and equiaxed grains, and similar carbide formation patterns were also evident along the dendritic structure. Equiaxed grains being produced and surrounded by intergranular carbide formation were also observed, as shown in Figure 4.1.3-6.

The silicon concentration seen in the elemental mapping (Figure 4.1.3-7) displayed higher concentrations of silicon in the matrix regions at the very edge of the grains, giving further evidence for the ejection of the non-matrix formers into the intergranular region during solidification of the matrix. The higher affinity of chromium and niobium for carbon leads to the carbide formations, whilst silicon remained in solution.

The morphology of the niobium carbides was more varied deeper into the alloy, with particulate, triangular carbides present, however they were also joined by carbides which appeared as long, thin veins. These were formed during slower solidification of the alloy, whereas the triangular carbides formed before solidification of the bulk alloy. These carbides were formed by ejection of niobium from the solidifying matrix grain into the intergranular region when solidification rates are slow enough.

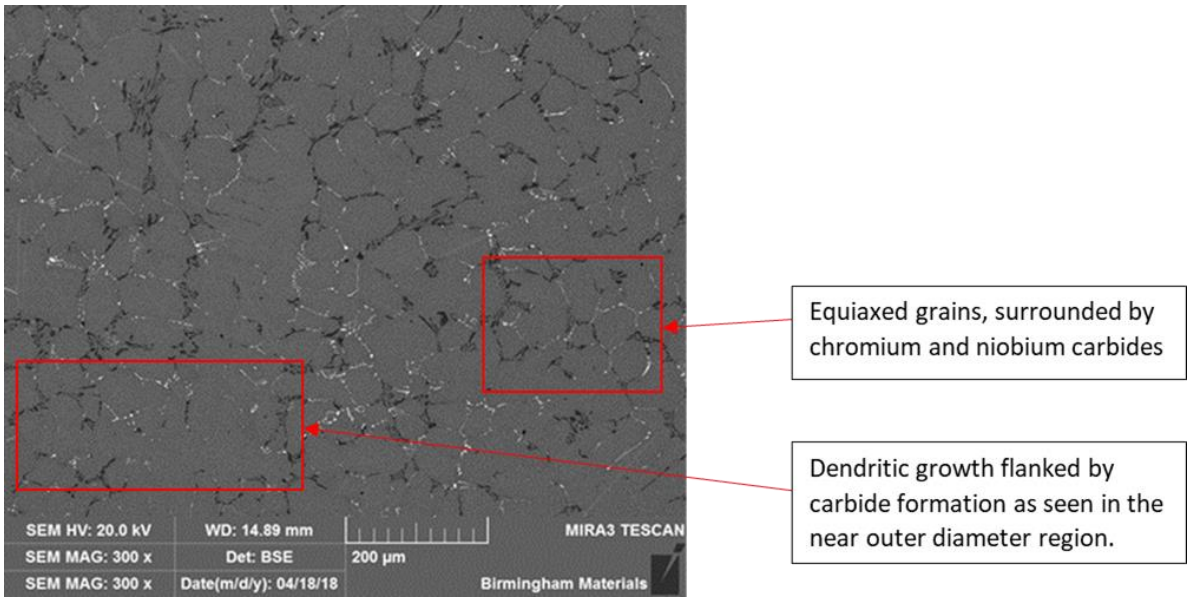

Figure 4.1.3-6 SEM backscattered image of Base displaying both dendritic and equiaxed grain structure and accompanying carbide formation.

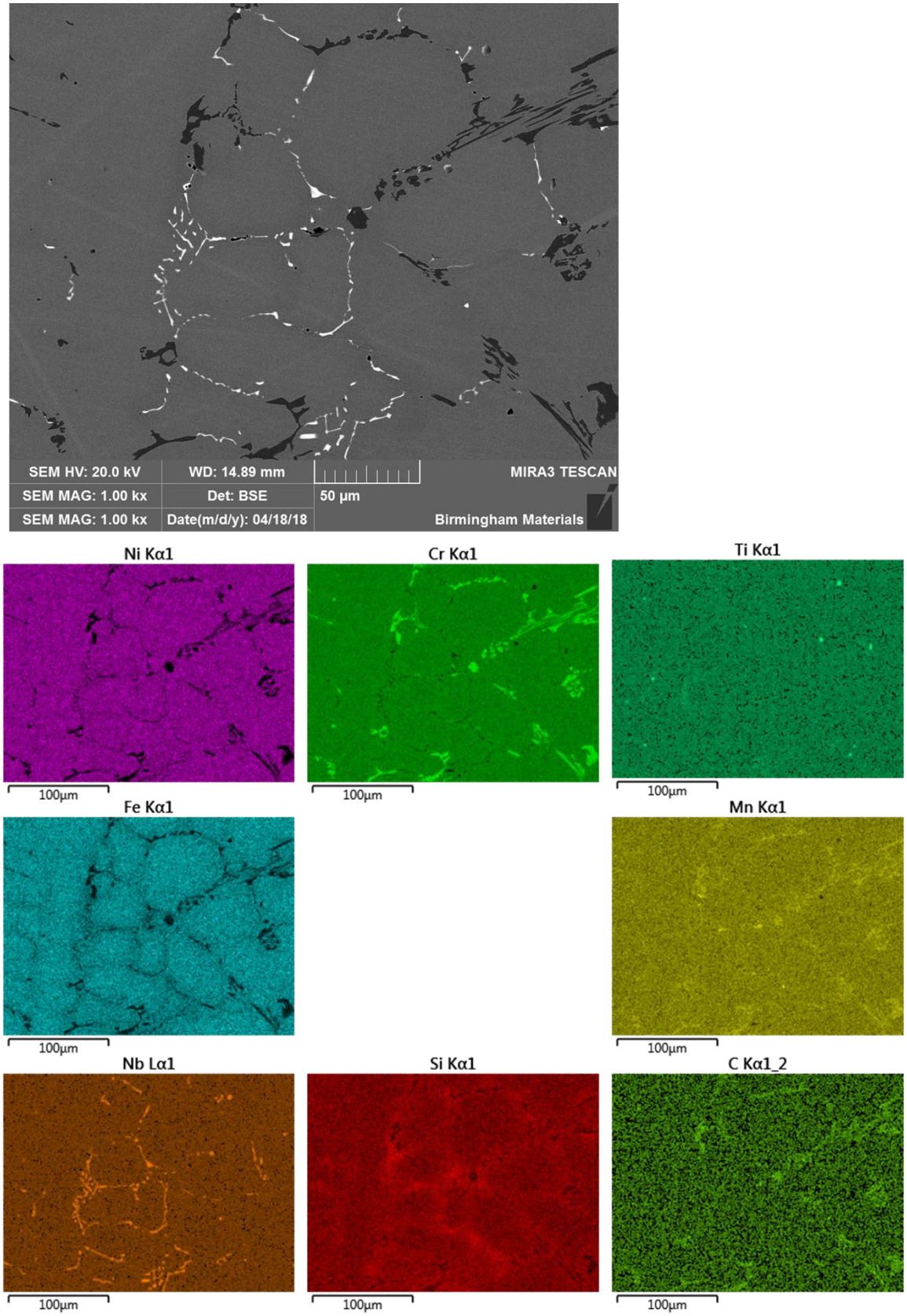

Figure 4.1.3-7 Elemental mapping of Base alloy in the crossover region, showing carbides, and silicon ejected to grain boundaries.

4.1.3.1.3 Near Inner Diameter Region

The near inner diameter region displayed equiaxed grains dominating the structure of the alloy, with carbides forming in the intergranular spaces. A new, square shaped particle was present in the near inner surface region of the alloy, as shown in Figure 4.1.3-8 b.

Intergranular carbides of both chromium and niobium were found in the near inner diameter region of the Base alloy. More of the vein-like niobium carbides were present at the inner diameter region due to the increased solidification times.

At the very inner surface, the square phase indicated in Figure 4.1.3-8 was shown to be a titanium carbonitride using elemental analysis (Figure 4.1.3-10) and observations of some oxide formation on the surface were made. The titanium carbonitride phase is very light, therefore these particles are pushed towards the inner diameter of the pipe by the centrifugal casting process. Rapid cooling rates can cause their entrapment within the matrix, while slower cooling allowed them to travel inwards at the solidification front. Like the triangular niobium carbides, these particles can act as nucleation sites for matrix grains if they are trapped in the solidifying matrix. The surface oxides were chromium and manganese oxides, with some thin sub-surface silicon oxides also being evident. These defects and unwanted phases are removed through machining after casting, therefore are insignificant with regards to impact in service.

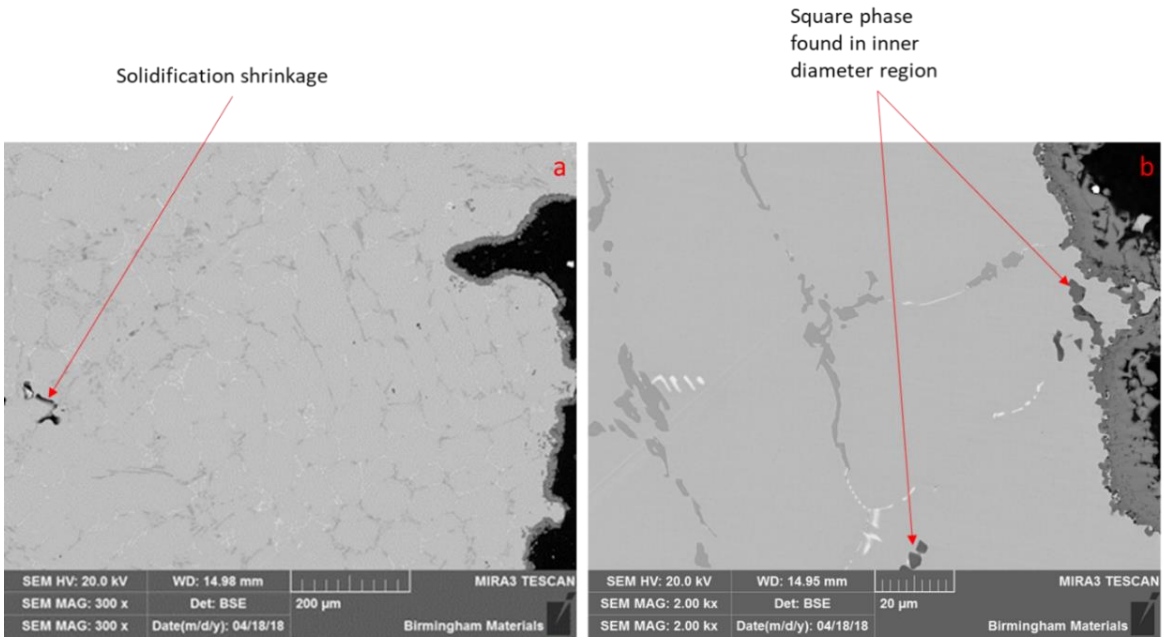

Figure 4.1.3-8 SEM backscattered image of the near inner diameter region of the Base alloy showing shrinkage porosity and square phase found at the very inner diameter surface.

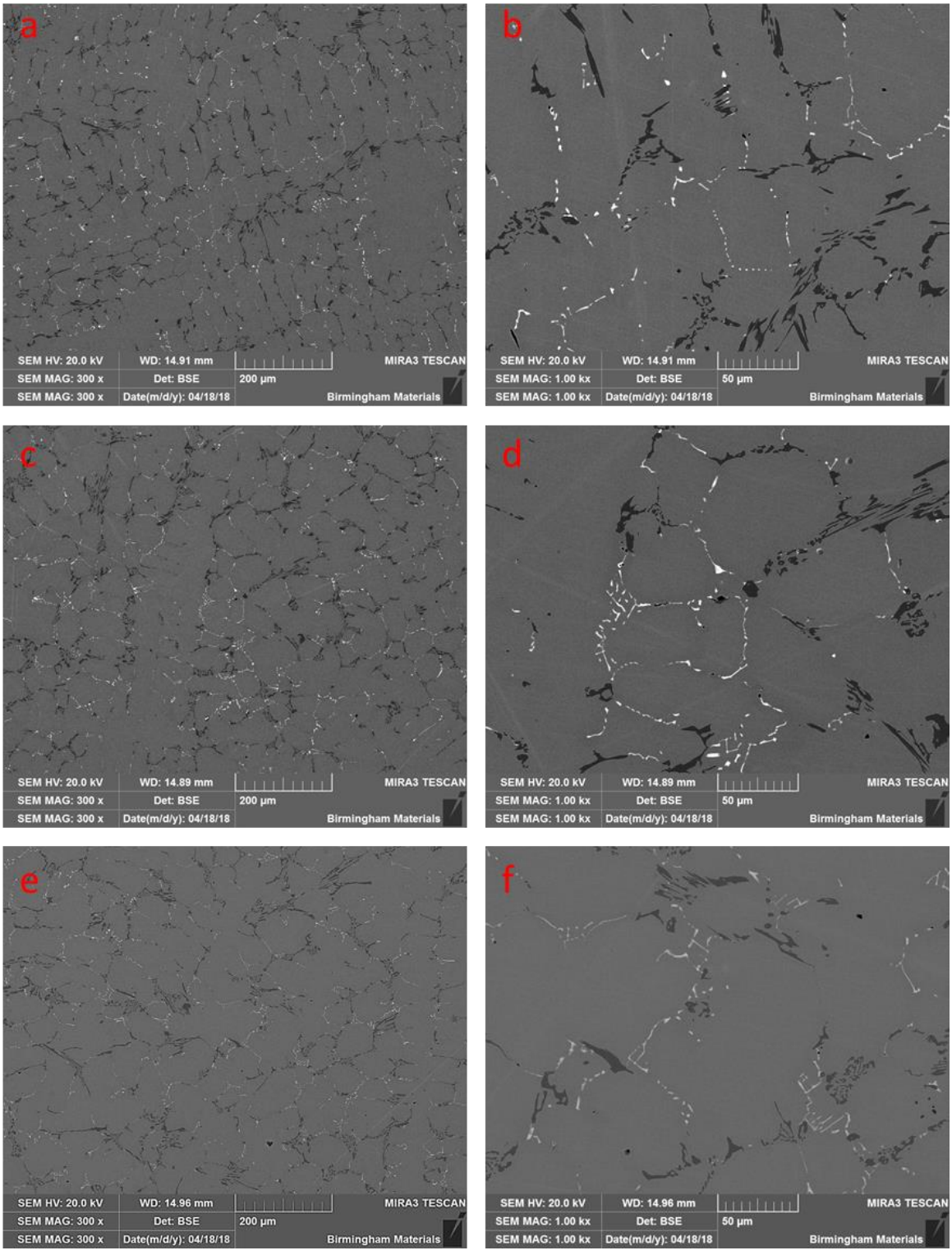

Figure 4.1.3-9: SEM backscattered images of the Base alloy; near outer diameter region (a & b); crossover region (c & d); and near inner diameter region (e & f). Shows change in carbide spacing and size at different regions of the alloy.

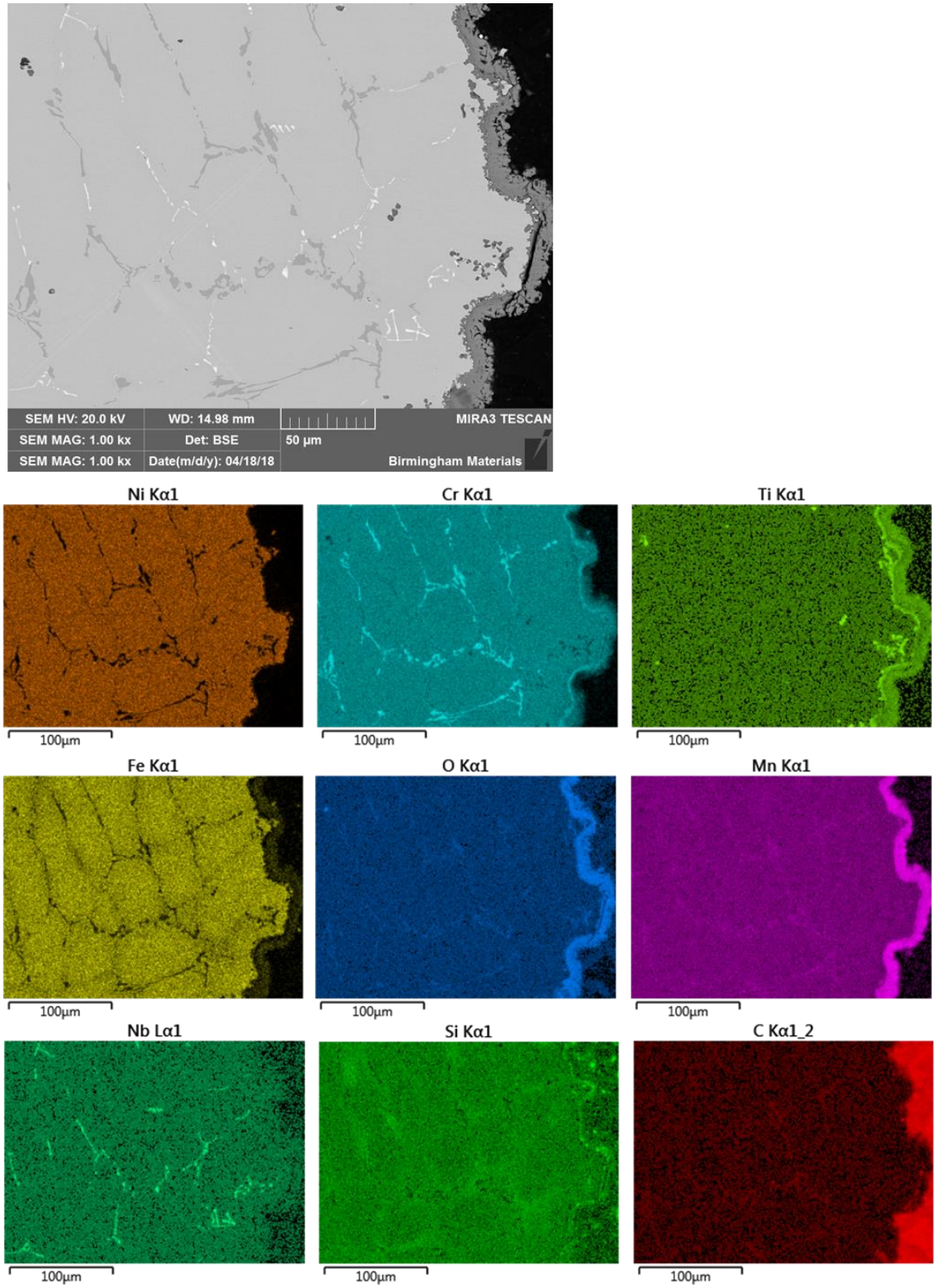

Figure 4.1.3-10 Elemental mapping of the near inner diameter region of the Base alloy, identifying titanium concentration at the inner surface, along with oxidized inner surface slag layer.

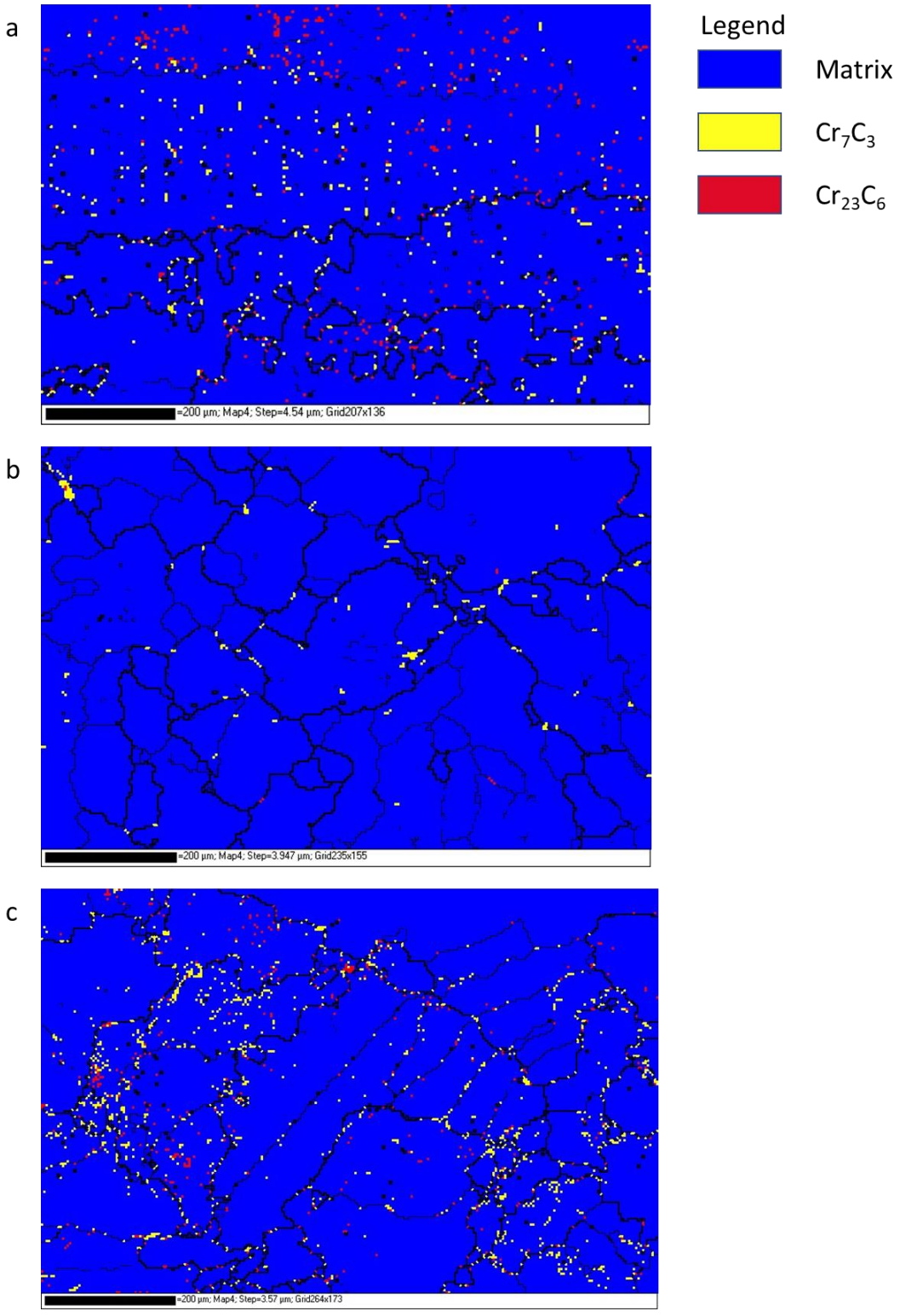

Figure 4.1.3-11: EBSD phase map of Base alloy at: (a) Outer diameter region; (b) cross-over region and; (c) inner diameter region showing grain structure and carbide location.

4.1.3.2 Low-Al alloy

As with the Base alloy, the Low-Al alloy was split into representative regions. Grain size and variations across this alloy were consistent with those of the Base alloy, with coarsening of grains .evident throughout the alloy due to the increasing solidification time, and there was little variation of grain size within the regions, as shown in Figure 4.1.3-12.

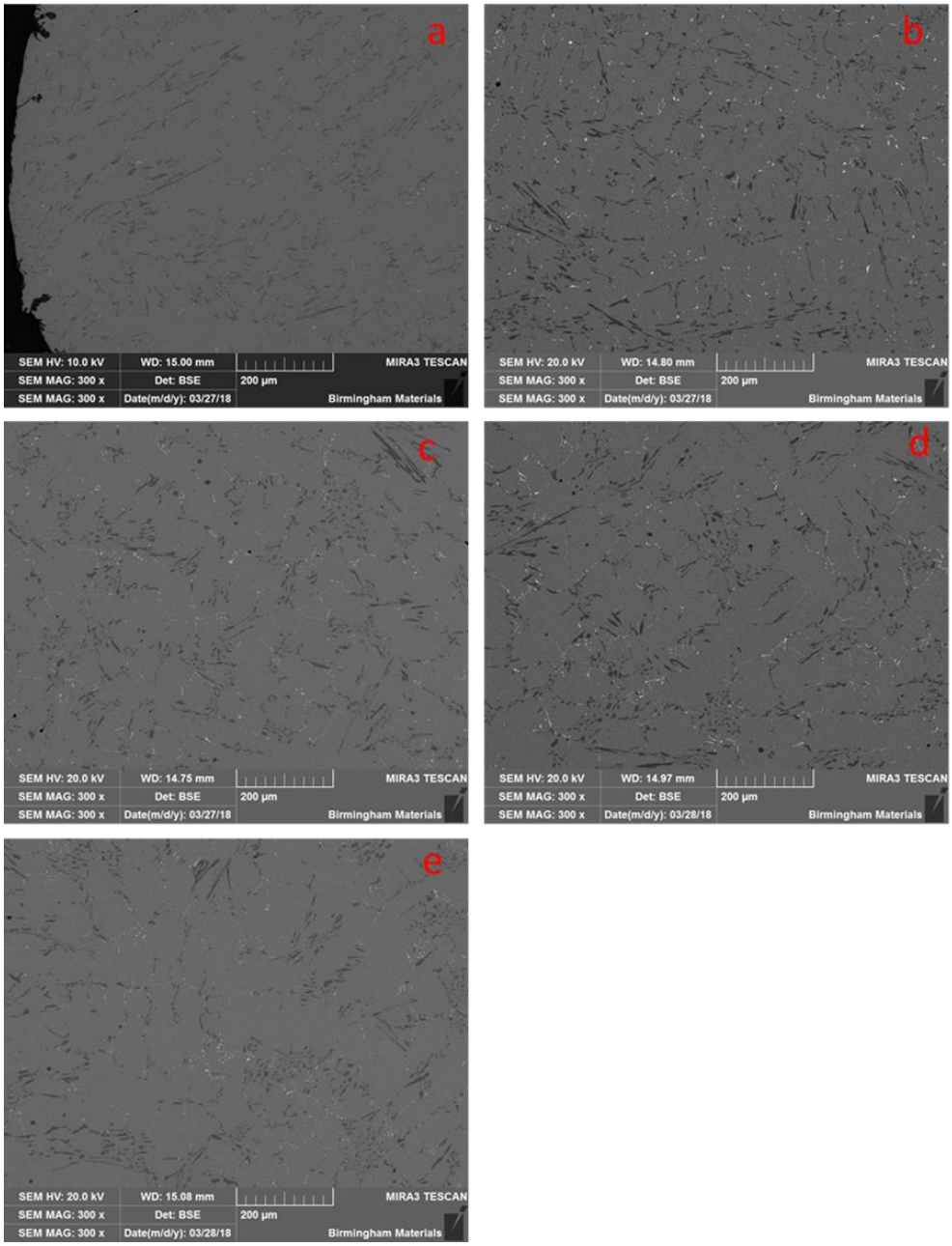

Figure 4.1.3-12: SEM backscattered images of Low-Al alloy in the as cast state: Outer diameter (a); 4mm depth (b); 8mm depth (c); 10mm depth (d); 12mm depth (e). Grain coarsening evident moving from the outer diameter inwards.

4.1.3.2.1 Near Outer Diameter Region

In the near outer diameter region, the microstructure displayed a similar pattern of dendritic matrix growth and interdendritic carbide formation, as seen in Figure 4.1.3-13, however these carbides were more acicular in appearance than those seen in the Base alloy.

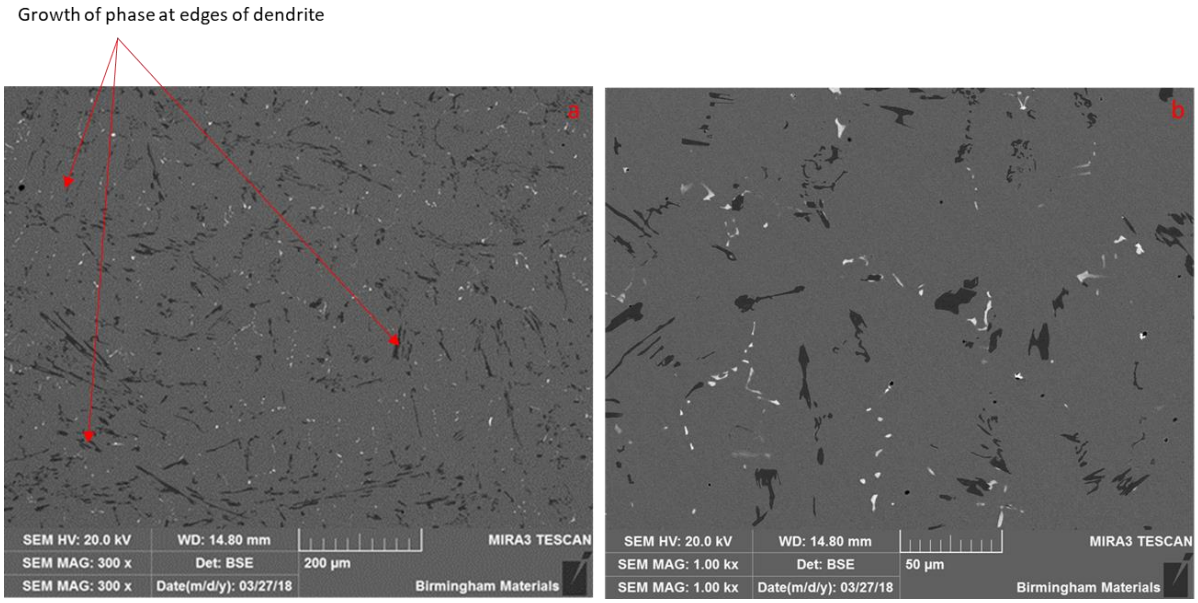

Figure 4.1.3-13 SEM backscattered image of the near outer diameter region of the Low-Al alloy showing interdendritic growth of carbides.

Chromium carbides and niobium carbides were present throughout the alloy. The volume of chromium carbides appeared to be reduced when compared to similar regions in the Base alloy. This could be expected due to the reduction in chromium content and increase in aluminium. However, as the elemental mappings in Figure 4.1.3-14 showed, there was no clear aluminium rich phase present in this region of the alloy, with the aluminium staying in solution in the matrix of the alloy. The chromium carbides were found to be acicular in nature, with the only discernible difference to be found their relative size – the chromium carbides in the Low-Al alloy appear to be larger in places than those seen in the Base alloy. This can be explained by the lowered chromium content leading to a larger region of dendrite that needs to eject chromium before formation of the carbide can occur, so this was formed over a larger area of the alloy.

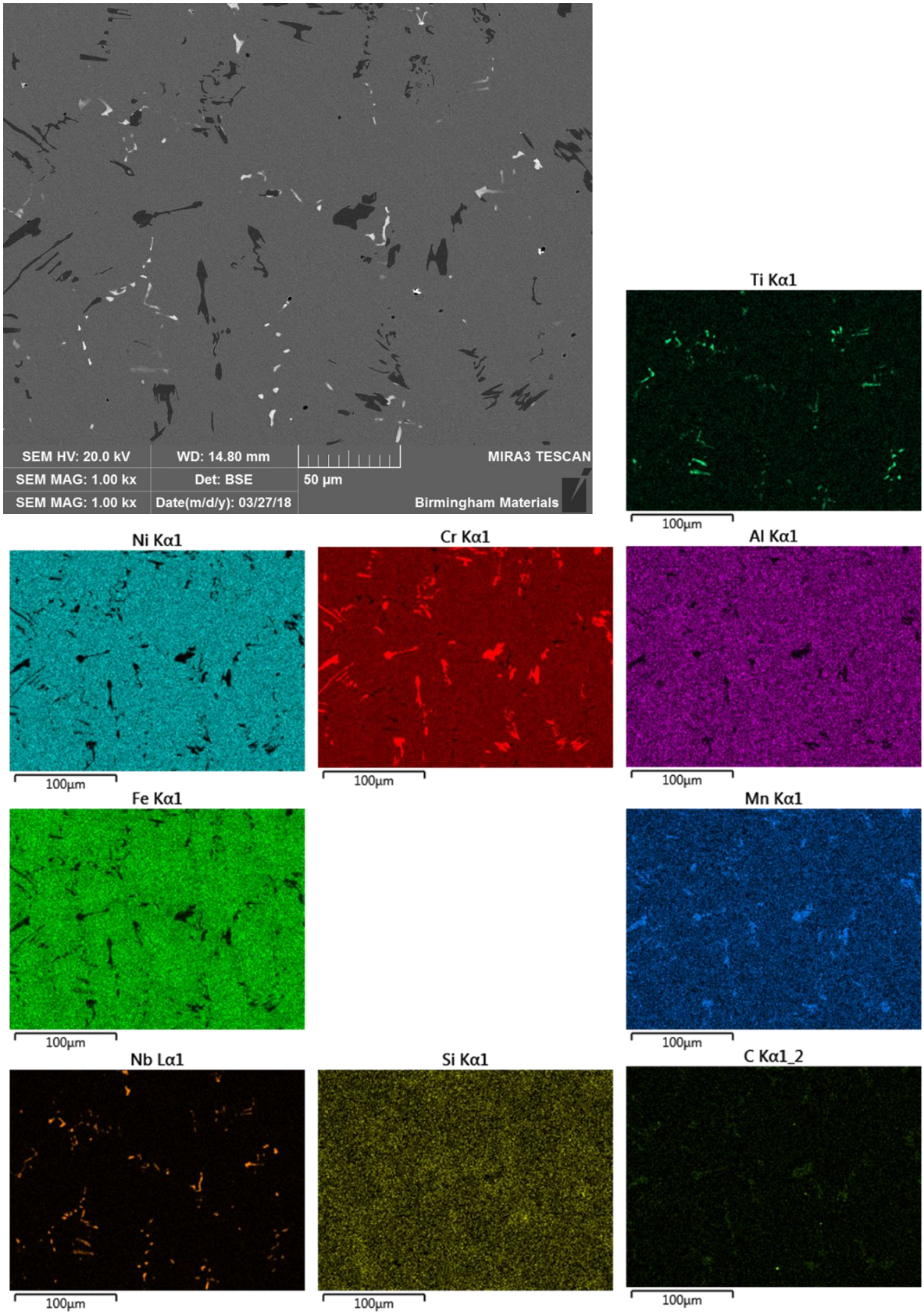

Figure 4.1.3-14 Elemental mapping of the near outer diameter region of the Low-Al alloy demonstrating aluminium presence in the matrix.

4.1.3.2.2 Crossover Region

The crossover region occurred in the 8mm to 10mm region of the Low-Al alloy, which had a combination of columnar and equiaxed grains. However, there was also a new secondary phase not present in the Base alloy, as indicated in Figure 4.1.3-15. This new secondary phase was again found in the intergranular areas as with the carbides, but it had a much lower volume fraction in comparison.

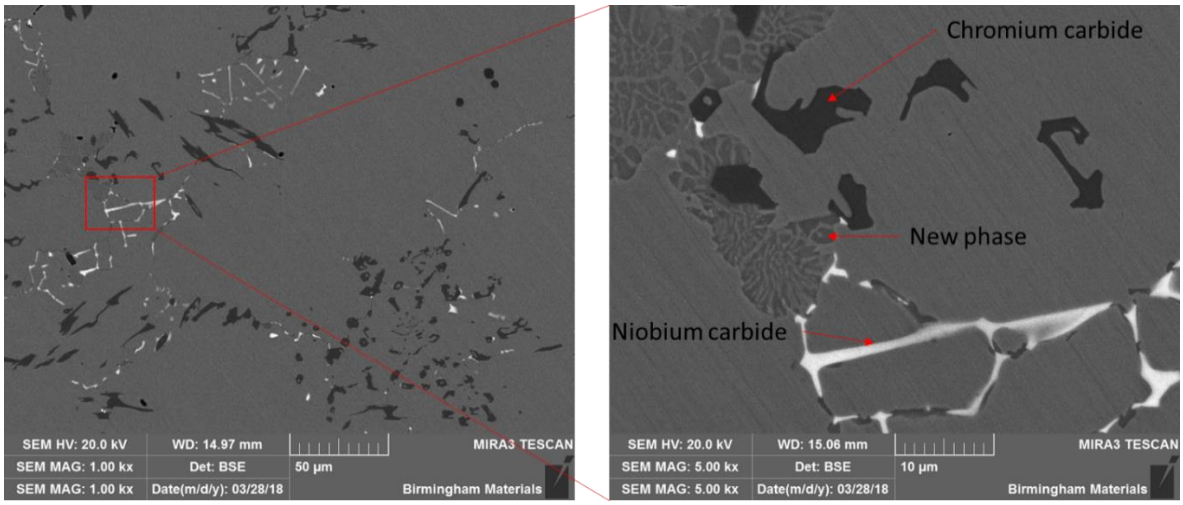

Figure 4.1.3-15 SEM Backscattered images of the crossover region of the Low-Al showing newly identified nickel and aluminium rich phase as predicted by the JMatPro model.

The new phase (indicated in Figure 4.1.3-15) present in the crossover region of the Low-Al alloy was not found to be present in the Base alloy or in the near inner diameter surface of this alloy. The elemental mappings in Figure 4.1.3-16 and Figure 4.1.3-17 showed this new phase appeared to be aluminium and nickel rich, as predicted by the JMatPro model (Figure 4.1.2-2). The appearance of this phase only at this deeper region can be explained by the casting process causing solidification from the outer diameter inwards, and more rapid solidification occurring at the outer diameter, with solidification times increasing through the pipes cross section. The slower solidification rate closer to the inner diameter allowed the formation of this phase.

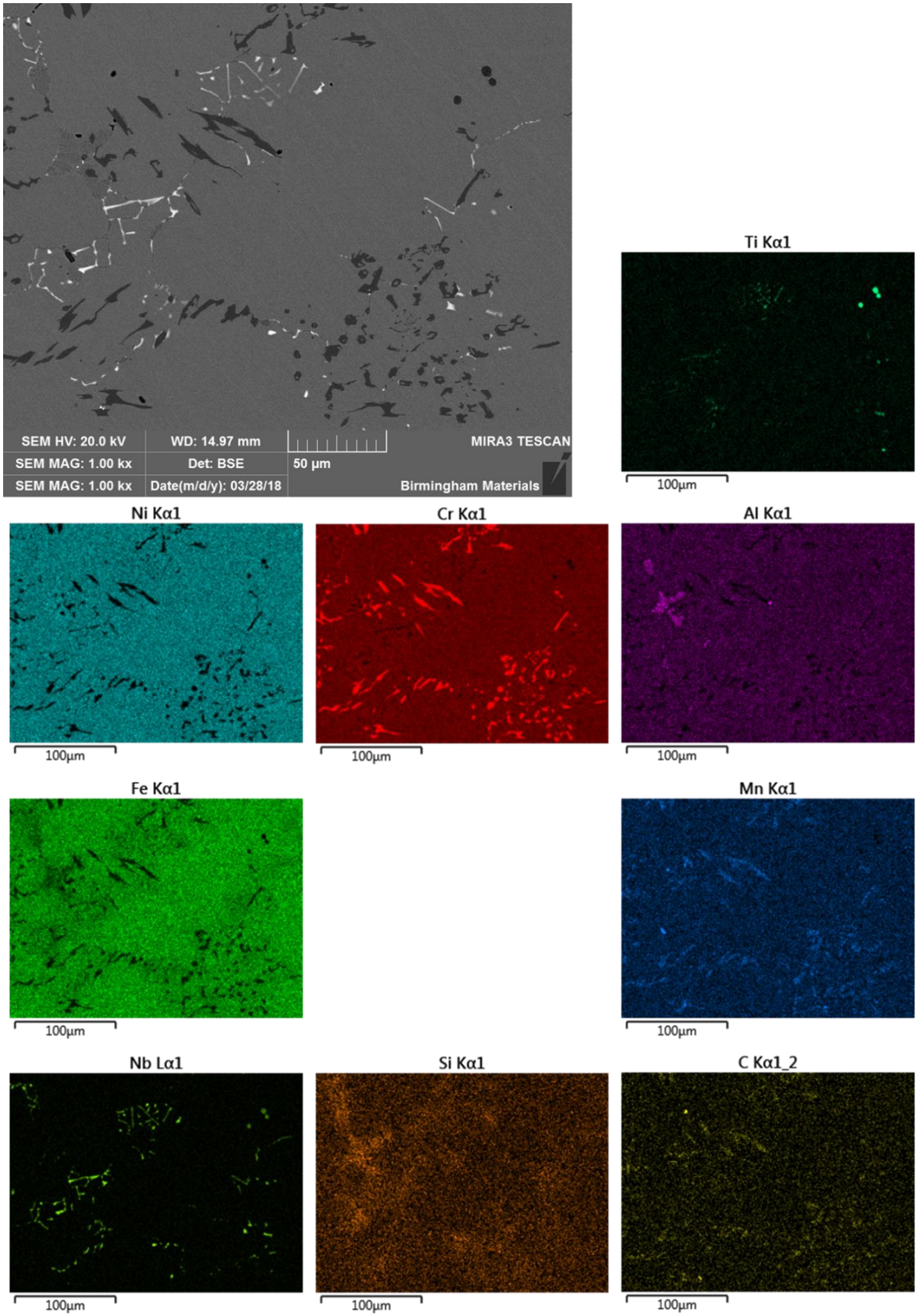

Figure 4.1.3-16: Elemental mapping of Low-Al alloy in the crossover region, showing the new nickel and aluminium rich phase.

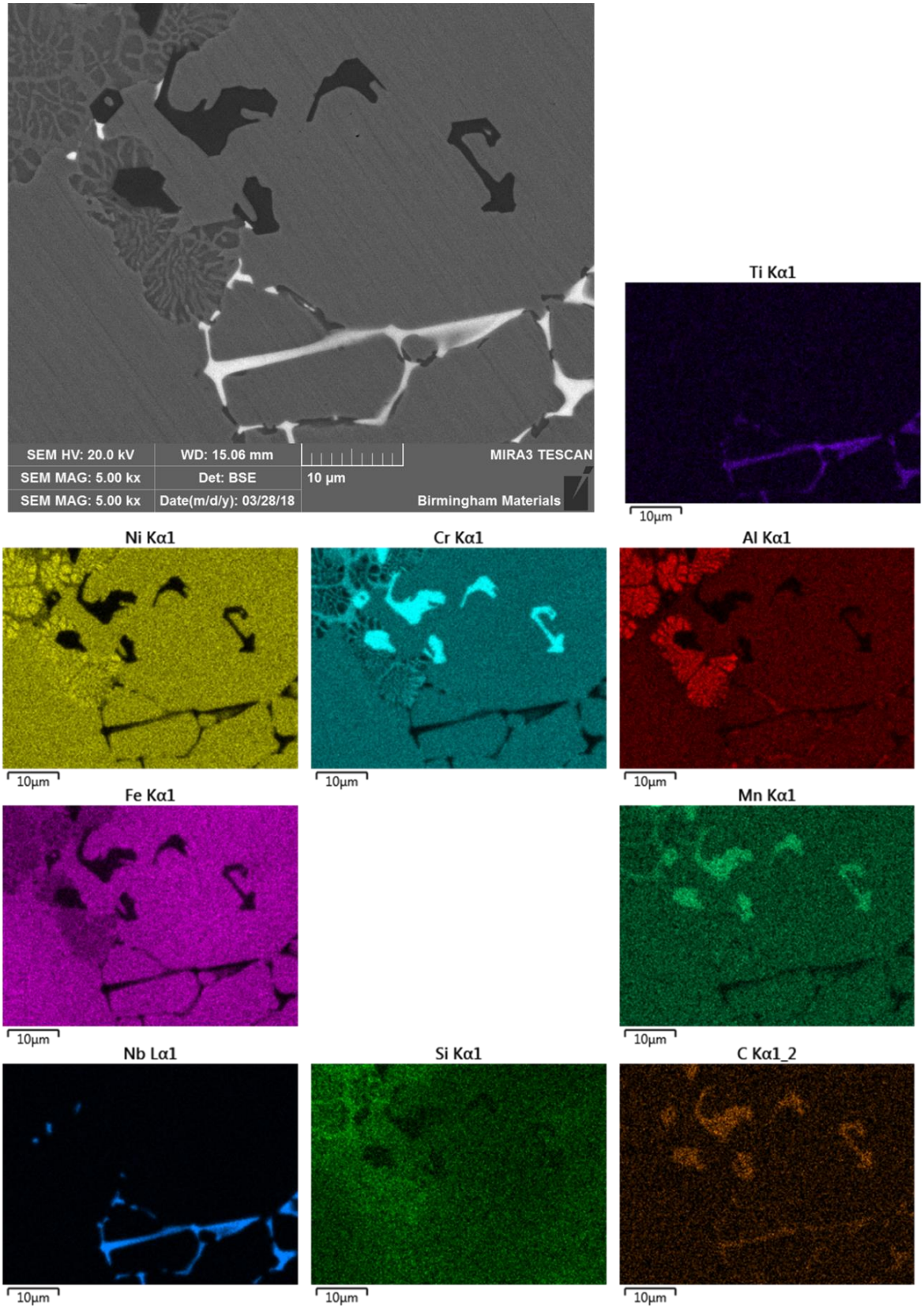

Figure 4.1.3-17 Higher magnification elemental mapping of the Low-Al alloy in the crossover region with the new phase.

4.1.3.2.3 Near Inner Diameter Region

At the near inner diameter region, the microstructure was similar to the Base alloy; with equiaxed grain structure and intergranular carbides. These maintained their more acicular nature compared with those in the Base alloy. The additional phase identified as a nickel and aluminium phase in the crossover region was also present, whilst the square titanium carbonitride phase identified in the near inner diameter region of the Base alloy was also found in the Low-Al alloy (Figure 4.1.3-18).

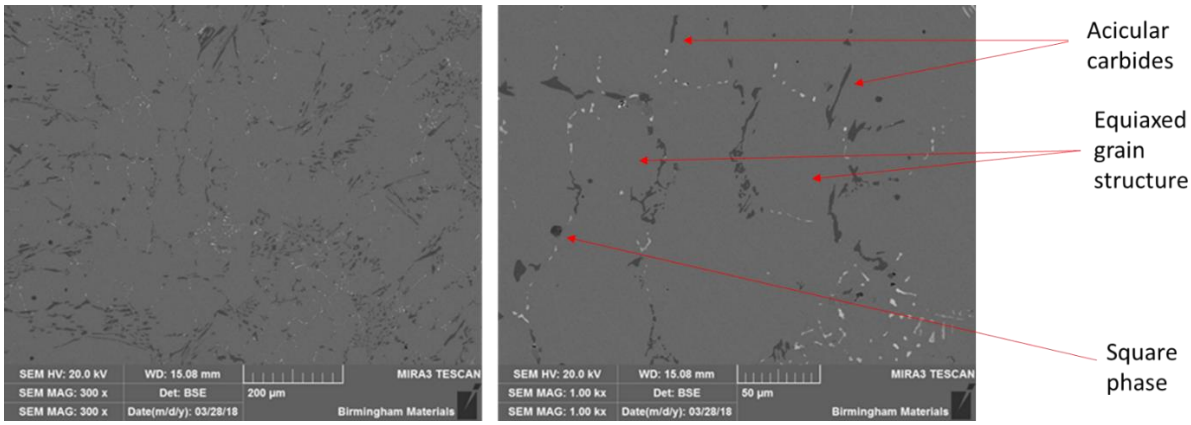

Figure 4.1.3-18 SEM backscattered images of near inner diameter region of Low-Al alloy highlighting features of the alloy microstructure.

Figure 4.1.3-20 shows the intergranular formation of the two carbides – chromium carbide and niobium carbide – and some formation of the nickel and aluminium phase in this near inner diameter region, as also seen in the crossover region. Titanium carbonitrides are again present in the near inner surface region of the alloy, indicated by the titanium elemental mapping in Figure 4.1.3-20.

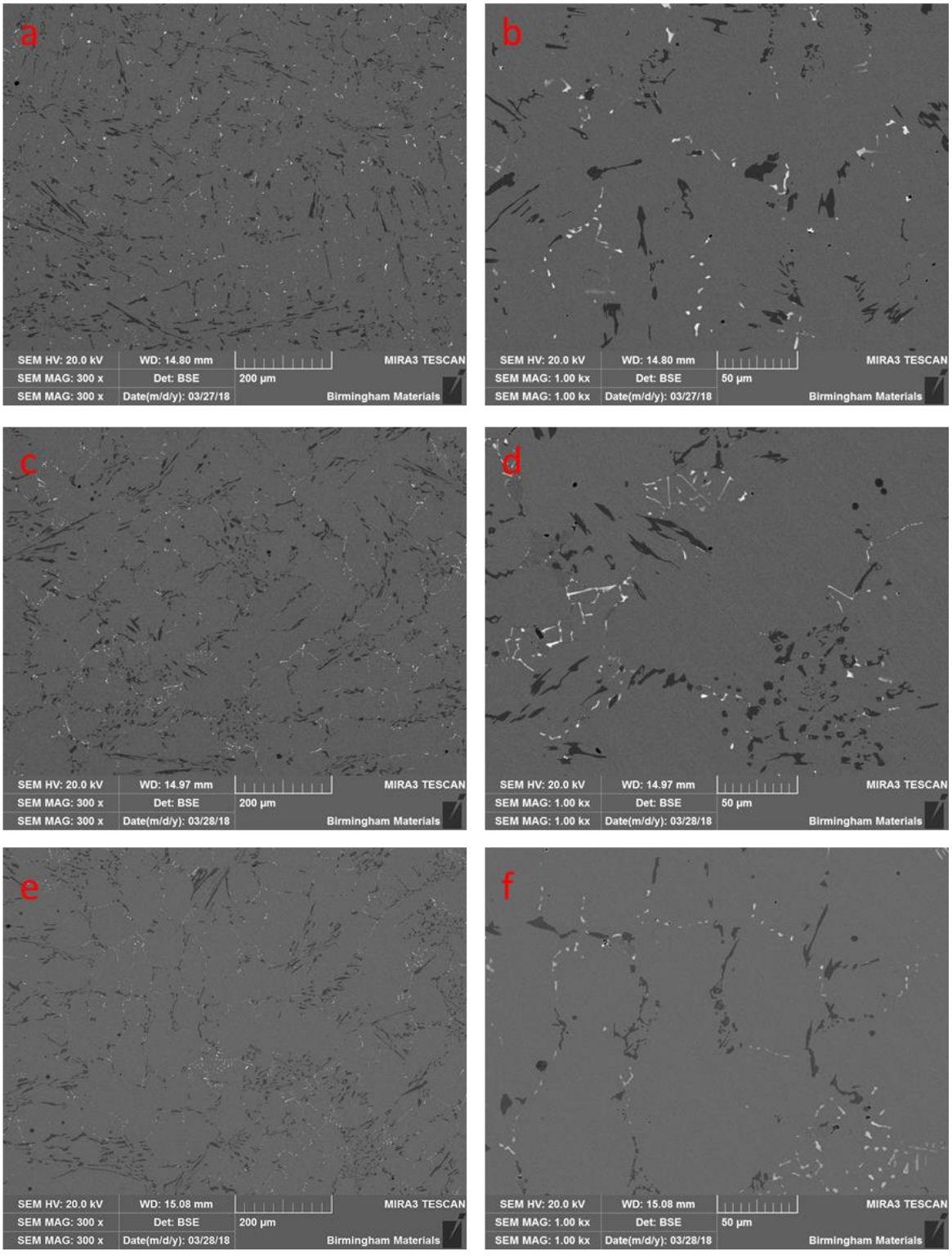

Figure 4.1.3-19: SEM backscattered images of the Low-Al alloy; near outer diameter region (a & b); crossover region (c & d); and near inner diameter region (e & f) showing the changing nature of the microstructure through the alloy.

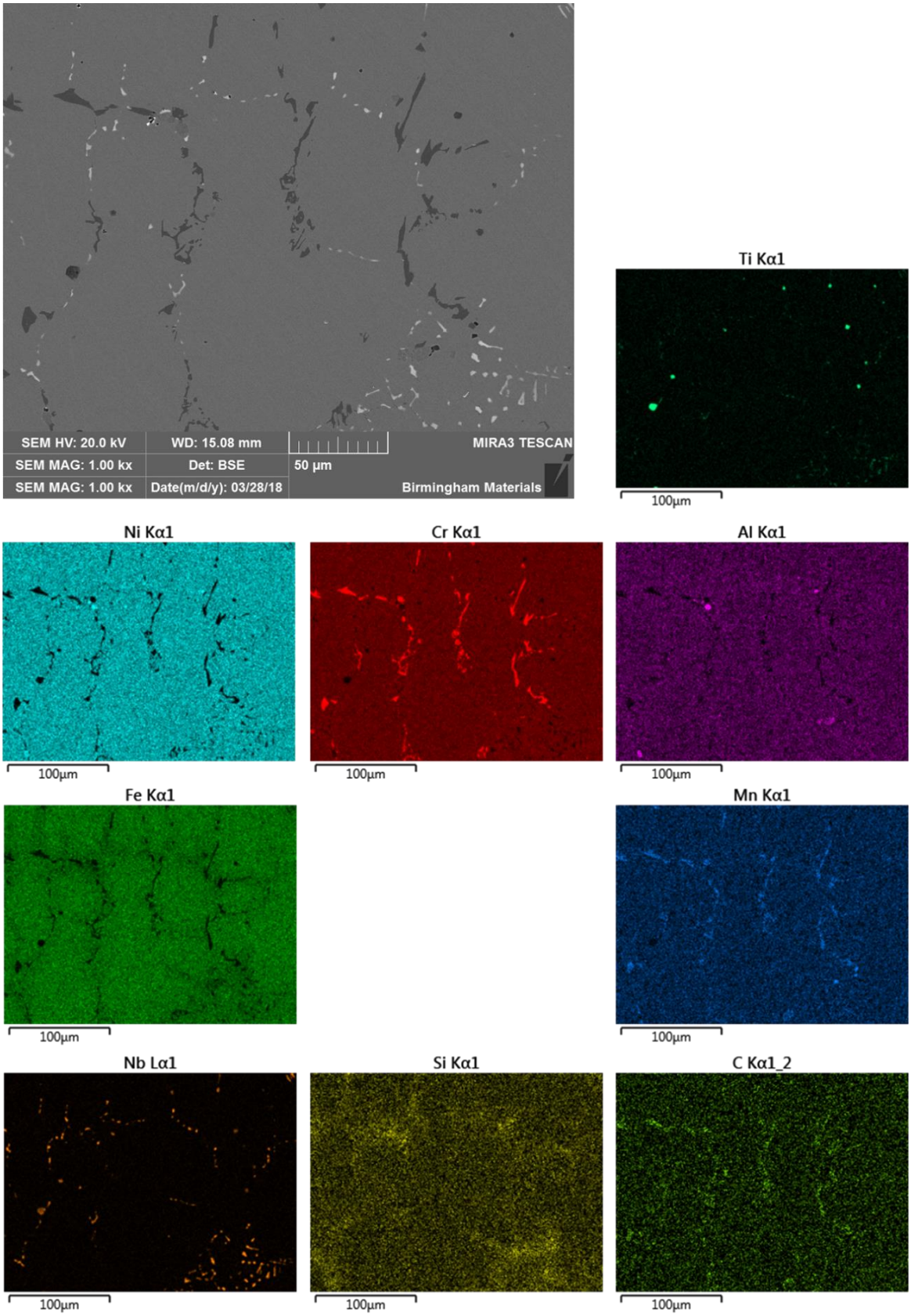

Figure 4.1.3-20 Elemental mapping of the near inner diameter region of the Low-Al alloy, showing titanium presence in the alloy

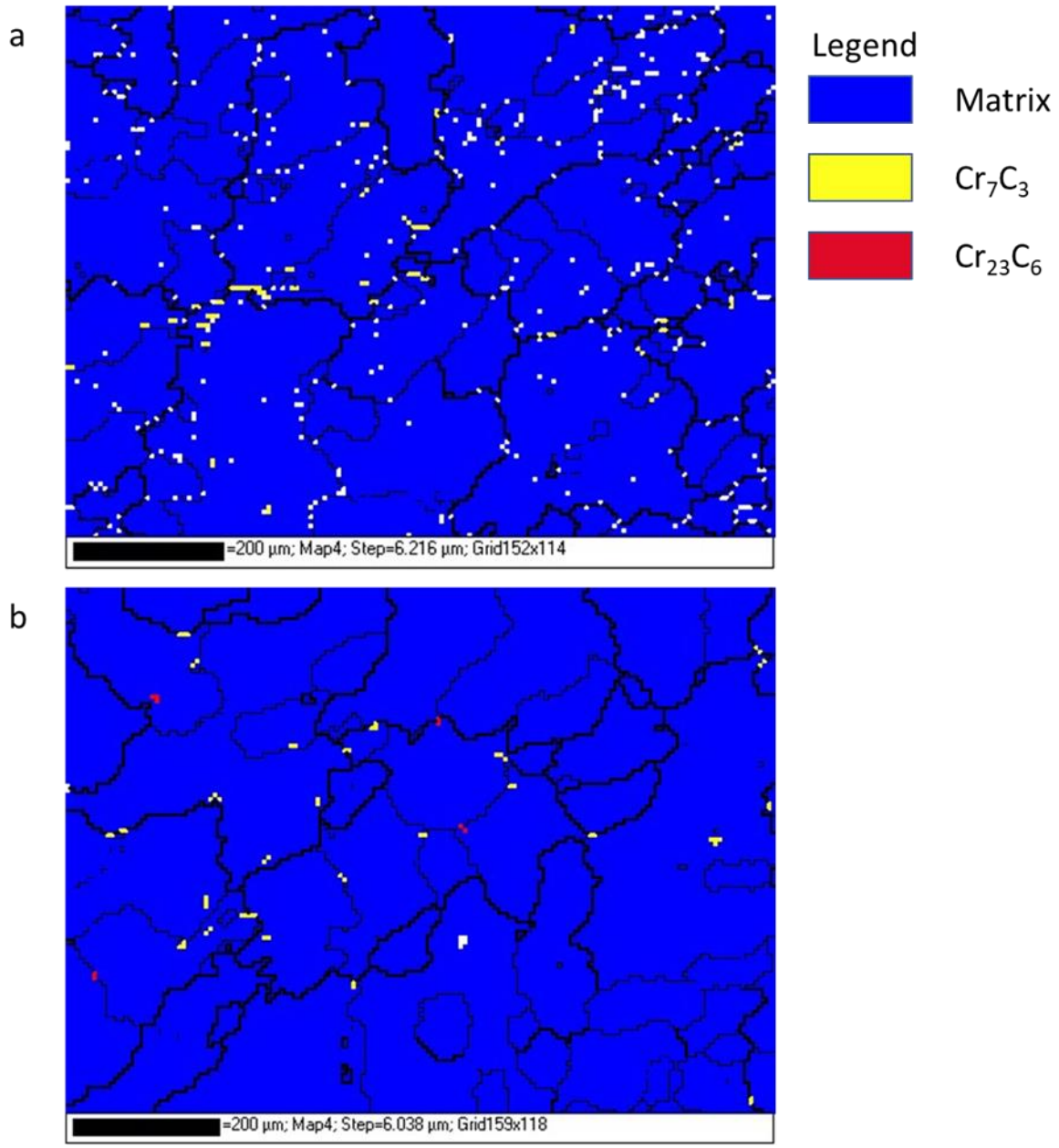

Figure 4.1.3-21: EBSD phase map of Low-Al alloy at: (a) Cross-over region and; (b) inner diameter region

4.1.3.3 High-Al alloy

The High-Al alloy displayed a dissimilar microstructure (Figure 4.1.3-22) to the two former alloys that were investigated; a dendritic structure in the near outer diameter region is evident, however fine carbide formation and widespread formation of the secondary phase is seen, which was only present sporadically through the crossover and near inner diameter region of the Low-Al alloy

(Figure 4.1.3-12 b-e). The carbides near the inner diameter showed large variability, with some faceted carbides seen in Figure 4.1.3-22 e and f measuring up to 50μm in diameter.

Grain size appeared more consistent throughout the alloy's depth; however, it displayed significantly large variability within regions - there were orders of magnitude of differences between the sizes of grains throughout the alloy, displaying an inconsistent nature in the grain growth. This could be due to the rapid formation of some of the abundant secondary phases before the solidification of the matrix, rather than after as was seen in the previous two alloys.

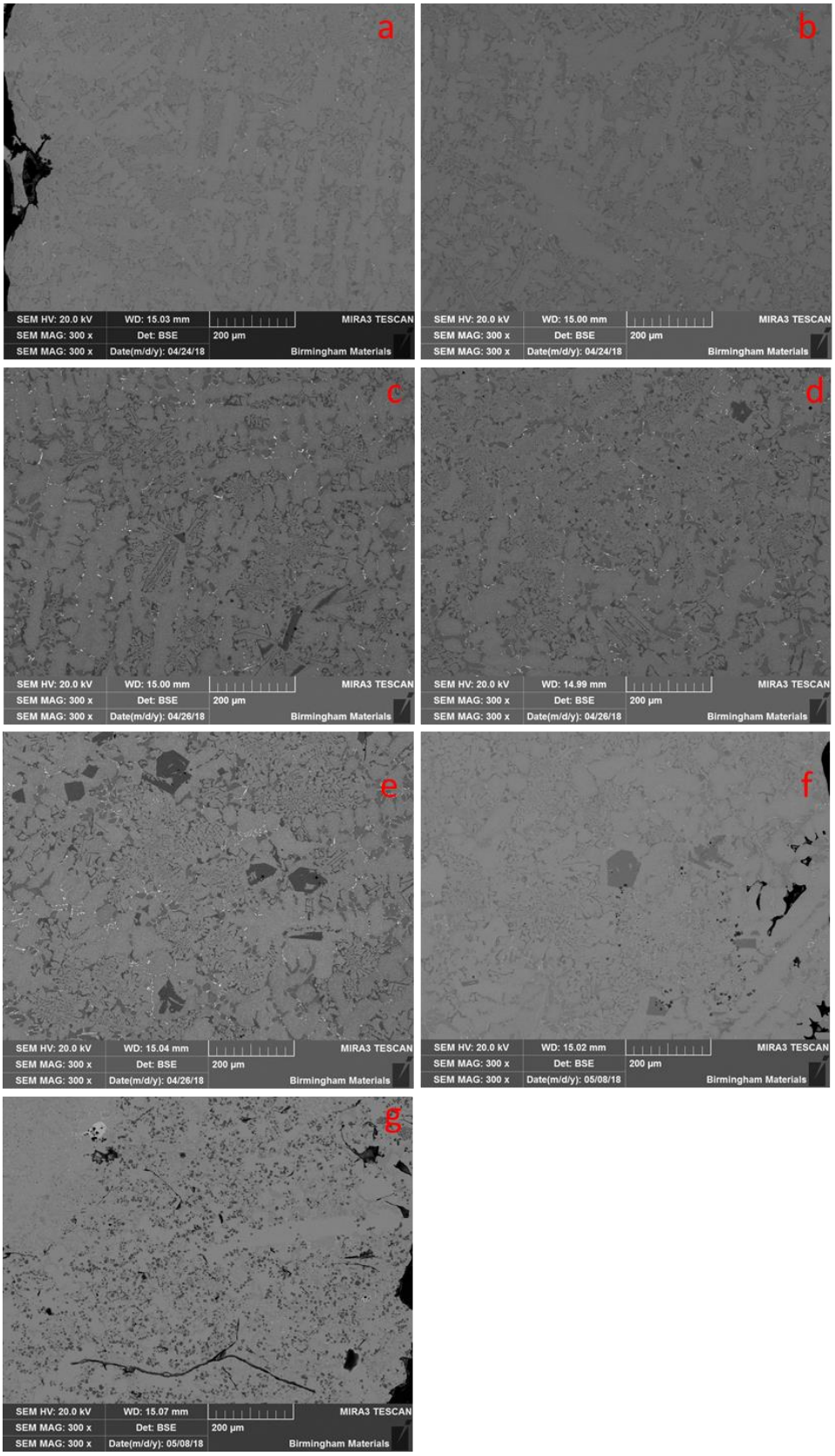

Figure 4.1.3-22 SEM backscattered images of High-Al alloy in the as cast state: Outer diameter (a); 4mm depth (b); 6mm depth (c); 8mm depth (d); 10mm depth (e); 12mm depth (f); Inner diameter (g) displaying significantly different microstructure compared to the Base and Low-Al alloys, with widespread carbide precipitation.

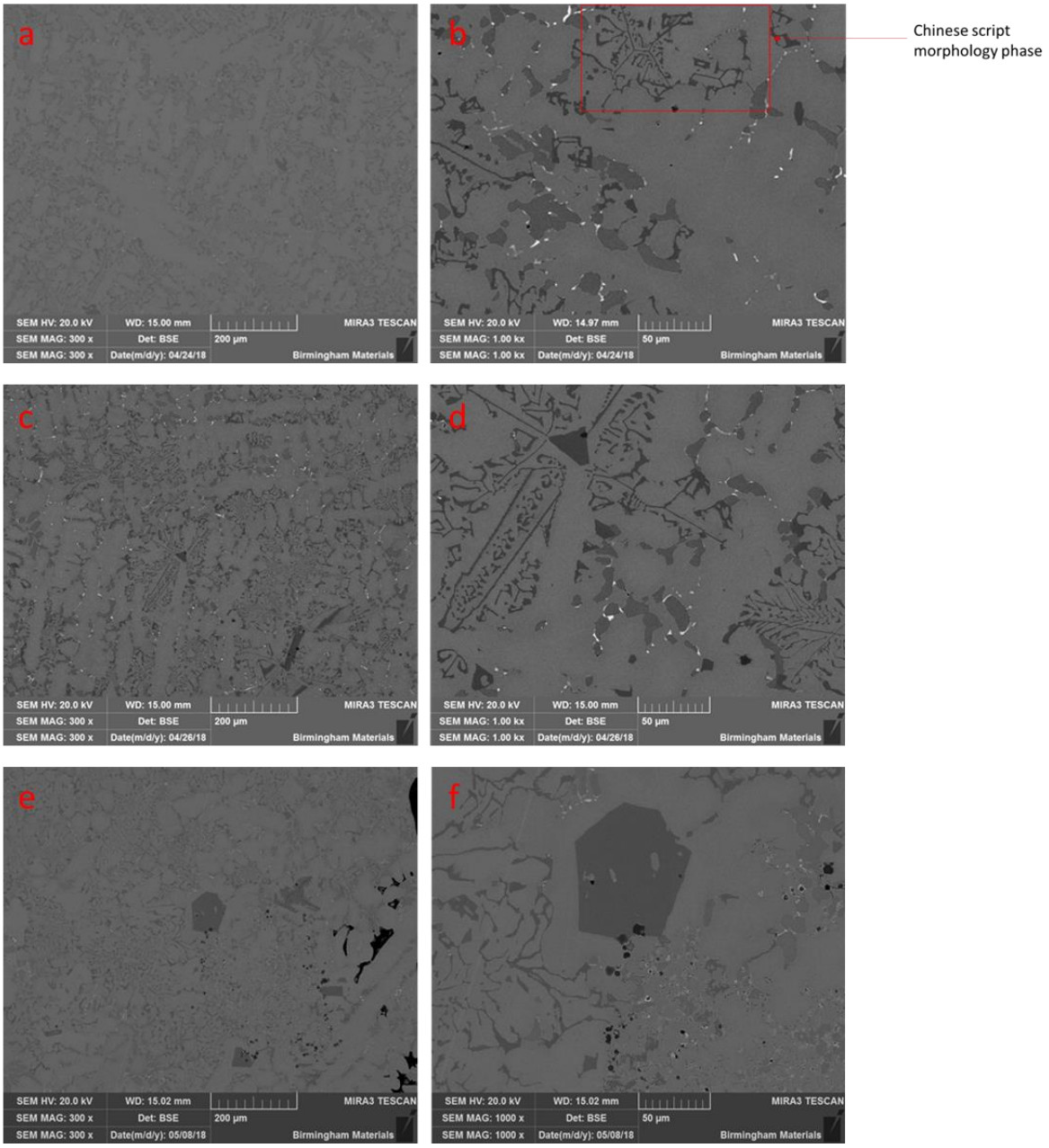

Figure 4.1.3-23:SEM backscattered image of High-Al alloy; near outer diameter region (a & b); crossover region (c & d); and near inner diameter region (e & f) showing facetted and Chinese scrip morphology carbides

4.1.3.3.1 Near Outer Diameter Region

The near outer diameter region (Figure 4.1.3-22 a-c) displayed a much higher volume fraction of the newly identified nickel and aluminium phase, whereas this was not present in the corresponding region of the Low-Al alloy. This falls in line with the JMatPro prediction of a four-fold increase in volume of the nickel and aluminium rich phase as displayed in Table 4.1.2-2. The other major difference between these two aluminium-containing alloys was the nature of the carbides.

Whilst they were found to be acicular in nature in the Low-Al alloy, in the High-Al alloy they are characterized as 'Chinese script' morphology, as indicated in Figure 4.1.3-23 a & b. This formation was a result of slower cooling rates of the alloy, which resulted in the interconnection of the carbides in the interdendritic space of the solidifying matrix (42).

The significant difference that was seen between the Low-Al and High-Al alloys was the alloy wide presence of the nickel and aluminium phase in the High-Al alloy, confirmed in Figure 4.1.3-24. This was sparse in the Low-Al alloy and only found closer to the inner diameter. This was due to the greater aluminium content in this alloy allowing for the formation of this phase even at the pipe's outer diameter surface. The microstructure was dissimilar, displaying the formation of the 'Chinese script' chromium carbides in this alloy, and they appeared to be less evenly spaced through the alloy, with the growth of the nickel and aluminium phase clearly developing preferentially in some regions.

The niobium carbides were again present, however they occurred much more readily on the surfaces of the nickel and aluminium phase, rather than in contact with the chromium carbide as was seen in the Low-Al and Base alloys.

This demonstrated the change in solidification sequence of the alloy, with the niobium carbide formed after the chromium carbide, with the chromium carbides found in significantly higher volumes, demonstrating the greater affinity for carbon of the chromium in this alloy. The niobium carbides only form after the chromium carbides, with more veined carbides indicating the formation due to ejection of niobium from the matrix and then subsequent carbide formation. This is confirmed by the reduced niobium carbide content in this alloy. These differences are evident in Figure 4.1.3-25.

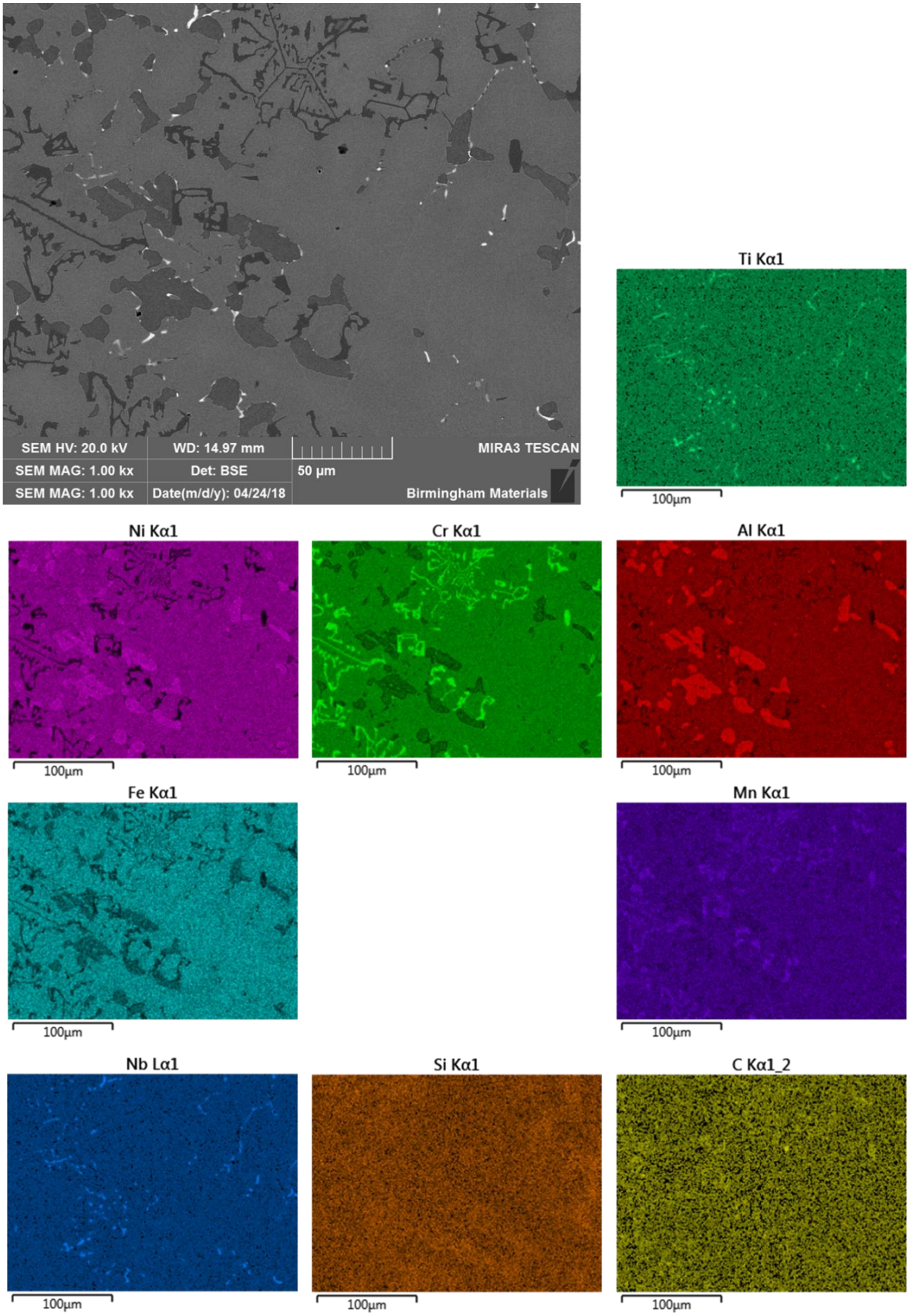

Figure 4.1.3-24 Elemental mapping of High-Al alloy in the near outer diameter region, with widespread aluminium and nickel rich phase and chromium carbide presence.

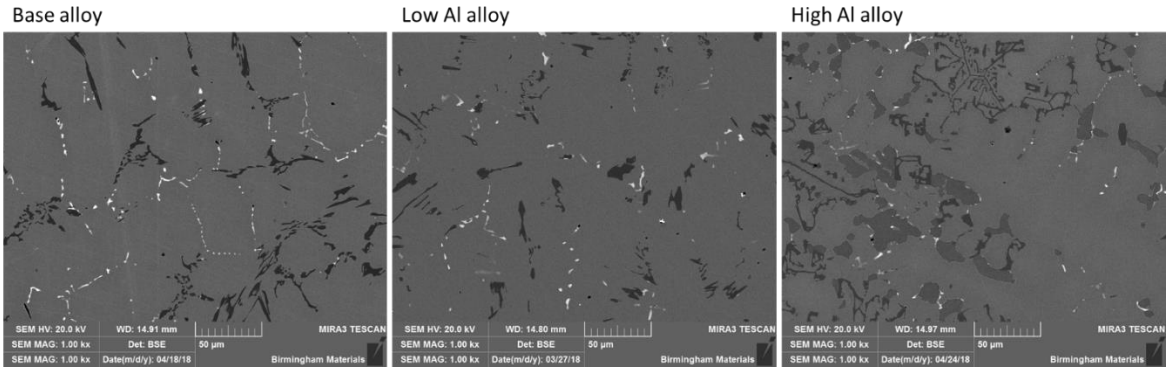

Figure 4.1.3-25: Backscattered images of Base, Low-Al and High-Al alloy matrix demonstrating change in volume of carbides between the three alloys.

4.1.3.3.2 Crossover Region

The crossover region from 6mm to 10mm (Figure 4.1.3-23 c & d) also showed a mixture of dendritic and equiaxed grain structure, and displayed the formation of much larger, faceted carbides in the alloy accompanying the 'Chinese script' carbides. The grains appeared significantly more varied in size than those seen in the previous two alloys, with some much larger grains present and regions of much finer grain structure overall, displaying a less consistent matrix than the previous two alloys. The faceted carbides demonstrated characteristic hexagonal morphology of the Cr_7C_3 carbide (127).

The prevalence of the aluminium and nickel phase appeared to be even greater in the area closer to the inner diameter of the pipe (Figure 4.1.3-26), again due to the lower atomic mass of the aluminium resulting in migration of the element closer to the inner diameter during the centrifugal casting process.

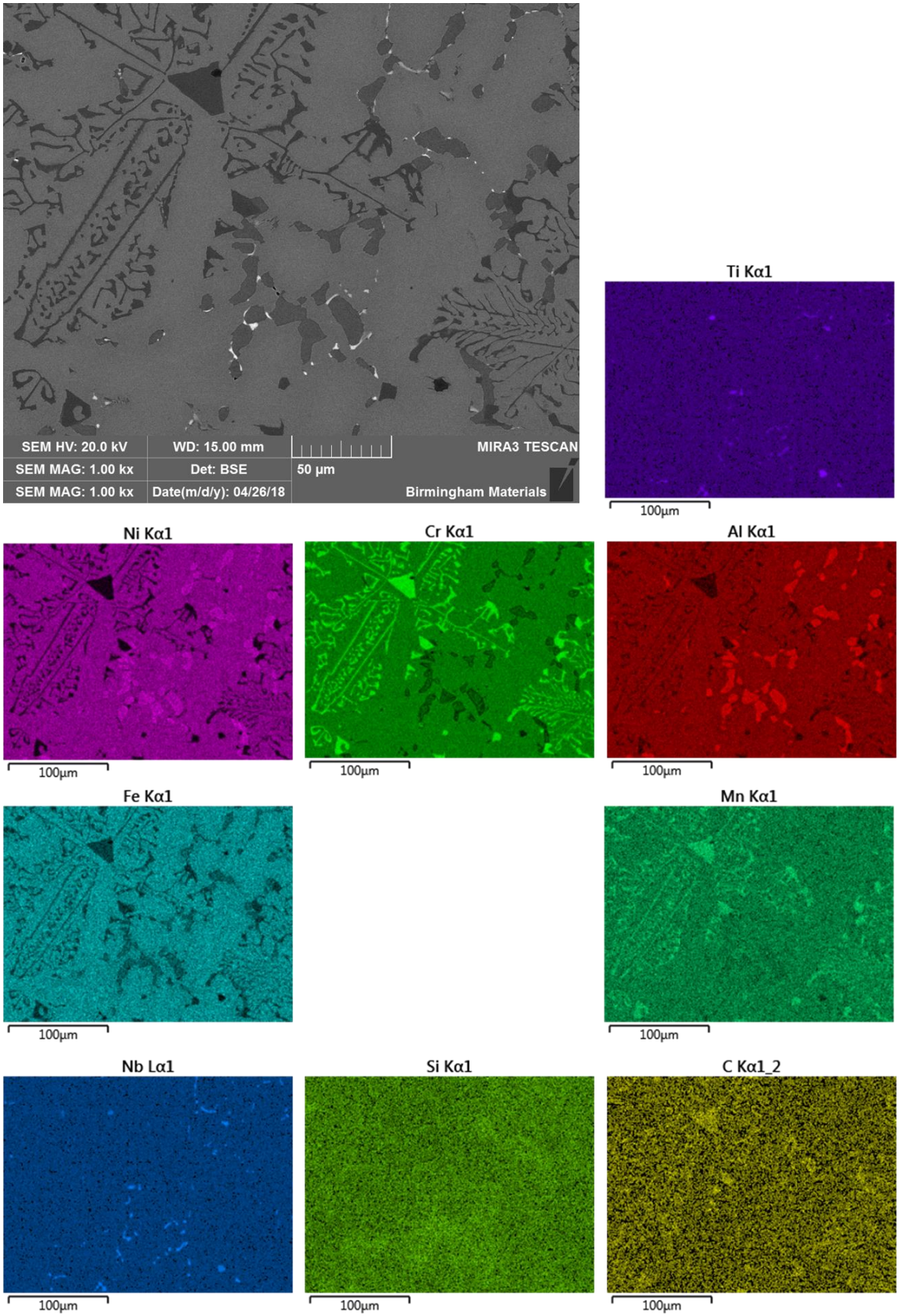

Figure 4.1.3-26 Elemental mapping of High-Al alloy in the crossover region, showing the facetted and scrip like carbides.

4.1.3.3.3 Near Inner Diameter Region

At the near inner diameter region (Figure 4.1.3-23 e & f), the microstructure was consistent with the other alloys investigated, with a fully equiaxed grain structure and the presence of the square phase, whilst overall the High-Al alloy maintained the inconsistent matrix nature, with differing carbide morphology. The carbides display two vastly differing morphologies; the Chinese script morphology as previously identified in the outer diameter region and the crossover region, and the large faceted carbides which are more frequently found in the cross over region and the near inner diameter region.

The near inner diameter region showed the equiaxed grain structure and the presence of square titanium carbonitrides. These titanium carbonitrides were formed during the casting process through the reaction between the constituent titanium and the nitrogen in the air atmosphere in which the casting took place. Due to the significantly high melting point of titanium carbonitride this phase solidified rapidly and formed as slag within the casting alloy. This phase is significantly lighter than the majority of the other elements in the alloy, and thus the centrifugal force acting towards the outer diameter acted on the heavier elements to a much greater degree, leading to the accumulation of the titanium carbonitride phase almost exclusively on the very inner surface of the pipe during casting. Another new phase found in this alloy was one of fine particles of yttrium oxide, as seen in Figure 4.1.3-27. This was caused by a reaction of the yttrium with oxygen in the air during casting. Despite the high density of yttrium, this phase finished close to the inner surface of the alloy after the completion of the casting process due to being pushed to the inner diameter on the melt front, rather than solidifying in the matrix. The presence of this phase was due to the significantly higher yttrium content added to this alloy compared to the other three alloys, as shown in Table 4.1.1-1.

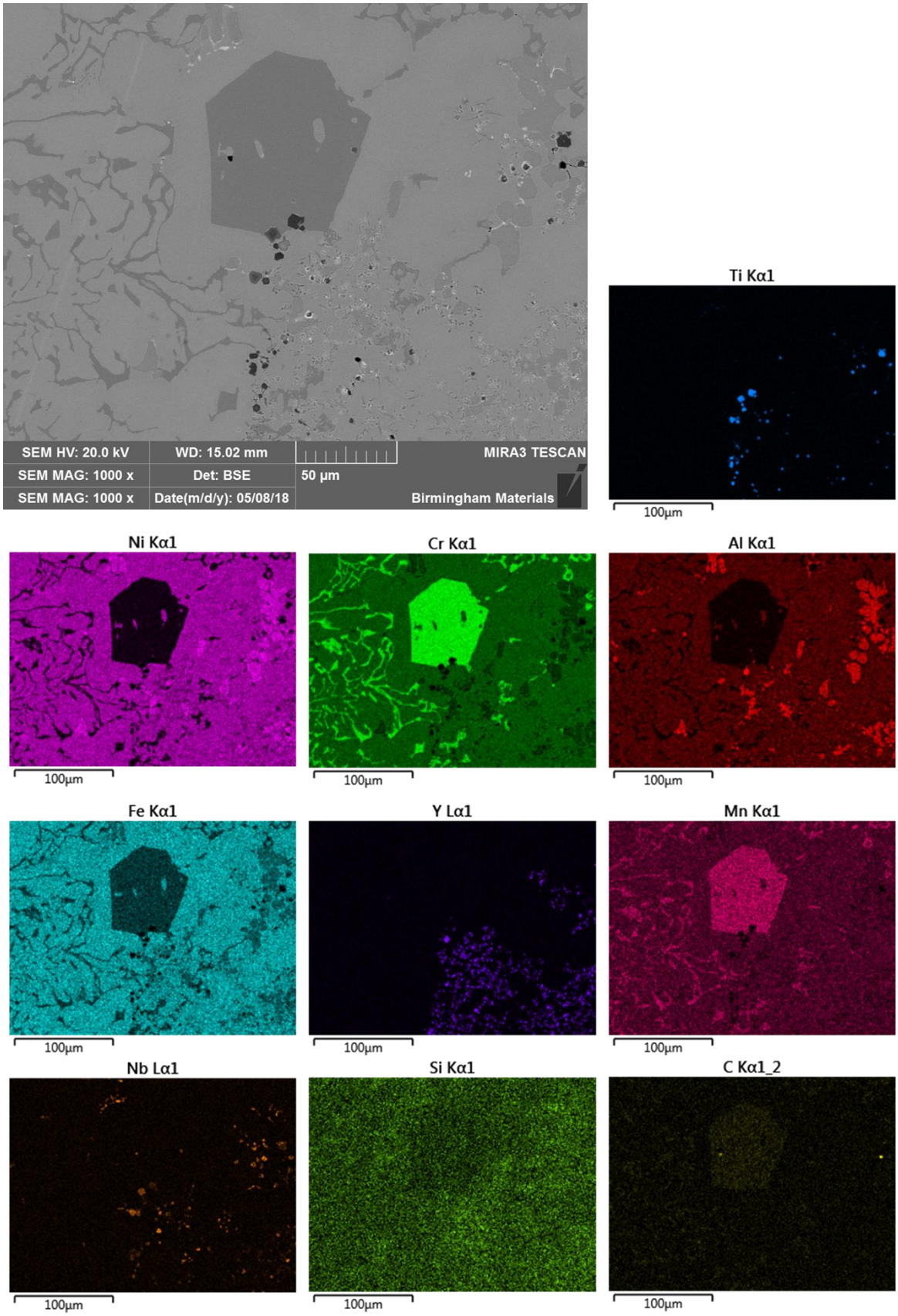

Figure 4.1.3-27 Elemental mapping of High-Al alloy in the near inner diameter region with a large faceted carbide, as well as titanium and yttrium presence.

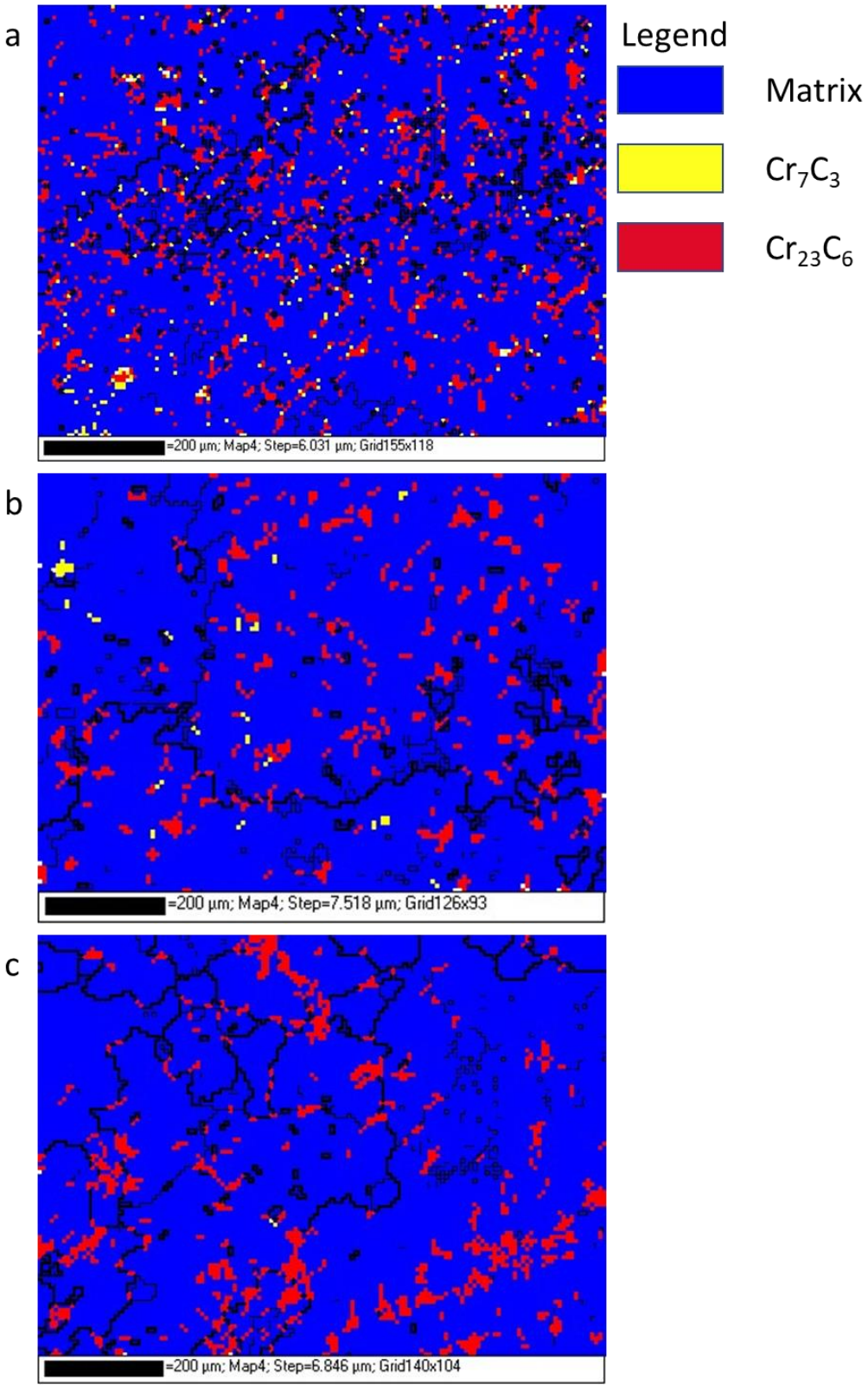

Figure 4.1.3-28: EBSD phase map of High-Al alloy at: (a) Outer diameter region; (b) cross-over region and; (c) inner diameter region

4.1.3.4 Optim-Al alloy

The Optim-Al alloy, similar to the other alloys, displayed the same dendritic grain growth characterized in the near outer diameter region by all four alloys, shown in Figure 4.1.3-33 a & b. The chromium and niobium carbides also appeared present, as with the other three alloys investigated, however they appeared to be significantly reduced in volume and decreased in size in comparison to the others. This matched the reduction of carbon in this alloy compared to the others investigated, resulting in a reduction in the carbide formation. This apparent raised matrix chromium content mentioned previously is in line with this finding, with more chromium staying in solution in the matrix with reduced availability of carbon present to form carbides. The carbide morphology was more similar in nature to that seen in the Base alloy when compared to the more acicular nature of the Low-Al alloy and the 'Chinese script' morphology seen in the High-Al alloy, which was caused by low cooling rates.

Thinner pipe thickness of the Optim-Al alloy compared to the other alloys resulted in faster cooling rates, which in turn has a large effect on the microstructure, as observed in the microstructure of the High-Al alloy.

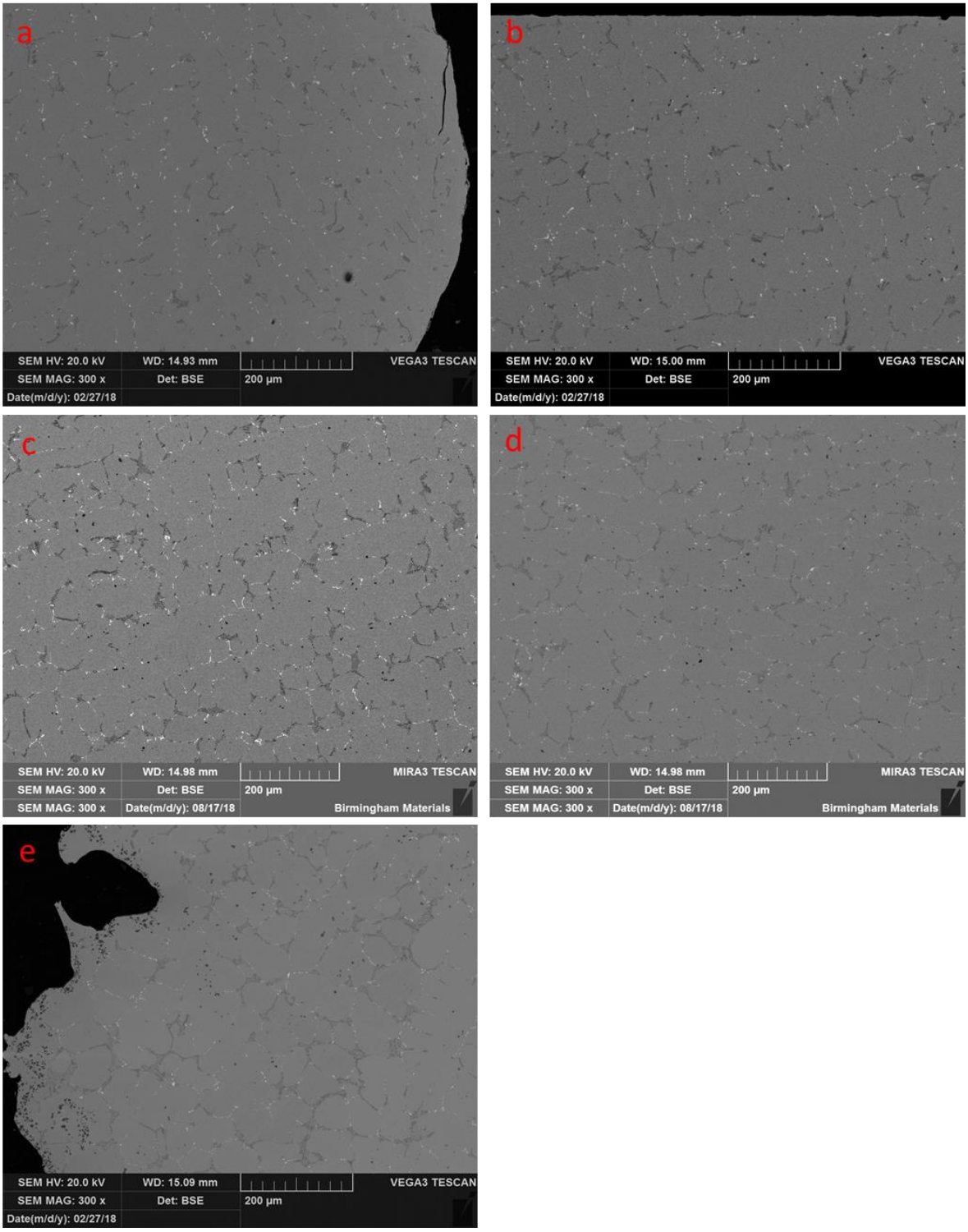

Figure 4.1.3-29 SEM backscattered images of Optim-Al alloy in the as cast state: Outer diameter (a); 4mm depth (b); 6mm depth (c); 8mm depth (d); Inner diameter (e) demonstrating the carbide morphology and position.

4.1.3.4.1 Near Outer Diameter Region

The reduction in carbon in this alloy (Table 4.1.1-1) is noticeable with the decrease in volume of carbides found in the alloy (Figure 4.1.3-29). The vastly reduced number of carbides compared to

the other three alloys was clearly evident in Figure 4.1.3-30, with chromium carbide size appearing marginally reduced compared to the Base and Low-Al alloys which displayed similar morphology carbides. This is reflective of the modelled composition, with total chromium carbide formation predicted to be between half and two thirds that of the other aluminium containing alloys (Table 4.1.2-2). The niobium carbides were also finer in appearance; both observations reinforcing the expected reduction due to the lower carbon content.

There is some formation of a yttrium rich phase, on the very outer diameter surface, which due to its heavy nature is much more likely to present at the outer diameter when cooling rates are high enough to entrap the particles, rather than moving with the melt front to the inner diameter, as was the case with the High-Al alloy. A titanium rich phase is present, which is seen across all four alloys, however it is usually found at the inner diameter (Figure 4.1.3-31). The titanium rich phase is present near the outer diameter in this alloy as the titanium is not fully oxidised, thus maintaining a more metallic nature, and being entrapped in the rapidly solidifying metal matrix. Furthermore, bonding to the heavy yttrium phase further reduces the ability to move towards the inner pipe diameter. These were both considered slag entrapments caused by the rapid cooling that occurs on contact with the surface of the mould, and therefore this slag was unable to travel through the molten alloy to end up on the inner surface.

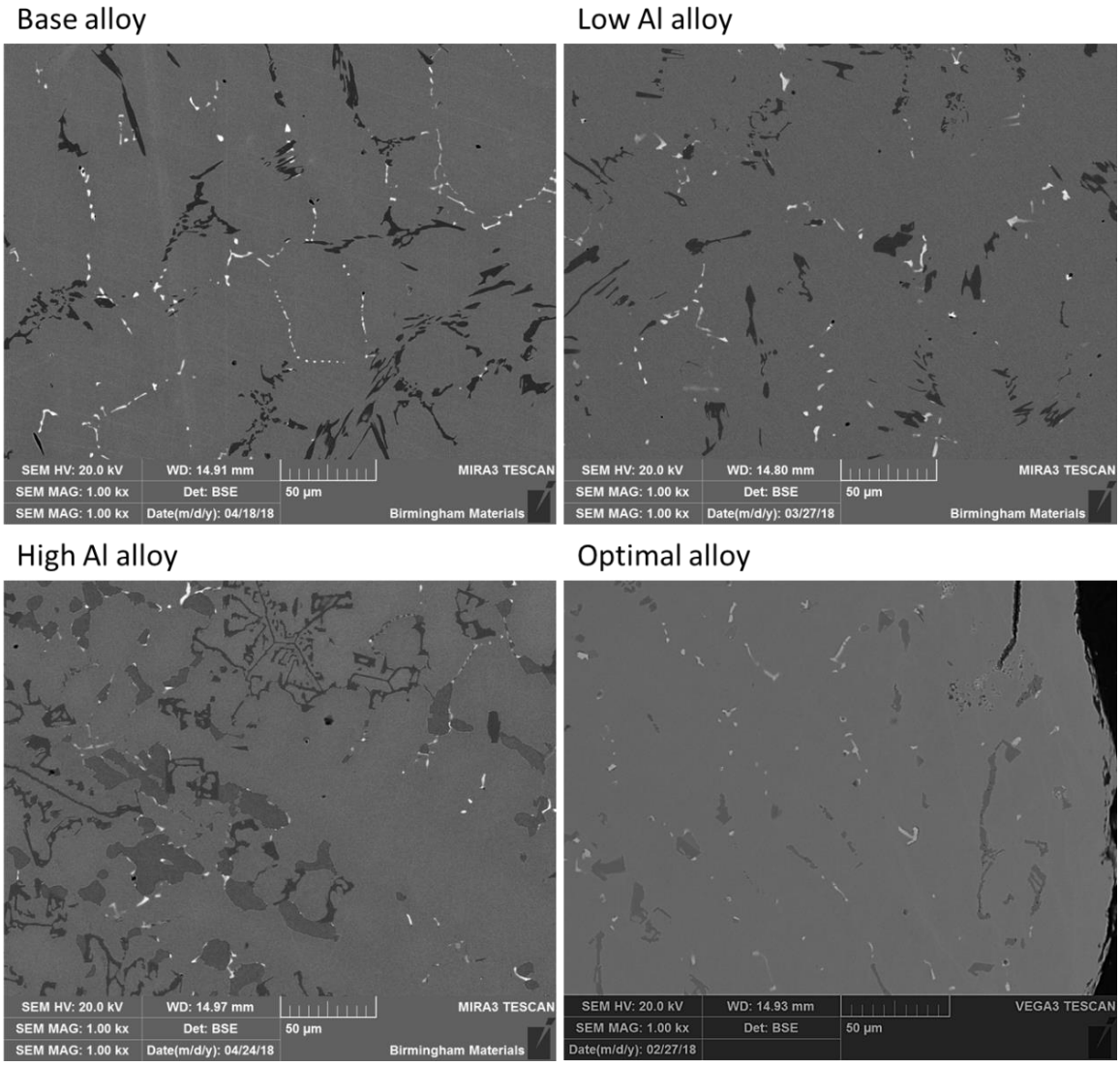

Figure 4.1.3-30: Backscattered images of all four alloys demonstrating differences in carbide size and distribution.

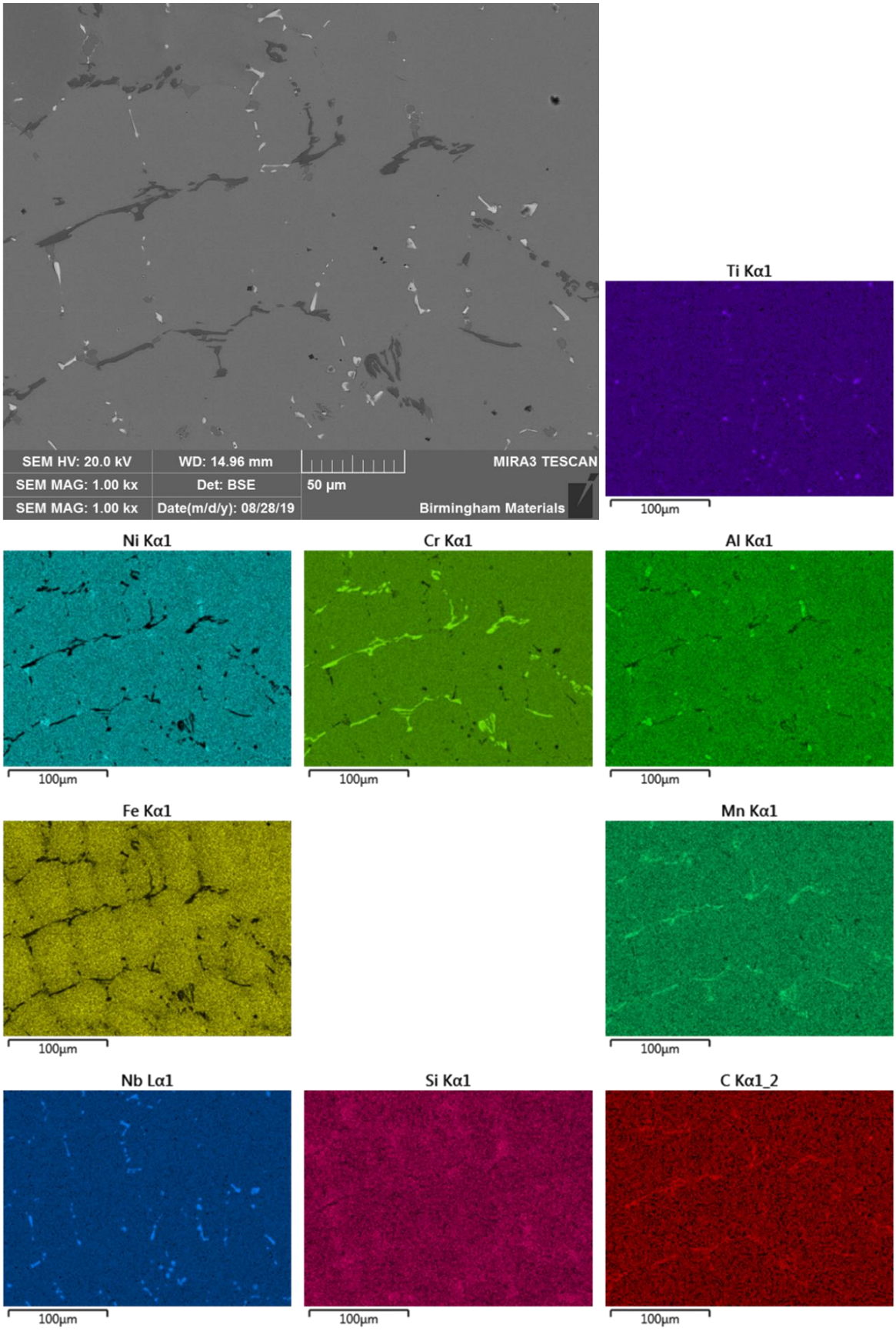

Figure 4.1.3-31 Elemental map of Optim-Al alloy near outer diameter region.

4.1.3.4.2 Crossover Region

The cross over region appeared to occur at a shallower depth compared with the other alloys, with some equiaxed grain growth evident in the 4mm region (Figure 4.1.3-29 b). The volume of the Ni_3Al phase appeared to be much more similar to that seen in the Low-Al alloy, with sparse formation of this phase found throughout the crossover region (Figure 4.1.3-33 d), and again a reduced carbide presence is observed.

Figure 4.1.3-32 shows continuation of the reduced presence of carbides throughout the alloy, and the presence of the nickel and aluminium phase in similar quantities compared to the Low-Al alloy. Other than this reduced carbide content the microstructure was widely similar to the Low-Al alloy. There was evidence of titanium carbonitrides being present throughout the alloy which was the main difference, with Figure 4.1.3-29 showing the dark, square phase occurring sporadically throughout the alloy, unlike the other alloys. This alloy contained five times the titanium content compared to the Base alloy (Table 4.1.1-1) therefore the increased prevalence of titanium rich precipitates was to be expected. The presence of titanium carbonitrides through the alloy is due to the more rapid cooling rate, entrapping the light particles rather than allowing them to all flow to the inner diameter at the melt front.

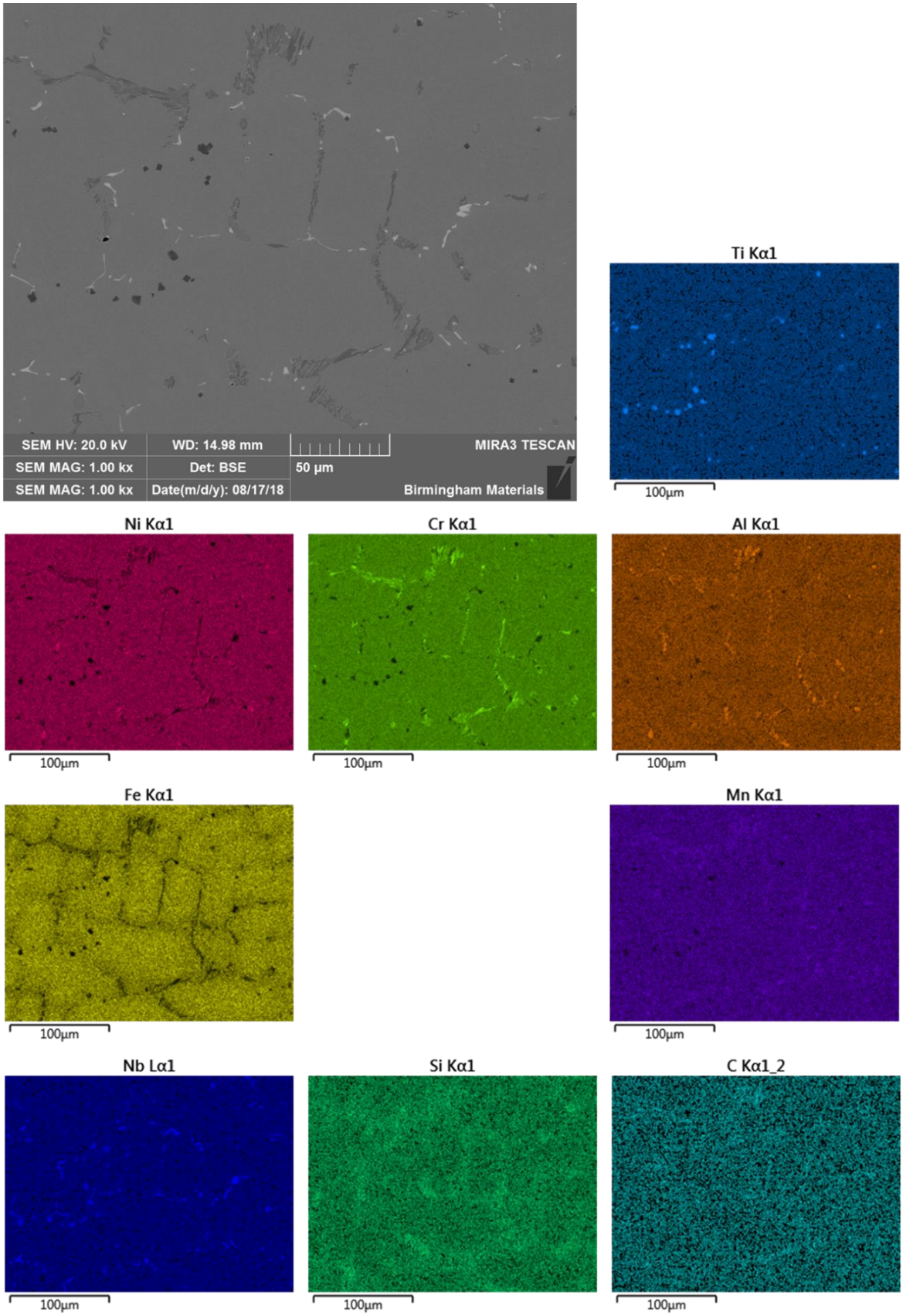

Figure 4.1.3-32 Elemental mapping of Optim-Al alloy crossover region showing titanium rich phase presence.

4.1.3.4.3 Near Inner Diameter Region

The depth of the near inner diameter region also appeared to be reduced, with the solely equiaxed grain structure only clearly present at the inner diameter (Figure 4.1.3-29 e, Figure 4.1.3-33 e & f). This is explained by the method of production of this alloy – the sample created was significantly thinner than the other three alloys, measuring at around 10mm in thickness, compared to 16mm average thickness of the other three alloys. With the faster cooling rates which accompanied this change, the depth of the fully equiaxed structure would be reduced, found solely close to the inner diameter as this has the longest cooling rate, however still faster than that of the other alloys at their inner diameters.

The secondary phases appeared to be very similar to those seen in the Low-Al alloy – the carbides, the Ni_3Al secondary phase and the square titanium carbonitride phase found solely at the extreme inner surface. The niobium carbides were found in contact with the chromium carbides, as was the case with the Base and Low-Al alloy, demonstrating the difference between these alloys and the High-Al alloy which had a slower cooling rate.

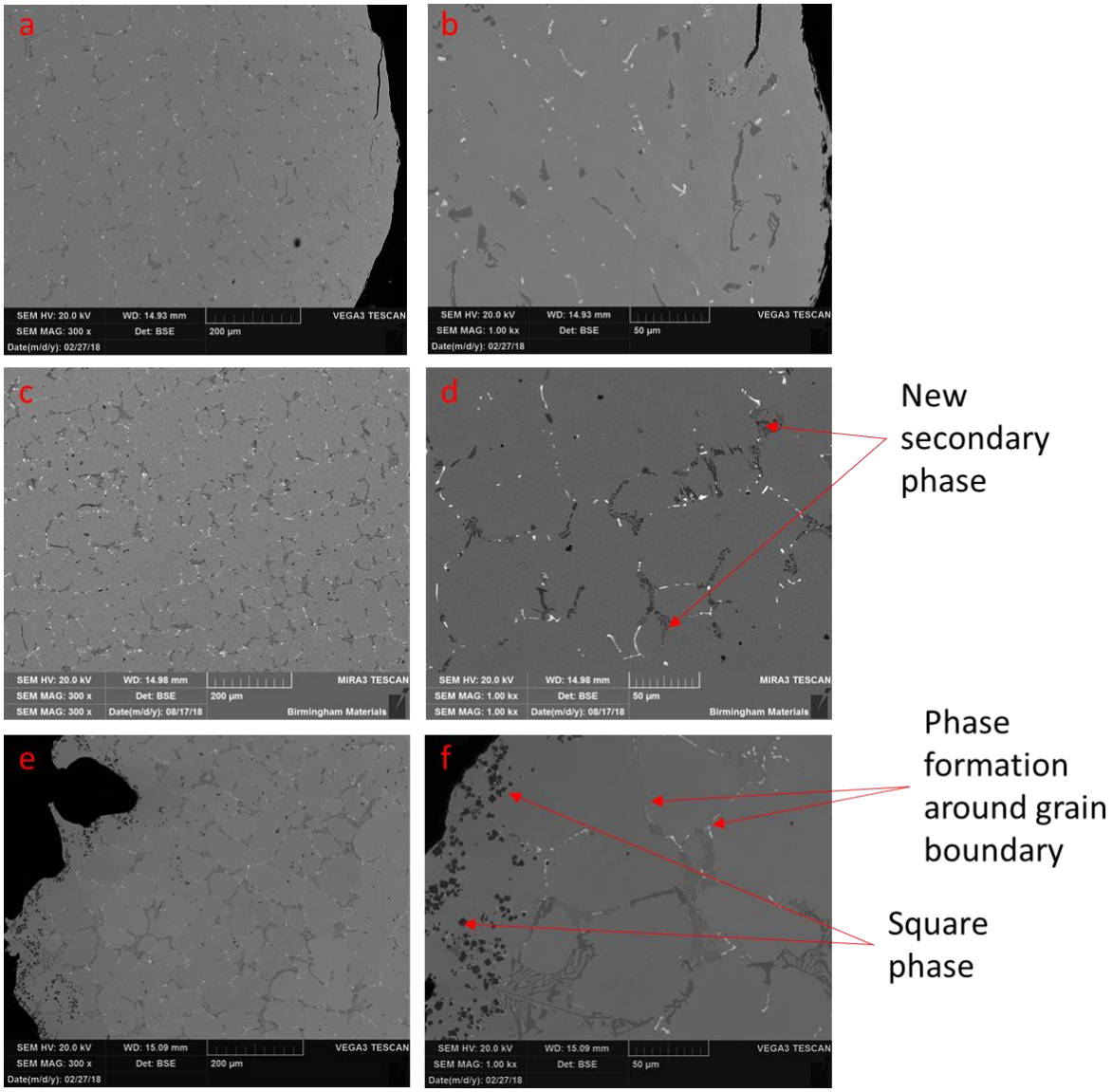

Figure 4.1.3-33: SEM backscattered images of the Optim-Al alloy; near outer diameter region (a & b); crossover region (c & d); and near inner diameter (e & f) displaying changes in microstructure features through the alloy thickness.

The near inner diameter region was broadly similar to the Base and Low-Al alloys, with titanium carbonitrides being present in large quantities near the surface (Figure 4.1.3-35), whilst similar secondary phases were identified throughout.

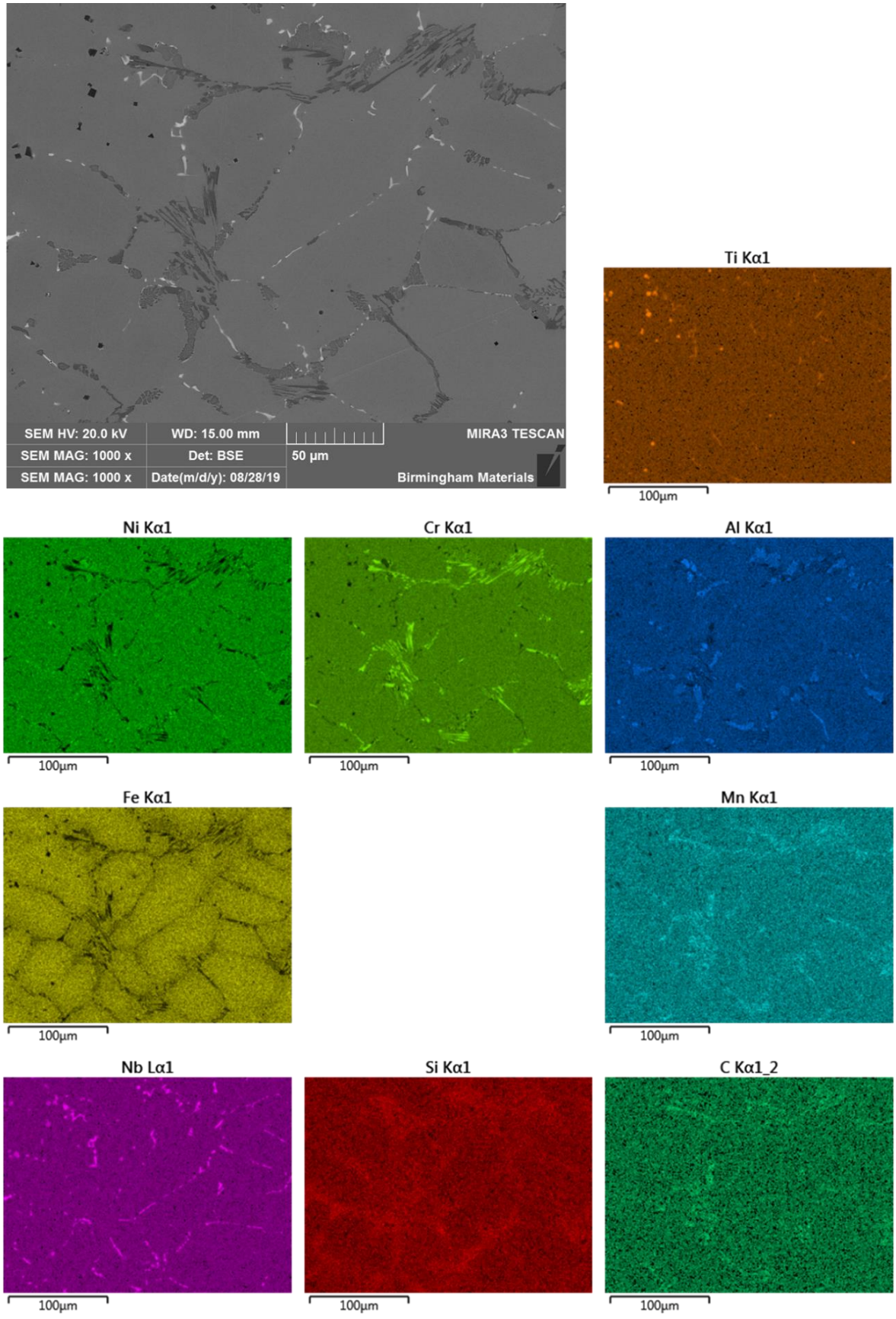

Figure 4.1.3-34: Elemental map of Optim-Al alloy at near inner diameter region

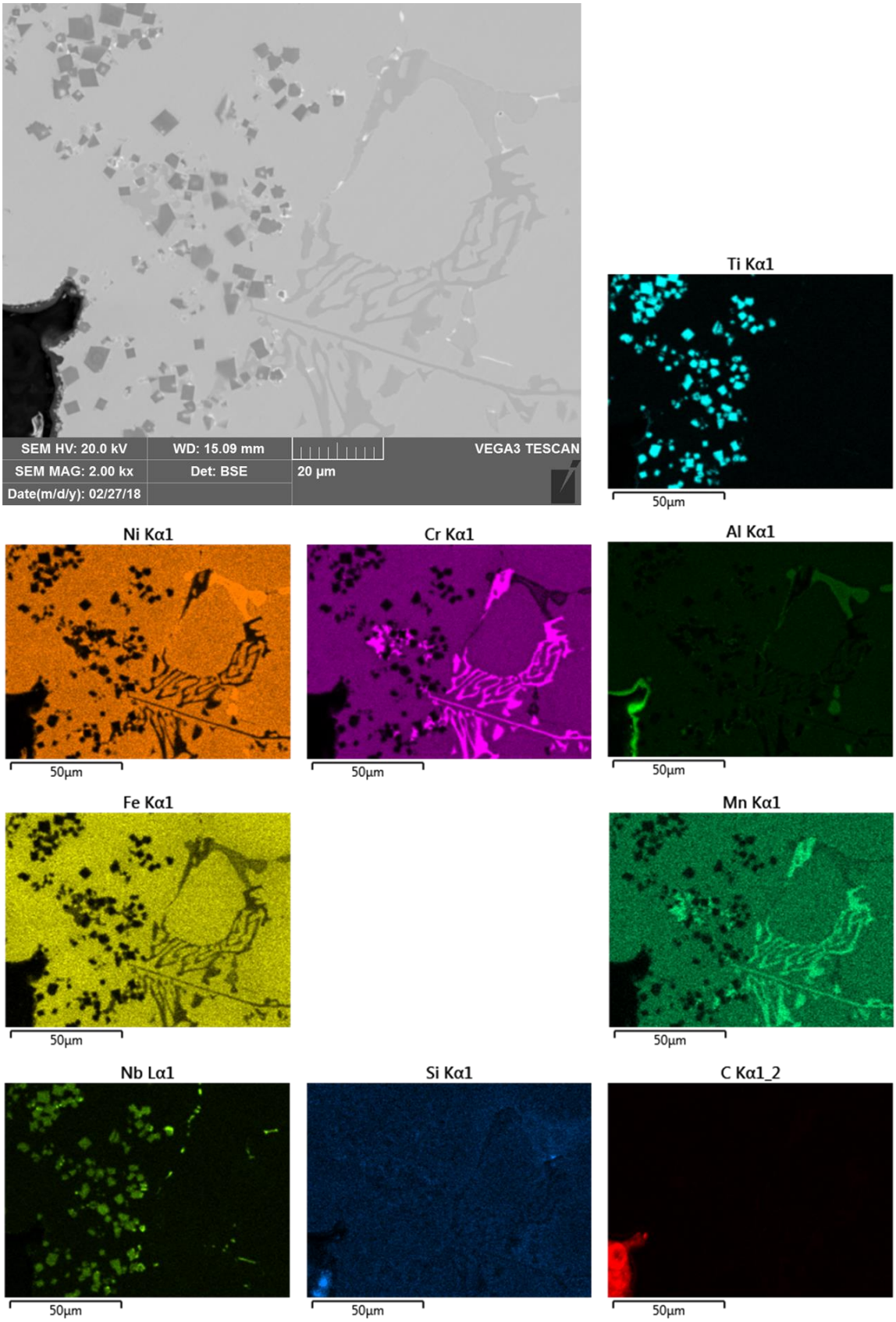

Figure 4.1.3-35: Elemental map of Optim-Al alloy at near inner diameter region higher magnification showing titanium and niobium rich phases at inner diameter surface,

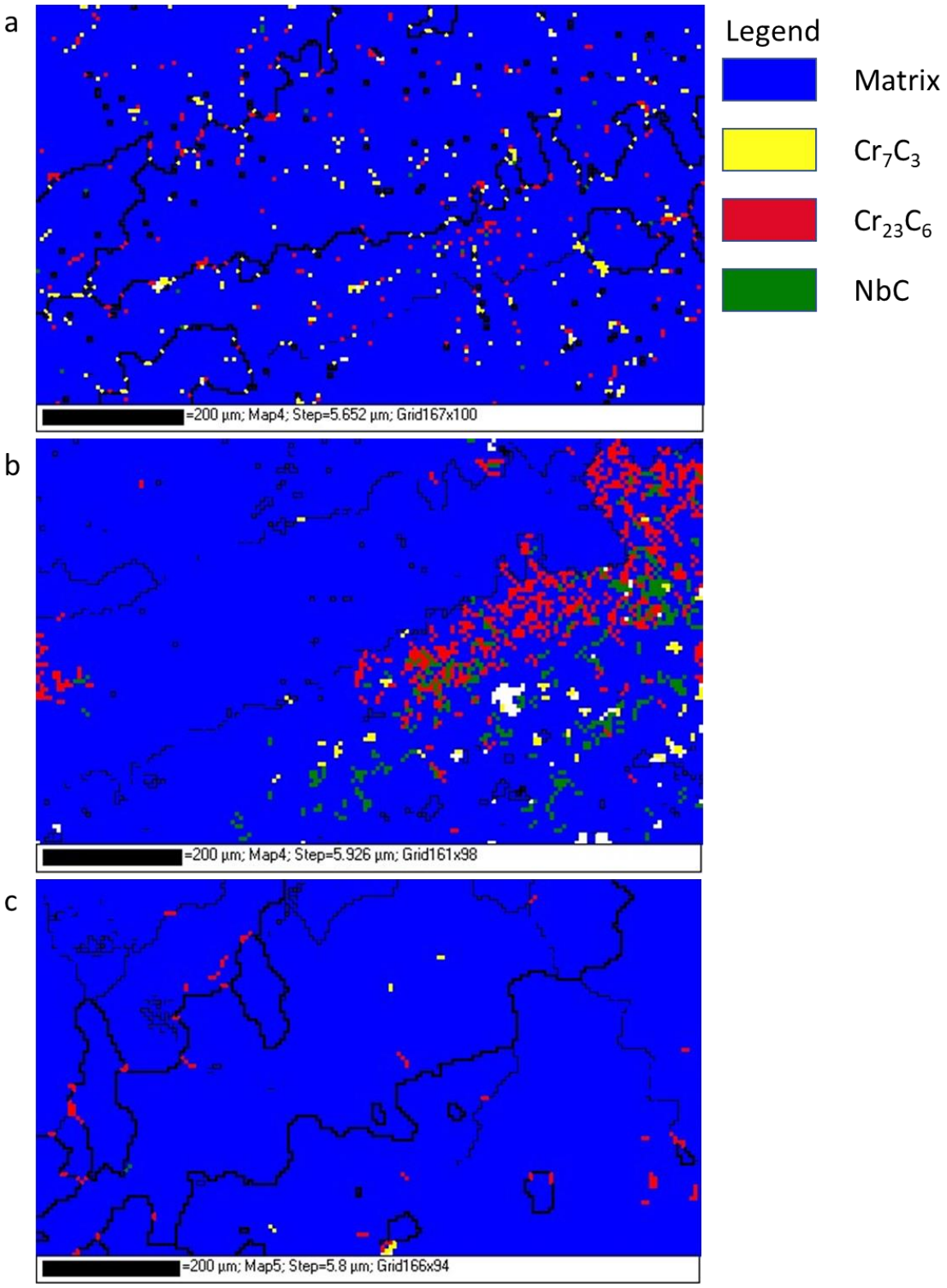

Figure 4.1.3-36: EBSD phase map of Optim-Al alloy at: (a) Outer diameter region; (b) cross-over region and; (c) inner diameter region

4.1.3.5 XRD analysis of alloy phases

X-ray Powder Diffraction, or XRD, is an analysis technique used for phase identification of crystalline materials. XRD was undertaken to confirm the matrix phase and investigate the other phases present across the four alloys, with the results displayed in Figure 4.1.3-37.

All four alloys displayed large peaks at 43.5° and 50.8°. These peaks correspond to the matrix consisting of the nickel and iron phase. A small peak at 39.2° was present, corresponding to the chromium carbide Cr_7C_3, whilst the peak at 44.4°, evident in the High-Al alloy, matches that of the aluminium and nickel rich phase Ni_3Al. This was in line with the widespread nickel and aluminium rich phase found across the High-Al sample in SEM and EDS analysis. The minor presence of this phase in the Low-Al and Optim-Al alloys was likely masked by the strength of the peak for the matrix at 43.5°.

The High-Al alloy also showed peaks correlating to the $Cr_{23}C_6$ form of chromium carbide, reinforcing the findings of the SEM analysis which found the carbide content of the High-Al alloy to be significantly greater than the other alloys. Therefore, both carbide forms were present in the alloy to a great enough extent to register in XRD analysis.

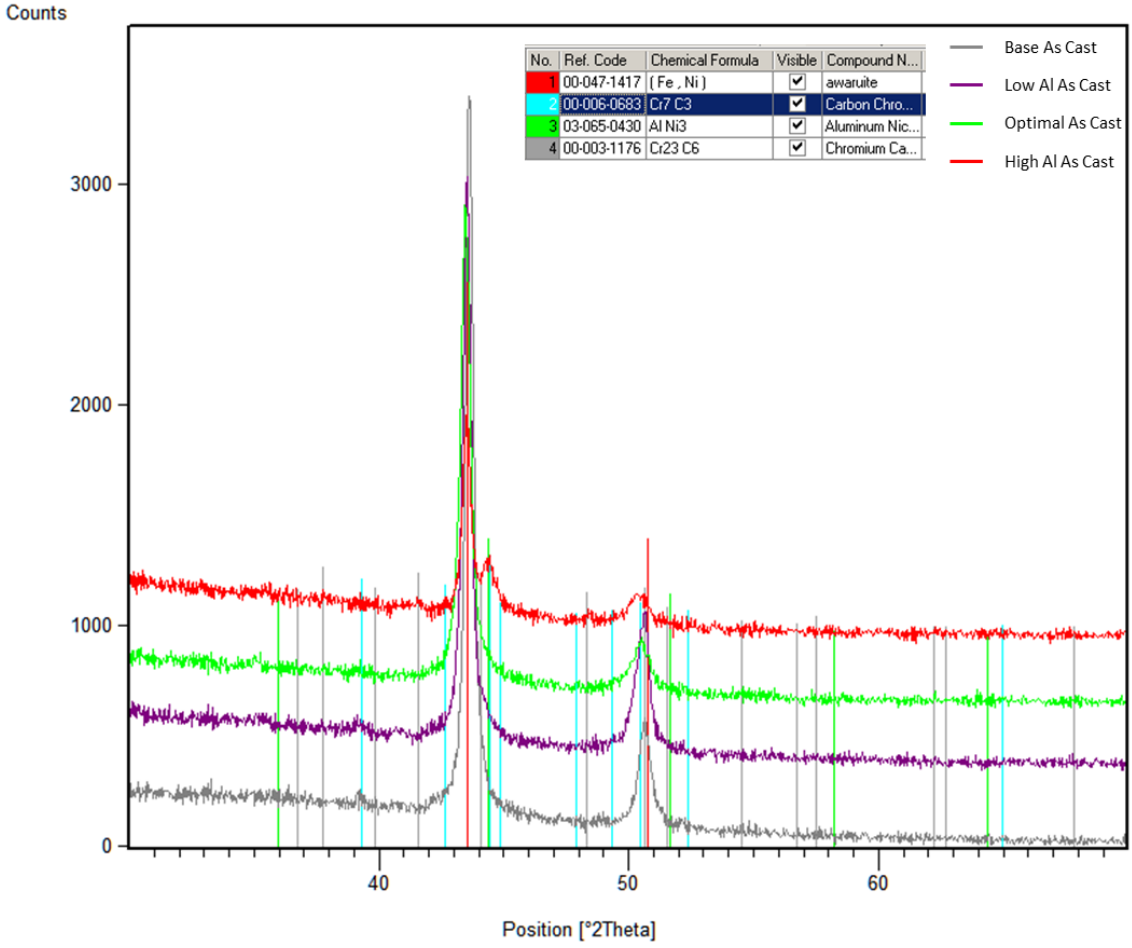

Figure 4.1.3-37: XRD traces of all four alloys in the as cast state, showing peaks for the matrix at 43.5° and 50.8°, whilst the High-Al alloy trace shows a peak at 44.4°, corresponding to the Ni_3Al phase, which was observed to be widespread in this alloy.

4.1.3.6 Summary of alloy microstructures

Across all four alloys under the current casting conditions as described in 3.1, the near outer diameter region was characterized by dendritic grain growth of columnar grains, growing away from the outer surface. This was a result of the temperature gradient introduced by the colder mould surface on the molten alloys. Carbides grew interdendritically after the solidification of the matrix as a result of localized raised carbide formers due to their ejection from the solidifying matrix. Slower cooling rates of the High-Al alloy resulted in a significantly different microstructure, with Chinese script style carbides replacing the more acicular carbides seen throughout the other alloys. Faster cooling rates in the other alloys resulted in an increased presence of triangular

niobium carbides which precipitate in the melt and are entrapped in the rapidly solidifying matrix. More vein-like carbides are present when cooling rates allowed the dissolved niobium to be ejected and carburise in the interdendritic region.

The Optim-Al alloy displayed finer carbide precipitation of both niobium and chromium, and chromium carbides had a significantly lower volume fraction. These observations were a result of the reduced carbon content in the alloy causing the lower volume fraction, coupled with the faster cooling rate which ensured finer carbide precipitates.

The High-Al alloy displayed widespread precipitation of the nickel aluminide (Ni_3Al) phase, which formed early, identifiable by the presence of niobium carbide growth on their surface, unlike the other alloys which saw niobium carbides in contact with the chromium carbides. This occurred due to the already precipitated niobium carbides acting as nucleation sites for the Ni_3Al phase.

The cross over region in all alloys showed a mixed microstructure of columnar grains and equiaxed grains. The columnar grains had carbide formation in the interdendritic regions, whilst the carbides formed more readily at the grain boundaries of the equiaxed grains. All the aluminium containing alloys displayed differing volume contents of the nickel aluminide phase in the crossover region, with the High-Al again showing widespread presence, whilst the Low-Al and Optim-Al alloys were significantly more sparsely populated.

The near inner diameter region of all four alloys was made up of equiaxed grains and carbide growth at the grain boundaries. Light phases, such as the observed square phase of TiCN, were present mainly at the very inner surface due to the centrifugal force of the casting process causing lighter phases to migrate to the inner surface of the melt. Due to the thinner pipe depth and faster cooling rates, the Optim-Al alloy displayed only a very small region of equiaxed grains.

In the three aluminium containing alloys, the prevalence of the nickel and aluminium rich phase separated them, with the High-Al alloy displaying vastly greater volumes of this phase, whilst the

Low-Al and Optim-Al alloys both had significantly reduced volumes. Furthermore, this phase was concentrated in the crossover region and the near inner diameter regions of the latter two alloys, but widespread throughout the High-Al alloy. This shall be discussed in more detail in section 5.1.

4.1.4 Illustration of microstructural impact on alloy properties

4.1.4.1 Thermal Properties

Differential scanning calorimetry was employed to assess the thermal events occurring in each alloy as they underwent non-isothermal heating. The samples were heated to 1450°C, well above the operating temperatures experienced in service. The samples were then cooled and re-heated, allowing for confirmation of phase change events to be identified. Endothermic events appear as peaks on the DSC trace.

The first minor peak observed in all four alloys (Figure 4.1.4-1 to Figure 4.1.4-4) occurred at 811°C, which was close to the reported precipitation temperature of the $Cr_{23}C_6$ carbide of 820°C by Li et al., 2018. The onset of this peak was seen between 750°C and 800°C across all four alloys, demonstrating the onset of carbide precipitation occurring just below 800°C. The variation of this peak from the expected precipitation temperature was due to the imperfect carbides – instead of being pure chromium and carbon, the phases contained a small fraction of other elements, most likely iron or nickel, which leads to a shift in the precipitation temperature. Table 4.1.4-1 shows the average composition of the carbides in the four alloys in the as cast state, as measured by EDS point elemental analysis. All four alloys displayed a quantity of iron or nickel in the chromium carbides. Whilst some of the signal is potentially being generated by the matrix in the EDS interaction volume beneath and around the carbide, there is enough evidence to confirm the impurities in the carbides.

Other than the precipitation of carbides, no other thermal events were obvious below 1280°C in any of the alloys. This was significantly higher than the service and cleaning temperatures, demonstrating the stability of the alloy throughout the required temperature range. Similarly, all

four alloys generated the same peaks during the second heating regime as the first, confirming these thermal events to be physical transformations of the alloys.

The Base alloy, High-Al alloy and Optim-Al alloy all displayed a dual peak in the range of 1280-1330°C (Figure 4.1.4-1, Figure 4.1.4-3 and Figure 4.1.4-4). This dual peak is characteristic of a quasi-peritectic reaction of the formation of the Cr_7C_3 carbide (129), whilst the single peak at 1315°C observed in Figure 4.1.4-2 for the Low-Al alloy was found to be the precipitation of the Cr_7C_3 carbide in hexagonal needle morphology. This precipitation temperature was seen to vary with different alloys in Thorpe and Chicco's work, and alternate alloys displayed this peak at 1259°C and 1199°C (129). It can therefore be considered that the precipitation temperature was variable dependent on the alloy's composition.

These temperatures were lower than predicted by the binary phase diagram of chromium and carbon (Figure 4.1.4-5), however the complex nature of the alloy resulted in differing conditions compared to the predicted ideals.

The other discernible change in the DSC traces were a result of the change in heating rate.

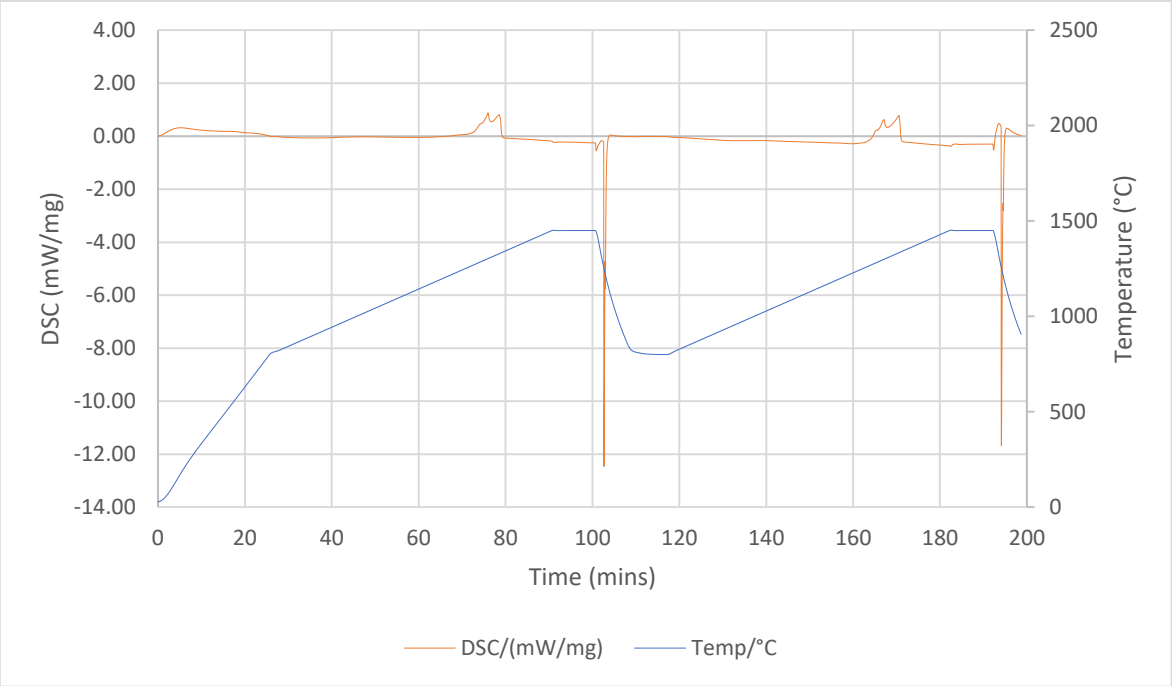

Figure 4.1.4-1: DSC trace and heating profile for Base alloy

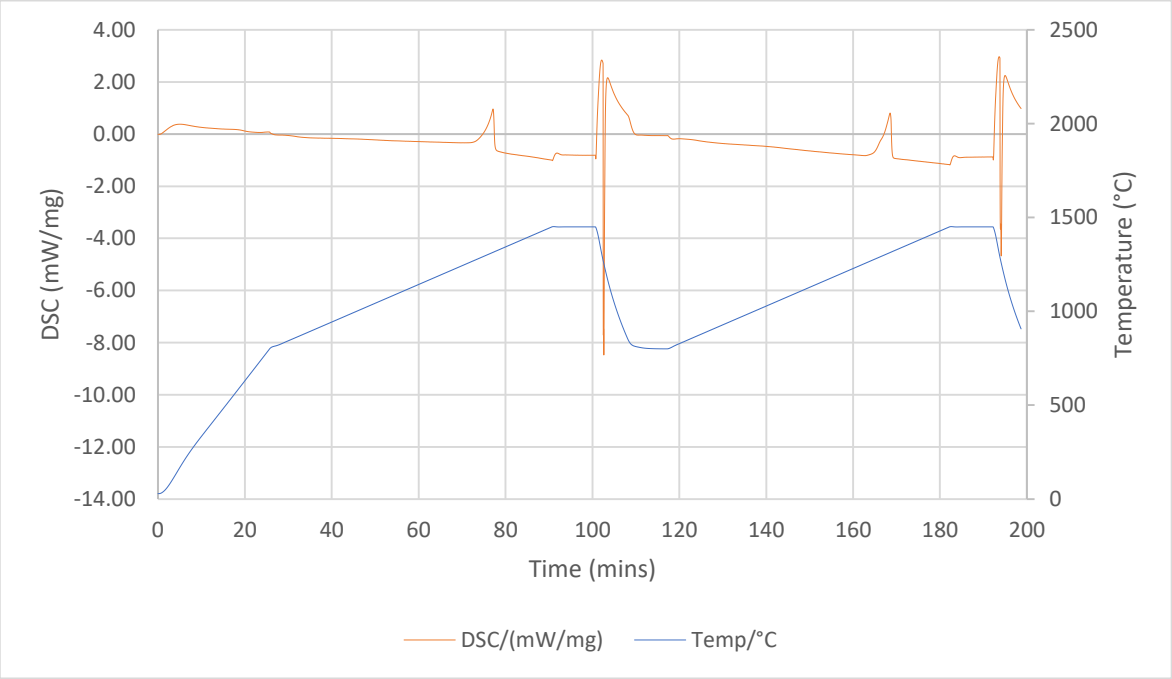

Figure 4.1.4-2: DSC trace and heating profile for Low-Al alloy

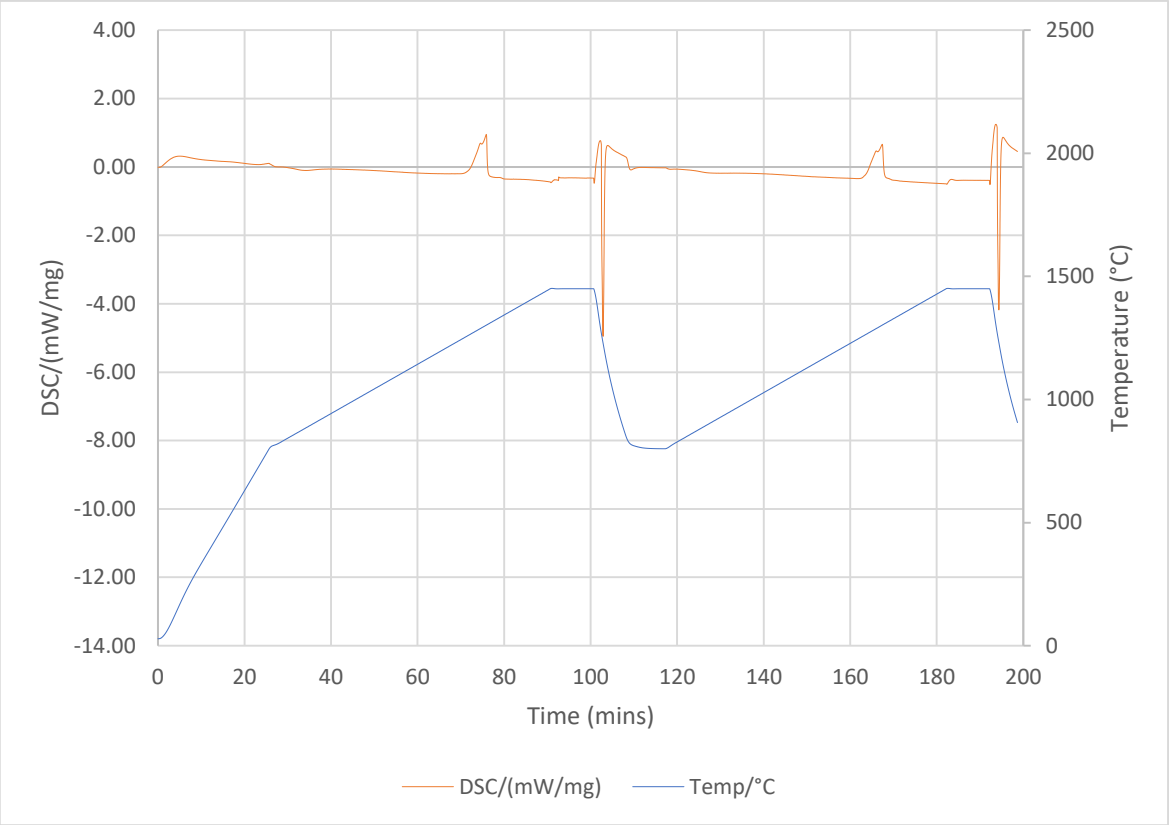

Figure 4.1.4-3: DSC trace and heating profile for High-Al alloy

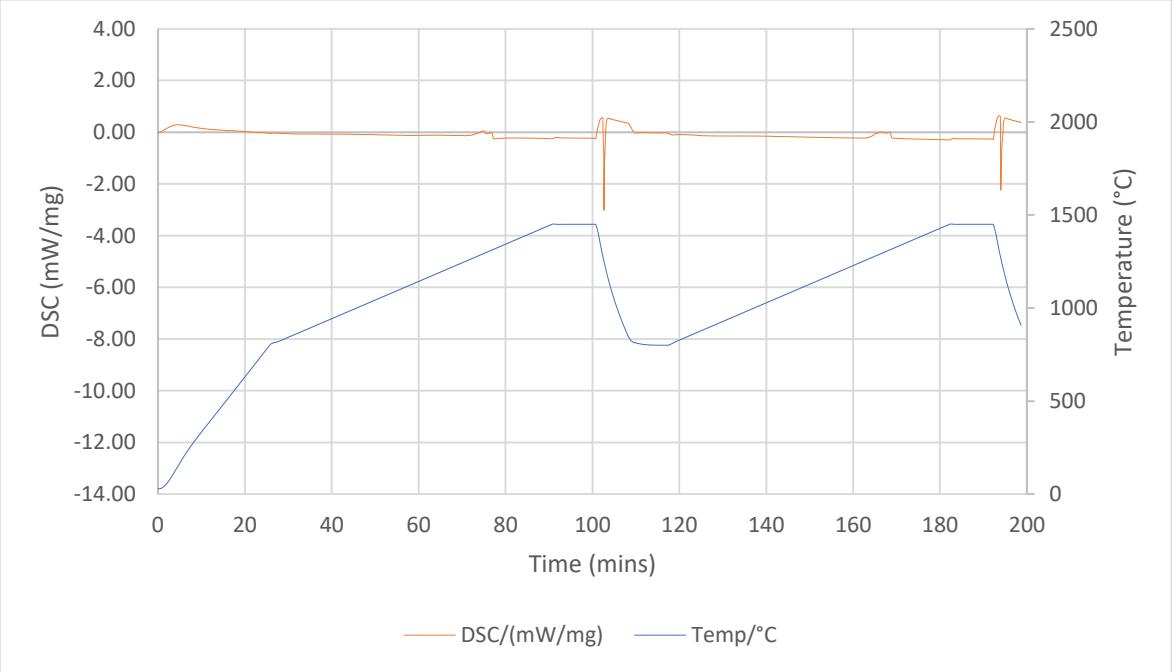

Figure 4.1.4-4: DSC trace and heating profile for Optim-Al alloy

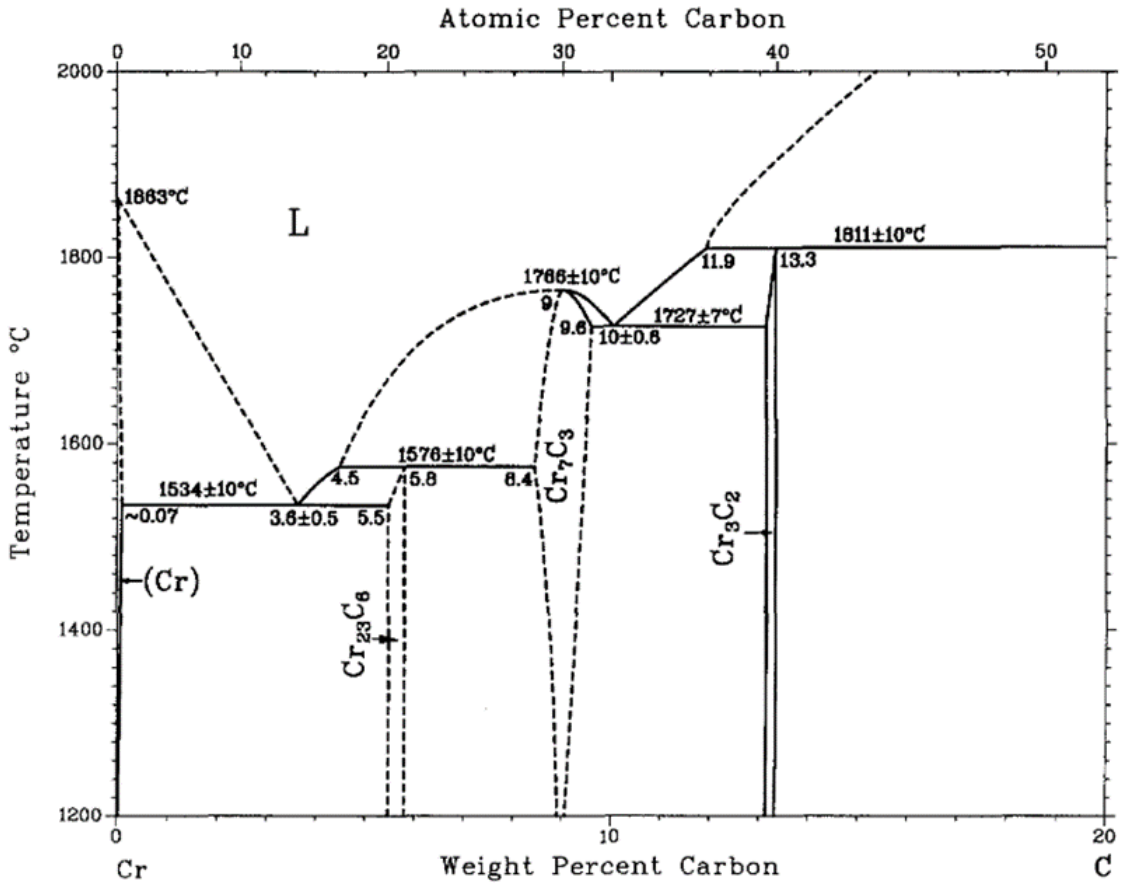

Figure 4.1.4-5: Chromium - Carbon phase diagram (40)

Table 4.1.4-1: Average composition of chromium carbides measured via EDS analysis

Element	Base Alloy	Low-Al Alloy	High-Al Alloy	Optim-Al Alloy
C	9.43	9.58	7.53	11.64
Al	0.00	0.19	0.15	0.27
Cr	83.06	81.34	79.06	77.81
Fe	4.48	6.04	7.83	5.43
Ni	2.94	2.73	5.35	4.65

4.1.4.2 Hardness

Service requirements of these alloys do not depend heavily on their material hardness, with the strength required to be endured only likely to occur during the transportation and installation of pipes, along with some internal impacts caused through coke removal during the cleaning cycle. However, the hardness measurement of the alloys throughout their thickness was a useful measure

to further observe how the alloy microstructure changed through its thickness and allowed these observations to be linked to the differences observed in the microstructure.

All the aluminium containing alloys (Figure 4.1.4-7, Figure 4.1.4-8 & Figure 4.1.4-9) had a greater average hardness than the Base alloy (Figure 4.1.4-6), possibly as a result of the solid solution strengthening effect of the aluminium dissolved in the matrix, as well as the addition of the nickel and aluminium phase. This acts as a precipitation hardener, something which the carbides bring to all four alloys. The hardness of all the alloys exceeded 200HV at all measured points, therefore the hardness of any of the alloys appears sufficient for the service requirements.

Both Base and Optim-Al alloys displayed a gradual decline in hardness, moving from the outer diameter to the inner diameter, which was due to the increasing grain size, resultant from the solidification times. The smaller the grains the greater the hardness, and this was reflected in both microstructural studies and hardness results. This reaffirmed the increased grain size that was observed, caused by the longer solidification times experienced towards the inner diameter of the pipe.

As would be expected due to the dissimilar microstructures, there appeared to be a relatively large difference in average hardness between the Low-Al alloy and the Optim-Al alloy. This was due to the reduced carbides in the Optim-Al alloy which act as precipitation hardeners, impeding dislocation movement. Therefore, the lower volume of carbides leads to a reduced hardness, despite the greater solid solution strengthening effect of increased dissolved chromium and aluminium in the Optim-Al alloy.

The variation in values of the same sample region seen in Figure 4.1.4-8 showed the variability of the microstructure of the High-Al alloy. This correlated with the observed microstructural inconsistencies in grain size and secondary phases, in accordance with the precipitation previously observed (4.1.3.3).

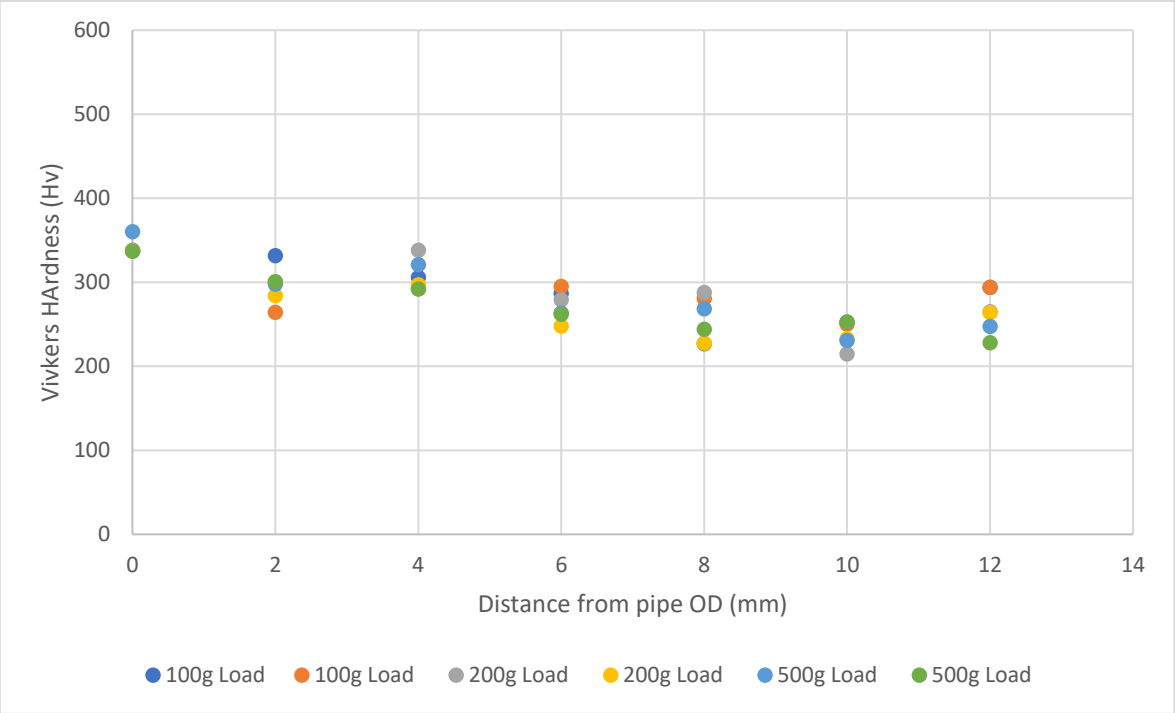

Figure 4.1.4-6 Hardness variation of Base alloy through depth of as cast alloy

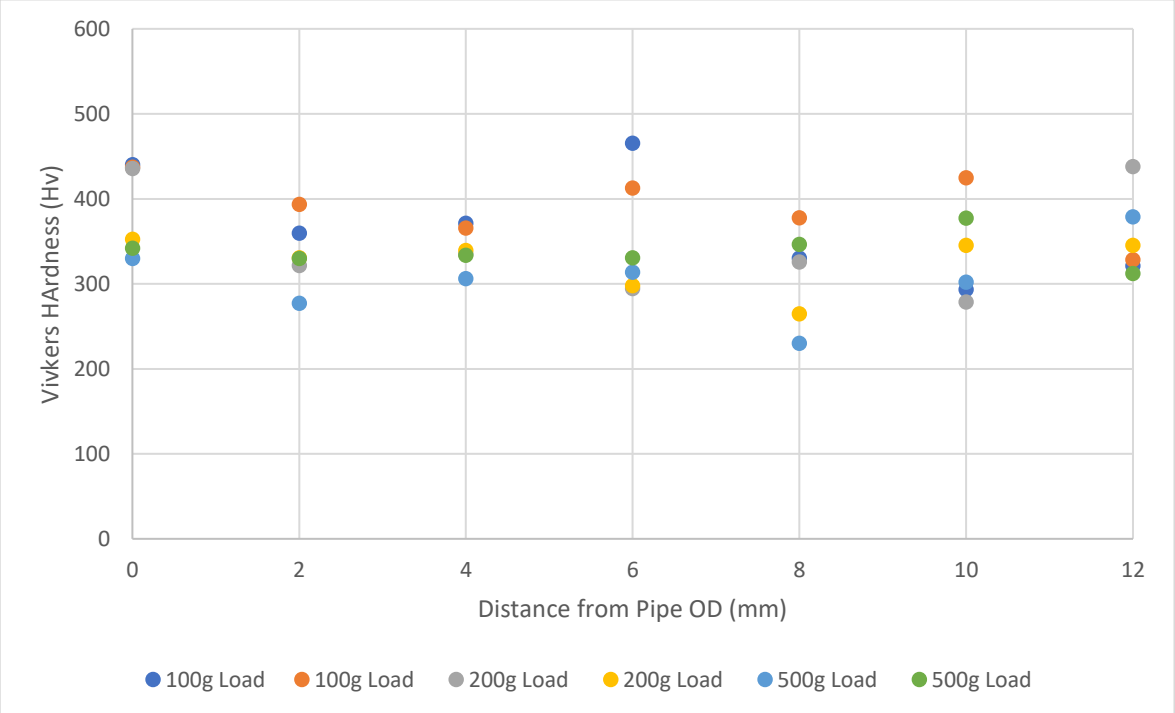

Figure 4.1.4-7 Hardness variation of Low-Al alloy through depth of as cast alloy

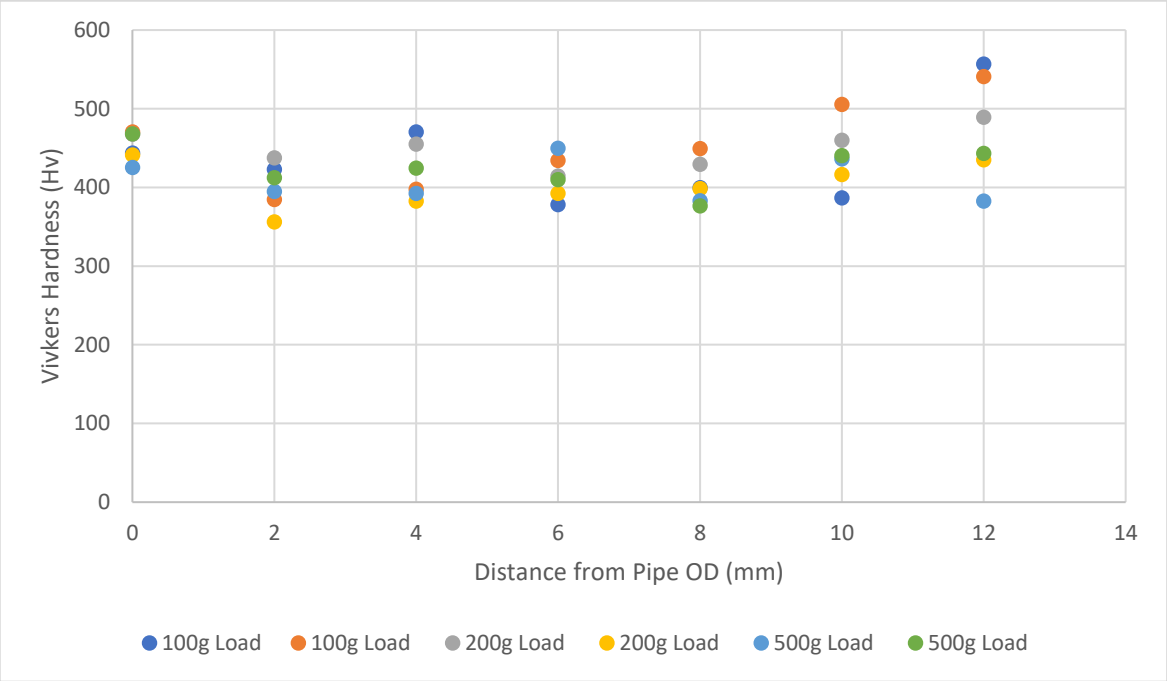

Figure 4.1.4-8 Hardness variation of High-Al alloy through depth of as cast alloy

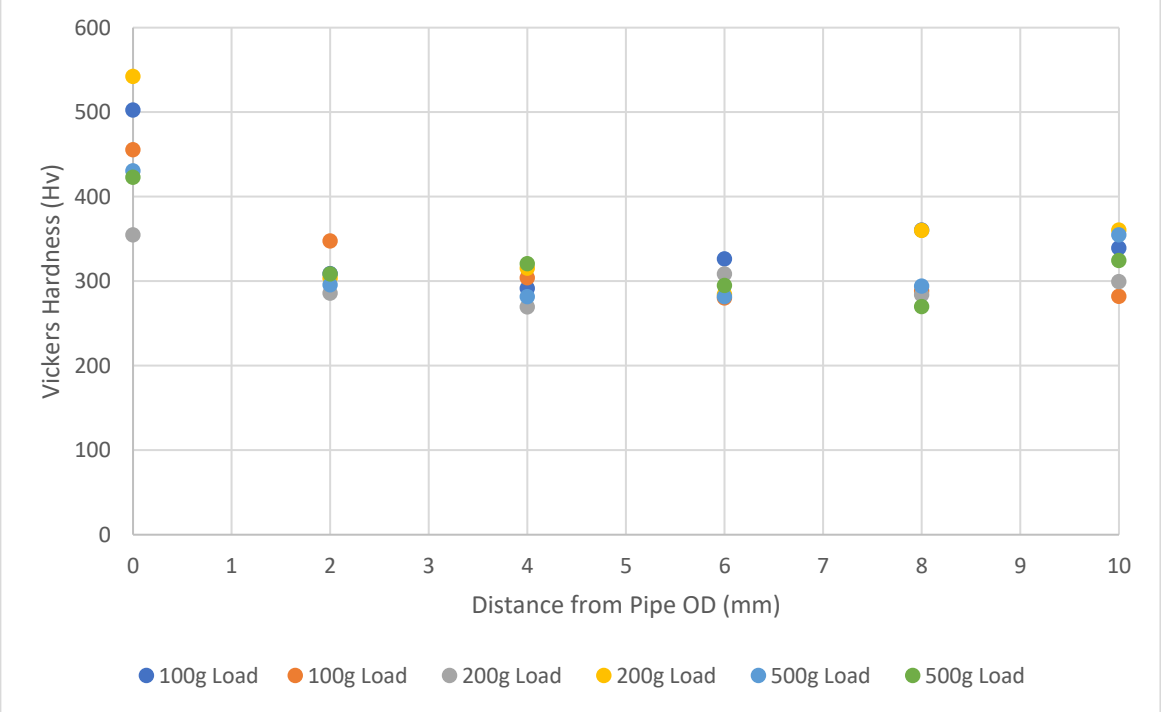

Figure 4.1.4-9 Hardness variation of Optim-Al alloy through depth of as cast alloy

4.1.4.3 Summary of illustration of microstructural impact on properties

All four alloys demonstrated precipitation of chromium carbides onset between 750°C and 800°C. The Base, High-Al and Optim-Al alloys displayed a quasi-peritectic reaction of the formation of the Cr_7C_3 carbide, whilst the Low-Al alloy

trace indicated the formation of the Cr_7C_3 carbide in hexagonal needle morphology.

Hardness differences between the alloys were closely linked to the carbide content of the alloys, with the High-Al alloy displaying a significantly greater hardness, matching the apparent greater volume fraction of carbides throughout that alloy. The hardness appeared greater at the inner and outer surfaces. The outer surface had a finer grain structure, resulting in greater hardness, whilst the inner surface contained titanium carbonitride particles, and experienced solid solution strengthening via the raised aluminium content.

4.2 Oxidation

To inhibit catalytic coking occurring, the elements that act as catalysts to cause this need to be separated from contact with the reactive gas stream when in service. The high temperature requirements of ethylene cracking mean nickel and iron are needed for the mechanical properties to remain consistent at working temperatures, however these two elements cause the catalytic coking action to occur. Therefore, it is necessary to have a physical barrier between the alloy matrix and the gas stream to prevent contact between the gas and the nickel and iron in the pipe material and arrest this catalytic coke formation.

A continuous, stable oxide which does not contain catalytic elements, formed on the inner surface of the pipe would be an ideal solution – protecting the gas from the matrix forming elements and not requiring complex and expensive treatments or coatings to be applied to the inner surface of the pipe.

A thick oxide with a coefficient of thermal expansion not in line with that of the bulk alloy will be susceptible to fracture via stresses induced in the oxide upon changes of temperature from those at which the oxide was formed. Most likely this will be during a cool down of the pipes, which leads to contraction of the pipe alloy and the oxide. If the oxide contracts to a greater degree than the pipe, the stresses generated in the oxide will be upon the oxide-alloy interface, resulting in potential debonding. Conversely, if the pipe contracts to a greater degree than the oxide, compressive stresses will be imparted into the oxide, potentially leading to fracture and spallation of the oxide. This issue is exacerbated with increasing oxide thickness, and is relatively negligible with a very thin oxide, therefore a thinner oxide which is protective is always more beneficial in the service applications.

The coefficient of thermal expansion of chromium oxide scale grown on a steel substrate was found to be 10.75×10^{-6} K^{-1} by Mougin et al. (130) which is larger than the generally reported values which

are usually up to 9.6 x10^{-6} C^{-1} as reported by Wang et al. (131). Similarly, the coefficient of thermal expansion of alumina when grown as a film was higher than generally reported bulk values, with Huntz et al. measuring it to be 10.7 x10^{-6} K^{-1} at 700°C, and rising not significantly above 11.5 x10^{-6} K^{-1} in the operational temperature range used in ethylene cracking (132).

As both coefficients of thermal expansion are of the same order of magnitude and very similar in actual value, the thickness of the oxide layer becomes significantly important, as the greater thickness of the oxide layer, the greater the volume change and therefore the more potentially detrimental the effect.

4.2.1 Oxide layer formation analysis

The oxidation behaviour of the four alloys were investigated to analyse and compare them, to assess which alloy would produce the most protective oxide on the pipe's inner surface for ethylene cracker furnace tubes.

All oxidised samples were cut, gold coated, and nickel plated before mounting of the sample for analysis of the layer structure of both the oxides and the alloy. The nickel-plating layer was clearly evident atop the external oxide on each sample image shown. This was used to maintain the oxide layer during the mounting process, and aid in distinguishing between the bakelite and the oxide layer on the surface of the samples.

4.2.1.1 Base Alloy

4.2.1.1.1 SEM Analysis

The effects of air oxidation of the Base alloy over 30 minutes, 8 hours and 24 hours at 1100°C are shown in Figure 4.2.1-1. The images show a clear oxide layer which had grown on the surface of the alloy which thickened with increased oxidation time, as displayed in Figure 4.2.1-2. The average oxide layer thickness was found to be 2.90µm ± 0.58µm after 30-minute oxidation, increasing to 7.83µm ± 1.48µm after 8 hours, demonstrating almost a 2.5x increase in the oxide layer thickness.

After 24 hours the oxide layer is measured at 13.16μm ± 1.41μm, which showed almost another doubling of the oxide layer thickness.

The longer oxidation period images distinctly show the formation of a sub-surface second phase (marked in Figure 4.2.1-1 c, f and i). There was evidence of both fracture of the oxide and regions where the oxide layer either has not formed or has formed and subsequently detached from the matrix.

Very fine chromium carbides precipitated during the treatment of the sample. These were much smaller than those seen in the as cast alloy (4.1.3), and appear to form closer to the grain boundaries than the centre of each grain, indicated in Figure 4.2.1-1 b and e. However, they were not exclusively found at the grain boundaries. The appearance of these carbides was in line with the typical morphology of $Cr_{23}C_6$ carbides (42,129). These fine precipitates were absent in the near surface region, and that region was also deeper, in line with the increased oxidation time. The depth of the region without the very fine precipitates was found to be almost the same depth as the deepest oxides within the sample.

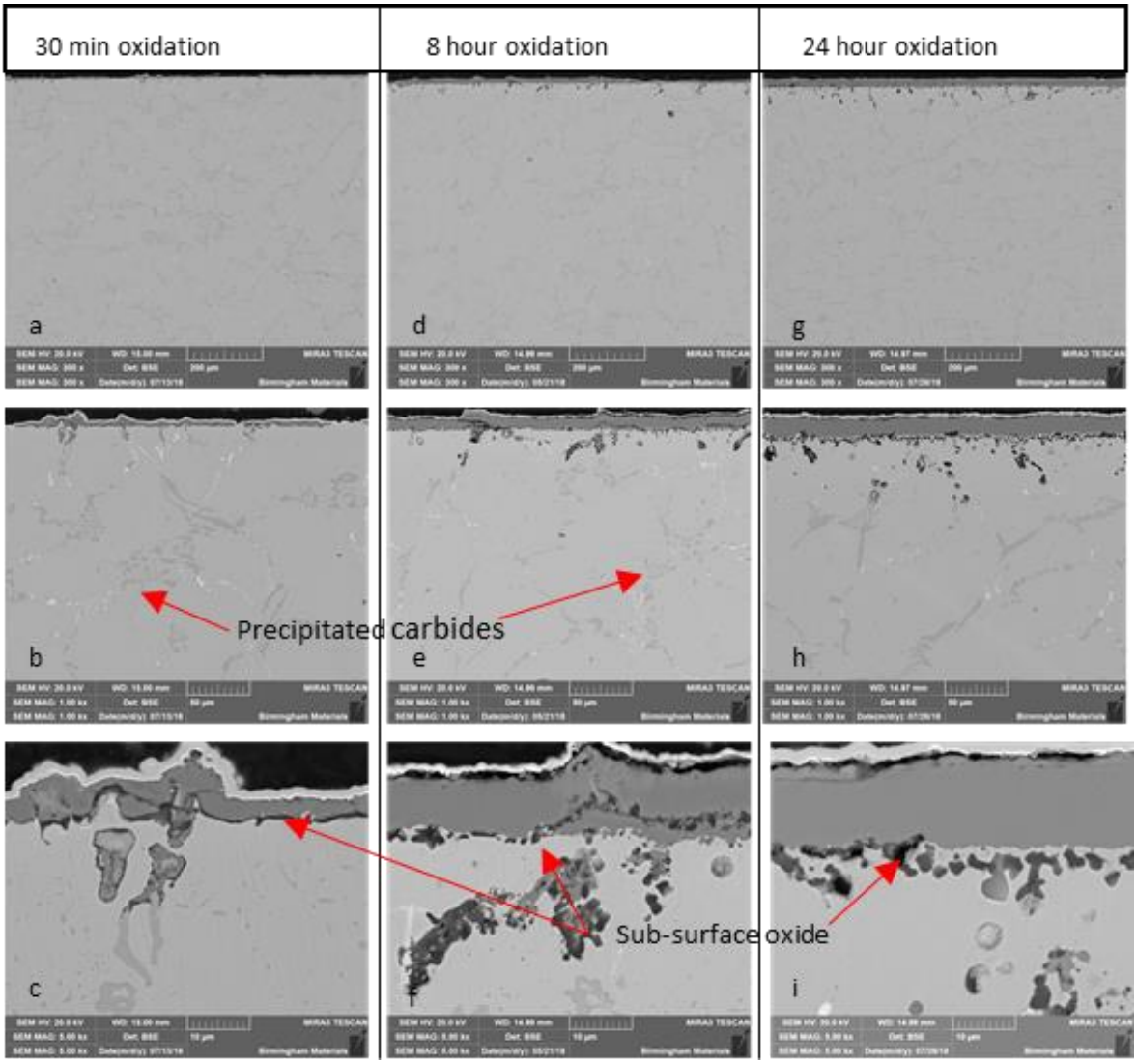

Figure 4.2.1-1: Base alloy oxidation after 30 minutes (a, b, c), 8 hours (d, e, f)and 24 hours (g, h, i) at 1100°C in air showing development of oxide layer and sub surface oxidation

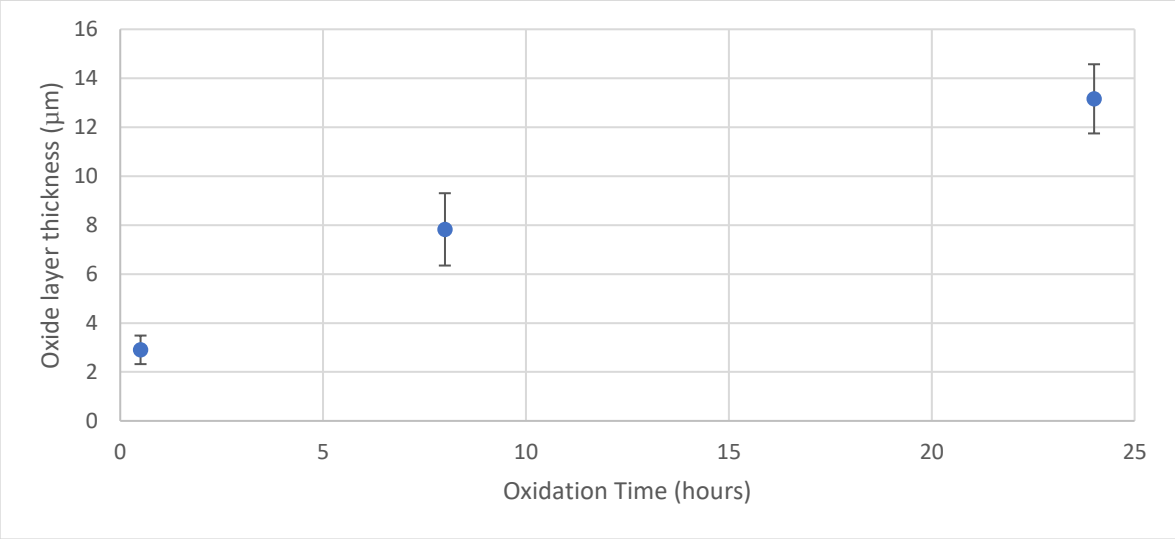

Figure 4.2.1-2: Oxide layer thickness of Base alloy after 30 minute, 8-hour and 24-hour oxidation

Figure 4.2.1-3 shows the surface oxide layer to be chromium and oxygen rich, sat beneath the nickel-plating layer which was applied after oxidation to retain the oxide and improve the contrast between the oxide and the bakelite on which the samples were mounted. The manganese elemental mapping (Figure 4.2.1-3) displayed significant concentrations on the very top surface of the oxide, suggesting a secondary oxide layer on the surface of the chromium oxide. This was expected to be manganese chromite ($MnCr_2O_4$). Manganese appeared to be present throughout the oxide, however the majority of this was due to the overlapping energy intensities of chromium and manganese, so only the regions of manganese which appeared significantly concentrated and were found in regions of lower chromium content were true representations of the presence of manganese.

Between the matrix and the chromium oxide a silicon rich layer formed under the chromium oxide. This also appeared to be another form of oxide.

The chromium elemental map also showed a clear chromium depleted zone beneath the oxide layer when compared to the rest of the matrix. The reduced chromium in this near oxide region explained the lack of fine chromium carbides, as the chromium was utilized in oxide formation, due to chromium oxide being more stable than chromium carbides, and thus the carbides are dissolved near the surface, and the chromium oxide layer was formed instead.

Large chromium carbides near to the sample surface had also undergone some oxidation, but this appeared to occur only in the carbides within 20 microns of the surface of the 30-minute oxidation of the Base alloy, with those deeper within unaffected, demonstrating that the oxygen penetration depth was limited to the near surface region.

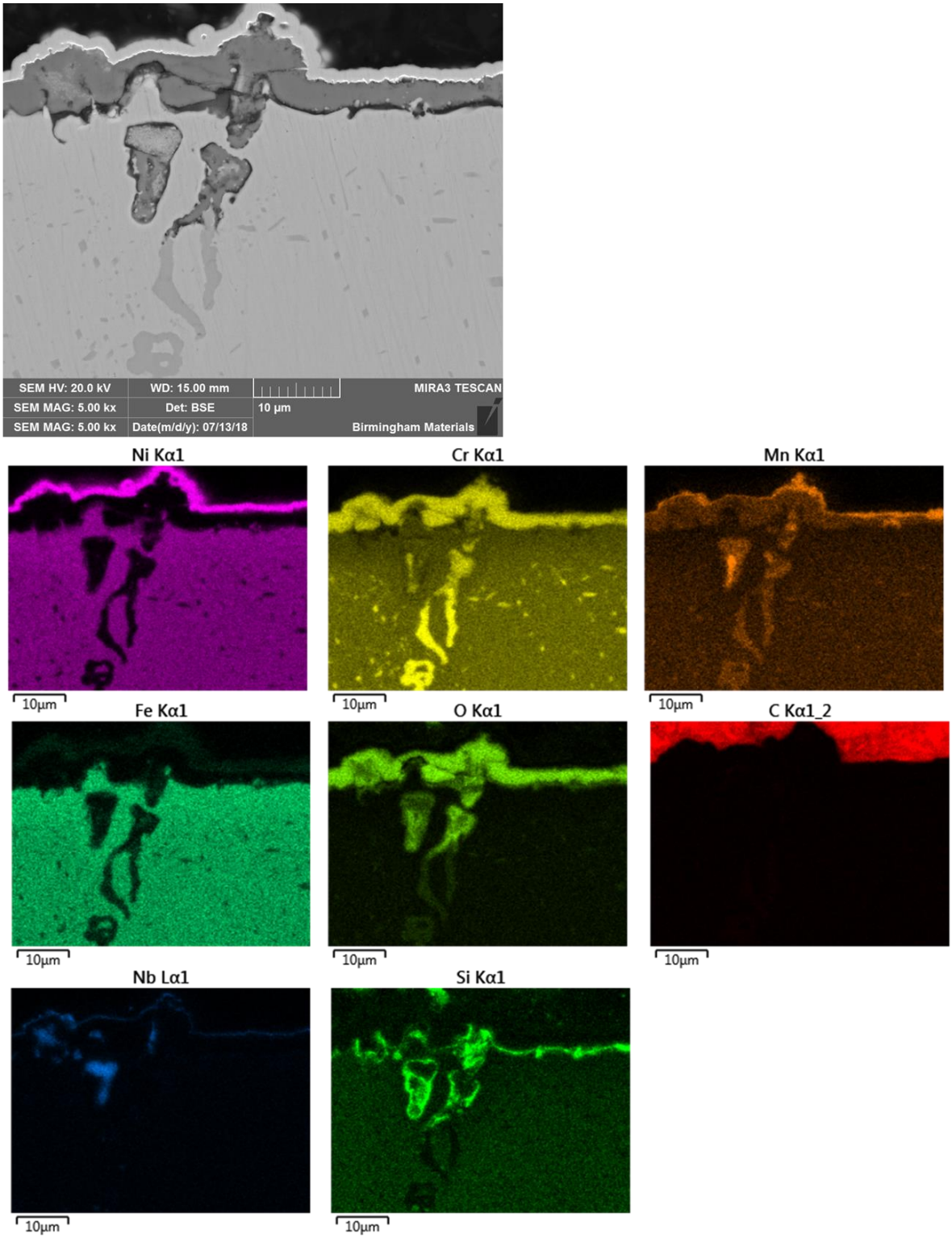

Figure 4.2.1-3: Base alloy 30-minute 1100°C oxidation elemental map showing chromium oxide surface layer and subsurface oxidized silicon.

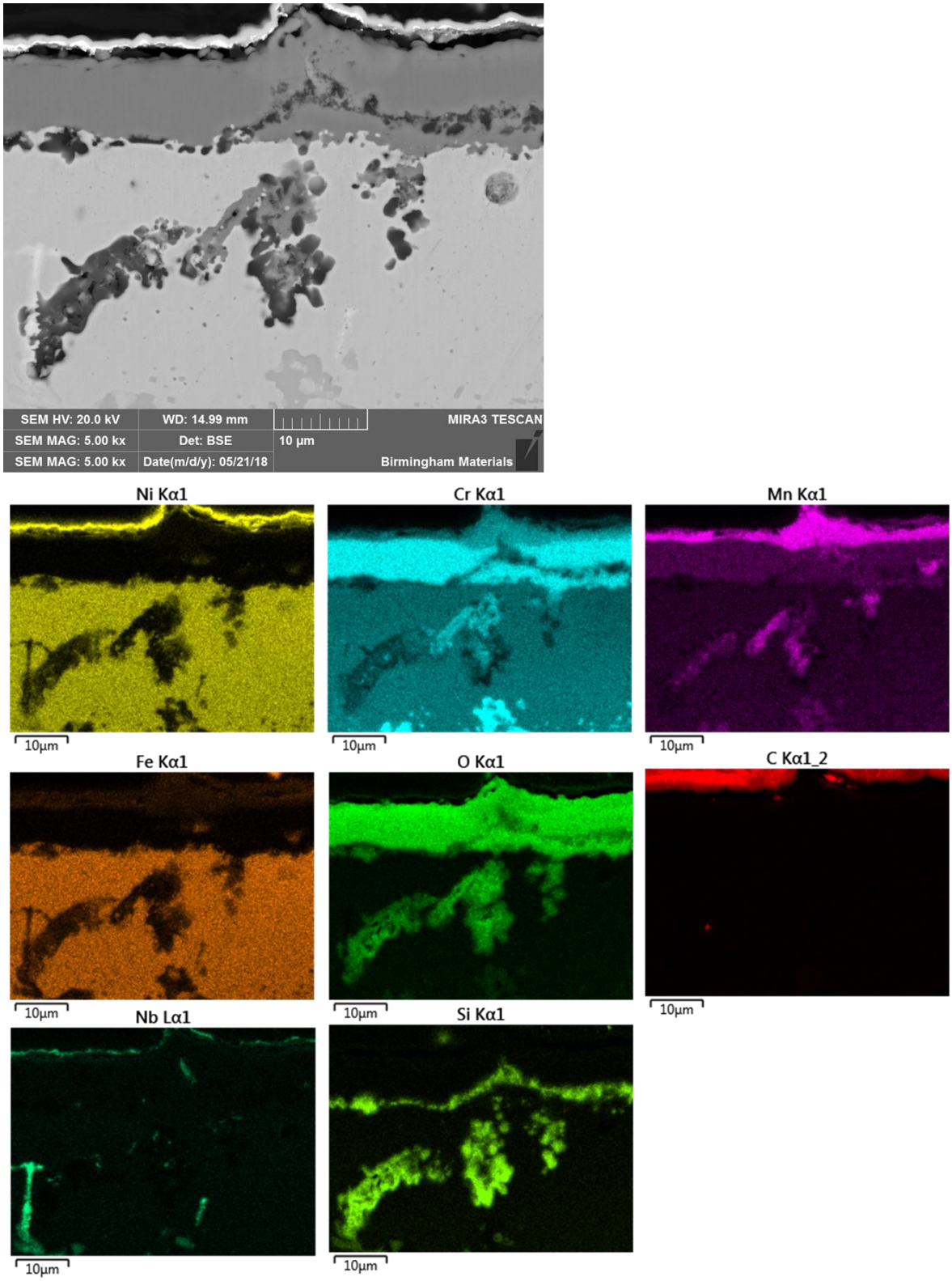

Figure 4.2.1-4: Base alloy 8h 1100°C oxidation elemental map showing manganese rich oxide on chromium oxide surface.

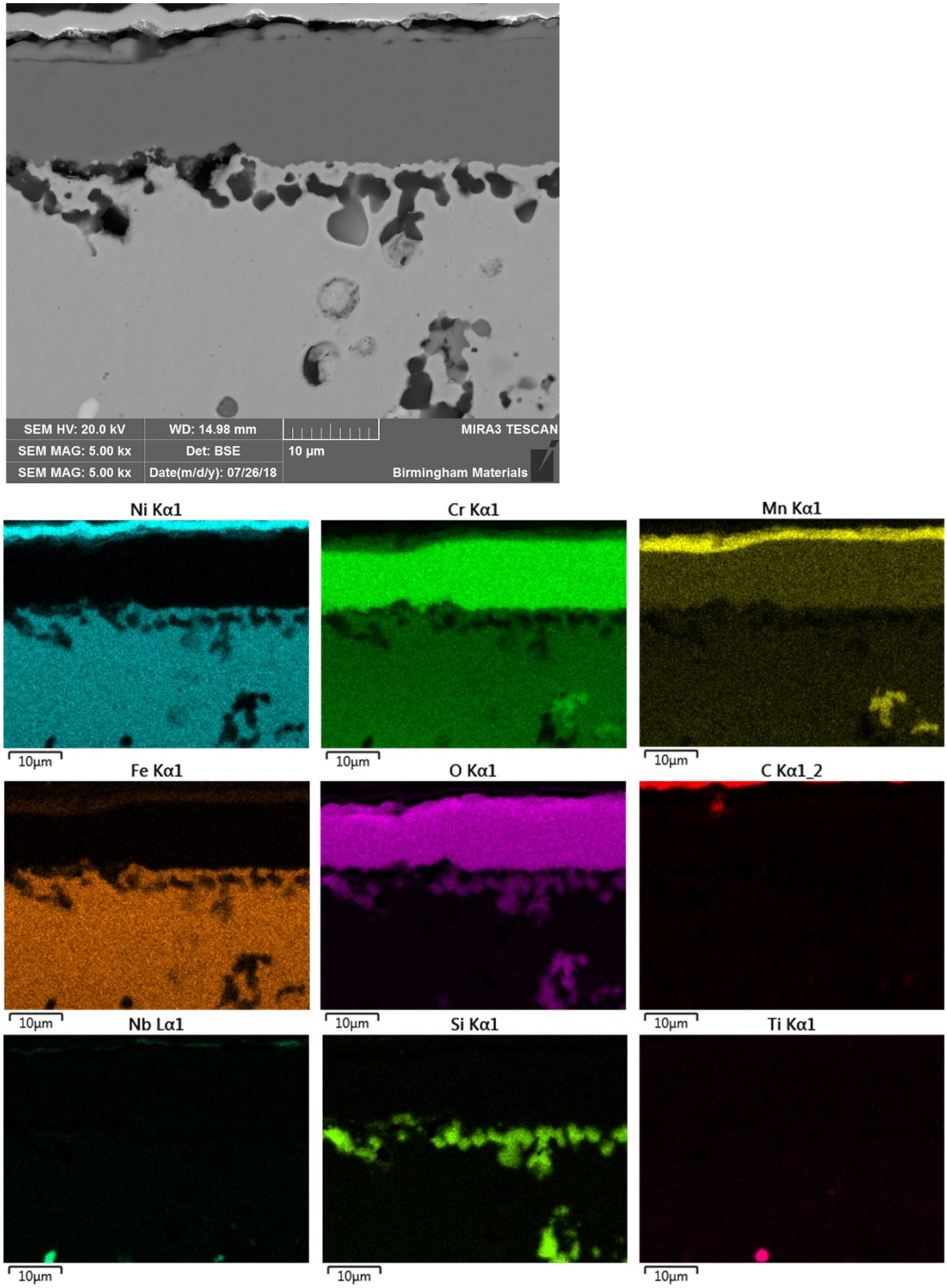

Figure 4.2.1-5: Base alloy 24h 1100°C oxidation elemental mapping demonstrating three clear oxide layers.

Figure 4.2.1-4 and Figure 4.2.1-5 show the EDS mapping of the surface layers of the Base alloy after 8 hours and 24 hours respectively at 1100°C in air. Both showed a transformation of the silicon oxide layer that was found beneath the chromium oxide after the 30-minute oxidation. The thin silicon oxide transformed from a continuous layer and became globular in nature, showing discrete phases measuring in the one to ten-micron range. They occurred either on or beneath the matrix-oxide interface, with some seen up to 30 microns deep into the matrix (Figure 4.2.1-1), suggesting that this silicon oxide phase was evidence of internal oxidation. This, along with deeper oxidised chromium carbides showed that the oxygen penetration depth was increased with longer oxidation time.

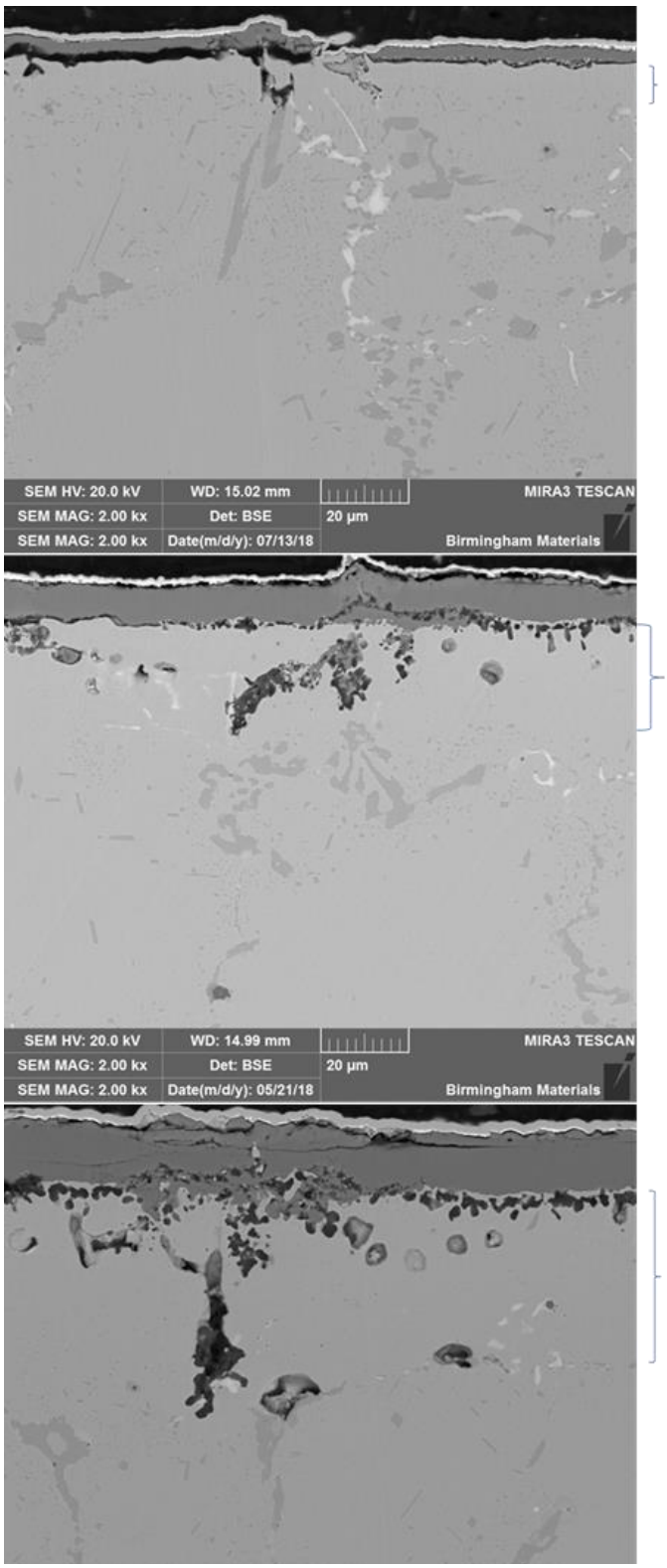

Figure 4.2.1-6: Absence of fine chromium carbide precipitation in 30-minute (top), 8-hour (middle) and 24-hour (bottom) oxidation samples of the Base alloy

The major oxide of chromium thickened with increased oxidation time, shown in Figure 4.2.1-6, and the surface manganese chromite appeared present, identified by the manganese elemental mappings in Figure 4.2.1-3 to Figure 4.2.1-5. Signs of

debonding of the manganese chromite from the chromium oxide were present in the 24-hour oxidation sample, seen as fractures parallel to the surface within the oxide layer in Figure 4.2.1-6.

Across all three oxidation states, the fine chromium rich precipitates that precipitated during the heating of the sample were absent closest to the sample surface. The depth of this absence increases with oxidation time, as indicated in Figure 4.2.1-6. This further demonstrated the depth of the chromium depleted zone in the alloys that formed during the oxidation process. This loss of carbides in the near surface region is due to chromium oxide being more thermodynamically favourable compared with chromium carbide, therefore the chromium present closest to the available oxygen preferentially oxidises instead, removing the carbides from the near surface region.

4.2.1.1.2 Phase Analysis

XRD (X-ray Powder Diffraction) was used for phase identification of the oxide layer on the surface of the Base alloy. This was employed to reinforce the findings of the EDS and SEM analysis, and to confirm the different oxides present on the surface of the alloy after the oxidation treatment. This was compared with the XRD results of the as cast alloy presented in 4.1.3.5.

Oxidation of the Base alloy for 8 hours at 1100°C showed significant presence of manganese chromite, with strong peaks at 35°, 42.7°, 56.4° and 62°. The oxidation sample also showed significant depressions in the matrix peaks, reinforcing the observations of a thick, dense oxide layer on the surface. This was further investigated in 4.2.2.1.3. The peak at 51° in all oxidised samples confirmed the chromium oxide layer as Cr_2O_3, as previously identified with EDS analysis.

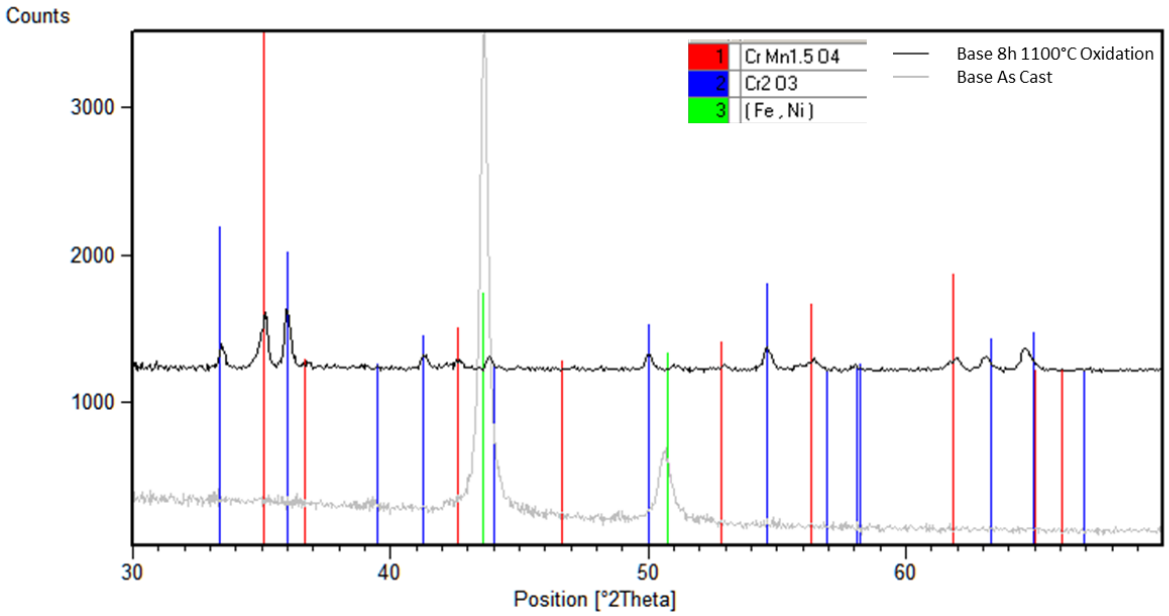

Figure 4.2.1-7: XRD traces of oxidised and as cast Base alloy with oxide products identified.

Transmission electron microscopy (TEM) was also undertaken on the Base alloy to confirm the phases present on the oxide layer. The surface chromium oxide was confirmed to be present, with the sub-surface silicon oxide found to be an amorphous silicon oxide. The manganese chromite layer was also confirmed to sit atop the chromium oxide layer.

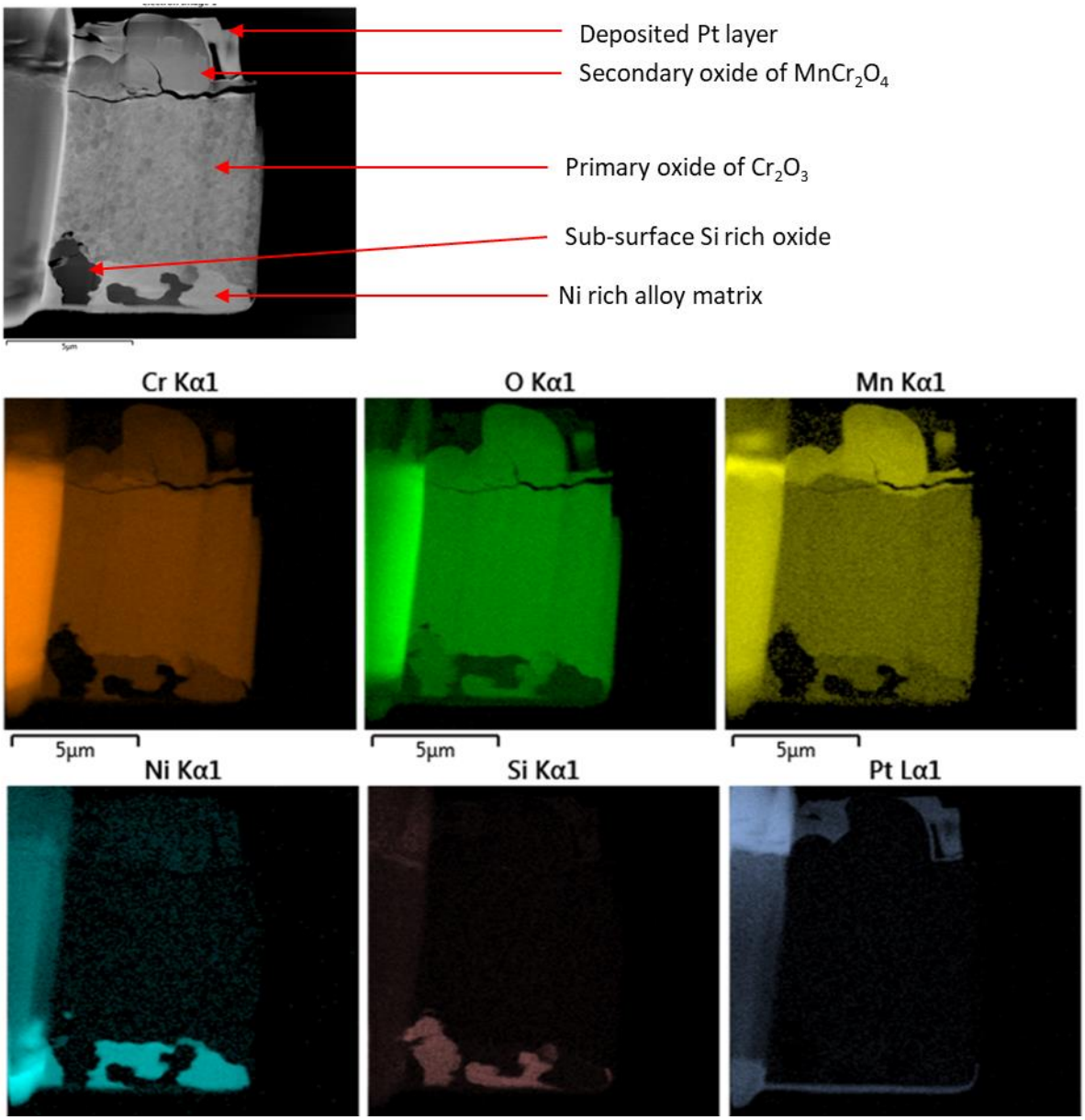

Figure 4.2.1-8: Scanning TEM image and EDS mapping of Base alloy oxide layer after oxidation at 1100°C for 8 hours displaying primary chromium oxide with secondary manganese chromite layer atop, and silicon rich oxide within the near surface matrix.

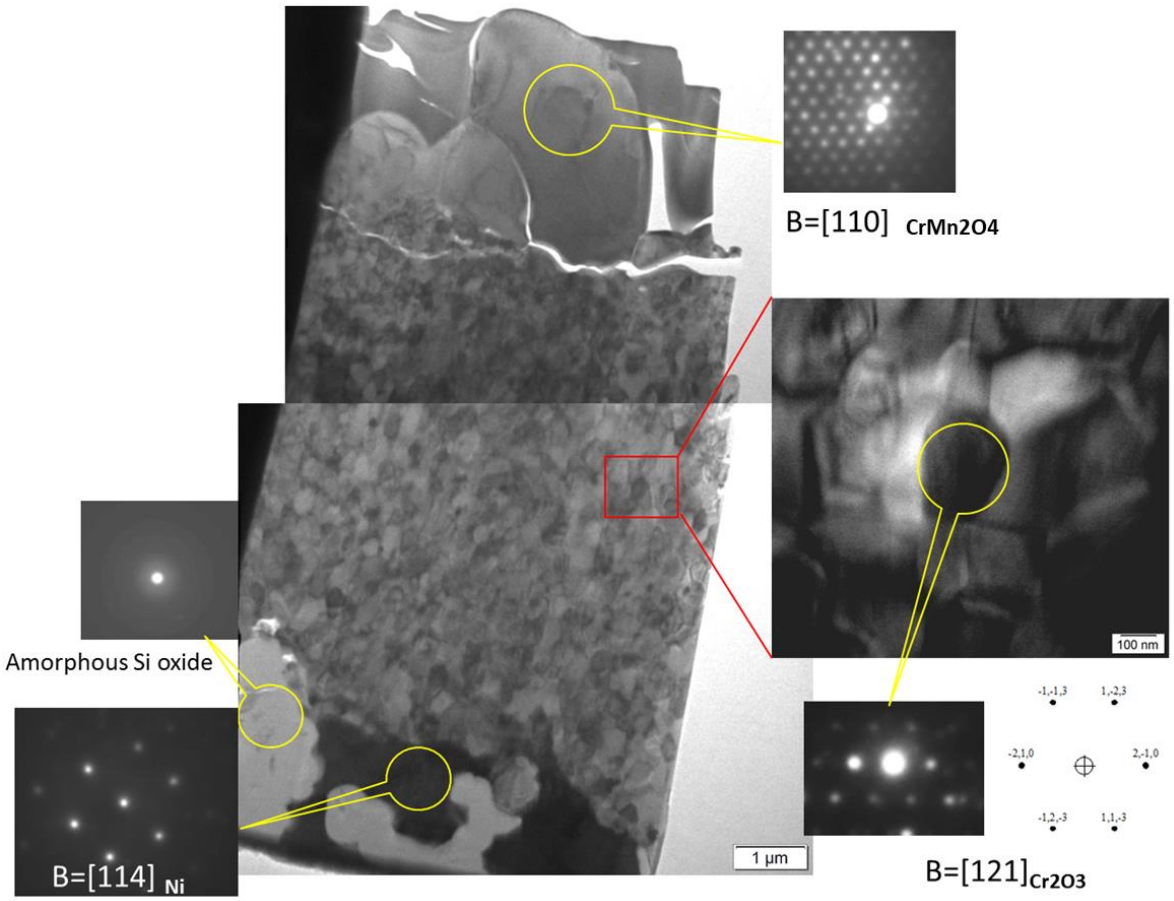

Figure 4.2.1-9: TEM image and corresponding selected area diffraction (SAD) patters of Base alloy oxidised at 1100°C for 8 hours, showing layer structure formed

4.2.1.2 Low-Al Alloy

4.2.1.2.1 SEM Analysis

Oxidation of the Low-Al alloy is shown in Figure 4.2.1-10. The matrix changes appeared very similar to those observed in the Base alloy, with a large volume of fine precipitates forming after a 30-minute heat treatment, precipitating out in an acicular morphology. The matrix of the 8-hour oxidation samples showed these precipitates to have coarsened and reduced in number. After the 24-hour oxidation the majority of the carbides had either re-dissolved or agglomerated to form larger, less structured carbides, with very fine precipitates only around the grain edges accompanying the larger carbides sitting on the grain boundaries.

The chromium oxide was present on the surface of the alloy (as in the Base alloy), however the oxide did not appear to be as continuous as that seen on the Base alloy, being noticeably patchy on the sample surface. A second layer beneath the chromium oxide was again present, but, as Figure 4.2.1-12 shows, this was no longer silicon rich, but now aluminium rich. The average oxide layer thickness was measured for the 30-minute oxidation as 1.96µm ± 2.27µm, with a doubling of the oxide layer seen after 8-hour oxidation, measured as 3.86µm ± 1.99µm. Average layer thickness again doubled to 7.28µm ± 4.10µm after 24-hour oxidation compared to the 8-hour oxidation. These increases were in line with the growth rate of the Base alloy, however the oxide was around half the thickness of the Base alloy, with significantly greater standard deviation. This is due to the patchy, inconsistent nature of the oxide, as well as the much thinner aluminium oxide being produced along with the chromium oxide, which utilized some of the available oxygen, partially stifling the chromium oxide growth.

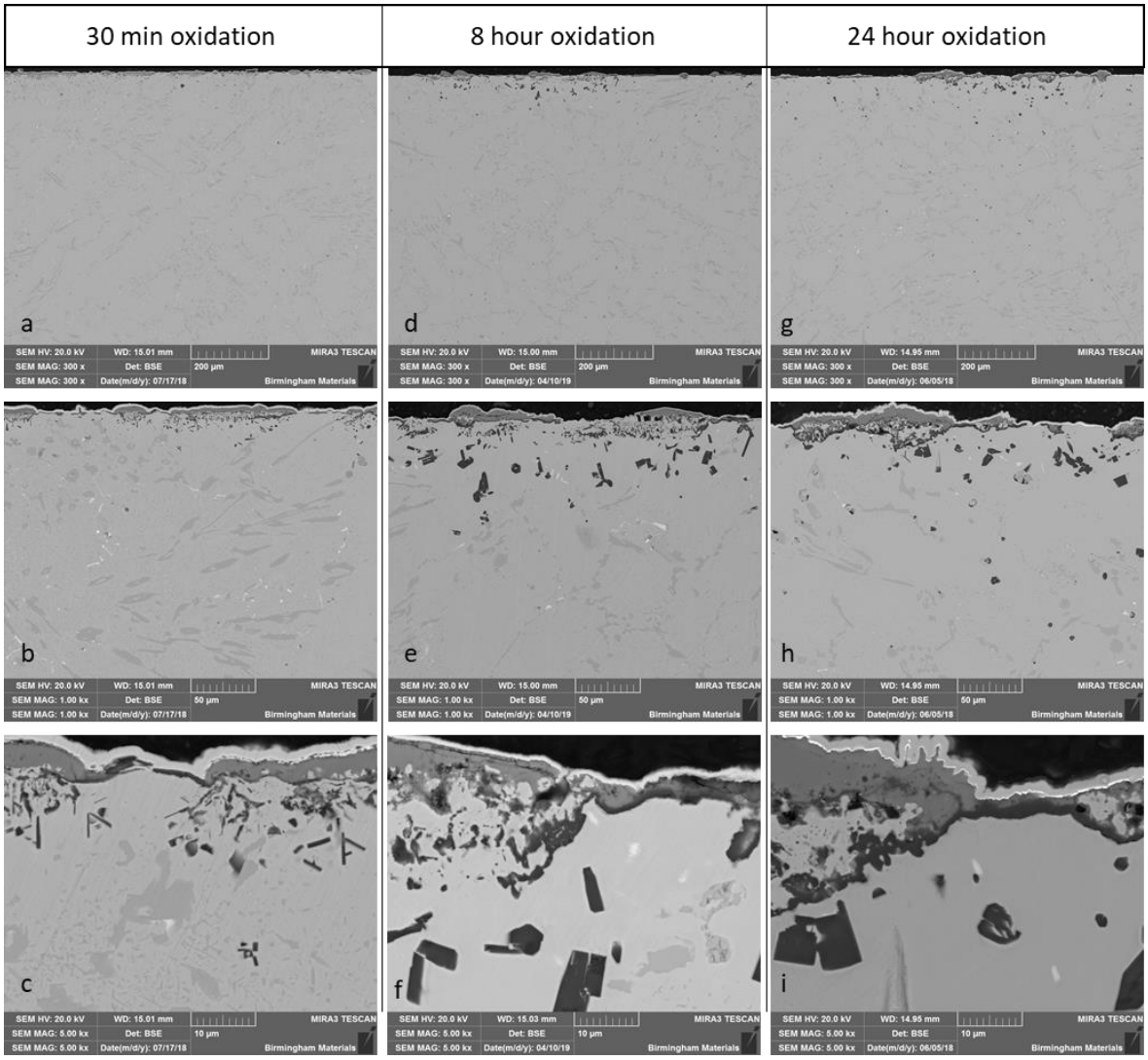

Figure 4.2.1-10: Low-Al alloy oxidation after 30 minutes (a, b, c), 8 hours (d, e, f) and 24 hours (g, h, i) at 1100°C in air

Whilst some silicon was still present in raised quantities at the matrix-oxide interface, the majority of the layer beneath the surface oxide was found to be aluminium rich (Figures Figure 4.2.1-12 and Figure 4.2.1-14). This surface oxide appeared to be chromium oxide, however some regions were devoid of this oxide and this left the sub-surface aluminium oxide exposed to the environment. This aluminium oxide was more characteristic of internal oxidation, rather than continuous surface oxidation. With longer oxidation times, the internal oxidation products agglomerated and formed regions of continuous, sub-surface oxide, but this was beneath regions of matrix, encapsulating a pocket of matrix sitting between the surface chromium oxide and the aluminium oxide layer (Figure

4.2.1-14 O and Al mappings). An aluminium and nitrogen rich phase, AlN, was also evident deeper than the aluminium oxide layer, presenting as very square or rectangular precipitates.

Areas with matrix fully exposed to the atmosphere were still present after all three oxidation treatments, indicating that the chromium oxide either formed on the surface spalled, or did not form at all.

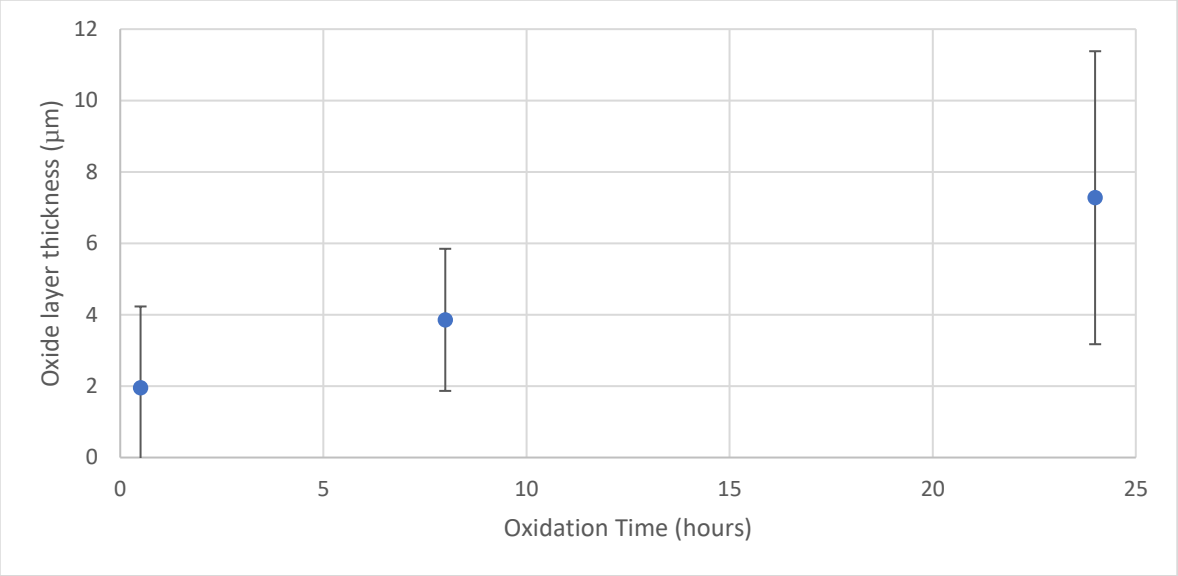

Figure 4.2.1-11: Graph of average oxide layer thickness of Low-Al alloy with increasing oxidation time

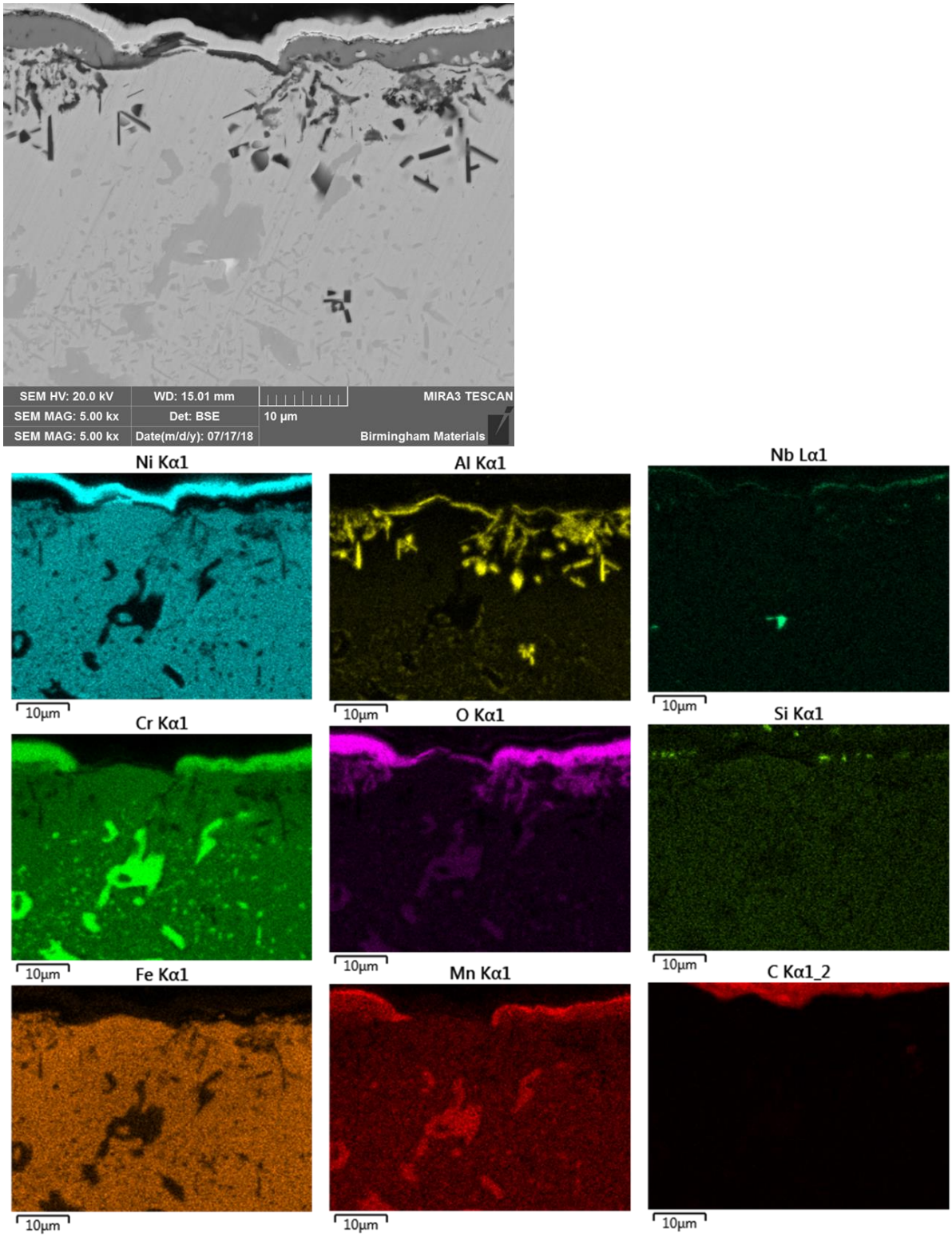

Figure 4.2.1-12: Low-Al 30-minute 1100°C oxidation elemental mapping showing mixed surface oxide with chromium oxide scales and disontinuous aluminium oxide.

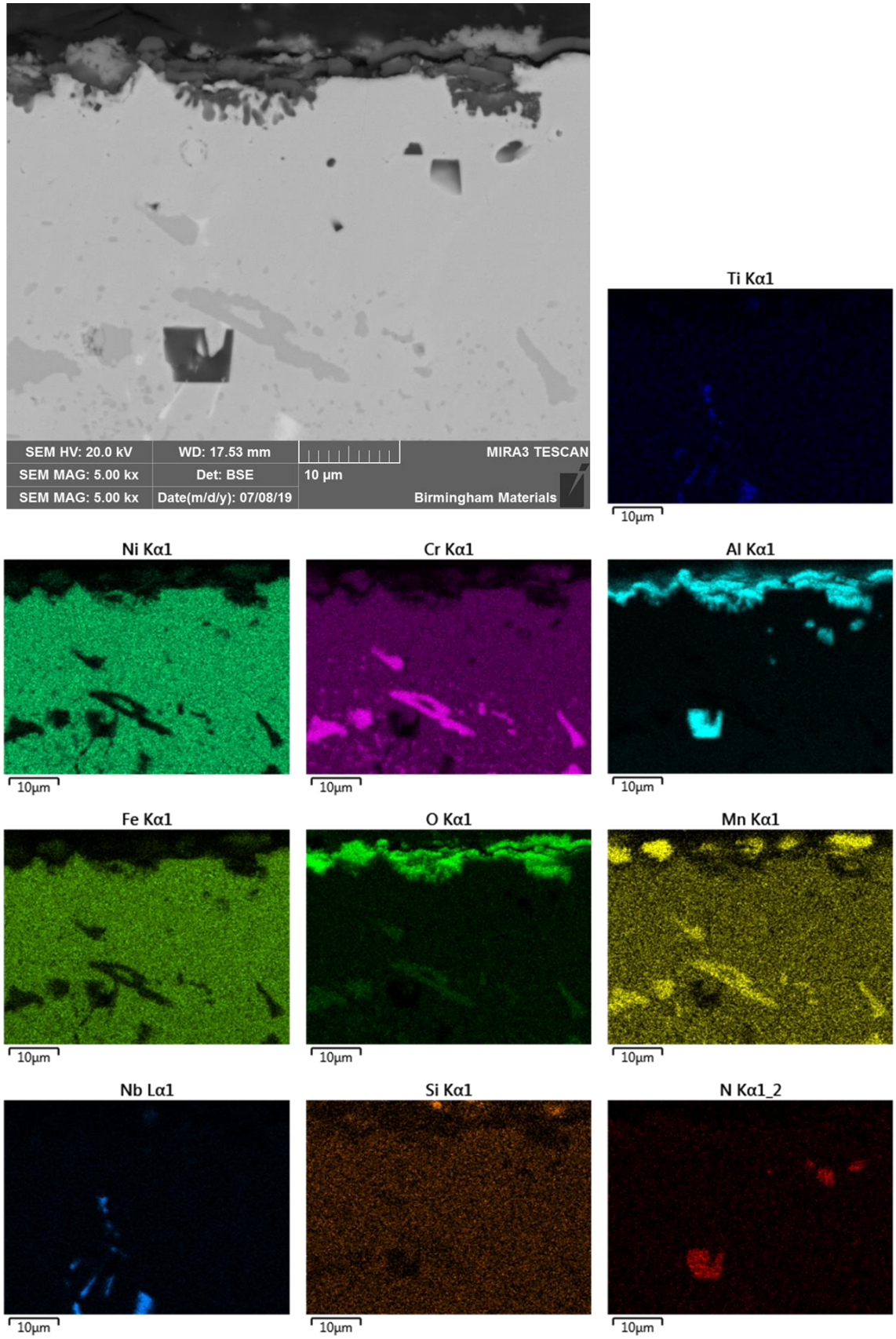

Figure 4.2.1-13: Low-Al 8-hour 1100°C oxidation elemental mapping with significant aluminium oxide near the surface.

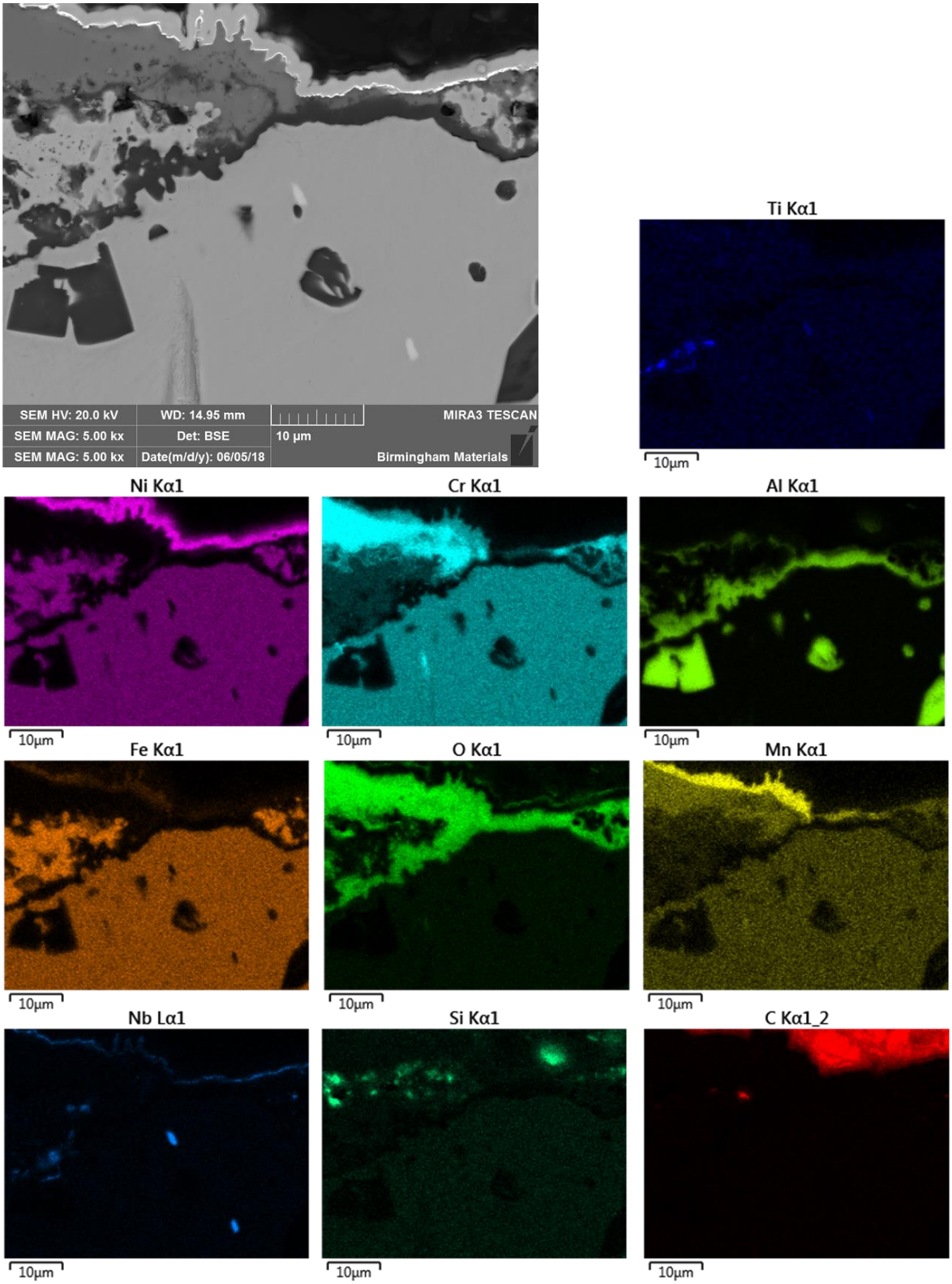

Figure 4.2.1-14: Low-Al 24h 1100°C oxidation elemental mapping demonstrating aluminium oxide beneath chromium oxide layer.

4.2.1.2.2 Phase Analysis

Figure 4.2.1-15 shows the XRD traces from the Low-Al alloy after oxidation compared to the as cast alloy. The matrix peaks showed a slight shift in position compared to the trace from the as cast alloy, a result of the diffusion of elements and the precipitation of phases which lead to changes in the d-spacing of the matrix.

Glancing angle XRD was used to gather greater signal from the surface of the sample, allowing clearer identification of surface phases. The peaks at 44°, 47° and 61° all confirm the presence of Al_2O_3 on the surface of the Low-Al alloy, whilst the peaks at 36.5° and 41.5° confirmed Cr_2O_3 formation after oxidation, reinforcing the EDS results. The peak at 35° also demonstrated the presence of $CrMn_{1.5}O_4$, despite the low volume making it difficult to resolve any other peaks.

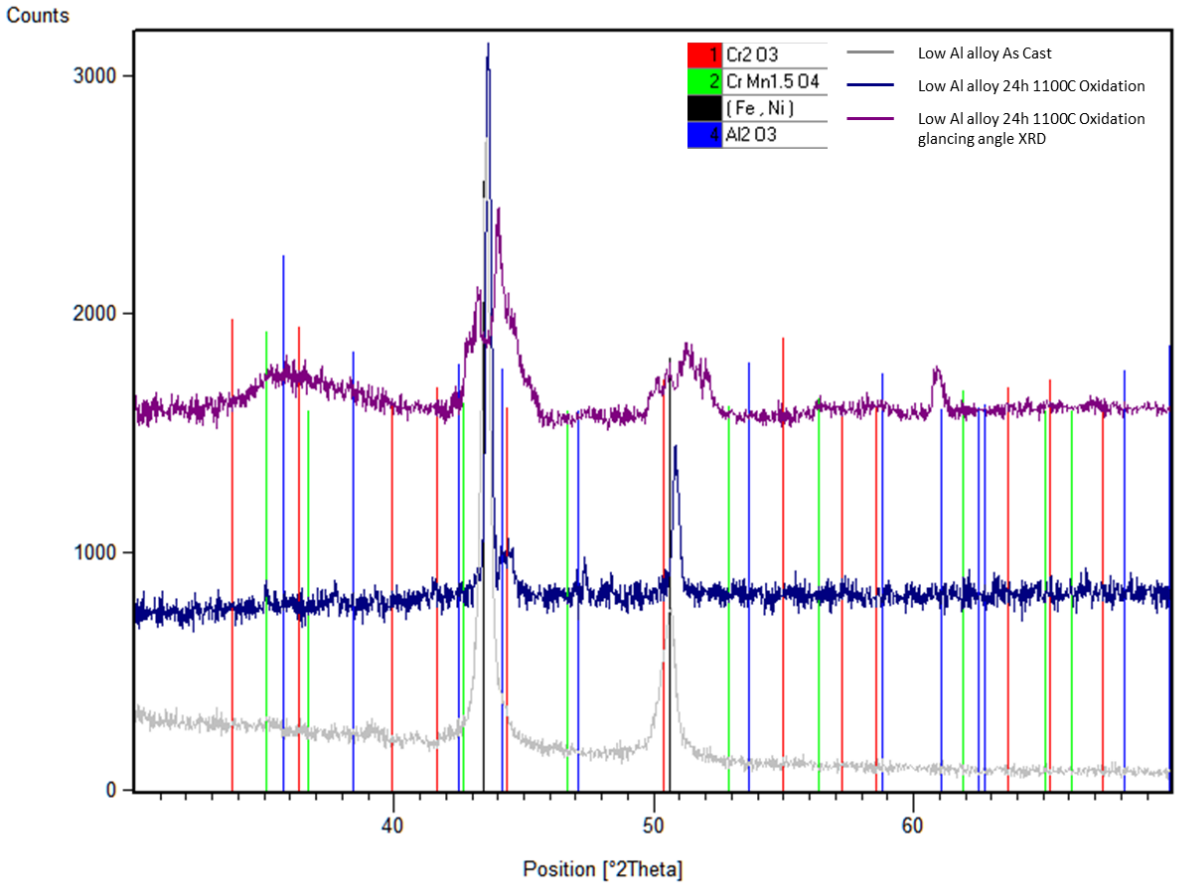

Figure 4.2.1-15: XRD traces of Low-Al alloy as cast and after 24h oxidation at 1100°C

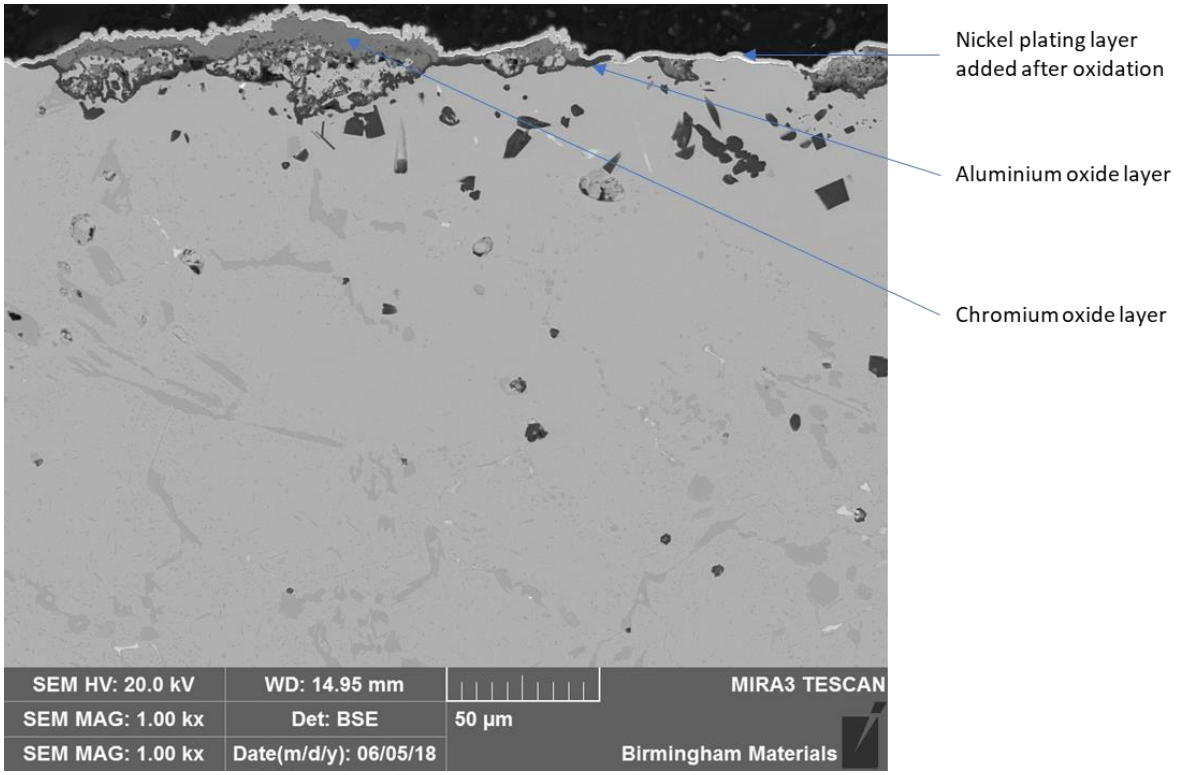

Figure 4.2.1-16: SEM backscattered image of Low-Al alloy sample oxidised for 24h at 1100°C analysed using XRD indicating oxide structure.

4.2.1.3 High-Al Alloy

4.2.1.3.1 SEM Analysis

Cross section images (Figure 4.2.1-17) showed the inconsistent and patchy production of an oxide layer on the surface of the alloy, with even less oxide coverage compared to the Low-Al alloy. This left a significant area of the matrix exposed at the surface, rather than forming the continuous oxide as desired. Some patches of oxide on the surface were present in places, and they followed a similar pattern to those seen in the Low-Al oxide alloy, with a surface chromium oxide and a subsurface aluminium oxide. The subsurface aluminium oxide appeared as interjoined internal oxidation after the 30-minute oxidation, however this became a continuous layer beneath the surface oxide with longer oxidation times. The continuity of the subsurface oxide layer was a significant improvement over the discrete globular silicon oxide layer that was seen on the Base alloy, because this layer gave complete coverage of the matrix in the regions where it was produced.

The areas covered by an oxide layer were measured, with the oxide layer 2.29μm ± 0.58μm in average thickness after 30-minute oxidation, 2.52μm ± 2.26μm after 8-hour oxidation and 8.13μm ± 5.70μm after 24-hour oxidation. The apparent minimal increase between 30-minute oxidation and 8-hour oxidation is due to the huge variation in the oxide thickness on the surface seen after 8-hour oxidation and reinforced by the standard deviation being almost 100% of the average thickness. The oxide layer thickness more than tripled between the 8-hour and 24-hour oxidation, however once again these figures are difficult to evaluate due to the nature of the oxide layer, again demonstrated by the large standard deviation of the measurements. Whilst the Base and Low-Al alloys displayed comparable measurements and changes in oxide layer thickness, the highly inconsistent nature of the oxide on the High-Al alloy results in much more unreliable results.

Comparing the appearance of the three oxidation times of the High-Al alloy and the Base alloy showed that whilst a thickening layer of the surface chromium oxide occurred, it was reduced in the aluminium containing High-Al alloy. The aluminium oxide produced was formed as a semi-continuous layer, compared to the dispersed particles of silicon oxide found in the Base alloy. This aluminium oxide layer was significantly thinner than the measured oxide thickness which included the chromium oxide layer. The thin aluminium oxide layer beneath the chromium oxide layer is what is desired, as a thinner oxide gives benefits due to the disparity of coefficients of thermal expansion between the oxide and the bulk alloy, aiding in oxide retention.

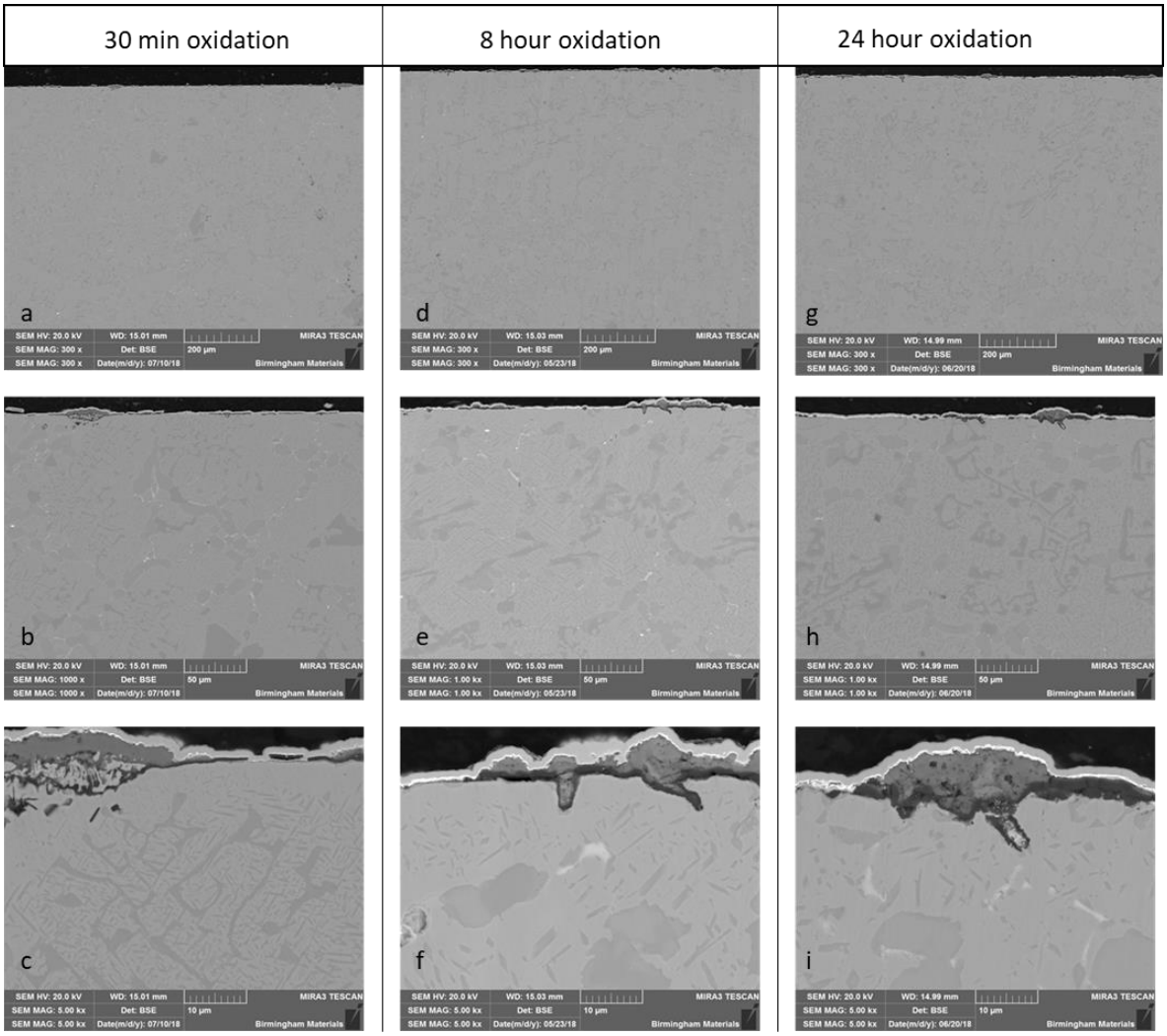

Figure 4.2.1-17: High-Al alloy oxidation after 30 minutes (a, b, c), 8 hours (d, e, f) and 24 hours (g, h, i) at 1100°C in air showing similar oxide structre to Low-Al alloy.

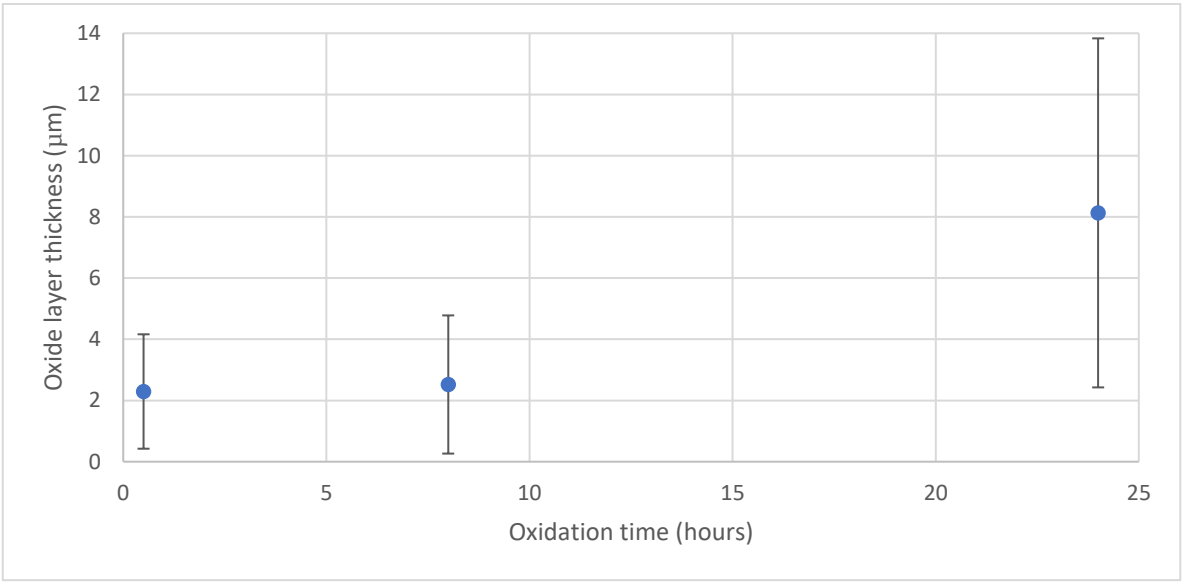

Figure 4.2.1-18: Graph of average oxide layer thickness of High-Al alloy samples oxidised at 1100°C with increasing time

Formation of intragranular carbides during the oxidation treatment is evident in Figure 4.2.1-17 c, with the carbide precipitation far more widespread than seen in the Base alloy, and greater than seen in the Low-Al alloy. The higher chromium content of this alloy compared to the Low-Al alloy, coupled with the greater carbon content compared to the Base alloy caused this amplification in carbide precipitation. These carbides were acicular as also seen in the Low-Al alloy. This is a characteristic morphology of the Cr_7C_3 carbide, compared to the $Cr_{23}C_6$ carbides that formed during the oxidation of the Base alloy (42,129). The formation of these carbides in both this alloy and the Low-Al alloy was concerning, as if they were found to be the acicular form of the Cr_7C_3 carbide, they are known to be deleterious to the stress rupture properties, therefore vastly impacting the viability of these alloys for use in service.

As well as the precipitation of fine carbides, the elemental mapping in Figure 4.2.1-19 also showed some of the needle-like phases to be nickel and aluminium rich, demonstrating precipitation of the nickel aluminide phase. This precipitation can be seen as positive, as these particles aid in creep resistance for the alloy, however they are very brittle, therefore may cause an issue in practice (18,104,133).

The elemental mapping of the 30-minute oxidation of the High-Al alloy (Figure 4.2.1-19) confirmed the surface chromium oxide and subsurface aluminium oxide layer, and also displayed manganese chromite atop the chromium oxide layer that was observed on the other alloys. Furthermore, the region which appeared to be matrix trapped between the internal oxidation and the chromium oxide, indicated in Figure 4.2.1-19, was primarily nickel and iron rich, being highly depleted of chromium compared to the matrix regions. This demonstrated that the chromium forming the oxide scale was all derived from this region, as no clear chromium depleted layer was seen elsewhere, as was the case with the Base alloy. Conversely, there was evidence of a depletion in

the near surface aluminium that corresponded to the aluminium oxide layer across the surface in the mapped region.

Longer oxidation time showed an agglomeration of the internal aluminium oxides that lead to the formation of a continuous layer of aluminium oxide beneath the surface oxide (Figure 4.2.1-20 and Figure 4.2.1-21). This was in keeping with scale formation described as type 4 by Stott et al.(134) (Figure 4.2.4-37), where the internal oxidation healed over beneath the surface oxide layer, leaving a complex mix of oxides above the aluminium oxide layer. This explained the presence of titanium, silicon and iron in the surface oxide regions, particularly those of the 24-hour oxidation, seen in Figure 4.2.1-21. Once the aluminium was exhausted in the sealed region the rest of the component elements were then oxidised. This resulted in a complex mixture of oxides above the “healing” oxide layer which separated them from the matrix.

The apparent presence of niobium across the surface of the oxide beneath the nickel plating in Figure 4.2.1-20 was actually the gold coating applied after oxidation treatment, but before the nickel plating procedure, with niobium and gold having very similar x-ray energies; niobium Lα=2.169 and gold Mα= 2.123. Figure 4.2.1-20 showed a titanium and niobium rich phase adjacent to a large chromium carbide. This is an imperfect (Nb,Ti)C formed in the latter stages of the cooling of the alloy during the casting process, with a raised localized concentration of these minor elements able to form on the carbide surface which minimizes the surface energies required for the phase formation.

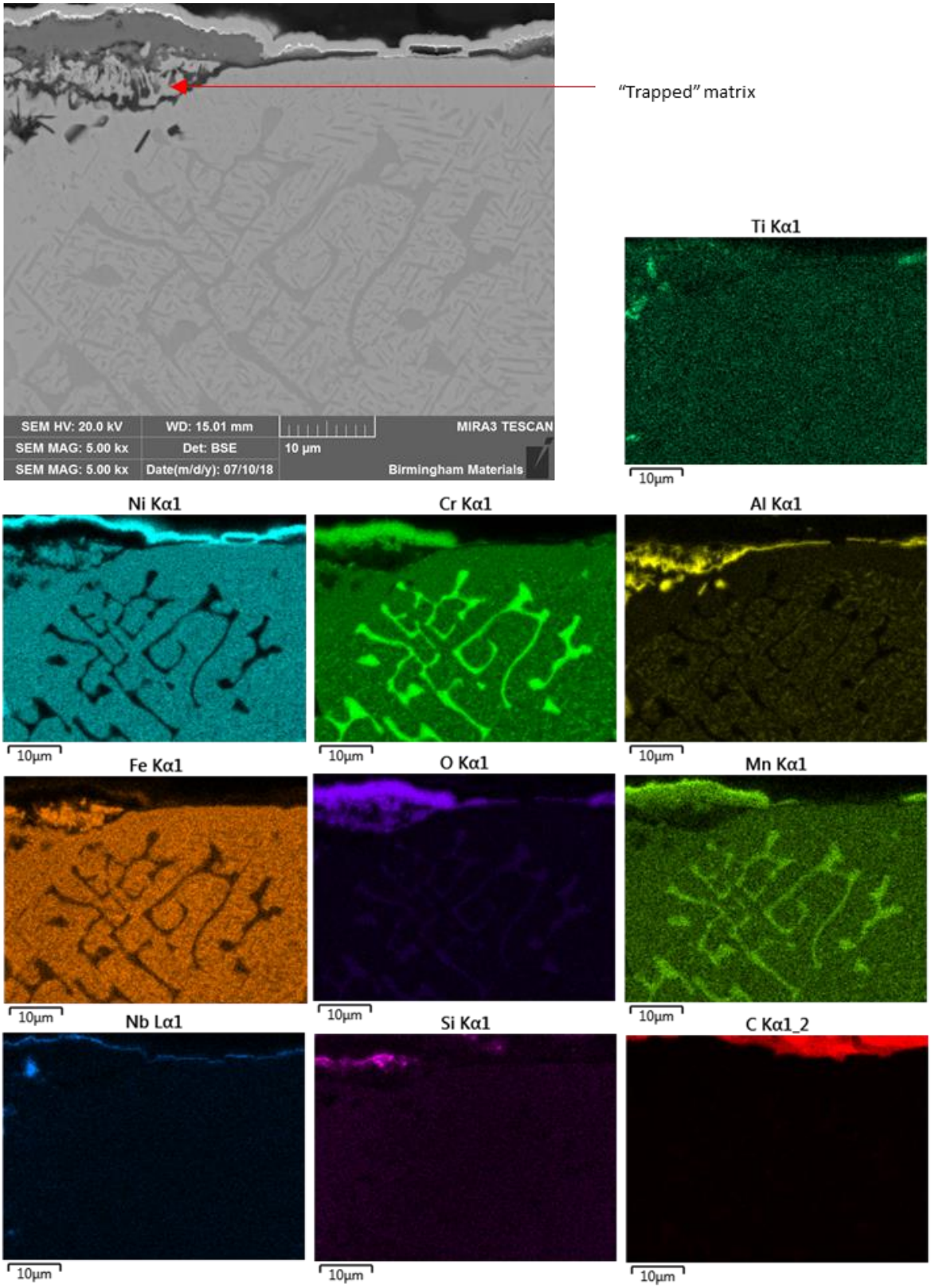

Figure 4.2.1-19: High-Al alloy 30-minute 1100°C oxidation elemental mapping showing matrix trapped between internal aluminium oxidation and surface chromium oxide scale.

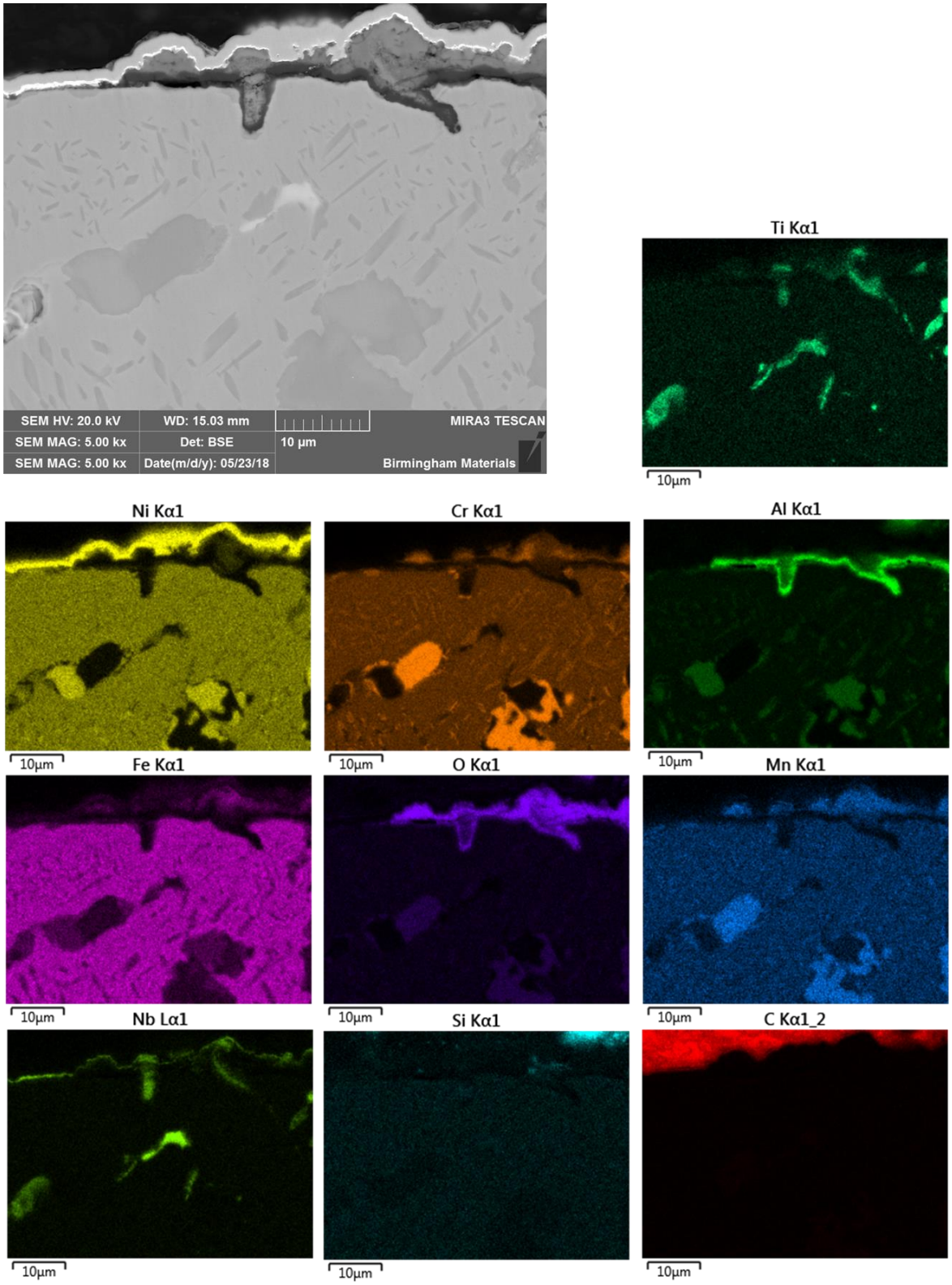

Figure 4.2.1-20: High-Al alloy 8-hour 1100°C oxidation elemental mapping

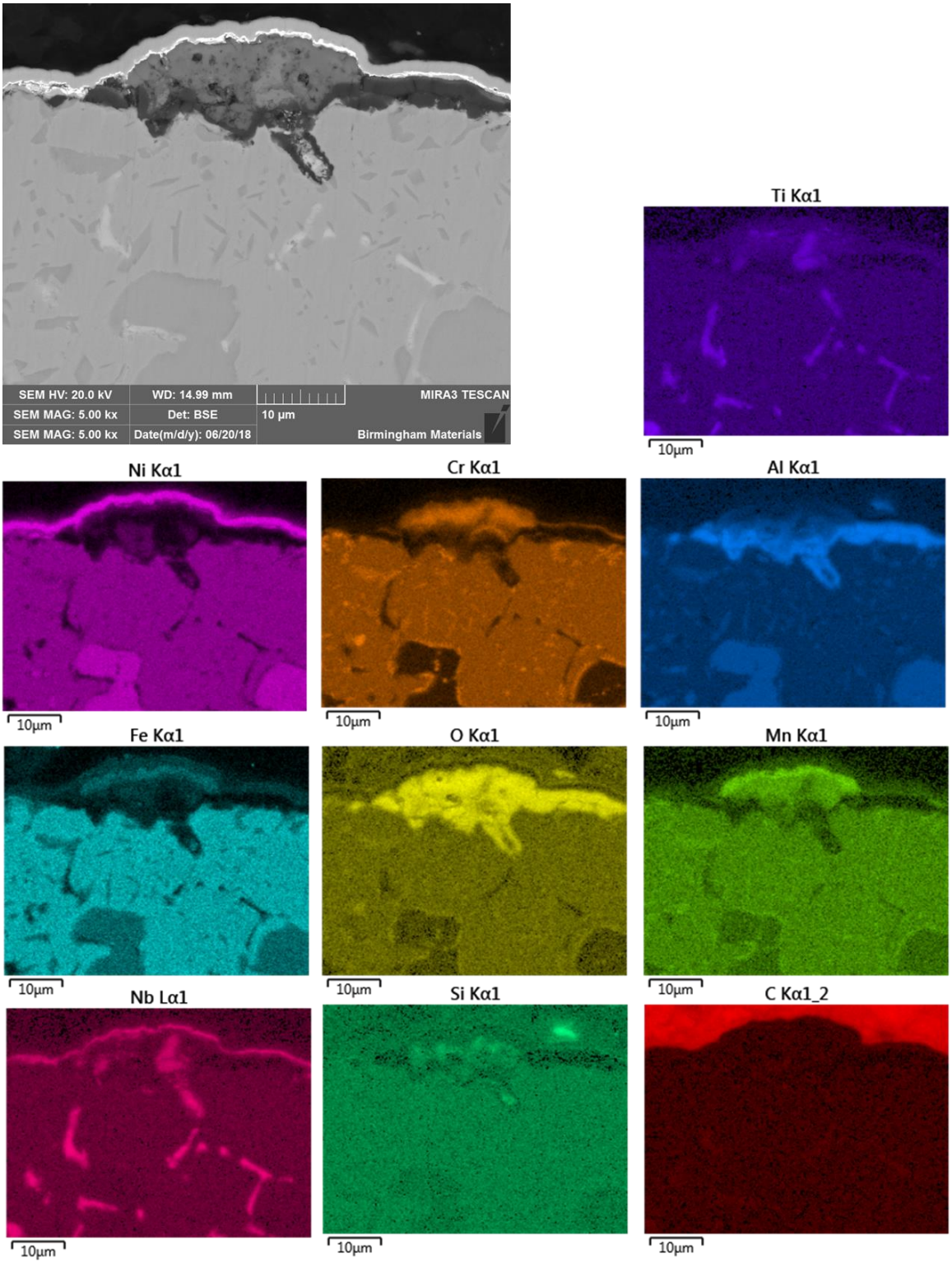

Figure 4.2.1-21: High-Al alloy 24-hour 1100°C oxidation elemental mapping with significant aluminium oxide benath chromium oxide layer.

4.2.1.3.2 Phase Analysis

Figure 4.2.1-22 shows the XRD traces of the as cast High-Al alloy and after 24-hour oxidation at 1100°C. Whilst the peaks of the matrix and the Ni_3Al phase were present in both alloys, the oxidised sample displayed peaks correlating to the presence of Al_2O_3 on the surface of the sample, as seen in SEM and EDS analysis. Some shift of the matrix peaks is evident, a result of the changes of d-spacing caused by the precipitation of the phases and diffusion of elements through the matrix.

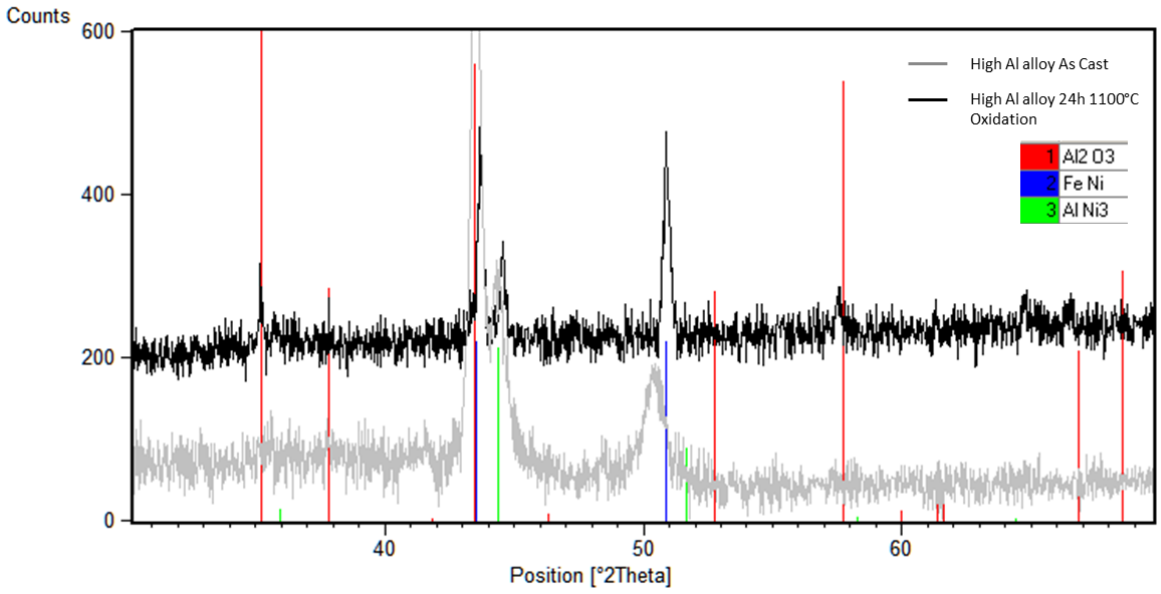

Figure 4.2.1-22: XRD traces of oxidised and as cast High-Al alloy

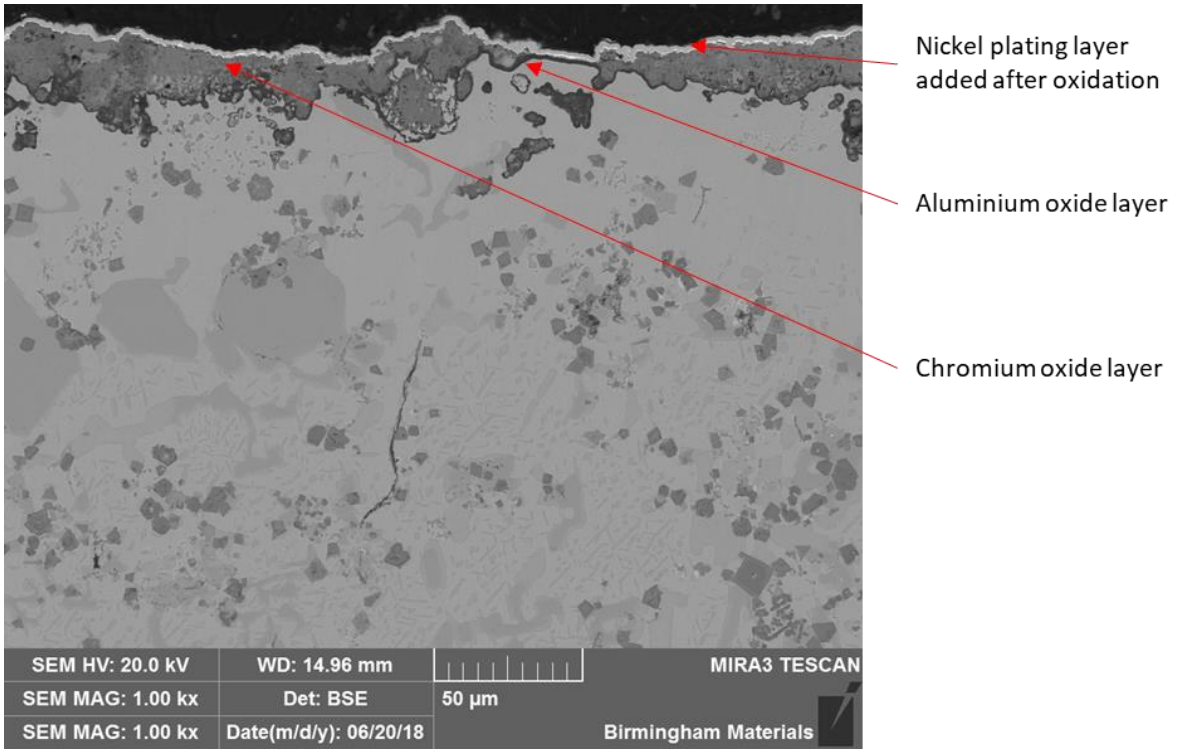

Figure 4.2.1-23: SEM backscattered image of surface of High-Al sample oxidised for 24h at 1100°C analysed for XRD with indication of oxide layers.

4.2.1.4 Optim-Al Alloy

4.2.1.4.1 SEM Analysis

Backscattered electron images of the Optim-Al alloy after three different oxidation lengths (30-minute, 8-hour and 24-hour) are shown in Figure 4.2.1-25. This displays a clear, continuous oxide across the surface of the alloy. The contrast of the layers in the backscattered image was very similar to the aluminium oxide seen beneath the chromium oxide scales in the Low-Al and High-Al alloys. The clear difference was that this alloy generated the aluminium oxide on the surface without the formation of a surface chromium oxide. Whilst some small chromium oxide scales were present, the aluminium oxide was clearly the dominant oxide, and appeared to form a complete covering of the alloy surface, as desired.

As was evident in Figure 4.2.1-25, an oxide was present across the surface, and formed around and beneath features on the surface of the sample, giving a complete barrier between the external environment and the bulk matrix of the alloy. Furthermore, this surface layer was significantly

thinner than that of the chromium alloy produced on the surface of the Base alloy, which, as discussed previously, is beneficial in the maintenance of the oxide layer during temperature changes. Moreover, there was the lack of any obvious loss of material or cracks in the surface oxide – these were present throughout the chromium oxide on the Base alloy but did not appear in this aluminium oxide layer.

The first obvious difference between the former two aluminium containing alloys and the Optim-Al alloy was the nature of the aluminium oxide after a short, 30-minute oxidation treatment. The Optim-Al alloy showed the aluminium oxide to be consistent and covering the full surface of the oxide, without any evidence of internal oxidation veins running perpendicular to the surface as was seen in both of the other aluminium containing alloys. The cause of these differences will be discussed later (5.2.2).

The thickness of the oxide layer was markedly lower when compared with the other alloys, with the oxide thickness 0.44μm ± 0.12μm after 30-minute oxidation, six times lower than that of the Base alloy, and more than four times thinner than the other aluminium containing alloys. After 8-hour oxidation the layer thickness was measured to be 1.25μm ± 0.46μm, displaying a similar 2- to 3-fold increase to the Base and Low-Al alloys, which were discussed previously as having a more similar microstructure than the High-Al alloy. After 24-hour oxidation the average oxide thickness was 1.80μm ± 0.69μm, a further growth of only around 50%, similar to the Base and Low-Al alloy, with a slightly greater reduction in growth rate. These measurements were in line with the SEM observations displaying the consistent, thin oxide growing across the surface.

The EDS mappings of all three different length oxidation treatments (Figure 4.2.1-26, Figure 4.2.1-27 and Figure 4.2.1-28) show evidence of only surface breaking niobium rich carbides, which, as previously discussed, are known to be present throughout the alloy and are unable to be sealed over with an aluminium oxide layer (marked in Figure 4.2.1-26). Instead the oxide grew beneath

these particles, maintaining a continuous oxide across the alloy. The absence of iron or nickel at the surface of the sample, which, as previously discussed, are the prime factors in catalytic coke formation, indicated that this alloy should be protective in service. The surface oxide provided a physical barrier between the catalytic elements and the active gas stream, minimizing the potential for catalytic coking.

Despite having surface breaking chromium carbides (indicated in Figure 4.2.1-26) which are, by their nature, chromium rich, no scale of chromium oxide appeared to grow on the surface of the alloy. Whilst a growth of chromium oxide would not necessarily be detrimental, it appeared that the lack of the chromium oxide allowed the ideal situation for growth of the aluminium oxide, without creating a competing oxide as with the previous two aluminium containing alloys.

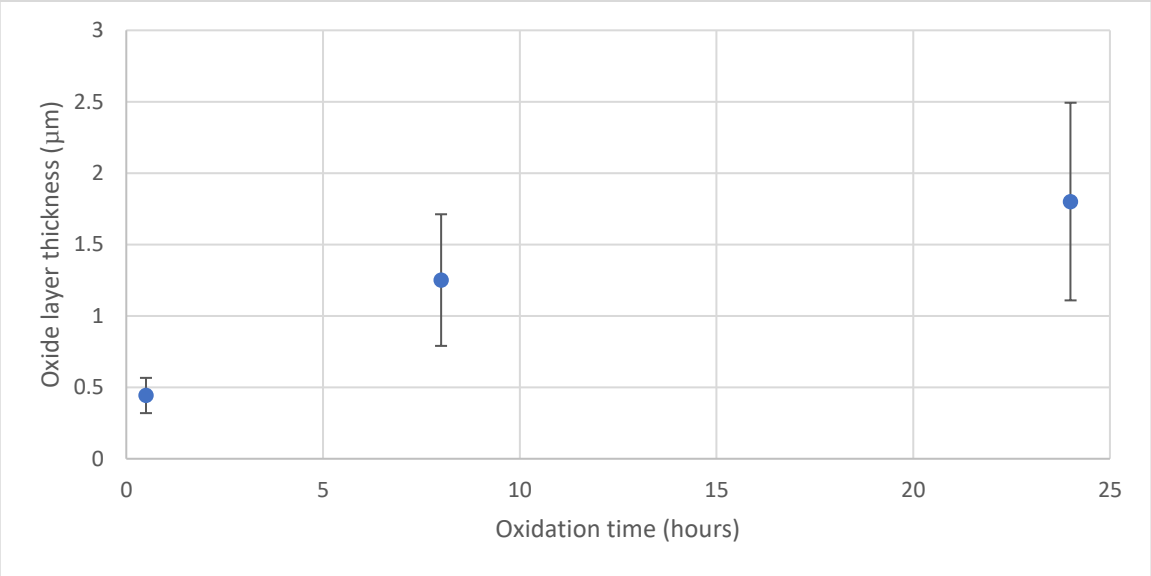

Figure 4.2.1-24: Graph showing average oxide layer thickness of Optim-Al alloy oxidised at 1100°C for increasing time

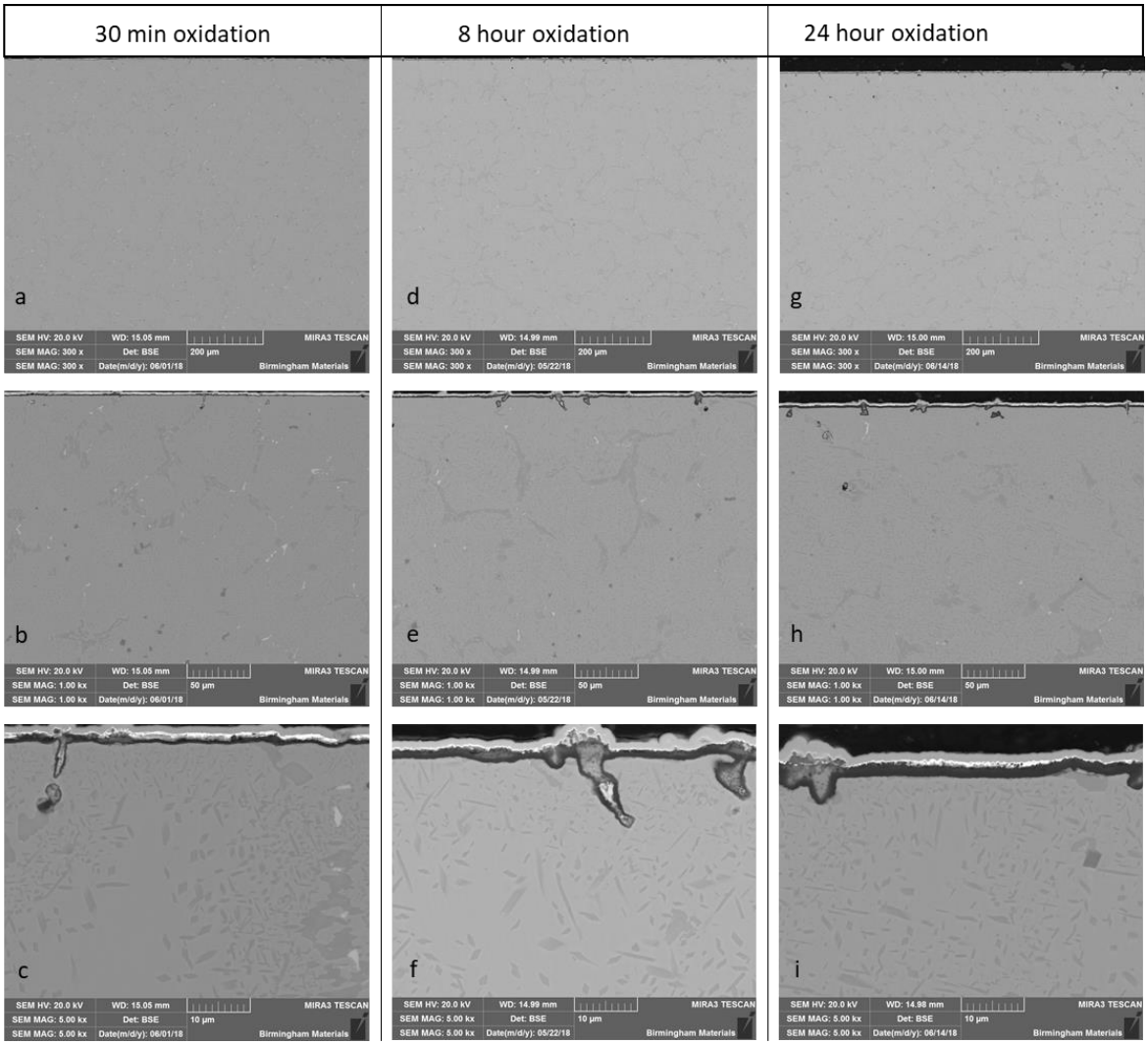

Figure 4.2.1-25: Optim-Al alloy oxidation after 30 minutes (a, b, c), 8 hours (d, e, f) and 24 hours (g, h, i) at 1100°C in air indicating surface coverage of single oxide layer.

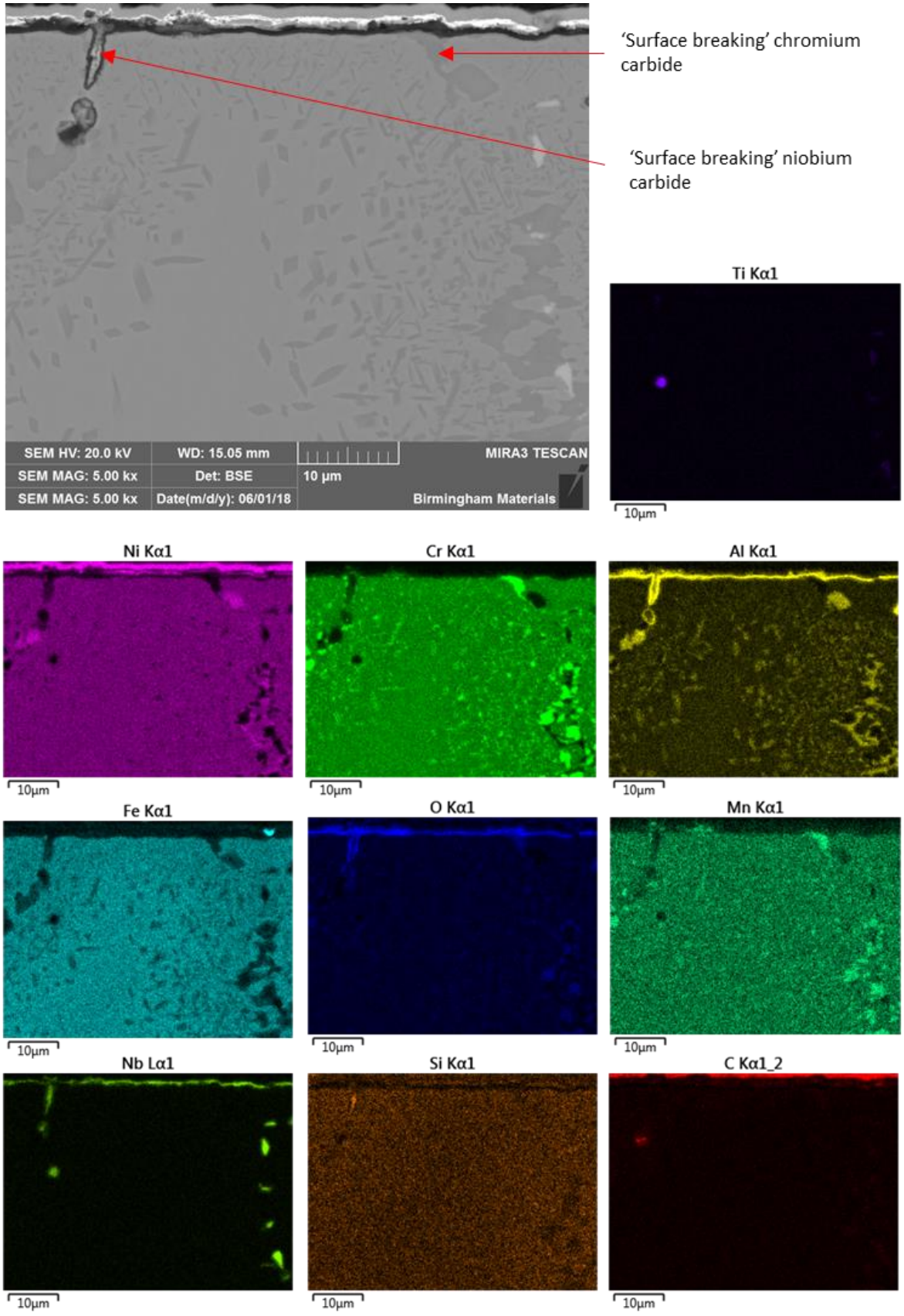

Figure 4.2.1-26: Optim-Al alloy 30 minute 1100°C oxidation elemental map with aluminium oxide across the surface unless a surace breaking niobium carbide is present.

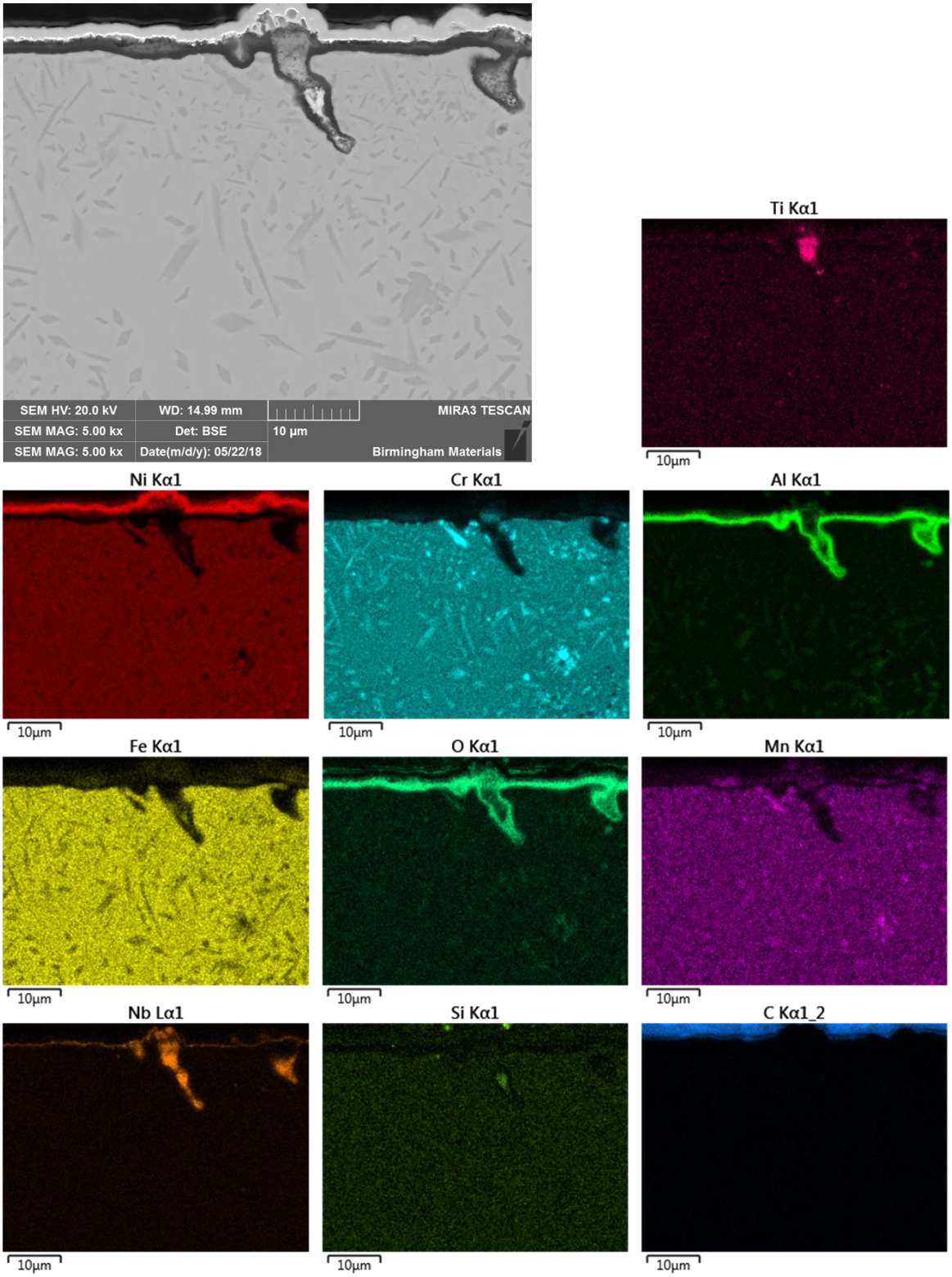

Figure 4.2.1-27: Optim-Al alloy 8-hour 1100°C oxidation elemental mapping, showing aluminium oxide protecting matrix beneath from surface.

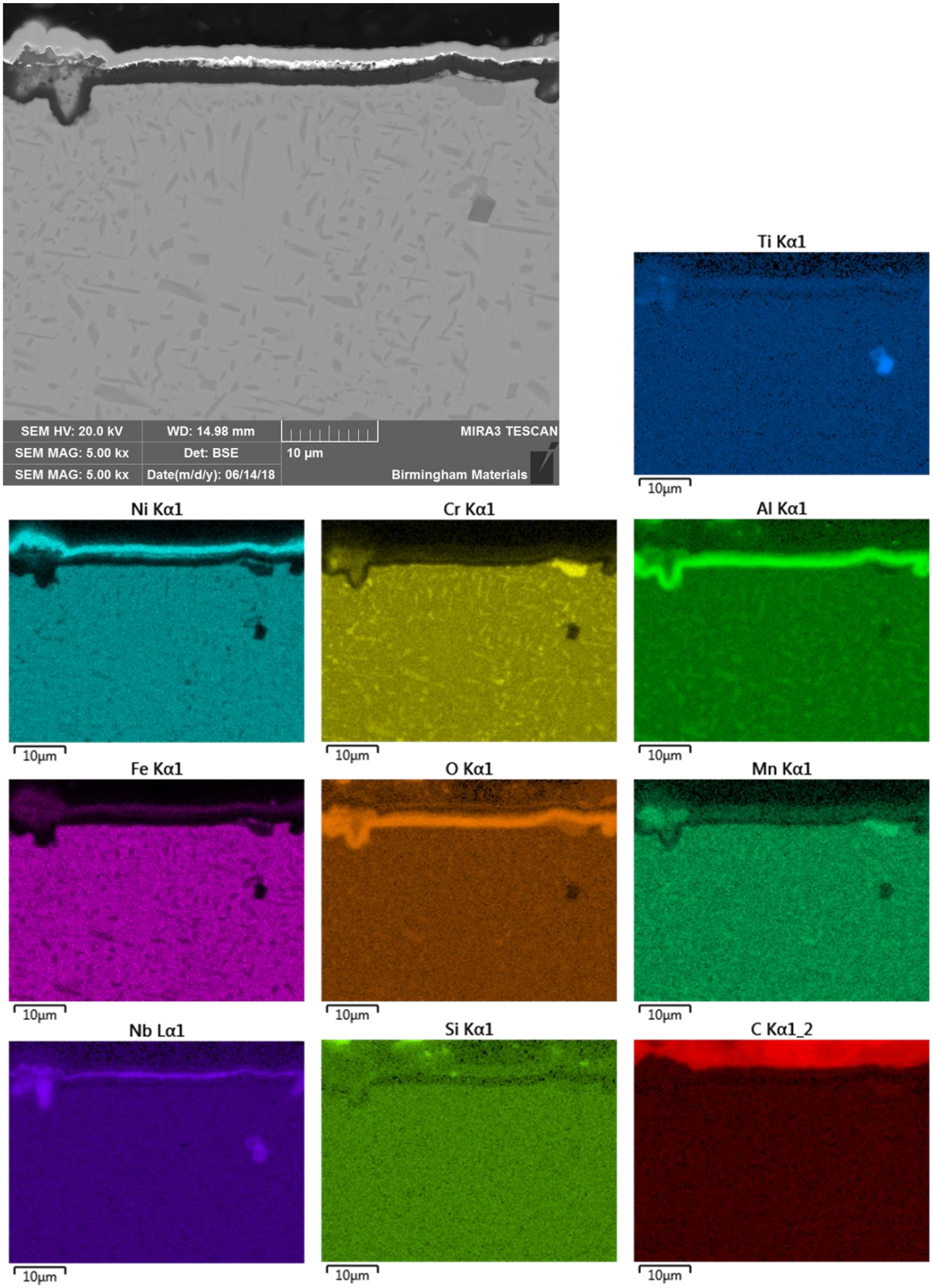

Figure 4.2.1-28: Optim-Al alloy 24-hour 1100°C oxidation elemental mapping, with surface layer showing two different phases, with an aluminum and nickel oxide apparet on the surface.

Whilst the formation of fine carbides was seen throughout the oxidised samples, and the nature of these carbides could be changed through adjustments of the cooling rates, the service conditions mean very gentle cooling rates were required to achieve the optimum product life. This is due to the disparity in thermal coefficients of expansion of the coke which builds up on the inner surface of the pipe, and the pipe itself, as discussed in 2.3.2, which is required to avoid premature failure. Due to this, no rapid cooling tests were undertaken as these would not occur in practice for the alloys. Furthermore, rapid cooling will cause greater loss of surface oxide material because of the dissimilar coefficients of thermal expansion of the oxide and matrix material.

4.2.1.4.2 Phase Analysis

XRD analysis of the Optim-Al alloy was undertaken to identify the different oxide phases produced on the surface of the alloy after the oxidation treatment.

Figure 4.2.1-29 shows the surface oxide previously presumed to be aluminium oxide to be confirmed as Al_2O_3 present on the surface of the samples in all oxidation treatments, with major peaks at 35° and 57.5°. The spinel phase $NiAl_2O_4$ was also present, particularly in the 48-hour oxidation sample, which is seen growing atop the aluminium oxide layer in Figure 4.2.2-38. This was identified by the peaks at 36.5° and 65°, with the 8-hour 1100°C oxidation sample also demonstrating this phase presence.

Furthermore, TEM analysis confirmed the Al_2O_3 oxide layer formed on the matrix, with presence of the $NiAl_2O_4$ atop the aluminium oxide layer (Figure 4.2.1-31 & Figure 4.2.1-30).

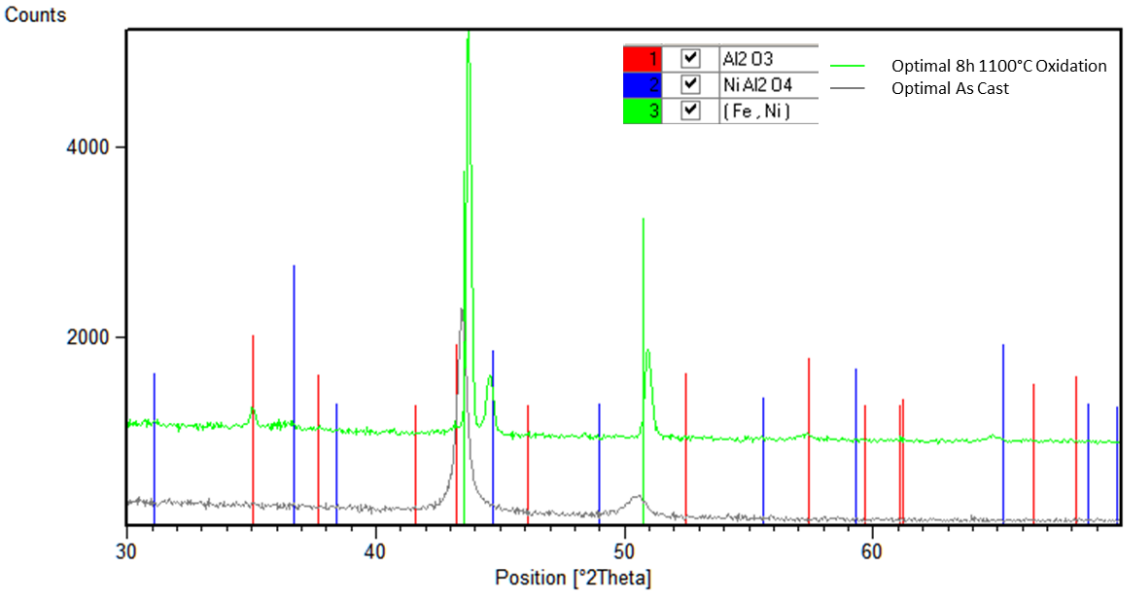

Figure 4.2.1-29: XRD traces of oxidised and as cast Optim-Al alloy

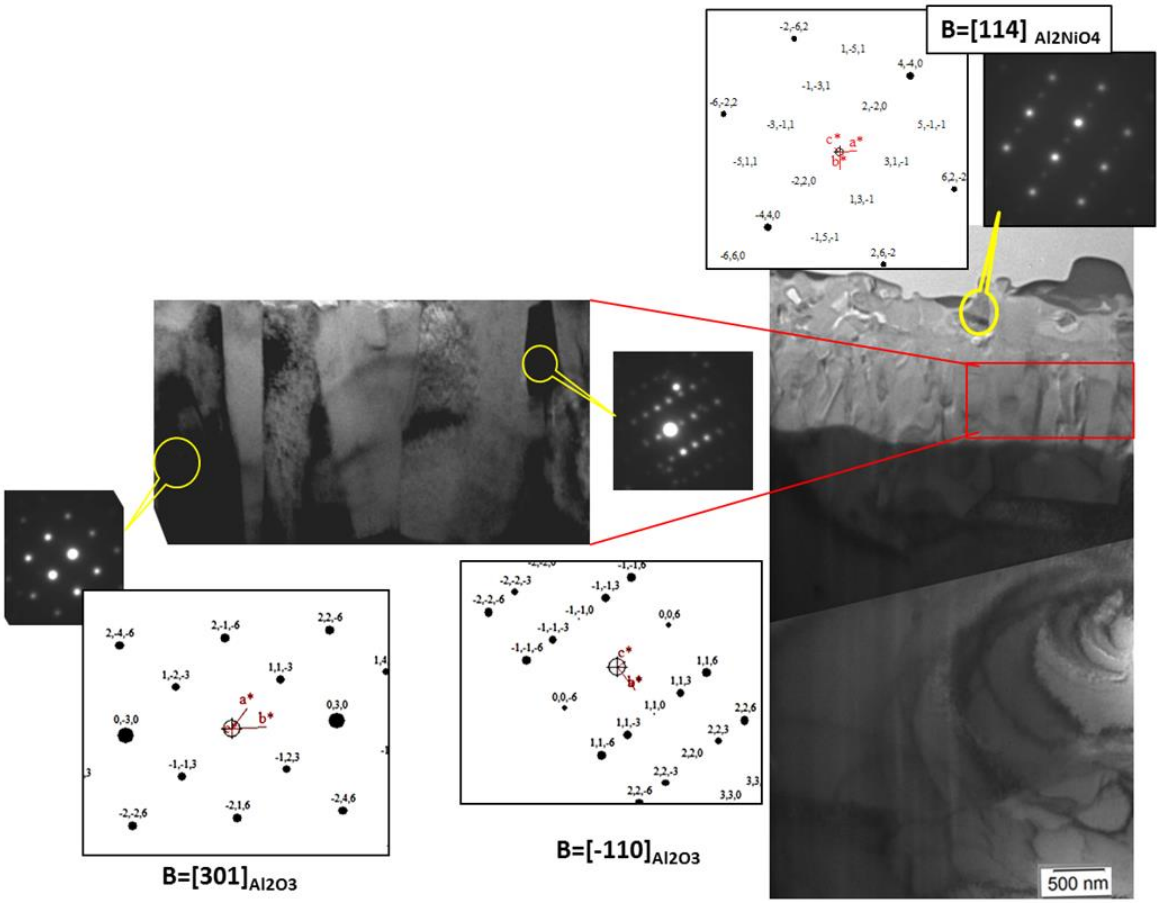

Figure 4.2.1-30: TEM image and corresponding selected area diffraction (SAD) patters of Optim-Al alloy oxidised at 1100°C for 8 hours, showing layer structure formed and identifying the different phases.

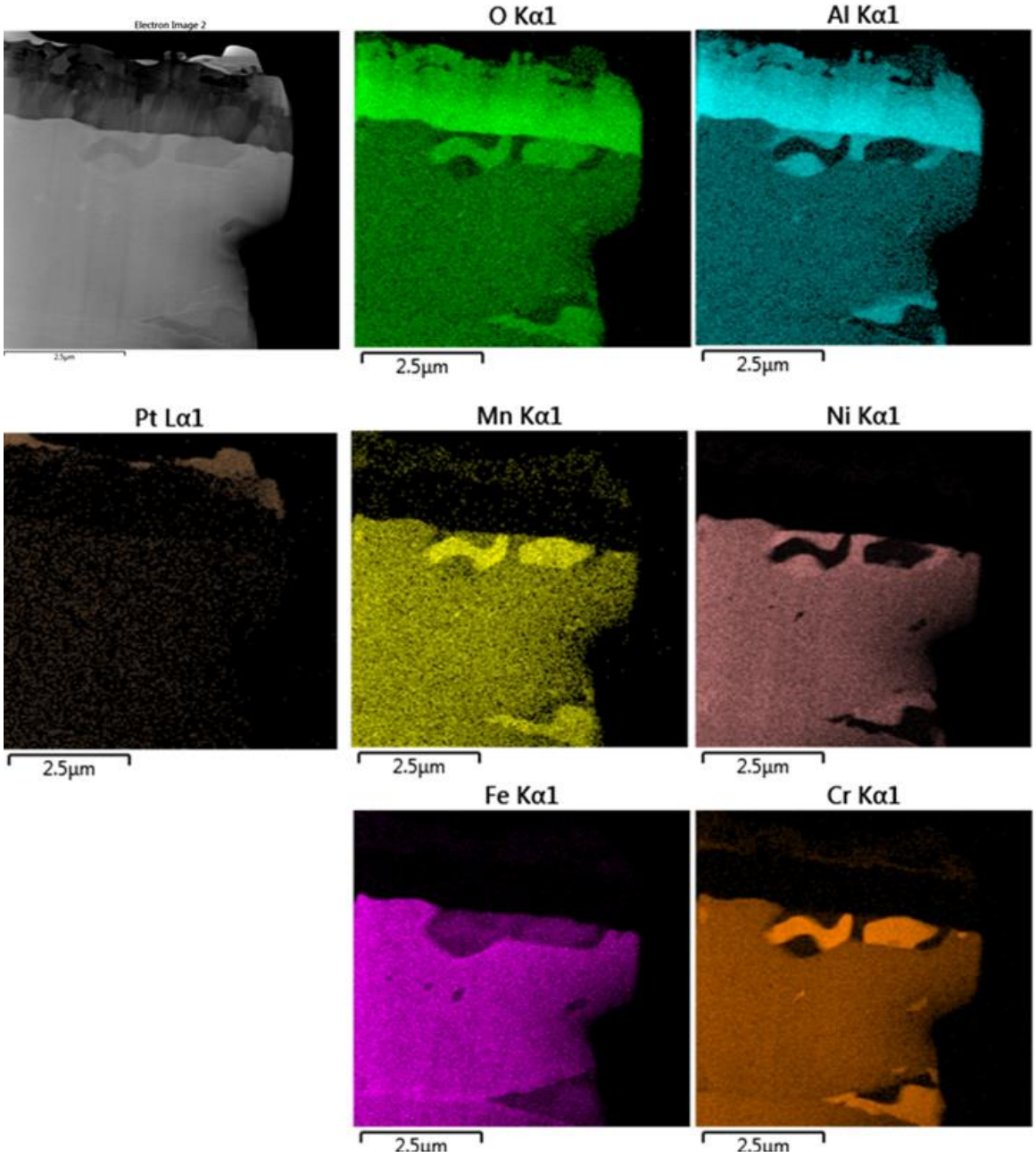

Figure 4.2.1-31: Scanning TEM image and EDS mapping of Optim-Al alloy oxide layer after oxidation at 1100°C for 8 hours

4.2.1.5 Summary of oxide layer analysis

The Base alloy produced a thick chromium oxide layer across the surface of the alloy. This chromium oxide layer was topped with a thin manganese chromite layer with extended oxidation time, whilst silicon oxide was present as a non-continuous sub-surface oxide.

The Low-Al and High-Al alloys displayed inconsistent surface coverage of an aluminium oxide which was topped with a chromium oxide. The silicon oxide formation seen in the Base alloy was no longer present in these alloys, having been superseded by the formation of aluminium oxide. Neither of the Low-Al or High-Al alloys presented with an oxide which fully covered the surface of the matrix.

The Optim-Al alloy on the other hand produced a dense, continuous aluminium oxide layer across the surface after all three treatment lengths. The aluminium oxide layer formed across the matrix surface, and over surface breaking chromium carbides. The only non-oxide phase which was present on the surface after oxidation were niobium carbides.

Oxide layer thickness of the aluminium oxide layer in the Optim-Al alloy was significantly lower than the chromium oxide layer formed on the Base alloy, as Table 4.2.1-1 displays a roughly six-fold difference between the two. The presence of chromium oxide and aluminium oxide on the Low-Al and High-Al alloy oxide layers resulted in significantly greater variability in oxide thickness, as indicated by the standard deviation of the oxide thickness. Excluding the High-Al alloy, due to the great standard deviation in the 8-hour oxidation average thickness, the other three alloys all displayed similar increases in the region of a three-fold increase between the 30-minute and 8-hour oxidation.

All the alloys displayed precipitation of secondary phases during the oxidation treatments, most commonly precipitation of fine chromium carbides, whilst nickel aluminides were seen to have precipitated in the High-Al alloy. The EDS mapping of the Base alloy displayed a clear chromium depleted layer in the matrix beneath the surface oxide layer, which was absent of precipitated chromium carbides due to the greater affinity of chromium for oxygen than carbon.

Table 4.2.1-1: Average oxide layer thicknesses of all four alloys after 30-minute, 8-hour and 24-hour oxidation

	Average Oxide Layer Thickness (µm)		
Alloy	30-minute	8-hour	24-hour
Base	2.90 ± 0.58	7.83 ± 1.48	13.16 ± 1.41
Low-Al	1.96 ± 2.27	3.86 ± 1.99	7.28 ± 4.10
High-Al	2.29 ± 0.58	2.52 ± 2.26	8.13 ± 5.70
Optim-Al	0.44 ± 0.12	1.25 ± 0.46	1.80 ± 0.69

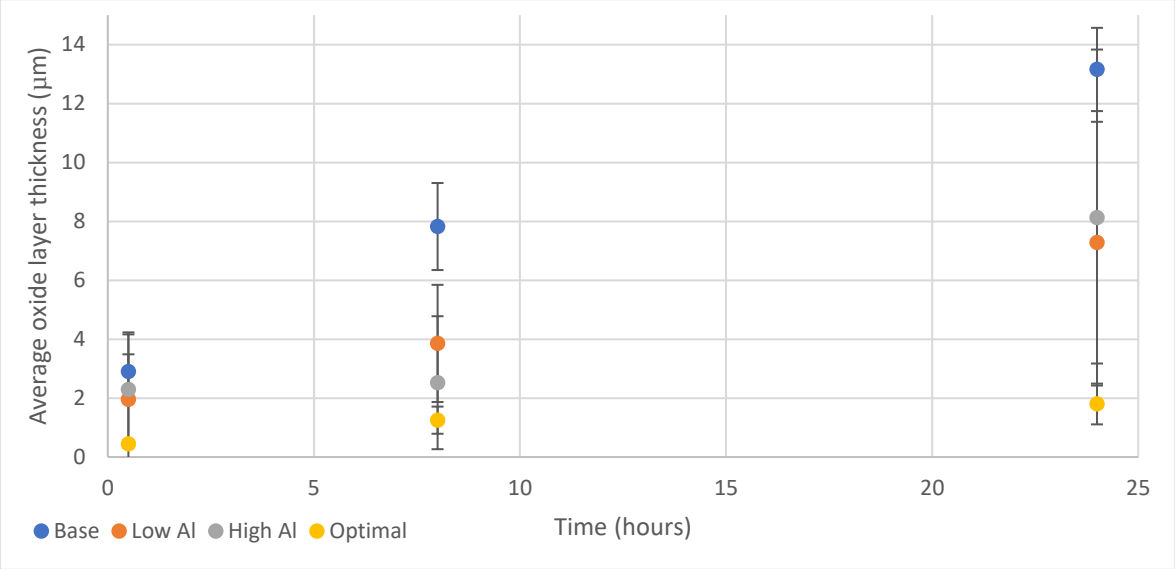

Figure 4.2.1-32: Graph of average oxide layer thickness progression for all 4 alloys

4.2.2 Effects of time and temperature on oxide layer growth

In order to evaluate the difference in the growth and nature of the oxides formed on the surface of the Base alloy and the Optim-Al alloy, oxidation of both alloys was undertaken at three temperatures – 800°C, 950°C and 1100°C, and over 8 different oxidation times: 1 hour, 2 hours, 4 hours, 8 hours, 16 hours, 24 hours, 36 hours and 48 hours. This procedure was undertaken to allow the evolution of the oxides to be observed, and for the most appropriate oxidation conditions to be determined. 800°C was selected to determine the potential evolution of the oxide in conditions similar to those used in service and to confirm that the oxide was able to withstand at least relatively short periods at the temperature necessary to achieve the desired protection. 1100°C was chosen as the high-end temperature as this is the peak temperature used in the cleaning cycle for the pipes. If the oxide is able to grow and maintain at 1100°C the cleaning cycle may be used as

a re-passivation step, reforming the oxide and maintaining the protection from catalytic coking occurring. If the scale could not withstand these conditions, another oxidation step would be necessary to reform the oxide layer after the cleaning cycle.

4.2.2.1 Base Alloy

The Base alloy, as previously discussed, formed a thick chromium oxide layer across its surface. This oxide showed evidence of incomplete coverage, fracturing, and loss of material. Oxidation over different temperatures and times allowed the nature and changes in the oxide layers formed to be explored.

4.2.2.1.1 800°C Oxidation

Comparing the surface appearance of the Base alloy oxidised at 800°C across the different oxidation times (Figure 4.2.2-1) showed little obvious change; the surface did appear to have a consistent oxide across the surface with no remarkable changes, especially after 4 hours. Whilst the oxide was thickening, there was very little evidence on the surface of any other major changes, with some sparse evidence of loss of oxide material, but this was not widespread.

Figure 4.2.2-2 more clearly illustrated that the oxide thickened and became more rounded in nature on the surface with increased oxidation time, but this change was gradual. The oxide grew in a relatively uniform manner, with the pattern of the machining marks on the surface of the sample still evident, as the 16-hour and 24-hour images in Figure 4.2.2-2 clearly illustrated the mirroring of the pattern of the machining marks. Figure 4.2.2-2 also shows the changing nature of the oxide with increased oxidation time, with the 16-hour and 48-hour showing the sample surface to be covered in small, angular scales of manganese chromite. This was found atop the chromium oxide, completely covering the surface of the samples oxidised for longer than 4 hours, demonstrated by Figure 4.2.2-4 and Figure 4.2.2-5. These show a manganese presence atop the chromium oxide layer.

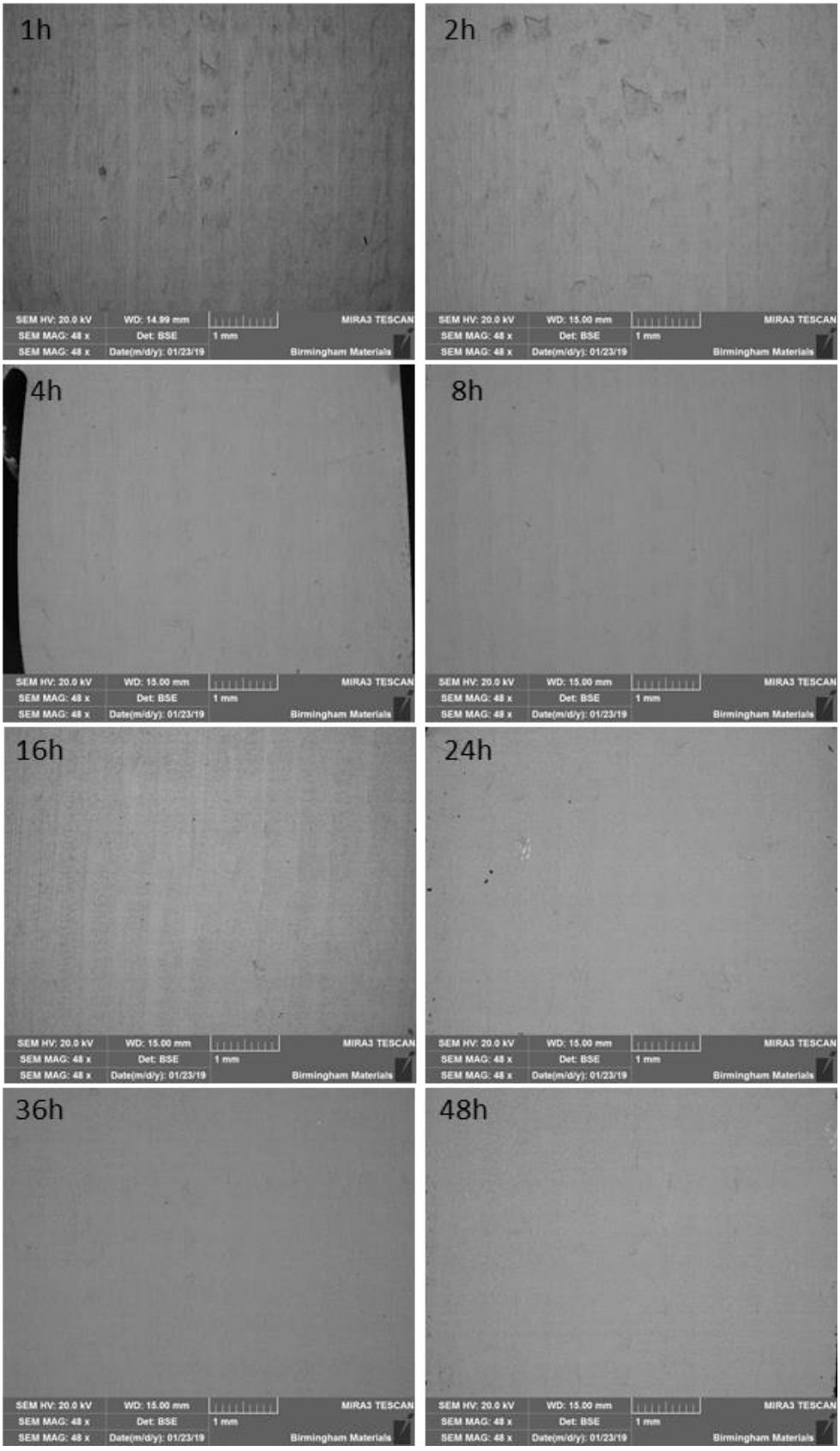

Figure 4.2.2-1: Base Alloy 800°C Oxidation progression surface images, with little difference clear throughout.

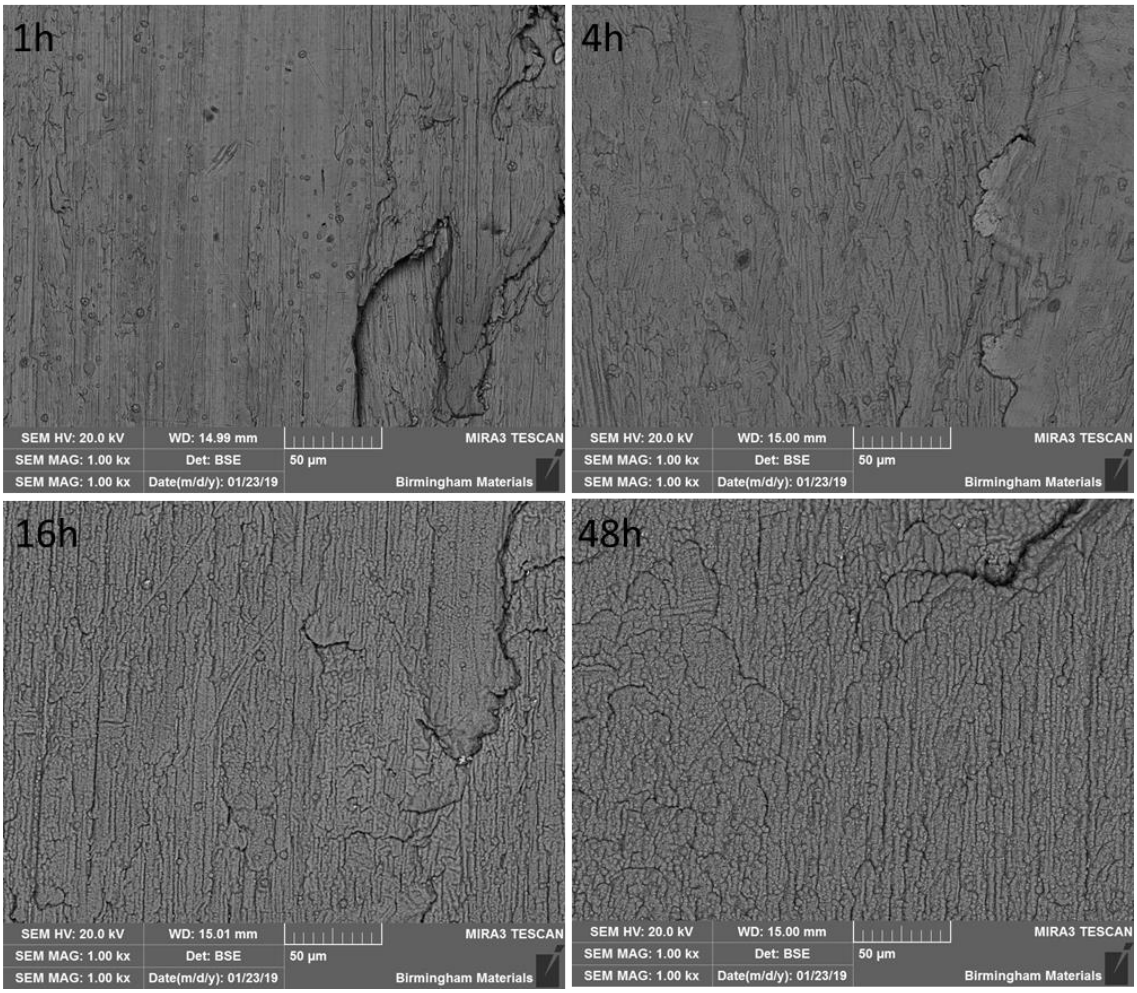

Figure 4.2.2-2: Base 800°C oxidation surface images higher magnification showing changing nature of surface texture, demonstrating oxide growth.

The cross-section images of the Base alloy shown in Figure 4.2.2-3 display a very thin oxide layer which thickened with oxidation time. However even after 48-hour oxidation the oxide layer thickness rarely reached 2 microns at its thickest point. Figure 4.2.2-6 shows the progression of the oxide growth, where there was a clear rapid thickening of the oxide layer during the first 8 hours of oxidation, followed by a more gentle increase in oxide layer thickness, with a plateauing at just over 0.8 microns. This plateauing could be a result of the depletion of near surface chromium, identified in Figure 4.2.1-6, limiting the chromium availability to continue the chromium oxide growth. Manganese is clearly present across the surface of the sample, as displayed in Figure 4.2.2-4, with notable differences between the manganese and the chromium mappings, confirming the manganese presence, rather than overlapping energy intensities giving false readings.

Furthermore, the cross-section EDS mapping shows manganese concentration atop the chromium rich layer in Figure 4.2.2-5.

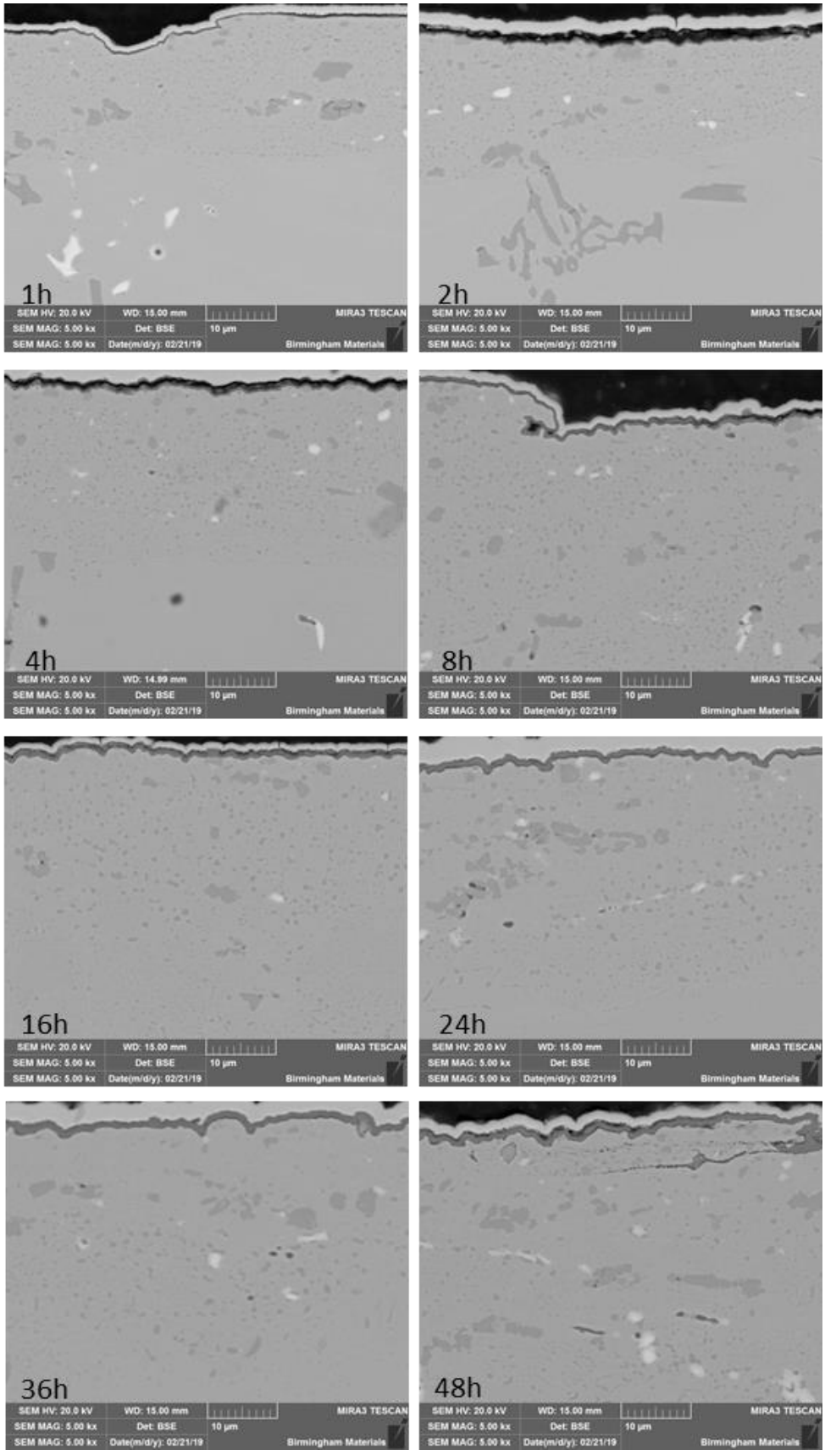

Figure 4.2.2-3: Base Alloy 800°C Oxidation progression cross section images showing thickness growth of surface oxide layer.

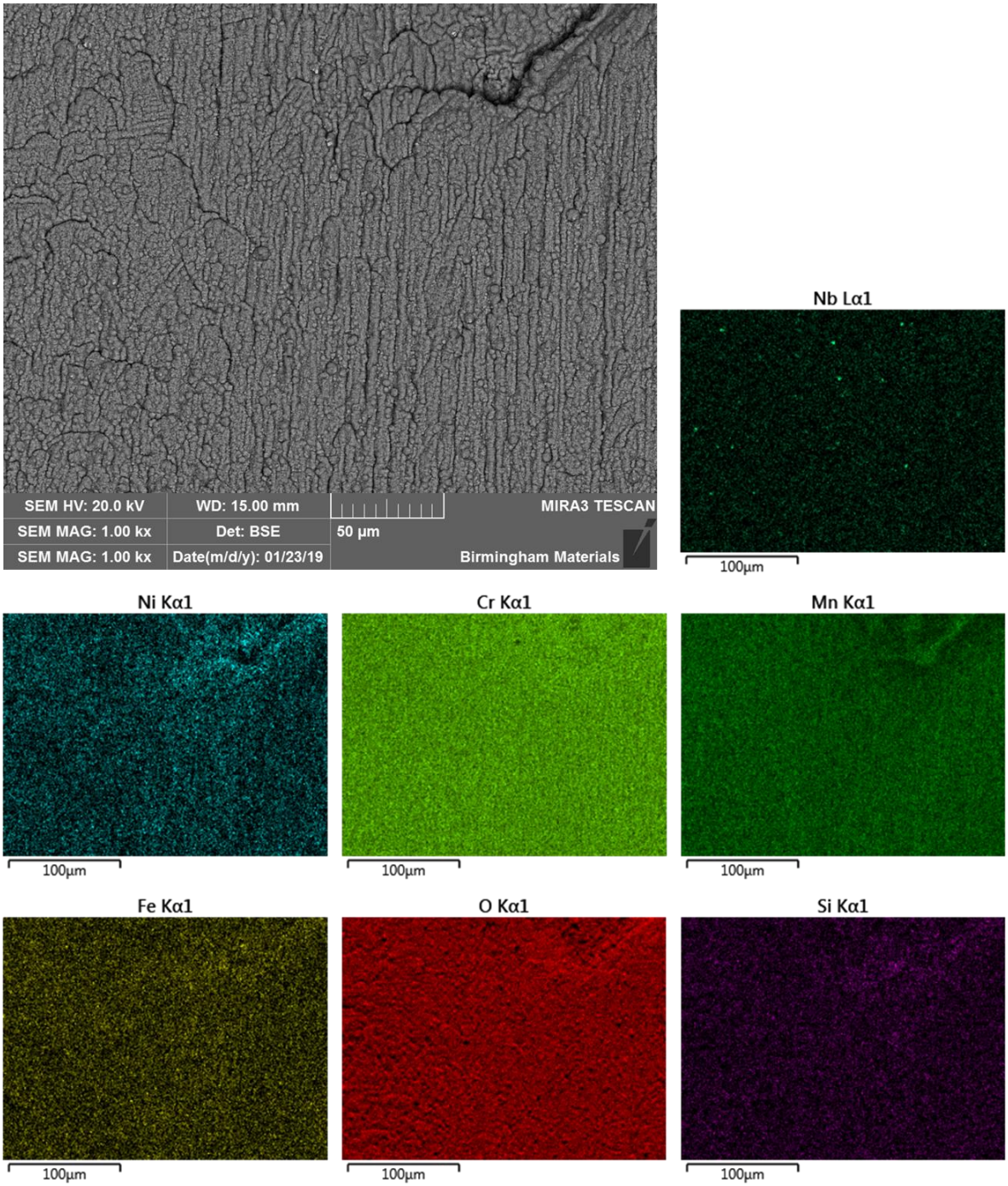

Figure 4.2.2-4: EDS elemental mapping of highly textured surface of Base alloy oxidised at 800°C for 48 hours

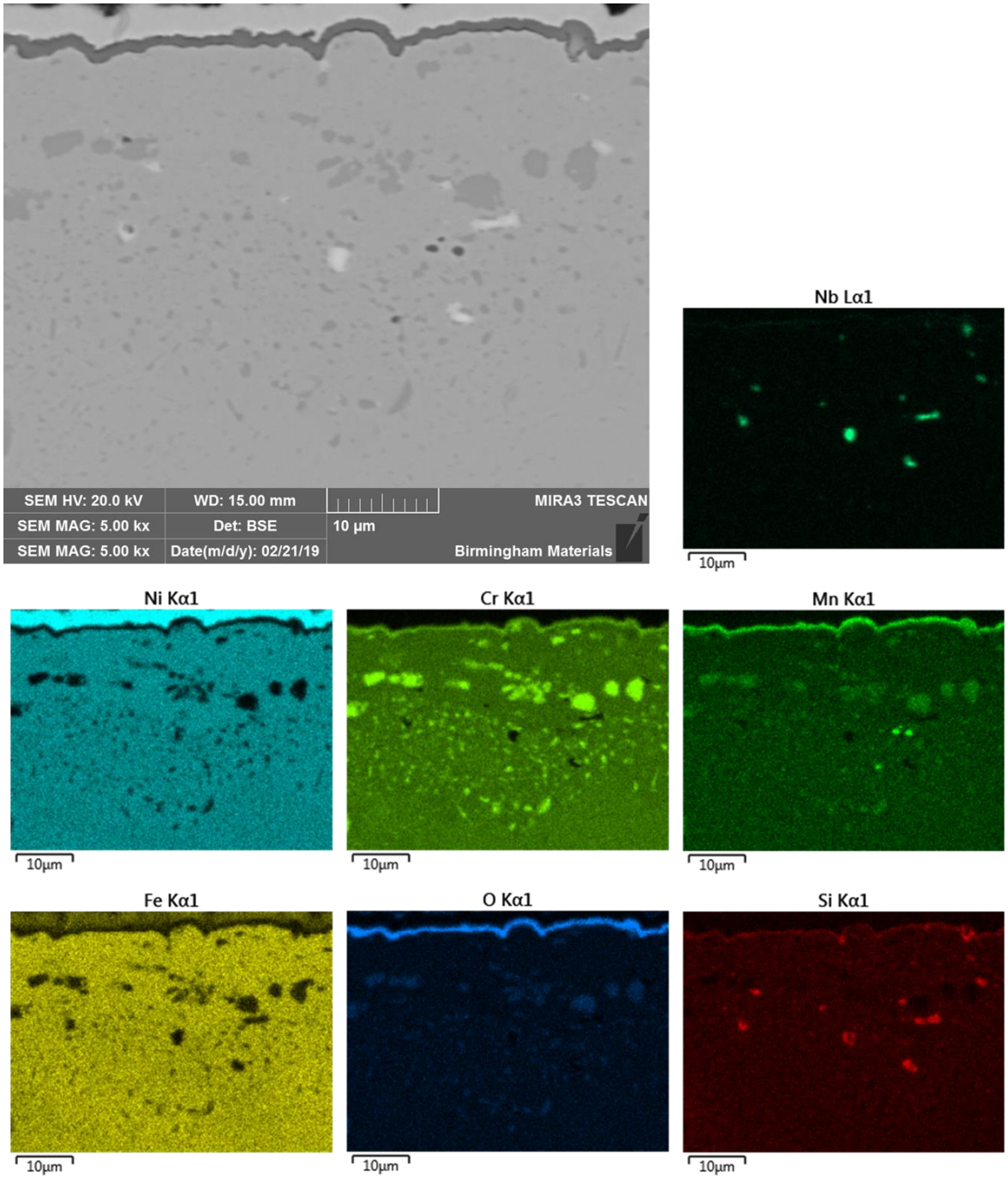

Figure 4.2.2-5: Cross section EDS elemental mapping of Base alloy oxide layer after 36h oxidation at 800°C

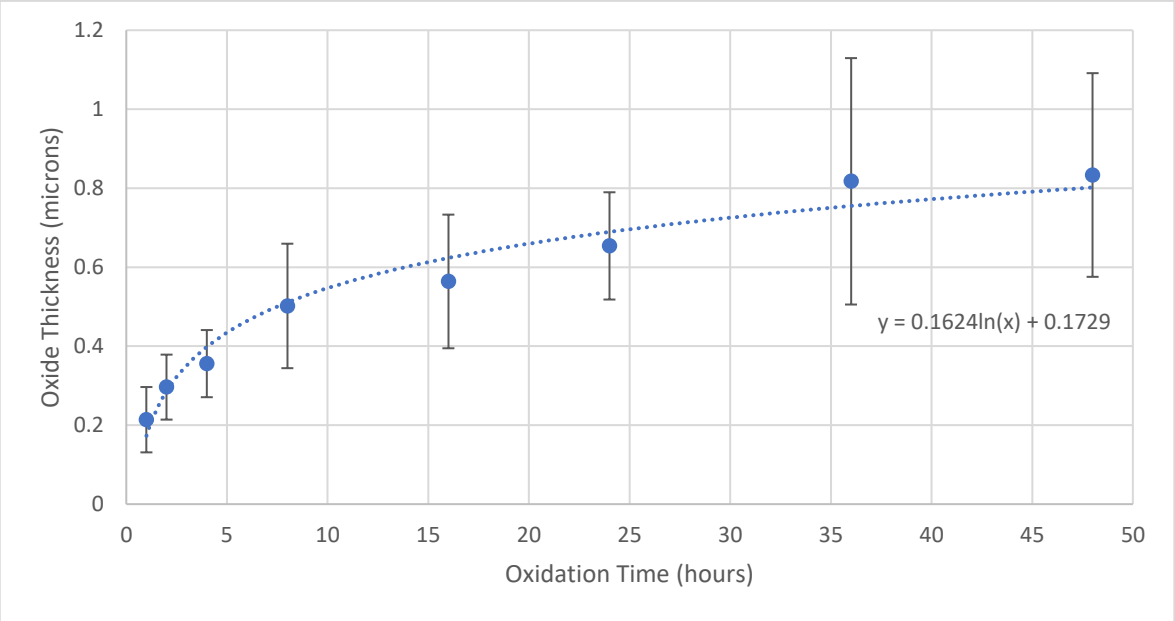

Figure 4.2.2-6: Average Oxide Thickness for Base Alloy 800°C Oxidation Progression

4.2.2.1.2 950°C Oxidation

An increase in the oxidation temperature saw a marked difference in the oxide produced on the surface of the samples. Figure 4.2.2-7 showed an oxide covering the surface of the samples, highlighted by the lost oxide which exposed the matrix material beneath. The lost material was concentrated around the machining marks on the sample surface; this will be discussed later (5.4). The surface was covered by manganese chromite (see Figure 4.2.2-9), which formed early along with the chromium oxide, rather than the manganese chromite developing after the chromium oxide. This demonstrated the increased oxidation kinetics due to the higher temperature which allowed this phase to form almost instantly.

The loss of oxide on the surface increased in volume with increased oxidation time. The cross sections of the samples (Figure 4.2.2-8) showed the thickening of the oxide layer over time, as also measured in Figure 4.2.2-10. This thickening is possibly the cause of the loss of material. Increased thickness of the oxide would exacerbate the effects of the differences in thermal oxidation between the matrix material and the superficial oxide. These differences would lead to stresses in the oxide layer and the interfacial bond, which, when the threshold levels are reached, will lead to fracture

and debonding of the oxide layer. This fracture of the oxide was seen in the cross-section images of Figure 4.2.2-8, particularly in the 24-hour and 36-hour samples. This loss of protective oxide at temperatures below those encountered during the cleaning process in industry demonstrated the need for a more durable and resilient oxide to maintain the protective nature throughout the life cycle of the alloy in use and thus allow elongated service interval times.

When comparing the thickness of the oxide developed at 950°C to the 800°C oxidation, as shown in Figure 4.2.2-11, it is seen that the oxide layer has increased roughly four-fold through the first 8 hours of oxidation at 950°C. The oxide layer thickness moved towards six and seven times that of the 800°C oxidation treatment sample at the longer oxidation treatments.

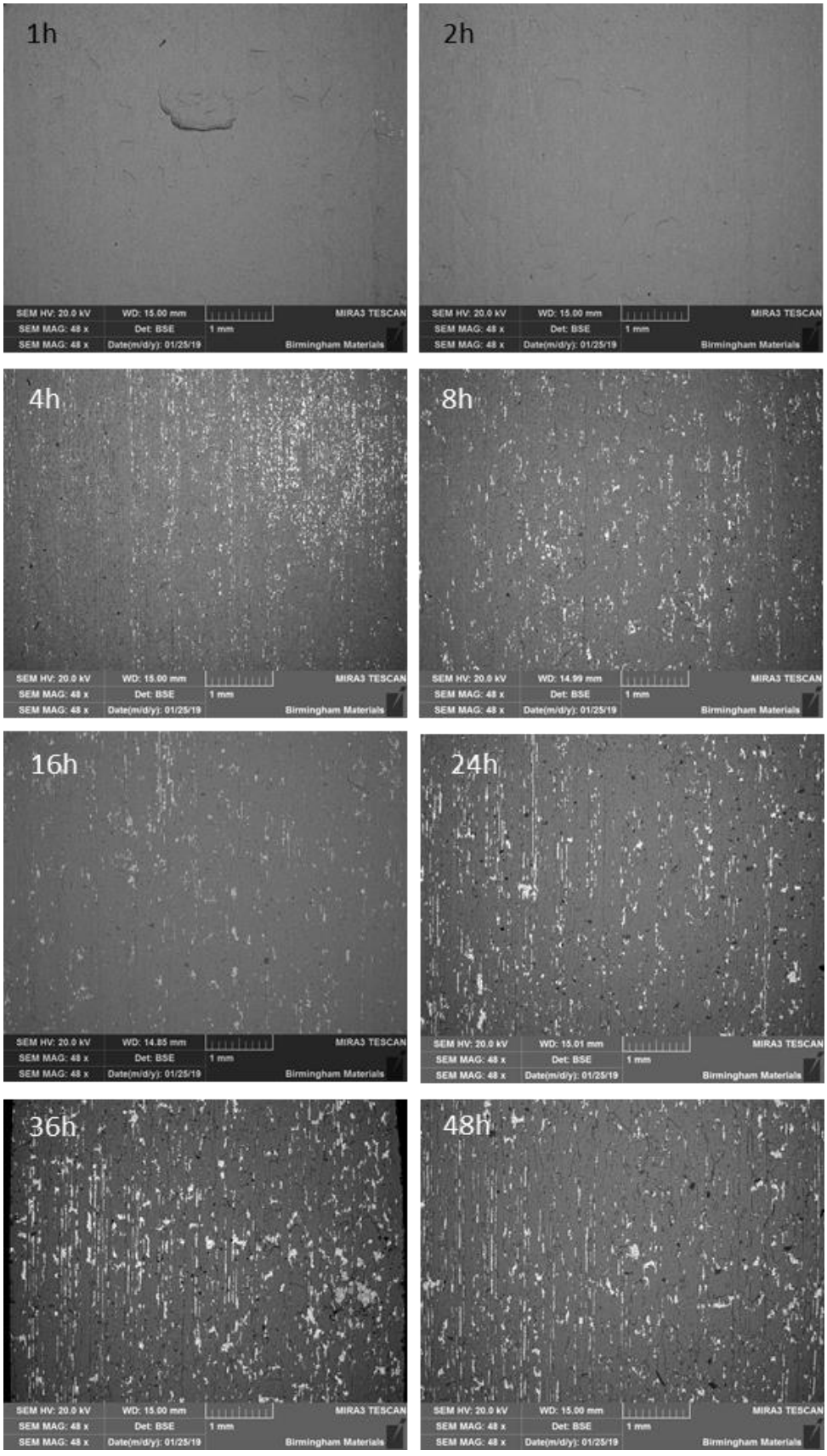

Figure 4.2.2-7: Base alloy 950°C oxidation progression surface images showing loss of surface oxide with longer oxidation times

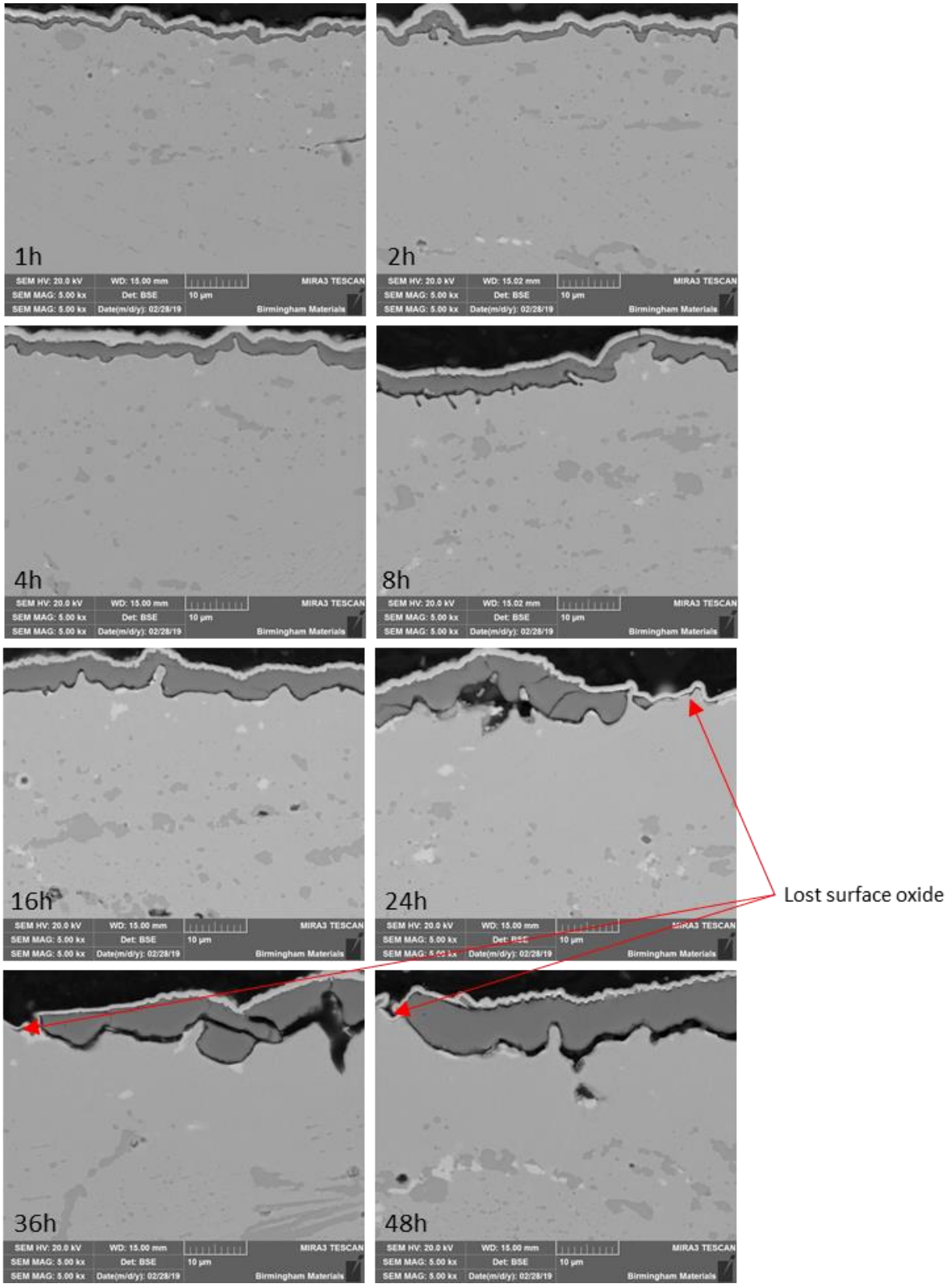

Figure 4.2.2-8: Base alloy 950°C oxidation progression cross section images indicating lost surface oxide.

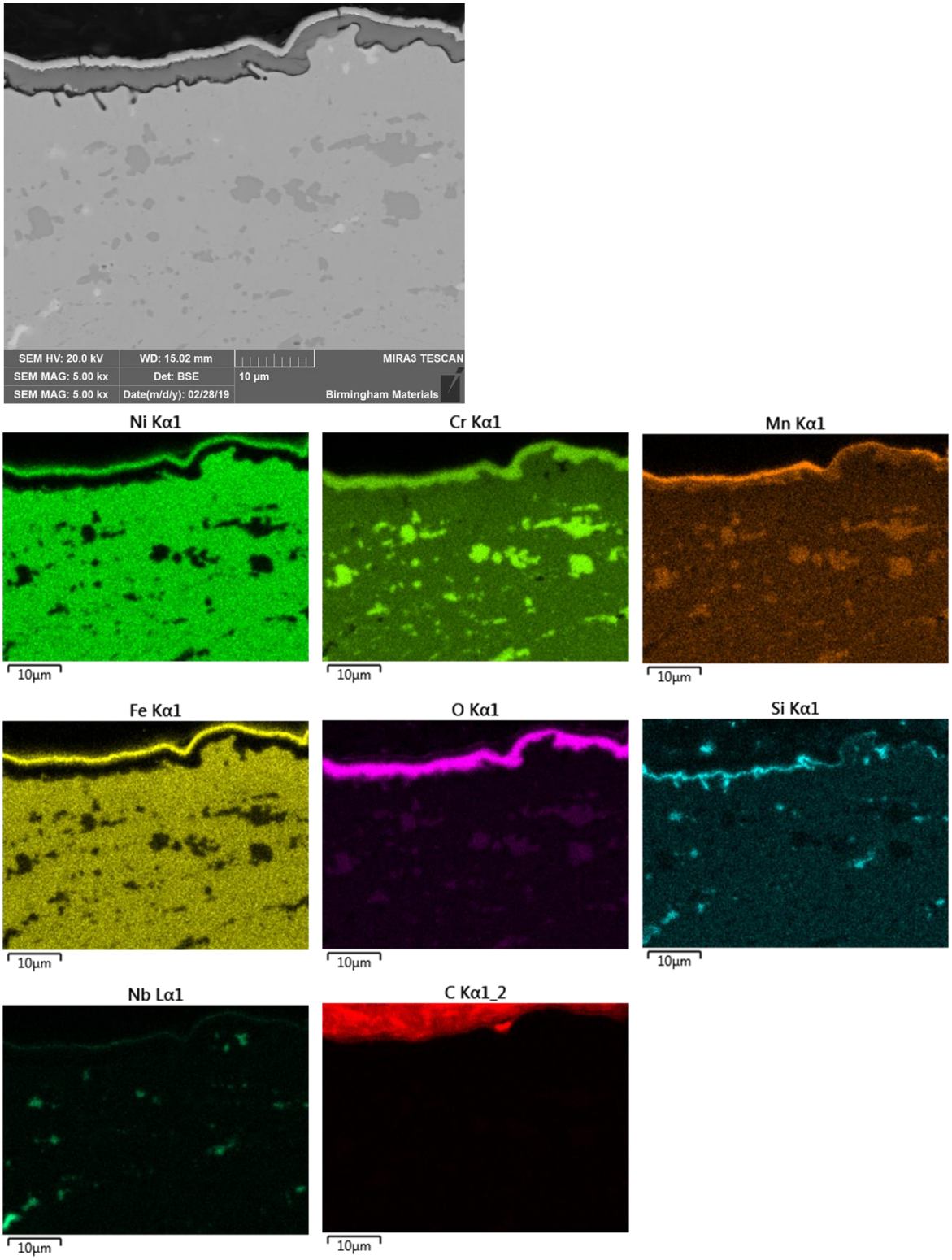

Figure 4.2.2-9: EDS mapping of Base alloy cross section oxidised at 950°C for 8 hours showing the three layers of surface oxide.

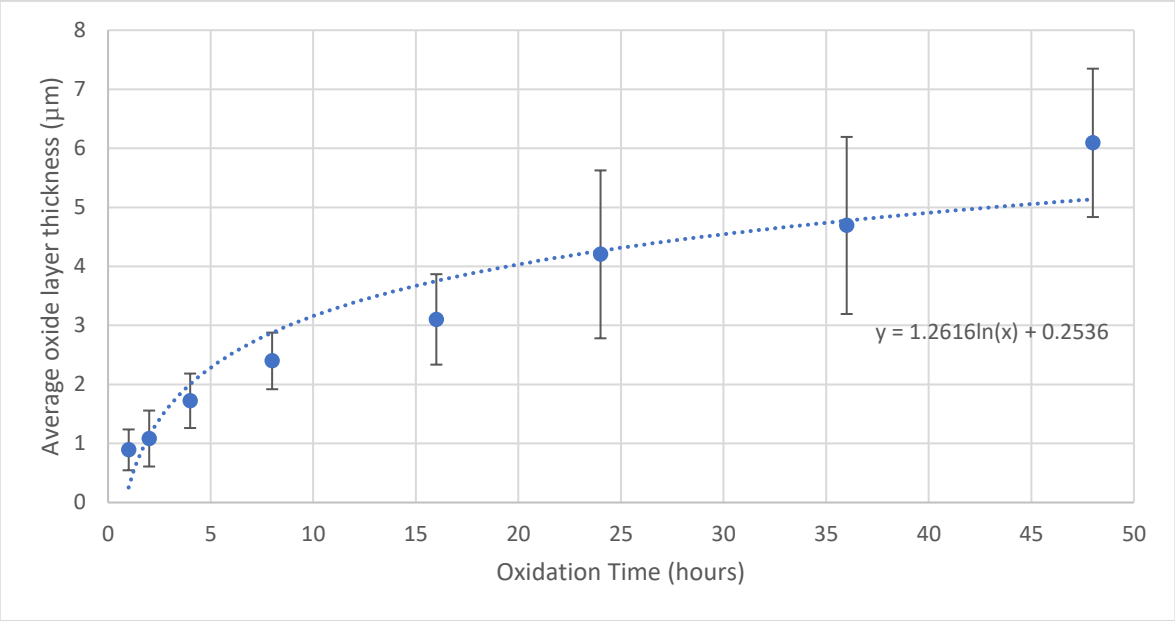

Figure 4.2.2-10:Average Oxide thickness of Base 950°C oxide layer

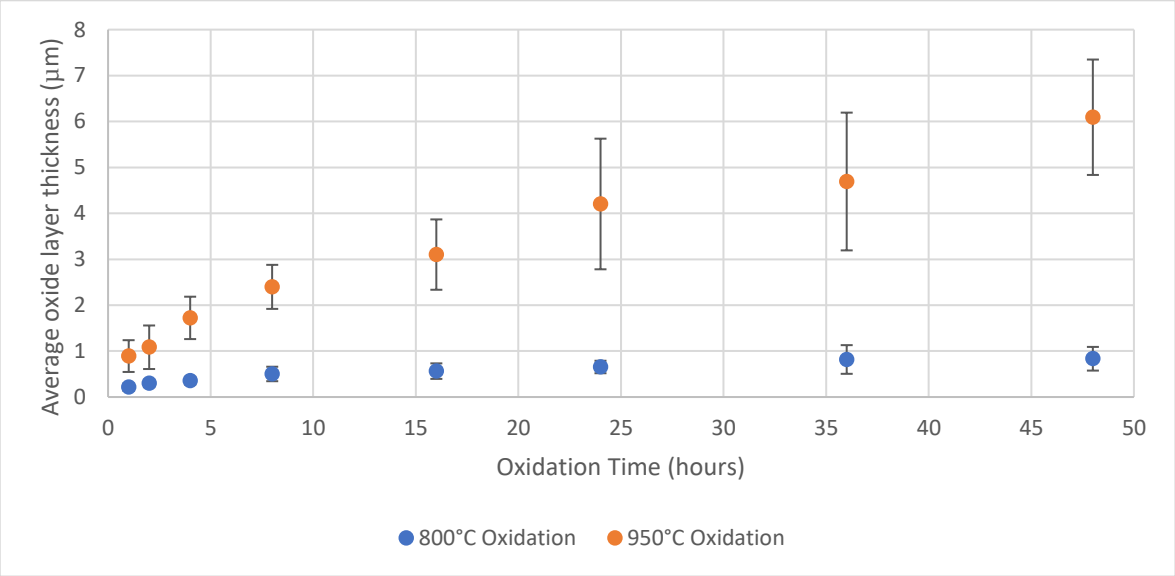

Figure 4.2.2-11: Comparison of average oxide layer thickness between Base alloy oxidised at 800°C and 950°C

4.2.2.1.3 1100°C Oxidation

Oxidation was undertaken at 1100°C to examine the effects of the temperature of the cleaning process on both the alloy and the oxide on its surface. Whilst the Base alloy was able to grow and maintain the oxide layer at 800°C (a commonly used operational gas temperature) an increase above these levels has been shown to be detrimental to the maintenance of the surface oxide in

this alloy. Figure 4.2.2-12 displays the surface of the alloy after oxidation at 1100°C over various times. The cleaning cycle in service is usually run at 1100°C for up to 48 hours, therefore the results of this oxidation treatment allowed comparison with the conditions that the alloy undergoes in service.

The surface images displayed evidence of the loss of oxide layer from the first hour of oxidation. This loss of material appeared to increase with longer oxidation times. As previously discussed, the increased stresses associated with the thicker oxide layer were the probable cause of the loss of material. The surface images of the oxidised samples (Figure 4.2.2-12) display a clear correlation between the area of lost surface oxide and the machining marks which run vertically down the samples in the images, particularly in the samples oxidised longer than 4 hours. This observation will be explored further in 4.2.2.3.

Elemental mapping of the surface of these oxides (Figure 4.2.2-14) illustrated the presence of the matrix forming elements, nickel and iron, on the surface in regions also rich with silicon. This silicon presence was the globular silicon oxide previously seen formed beneath the chromium oxide in the Base alloy. The discontinuous nature of this phase (as seen previously) is evident in both the elemental mapping and the cross-sectional images (Figure 4.2.2-14 and Figure 4.2.2-15), leaving small pockets of matrix exposed in the regions where the oxide was lost. This silicon oxide was widespread in the Base alloy oxidised at 1100°C, however it did not present at all in the 800°C oxidation samples and did not form initially in the 950°C oxidation samples. The nature of this phase in the 950°C oxidation sample was also very different; forming a thin, continuous phase beneath the chromium oxide, rather than the rounded form seen in the 1100°C oxidation.

Manganese chromite was clearly seen on the surface of the chromium oxide layer (Figure 4.2.2-16), appearing as much smaller, smooth, angular scales atop the chromium oxide. Shorter oxidation time samples displayed almost complete surface coverage of manganese chromite, however this

phase was lost from the region surrounding the exposed matrix, leaving exposed chromium oxide, as illustrated in Figure 4.2.2-13. This phenomenon also occurred in the 950°C oxidation samples, however significantly less manganese chromite was lost, suggesting that the energy released in the fracture of the thicker oxides produced at the higher temperatures, lead to greater debonding and loss of manganese chromite from the sample surface around the fracture sites. This was in line with XRD findings discussed previously, where 48-hour oxidation at 1100°C saw a large drop in XRD signal for the manganese chromite phase (4.2.1.1).

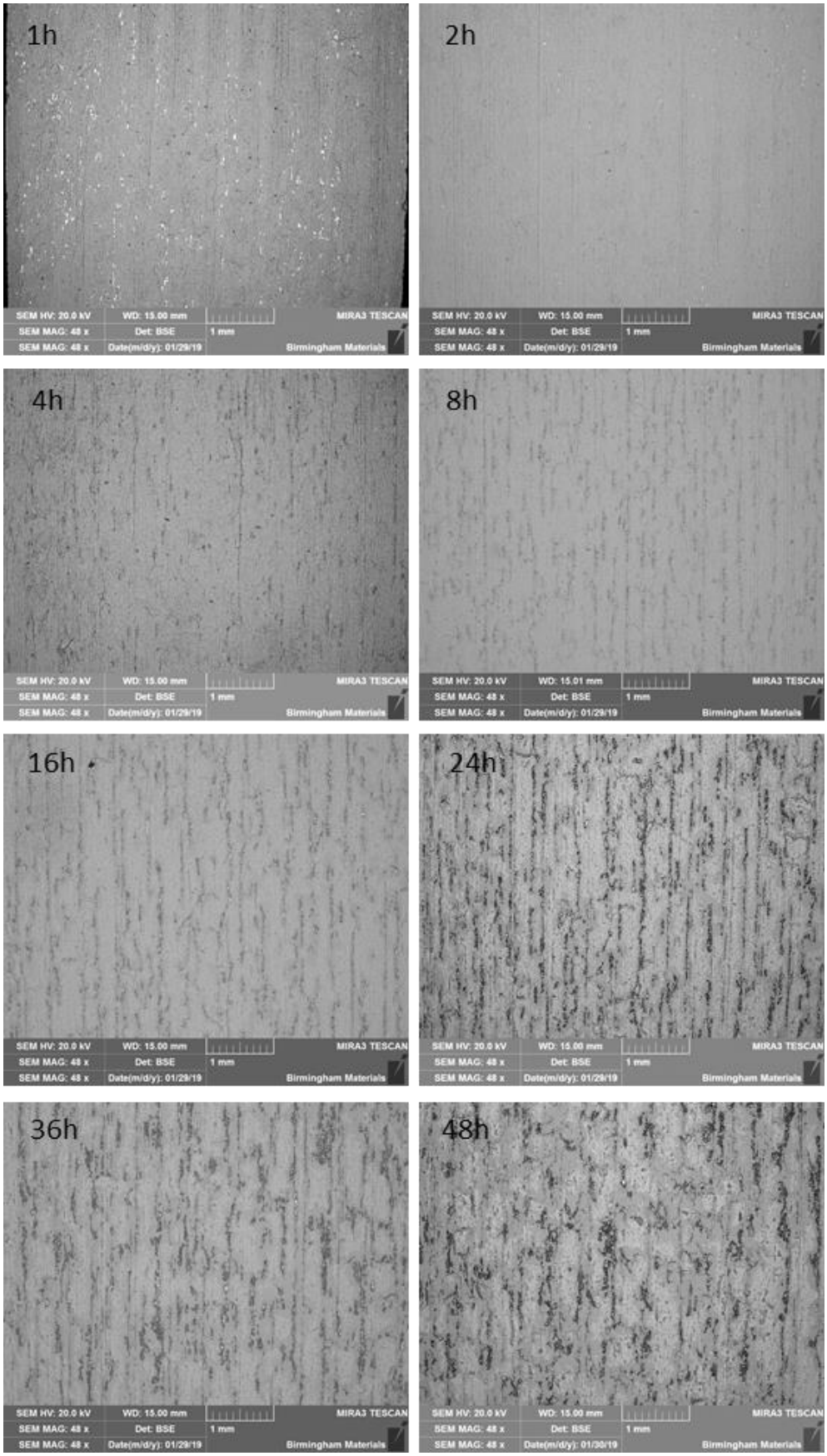

Figure 4.2.2-12: Base alloy 1100°C oxidation progression surface images, again showing clear loss of surface oxide

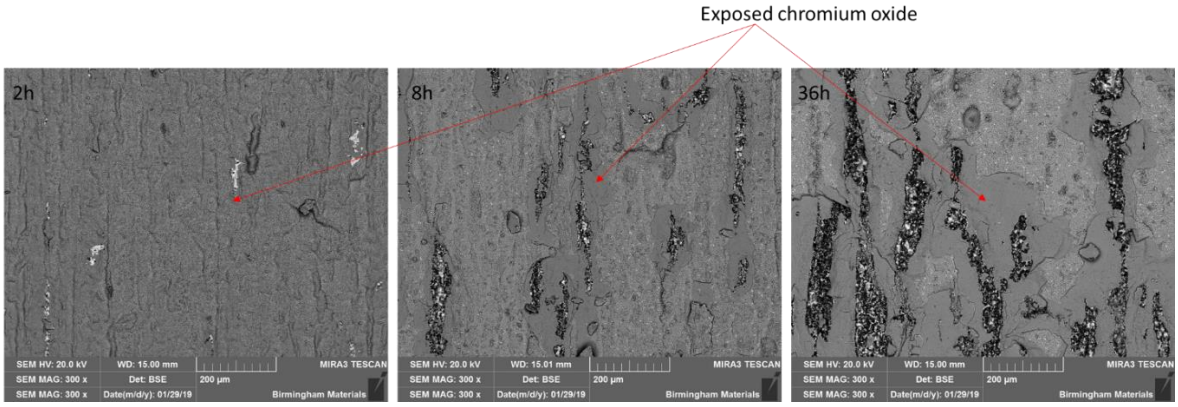

Figure 4.2.2-13: Surface of Base alloy oxidised at 1100°C for 2h, 8h and 38h showing the loss of manganese chromite around the area where the chromium oxide was lost

The cross-sectional images paired with the average oxide thickness graph show that the growth rate of the oxide displayed a consistent pattern of more rapid early oxidation, with continued thickening of the oxide layer with time. No clear complete plateauing of the oxide growth was seen in the plots, therefore further oxidation could be reasonably expected to occur throughout exposure to temperatures in the service range.

Thermogravimetric analysis (TGA) was undertaken to measure the mass gain over time with oxidation of the alloy. This was done to compare with the oxide thickness measurements taken and confirm the observed oxidation behaviour of the alloy. When comparing the average thickness measurements to the mass gain over time as measured by the TGA (Figure 4.2.2-20) there was a large step up in mass at around 21 hours of oxidation at 1100°C. This will be discussed later (5.2.1).

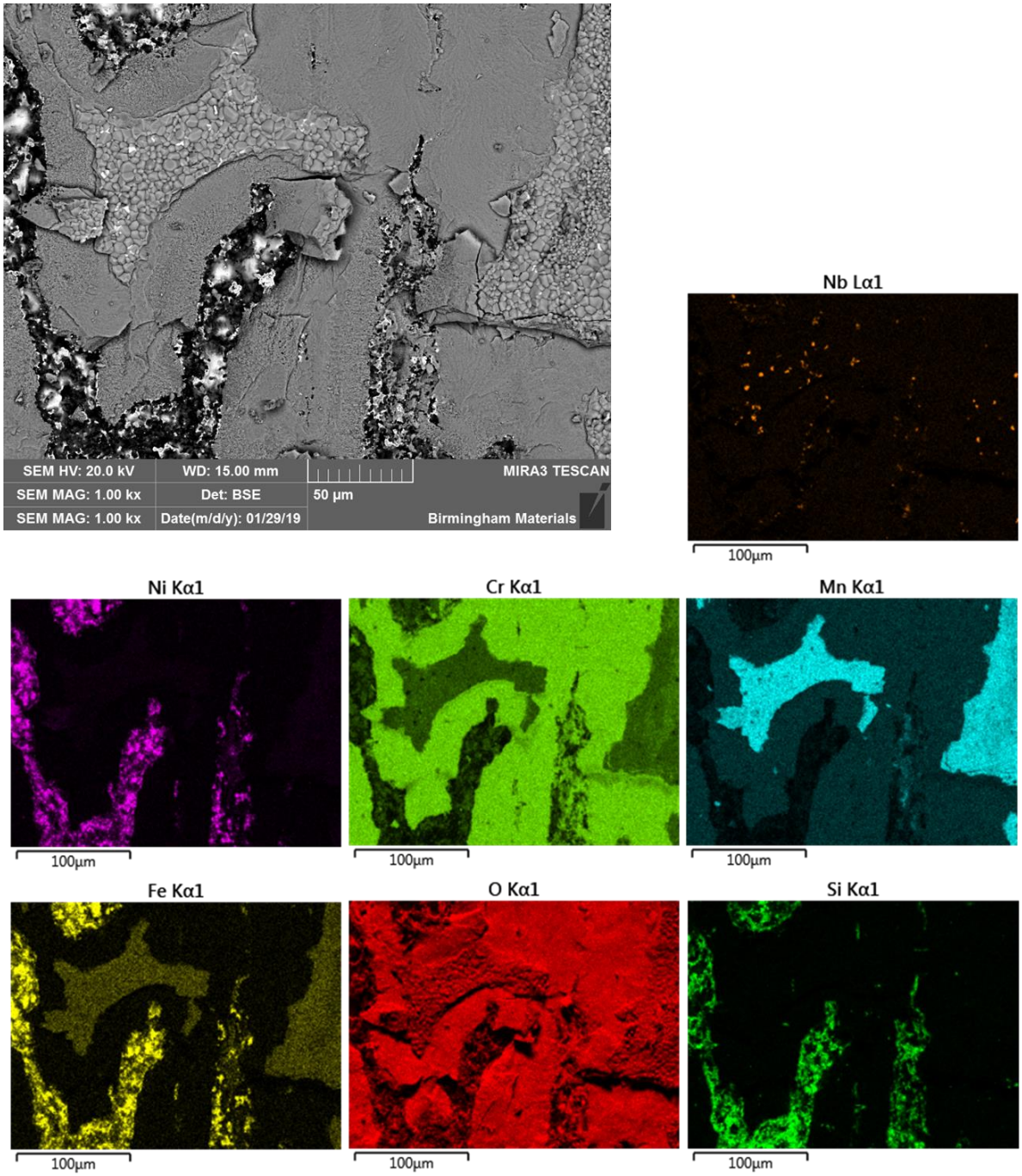

Figure 4.2.2-14: Elemental mapping of Base alloy 24 hour oxidation at 1100°C indicating regions of exposed matrix, chromium oxide and manganese chromite.

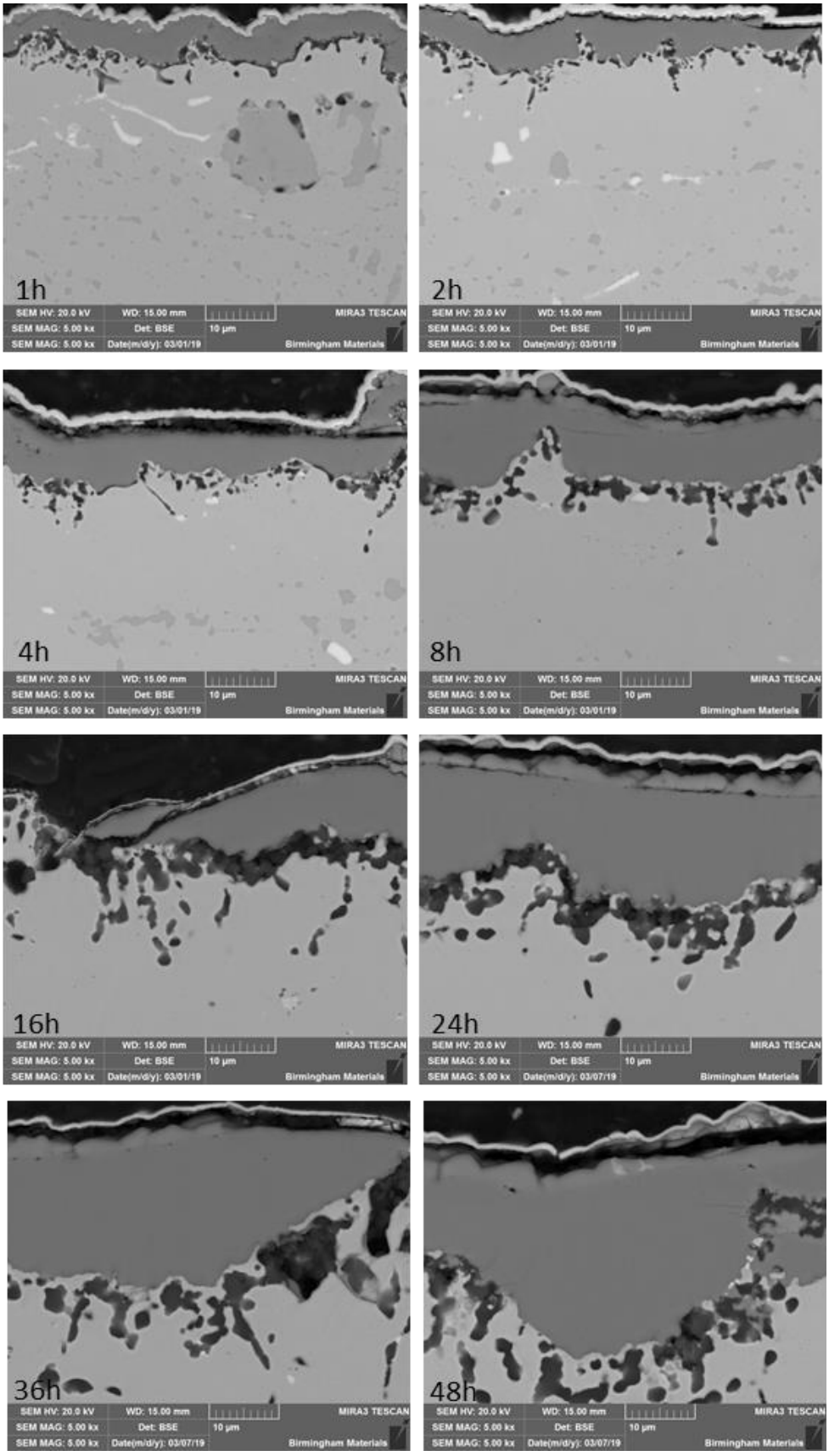

Figure 4.2.2-15: Base alloy 1100°C oxidation progression cross section images showing thickening of surface oxide and subsurface oxides.

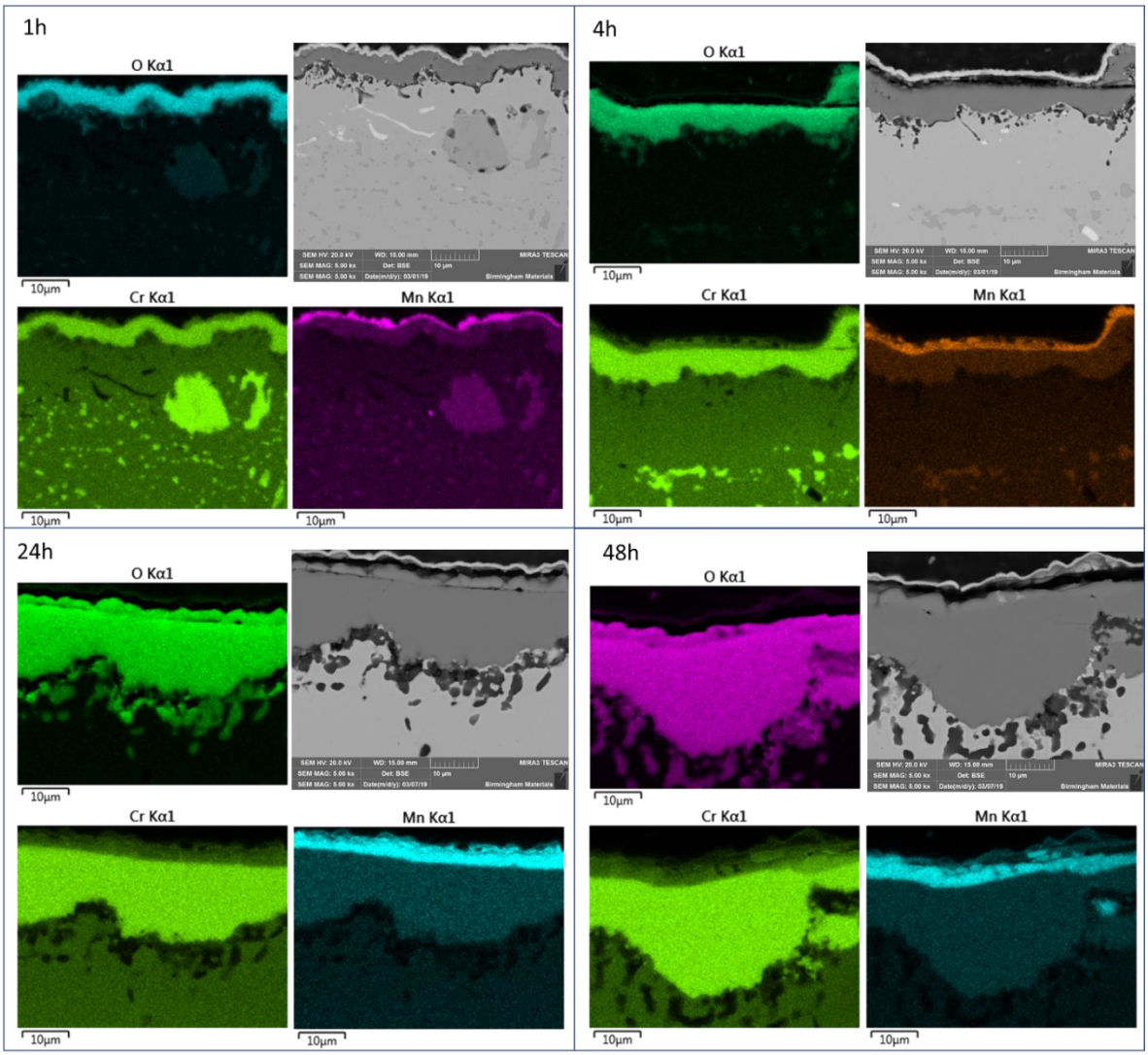

Figure 4.2.2-16: EDS mappings showing manganese chromite atop chromium oxide throughout 1100°C oxidation of the Base alloy

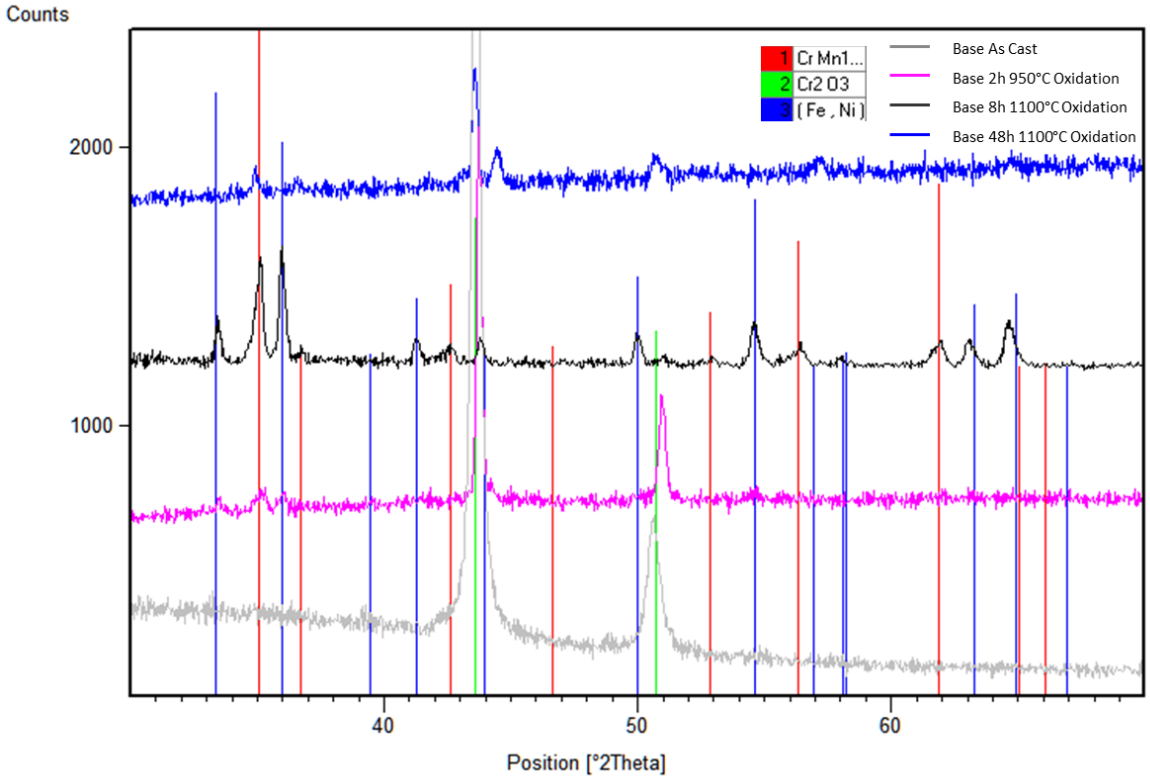

Figure 4.2.2-17: XRD traces of Base alloy as cast and after different oxidation treatments, identifying the manganese chromite and chromium oxide layers.

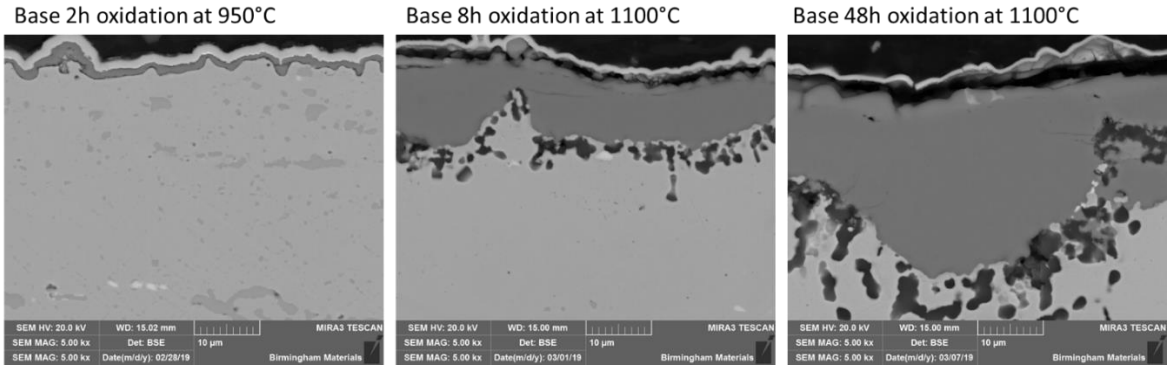

Figure 4.2.2-18: Cross section images of oxide layer of the samples analysed by XRD, showing three different oxide layer structures.

Samples which had undergone differing temperature and time oxidation treatments, demonstrating three different surface conditions of the oxide layer, were analysed via XRD to confirm the different phases present on the sample surface; the oxide layer produced during the initial stages of oxidation, with widespread coverage of the manganese rich layer on the surface of the oxide layer was present, and after spallation had occurred.

As previously identified, oxidation of the Base alloy for 8 hours at 1100°C showed significant presence of manganese chromite, with strong peaks at 35°, 42.7°, 56.4° and 62°. These peaks were found to be significantly depressed after 48-hour oxidation. This suggested the loss of the manganese chromite phase from the surface, a result of spallation or debonding of this layer, as observed in Figure 4.2.2-13. The 8-hour oxidation sample showed significant depressions in the matrix peaks, reinforcing the observations of a thick, dense oxide layer on the surface. The larger matrix peaks seen after 48-hour oxidation is evidence of the spallation of the oxide layer, which allowed more signal from the matrix. The peak at 51° in all oxidised samples confirmed the chromium oxide layer as Cr_2O_3, as previously identified with EDS and TEM analysis.

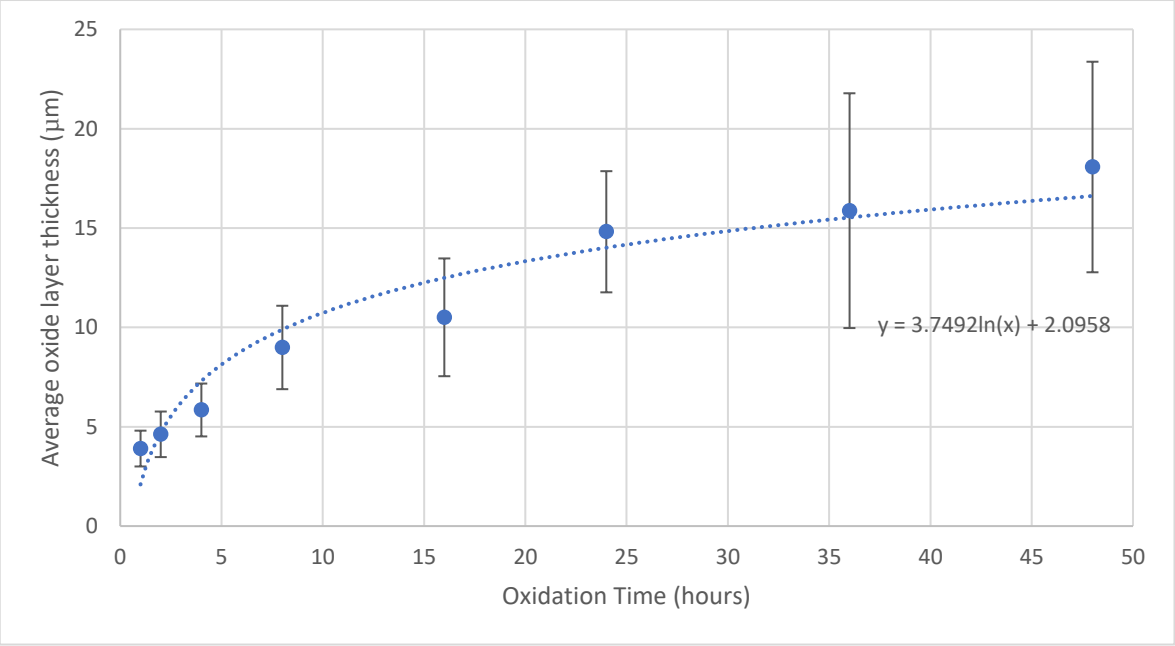

Figure 4.2.2-19: Average Oxide thickness of Base 1100°C oxide layer

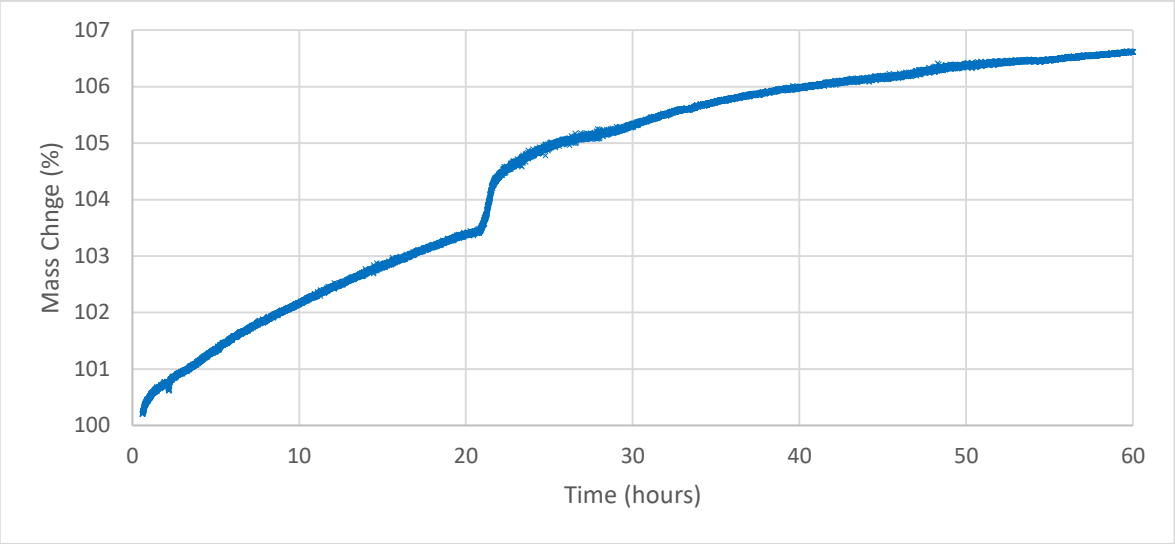

Figure 4.2.2-20: Graph of TGA (thermogravimetric analysis) of oxidation of Base alloy at 1100°C for 60 hours

Figure 4.2.2-21 clearly illustrates the significant difference in oxide layer thickness growth between oxidation temperatures and times, with all three temperatures displaying an increased rate of oxidation in the early stages, but all maintaining oxide growth throughout the experiment. As mentioned previously, the oxide layer thickness increased by between four to six times with the increase from 800°C to 950°C. Increasing the temperature from 950°C to 1100°C saw a thickness increase of between three and four times.

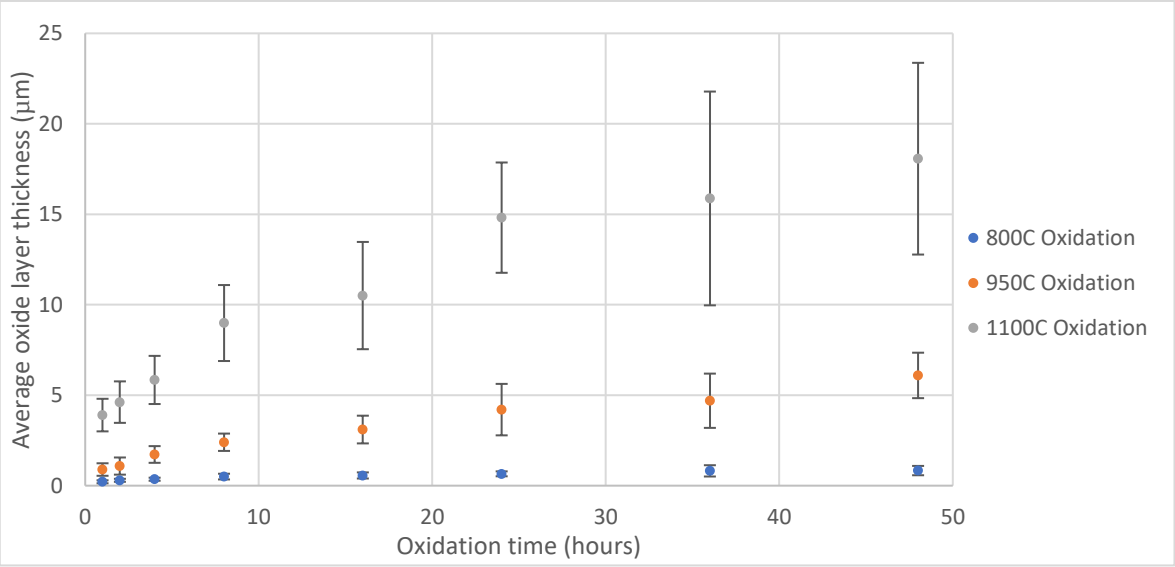

Figure 4.2.2-21: Graph comparing growth rates of oxide layer in Base alloy at 800°C, 950°C and 1100°C

4.2.2.2 Optim-Al Alloy

4.2.2.2.1 800°C Oxidation

Surface images of the Optim-Al alloys oxidised at 800°C for various times (Figure 4.2.2-22) did not generate any significant information, with signs of an oxide formed on the surface but little evidence available to allow major distinctions between the samples. EDS mapping of the regions displayed concentrations of aluminium and oxygen across the sample, however due to the interaction volume of the SEM, and the sub-micron scale of the oxide, much of the information gathered was from the subsurface region. A lower accelerating voltage being used would have allowed for more surface information to be gathered, and less subsurface signal to be generated.

Figure 4.2.2-23 shows evidence of fine chromium precipitates, which are known to form during the heat treatment in the near surface region, however they were not all surface-breaking, as the EDS mapping suggested. The presence of aluminium across the surface gave evidence of the presence of an aluminium oxide covering the surface of the sample. This was backed up by the cross-sectional images of the samples (Figure 4.2.2-24).

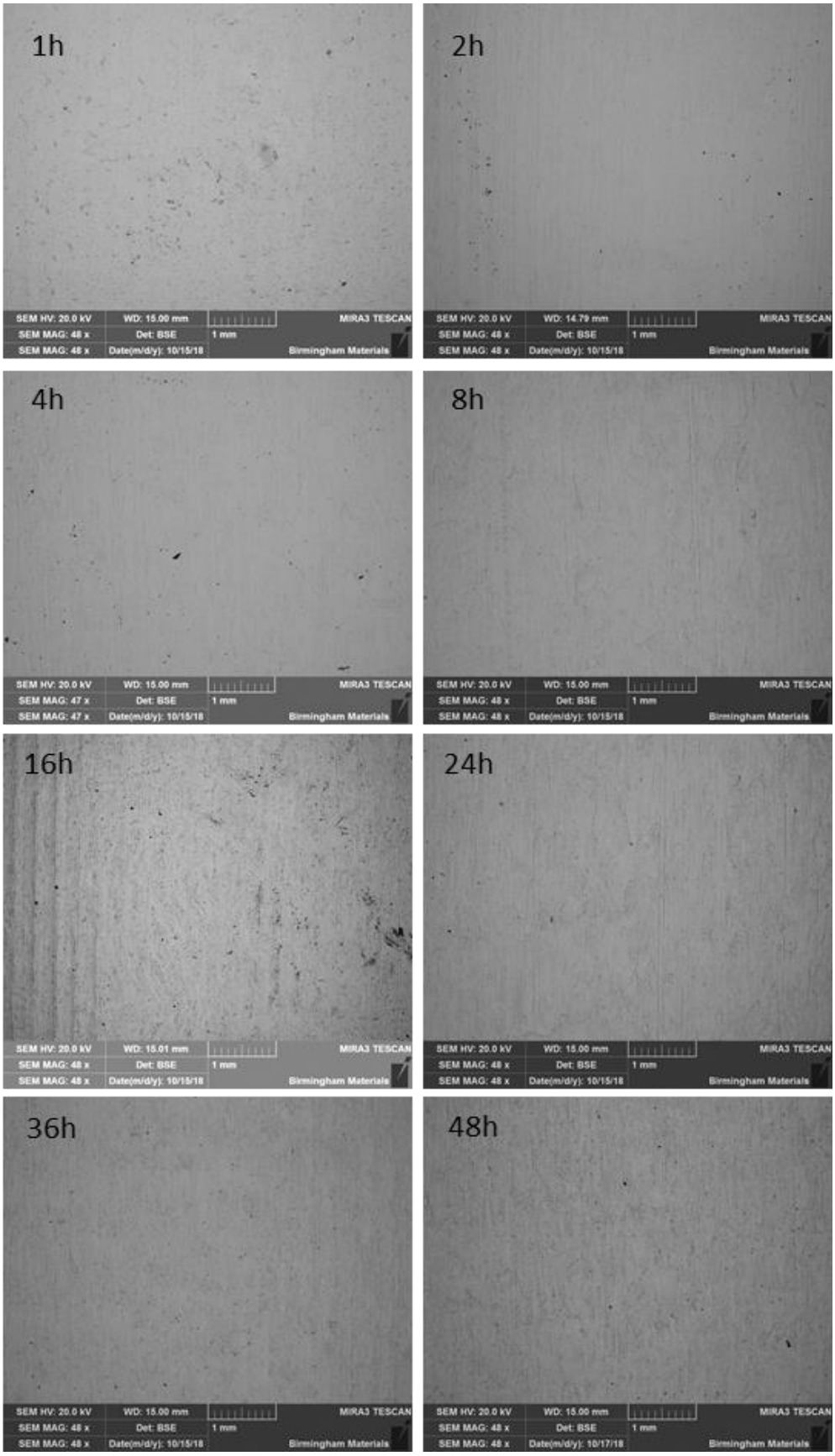

Figure 4.2.2-22: Optim-Al 800°C Oxidation progression surface images, with some surface texture changes visible.

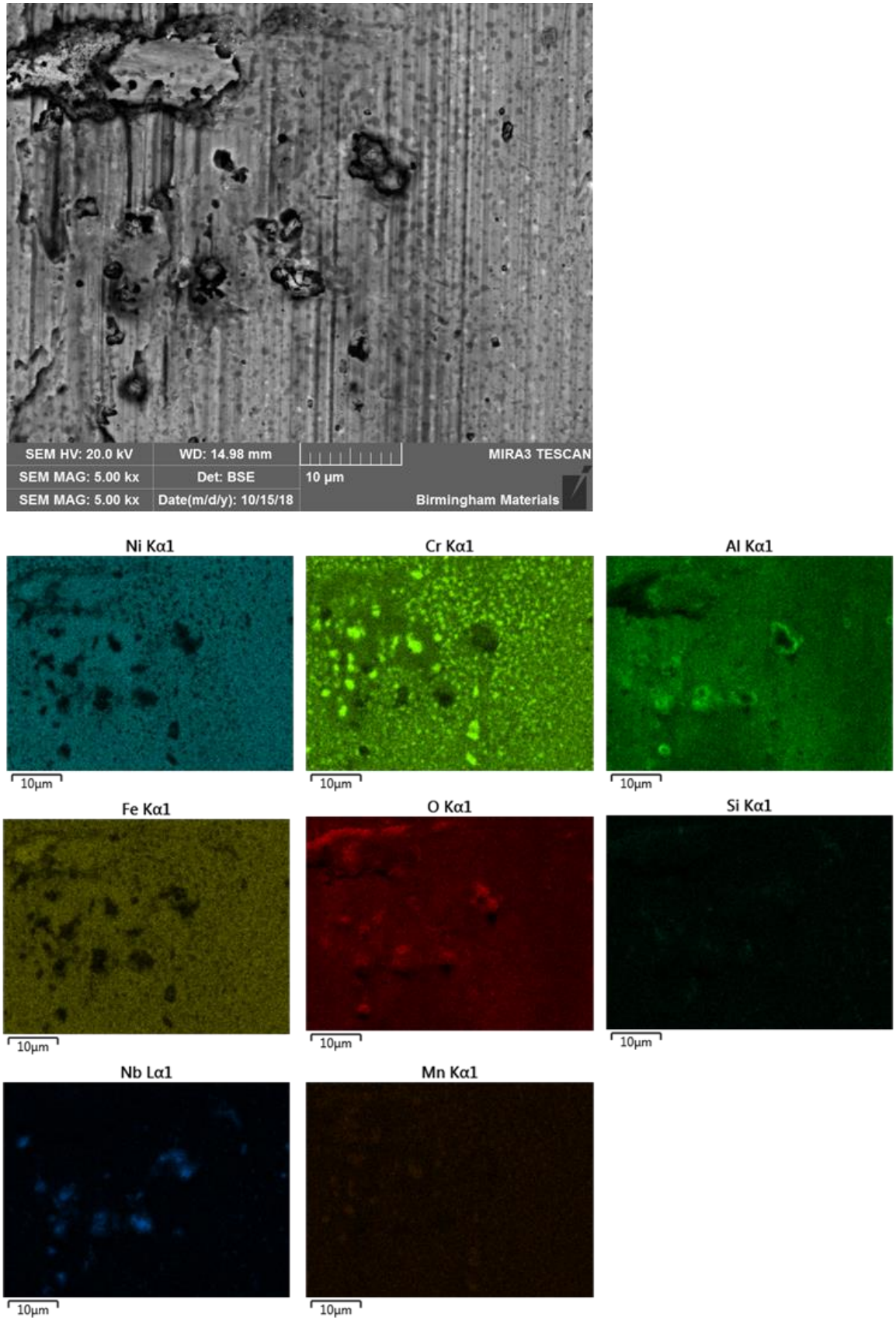

Figure 4.2.2-23: Surface EDS Mapping of Optim-Al alloy oxidised at 800°C for 36 hours, highlighting subsurface chromium carbides

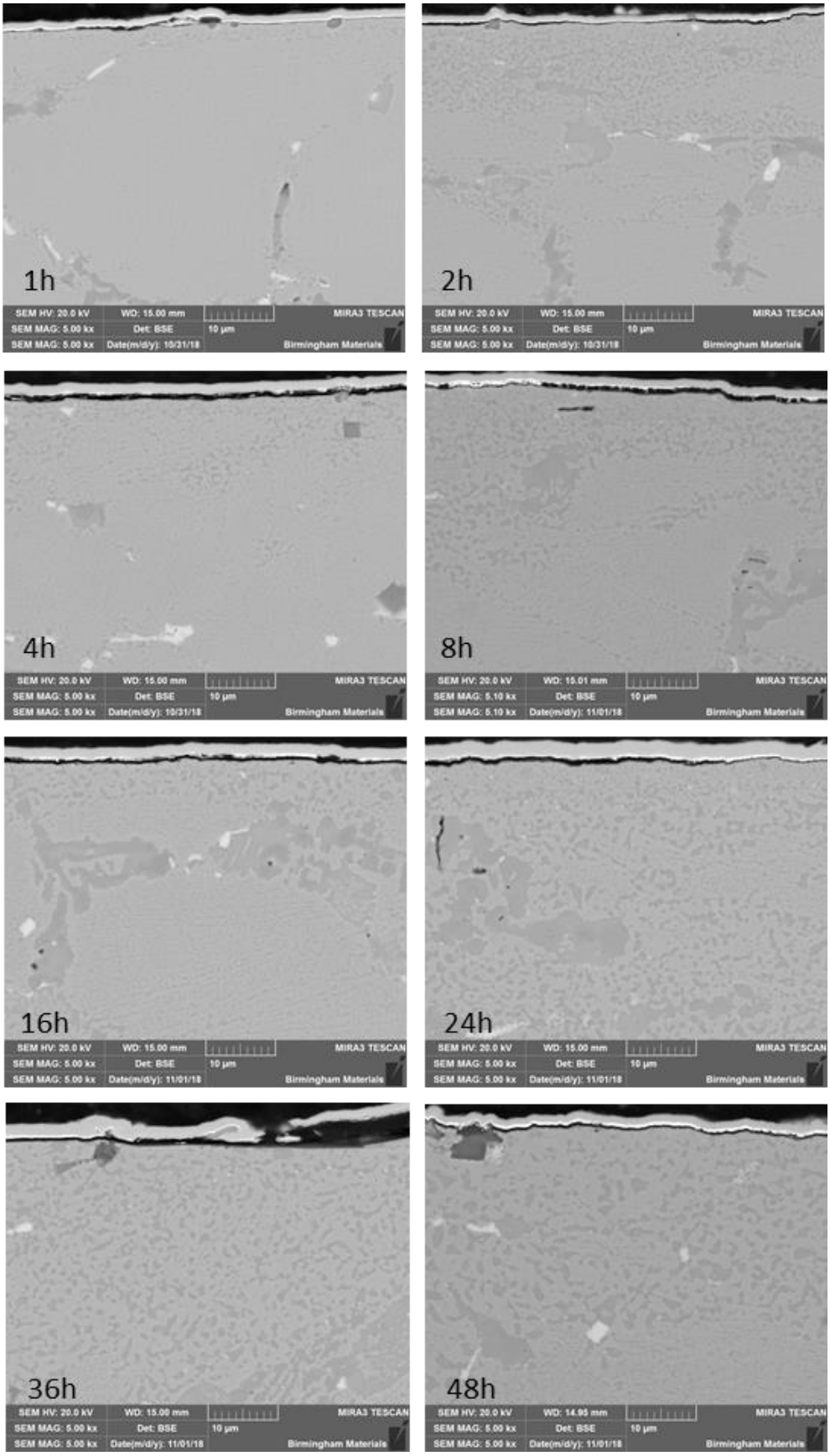

Figure 4.2.2-24: Optim-Al 800°C Oxidation progression cross section images showing much thinner oxide layer than Base.

Figure 4.2.2-24 shows the thin oxide layer atop the matrix in the Optim-Al alloy after oxidation at 800°C. Whilst difficult to resolve in the backscattered SEM images, EDS mapping of the sample oxidised for one hour (Figure 4.2.2-25) indicated concentrations of oxygen and aluminium on the surface, beneath the protective gold and nickel layers that were added after the oxidation treatment. This demonstrated that, despite minimal oxidation treatment time, the aluminium oxide layer still formed. Note that some lateral drift of the sample occurred during the mapping process, however the surface oxide layer is still evident.

Figure 4.2.2-26 displays the oxide thickness changes with time for the Optim-Al alloy. This oxide growth follows a similar pattern to that seen in the Base alloy, characterized by more rapid oxide growth in the initial oxidation period, followed by plateauing. When comparing the thickness of the Optim-Al alloy to the Base alloy in the same conditions, the oxide thickness was in the range of four times thinner than that of the Base alloy (Figure 4.2.2-27). This is beneficial to the service properties of the alloy, as previously discussed, due to reduced stress generation between the oxide and the bulk material during contraction during cooling, leading to greater retention of the oxide on the pipe surface.

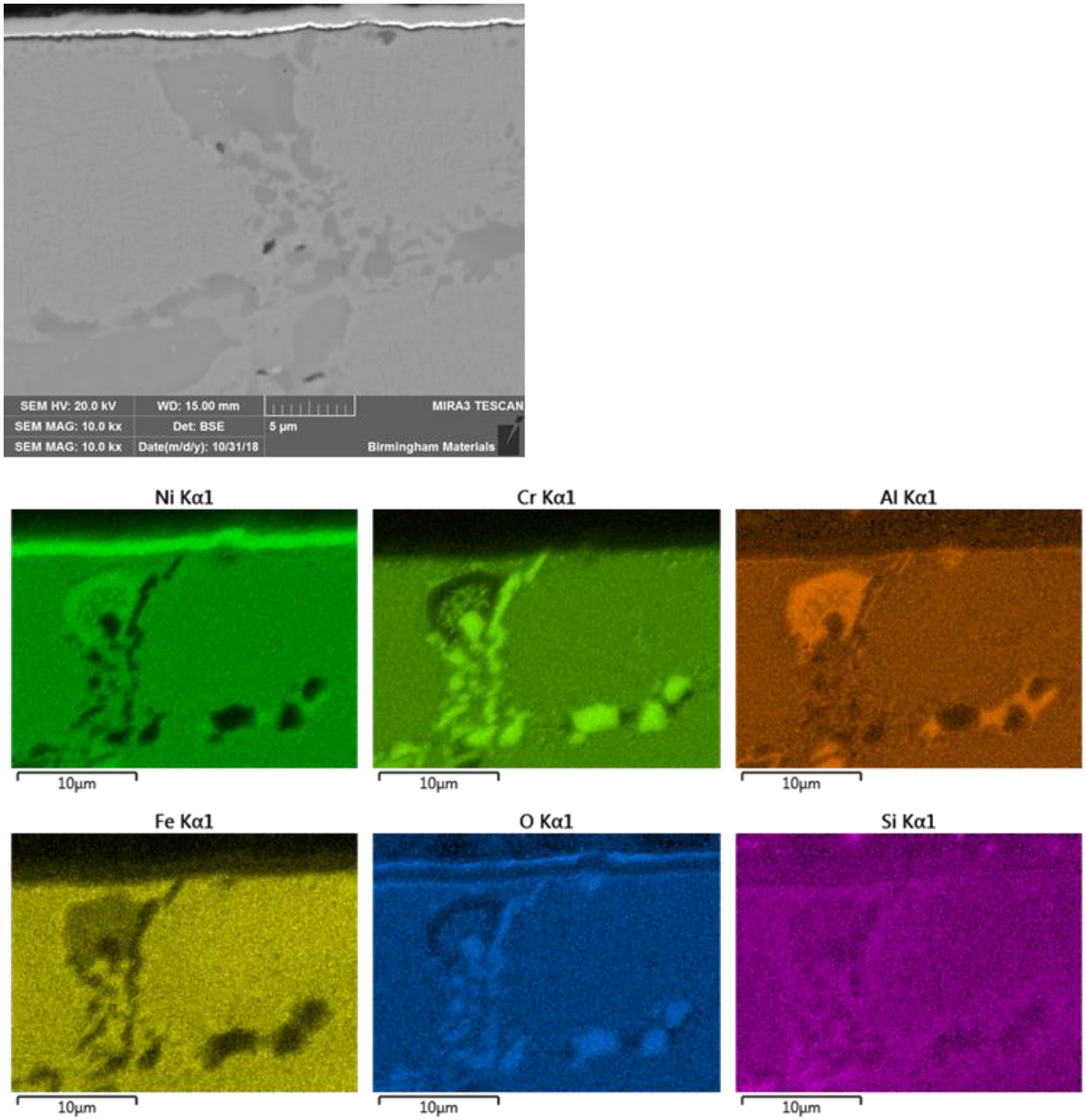

Figure 4.2.2-25: EDS mapping of Optim-Al alloy oxidised at 800°C for 1 hour, showing a very thin aluminium oxide layer present on the surface after short oxidation time.

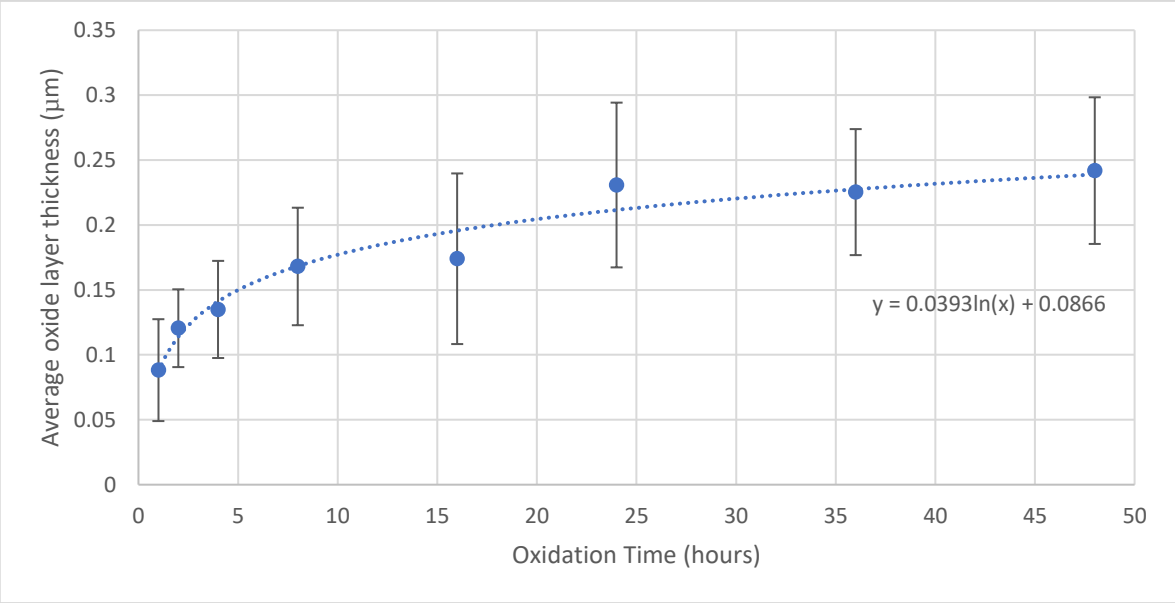

Figure 4.2.2-26: Graph of Average Oxide thickness of Optim-Al alloy oxidised at 800°C

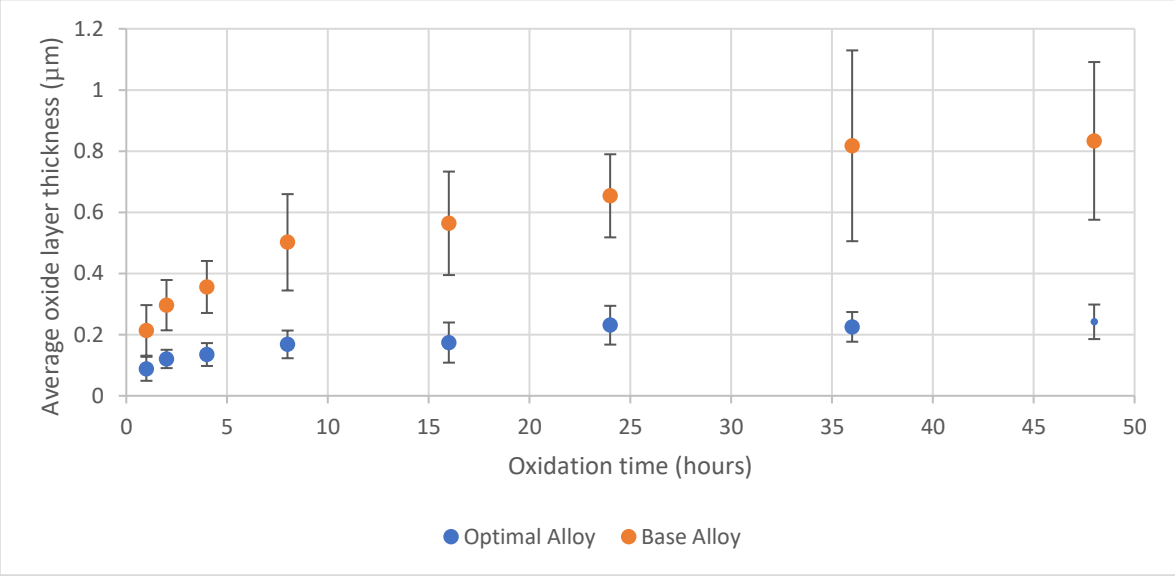

Figure 4.2.2-27: Comparison of average oxidation oxide layer thickness of Base alloy and Optim-Al alloy after oxidation at 800°C

4.2.2.2.2 950°C Oxidation

Surface images of the Optim-Al alloy oxidised at 950°C (Figure 4.2.2-28) showed significantly more changes between one another than those of the 800°C oxidation. An oxide layer was present across the surface of all the samples, as was the case in the 800°C oxidation. However, variations in thickness of the oxide were observed in the backscattered images in Figure 4.2.2-28, with the thicker oxide layer appearing as darker regions on each image. This is a result of the lower atomic

mass of the aluminium oxide compared to the matrix beneath, meaning fewer backscattered electrons are generated by interaction with the surface aluminium oxide. When the oxide was thicker, less of the signal was received from the subsurface matrix, thus creating a darker region on the backscattered image. It was therefore observed that the oxide, whilst being present across the samples, was not uniform in growth.

These observations were reinforced by the EDS mapping, Figure 4.2.2-29, where the darker regions of the backscattered image correlated to regions with a greater presence of aluminium.

Cross sections of the oxidised samples displayed the oxide layer beneath the nickel plating, atop the matrix (Figure 4.2.2-30). This oxide layer was significantly thicker than that seen on the Optim-Al samples oxidised at 800°C, with average oxide thickness measured at around three times thicker at all oxidation times. When compared to the Base alloy, the oxide layer was still significantly thinner on the Optim-Al alloy, measuring at between three and four times thinner than the Base alloy through the first 8 hours of oxidation, and increasing to over seven times the thickness of the Optim-Al alloy by 48 hours, due to the continually growing nature of the Base alloy oxide layer, compared to the plateauing seen in the growth of the Optim-Al alloy oxide layer(Figure 4.2.2-32).

As with the Optim-Al alloy oxidised at 800°C, the oxide appeared to be continuous across the surface, with no evidence of fracture or regions of exposed matrix. This observation was particularly important for the maintenance of protection afforded by the oxide in service, as the oxide will maintain its presence at operating service temperatures, forming the physical barrier necessary to inhibit catalytic coke formation.

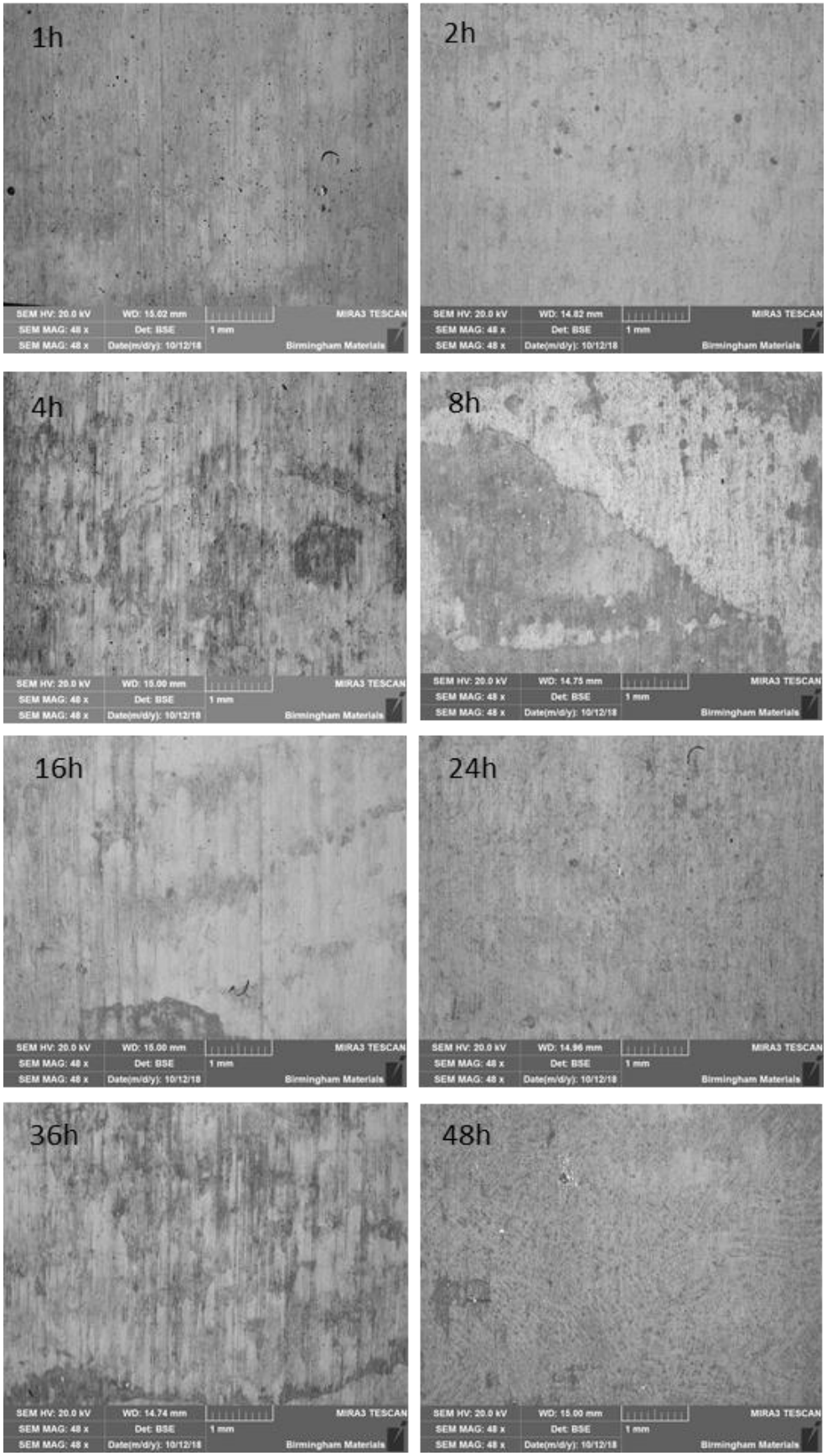

Figure 4.2.2-28: Optim-Al 950°C Oxidation progression surface images, showing varied surface appearance.

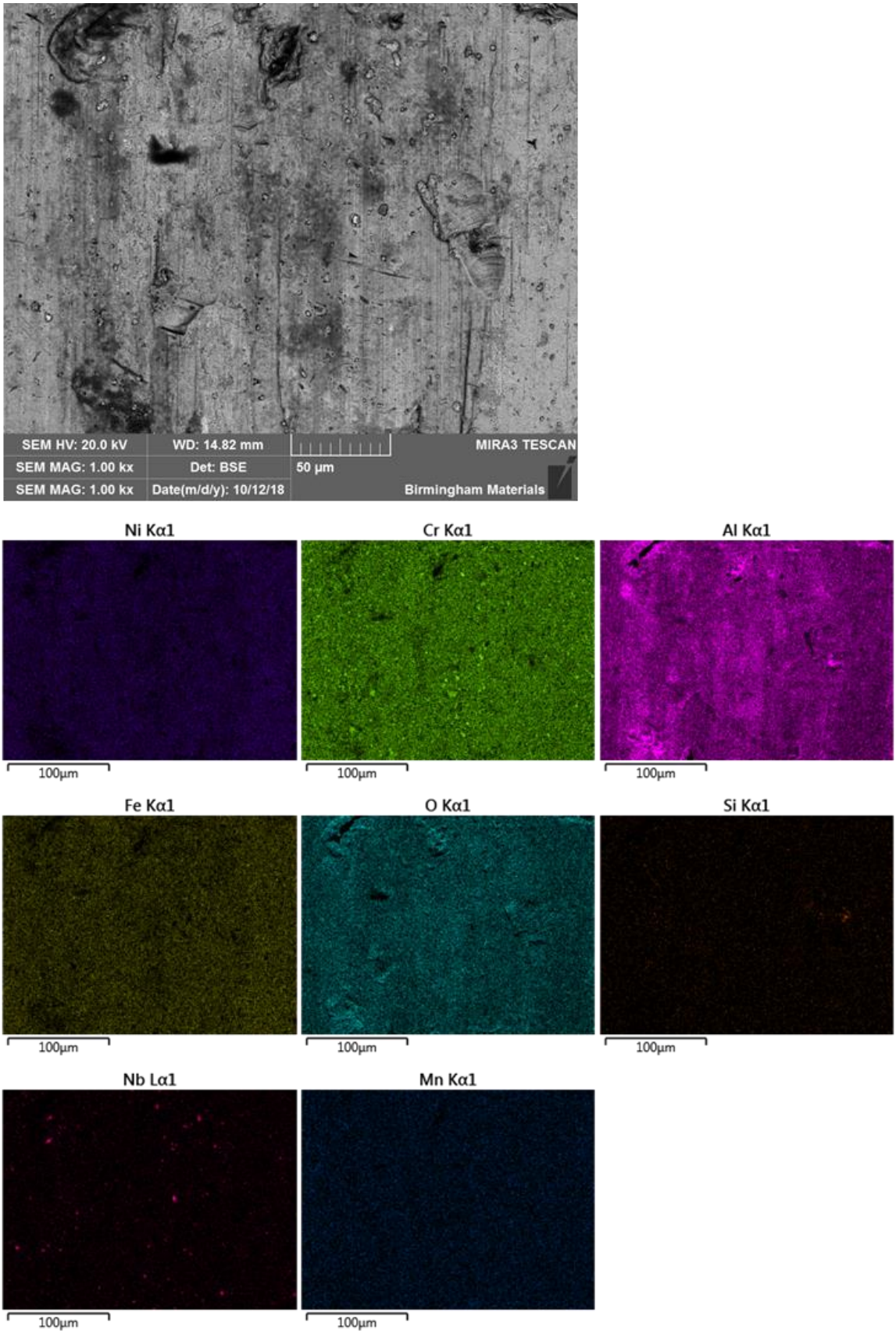

Figure 4.2.2-29: Optim-Al Alloy EDS Mapping after oxidation at 950°C for 2 hours demonstrating mixed thickness of oxide through aluminium concentration.

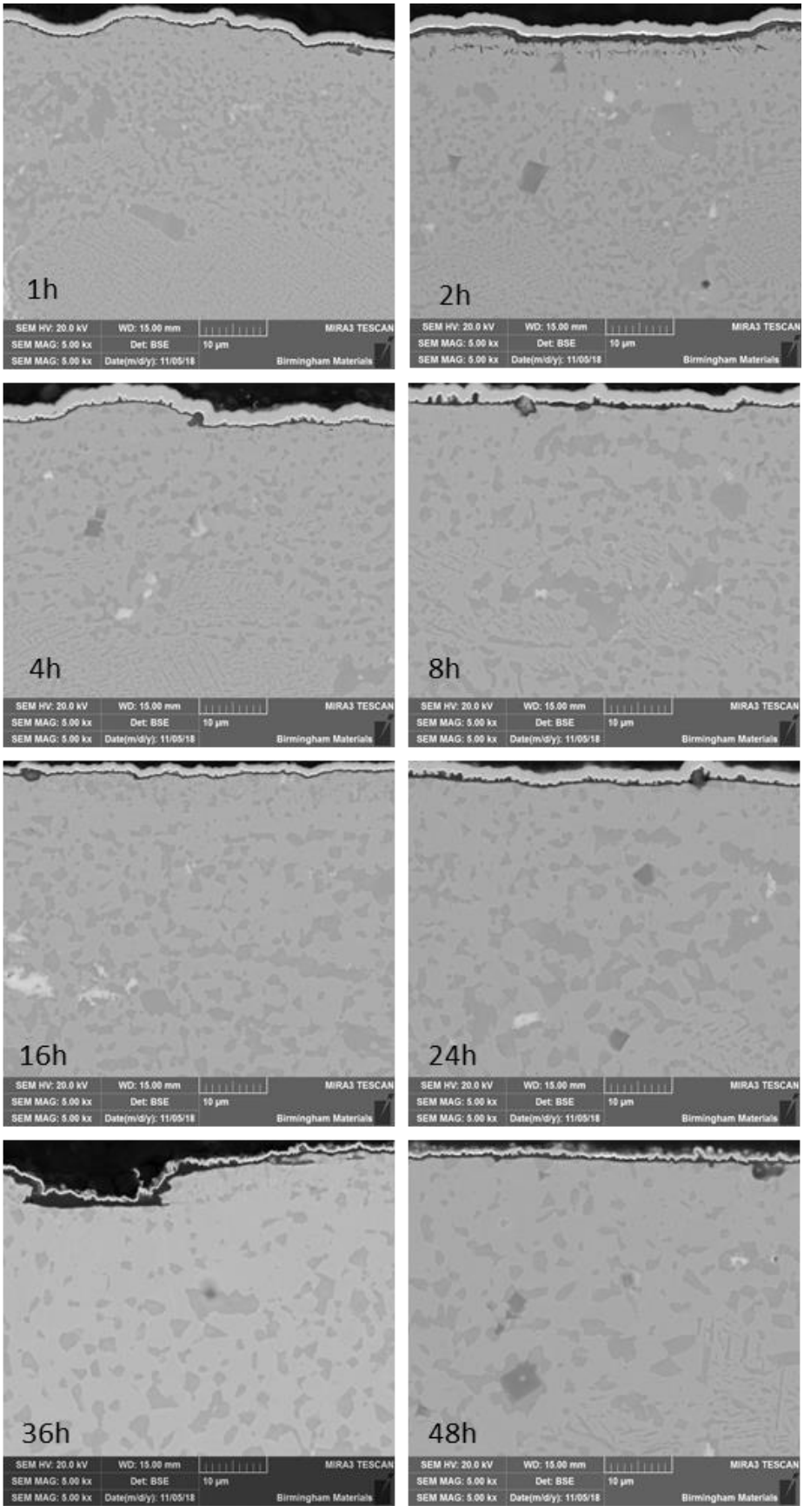

Figure 4.2.2-30:Optim-Al 950°C Oxidation progression cross section images, showing increasing oxide thickness.

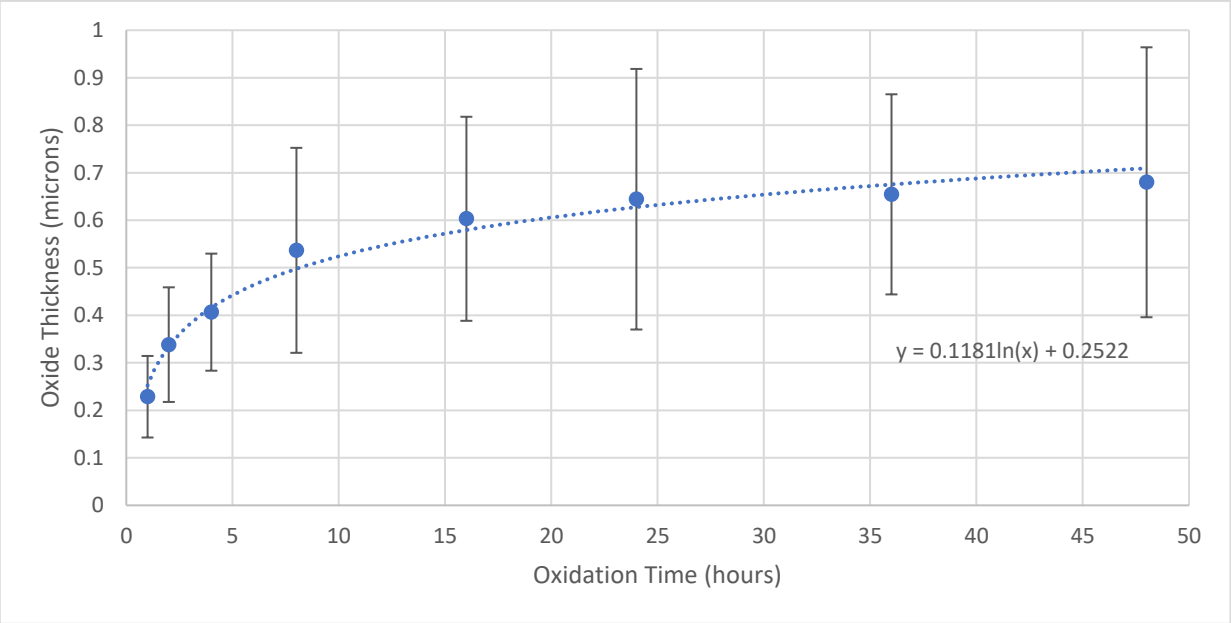

Figure 4.2.2-31: Graph of oxide thickness with increasing oxidation time of Optim-Al alloy at 950°C

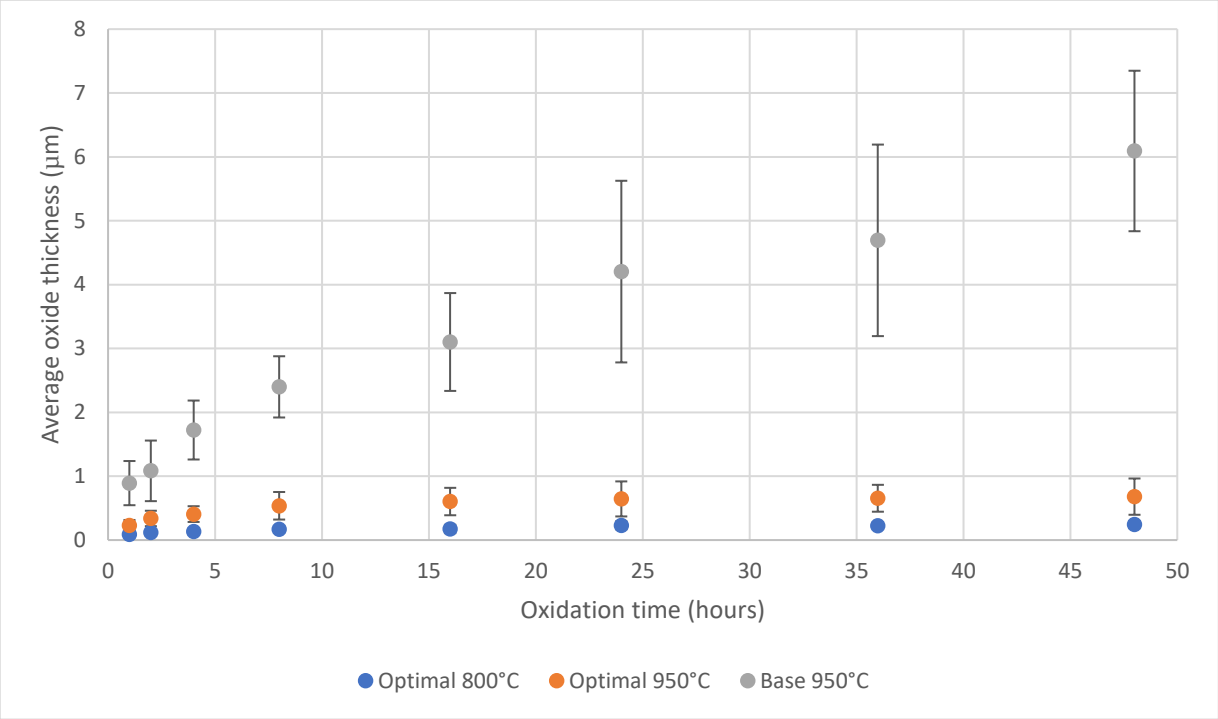

Figure 4.2.2-32: Graph comparing average oxide thickness of Optim-Al alloy oxidised at 800°C and the Optim-Al and Base alloys oxidised at 950°C

4.2.2.2.3 1100°C Oxidation

Surface images of the Optim-Al alloy oxidised at 1100°C displayed oxide across the majority of the sample, however there were clear regions of lost material, as seen previously with the Base alloy. The loss appeared greatest in the 48-hour oxidation treatment, but the losses were similar in

volume from the 4-hour through to the 36-hour samples. As seen previously with the Base alloy, the oxide layer appeared to be lost primarily along the machining marks present on the surface of the alloy. This will be discussed in more depth later (5.4).

The nature of the aluminium oxide layer is to grow significantly thinner than that of the chromium oxide. This leaves potential for the contrast seen in the image to be due to signal being picked up from the matrix, beneath the thin surface aluminium oxide. When examining the cross sections of the Optim-Al alloy (Figure 4.2.2-35), no immediate evidence of lost material was present. The oxide covered the surface of all the samples, increasing in thickness with increased oxidation time.

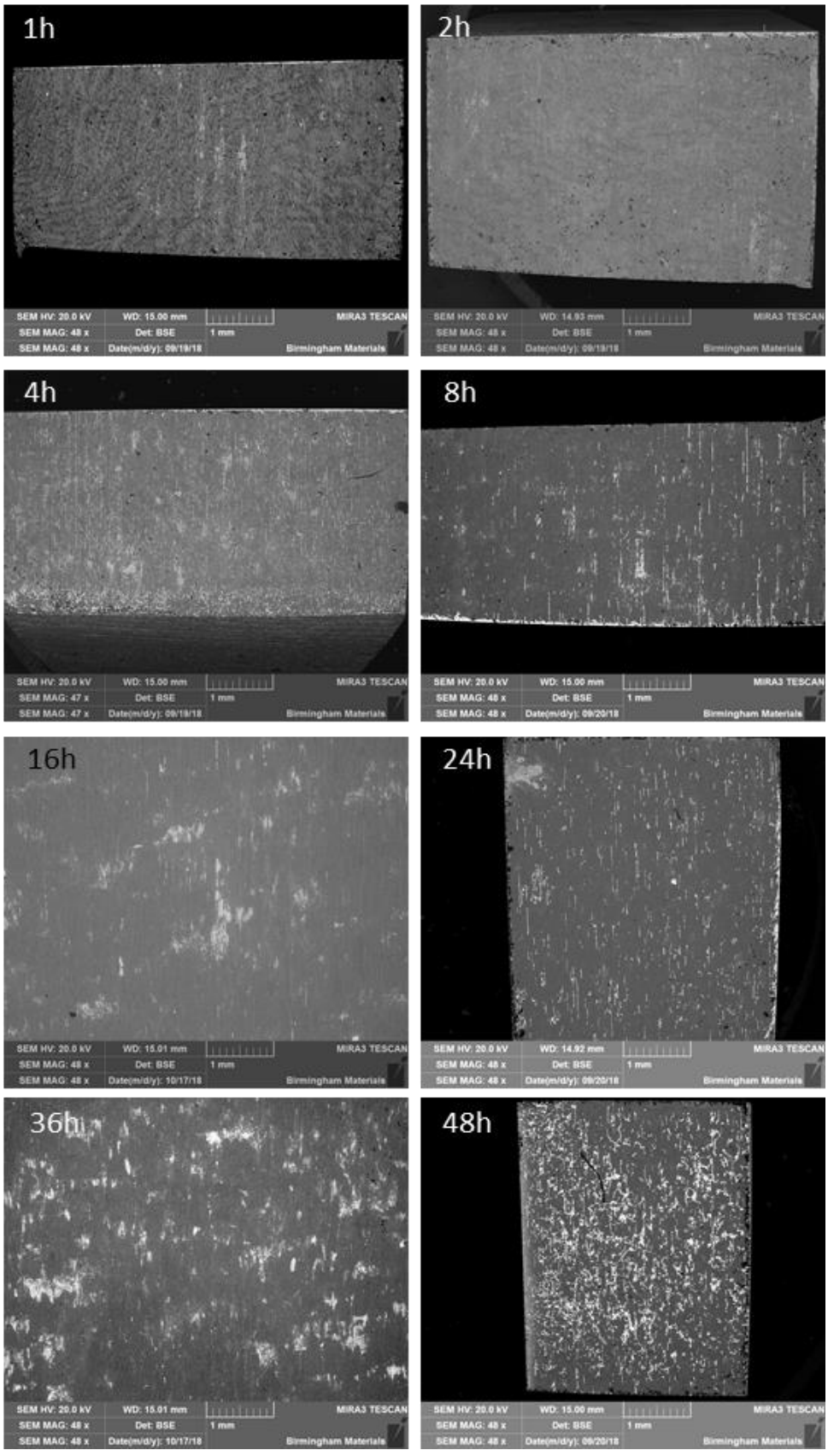

Figure 4.2.2-33: Optim-Al 1100°C Oxidation progression surface images displaying apparent lost oxide layer

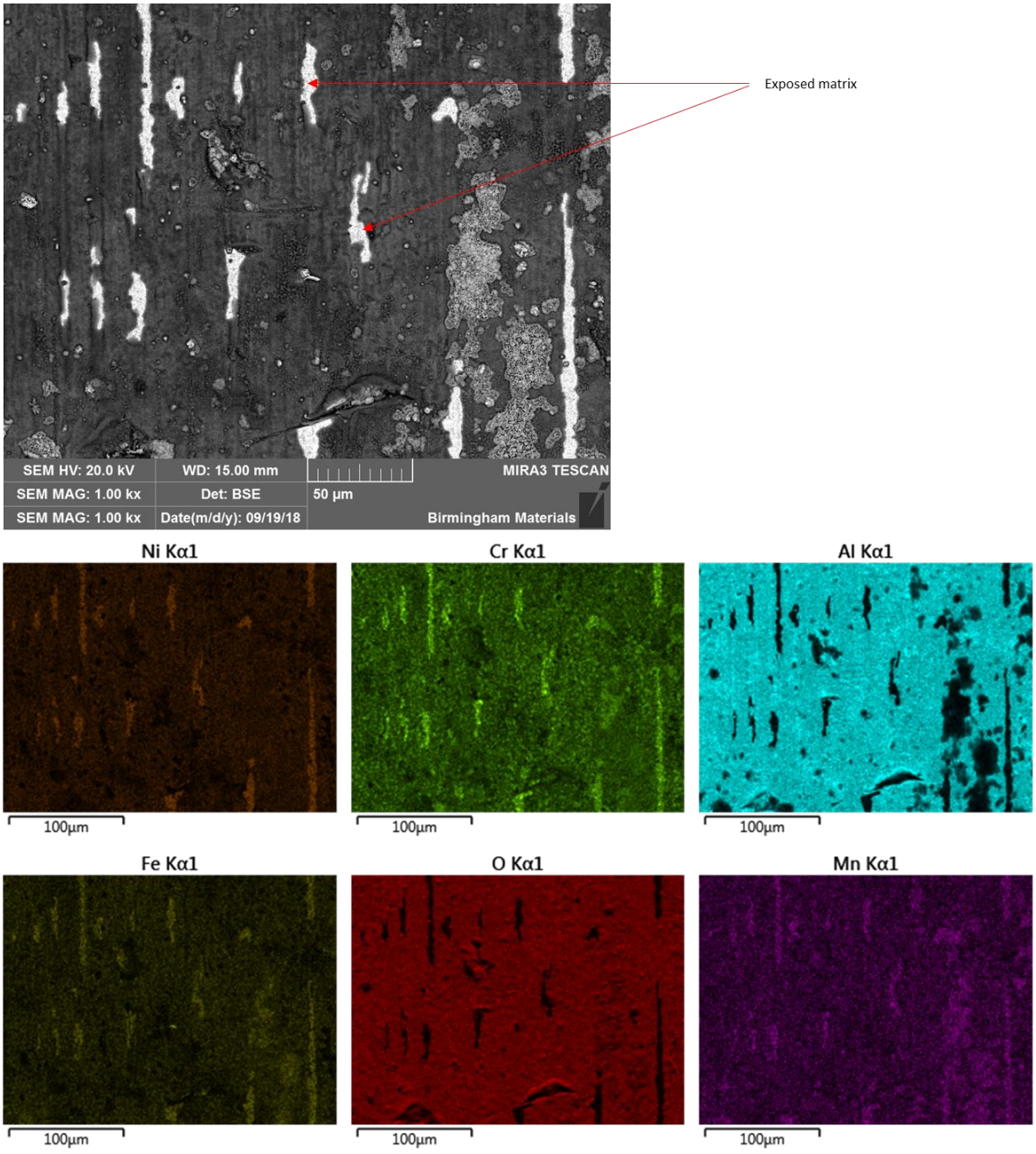

Figure 4.2.2-34: EDS mapping of Optim-Al alloy surface after 4-hour oxidation at 1100°C examining the loss of oxide layer.

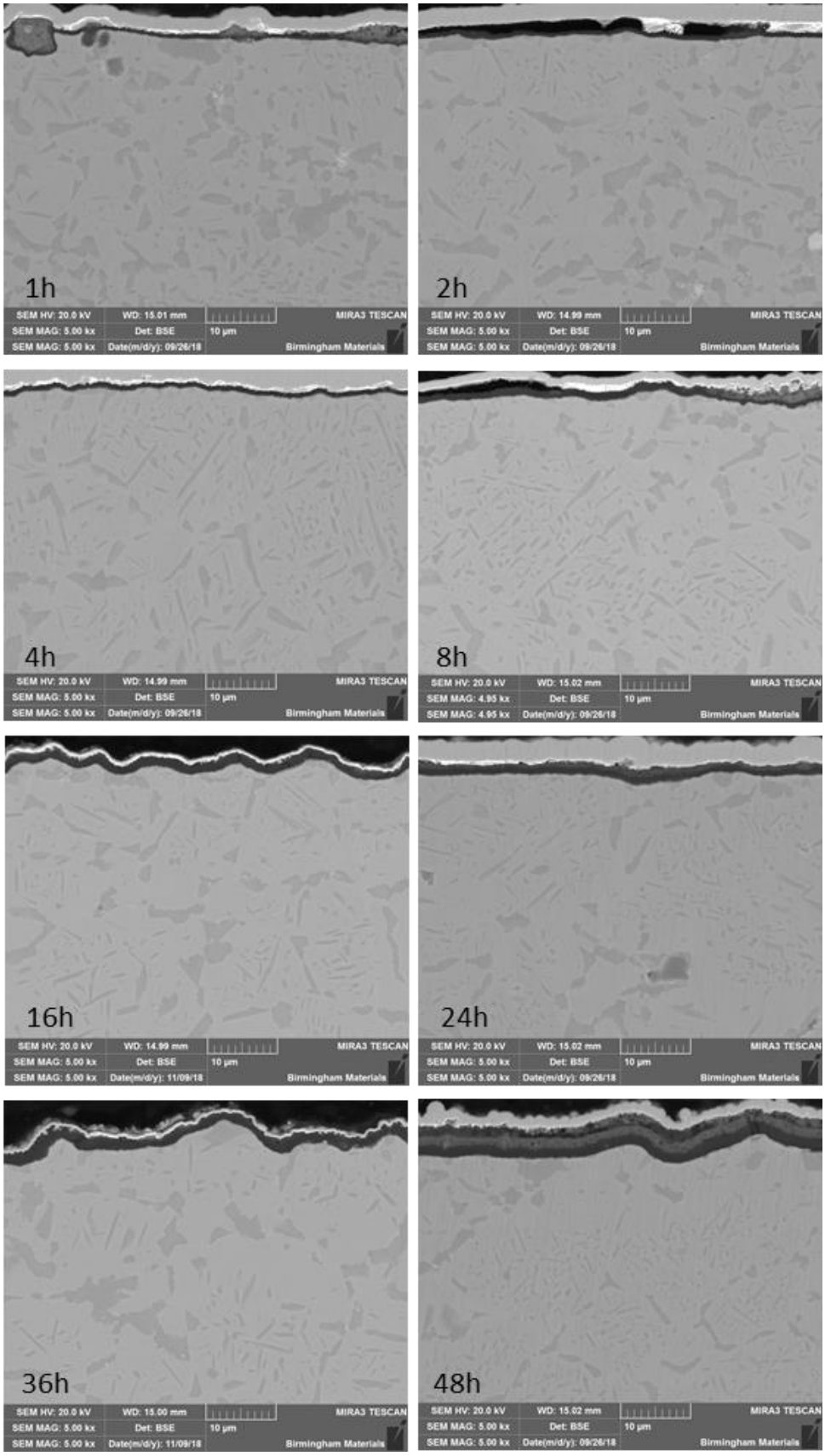

Figure 4.2.2-35: Optim-Al 1100°C Oxidation progression cross section images showing significant thickening and changing nature of the oxide layer by 48 hour oxidation.

Further examination of the 48-hour sample showed a clear difference in the oxide layer, with two separate oxides present. Figure 4.2.2-36 showed the oxide on the immediate surface of the matrix appearing to be the dense, continuous aluminium oxide seen elsewhere on the sample. However, above this aluminium oxide, a second oxide was formed. The EDS mapping suggested a composition of primarily nickel, aluminium and oxygen. The presence of nickel in this outer oxide was concerning, as nickel is a catalyst for catalytic coking. However, its presence as an oxide rather than in the matrix alters its effect, as this $NiAl_2O_4$ (nickel aluminide) spinel phase has been investigated as a catalyst for steam reforming of hydrocarbons. The nickel aluminide layer appeared to only form at higher temperatures after prolonged treatment times, as it was not evident in the shorter oxidation treatments or in any of the samples oxidised at lower temperatures. Thus, service temperatures of the order of 800°C are unlikely to elicit rapid formation of this secondary oxide. It is possible that the nickel aluminide will form during service after significant time at operational temperatures, beyond the timescales investigated. More likely is during the cleaning cycle; it runs at temperatures and times in the range of this experiment; therefore the production of this spinel phase could be expected.

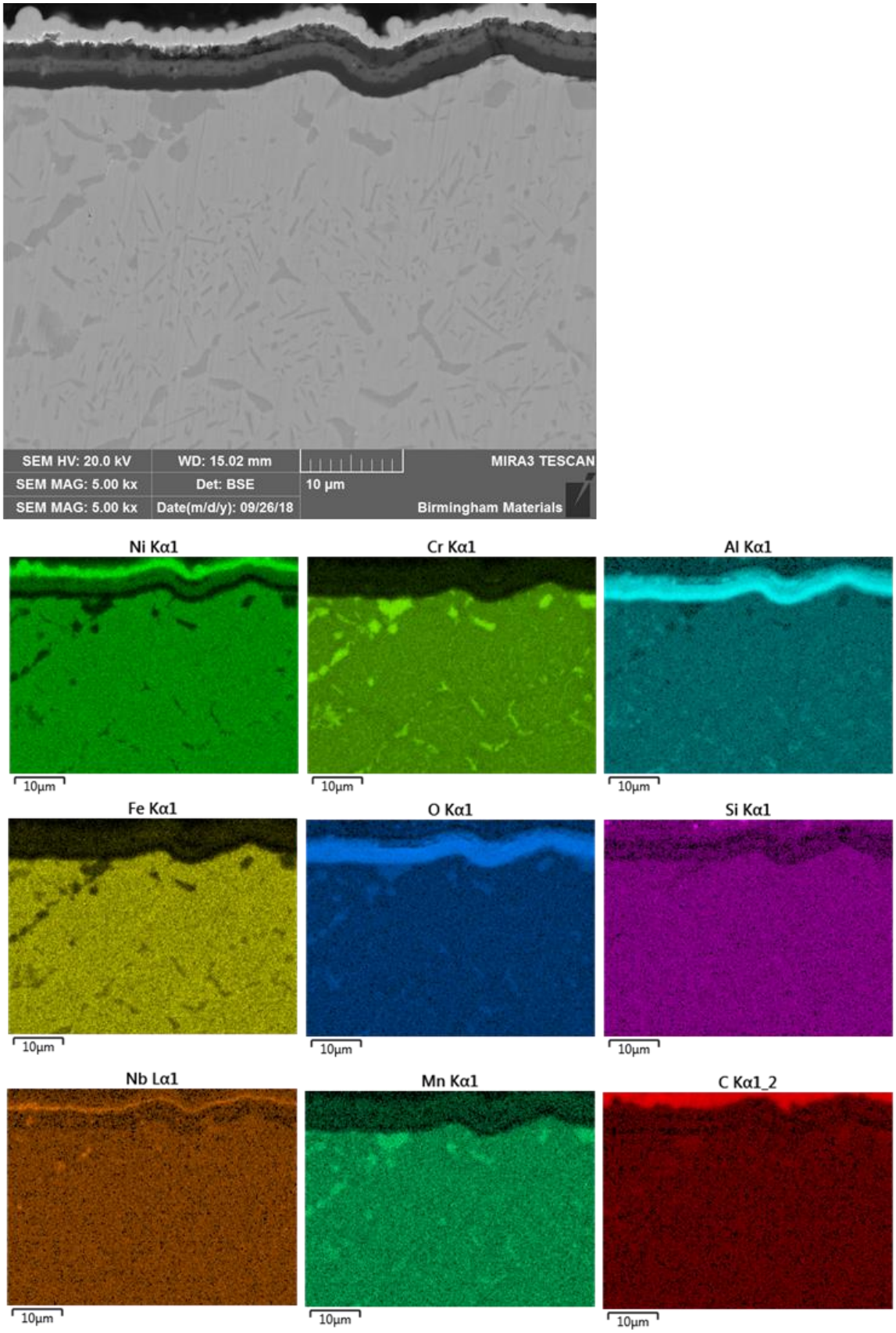

Figure 4.2.2-36: EDS mapping of 48-hour 1100°C oxidation of Optim-Al alloy examining the two differing oxide layers on the sample surface

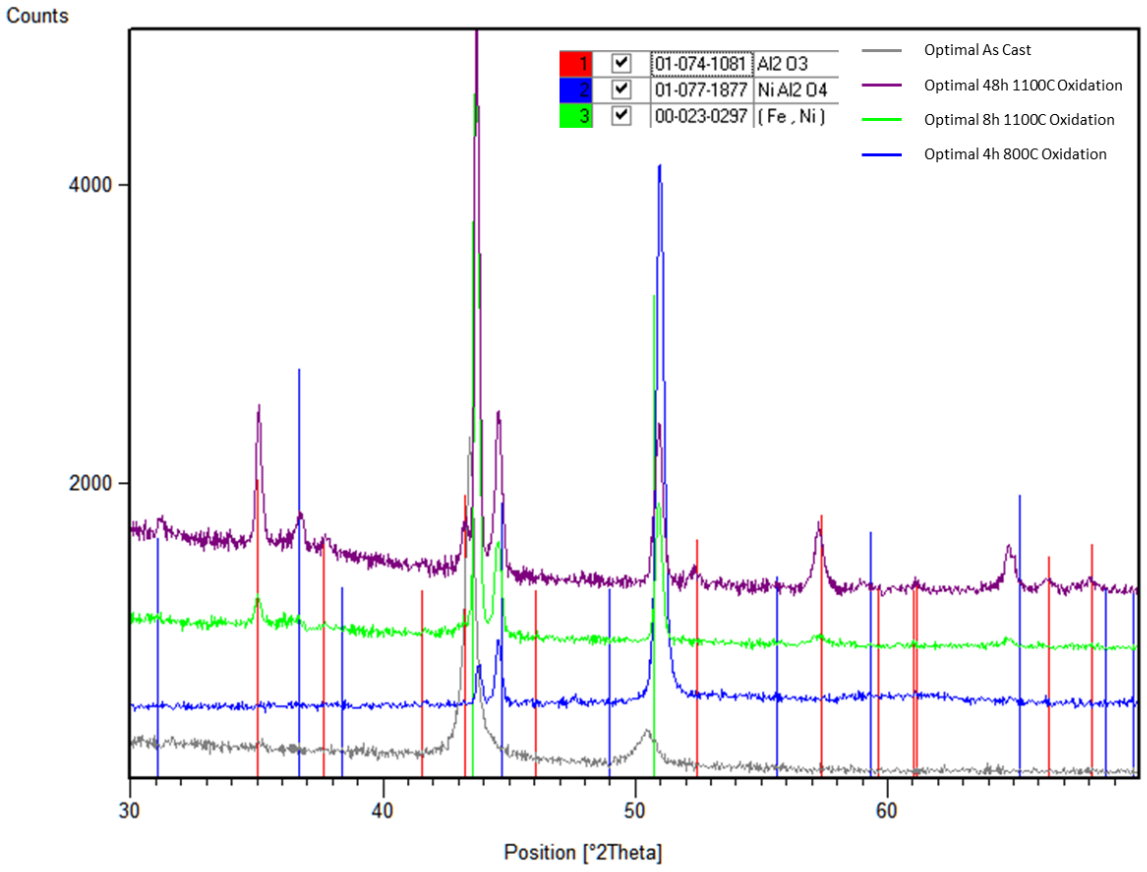

Figure 4.2.2-37: XRD traces of Optim-Al alloy as cast and after three different oxidation treatments identifying the surface oxides.

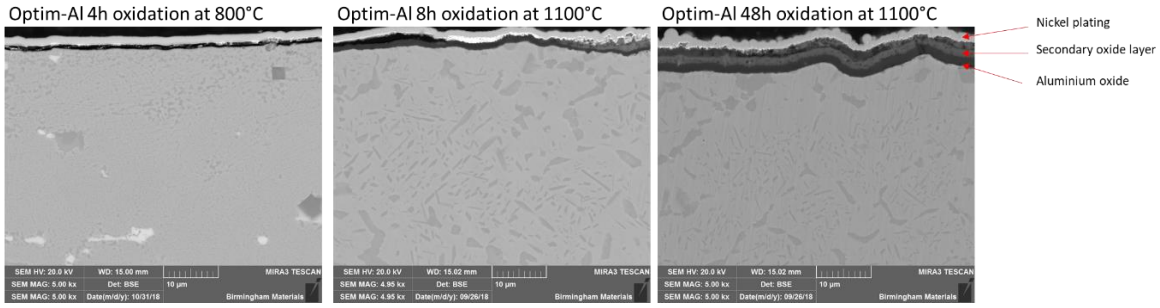

Figure 4.2.2-38: Cross section SEM backscattered images of Optim-Al alloy samples investigated by XRD analysis, displaying the identified phases.

XRD was undertaken on three samples to confirm the changes of the oxide layer. As with the Base alloy, a lower temperature oxidation sample was analysed to evaluate the oxide layer produced early in the oxidation process. The longer oxidation treatment sample was included to identify the secondary oxide layer which appeared on the sample surface after extended oxidation times.

Figure 4.2.2-37 showed major peaks at 35° and 57.5° which correlated to Al_2O_3 on the surface of the samples in all oxidation treatments. The spinel phase $NiAl_2O_4$ was also present, particularly in the 48-hour oxidation sample, which was seen atop the aluminium oxide layer as the second oxide identified in Figure 4.2.2-38. This was identified by the peaks at 36.5° and 65°, with the 8-hour 1100°C oxidation sample also demonstrating this phase presence.

The oxide thickness measurements (Figure 4.2.2-39) show a consistent increase in oxide thickness with time during the short oxidation times. This continued but tailed off after 8 hours, with the graph slowly arcing to a progressively reduced oxide growth rate.

Similarly, the thermogravimetric analysis (TGA) test displayed similar growth rate and pattern, as displayed in Figure 4.2.2-40. The small dip seen within the first 2 hours of the TGA test was identified as cause by the correction curve of the alumina crucible, and was also present on the curve for the Base alloy (Figure 4.2.2-21). This is illustrated in Figure 4.2.2-41, showing the correction curve to have a dip which is then translated onto the results for both alloys. This dip on both alloys can therefore be ignored as significant.

The comparison of the Base alloy and the Optim-Al alloy's oxide thickness and mass gain at 1100°C showed roughly a six-fold decrease in mass gain and oxide thickness for the Optim-Al alloy compared to the Base alloy, with a significantly thinner oxide on the surface (Figure 4.2.2-43). As formerly discussed, the benefits of thinner oxide layers are significant if the oxide performs just as well, let alone if the oxide displays greater consistency, coverage of the matrix, and increased durability.

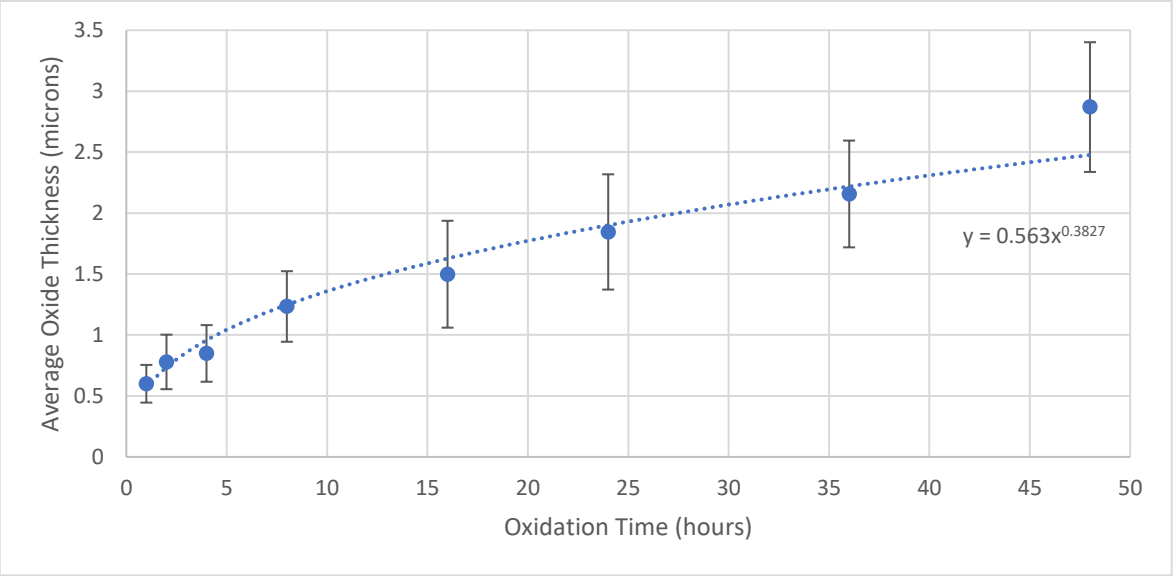

Figure 4.2.2-39: Oxide thickness progression of Optim-Al alloy oxidation at 1100°C

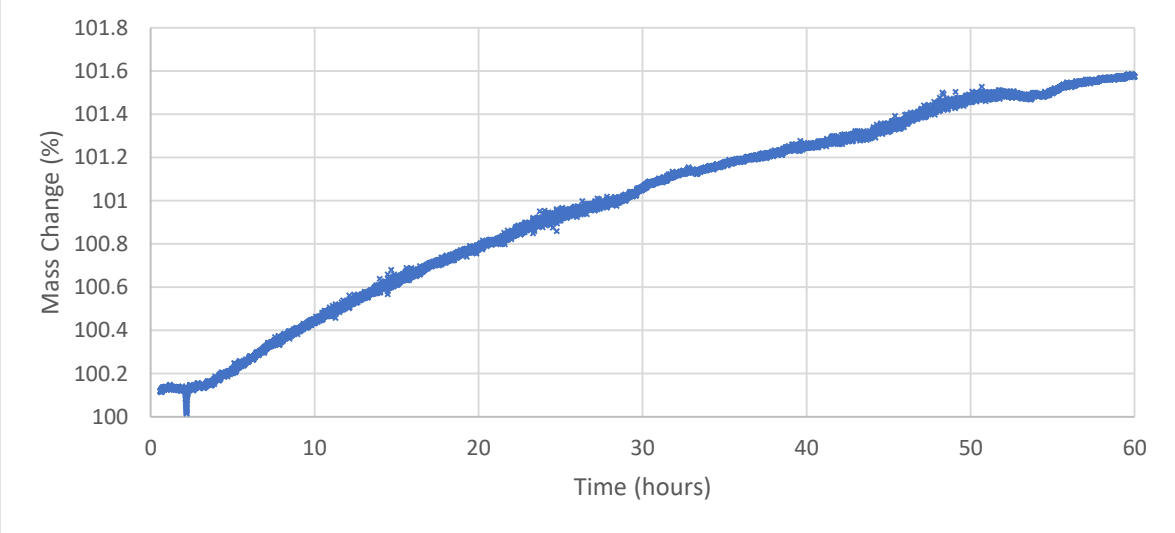

Figure 4.2.2-40: Graph of TGA (thermogravimetric analysis) measurement of Optim-Al alloy oxidised at 1100°C for 60 hours

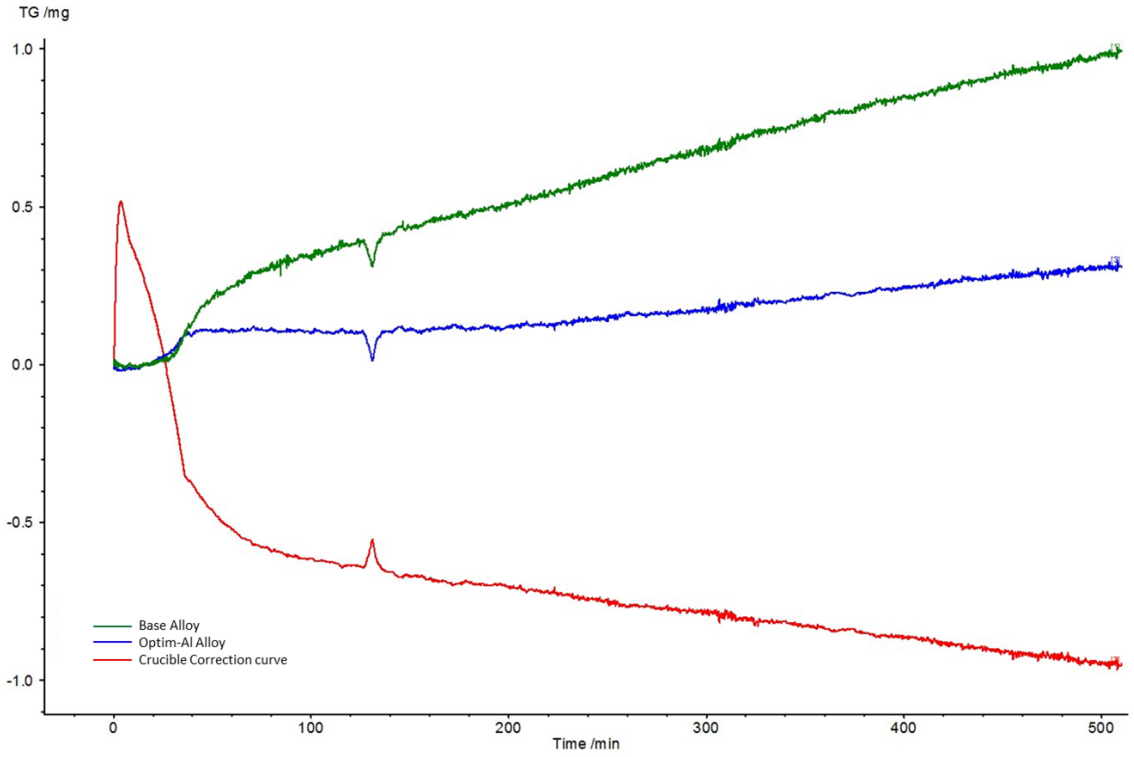

Figure 4.2.2-41: TGA traces of Base and Optim-Al alloy along with the crucible correction curve (red), demonstrating the cause of the apparent mass loss around two hours into the oxidation treatment.

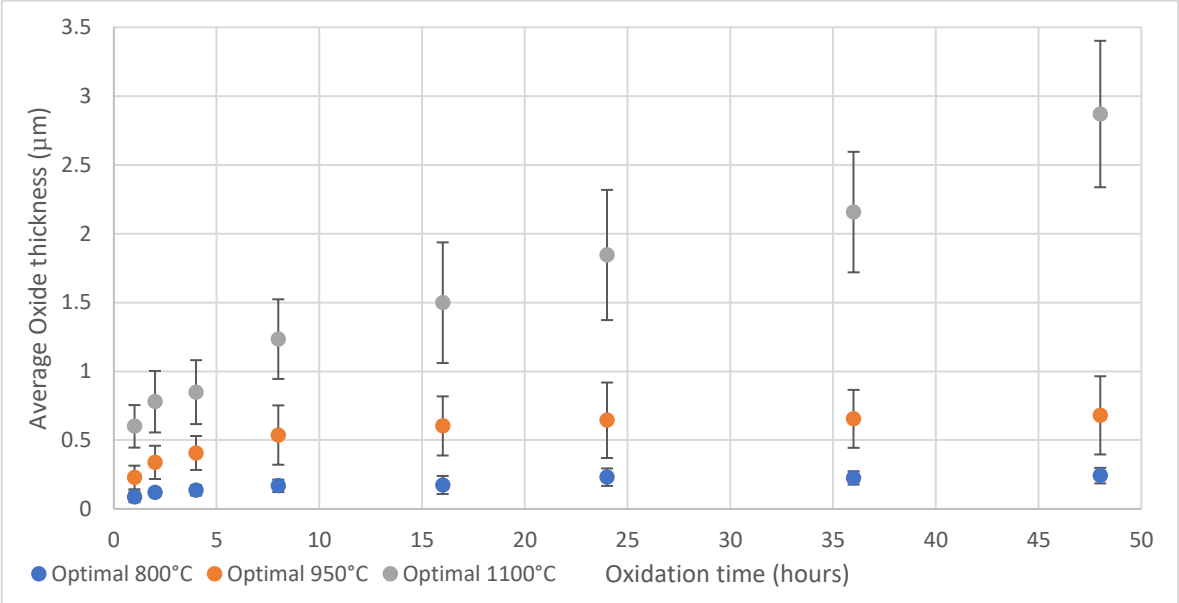

Figure 4.2.2-42: Graph comparing Optim-Al alloy average oxide layer thickness over time at 800°C, 950°C and 1100°C

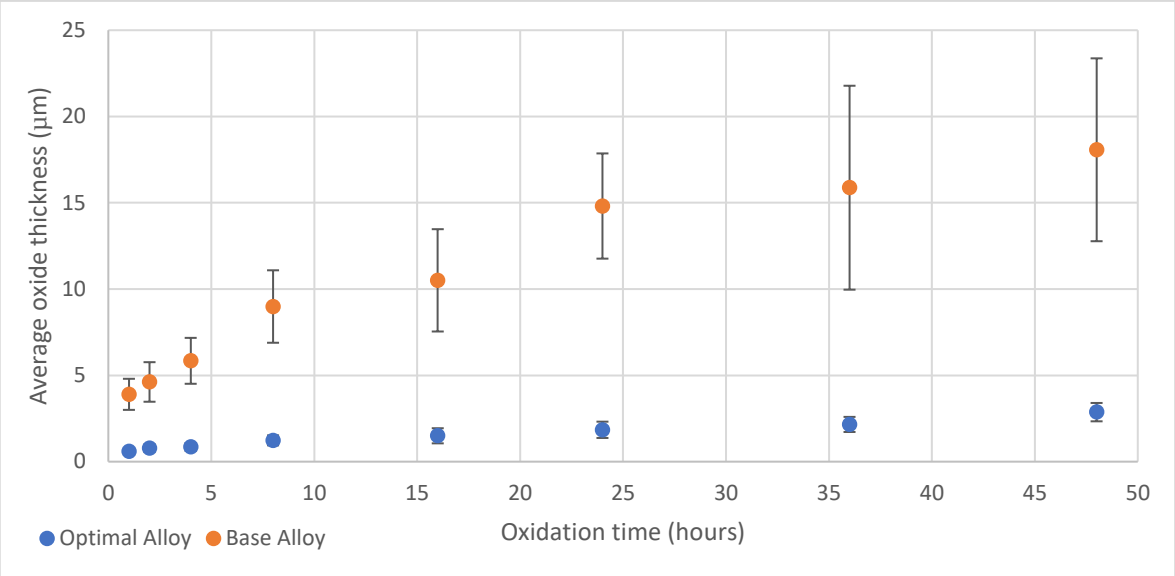

Figure 4.2.2-43: Comparison graph of oxide layer thickness between Base alloy and Optim-Al alloy after oxidation at 1100°C

4.2.2.3 Summary of effects of time and temperature on oxide layer growth

The Base alloy showed significantly thicker oxide growth at all compared temperatures and times, producing the chromium oxide layer previously identified in 4.2.1, compared to the aluminium oxide layer produced by the Optim-Al alloy. Oxidation rate was found to be generally parabolic, howeve a step change in the Base alloy oxidation was observed after around 21 hours of oxidation at 1100°C. This will be discussed later (5.2.1).

Both alloys displayed some evidence of spalled oxide layer, however this was much more widespread for the Base alloy and occurred at lower temperatures and shorter oxidation times. Furthermore, repassivation of the oxide layer appeared to occur with the Optim-Al alloy, whilst that was not consistently the case with the Base alloy.

4.2.3 Adhesion of oxide layer

As was observed in 4.2.2, the oxide layer on the Base alloy and the Optim-Al alloy displayed lost oxide from the surface of the pipe, particularly with higher temperatures and the longer oxidation treatments. Furthermore, the oxide clearly appeared to be lost around the machining marks on the inner diameter surface of the processed pipes (observed primarily in Figure 4.2.2-12 and Figure

4.2.2-33). Therefore, the effect of the surface to be oxidised, and the adhesion of the oxide to the substrate were investigated.

4.2.3.1 Effect of surface roughness on oxide adhesion

As identified previously, the alloys lose the oxide from the surface in specific regions, apparently related to the machining marks on the sample surfaces. The Optim-Al alloy was oxidised with differing sample surface preparations to assess the oxide adhesion. Three preparations were analysed; ground with 120 grit paper; as machined; and ground with 1200 grit paper. All three samples were oxidised for 24 hours at 1100°C.

Table 4.2.3-1: Roughness measures of Optim-Al samples before oxidation

Sample	Average Ra
Optim-Al 120 grit grind	0.73
Optim-Al machined	0.52
Optim-Al 1200 grit grind	0.11

Table 4.2.3-2: Average % area of Optim-Al sample surface without oxide layer present

Surface finish	Average % area without oxide
120 grit	1.87
Machined	9.98
1200 grit	1.54

All three samples displayed evidence of material loss (Figure 4.2.3-1, Figure 4.2.3-3 and Figure 4.2.3-5), however this loss greatly varied between surface finishes. The sample with the smoothest finish, the 1200 grit paper, displayed the lowest level of lost oxide from the surface (1.54%), whilst the machined sample displayed the greatest loss (9.98%), as displayed in Table 4.2.3-2, as calculated using ImageJ software.

The other features seen in Figure 4.2.3-5 which were not the surface oxide layer, nor the exposed matrix beneath, were identified by EDS mapping (Figure 4.2.3-6) as surface breaking niobium carbides. The presence of these is in line with the oxidation observations made in 4.2.1.4, where it

was seen that the oxide layer formed beneath niobium carbides which were exposed to the environment, rather than forming the aluminium oxide layer atop them as seen across the rest of the sample.

In all three samples, the lost material shared at least one border with a scratch, machining mark, or other defect on the surface of the sample. It is hypothesized that as the sample surface oxidises, the walls of the scratch or machining mark will also oxidise, and as the oxide layer thickens, pressure builds up as the two opposing oxides come into contact with one another in the scratch. As the oxide continues to thicken with time, the pressure reaches a critical point at which the oxide ruptures outwards, and in doing so fractures the oxide and debonds it from the bulk material. This process is illustrated in Figure 4.2.3-7.

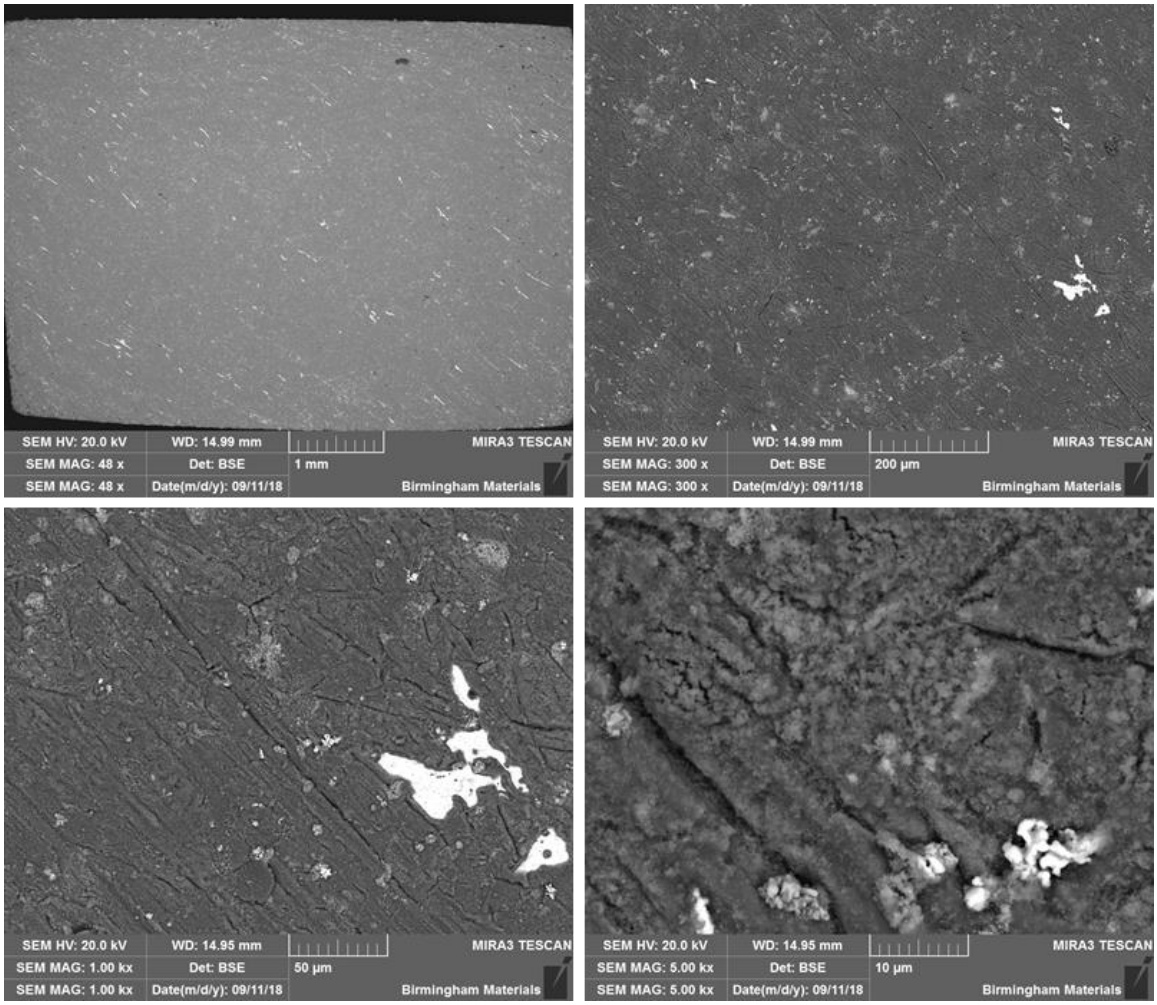

Figure 4.2.3-1: Optim-Al alloy oxidised. 120 grit paper finish. Patches of lost oxide identifiable.

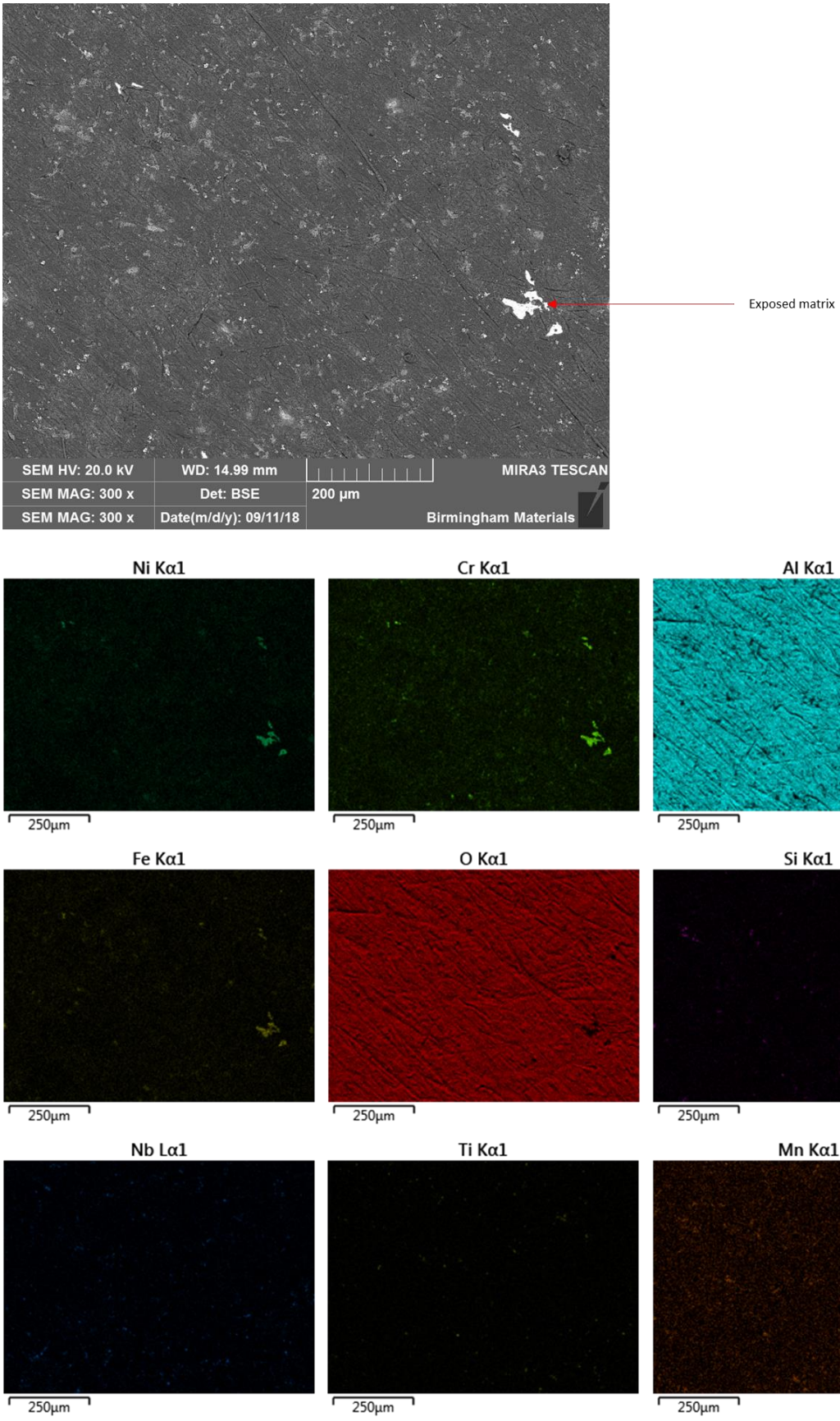

Figure 4.2.3-2:EDS mapping of Optim-Al oxidised after 120 grit paper finish identifying exposed matrix material.

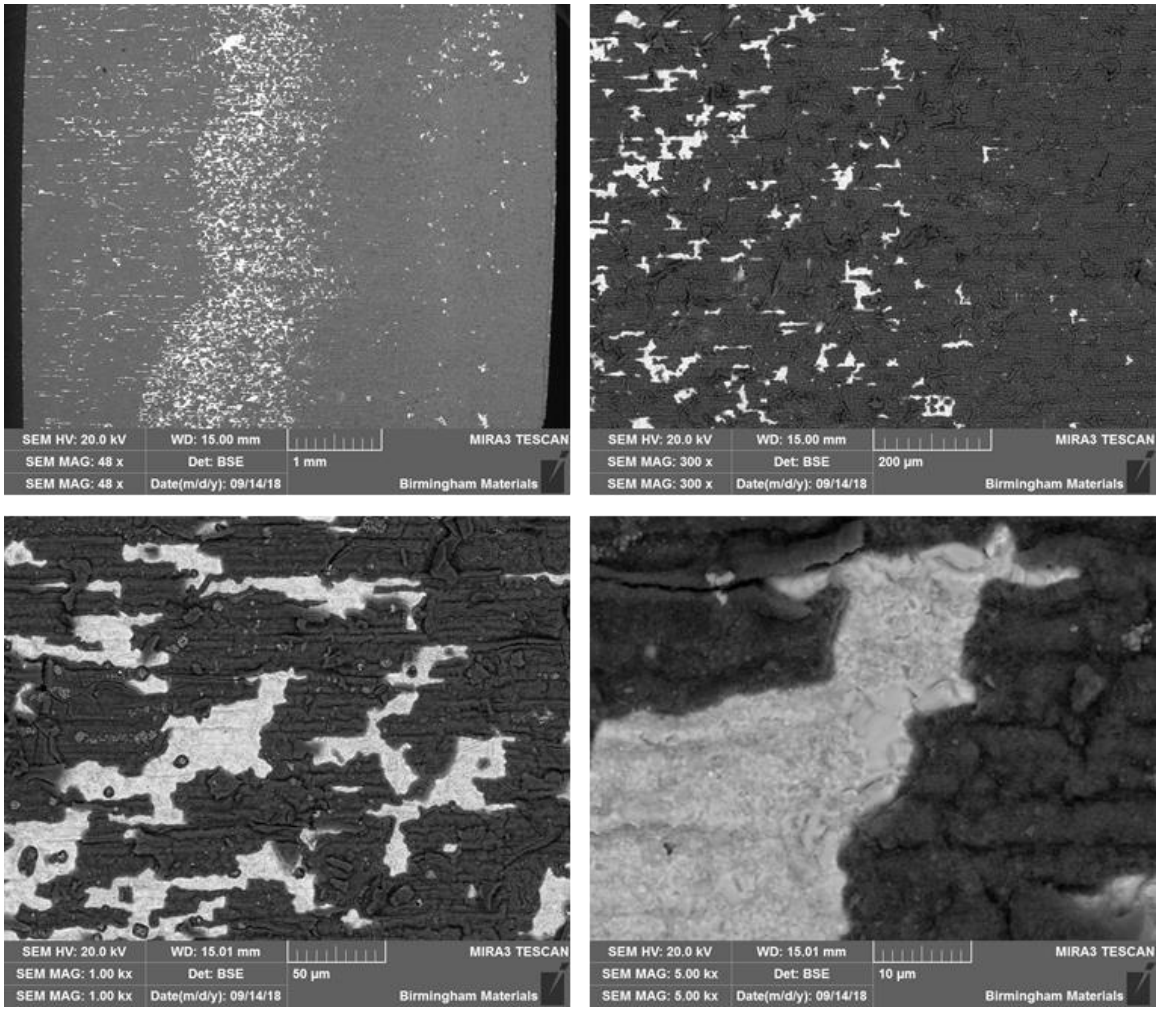

Figure 4.2.3-3: Optim-Al alloy oxidised. As machined finish. Showing widespread oxide removal from surface.

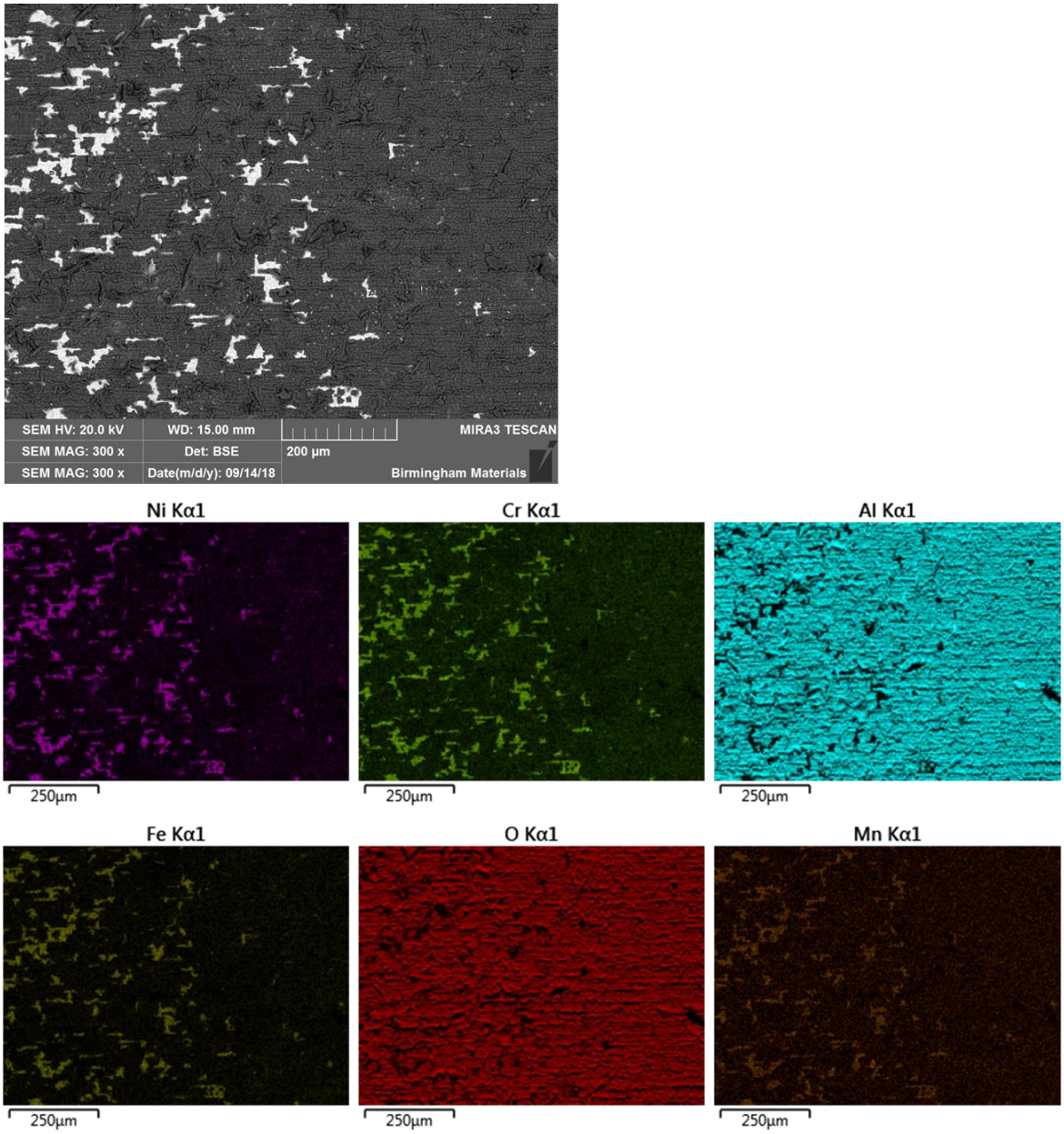

Figure 4.2.3-4: EDS mapping of as machined Optim-Al alloy indicating exposed matrix material.

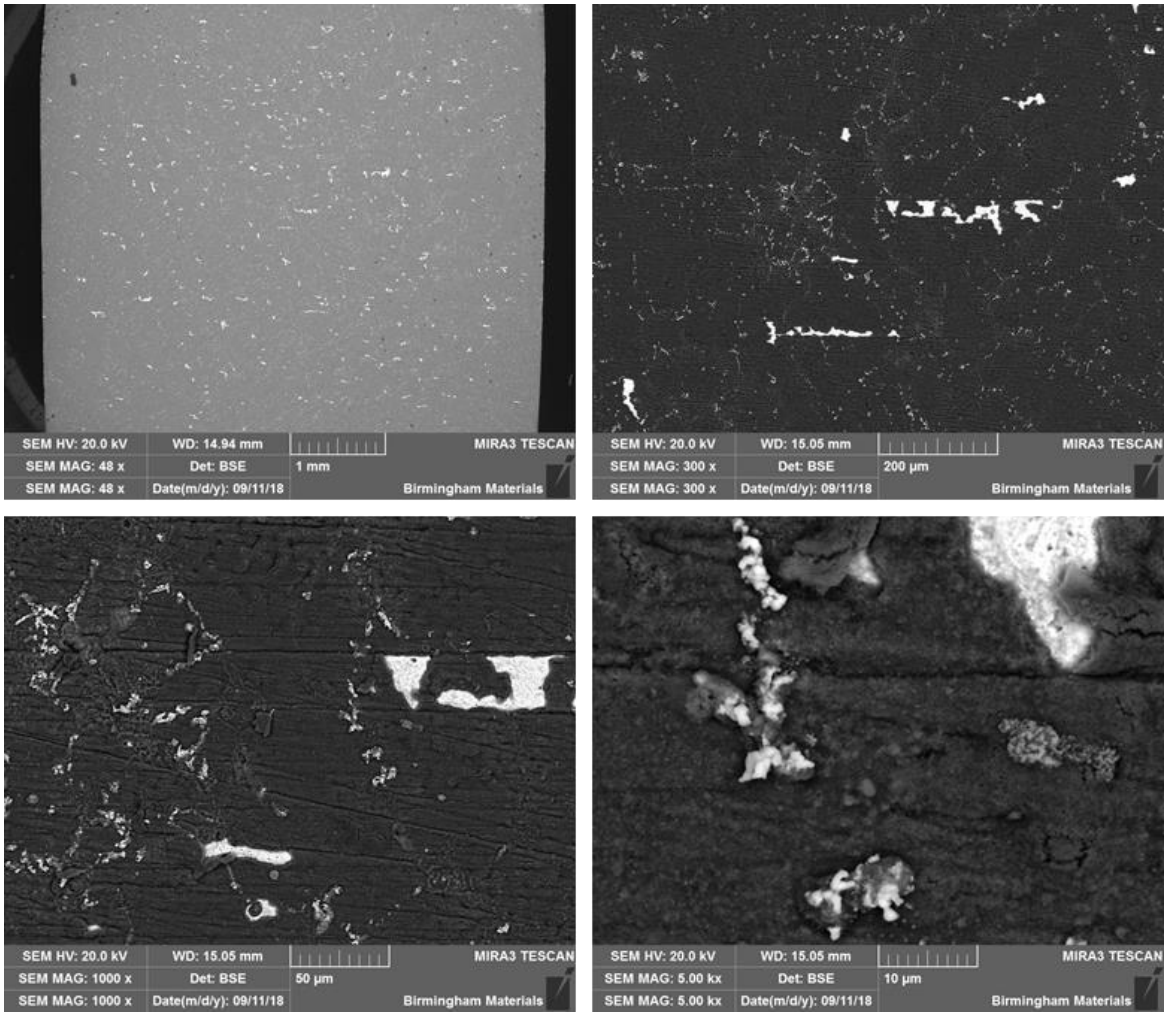

Figure 4.2.3-5: Optim-Al alloy oxidised. 1200 grit paper finish. Showing limited oxide layer loss from surface.

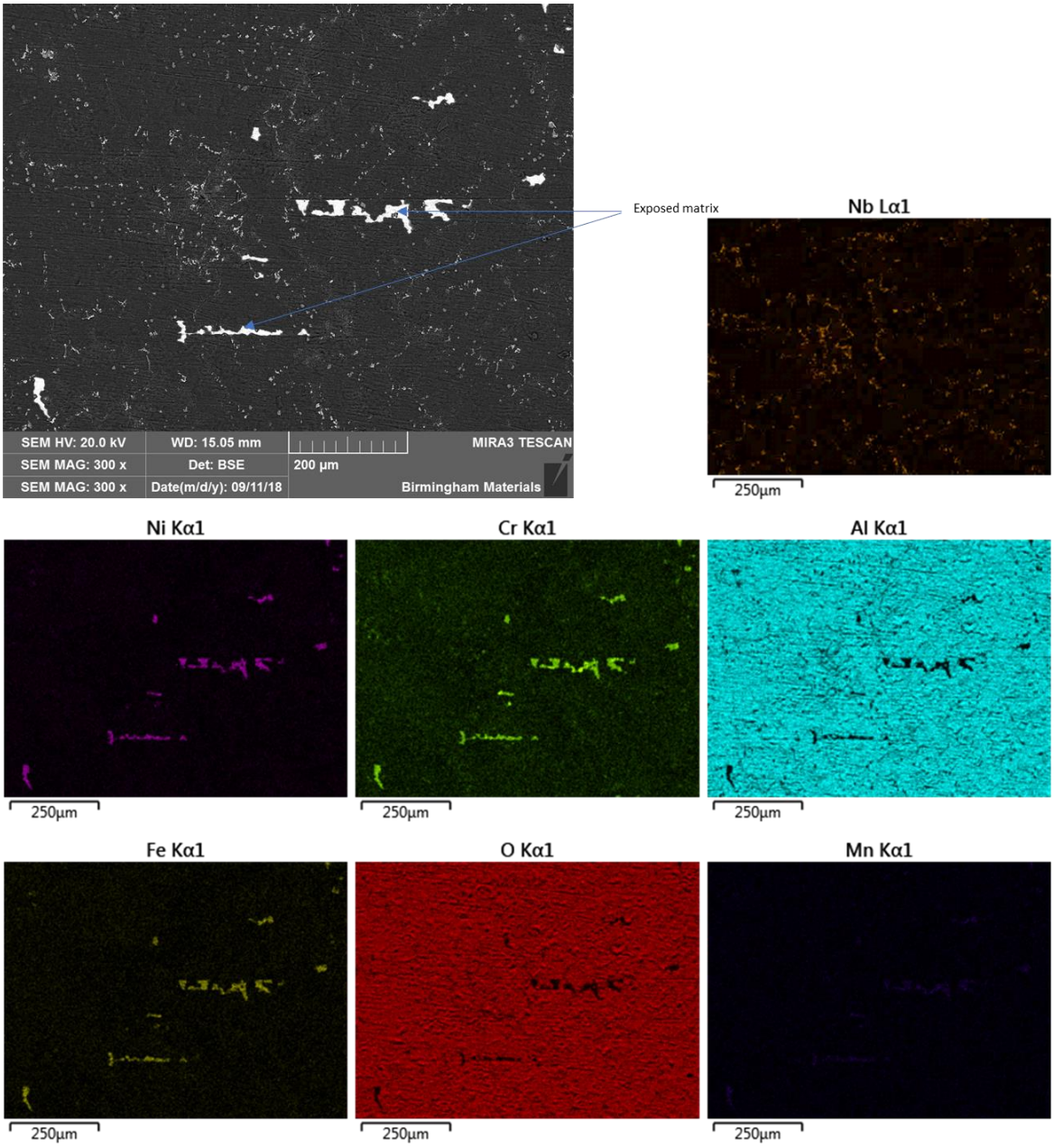

Figure 4.2.3-6: EDS mapping of Optim-Al alloy oxidised surface. 1200 grit paper finish identifying exposed matrix.

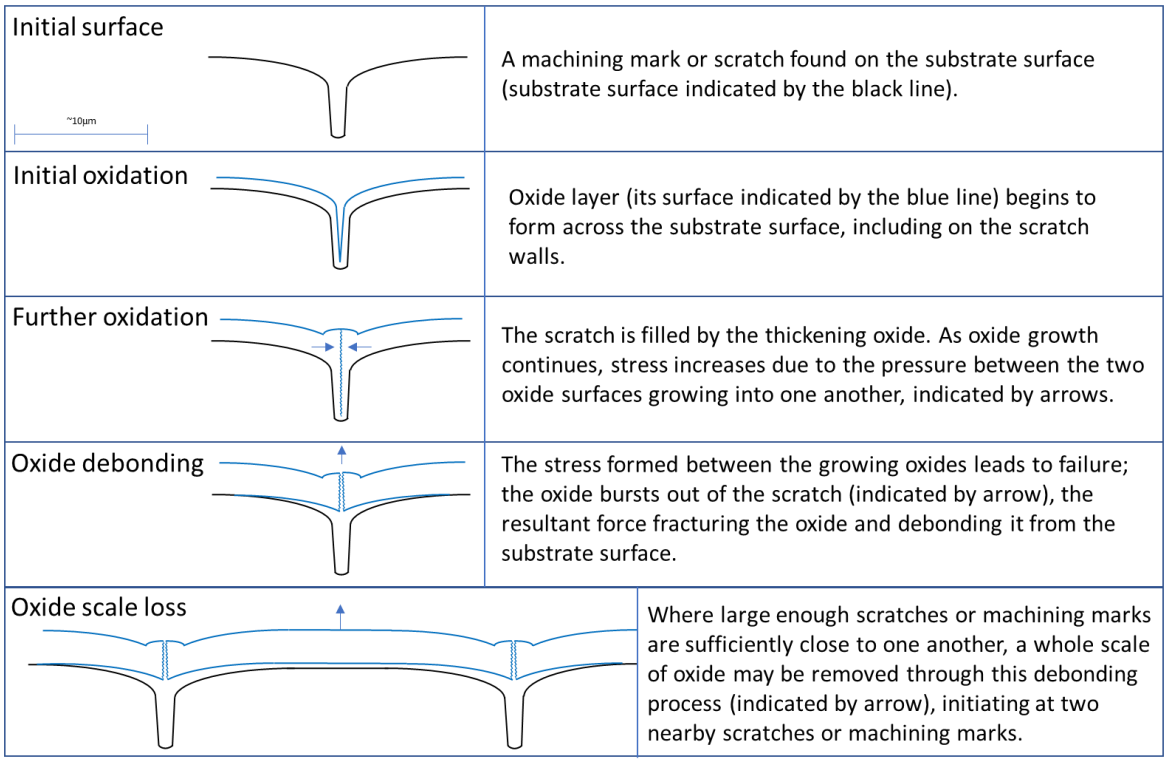

Figure 4.2.3-7: Diagram of proposed mode of failure and material loss due to surface imperfections during the high temperature oxidation of the alloys. Stresses forming from two oxide surfaces in contact with one another lead to fracture and debonding of the oxide layer.

These results suggested that minimizing surface scratches and machining marks will significantly improve the oxide layer retention on the surface of the samples.

4.2.3.2 Scratch tests

To further evaluate the adhesion of the oxide layer, scratch tests were undertaken. Scratch tests are used to assess the adhesion of a surface layer on a material, and the failure mechanism of the surface layer. A force is applied by a diamond tip at an increasing rate; either a linear increase or a stepped increase, until failure of the surface layer. Friction and acoustic emission of the test are regularly measured, and the scratch tracks are examined after the test. The European Standard EN 1071-3 describes the scratch test procedure (121). This test was used to more accurately quantify the differences in adhesion of the oxide layer between the chromium oxide layer on the Base alloy, and the aluminium oxide layer on the aluminium containing alloys, as well as determine the failure mechanisms of the oxide layers under applied force. Greater adhesion of the oxide layer indicates

a lower likelihood of spallation, with greater stress build up from thermal expansion or contraction required to cause debonding.

Samples of all four alloys at the machined inner diameter depth were polished and oxidised under different conditions to one another to elicit the greatest coverage of surface oxide on all samples. The samples underwent scratch tests from 0N-60N force in a linearly increasing rate.

Examination of the Base alloy scratch tests showed significant loss of surface oxide from low pressures, with damage to the oxide apparent from the very beginning of the scratch test (Figure 4.2.3-8). Figure 4.2.3-9 displays the surface presence of matrix forming elements, confirming the exposure of the matrix and removal of the oxide from the sample surface. These results signify poor bonding adhesion between the oxide and the substrate beneath. The appearance of the scratch test marks produced are in line with buckling failure followed by spallation buckling failure of the oxide, as described by Bull (135,136) and displayed in Figure 4.2.3-13. This is characterized by failure in an arc ahead of the contact point, followed by lateral spread of the scratch track of the spalled material. This failure indicates high tensile stresses within the oxide layer, released by through-thickness cracks created by the stress applied in the test. The greater thickness of the chromium oxide layer compared to the other alloys is also likely to be a factor with its potential for greater internal stresses.

Half of all surface oxide layer material in the scratch track was lost at an average force of 10N across the three scratches on the Base alloy. This is a significant concern, as the bonding between the oxide and matrix is clearly poor, and the oxide is likely to experience some impact forces during the cleaning process, where the coke layer is burned out, with debris moving through the pipe at a significant speed, and therefore impacts with the pipe are likely to lead to removal of the protective oxide layer.

The Low-Al alloy, whilst not having a consistent oxide across the sample surface, as discussed previously (4.2.1.2), showed the oxide layer remaining intact through to 25N of force, displaying significantly greater adhesion to the matrix than the Base alloy. Failure of the oxide appears to be buckling, with buckling spallation occurring at forces above 40N, a similar failure mechanism to the Base alloy, however, it showed much greater adhesion and resilience to damage at lower forces.

The High-Al alloy, similar to the Low-Al alloy, maintained surface oxide throughout the low applied force range, with no noticeable damage evident until stresses over an average of 20N were applied (Figure 4.2.3-11). This was a similar range to the Low-Al alloy, and significantly greater than the Base alloy. With some oxide material found outside the scratch wear track, this appeared to once again be buckling, however there is very little evidence of buckling spallation.

The Optim-Al alloy scratch test appeared more resilient than the other tested alloys, as no visible damage or oxide removal occurred until 30N of force was applied. The oxide layer displayed conformal cracking, rather than buckling of the oxide as observed with the other three alloys. The oxide layer was not removed from its initial site, instead the force of the scratch test led to fracturing of the oxide in place, demonstrating significantly greater adhesion between the oxide layer and the bulk matrix, with through thickness failure occurring without debonding. This result further suggests a significantly better oxide maintenance for the Optim-Al alloy than that seen with the Base alloy, a significant indicator of potential improved performance in service.

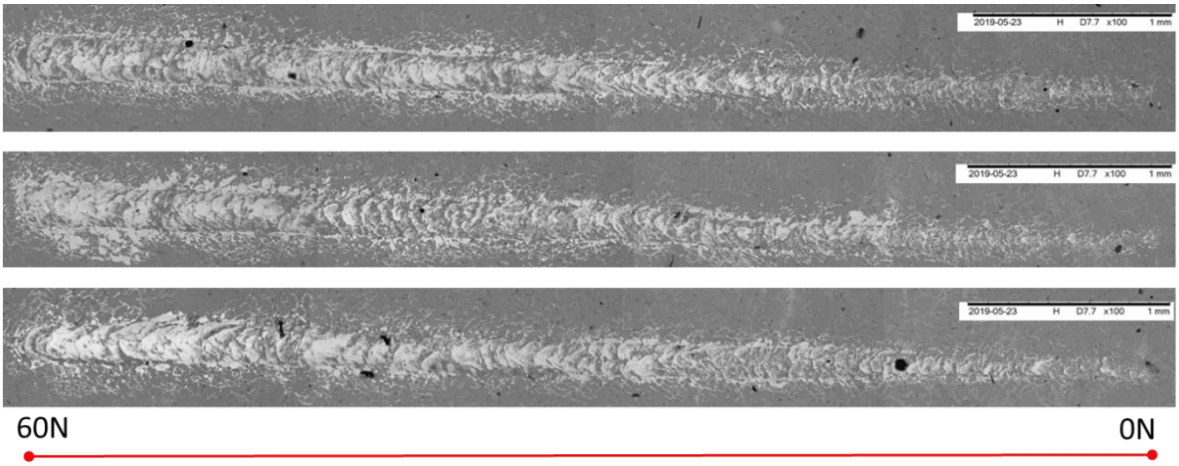

Figure 4.2.3-8: Base alloy scratch tests backscattered images displaying loss of surface oxide from low loads onwards.

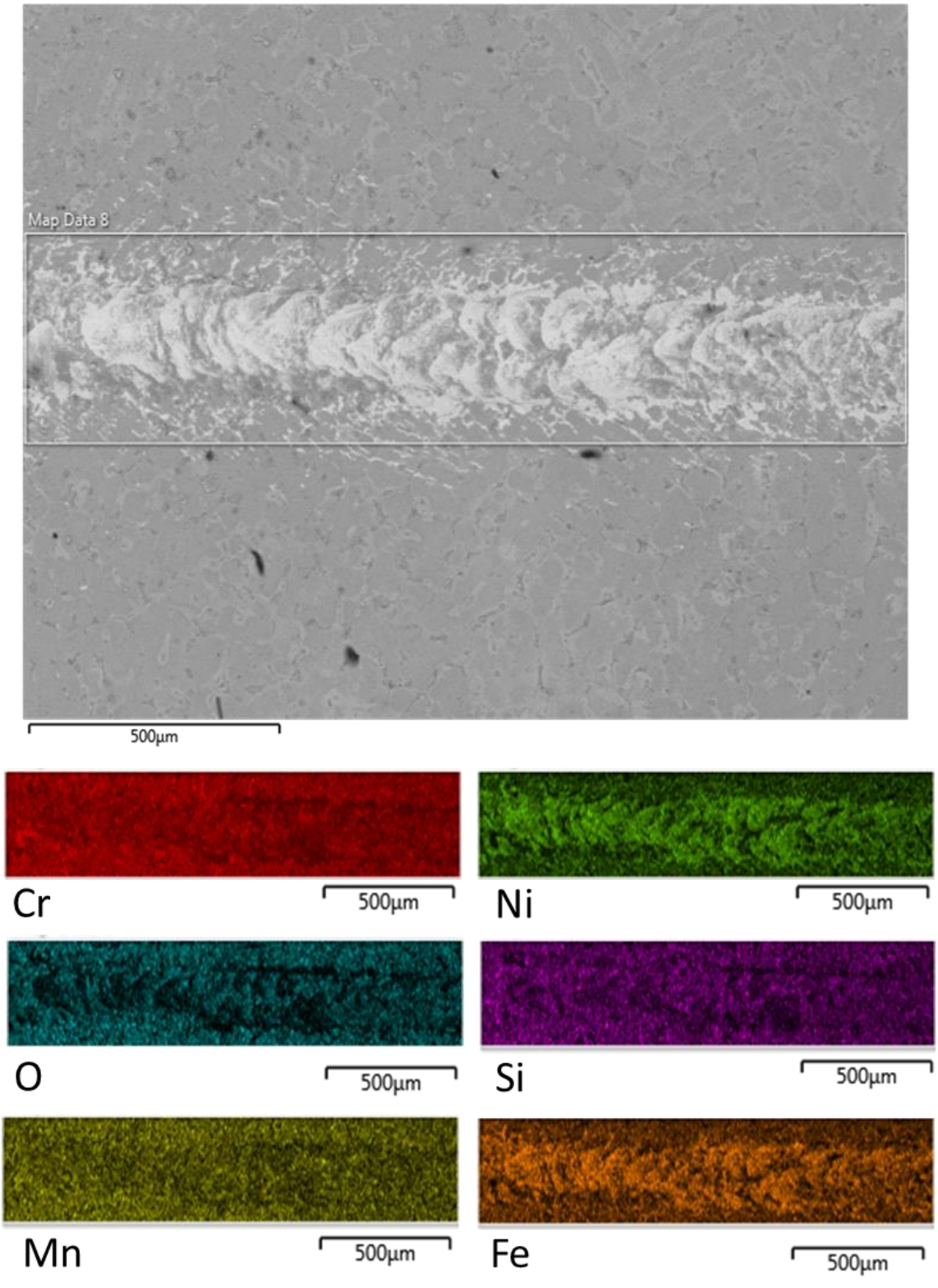

Figure 4.2.3-9: EDS mapping of scratch track of Base alloy scratch test in 30-45N range, demonstrating matrix exposure.

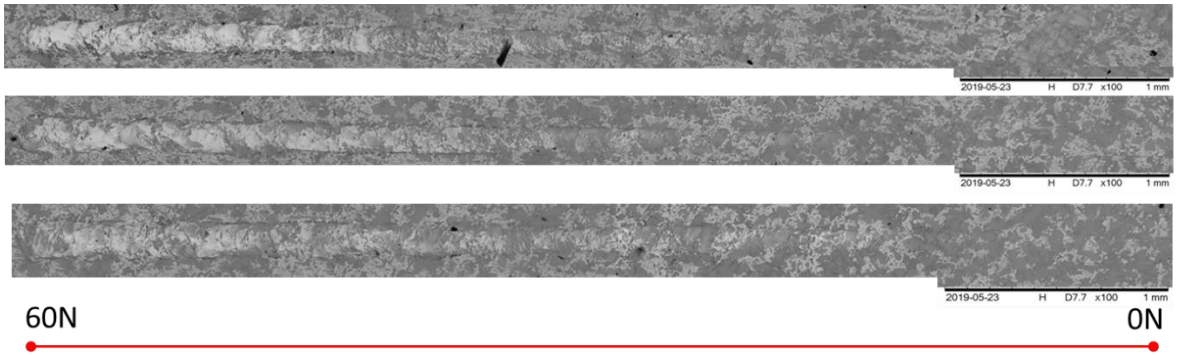

Figure 4.2.3-10: Low-Al alloy scratch test backscattered images showing some resilience to loss of oxide at low force.

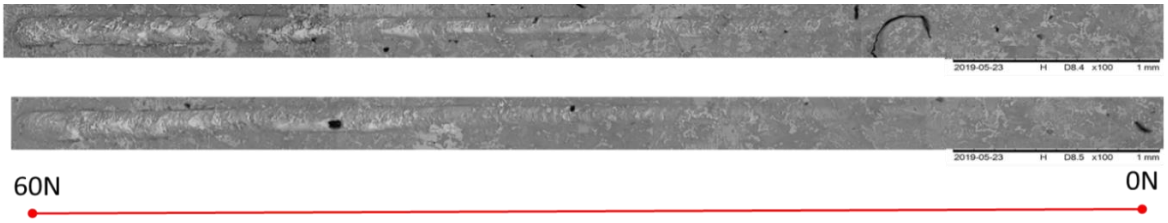

Figure 4.2.3-11: High-Al alloy scratch test backscattered images showing some resilience to loss of oxide at low force.

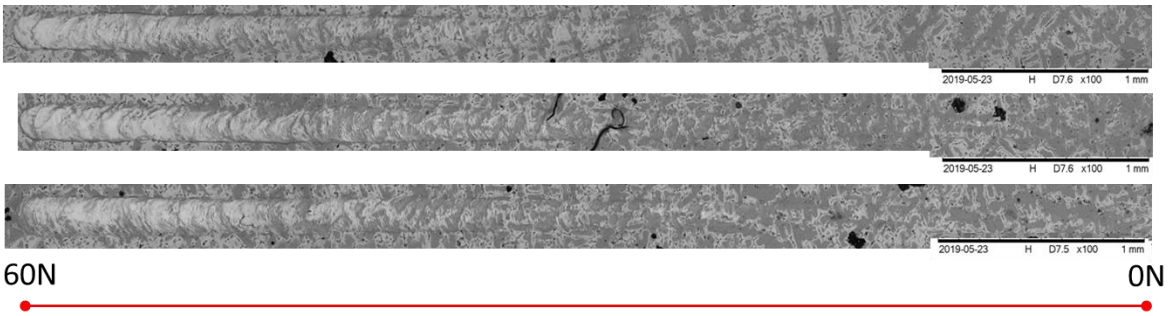

Figure 4.2.3-12: Optim-Al alloy scratch test backscattered images showing good adhesion at low and moderate forces, and differing failure patterns to the other three alloys.

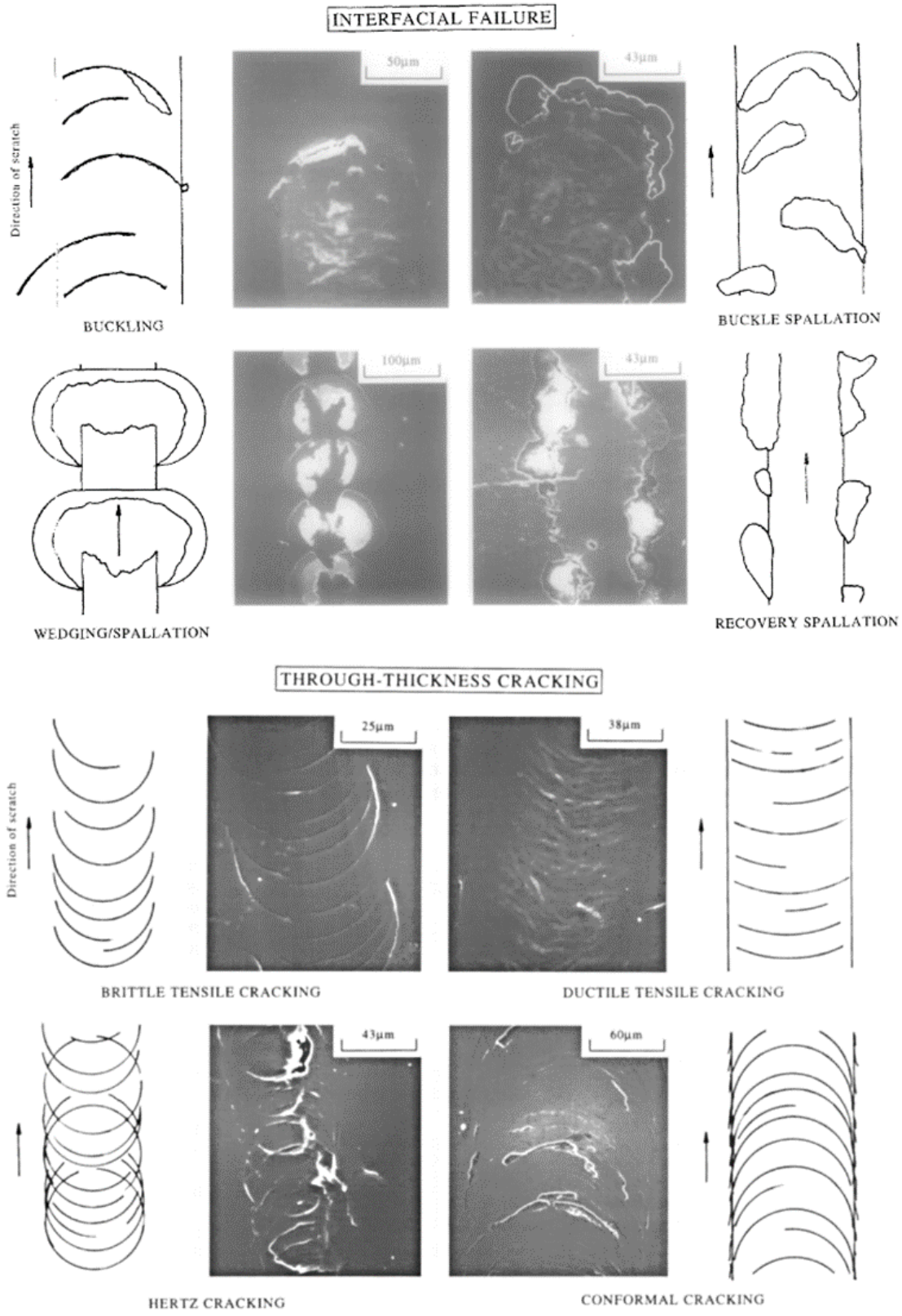

Figure 4.2.3-13: Failure modes in scratch tests (135)*. Demonstrating the 8 common failure modes in scratch tests, split between interfacial failure modes and through thickness cracking modes. The chromium oxide forming alloys of Base, Low-Al and High-Al all displayed buckling and some degree of buckle spallation, whereas the alumina forming Optim-Al displayed conformal cracking.*

4.2.3.3 Pilling-Bedworth Ratio

Maintenance of adhesion of an oxide to a substrate with regards to the difference in densities of the oxide compared to the substrate matrix are evaluated using the Pilling-Bedworth Ratio (PBR). A PBR below 1 indicates a porous or cracked, discontinuous oxide on the substrate surface. A PRB of over 2 suggests a spalling oxide, whilst a PBR between 1 and 2 will usually be a protective oxide to the surface (137). The PBR was calculated for the different alloys and their respective oxides. Due to the complex nature of the alloy compositions, some assumptions and simplifications were required to give an appropriate calculation.

Equation 1: Pilling-Bedworth Ratio

$$R_{PB} = \frac{V_{oxide}}{V_{metal}} = \frac{M_{oxide} \times \rho_{metal}}{M_{metal} \times \rho_{oxide}}$$

Where V=molar volume, M=molecular mass and ρ=density.

As XRD analysis of the as cast alloys showed, the matrix was found to be Ni_2Fe, which has a density of 7.74g/cm^3. Calculating an experimental density of the Optim-Al alloy from the composition found using EDS spot identification is shown in Table 4.2.3-3. Taking into consideration the high carbon content readings, a pitfall of EDS analysis, it can be assumed that the calculated theoretical density of the Optim-Al matrix is congruent to the known density of Ni_2Fe of 7.74g/cm^3.

Table 4.2.3-3: Optim-Al matrix composition and theoretical density

Element	Atomic mass	weight %	density, ρ (g/cm^3)	weight % x density
C	12.011	7.25	2.26	16.385
Al	26.982	3.95	2.702	10.673
Si	28.085	0.54	2.33	1.258
Cr	51.996	27.39	7.19	196.934
Mn	54.938	0.76	7.43	5.647
Fe	55.845	19.69	7.874	155.039
Ni	58.963	40.11	8.9	356.979
Total				742.915
Theoretical Density				7.452 g/cm^3

Table 4.2.3-4: Densities of matrix and oxide compaounds

Compound	density, ρ (g/cm^3)
Ni_2Fe	7.74
Al_2O_3	3.987
Cr_2O_3	5.22

Using the atomic mass data in Table 4.2.3-3, the molecular mass of Ni_2Fe is calculated to be 173.231, whilst Al_2O_3 is 101.964 and Cr_2O_3 151.992. Therefore, the PBR for Al_2O_3 on the alloys is $PBR = \frac{101.964 \times 7.74}{173.231 \times 3.987} = 1.143$. This is clearly in the protective oxide range, demonstrating that the aluminium oxide layer produced on the alloy surface of Optim-Al should maintain adhesion without spalling, and will cover the alloy surface without fracture or porosity. The PBR for $Cr_2O_3 = \frac{151.992 \times 7.74}{173.231 \times 5.22} = 1.300$, similarly in the protective and adhered range. The higher PBR score for the chromium oxide shows a greater disparity in volume between the chromium oxide and the matrix, therefore this oxide is more likely to spall than the aluminium oxide; in line with previous observations.

4.2.3.4 Summary of adhesion of oxide layer

Spallation was found to centre around deep scratches or machining marks on the surface of the substrate. The smoother the surface, the greater the maintenance of the oxide layer appears to be.

The adhesion of the aluminium oxide layer to the alloy matrix was found to be significantly greater in all three aluminium containing alloys than the adhesion of the chromium oxide layer to the Base alloy.

4.2.4 Effect of oxidation conditions on oxidation behaviour

Air oxidation was shown to produce various oxide products in the different alloys, however pre-treatment with controlled oxygen levels and conditions may allow for different oxides to form on

the sample surfaces. Moreover, after installation of new pipes in a furnace, the protective oxide layer may then be formed in situ, therefore understanding the best conditions for this oxide development is paramount. The effect of vastly reducing the available oxygen for oxidation of the alloys is to allow the Low- and High-Al alloys to form aluminium oxide on their surfaces rather than the chromium oxide which has appeared to be dominant.

Furthermore, the alloys will likely undergo cycles of differing thermal events between service temperatures, cleaning temperatures and cool downs, which have a dramatic effect on the stability and life of the alloy and its oxide.

4.2.4.1 Effect of low partial pressure of oxygen on oxidation behaviour

Each element has a different limit of oxygen availability at a particular temperature for the oxide to form at equilibrium. Figure 4.2.4-1 shows the limits of oxygen partial pressures for chromium, aluminium, titanium, silicon and manganese at 800°C. This suggests that aluminium has a significantly lower oxygen presence dependency, in the order of $PO_2 = 10^{-45}$ (red line), whilst chromium is significantly higher at around $PO_2 = 10^{-27}$ (green line), and silicon sits between the two at around $PO_2 = 10^{-35}$ (purple line). Manganese showed a limit slightly below chromium, of the order of $PO_2 = 10^{-29}$ (yellow line). As titanium sits between aluminium and chromium (blue line), it was used to preferentially oxidize before chromium was able to, whilst allowing aluminium to continue to oxidize in the conditions.

To limit the formation of chromium containing oxides and therefore promote the aluminium or silicon oxide growth on the sample surfaces, all of the samples were oxidised with titanium upstream at $PO_2 = 10^{-25}$ and without titanium at $PO_2 = 10^{-23}$ for 24 hours at 800°C, very close to the oxygen limit of chromium oxide production, whilst still in the working temperature range of the alloys in service.

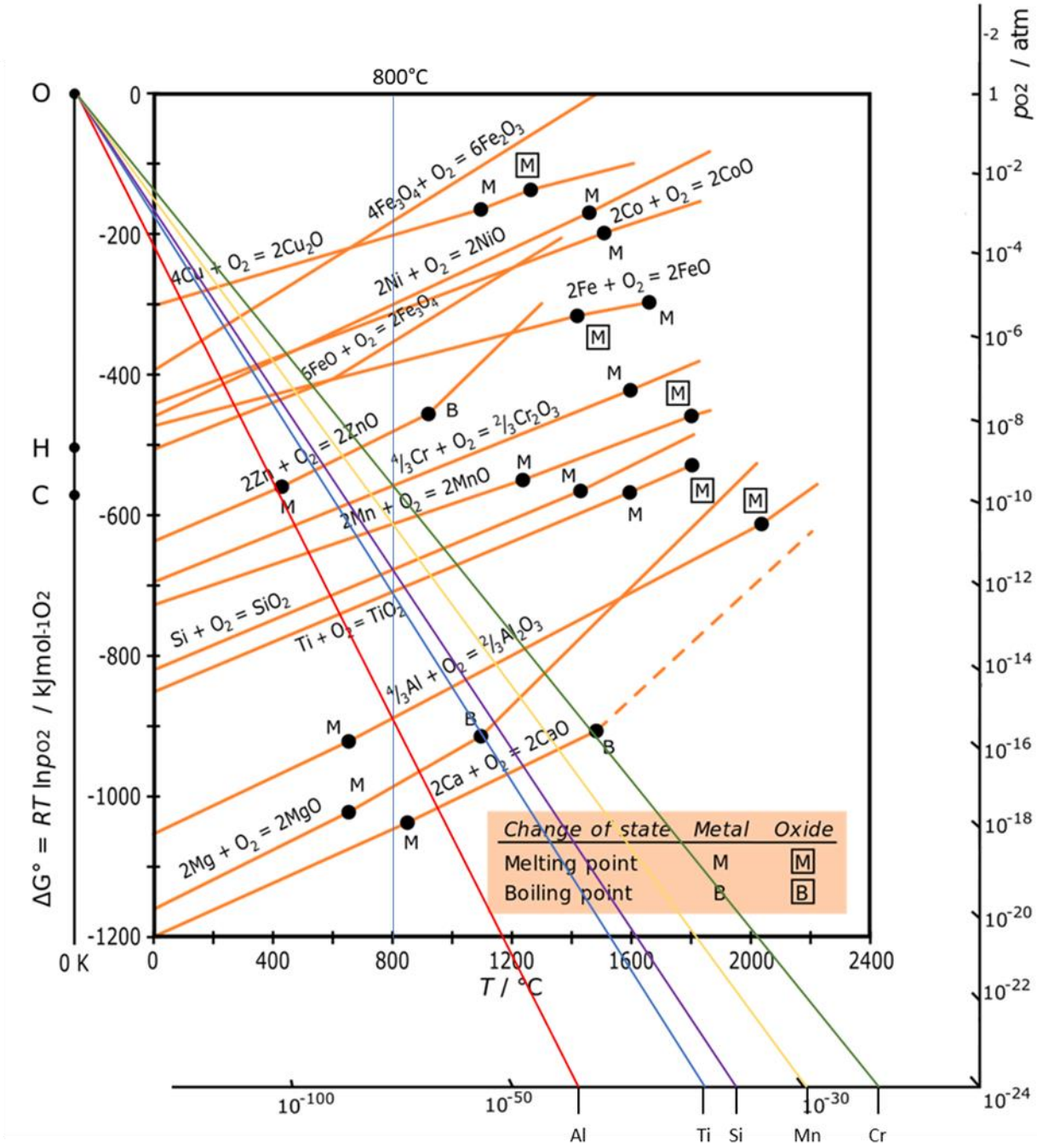

Figure 4.2.4-1: Ellingham diagram displaying the limits of partial pressures of oxygen required to oxidise chromium, aluminium, titanium, manganese and silicon at 800°C.

4.2.4.1.1 Base Alloy

4.2.4.1.1.1 Oxidation: $PO_2 = (10^{-25})$

The Base alloy appeared to have formed an oxide layer at this lowest partial pressure of oxygen, after treatment for 24 hours at 800°C, and the regions with a surface oxide formed an oxide layer

of a similar thickness to that seen after the same temperature and time oxidation in atmospheric pressure air, as seen in Figure 4.2.4-3. The chromium however was limited to mainly surface breaking carbides, whereas the oxide appears to be manganese heavy, with some presence of silicon and chromium. This suggests the oxide could either be the manganese chromite, common on the surface of the chromium oxide produced in air, or it could be a manganese oxide, produced preferentially due to the limited oxygen preventing the formation of chromium oxide.

As discussed previously, glow discharge optical emission spectroscopy (GDOES) allows the composition of a conductive material to be measured by plasma sputtering of the top layer of the material and recording the resultant photons. This allows the surface layer of the treated samples to be chemically analysed through the surface to the bulk alloy. GDOES was used to investigate the composition of the surface layers produced after the low partial pressure of oxygen oxidation treatments, as the composition measurements gave additional evidence in identifying the thin surface oxide composition alongside EDS analysis.

When examining the GDOES trace of the surface of the sample, shown in Figure 4.2.4-5, the manganese levels are clearly elevated on the sample surface, along with chromium and oxygen, before being taken over by mainly chromium and oxygen. This reinforces the evidence for manganese chromite or manganese oxide production on the very surface of the sample.

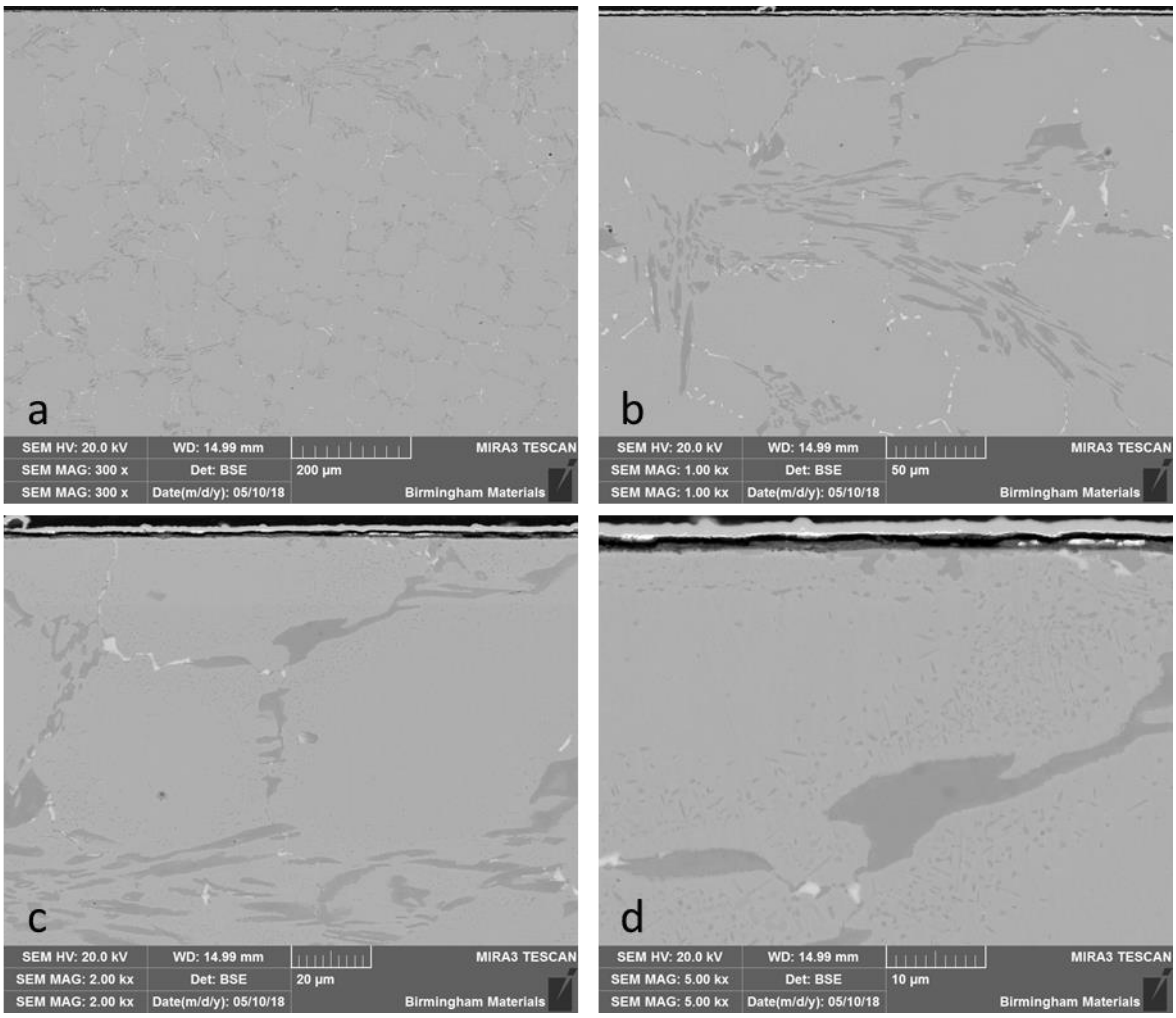

Figure 4.2.4-2: SEM images of Base alloy oxidised at $PO_2=10^{-25}$ with some discernible surface oxide present

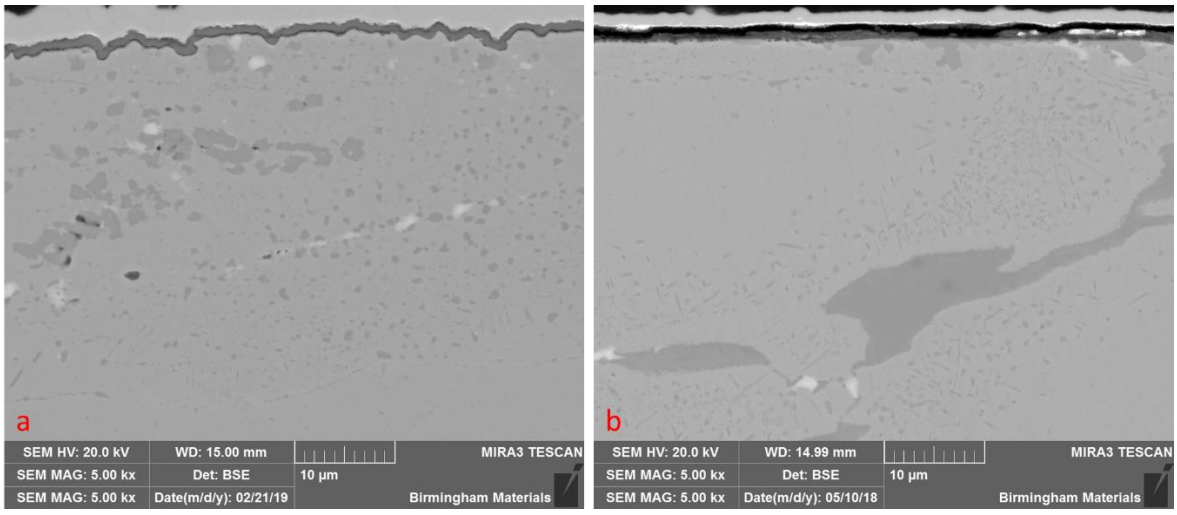

Figure 4.2.4-3: Comparison of Base alloy after; (a) air oxidation; (b) $PO_2=10^{-25}$ oxidation at 800°C for 24 hours showing similar growth rate but poorer surface coverage when oxidized at lower oxygen availability.

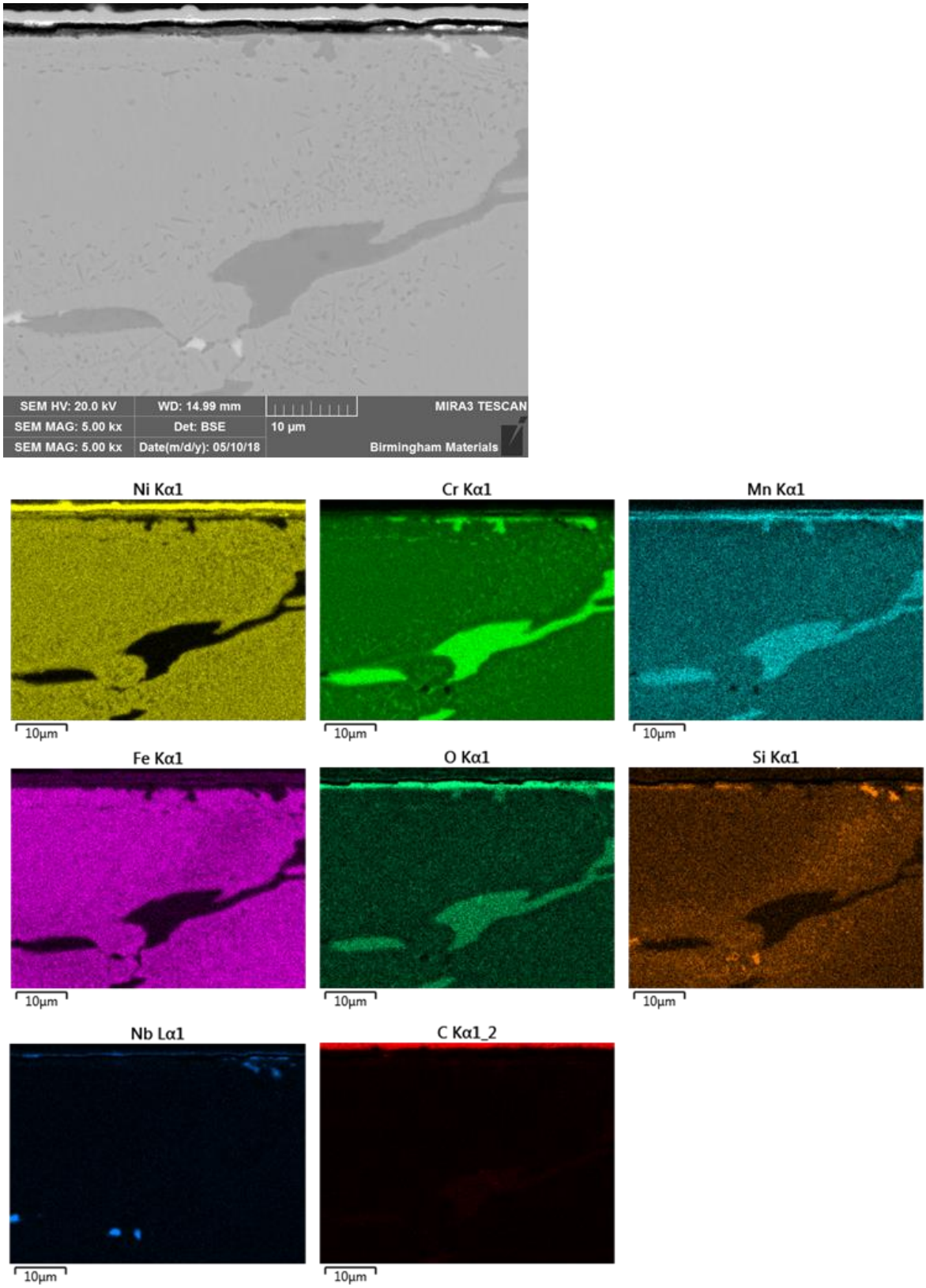

Figure 4.2.4-4: EDS Mapping of Base alloy oxidised at $PO_2=10^{-25}$ showing manganese rich surface oxide.

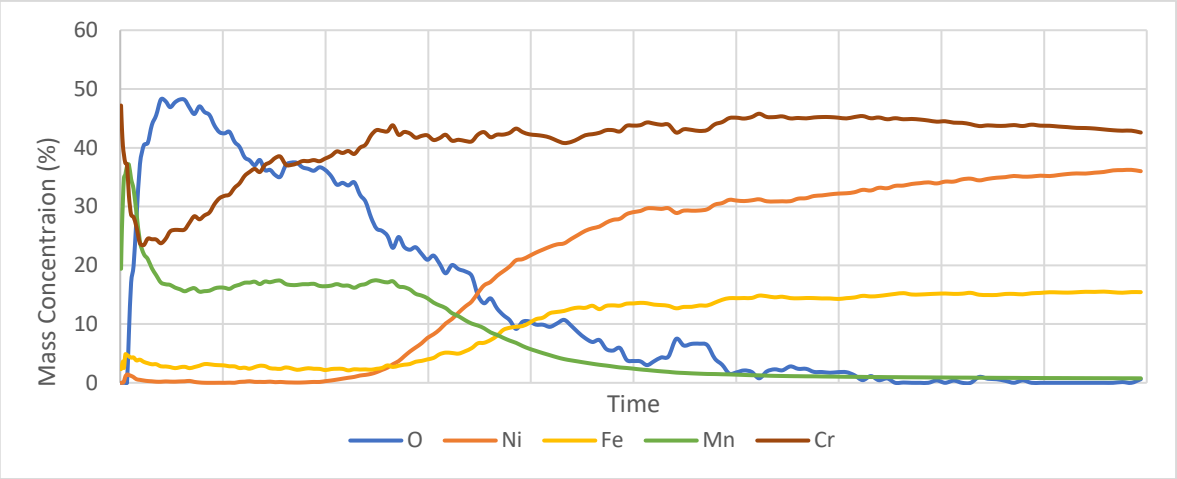

Figure 4.2.4-5: GDOES of inner surface of Base alloy oxidised at $PO_2 = 10^{-25}$ with heightened manganese content at the surface of the sample.

The matrix changed in a very similar way to that when oxidised in air, with the precipitation of fine chromium carbides around the edge of the grain. This was to be expected, as the thermal profile of the heat treatment had not been altered, only the atmospheric environment, therefore only the surface reactions would be expected to differ.

4.2.4.1.1.2 Oxidation: $PO_2 = (10^{-23})$

The raised oxygen content increased the possibility of chromium oxidation occurring compared to the conditions in the previous oxidation. The SEM images showed a surface oxide layer was produced, once again a similar thickness to that produced after the same time and temperature oxidation in air (Figure 4.2.4-7). The EDS mapping scans in Figure 4.2.4-8 confirmed the presence of an oxide layer. The mappings show primarily chromium and manganese present, with evidence suggesting that nickel and iron were also oxidised at the surface.

These results demonstrated that lower oxygen availability can reduce the formation of certain oxides and promote others. However, in this alloy, the presence of nickel and iron on the surface indicated that this alloy did not benefit from low oxygen oxidation by forming a more beneficial oxide for coking protection. This was to be expected with no aluminium in this alloy, as the low

oxygen availability would be beneficial in promoting the growth of aluminium oxide on the sample surface.

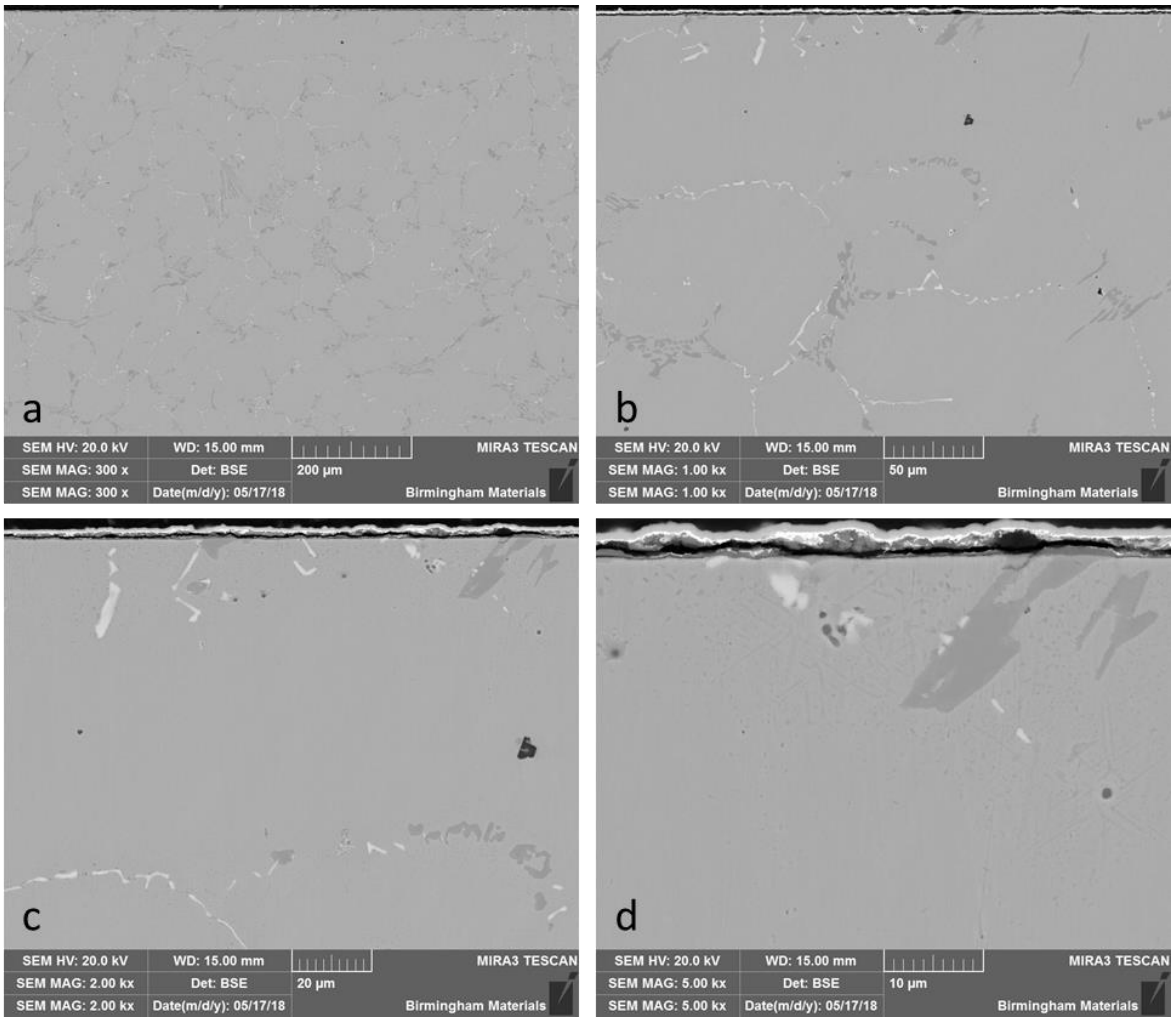

Figure 4.2.4-6: SEM images of Base Alloy oxidised at $PO_2 = 10^{-23}$

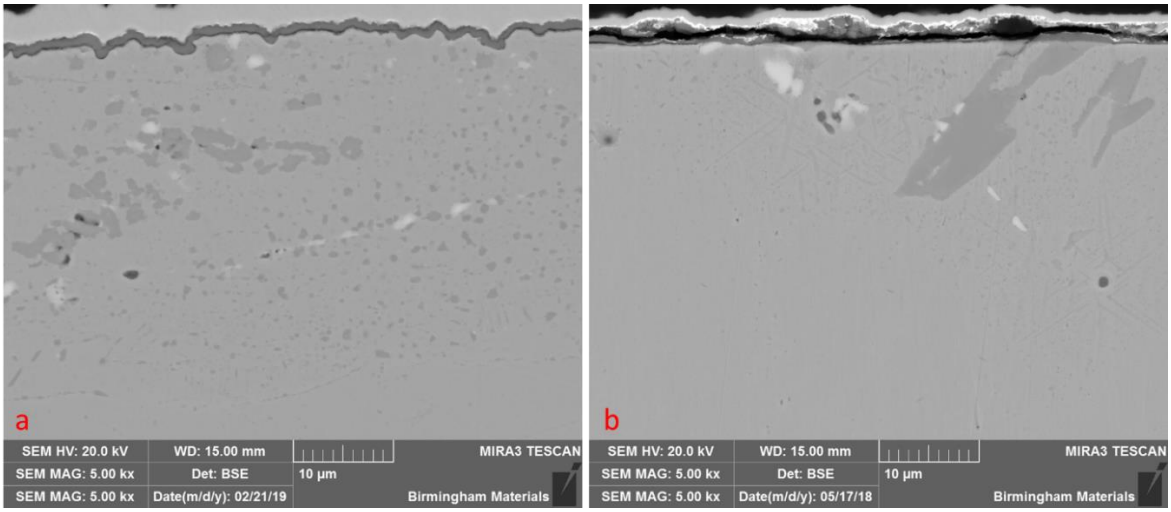

Figure 4.2.4-7:Comparison of Base alloy after; (a) air oxidation; (b) $PO_2=10^{-23}$ oxidation at 800°C for 24 hours

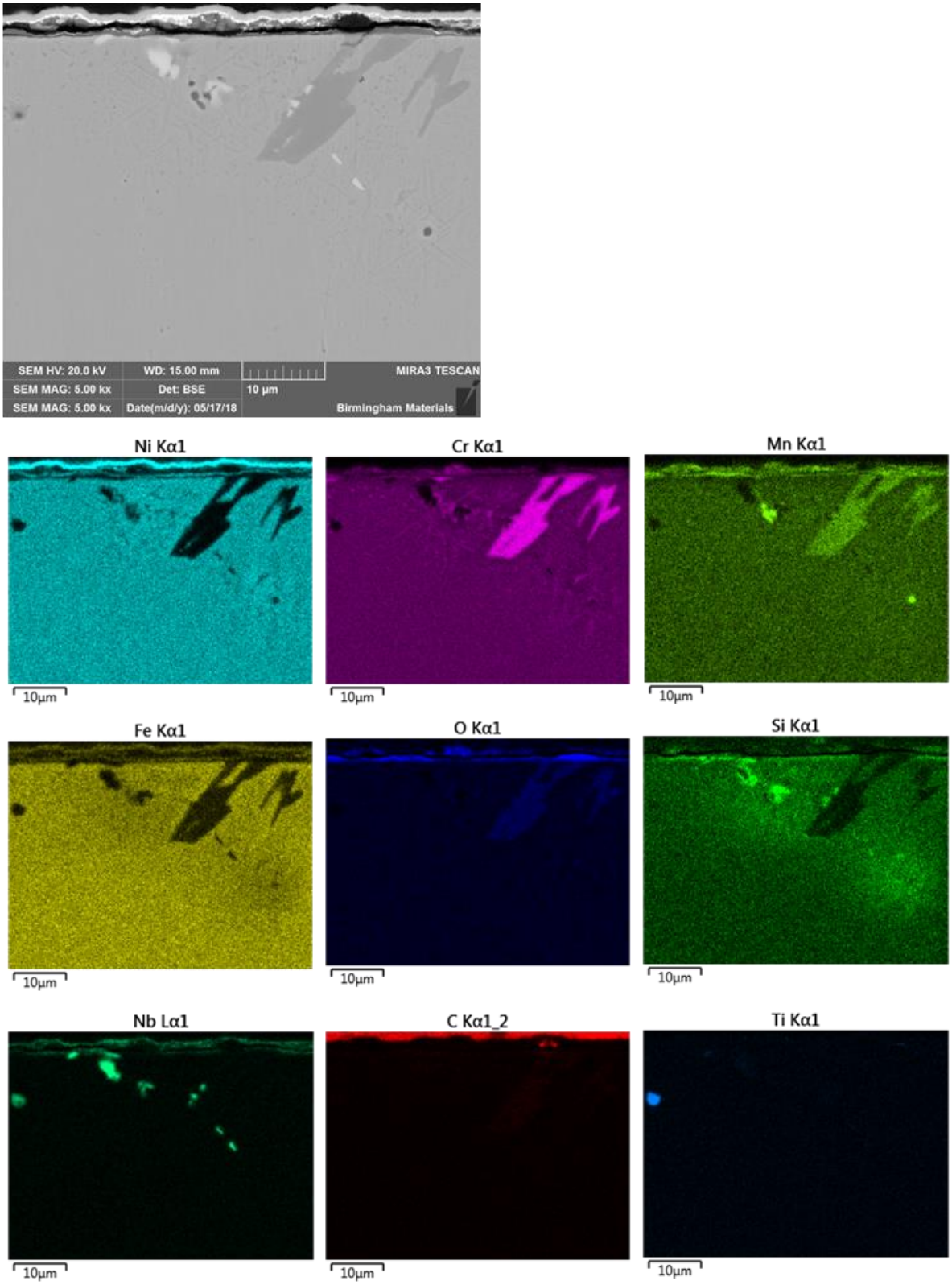

Figure 4.2.4-8: EDS Mapping of Base alloy oxidised at $PO_2=10^{-23}$

4.2.4.1.2 Low-Al Alloy

4.2.4.1.2.1 Oxidation: $PO_2 = (10^{-25})$

The aluminium containing alloys were expected to produce more beneficial results from low PO_2 oxidation conditions than those of the Base alloy, with the oxygen availability well above the limit for aluminium oxidation, as displayed in Figure 4.2.4-1. The images of the Low-Al alloy (Figure 4.2.4-9) showed an oxide across the surface of the alloy, beneath the nickel coating layer that was added after oxidation.

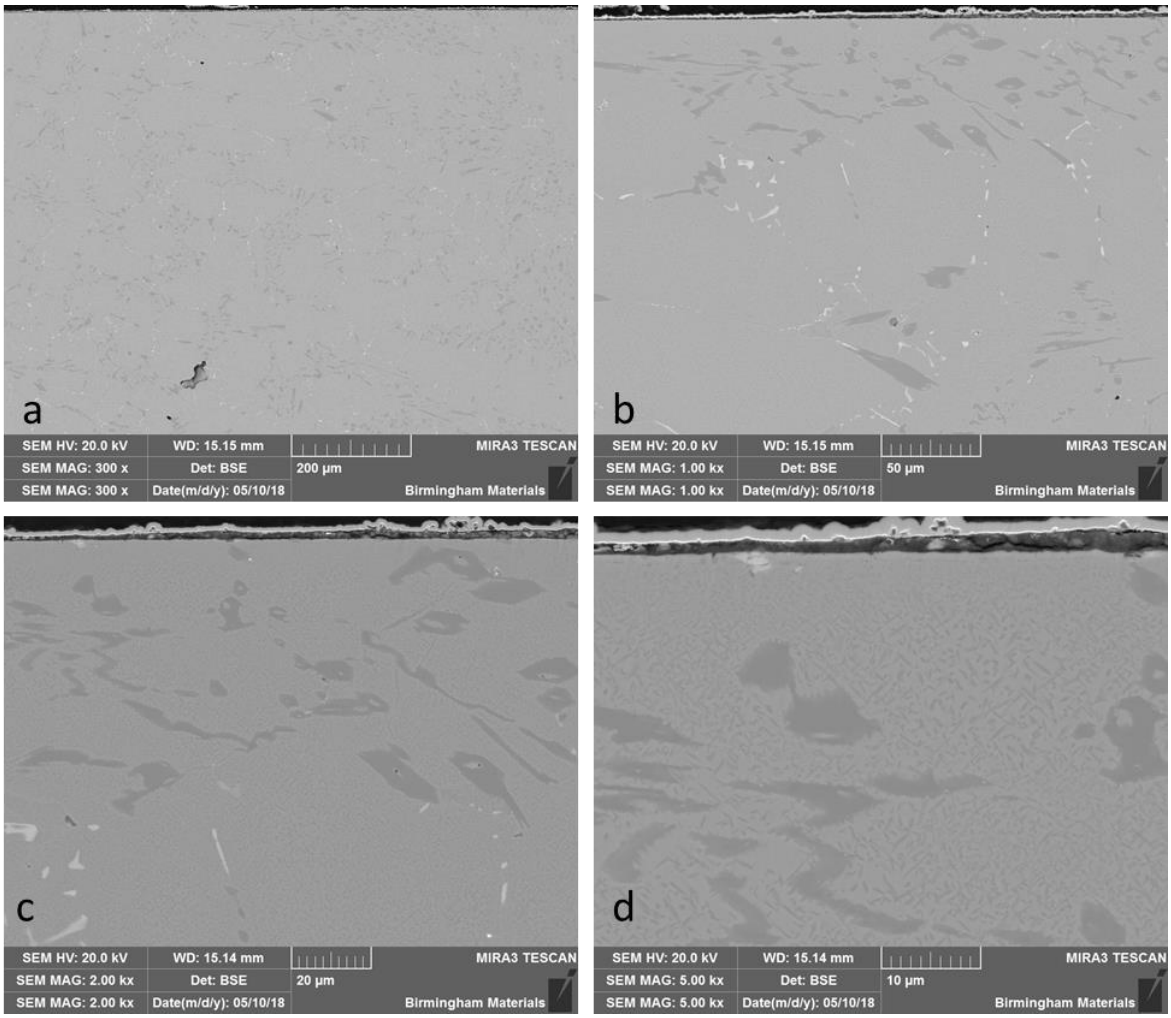

Figure 4.2.4-9: SEM images of Low-Al alloy oxidised at $PO_2 = 10^{-25}$

EDS mapping confirmed the oxide presence across the surface of this alloy, with aluminium being the clear oxide former compared to the other elements present, with some patches of a manganese

rich oxide atop the aluminium oxide. This was probably either a manganese chromite or manganese oxide, as seen on the Base alloy. This showed a major improvement compared to the same alloy oxidised at the same time and temperature in air, where the alloy formed surface chromium oxide in some regions. The oxide layer did not fully encapsulate the surface after air oxidation, however it was able to with low oxygen oxidation, as evident in Figure 4.2.4-9. Furthermore, the aluminium oxide was formed on the alloy surface, rather than as an internal oxidation product which agglomerates over the oxidation period, as was observed to occur after the air oxidation.

Figure 4.2.4-11 shows the GDOES results on the surface of the alloy, displaying a rise in aluminium and oxygen at the surface, along with a rising peak of chromium. The chromium appears present at the surface due to the patchy oxide layer and some variation occurring due to differing sputtering rates and oxide thicknesses on the sample surface.

The concern highlighted by these results was the apparent fracturing of the aluminium oxide along its length in some regions, as highlighted in Figure 4.2.4-10. The oxide had not fractured at the oxide-matrix interface, which is positive for the interfacial bonding, however the fracture is a concern for the maintenance of an oxide across the surface. This fracture was probably caused in the cooling stage of the treatment, with internal stresses reaching breaking point with the thermal contraction on cool down.

As with the Base alloy, the matrix changes were in line with those seen in the air oxidation treatments of the alloy.

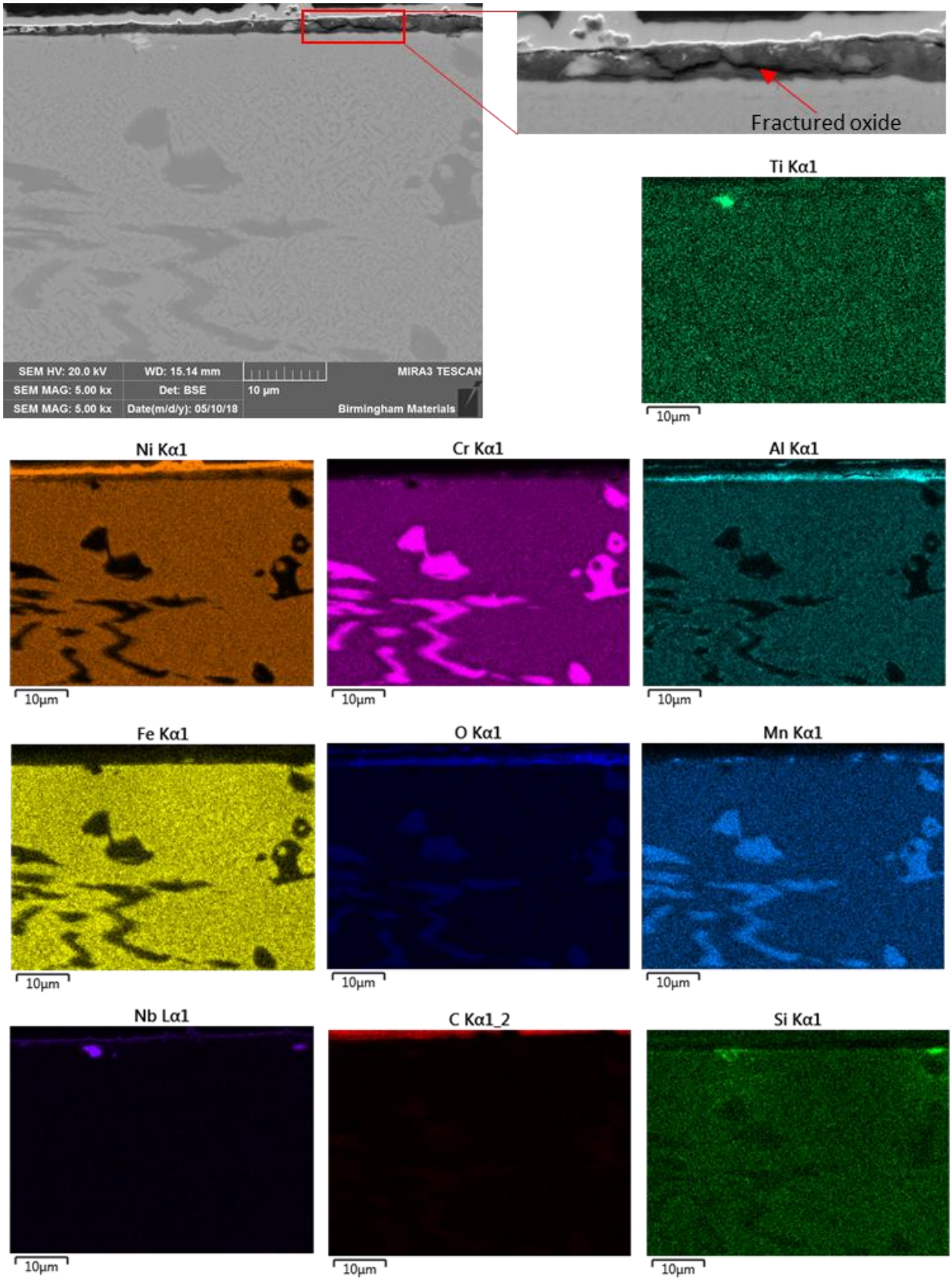

Figure 4.2.4-10: EDS Mapping of Low-Al alloy after oxidation at $PO_2 = 10^{-25}$ showing fracture in the oxide layer.

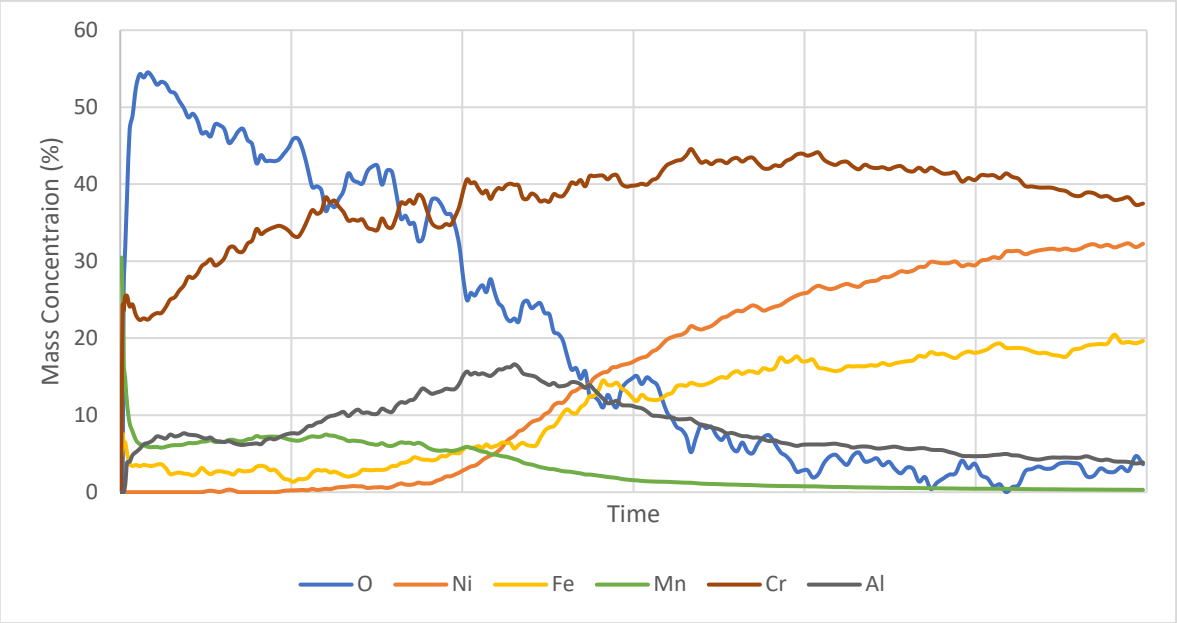

Figure 4.2.4-11:GDOES of inner surface of Low-Al alloy oxidised at PO2 = 10-25

4.2.4.1.2.2 Oxidation: $PO_2 = (10^{-23})$

The lower oxygen availability compared to air didn't allow for the influx of oxygen into the Low-Al alloy, therefore the oxide cannot form around or over features on the alloy surface, as was seen in air oxidation in the Optim-Al alloy. However, the surface was mainly covered by an aluminium oxide, as shown by the EDS mapping in Figure 4.2.4-13. The increased oxygen availability compared to the previous test due to the lack of titanium as an oxygen scavenger allows surface chromium carbides to supply the necessary chromium for chromium oxide to form on the surface in these regions, breaking up the continuous aluminium oxide seen in the lower oxygen oxidation treatment. Whilst there appeared to be oxide present across the surface of the alloy (which was not the case when oxidised in an air environment) the increase in oxygen availability led to a less consistent surface, with aluminium oxide no longer the sole barrier to the external environment.

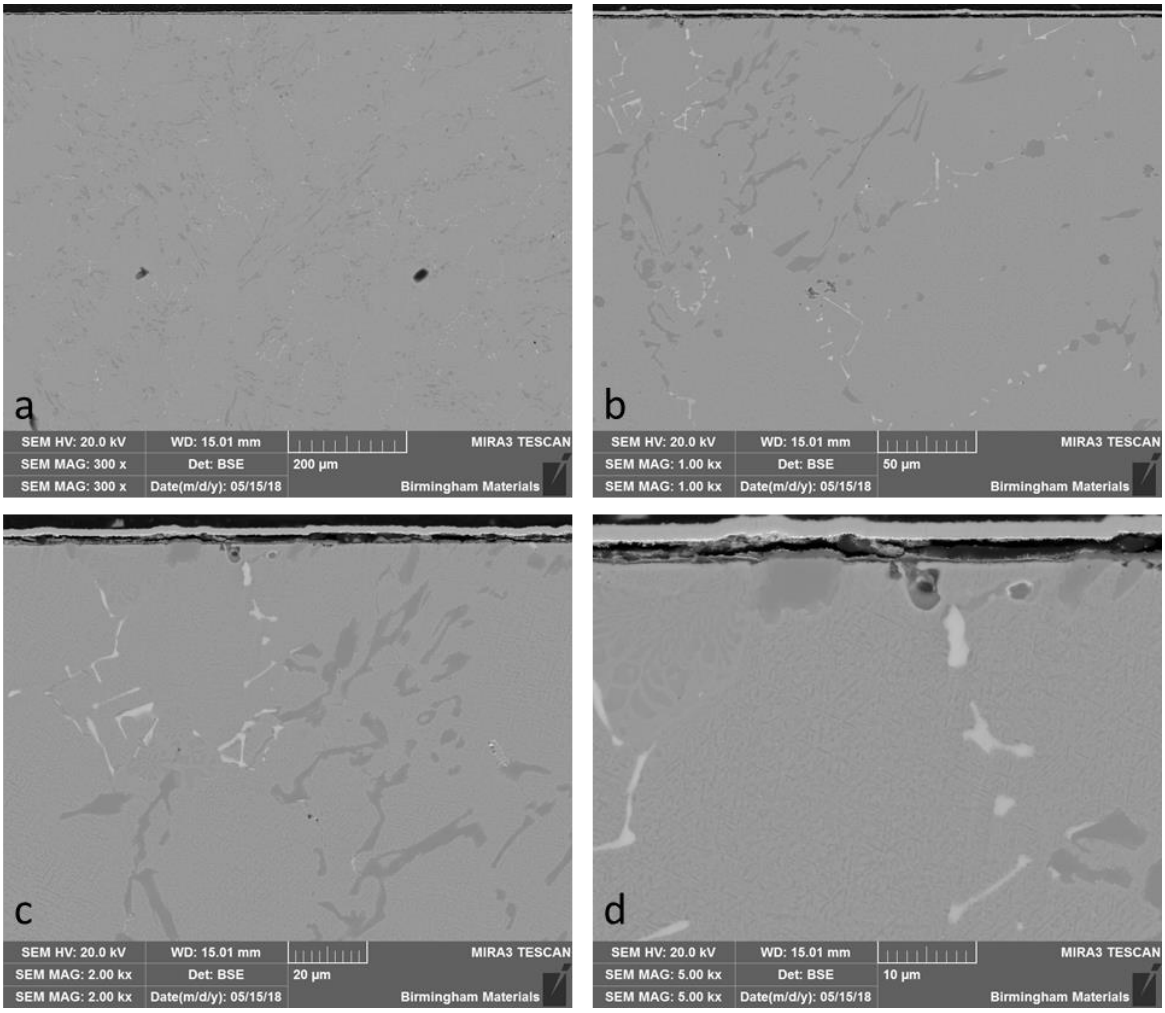

Figure 4.2.4-12: SEM images of Low-Al alloy oxidised at $PO_2 = 10^{-23}$

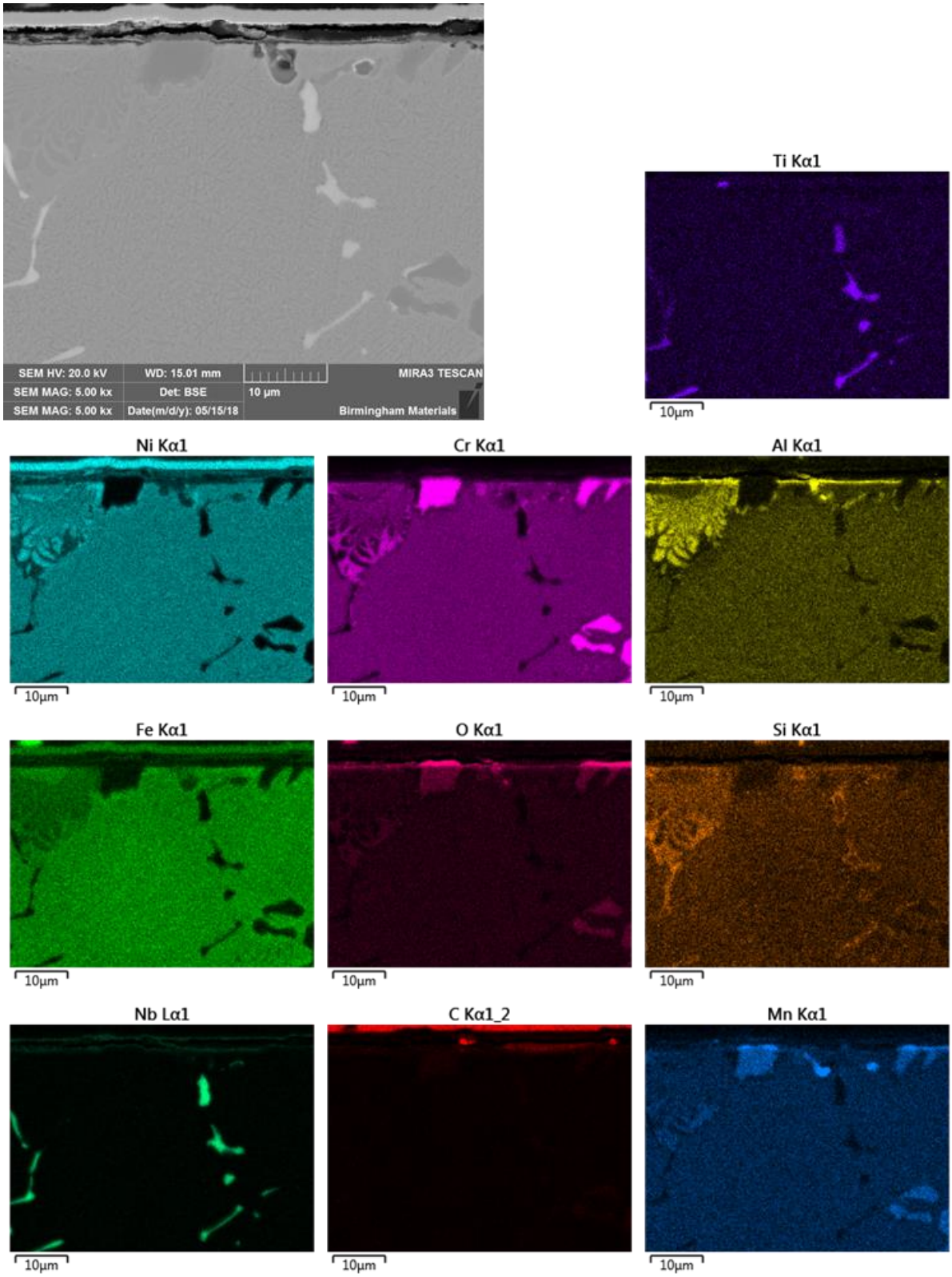

Figure 4.2.4-13: EDS mapping of Low-Al alloy oxidised at $PO_2 = 10^{-23}$ Identifying surface aluminium oxide layer.

4.2.4.1.3 High-Al Alloy

4.2.4.1.3.1 Oxidation: $PO_2 = (10^{-25})$

The higher aluminium content in this alloy should facilitate the growth of a surface aluminium oxide more readily than the Low-Al alloy, as it contains a higher percentage of aluminium both in the cast material, and available in the matrix (Figure 4.1.1-6), despite the widespread formation of the nickel and aluminium rich phase.

Figure 4.2.4-14 showed an oxide layer across the sample's surface, which didn't grow beneath the chromium oxide as in the samples oxidised in air, but instead grew alone. Figure 4.2.4-15 confirmed the oxide to be aluminium rich, absent of the surface chromium oxide, and only a small region showing a second oxide product, which, like the Low-Al alloy, appeared to be manganese rich; either manganese chromite or a manganese oxide. As demonstrated in Figure 4.2.4-1, manganese is able to oxidize at lower oxygen partial pressures when compared to chromium.

The GDOES trace in Figure 4.2.4-16 showed a significantly higher aluminium content at the surface of the alloy compared to the Low-Al alloy, and no peak in chromium in the near surface area. This suggested a thicker and more widespread aluminium oxide layer across the surface compared to the Low-Al alloy.

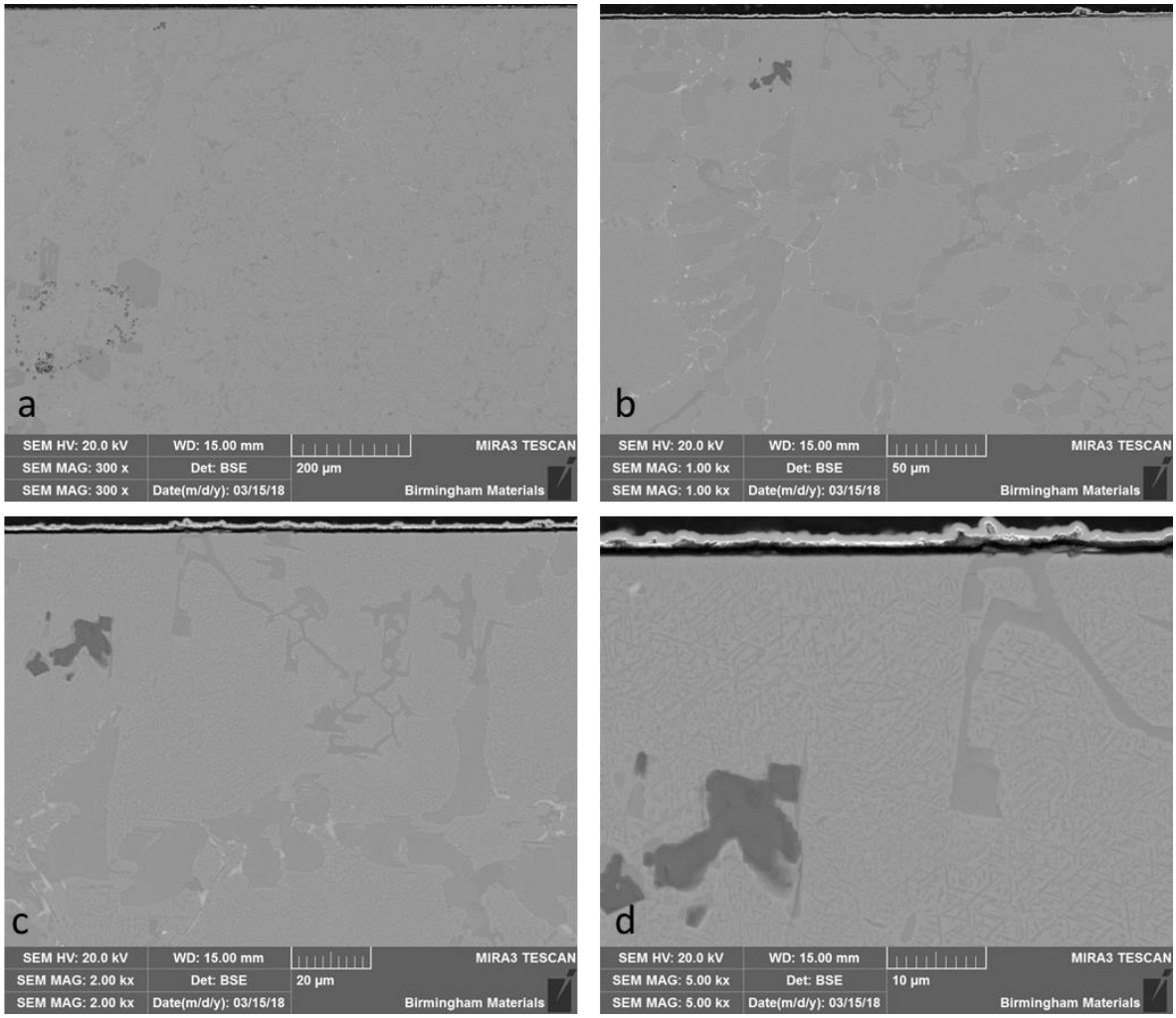

Figure 4.2.4-14: SEM images of High-Al alloy oxidised at $PO_2 = 10^{-25}$

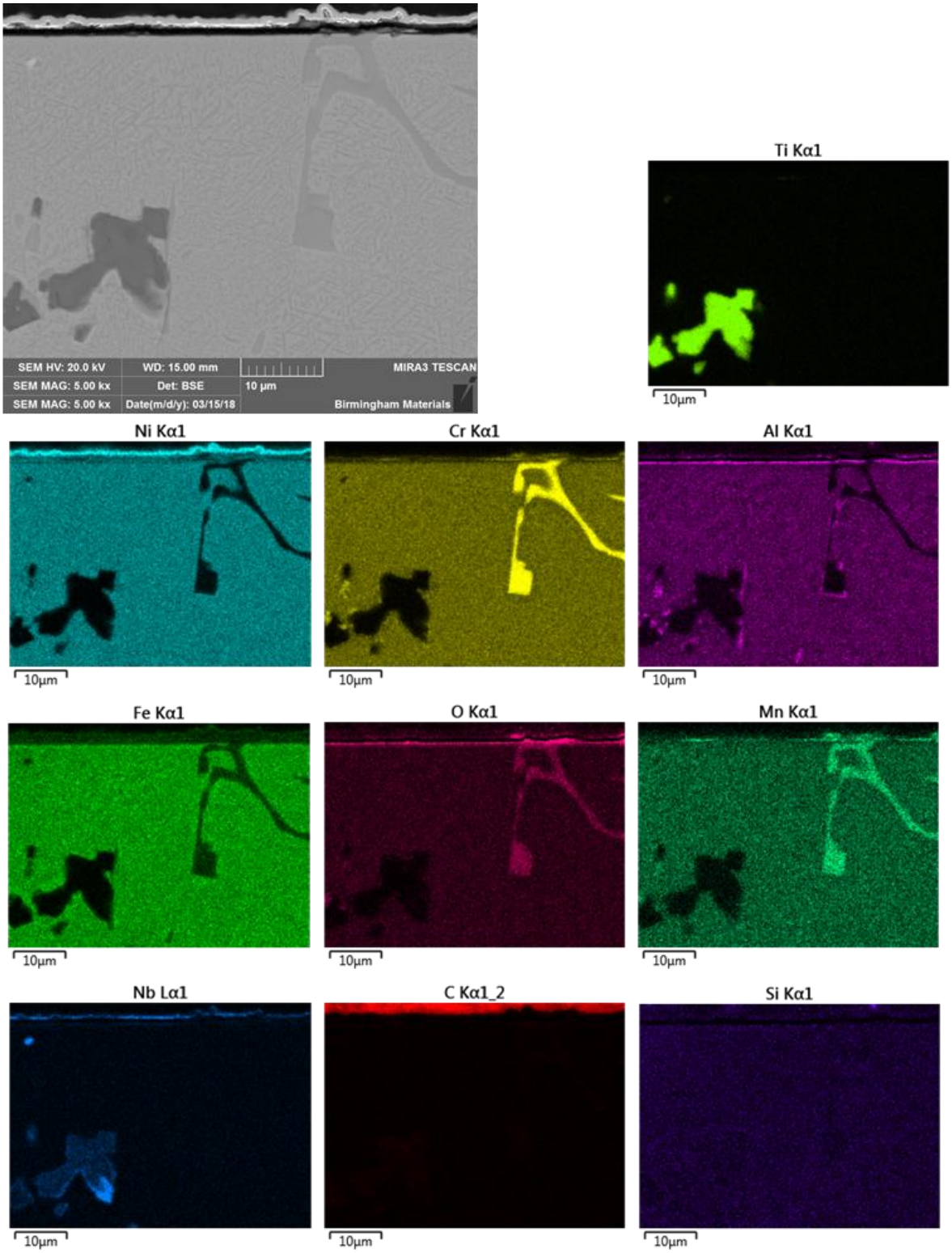

Figure 4.2.4-15: EDS mapping of High-Al alloy oxidised at $PO_2 = 10^{-25}$ indicating growth of a thin aluminium oxide across the surface of the sample.

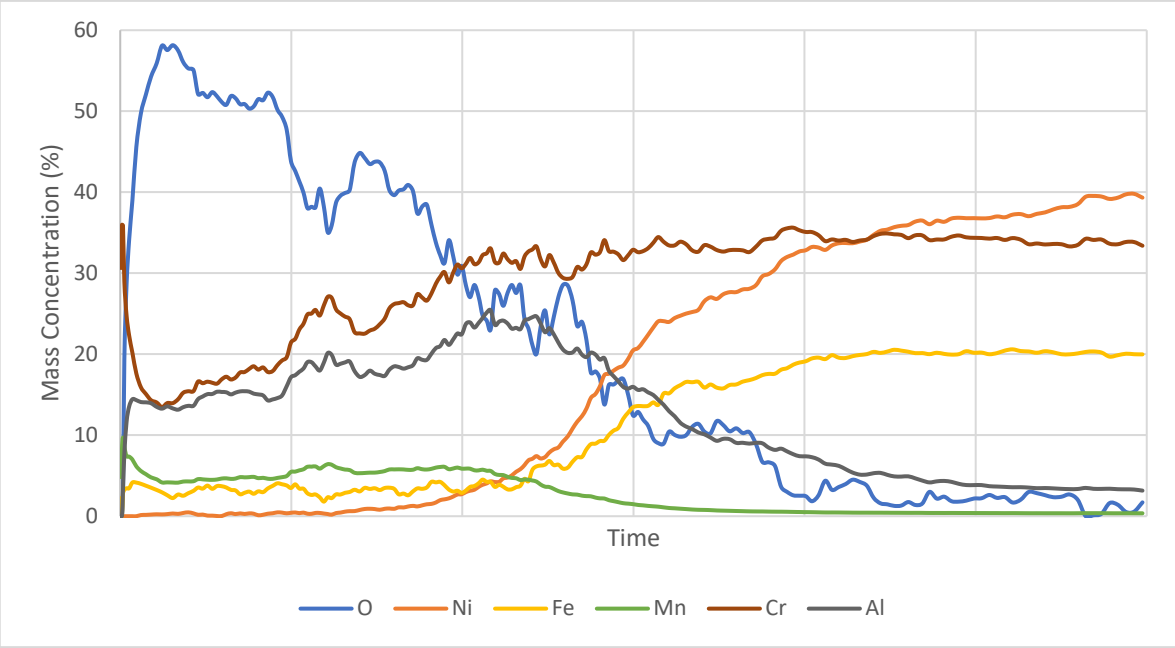

Figure 4.2.4-16: GDOES of inner surface of High-Al alloy oxidised at $PO_2 = 10^{-25}$

4.2.4.1.3.2 Oxidation: $PO_2 = (10^{-23})$

Greater oxygen availability in this treatment increased the ability of chromium to oxidise on the sample surface. That was observed to occur in the regions where the matrix material was exposed on the surface. Whilst an aluminium oxide was present on the surface where there was a surface-breaking nickel and aluminium rich phase and the surrounding region, areas of exposed matrix allowed the formation of a chromium rich oxide on the surface as seen in Figure 4.2.4-18.

Whilst aluminium oxide was present across the surface of the alloy after oxidation at lower oxygen levels, the raise in oxygen availability allowed the chromium to oxidise.

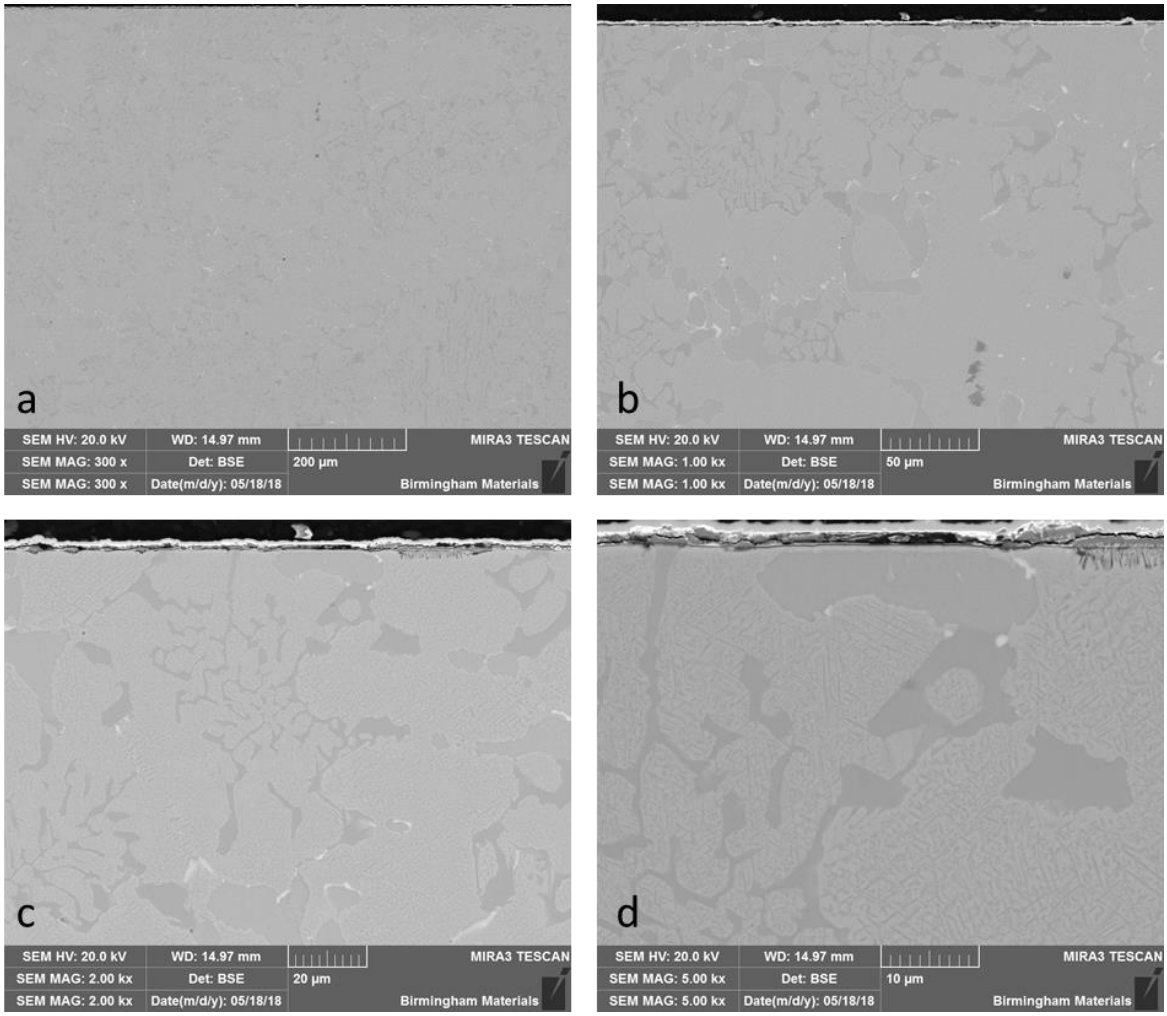

Figure 4.2.4-17: SEM images of High-Al alloy oxidised at $PO_2 = 10^{-23}$

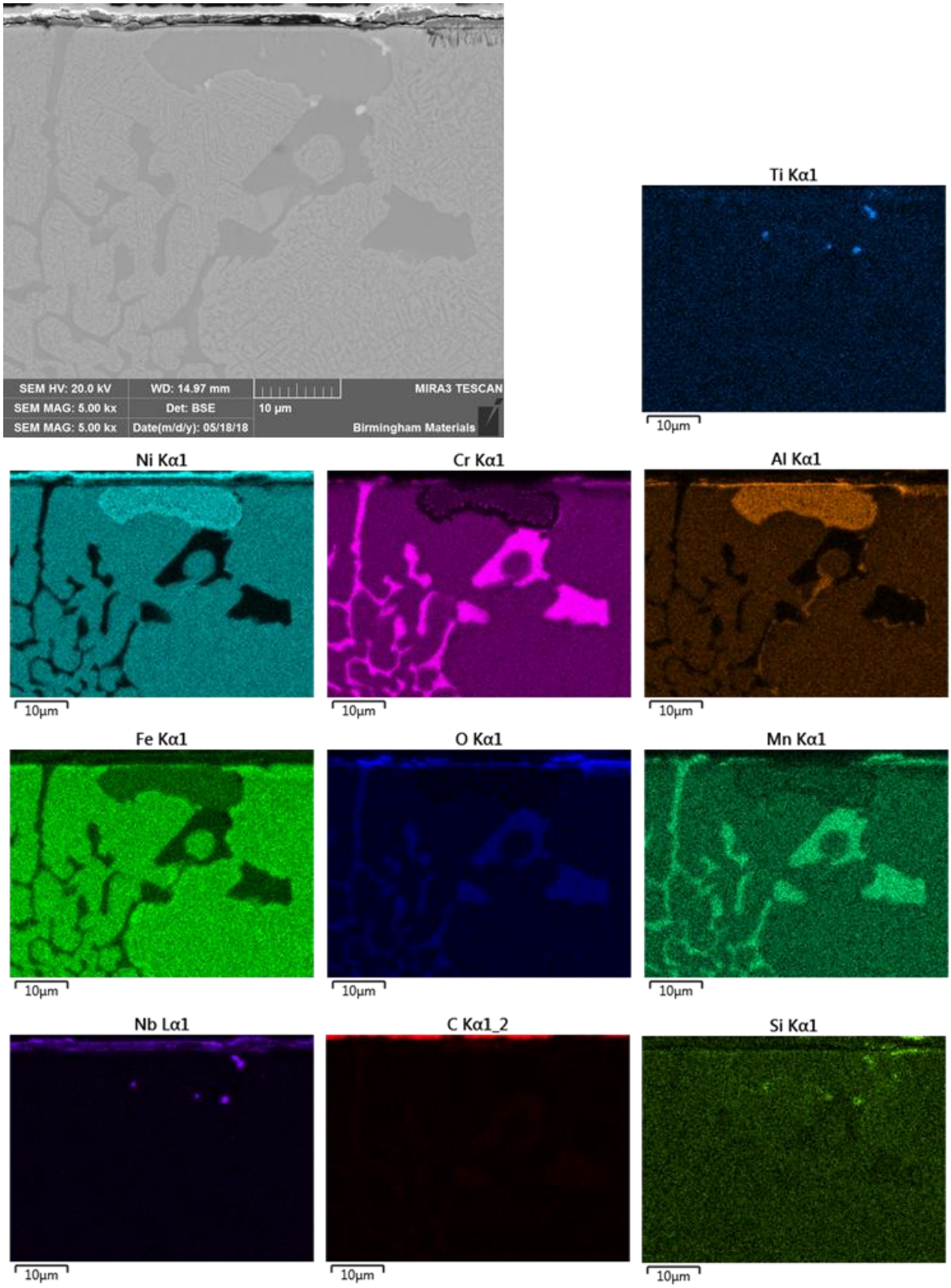

Figure 4.2.4-18: EDS mapping of High-Al alloy after oxidation at $PO_2 = 10^{-23}$ showing mixed surface oxide products.

4.2.4.1.4 Optim-Al Alloy

4.2.4.1.4.1 Oxidation: $PO_2 = (10^{-25})$

The Optim-Al alloy showed formation of an aluminium oxide across the sample surface, as expected when referring to the Ellingham diagram in Figure 4.2.4-1, and there appeared to be precipitation of chromium carbides beneath the surface of the alloy. The carbide morphology was the main difference observed between the air oxidation and low partial pressure of oxygen oxidation samples, as compared in Figure 4.2.4-20. There was a clear difference between the carbides formed immediately beneath the oxide at the surface of the alloy and those found deeper in the alloy. In the bulk of the alloy, the acicular carbides, which were observed regularly in other oxidation treatments, are evident. These acicular, needle-like carbides are characteristic of the Cr_7C_3 phase, as discussed previously, whilst the near surface carbides appear to be of the $Cr_{23}C_6$ phase.

The formation of this near surface carbide was also seen in the Optim-Al alloy when oxidised in air with the same time and temperature, however it did not noticeably occur in other states. It is hypothesized this was a result of degradation of the near surface carbides from the Cr_7C_3 form to the $C_{23}C_6$ form as a result of the aging.

The GDOES trace shows the aluminium presence on the surface to be significantly higher than the other two aluminium containing alloys, with manganese and chromium both lower. This demonstrates the continuous nature of the aluminium oxide layer on the Optim-Al alloy compared to the others, giving further evidence of the improved coverage of the oxide layer.

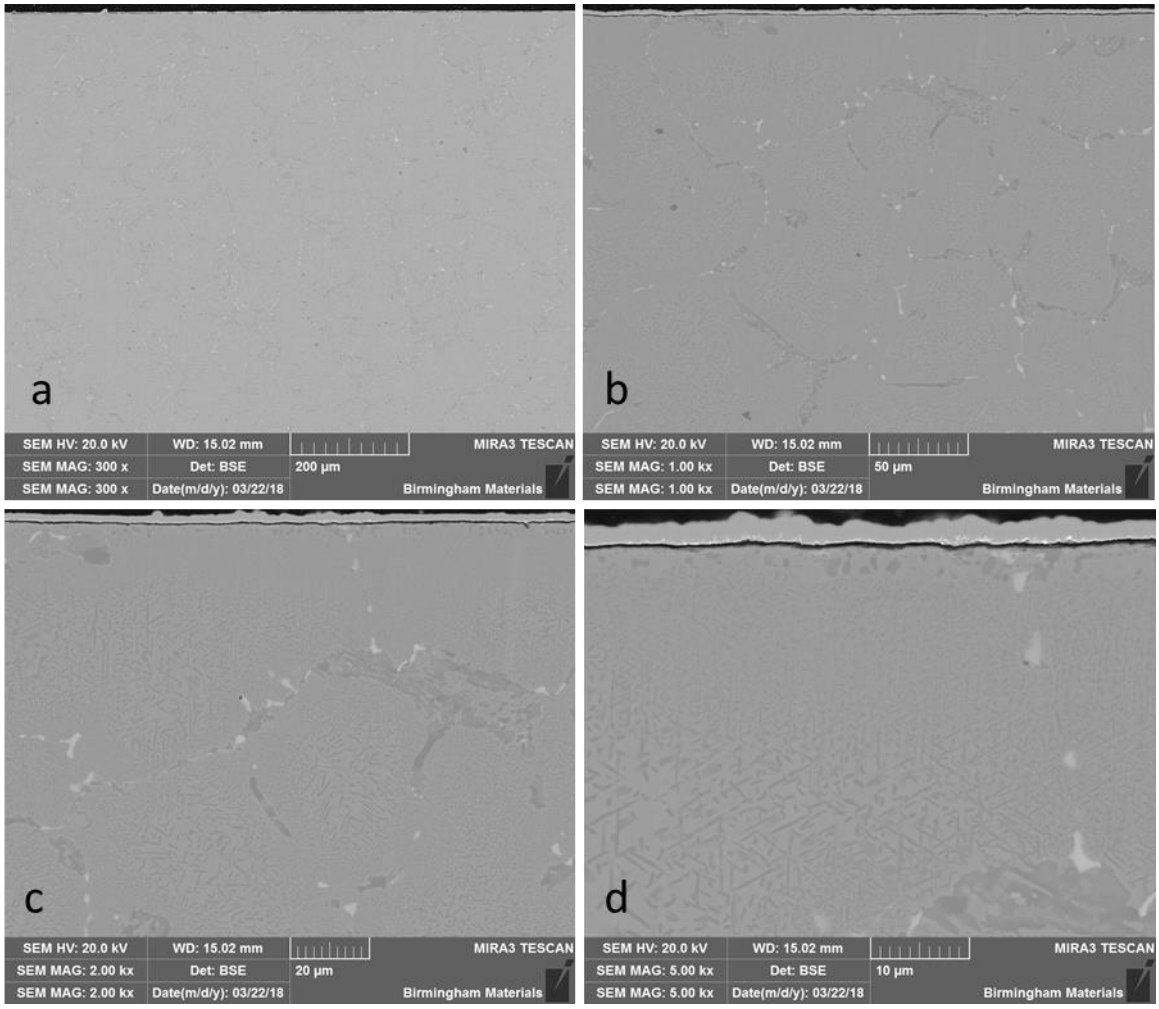

Figure 4.2.4-19:SEM images of Optim-Al alloy after oxidation at $PO_2 = 10^{-25}$with apparent continuous surface oxide.

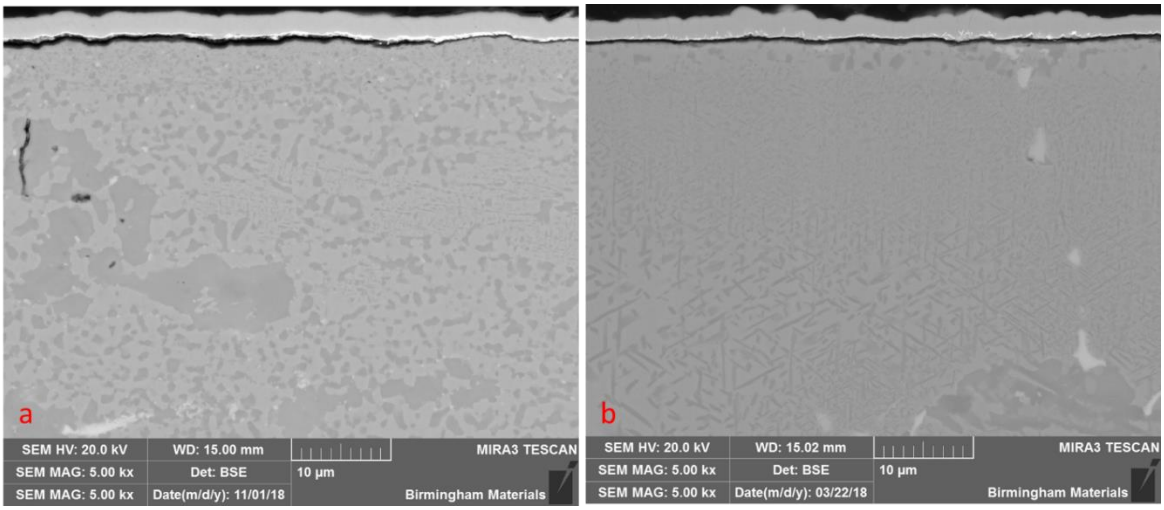

Figure 4.2.4-20: Comparison of Optim-Al alloy after; (a) air oxidation; (b) $PO_2=10^{-25}$ oxidation at 800°C for 24 hours demonstrating similar microstructure changes in the ner surface matrix.

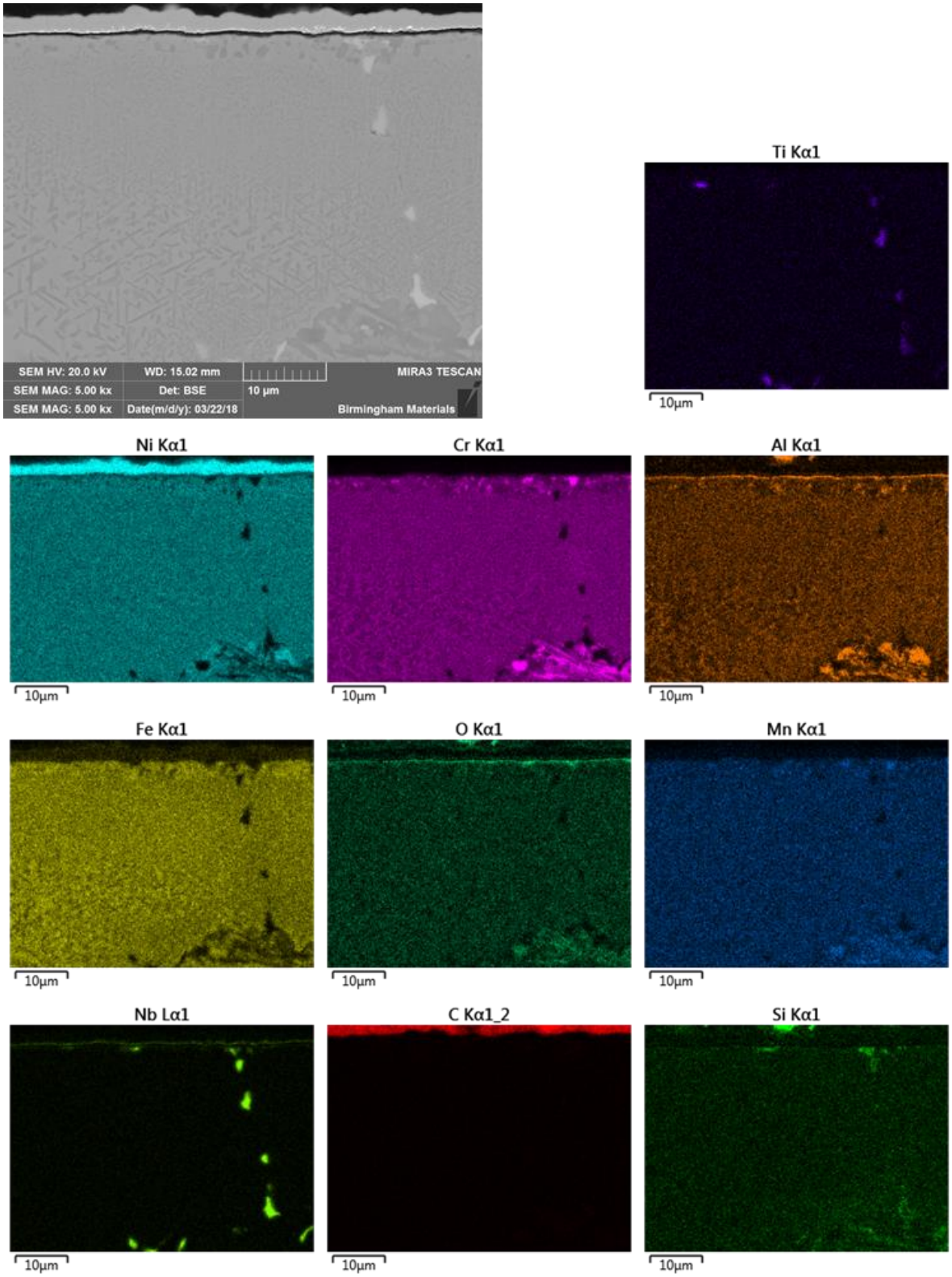

Figure 4.2.4-21: EDS Mapping of Optim-Al alloy after oxidation at $PO_2 = 10^{-25}$ with thin aluminium rich surface oxide layer present.

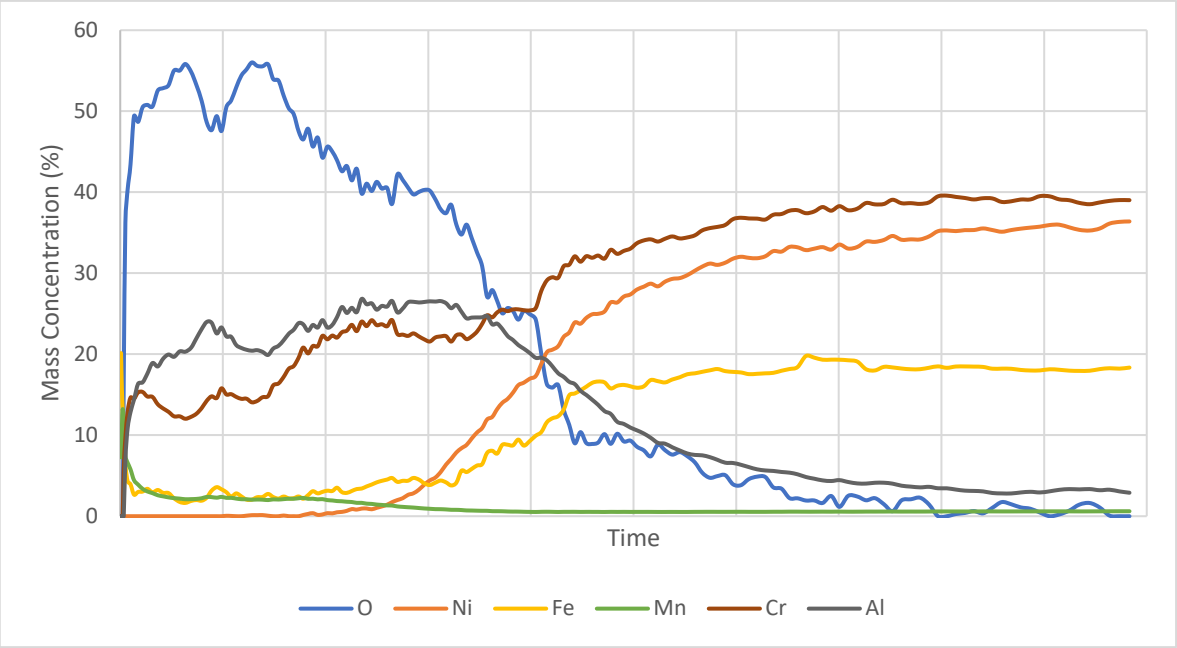

Figure 4.2.4-22: GDOES of inner surface of Optim-Al alloy oxidised at PO2 = 10-25

4.2.4.1.4.2 Oxidation: $PO_2 = (10^{-23})$

The increase in oxygen availability allowed the formation of chromium oxide on the surface of the other alloys. However, the Optim-Al alloy maintained its surface aluminium oxide, with no evidence suggesting any competing oxide growth in this low oxygen availability oxidation treatment.

Similar to the previous sample oxidised at $PO_2=10^{-25}$, the most noticeable difference between the alloy oxidised in air and that in the low partial pressure of oxygen was the nature of the secondary carbide precipitation (Figure 4.2.4-24).

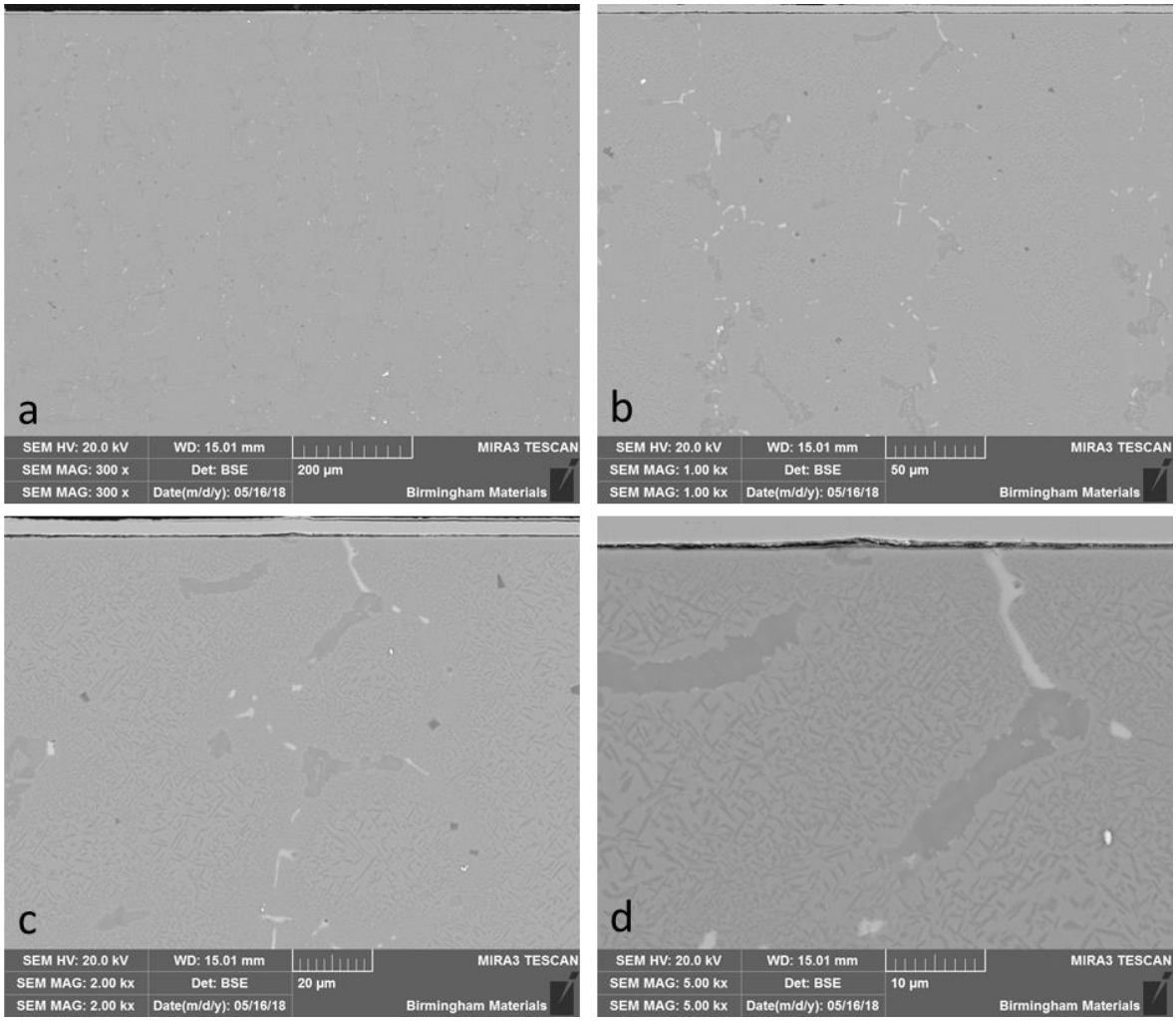

Figure 4.2.4-23: SEM images of Optim-Al alloy after oxidation at $PO_2 = 10^{-23}$

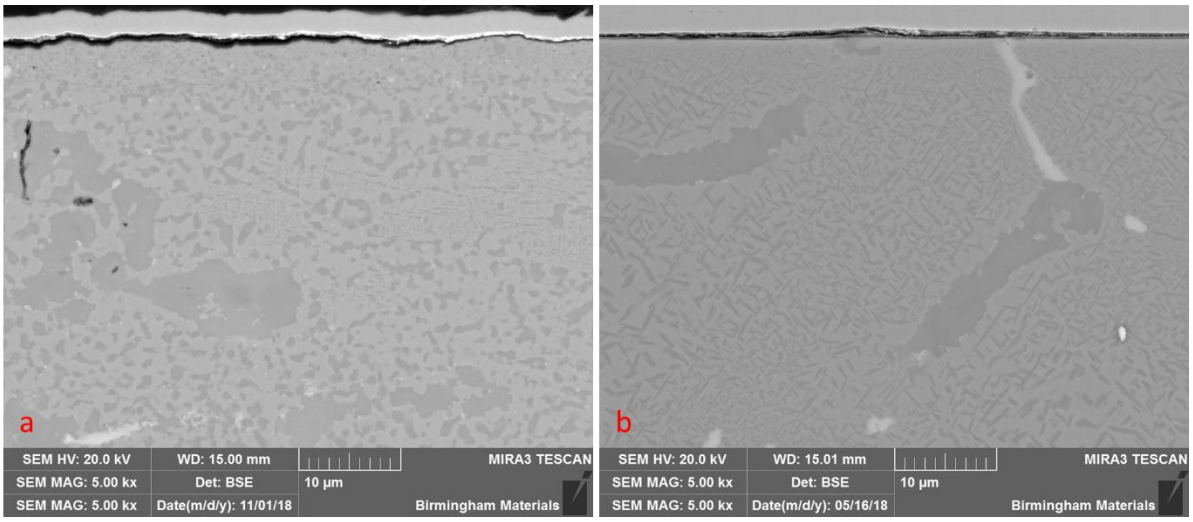

Figure 4.2.4-24: Comparison of Optim-Al alloy after; (a) air oxidation; (b) $PO_2=10^{-23}$ oxidation at 800°C for 24 hours

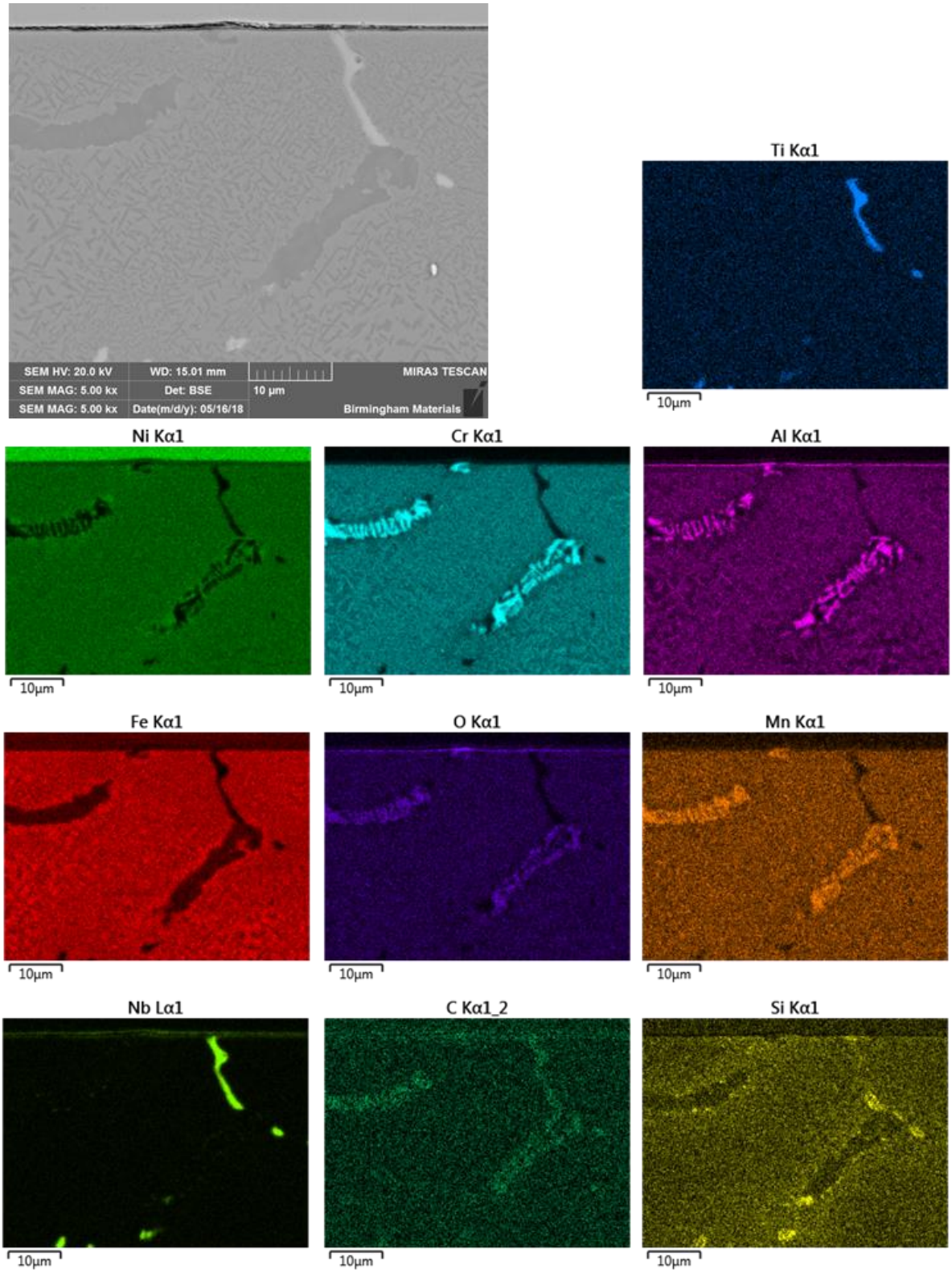

Figure 4.2.4-25: EDS elemental mapping of Optim-Al alloy after oxidation at $PO_2 = 10^{-23}$ with surface aluminium oxide layer.

4.2.4.2 Cyclic Oxidation

The Optim-Al alloy was consistently shown to be the most protective of the alloys with regards to the production and maintenance of a surface oxide layer acting as a barrier between the matrix and the reactive gas stream in service. To this point only single oxidation treatments had been evaluated, therefore cyclic oxidation treatment was undertaken on the Optim-Al alloy, to allow further assessment of the formation and adherence of the oxide layer to the sample surface. The inner diameter of the machined sample was analysed, allowing the results to be representative of the alloy in service.

The sample was pre-oxidised at 875°C for 48 hours at $PO_2 = 10^{-27}$, before cyclic oxidation between 1150°C ad 25°C for 45 minutes and 25°C for 15 minutes, for 50 cycles (see Figure 4.2.4-26). This treatment was highly stressful on the alloy, vastly exceeding the recommended maximum cooling rates in service of 100°C/hour, therefore some damage to the bulk material was possible, however this was necessary to facilitate the desired extreme testing conditions.

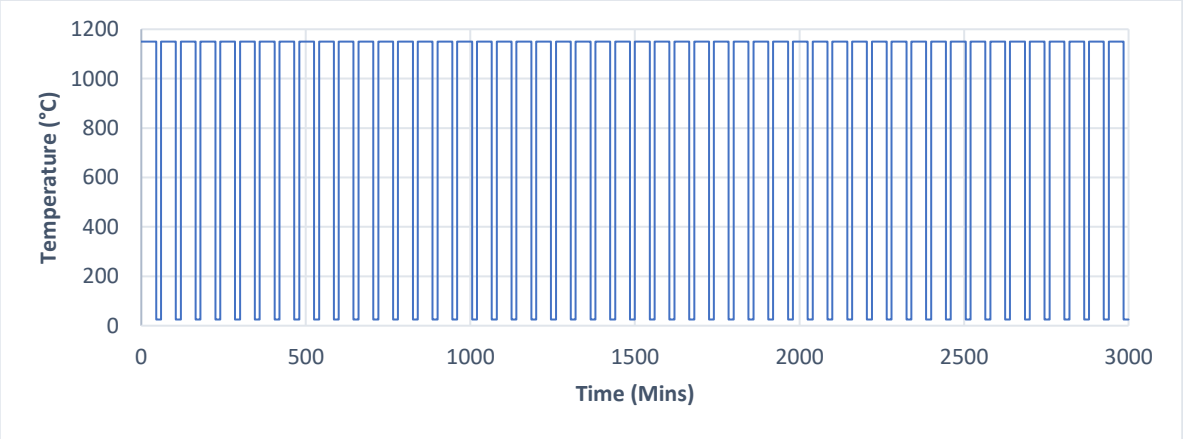

Figure 4.2.4-26: Graph showing temperature change profile of cyclic oxidation treatment, illustrating all 50 cycles.

4.2.4.2.1 Effect of cyclic oxidation on matrix structures

As seen previously, increased oxidation treatment times lead to precipitation and spherification of the chromium carbide phases within the matrix. This was observed to continue, with Figure 4.2.4-27 displaying very rounded, almost circular carbides throughout the matrix, with both the primary

carbides formed during casting, and the secondary carbides precipitated during the heat treatment appearing rounded. This, as discussed before, was a result of the carbides minimizing their surface energies. This phenomenon was not seen with the aluminium and nickel rich phase, which appeared to maintain its as cast morphology.

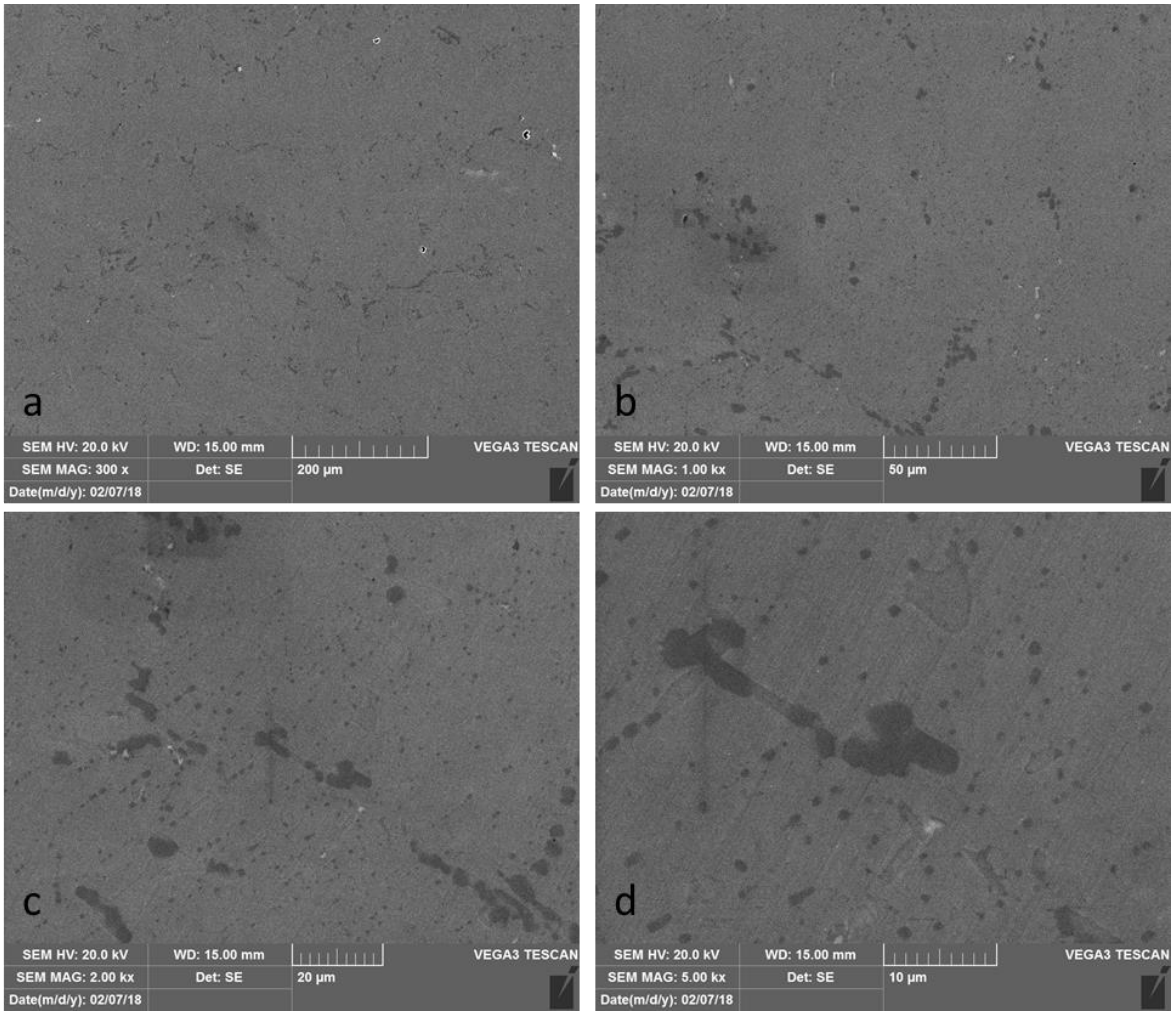

Figure 4.2.4-27: SEM images of Optim-Al alloy matrix after cyclic oxidation treatment showing rounded carbides within the matrix.

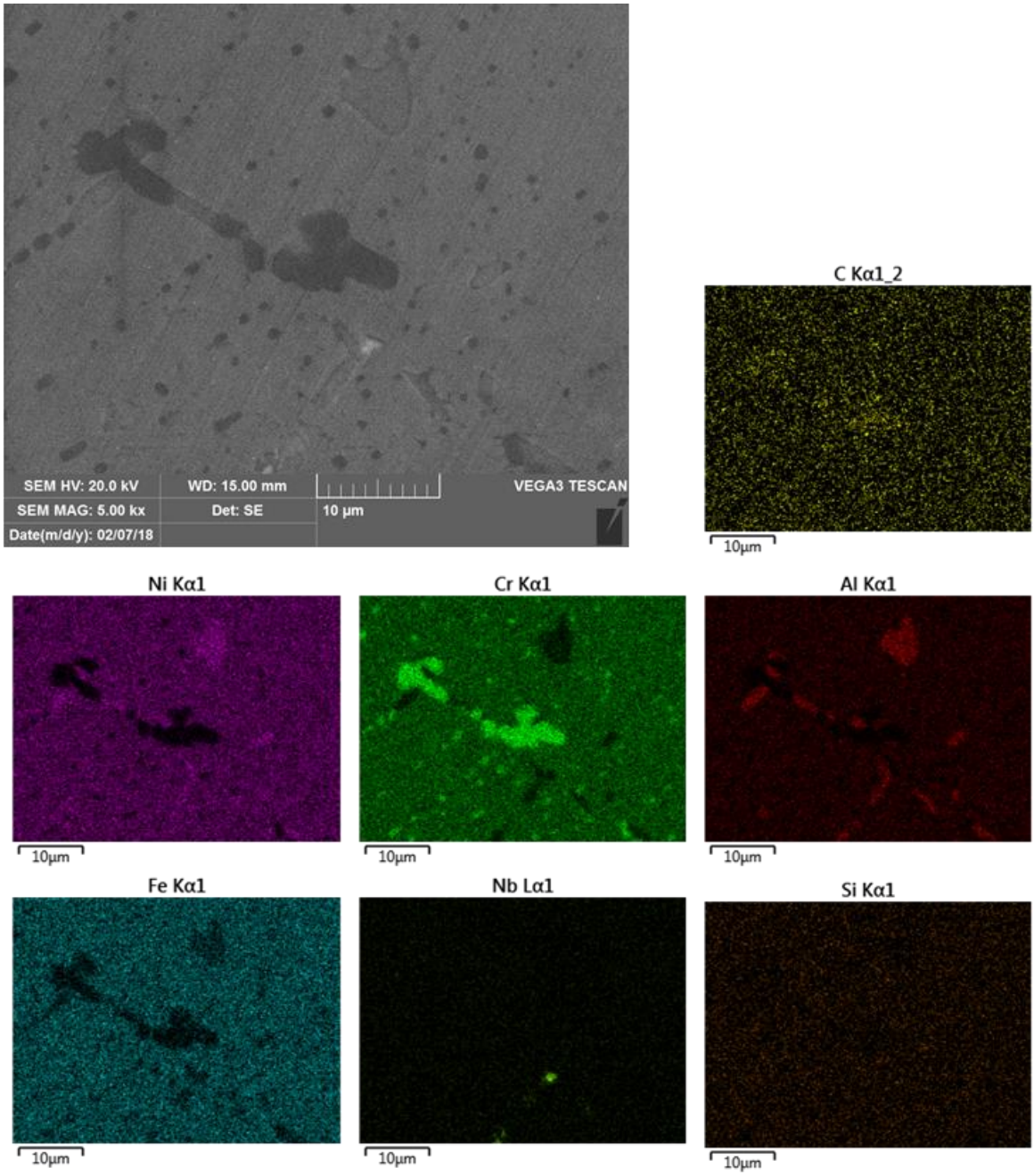

Figure 4.2.4-28: EDS Mapping of the Optim-Al alloy matrix after cyclic oxidation showing alteration of carbide morphology.

4.2.4.2.2 Oxide Layer formation and maintenance with cyclic oxidation

Examination of the surface of the Optim-Al alloy after the cyclic oxidation treatment displayed a thick, consistent aluminium oxide covering most of the sample surface, as shown in Figure 4.2.4-29. Some areas showed the surface oxide fracturing and detaching from the sample surface, however this was still found to be coated with the nickel-plating layer. This indicated the fracture occurred

during sample preparation for imaging and was present and adhered to the sample surface before the mounting and polishing procedures.

The widespread presence and adherence of the oxide is highly promising for the effective protection of the alloy in service. The oxide layer thickened over the treatment time, indicating the oxide had not spalled and regrown, or fractured and been removed during the treatment, but had thickened and maintained the bond to the bulk sample. Figure 4.2.4-29 shows signs of fracturing of the bulk alloy; a result of the rapid temperature changes in the treatment, however the EDS mappings show that even this exposure of matrix material to the atmosphere was followed by oxidation of the exposed surface, demonstrating repassivation and therefore protecting the matrix from the environment.

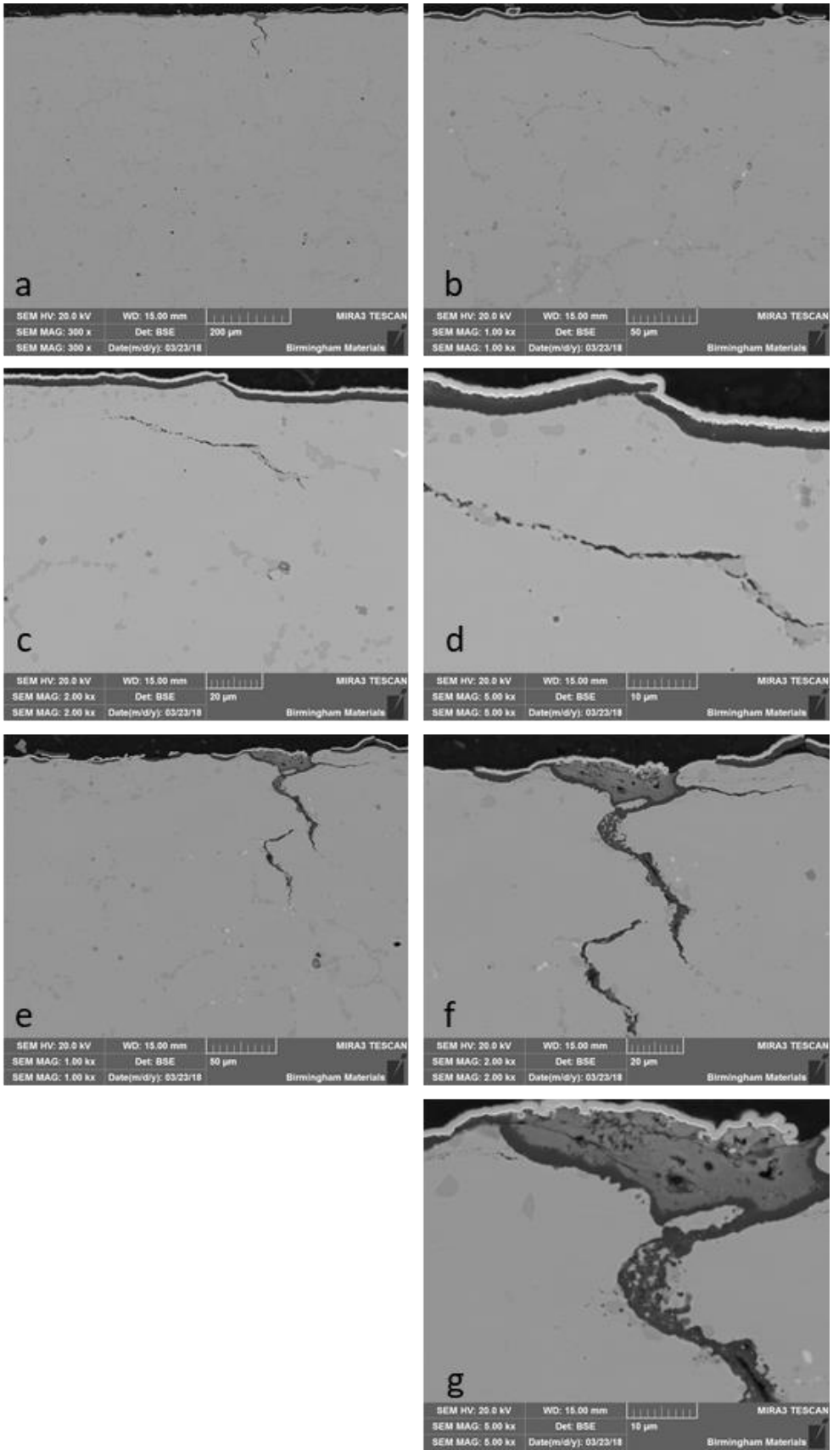

Figure 4.2.4-29: SEM images of Optim-Al alloy machined internal diameter cross section after cyclic oxidation treatment, showing a region with a crack on the surface.

The EDS map (Figure 4.2.4-30) shows that an internal fracture occurred along a grain boundary populated with chromium carbides. These boundaries between the matrix and the secondary phase were the weaknesses in the bulk alloy. This fracture however subsequently appeared to have been oxidised, with evidence of raised aluminium content along the fracture line, albeit a smaller level than that seen on the alloy surface. This was probably in part due to reduced space for growth and significantly reduced oxygen availability, as well as through the reduced aluminium availability with much of the available aluminium in the near surface region having already been oxidised on the surface. Apparent niobium presence atop the oxide was once again due to overlapping energy intensities between niobium and the gold used to coat the sample before nickel plating.

Figure 4.2.4-31 examines a surface breaking fracture in the alloy, which was probably a result of the rapid change in temperature during the treatment. The crack is flanked by chromium carbide particles, which appear to present the path of lowest energy for the crack to propagate. With this site surface breaking, both greater oxygen availability and room for oxide growth allowed a thicker aluminium oxide to form across the entire crack surface. This was more positive evidence for the repassivation on the surface of fractures and exposed material in the case of minor failures of the pipe or loss of surface oxide material.

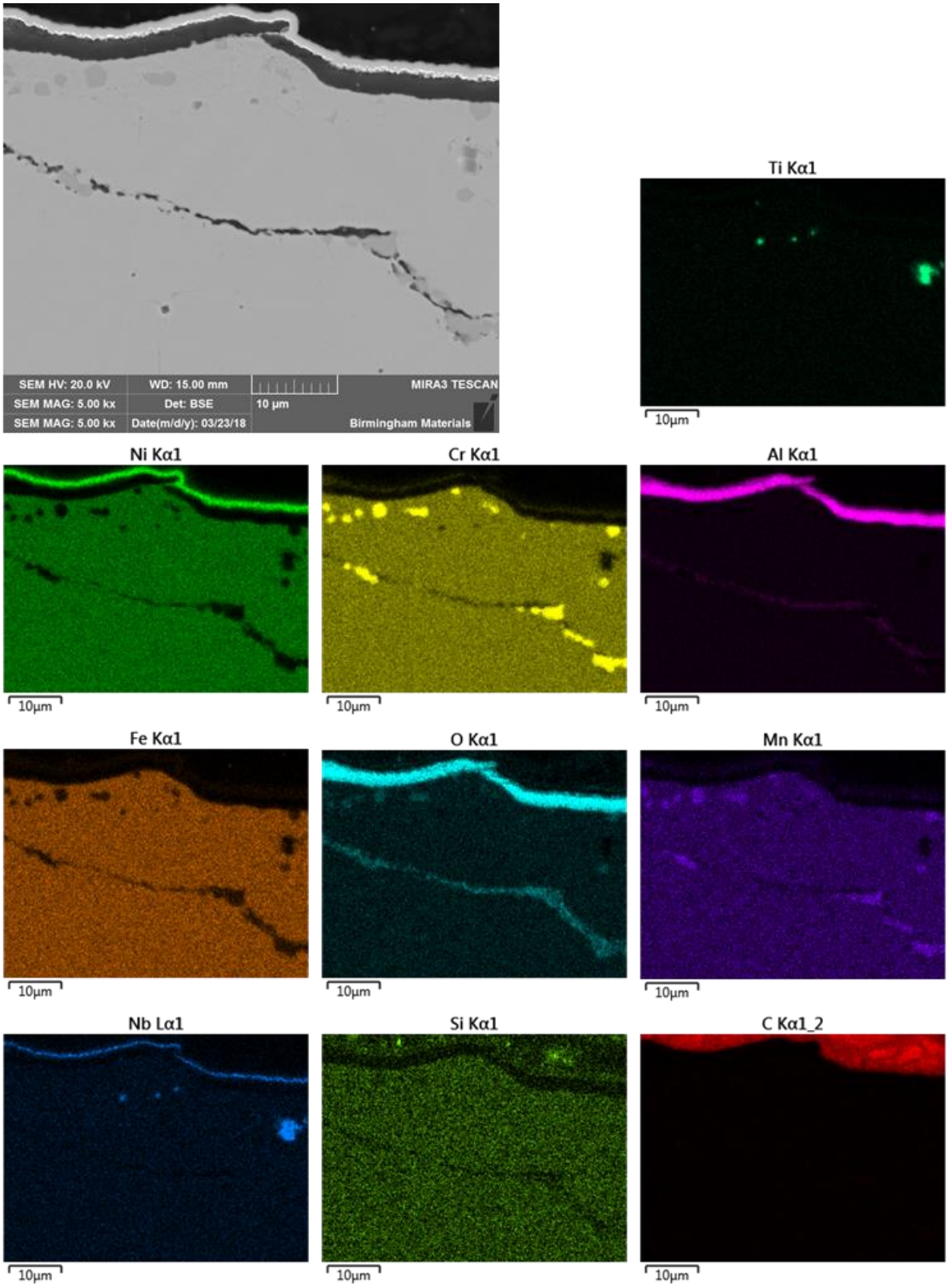

Figure 4.2.4-30: EDS mapping of Optim-Al alloy cross section after cyclic oxidation illustrating a dense aluminium oxide layer atop the sample surface.

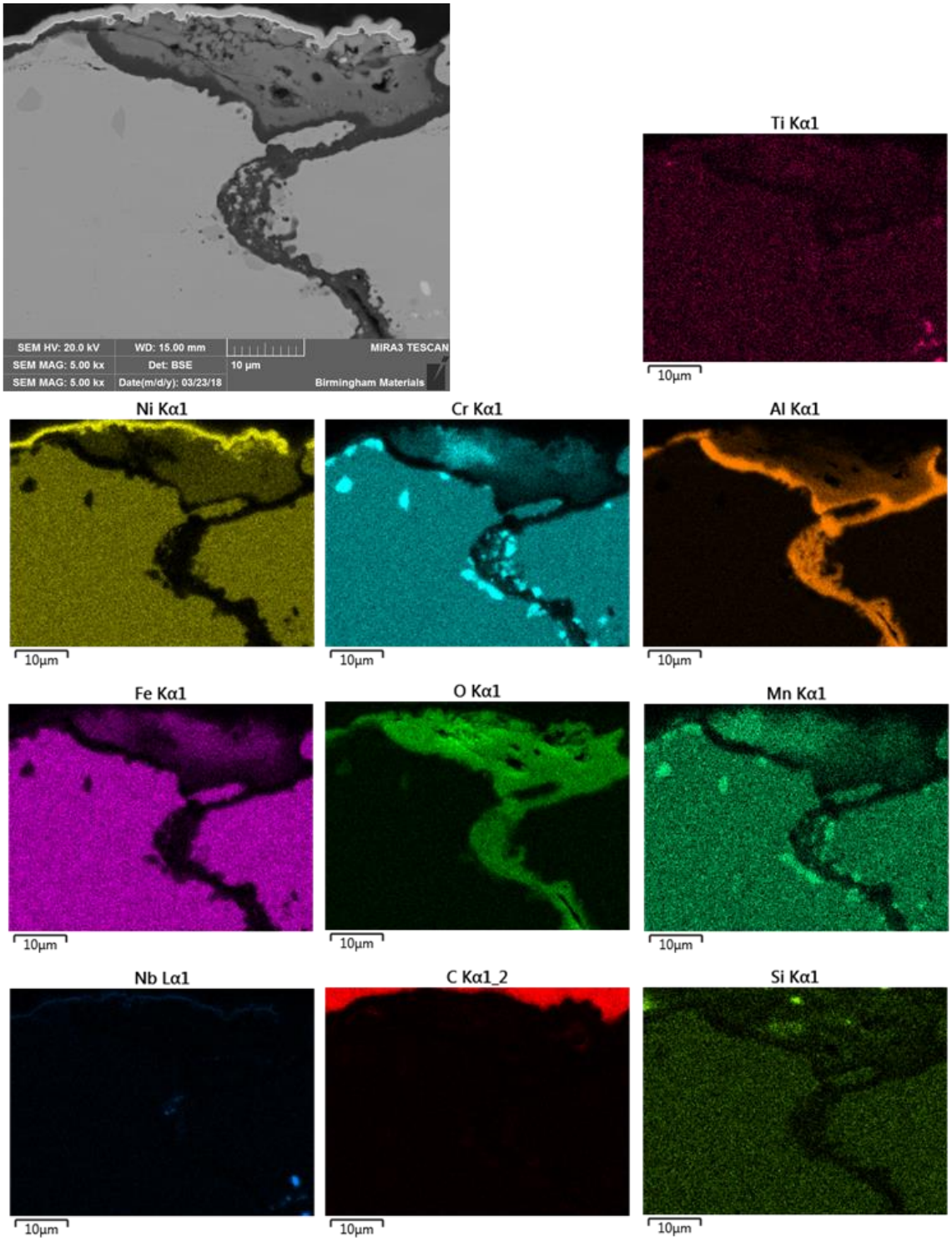

Figure 4.2.4-31: EDS mapping of Optim-Al alloy after cyclic oxidation on crack showing growth of aluminium oxide across the crack surface, maintaining the oxide protection of the alloy.

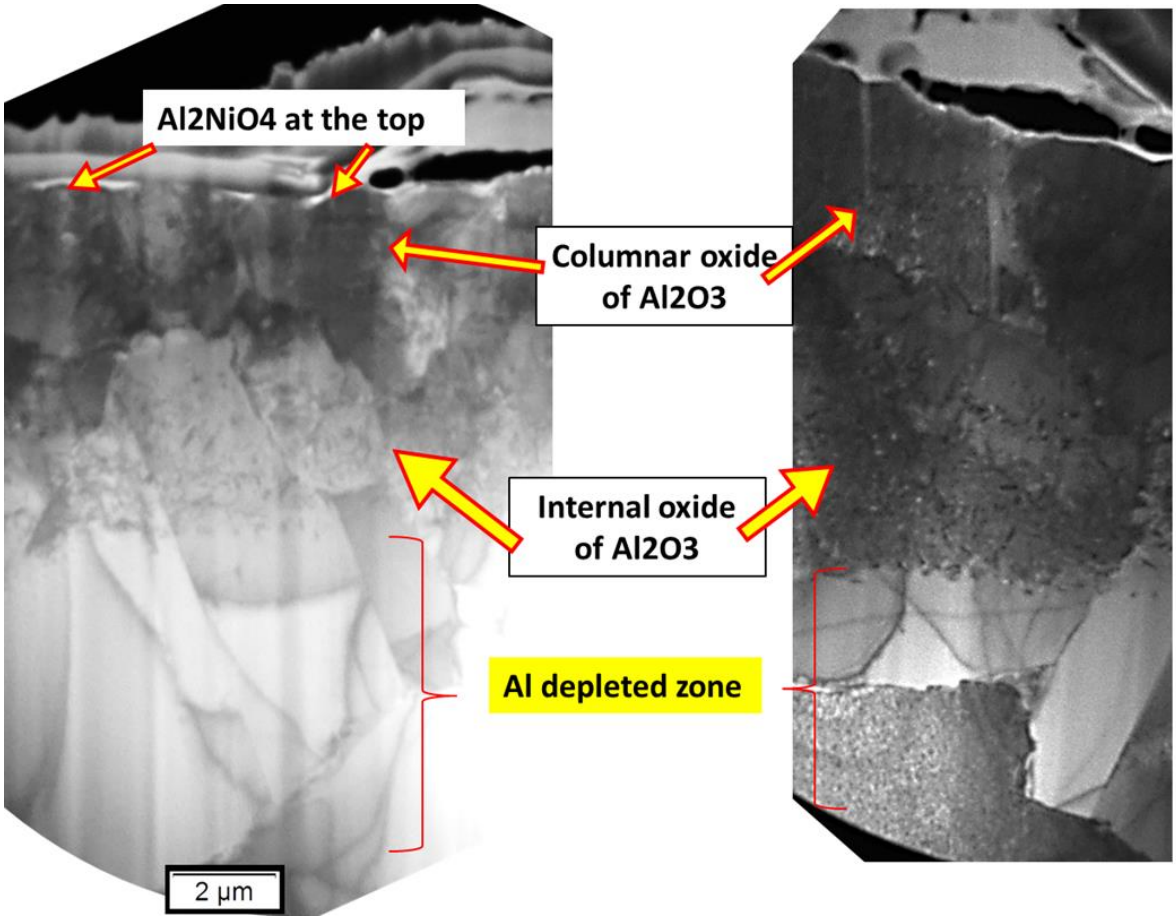

Figure 4.2.4-32: Cross-sectional TEM microstructure of Optim-Al alloy after pre-oxidation (875°C, 48h $PO_2=10^{-27}$), then cyclic oxidation for 50 cycles (1150°C , 45 mins-room temperature,15 mins) indicating the phases found.

The region above the surface aluminium oxide displayed formation of a secondary oxide layer atop the aluminium oxide. The presence of chromium and oxygen was evident, however there was also some nickel and iron in this layer. This was similar to the secondary oxide which was produced on the Optim-Al alloy after elongated oxidation treatment at very high temperatures, where a secondary oxide consisting mainly of nickel, aluminium and oxygen formed atop the aluminium oxide.

TEM examination found this upper oxide to be $NiAl_2O_4$, the same oxide layer present after extended oxidation treatments at high temperature. This layer sat atop the Al_2O_3 aluminium oxide layer as identified previously, demonstrating maintenance of the oxide layer during the highly stressful conditions of the cyclic oxidation testing.

The secondary oxides of $NiAl_2O_4$ do not appear to be present across the inner diameter surface of the entire sample, however they are much more prevalent on the sample edges, the area illustrated in Figure 4.2.4-33. This is shown in Figure 4.2.4-34 where, whilst still clearly displaying the dark aluminium oxide on the bulk matrix surface, the two additional oxide layers are clearly visible.

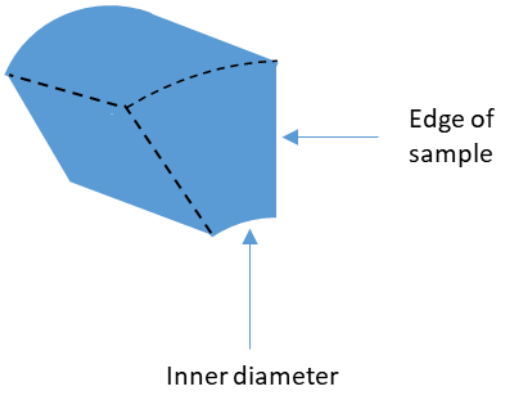

Figure 4.2.4-33: Schematic diagram of edge of sample analysed compared to inner diameter

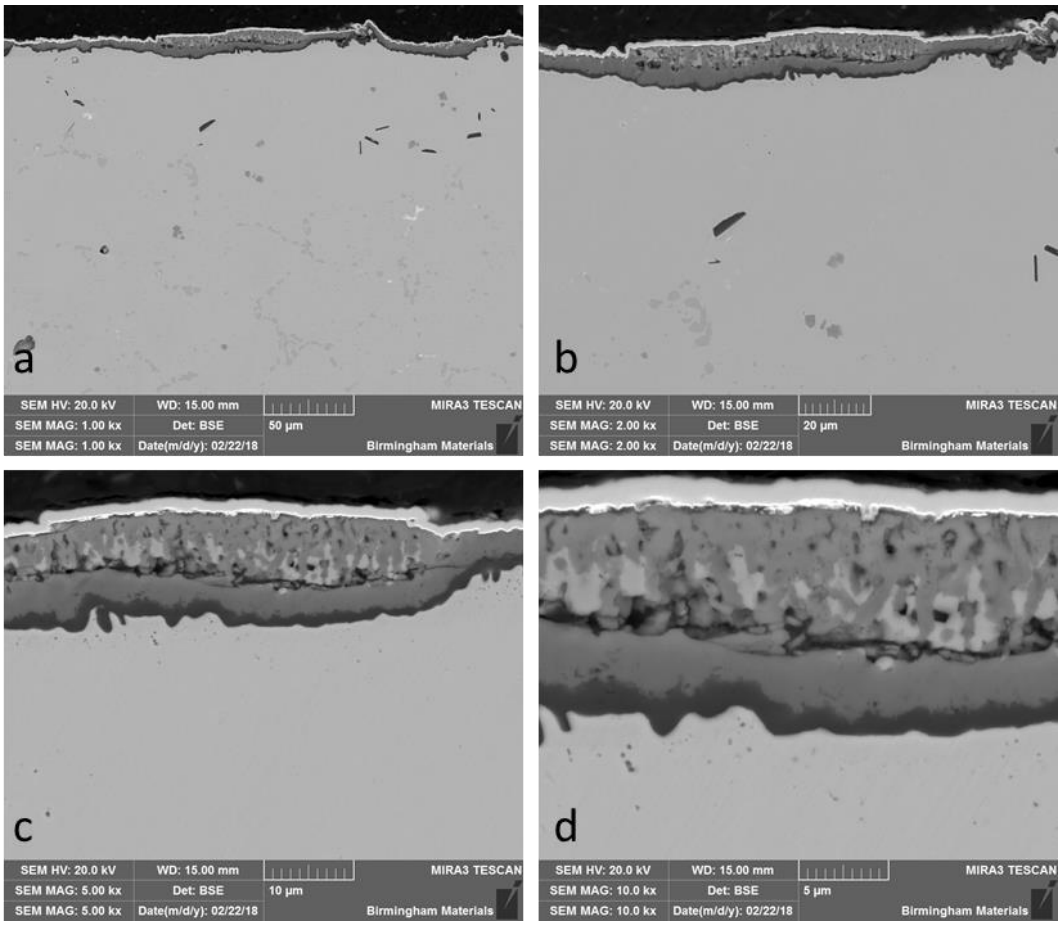

Figure 4.2.4-34: Cross section SEM imaging of cyclically oxidised Optim-Al alloy along sample edge, showing mixed oxide above the aluminium oxide layer.

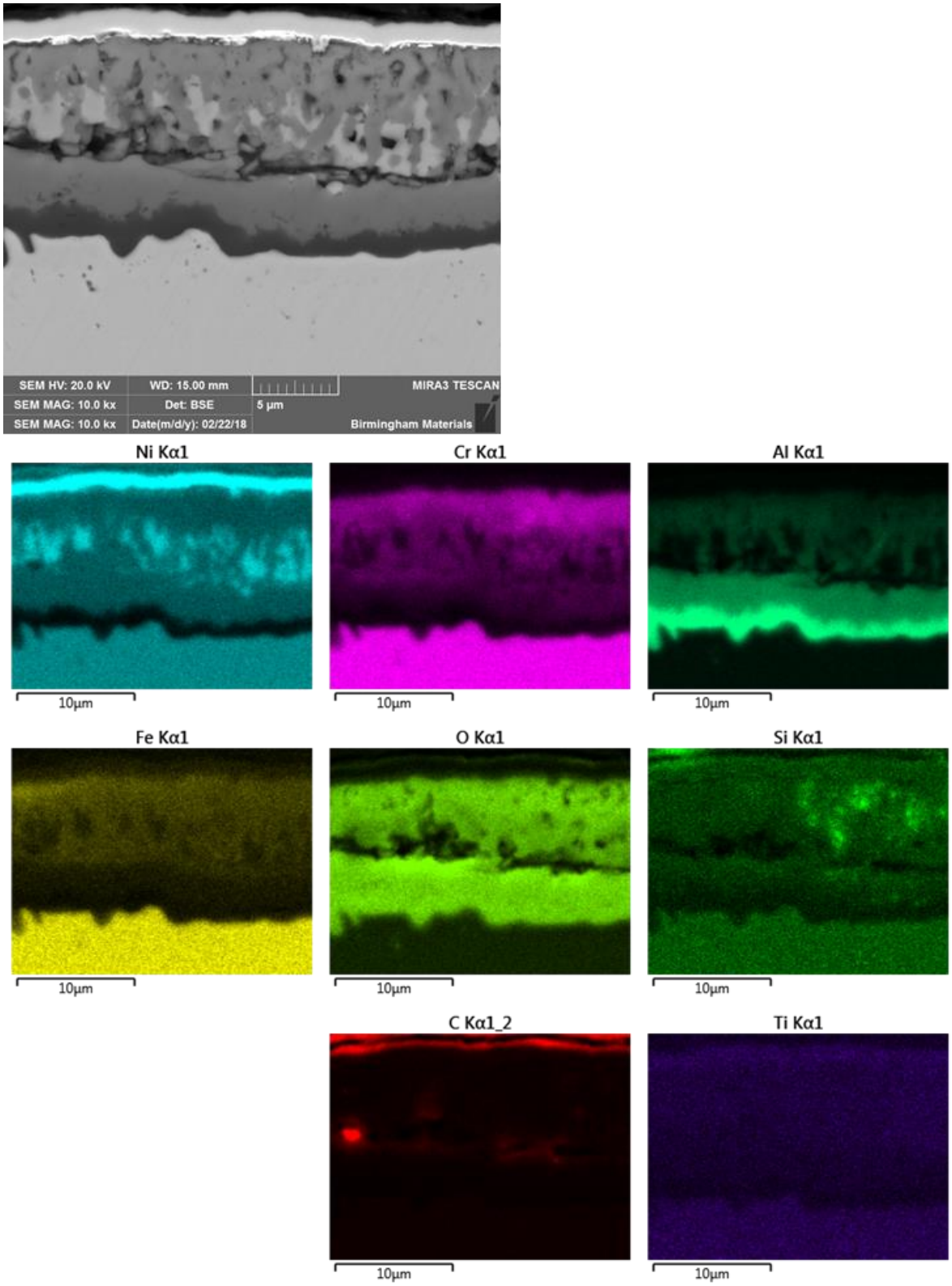

Figure 4.2.4-35: EDS mapping of cyclically oxidised Optim-Al alloy edge identifying the mix of oxide products within the trapped matrix region.

As Figure 4.2.4-35 shows, the aluminium oxide layer was topped by a consistent second oxide which was identified as $NiAl_2O_4$, as formerly seen in the 48-hour 1100°C oxidation tests. This sits beneath a third layer which appears to be columnar aluminium oxide and $NiAl_2O_4$, as identified in Figure 4.2.4-32. Examining the edge of a pre-oxidised sample in comparison to the cyclically oxidised sample, shown in Figure 4.2.4-36, regions of internal oxidation were seen to be formed after the initial oxidation. The pattern of the matrix between the internal oxidation products matches that seen in the mixed, upper oxide region seen in some areas of the cyclically oxidised sample. These observations suggest the aluminium oxide layer can fully form along the lower boundary of the internal oxidation 'arc', formed by more rapid diffusion of oxygen along the gaps between secondary dendrites, parallel to the inner diameter of the pipe. The aluminium depleted matrix above this arc is separated from the bulk material and hence exposed to oxygen during the treatment, where the different oxides are able to form. This internal oxidation was seen in both the Low-Al and High-Al alloys in the single oxidation treatments, however was not evident in the Optim-Al alloy oxidation treatments.

This evidence suggested that the region of alloy displayed in Figure 4.2.4-31 on the inner surface of the sample has undergone a similar process of the isolation of a region of matrix on the surface, due to the fracture. The isolation of this region, separated from the bulk material by the fracture and potential internal oxidation, was then oxidised continually and preferentially the aluminium containing oxides formed initially, and subsequently the remaining matrix elements formed other oxides.

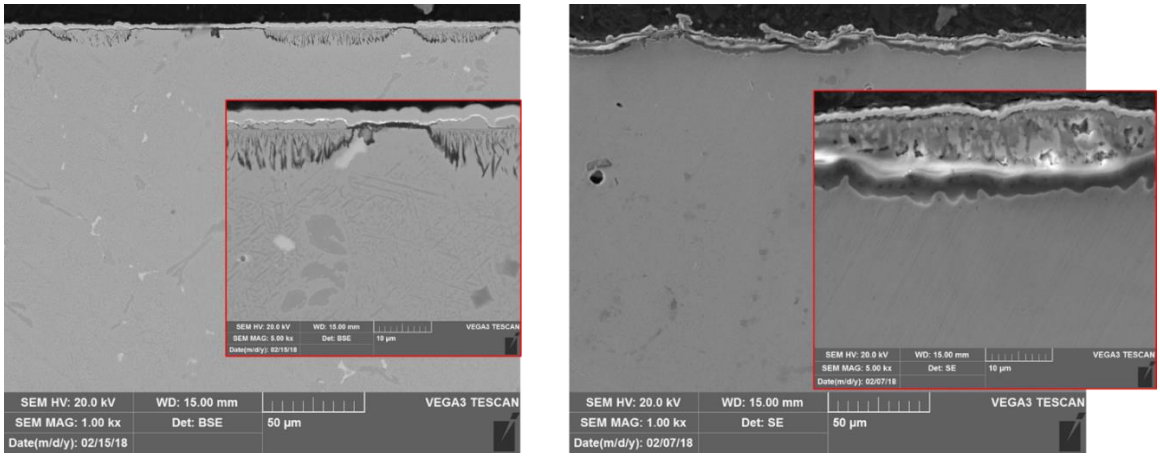

Figure 4.2.4-36: Comparison between edge of sample after pre-oxidation and cyclic oxidation of the Optim-Al alloy

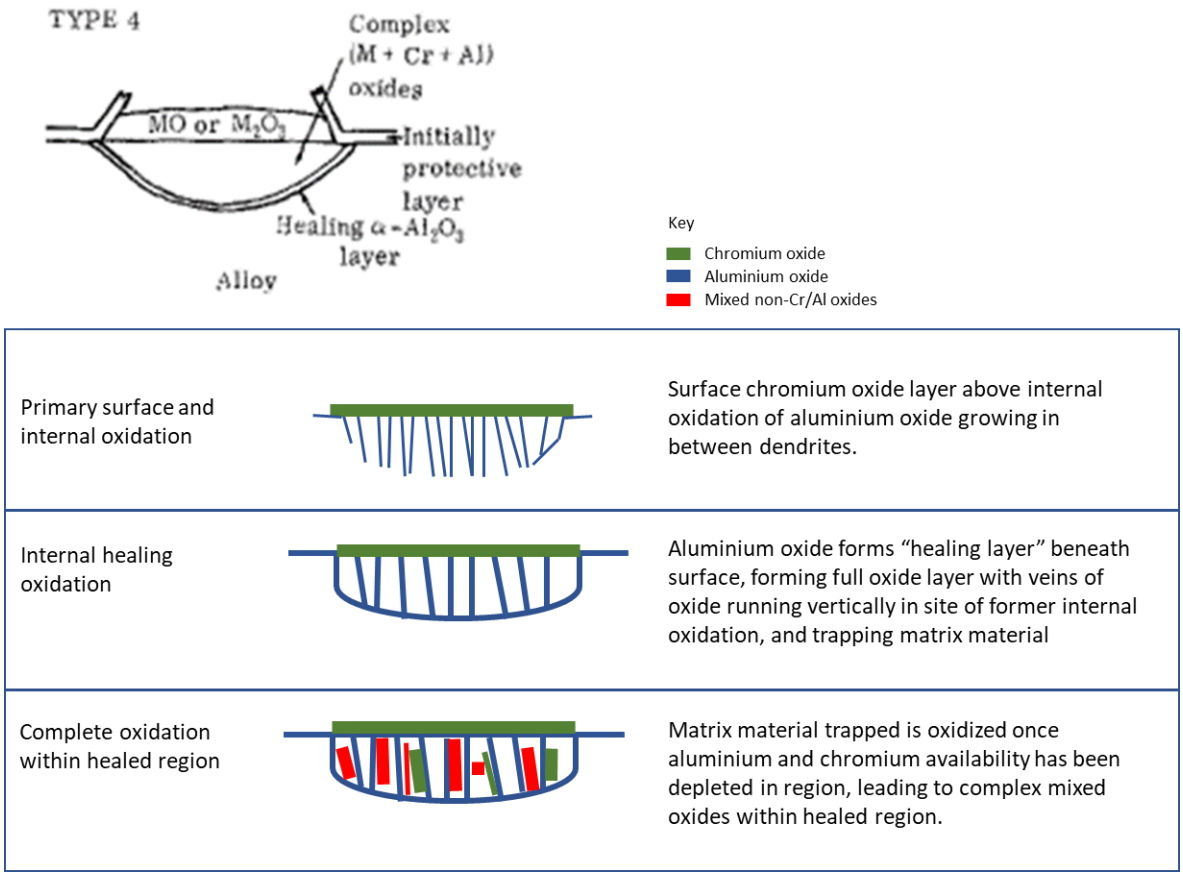

Figure 4.2.4-37: Scale formation modes adapted from Stott, Wood and Hobby, 1971 (134)*, showing Schematic diagrams of the morphology of mode 4 of scale formation on Co-Cr-Al, Fe-Cr Al, and Ni-Cr-Al alloys. Schematic demonstrates the progression of the formation of the mixed internal oxides near the alloy surface as seen in Figure 4.2.4-36.*

The presence of internal oxidation on the sides of the sample and the absence of it on the inner diameter could also due to the processing which took place on the inner diameter. The pipe, after being cast, is bored out to remove the internal layer containing the slag and inclusions which

develop in the casting process, leaving the inner diameter surface. This machining causes some degree of work hardening to this surface, which causes the formation of higher concentrations of dislocations on the sample surface. This in turn enables easier flow of interstitial oxide formers, in this case aluminium, to the surface faster than the influx of oxygen into the sample, and therefore avoids internal oxidation on the inner surface.

The previously outlined potential cause for the internal oxidation along the side of the sample is the direction of the dendrites. The internal oxide phase runs adjacent to the sample edge; this is in parallel with secondary dendrite growth of the alloy. The edge of the sample therefore has small, secondary dendrites, and corresponding interdendritic regions exposed along the length of the sample. These act as channels for oxidation to occur within the sample. As this aspect of the sample would not be exposed during service, this does not pose an issue to the protective nature of the alloy.

4.2.4.3 Summary of effect of oxidation conditions on oxidation behaviour

Oxidation in atmospheres with sufficiently low partial pressures of oxygen can inhibit the formation of chromium rich oxides on all alloys. In the Low-Al and High-Al alloys this allows the aluminium oxide to be formed across the substrate surface, unlike in air oxidation. There was no significant difference in the oxide layer for the Optim-Al alloy however. The Base alloy was unable to form a chromium oxide layer when the oxygen availability was on the limit of chromium oxidation, therefore a manganese rich oxide was formed in its place.

Cyclic oxidation of the Optim-Al alloy demonstrated the ability for the alloy to maintain and repassivate its oxide layer.

5 Discussion

5.1 Microstructure of the alloys

As reported in 4.1, the four alloys displayed similar phases, made up of an iron and nickel matrix with dissolved chromium and other additional alloying elements, with chromium carbides and niobium carbides formed in the interdendritic areas of the alloy, whilst a nickel aluminide phase was also present in the aluminium containing alloys. The microstructure of the four alloys differed in numerous ways, driven by their chemical composition and by the cooling rates they experienced.

All four alloys displayed three distinct regions: the outer diameter region, characterised by dendritic grain growth and long grains perpendicular to the outer surface of the pipe, and interdendritic carbide formation; the inner diameter region, composed of equiaxed grains, larger than those seen at the outer surface, coupled with carbides formed at the grain boundaries; and the cross-over region, where there is a mix of the equiaxed grains and the dendritic grain growth.

The chromium carbides displayed significant variation between the alloys, with the Optim-Al alloy displaying a significantly reduced volume fraction, due to the reduced carbon content (Table 4.1.1-1). The Cr_7C_3 carbides and $Cr_{23}C_6$ carbides were seen in all alloys (4.1.3), with the most common being $Cr_{23}C_6$ in Base and Optim-Al.

Aluminium content was raised at the outer and inner diameters but reduced through the middle of the alloy, illustrated in Figure 5.1-1. This was caused by the rapid solidification at the outer diameter due to contact with the die causing aluminium to be trapped at the outer diameter. However, as the solidification rates reduce moving towards the inner diameter, the aluminium has time to be ejected from the solidifying grains. It is then pushed towards the inner diameter of the tube due to the centrifugal forces as it is lighter than much of the constituent elements of the alloy. This results in the higher concentration of aluminium at the outer and inner diameters, with reduced content

in the cross-over region. This increase at the inner diameter is beneficial for aluminium oxide formation, increasing the aluminium availability at the oxidation site.

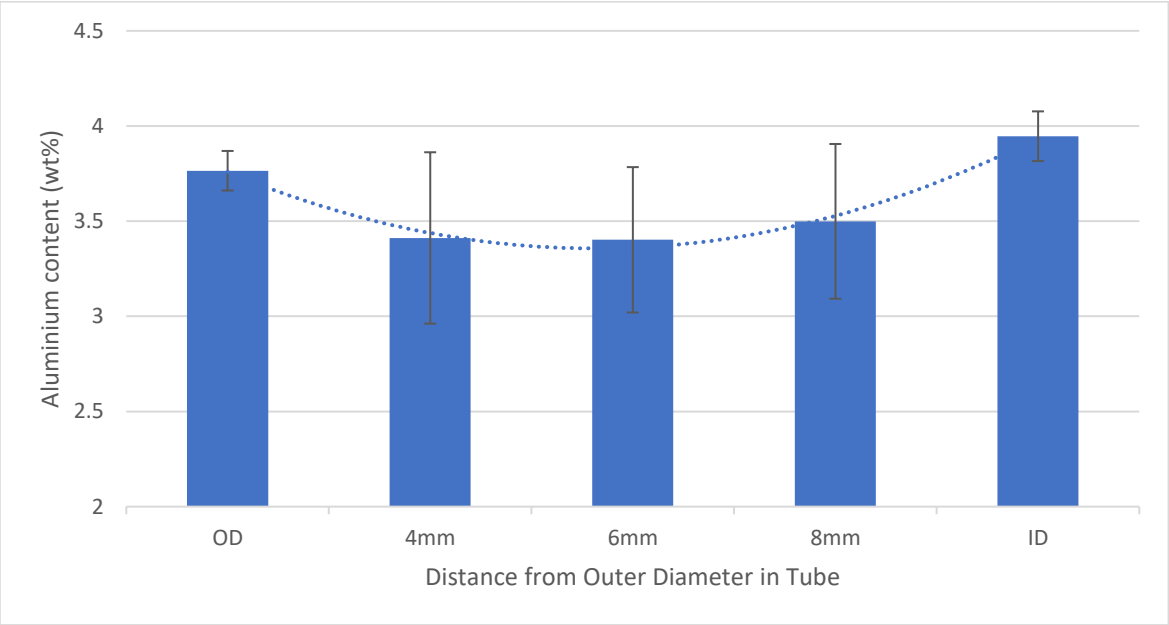

Figure 5.1-1: Graph showing aluminium content of Optim-Al alloy as cast between inner and outer diameter of the tube, as measured by EDS point analysis, demonstrating rise in aluminium content at the inner and outer diameters.

Silicon content was observed to be greater at the grain boundaries in all four alloys, due to ejection from the solidifying matrix grains leading to its concentration towards the grain boundaries. This grain boundary silicon concentration has been found to be beneficial for the welding properties of the alloys (138).

5.1.1 Effect of aluminium addition on microstructure

Comparing the Base alloy to the other three aluminium containing alloys allows for the effect of aluminium addition to the microstructure to be evaluated. The primary difference observed was the formation of the nickel aluminide phase which was seen in all three aluminium containing alloys in varying volume fractions.

As shown in 4.1.2, modelling of the solidification of the three aluminium containing alloys suggests that the raise in aluminium content of the High-Al alloy would lead to a significantly greater volume fraction of nickel aluminide. This was the observed result when compared with the Low-Al and

Optim-Al alloys. This increase in volume fraction of the nickel aluminide phase, identified as the intermetallic Ni_3Al by the XRD analysis (Section 4.1.3.5 and Figure 4.2.1-22), leads to a significantly more brittle alloy, therefore widespread formation must be avoided for an alloy to be suitable for service (29). This demonstrates a limit for aluminium content, and the requirement for careful control of the casting parameters to limit the formation of this Ni_3Al phase.

A reduction in aluminium content from the 5.56% of the High-Al alloy to 4.49% in the Optim-Al alloy saw a reduction in the onset of formation temperature (as predicted by the JMatPro model) from 1260°C to 1230°C, leading to a shorter window of precipitation for the Ni_3Al phase. This in turn caused a significant reduction in volume fraction of the nickel aluminide phase, from a volume fraction of 0.0333 in the High-Al alloy to 0.0067 in the Optim-Al alloy at solidus temperature. This predicted five-fold decrease in volume fraction is in line with the observed as cast microstructure, and therefore is expected to yield a much more ductile alloy. The brittle nature of the High-Al alloy is evidenced by the hardness measurements, with its hardness measured in the region of 1.5 times that of the Optim-Al alloy (Figure 4.1.4-6 to Figure 4.1.4-9).

The Low-Al alloy, with aluminium concentration of 3.79%, was not predicted to form any nickel aluminide phase by the model, however there was some evidence of a very small volume fraction of this phase in the alloy, shown in Figure 4.1.3-17 and Figure 5.1.1-1. This presence is explained by the ejection rates of elements from the solidifying matrix. As the matrix grains solidify, non-matrix formers are ejected from the grain into the melt, leading to localized regions of the solidifying alloy having a greater aluminium content than the bulk composition. In these regions, the nickel aluminide phase is able to precipitate during solidification of the alloy.

Differences in the shape, volume and distribution of the nickel aluminide are evident when comparing the phase in the Optim-Al and High-Al alloys to the Low-Al alloy. Whilst the morphology of the phase in the High-Al and Optim-Al alloys is very similar, displaying relatively round patches

of the phase with no distinct variation, those seen in the Low-Al alloy appear similar to a delta landform, with channels running between patches of the phase (Figure 5.1.1-1). More thorough observation of this phase showed it to be a combination of two phases; the Ni_3Al phase sat within a silicon and chromium rich intermetallic. As reported by Tripathi et al. (139) formation of the intermetallic phases Ni_3Al and $CrSi_2$ together has been observed in an oxygen free environment under certain conditions. This finding is supported by the $CrSi_2$ phase having the most negative effective heat of formation of all chromium-silicon compounds, therefore the most likely phase to form (140). The work done by Tripathi et al. demonstrated the adhesive effect of the formation of the two intermetallic compounds at a boundary, probably due to co-precipitation of the compounds creating mechanical interlocking, which is in line with the interlocking phases seen in the precipitated phase in the Low-Al alloy.

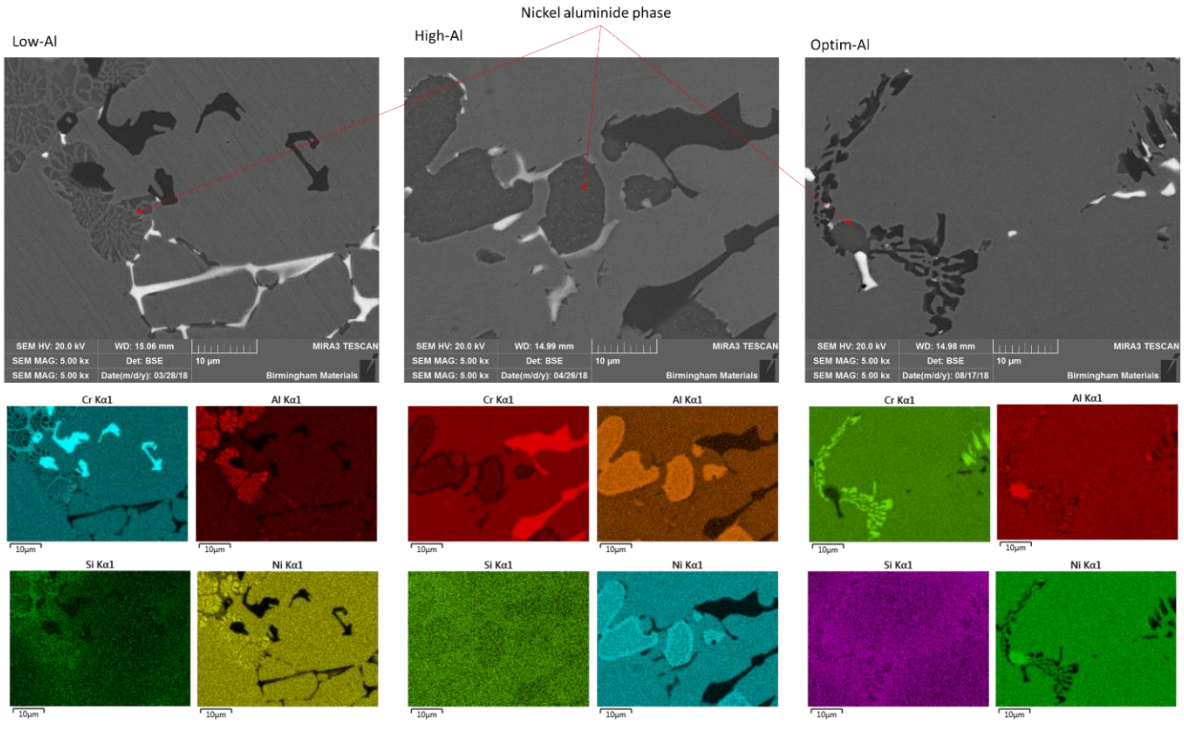

Figure 5.1.1-1: EDS mapping and backscattered electron SEM image of nickel and aluminium rich phase in all three aluminium containing alloys

An increase in aluminium content was also seen to lead to increased chromium carbide content in the alloys. This effect is due to the aluminium being preferentially dissolved into the alloy matrix in

favour of the chromium atoms, due to their significantly smaller size and therefore reduced stress on the matrix crystal lattice. This causes less chromium to be dissolved and therefore it is available for reacting with the available carbon.

Evaluation of the Hume-Rothery rules for solid solubility (141) of aluminium and chromium in the austenitic matrix confirm this expectation, using the properties in Table 5.1.1-1.

Table 5.1.1-1: Hume-Rothery parameter properties of Ni, Fe, Al and Cr

Element	Atomic Radius (pm)	Crystal Structure	Valency	Electronegativity
Ni	124	FCC	+2	1.91
Fe	132	FCC	+2, +3	1.83
Al	121	FCC	+3	1.61
Cr	139	BCC	+2, +3, +6	1.66

Rule 1: <15% difference in atomic radius of the atoms. As the matrix is an austenitic stainless steel, the atomic radii of both iron and nickel will be compared with aluminium and chromium.

Rule 1: $\frac{r_{solute}-r_{solvent}}{r_{solvent}} \times 100 \geq 15\%$

Al in Fe = $\frac{121-132}{132} \times 100 = -8.3\%$

Al in Ni = $\frac{121-124}{124} \times 100 = -2.4\%$

Cr in Fe = $\frac{139-132}{132} \times 100 = 5.3\%$

Cr in Ni = $\frac{139-124}{124} \times 100 = 12.1\%$

The calculations confirm that both chromium and aluminium are within the limit of disparity in atomic radius, with aluminium being closely matched in size to nickel, whilst there is a much larger disparity between chromium and nickel.

Rule 2: Identical crystal structure of the solute and solvent atoms leads to greater solubility. Aluminium displays an FCC (face centred cubic) crystal structure, as does the austenitic steel matrix,

however chromium forms in a BCC (body centred cubic) crystal lattice, therefore it will be less likely to be soluble in the austenitic matrix.

Rule 3: A greater valency of the metals increases their likelihood for solid solution. If the solute and solvent metals have the same valency, solubility is greatest. The valency of nickel and iron in the matrix phase can vary; however, it is typically +2 for nickel, and either +2 or +3 for iron. Aluminium typically has a valency of +3, whilst chromium may have a valency of +2, +3 or +6 depending on its state. This showed that both solute atoms can have similar or identical valencies as the solvent atoms, therefore neither hinder the potential for solution.

Rule 4: Electronegativity difference being close to zero increases the solubility. As shown in Table 5.1.1-1, the electronegativity of aluminium and chromium are very similar, with chromium being marginally closer to the matrix elements of nickel and iron, however there is not a major difference.

All of the above demonstrate that aluminium and chromium have a similar ability to dissolve in the matrix of the alloys, with aluminium showing greater solubility due to its matching crystal structure, and a smaller variance in atomic radius. This effect is identifiable when comparing the Low-Al and High-Al alloys. They have a measured carbon content of 0.49% and 0.48% respectively, with the major difference between the two being the aluminium content, allowing the effect of the addition of aluminium to be determined. The Low-Al alloy contained 3.79% Al, compared to 5.56% within the High-Al alloy.

Comparison of the predicted phase composition of these two alloys showed a large disparity between projected chromium carbide content; at solidus temperature, the High-Al alloy was predicted to contain a volume fraction of 0.677 chromium carbides, whilst the Low-Al alloy was predicted to contain a volume fraction of just 0.054 at solidus temperature. This is a 12.5 times difference in expected carbide content between the alloys. As the model is a prediction of the alloy at equilibrium, the kinetics of the solidification also play a part in the resultant alloy. Therefore the

actual observed microstructure does not display this significant a difference, however, the carbide content in the High-Al alloy was clearly higher when comparing the two, as shown in Figure 4.1.3-25.

Figure 5.1.1-2 shows the solidus and liquidus temperatures of the four alloys, as predicted by the model. With increasing aluminium content, both the solidus and liquidus temperatures are seen to decrease, with the High-Al alloy displaying the lowest and the Base alloy the highest.

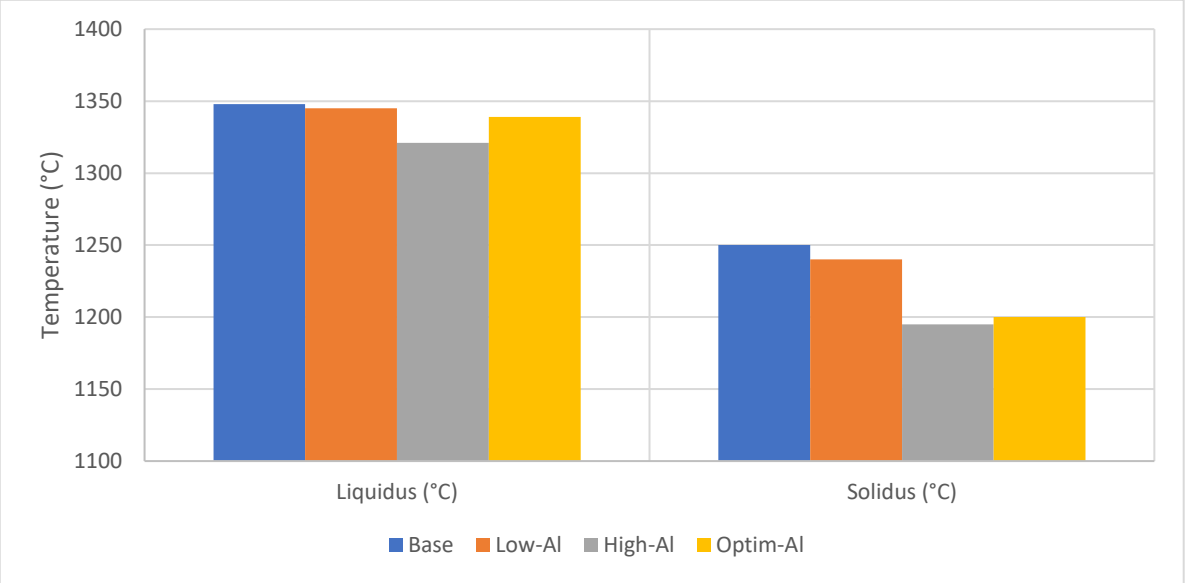

Figure 5.1.1-2: Graph showing solidus and liquidus temperatures of all four alloys as predicted by JMatPro model

The lower solidus temperature of the High-Al alloy results in slower solidification of the alloy under the same conditions, which in turn allows greater carbide precipitation during solidification. This means the increased aluminium content causes carbide formation to occur to a greater extent, which is in line with the observed microstructure and the findings of Kiani-Rashid and Delagnes et al. (142,143).

As this change in solidus and liquidus temperatures impacts the solidification, it causes changes in the morphology of the carbides between the alloys. The slower cooling rates due to the lower solidus temperatures of the High-Al alloy results in interconnection of the acicular carbides in the interdendritic regions, forming the Chinese script morphology of the chromium carbides in this alloy (18,42,144). Furthermore, the large facetted carbides in this alloy form due to the longer

precipitation times available, as the carbides nucleate in the interdendritic space of the solidifying alloy. However, slow enough movement of the melt interface causes the carbide to be pushed towards the inner diameter and allowed to grow further without being instantly trapped within the solidifying matrix (145). Both described carbide morphologies are shown in Figure 4.1.3-23.

The niobium carbide content is also affected by the aluminium content, with a significantly greater niobium carbide (NbC) volume fraction observed in the Base alloy compared to the aluminium containing alloys. The High-Al alloy microstructure investigation displayed a very limited presence of NbC when compared to the others. This trend is reinforced by the JMatPro model (4.1.2), with the niobium carbide content inversely proportional to the aluminium content. This finding is explained by the increased chromium carbide volume fraction that is observed with increased aluminium concentration; the greater volume fraction of chromium carbides uses up a greater volume of the available carbon in the alloy to form carbides, therefore greater chromium carbide content causes a reduction in niobium carbide content.

This reasoning is further reinforced by the model of phase solidification, where chromium carbides initiate formation at higher temperatures than niobium carbides in all four alloys, confirming that the chromium carbides begin to form before the niobium carbides.

5.1.2 Effect of other alloying elements on microstructure

Carbon content of the alloys has a significant impact on the microstructure, acting as the second variable dictating the nature of the carbides in the alloy. Comparing the Low-Al and High-Al alloys, which have carbon contents of 0.49% and 0.48% respectively, to the Optim-Al alloy, which contains just 0.26% carbon, the effect of the carbon content can be observed.

The large difference in carbide content which accompanies the increased aluminium content, as previously discussed, is counteracted by a reduction in carbon content in the Optim-Al alloy, reducing the carbon available to react with the chromium, and leading to a predicted chromium

carbide content of just 0.038, two thirds that of the Low-Al alloy. Therefore, despite containing a greater amount of aluminium which was previously shown to cause an increase in chromium carbides, as the carbon content in the Optim-Al alloy is half that of the Low-Al alloy it supresses the carbide content.

The titanium content impacts the niobium carbide (NbC) presence in the alloys. As titanium content increases, the volume fraction of NbC in the alloys decreases, as predicted by the model (4.1.2) and seen in the microstructural observations (Figure 4.1.3-25). This is due to titanium being more stable as a carbide, and therefore producing (Ti,Nb)C, and leaving niobium to dissolve into the matrix, and available for potential oxidation (146). A reduction in niobium carbide content in the alloys is detrimental to the oxidation properties of the alloy, as these niobium carbides act as barriers at the grain boundaries to iron and nickel movement to the surface, and therefore aid in keeping these catalytic elements from reaching the surface of the sample (146). The titanium presence, whilst aiding creep resistance in the alloys, can lead to detrimental effects on the microstructure. An increased titanium concentration promotes the NbC phase to precipitate in a finer morphology, whereas greater niobium coupled with reduced titanium presence leads to the Chinese script morphology (18) observed in the Base, Low-Al and Optim-Al alloys (0.03%, 0.16% and 0.15% Ti respectively). This was not the case in the High-Al alloy which contained 0.36% Ti.

5.2 Oxidation Behaviour

The oxidation behaviour was investigated across all four alloys. As has been discussed in 2.4.1, a continuous, stable oxide layer which does not contain catalytic elements on the inner surface of the pipe would be an ideal solution to reduce catalytic coking – protecting the gas from the matrix forming elements and not requiring either complex and expensive treatments or coatings to be applied to the inner surface of the pipe.

A thick oxide layer with a coefficient of thermal expansion which is not in line with that of the bulk alloy will be susceptible to fracture via stresses induced in the oxide upon changes of temperature from those at which the oxide was formed. This is most likely to occur during heating up or cooling down of the pipes, which leads to different levels of contraction of the pipe alloy and the oxide due to differences in their coefficients of thermal expansion. Typically, the coefficient of thermal expansion of surface oxide ceramic is smaller than that of the metallic nickel alloy substrate. During heating up, if the pipe expands to a greater degree than the surface oxide layer, the stresses generated in the oxide will result in cracks and/or potential debonding under the tensile stresses in the oxide layer. Conversely, when cooling down, if the pipe contracts to a greater degree than the oxide, compressive stresses will be imparted into the oxide, potentially leading to buckling fracture and spallation of the oxide. This issue is exacerbated with increasing oxide thickness, but is relatively negligible with a very thin oxide, and therefore a protective thinner oxide is always more beneficial in the service applications.

The reported coefficient of thermal expansion of nickel alloys is around 17-18x10^{-6} K^{-1} in the temperature range of 100°C-1200°C (11,147,148).The coefficient of thermal expansion of chromium oxide scale grown on a steel substrate was found to be 10.75x10^{-6} K^{-1} by Mougin et al. (130) which is larger than the generally reported values which are usually up to 9.6 x10^{-6} K^{-1} as reported by Wang et al. (131). Similarly, the coefficient of thermal expansion of alumina when grown as a film was higher than generally reported bulk values (149), with Huntz et al. measuring it to be 10.7 x10^{-6} K^{-1} at 700°C, and rising not significantly above 11.5 x10^{-6} K^{-1} in the operational temperature range used in ethylene cracking (132).

As both coefficients of thermal expansion are of the same order of magnitude and very similar in actual value, the thickness of the oxide layer becomes significant, as the greater the thickness of

the oxide layer, the greater the volume change and therefore potentially more detrimental to the maintenance of a consistent oxide layer.

5.2.1 Oxidation behaviour of the Base alloy

As shown in Figure 4.2.1-1, the Base alloy displays consistent oxidation characteristics, with a dense chromium oxide (Cr_2O_3) layer forming across the sample surface, confirmed by TEM and XRD results (4.2.1.1.2). This oxide is an outwardly growing oxide, as the inward flux of oxygen was found by Yan et al. to be three orders of magnitude lower than the diffusion of chromium to the surface (150). Chromium supply for the continued oxidation on the surface is fulfilled by the dissolution of near surface chromium carbides, after the solid solution chromium supplies in the surface matrix are exhausted. This results in a chromium depleted zone beneath the oxide layer (Figure 4.2.1-6), coupled with a loss of chromium carbides in this region, known as denuding (52,91,150–152).

Typical chromium, nickel and iron based alloys are known to produce this chromia layer after oxidation, with TiO_2, or rutile, often found atop the chromium oxide (91,92). This is not the case in the Base alloy, which contains only 0.03% titanium. Instead, a manganese and chromium spinel phase, manganese chromite ($MnCr_2O_4$), was observed to be present across the surface of the chromium oxide, particularly with extended oxidation times. This is a commonly found surface phase (35,101,153,154).

This phase formation, which was found to occur after initial chromium oxidation formation when examining the 800°C oxidation cross-section images, confirms the ability of manganese to rapidly diffuse through the chromium oxide layer. It is therefore available at the surface/atmosphere interface to oxidise (101,155). Manganese was found to diffuse through chromia significantly quicker than any other constituent cation (155). The presence of this manganese chromite atop the chromium oxide is particularly favourable, due to its reported anti-coking behaviour being greater than chromium oxide (36,88–90,99,100,102).

Analysis of the growth of the oxide layer over time on the Base alloy displayed a thickening of the oxide with increased temperatures and oxidation times. As illustrated in Figure 4.2.2-20, when oxidised at 1100°C, after 21 hours there was a step-change in mass gain as registered by the TGA (thermogravimetric analysis) of the oxidation. When analysing the cross-section images of this oxide layer over this time period and beyond, an arrest in the thickening of the manganese chromite layer appeared to occur, coupled with further thickening of the chromium oxide layer. This was theorized to be a result of the manganese chromite reaching a limit in thickness, due to availability of reactants, and therefore the chromium oxide was able to grow without competition. This observation is reinforced by previous findings, demonstrating the effect of the $MnCr_2O_4$ layer inhibiting the growth of the chromium oxide layer on these alloys (36,88,99,100,102).

The subsurface presence of an amorphous silicon oxide layer, SiO_2, was evident throughout oxidation testing of the Base alloy. This oxide is produced beneath the chromium oxide layer as silicon has very low solubility within chromia, unlike manganese, and therefore the silicon is ejected into the matrix at the oxide/matrix interface, leading to a greater concentration of silicon in the matrix immediately beneath the chromia layer (150). There are differing reports of the effect of silicon on the adhesion of the chromium oxide layer to the matrix, with Alnegren (30) suggesting silicon decreases adhesion, whilst other reports conversely suggest the silicon oxide layer acts to increase adhesion to the surface (156).

Adhesion of the $MnCr_2O_4$ layer to the surface of the Cr_2O_3 layer does not appear to have been investigated previously. The oxidation results gathered in this investigation clearly displayed a trend of the manganese chromite to fracture around the spalled oxide region (Figure 4.2.2-13 and Figure 4.2.2-14). Spallation of the chromium oxide layer occurred along the machining marks of the alloy surface, leaving matrix material exposed to the surface (Figure 4.2.2-12 and Figure 4.2.2-14). The manganese chromite layer atop the chromium oxide layer was seen to be lost around the site of

spallation, resulting in greater manganese chromite loss compared to chromium oxide. This observation suggests that the adhesion between the manganese chromite and the chromium oxide layers is poorer than that of the chromium oxide to the matrix of the alloy, as the force generated in the spallation of the chromium oxide caused the removal of a greater area of manganese chromite.

The loss of this manganese chromite from the surface of the alloy would be expected to elicit poorer protection from catalytic coking in ethylene cracker furnaces, as the manganese chromite layer has been consistently shown to provide greater protection from catalytic coking. Furthermore, the exposed matrix caused by the spallation of the chromium oxide layer clearly leaves significant nickel and iron in contact with the reactive gas stream, therefore catalytic coking can occur.

5.2.2 Effect of aluminium on oxidation behaviour

Addition of aluminium to the alloy caused significant differences to the oxidation behaviour of the alloys. The first observation was that of the reduced surface coverage of the chromium oxide layer, as seen on the Low-Al and High-Al alloys (Figure 4.2.1-10 and Figure 4.2.1-17 respectively), when compared to the Base alloy (Figure 4.2.1-1). This difference is summarized in Figure 5.2.2-1, which displays the reduced oxide layer thickness of the Low-Al and High-Al alloys. It also demonstrates the much greater variability in oxide layer thickness by the significantly greater standard deviation. This deviation illustrates the inconsistent nature of the oxide layer on the alloy, with some oxide patches having a similar thickness to those seen on the Base alloy, whilst other regions are entirely free from oxide formation (Figure 4.2.1-16).

The reduction in chromium oxide on the surface is linked to the microstructural changes previously discussed; the addition of aluminium leads to greater chromium carbide formation. This results in a reduced chromium content readily available for oxidation in the matrix, and therefore less chromium oxide is able to form on the alloy surface.

Furthermore, the reduction in niobium carbides observed in these two alloys compared to the Base alloy also significantly impacts the oxidation behaviour. Niobium carbides act as barriers to the movement of other matrix elements through the alloy, such as nickel and iron (146). By restricting their movement, the chromium is able to more readily oxidise. Therefore, conversely, the reduced volume fraction of niobium carbides in the Low-Al and High-Al alloys results in a reduction in the ability of chromium to oxidise on the alloy surface, leading to a reduction in surface oxide.

The silicon oxide layer which was found beneath the chromium oxide layer in the Base alloy was replaced by aluminium in the Low-Al and High-Al alloys. This aluminium oxide layer presence also confirms the lack of oxide growth across regions of the alloys; as the aluminium oxide layer forms beneath patches of chromium oxide, it can be used to evaluate whether the oxide layer has spalled, leaving either aluminium oxide on the surface, or a deep loss of material. If there is no aluminium oxide on the surface and the surface appears to be consistent with the original, it can be determined that no oxide growth occurred.

This aluminium oxide layer was found to appear as internal oxidation beneath the surface chromium oxide. Internal oxidation occurs when the movement of oxygen inwards in the alloy is significantly greater than the diffusion of reactive species to the surface of the sample (157,158).

Manganese chromite was again found atop the chromium oxide layer for both the Low-Al and High-Al alloys, demonstrating similar oxidation behaviour in the regions of oxide growth, with the major difference being the inconsistent nature of the oxide layer and the substitution of the silicon oxide with an aluminium oxide layer.

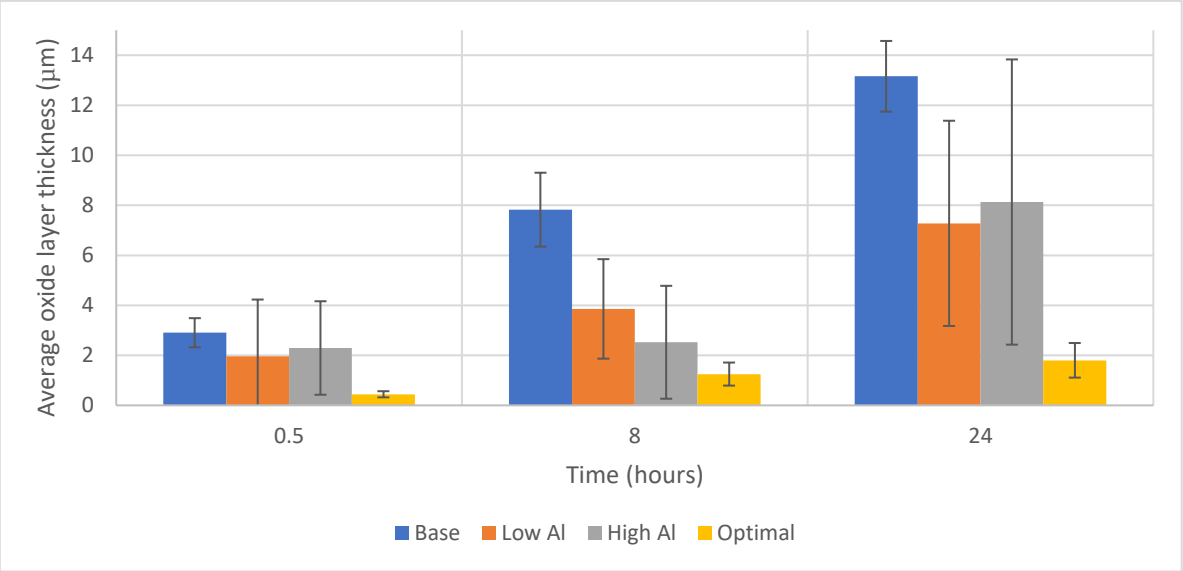

Figure 5.2.2-1: Average oxide layer thickness of all four alloys after 30-minute, 8-hour and 24-hour oxidation at 1100°C

Giggins and Petit (110) reported three different oxidation results when investigating Ni-Cr-Al alloys, dependent on the composition of the oxidised alloy, which were separated into three groups. Group I alloys displayed a NiO surface layer, atop significant internal oxidation, made up of multiple different internal oxidation products. This occurs if the quantity of both aluminium and chromium in the alloy is low. Group II alloys displayed a continuous Cr_2O_3 surface layer, with discontinuous Al_2O_3 internal oxidation beneath, whilst Group III alloys formed a continuous Al_2O_3 layer across the surface of the sample. None of these three groups accurately match the oxidation behaviour seen in the Low-Al and High-Al alloys. Instead, Giggins and Petit describe the observations of oxidation seen in what they described as “transition alloys”; alloys found to have compositions at the boundaries between the different groups. In these transition alloys, the oxide layer was nonuniform and displayed characteristics of each of the different groups (110).

The Optim-Al alloy displayed markedly different oxidation behaviour when compared to both the Base alloy, and the other two aluminium-containing alloys. Whilst all three of the other alloys displayed the formation of chromium oxide on the surface of the alloy, the Optim-Al alloy did not display formation of chromium oxide on the surface, instead producing an aluminium oxide layer across the sample surface (Figure 4.2.1-26-Figure 4.2.1-28). This oxide layer product was confirmed

by the TEM investigation, shown in Figure 4.2.1-31. Instead of being found primarily beneath a chromium oxide, as was the case with the Low-Al and High-Al alloys (Figure 4.2.1-12 and Figure 4.2.1-19), the aluminium layer was consistent across the surface of the alloy, except for where surface breaking NbC particles were present. In these areas, the aluminium oxide layer was formed beneath the NbC particle, maintaining the oxide barrier across the whole sample. This was consistent with the characterisation of Group III alloys (110). This showed that the composition of the Optim-Al alloy has the requisite content of chromium and aluminium to facilitate these oxidation behaviours.

On initial inspection, the Optim-Al alloy does not appear to have greater chromium and aluminium content when compared to the High-Al alloy, and therefore does not logically fit the theory; however, it can be explained by the compositional and microstructural differences of the Optim-Al alloy compared to the Low-Al and High-Al alloys. Whilst chromium content was similar across all three, the content of chromium found in the matrix phase was greater in the Optim-Al alloy than the other two. This, as discussed previously, is a result of the reduced carbon content in this alloy leading to a reduction in chromium carbides throughout, coupled with an increase in the niobium carbide content; both increasing the matrix chromium content (151). The increasing niobium carbide content also further promotes oxide layer formation(159).

This raised chromium in the matrix would initially be assumed to favour the formation of chromium oxide on the surface, but the chromium allows for the third-element effect to occur. This phenomenon is not fully understood; however, its effects have been repeatedly reported (151,160,161). The addition of chromium to an aluminium containing, nickel-based alloy allows the volume of aluminium necessary to form an aluminium oxide to be reduced. Initial expectations would be that the chromium would compete for oxidation, but this is not the observed case. The most common theory is that the chromium, or third element, acts as an oxygen getter, providing

greater oxygen availability at the surface of the alloy and reducing flux of oxygen deeper into the alloy, therefore allowing the aluminium more time to replenish at the surface after initial oxidation (161).

The aluminium oxide layer which forms across the Optim-Al surface is significantly thinner than the chromium oxide layer found atop the Base alloy after oxidation, as demonstrated in Figure 5.2.2-1. As previously discussed, the reduced oxide thickness aids greatly in adhesion of the oxide layer to the matrix during temperature changes, resisting spallation to a greater degree through a reduced stress concentration within the oxide layer or at the interface between the oxide layer and the substrate.

5.3 Effect of conditions on oxidation behaviour

5.3.1 Effect of oxygen partial pressure on oxidation behaviour

As previously discussed, the oxidation behaviour in air is largely dependent on the composition and microstructure of the alloy. The oxidation behaviour can also be affected by the oxidation conditions. Hence, in this research the four alloys were also oxidised at low partial pressures of oxygen to assess the possibility of manipulating the oxidation conditions to form alternate oxidation products than those seen after air oxidation. Some investigations have been done on oxidation of similar alloys in low-PO_2 environments, but these were done at higher partial pressures of oxygen as they were used to inhibit the formation of NiO_2 (101,162). As the formation of nickel oxide has not been observed in the air oxidation due to the high chromium and aluminium contents of the alloys, even lower partial pressures of oxygen, close to the limit of chromium oxidation, were used in this work to inhibit the formation of the chromium oxide and form alternate oxide layers.

It is known that each element has a different limit of oxygen availability at a particular temperature for the oxide to form at equilibrium. Figure 4.2.4-1 shows the Ellingham diagram, displaying the limits of oxygen partial pressures for chromium, aluminium, titanium, manganese and silicon at

800°C. This suggests that aluminium has a significantly lower oxygen presence dependency, in the order of $PO_2 = 10^{-45}$ (red line), whilst chromium is significantly higher at around $PO_2 = 10^{-27}$ (green line), and silicon sits between the two at around $PO_2 = 10^{-35}$ (blue line).

To limit the formation of chromium containing oxides and therefore promote the aluminium or silicon oxide growth on the sample surfaces, all the samples were oxidised at $PO_2 = 10^{-25}$ and $PO_2 = 10^{-23}$ for 24 hours at 800°C, very close to the oxygen limit of chromium oxide production, yet within the working temperature range of the alloys in service.

In both $PO_2=10^{-25}$ and $PO_2=10^{-23}$ oxidation treatments, the Base alloy displayed the formation of an oxide layer on the surface of the oxide (Figure 4.2.4-3 and Figure 4.2.4-7) which was of similar thickness to the oxide layer produced under the same time and temperature conditions. However, this oxide layer was found to be manganese rich, rather than a chromium oxide, with silicon oxide also present. Chromium was only present at the surface when formed as an oxide over a chromium carbide on the exposed surface. This showed that when the oxygen content was on the borderline of the limit for oxidation of chromium, manganese and silicon were able to oxidise preferentially over the chromium, with both elements having a lower limit of oxygen for oxidation.

The Low-Al and High-Al alloys both displayed mixed oxidation when oxidised in air, characterised as “transition alloy” oxidation as described by Giggins and Petit (110). However, by reducing the oxygen content of the environment, the oxidation behaviour of these alloys was markedly changed. The Low-Al alloy displayed a continuous aluminium oxide layer across the surface of the sample, a significantly different outcome when compared to the patchy chromium oxide scale with subsurface internal oxidation of aluminium observed after air oxidation. This oxidation treatment created an oxide layer much more similar to that produced on the Optim-Al alloy, with an aluminium oxide layer across the sample surface. The lower partial pressure of oxygen results in a

reduced oxygen flux into the alloy, and therefore oxidation around surface-breaking NbC particles was not observed, whereas this did occur in air oxidation of Optim-Al.

The High-Al alloy similarly produced an aluminium rich oxide layer across the surface of the alloy after the $PO_2=10^{-25}$ oxidation, unlike the oxide produced after air oxidation. However, when the oxygen partial pressure was raised to $PO_2=10^{-23}$, evidence of the chromium oxide surface scale with subsurface aluminium oxide internal oxidation was present, demonstrating that this alloy will readily oxidise in this manner if the oxygen availability is great enough.

The Optim-Al alloy produced very similar results to air oxidation for both low partial pressures of oxygen oxidation conditions. A thin, continuous oxide was formed across the sample surface, with little evidence of defects or spallation (Figure 4.2.4-21 and Figure 4.2.4-25). This shows the production of the aluminium oxide layer as seen in the air oxidation treatments is not limited by a reduction in oxygen presence to any degree close to service conditions. The aluminium oxide layer is even produced in conditions where very limited oxygen is present. Cai et al. showed that the alumina layer will grow to a thickness limit, dependent on the oxygen pressure, however the growth before that will be uniform, which is in agreement with these observations (65).

These observations of the ability of Optim-Al to form aluminium oxide across the surface in low oxygen environments were further supported by the results of carburisation testing. The Optim-Al alloy was pack-carburised at 1100°C for 200-hours, and despite these conditions, the alloy still produced a surface aluminium oxide layer, as shown in Figure 5.3.1-1. Some loss of surface oxide is evident; however, this is caused by rapid cooling leading to fracture of the oxide. This will be discussed in greater detail later (5.4).

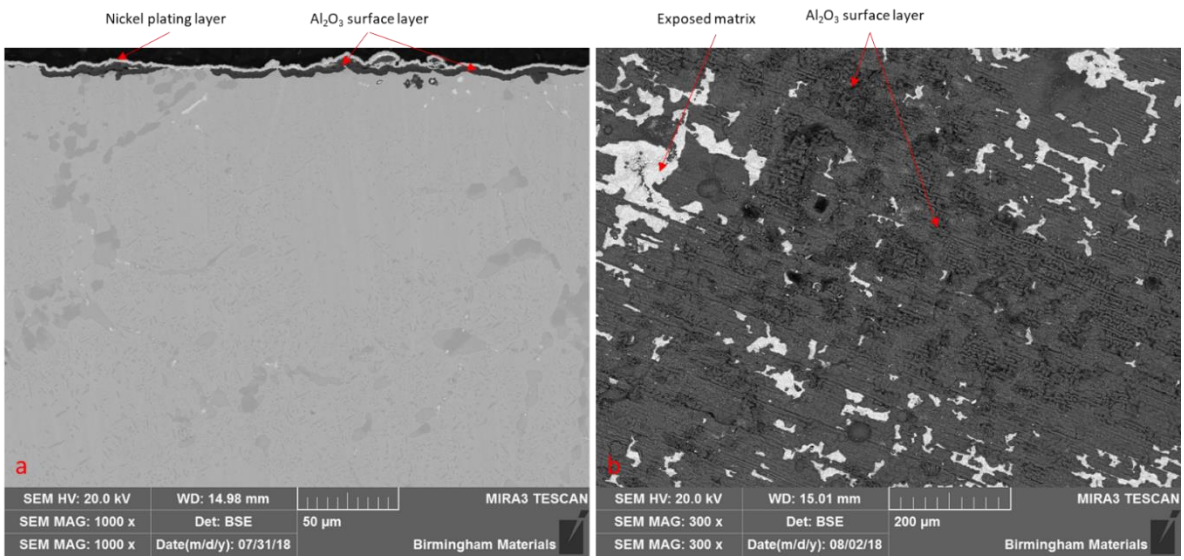

Figure 5.3.1-1: SEM backscattered images of gas carburised Optim-Al alloy; (a) cross section and; (b) surface

5.3.2 Effect of time and temperature on oxidation behaviour

High temperature oxidation of all four alloys proved that the Optim-Al alloy produced the most consistent aluminium oxide layer, and therefore the effect of differing temperatures and times on oxidation behaviour of this alloy compared to the Base alloy was undertaken. The alloys were oxidised at 800°C, 950°C and 1100°C for times ranging from 1 hour to 48 hours to track the changes of the oxide layer over time.

The Base alloy displayed growth of a chromium oxide, which was topped by a manganese chromite layer, evident in all samples oxidised for longer than 4 hours at 800°C, and at all times for the higher temperatures. This shows the initial formation of the chromium oxide layer precedes that of the manganese chromite layer, which grows atop the chromium oxide during oxidation.

The subsurface silicon oxide layer changed drastically in nature between the temperatures. In the 800°C and 950°C oxidation treatments, the silicon layer was found in a thin layer beneath the chromium oxide layer at all oxidation times. However, oxidation at 1100°C resulted in the silicon oxide forming as internal oxidation, appearing globular in nature and within the matrix just beneath the chromium oxide layer. This shows that the increased oxidation temperature allows the

oxidation of silicon to occur more rapidly than the flux of silicon to the matrix-chromia interface, therefore the silicon oxidises deeper than that seen at the lower temperatures.

Thickness and growth rate of the chromium oxide layer increases significantly with increased temperature. All three oxidation temperatures displayed a similar parabolic pattern of growth, with a rapid initial growth rate through the first 8 hours, followed by a reduction (shown in Figure 5.3.2-1). This parabolic growth rate suggests that the oxidation kinetics are governed by diffusion (163) which reinforces the observations of the change in nature of the silicon oxide layer.

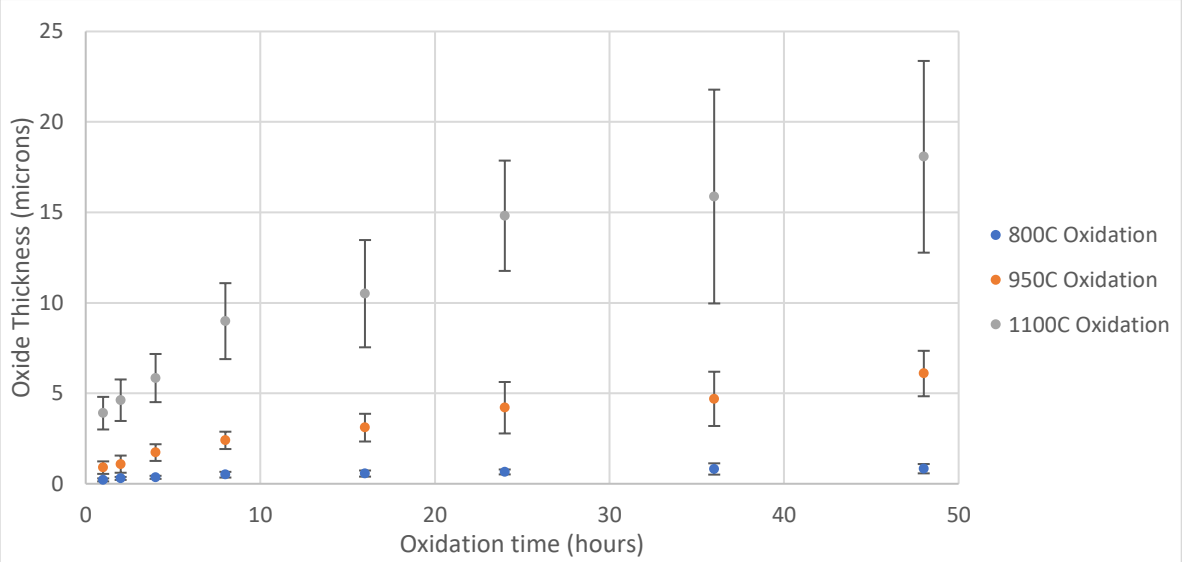

Figure 5.3.2-1: Graph comparing growth rates of oxide layer in Base alloy at 800°C, 950°C and 1100°C

The 1100°C oxidation oxide thickness growth graph appears to show a step up between the 16-hour and 24-hour oxidation, which initially was interpreted as an outlier, however the alloy was also tested in the same conditions by thermogravimetric analysis, which confirmed the rapid increase in mass gain at around the 21-hour mark (Figure 5.3.2-2). When comparing this to the cross-sectional images, there appeared to be no significant change in the manganese chromite thickness between the 16-hour oxidation and the 48-hour oxidation, whereas the chromium oxide layer continued to grow. This sudden jump in mass gain is proposed to be a result of the exhaustion of available manganese in the near surface region, and therefore the chromium oxide was able to

grow without competition for the first time at this temperature. This allowed growth rates similar to the initial rate for a short period, before tapering off to a similar, consistent oxide thickening (as seen previously).

The rapid mass gain at this temperature is thought not to be a result of spallation allowing fresh matrix to be exposed to the air environment, as the magnitude of the mass gain was greater than the initial oxidation rate. Furthermore, as seen previously, the volume of spalled oxide increases over time rather than occurring at a singular event, whereas this step change suggests a unique change in oxidation behaviour at this point.

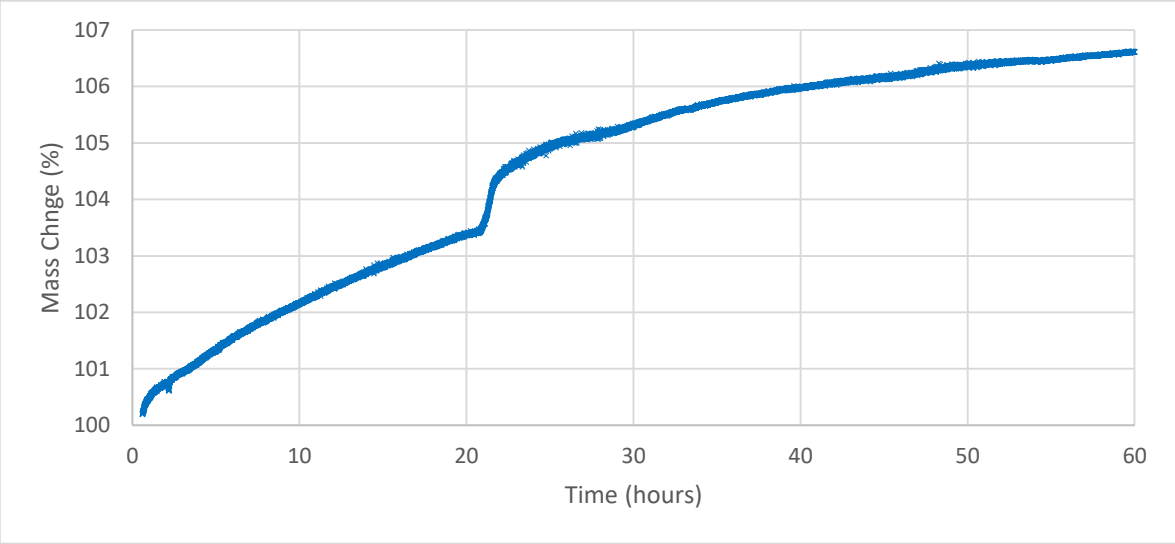

Figure 5.3.2-2: Graph of TGA (thermogravimetric analysis) of oxidation of Base alloy at 1100°C for 60 hours

Whilst the oxide layer of the Base alloy showed increased oxide thickness as both oxidation time and temperature were increased, the oxide layer clearly suffered from spallation with these increases. All samples oxidised at 800°C displayed maintenance of the oxide layer across the entire sample surface, however all the samples oxidised at 950°C for 4 hours and longer, as well as all samples oxidised at 1100°C regardless of time, displayed increasing volumes of spalled material, exposing the matrix beneath. This spallation consistently occurred around surface features of the sample, in this case the machining marks on the surface of the internal diameter of the pipe. The cause for this will be discussed later.

The Optim-Al alloy displayed formation of the aluminium oxide layer, rather than the chromium oxide layer, without a sub-surface oxide layer. This layer covered the entire surface of the samples except for where NbC particles were present at the surface. At these points, the aluminium oxide layer was formed beneath the NbC particle, maintaining a protective layer across the matrix throughout the alloy. This demonstrates ideal behaviour for creating a physical barrier between the matrix and the gas stream in service.

The aluminium oxide layer maintained the same appearance throughout all oxidation lengths at 800C° and 950°C, however after longer oxidation times (beyond 16 hours) at 1100°C a secondary oxide layer was observed to form. This secondary oxide was identified as being the spinel phase $NiAl_2O_4$, which formed atop the aluminium oxide layer. This secondary oxide did not appear to have any effect on the aluminium oxide layer beneath, but instead grew atop the first oxide. The formation of this secondary oxide with elongated oxidation times and high temperature is due to the solubility of nickel in the aluminium oxide coupled with the depletion of available aluminium, resulting in the spinel phase evolution becoming kinetically favourable, facilitated by the high temperature. This phase has been studied as a catalyst for steam reforming of other hydrocarbons, therefore its presence is seen as potentially beneficial, rather than deleterious (77).

The spallation and loss of oxide from the surface during oxidation was significant for the Base alloy, particularly at higher temperatures and oxidation times. The Optim-Al alloy did display some oxide loss after oxidation at 1100°C, particularly after the 8-hour oxidation and longer, however this is a much more stressful onset condition compared to the Base alloy, and the volume of oxide lost was significantly lower for the Optim-Al alloy compared to the Base alloy.

The oxide layer growth rate, as show in Figure 5.3.2-3, demonstrates the formation of the spinel phase with the oxide layer growth rate being maintained for longer than the Optim-Al alloy when oxidised at lower temperatures. The 800°C and 950°C samples initially displayed more rapid growth

rate, before plateauing at around 16-hours, whereas the growth of the oxide layer on the samples oxidised at 1100°C showed prolonged maintenance of this higher growth rate, which was mirrored in the mass gain plotted from the TGA (thermogravimetric analysis) experiments Figure 5.3.2-4. The slight drop at around 2 hours in was explained in 4.2.2.2.3.

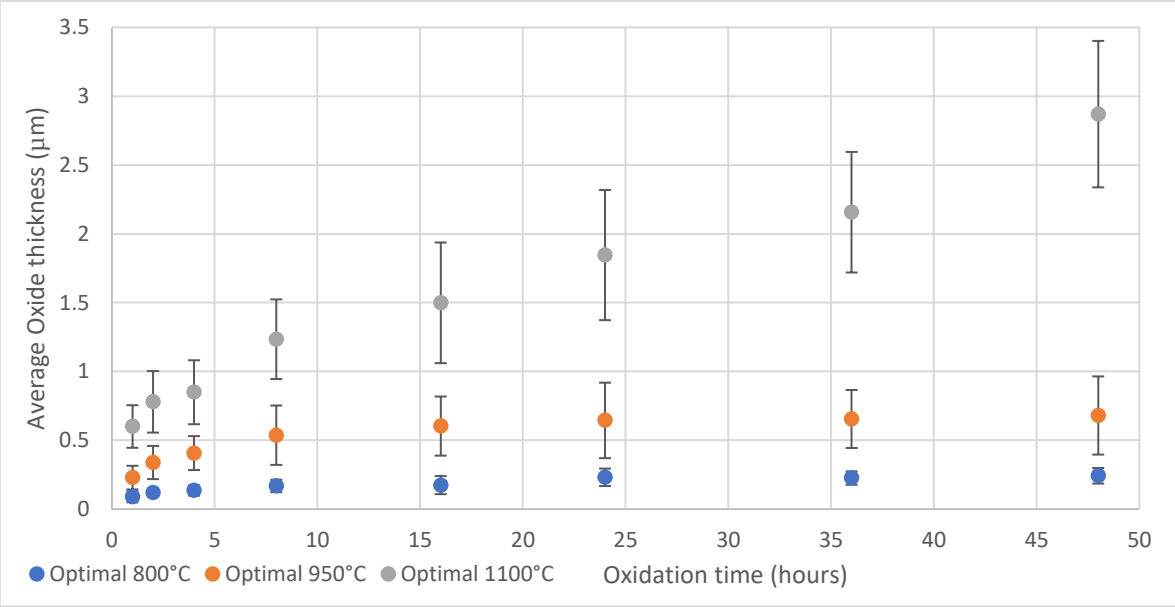

Figure 5.3.2-3: Graph comparing Optim-Al alloy average oxide layer thickness over time at 800°C, 950°C and 1100°C

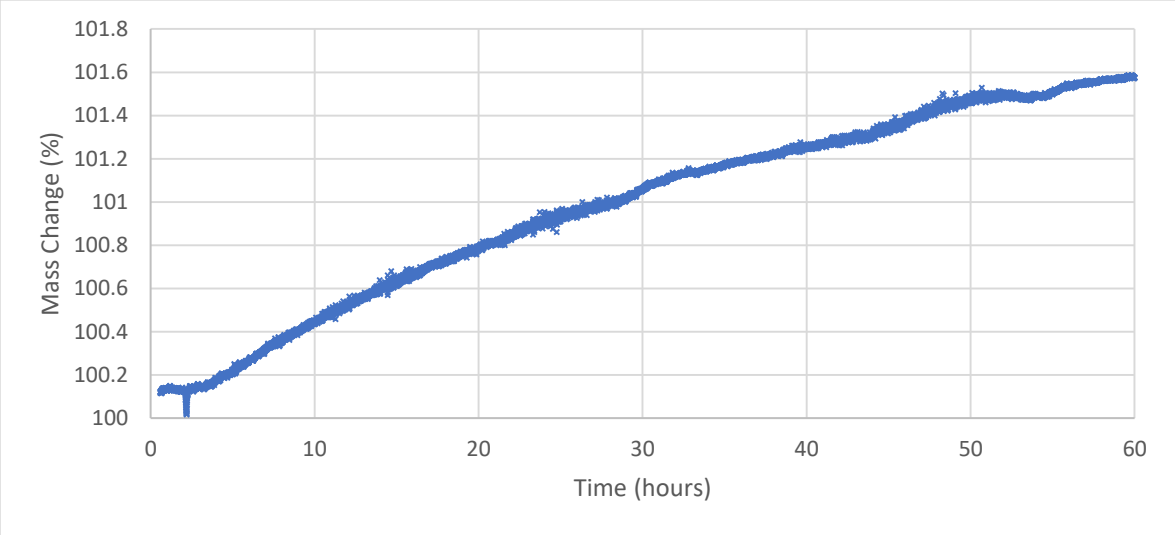

Figure 5.3.2-4: Graph of TGA (thermogravimetric analysis) measurement of Optim-Al alloy oxidised at 1100°C for 60 hours

The difference in oxide layer thickness between the Base alloy and Optim-Al alloy was stark, as seen in Figure 5.3.2-5. The chromium oxide layer on the Base alloy was thicker at all oxidation times for

the same temperature than the aluminium oxide layer on the Optim-Al alloy. Furthermore, the oxide layer of the Base alloy oxidised at 950°C was twice as thick as that on the Optim-Al alloy oxidised at 1100°C, demonstrating the significant difference seen in both oxide layer thickness and oxide growth rate. This distinct reduction in oxide layer thickness produced on the Optim-Al alloy signifies a much greater likelihood for oxide layer maintenance due to reduced spallation, with a lower chance of fracturing and loss of oxide during cool down of the pipes, as discussed previously.

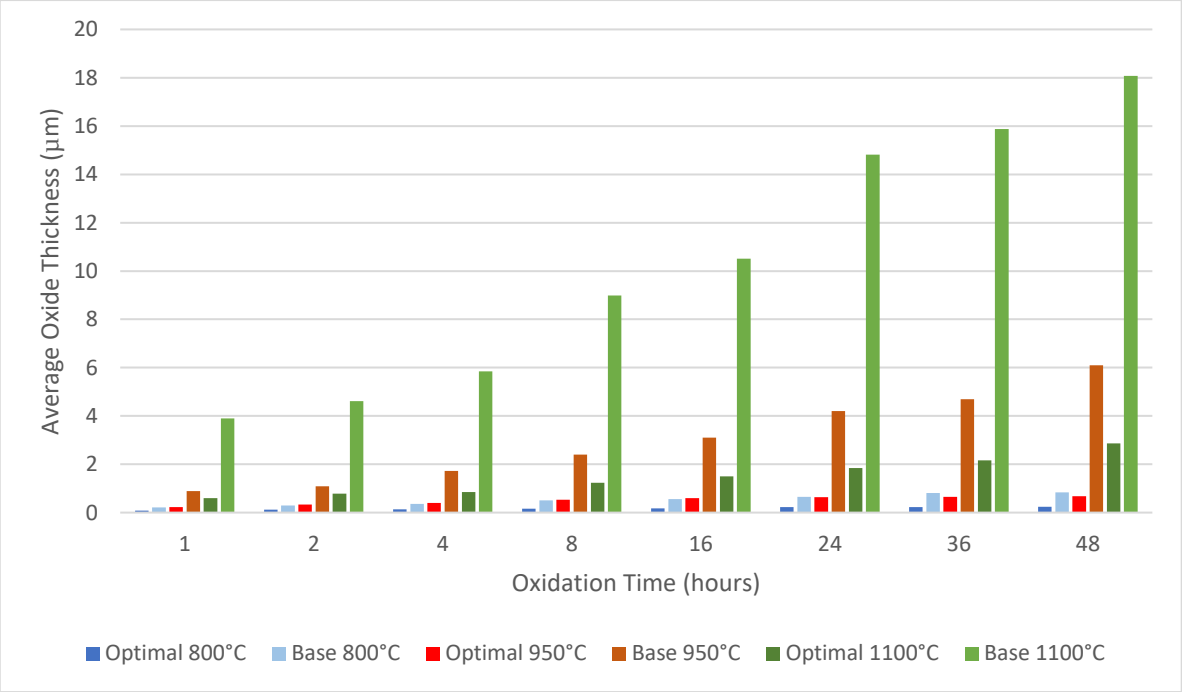

Figure 5.3.2-5: Graph of average oxide layer thickness for Base and Optim-Al alloys oxidised at 800°C, 950°C and 1100°C

5.4 Oxide layer adhesion

The adhesion or bonding of surface oxide layers to the substrate is paramount for the protective properties of the tube alloy from catalytic carburisation. As identified previously, both the Base and Optim-Al alloy displayed complete coverage of the sample surface after oxidation, but they both showed some signs of spallation and loss of oxide layer from the surface to varying degrees. As reported in 4.2.2.3, the Base alloy displayed widespread oxide loss, centred around the machining marks on the surface of the alloy at both 950°C and 1100°C oxidation, increasing in volume with increased time and temperature. This spallation of oxide layer is in keeping with Evans'

observations of chromium oxide spallation. He found that a chromia layer 6μm in thickness would spall after a temperature change of around 200°C, whilst the oxide thickness of the Base alloy was measured up to 18μm after 48 hour oxidation at 1100°C, demonstrating clear prospects of spallation during cool down (103).

Meanwhile, the Optim-Al alloy only displayed oxide losses at 1100°C oxidation, and this loss was once again found around the machining marks on the alloy surface. Cross sectional imaging of the Optim-Al alloy showed no signs of matrix exposed at the surface (see Figure 4.2.2-35), suggesting the ability of the alloy to re-passivate, and the apparent exposed matrix was just the site of much thinner aluminium oxide, with much of the SEM interaction volume occurring in the matrix beneath (similar to that observed in Figure 4.2.2-22 after oxidation at 800°C). In contrast, both the Low-Al and High-Al alloys formed patchy, discontinuous oxides on the surface, leaving areas of matrix exposed after oxidation.

Scratch tests on all four alloys were completed to evaluate the bonding strength and adhesion of the oxide layer to the bulk matrix beneath, and hence demonstrate a greater resistance to spallation and oxide loss.

The appearance of the scratch test marks on the Base alloy are in line with buckling failure followed by spallation buckling failure of the oxide, as described by Bull, illustrated in Figure 4.2.3-13 (135,136). This is characterised by failure in an arc ahead of the contact point, followed by lateral spread of the scratch track of the spalled material. This failure indicates high tensile stresses within the oxide layer, released by through-thickness cracks created by the stress applied in the test. The greater thickness of the chromium oxide layer compared to the other alloys is also likely to be a factor, with its potential for greater internal stresses.

As half of all surface oxide layer material in the scratch track was lost at an average force of 10N across the three scratches on the Base alloy, the bonding between the oxide and matrix can clearly

be considered as poor. The oxide is likely to experience some impact forces during the cleaning process, where the coke layer is burned out, with debris likely to be moving through the pipe at a significant speed, and therefore impacts with the pipe are likely to lead to removal of the protective oxide layer beyond that lost through spallation.

Both the Low-Al and High-Al alloys, whilst not demonstrating formation of a fully encapsulating oxide, showed significantly greater resistance to oxide loss compared to the Base alloy, maintaining the formed oxide through to forces of 25N and 20N respectively - more than twice that of the Base alloy. When considering the nature of the oxides formed, this suggest that the aluminium oxide layer produced beneath the scales of chromium oxide on the Low-Al and High-Al alloy has a greater bond to the matrix than the silicon oxide layer does beneath the chromium oxide on the Base alloy, as the matrix was protected until a significantly greater force was applied.

The Optim-Al alloy showed the greatest resilience to the scratch test, maintaining an oxide across the sample until applied forces were greater than 30N, three times that of the Base alloy. The oxide layer also displayed conformal cracking, rather than buckling of the oxide as observed with the other three alloys. The oxide layer was not removed from its initial site, instead the force of the scratch test led to fracturing of the oxide in place, demonstrating significantly greater adhesion between the oxide layer and the bulk matrix, with through thickness failure occurring and without debonding.

The results of the adhesion of the oxide layer and the observed spallation differences between the Base and Optim-Al alloys reinforce the Pilling-Bedworth ratio calculations (4.2.3.3). These confirmed that although both oxides were in the adherent range, the aluminium oxide was closer to a one to one match in volume, therefore generating less internal stresses upon formation on the alloy surface. Greater internal stresses would lead to easier oxide fracture and debonding, as demonstrated in the chromium oxide when compared to the aluminium oxide.

As the spallation in the high temperature oxidation treatments was found to be centred around the machining marks, the effect of surface roughness of the sample on oxide adhesion was undertaken for the Optim-Al alloy. Whilst the machined sample had a roughness of Ra=0.52, it displayed significantly greater loss of oxide than the Optim-Al alloy with lower roughness. At all three roughness levels, the lost material shared at least one border with a scratch, machining mark, or other defect on the surface of the sample. The machined sample had significantly deeper scratch marks than the other two ground samples, by nature of the machining process. It is hypothesized that as the sample surface oxidises, the walls of the scratch or machining mark will also oxidise, and as the oxide layer thickens, pressure builds up as the two opposing oxides come into contact with one another in the scratch. As the oxide continues to thicken with time, the pressure reaches a critical point at which the oxide ruptures outwards, and in doing so fractures the oxide and de-bonds it from the bulk material. This process is illustrated in Figure 4.2.3-7. This proposed mechanism is similar to that described by Evans on the spallation of oxide scale under compression in a concave curved section (103).

5.5 Industrial benefits of the Optim-Al alloy

Whilst no specific anti-coking tests were completed in this investigation, alumina has continually been shown to provide greater protection than chromia, particularly in the humid environments such as those experienced during ethylene steam cracking (23,64,105,113,164–166). It was important therefore that the oxidation behaviour of the alloys being investigated showed the following requirements – ease of formation, strong adhesion and resistance to spallation.

This investigation found the Optim-Al alloy produced a stable, adherent and dense oxide layer covering the surface of the substrate. Han et al. investigated an alloy which was unable to maintain the aluminium oxide, which spalled and eventually gave way to chromium oxide and then nickel through subsequent aluminium and chromium depletion (167). The Optim-Al alloy has shown the

ability to maintain a protective aluminium oxide layer across the sample surface, particularly at temperatures in the operating range of ethylene cracker furnaces. Furthermore, despite evidence of spallation at higher temperatures, the oxide layer appeared to re-passivate (as also found by Chyrkin et al. (111)), demonstrating the ability for the Optim-Al alloy to potentially heal over regions of spalled oxide scale, further supported by the cyclic oxidation testing (4.2.4.2.2). This is reinforced by the observations of alumina forming alloys which did not demonstrate an aluminium depleted zone beneath the surface oxide in the way that chromium does (107,168,169).

Whilst low partial pressure of oxygen oxidation regimes were investigated and found to be beneficial for promotion of an aluminium oxide layer on the surface of the Low-Al and High-Al alloys, such conditions were proven to be unnecessary for the Optim-Al alloy. This was successful when oxidising in forming an adherent, dense aluminium oxide layer across the alloy surface when oxidised in air conditions. This is significantly important, as this foregoes the need for expensive or complex pre-service treatments to elicit the production of the desired protective oxide layer on the Optim-Al alloy. Furthermore, the investigation into effect of oxidation time and temperature (4.2.2.2) demonstrated the oxidation conditions required for optimal oxide growth to be in the region of 800°C, the typical operating temperature. The pre-oxidation time also appears to be minimal, with a fully covering, albeit very thin, oxide layer formed after just one-hour oxidation at 800°C being observed in Figure 4.2.2-25. These results all demonstrate the significant improvement in anti-coking protection of the Optim-Al alloy over those currently used in the industry.

Surface finish of the inner diameter of the pipes appears to play a significant role in the adhesion and maintenance of the oxide layer on the pipe surface. A smoother internal finish limits the initiation sites for spallation to occur through build up in stresses in the oxide. A smoother surface will enable the oxide layer to be maintained and therefore continue to provide a barrier between the gas stream and the catalytic elements of nickel and iron in the matrix.

6 Conclusions and future work

6.1 Conclusions

- Addition of aluminium to the Ni-Cr-Fe alloy in too great a quantity results in the formation of the brittle Ni_3Al phase. If this phase is formed throughout the alloy in large volume fractions, the alloy will not have the properties required for service conditions.
- Increased aluminium content causes an increase in volume of carbides in the alloy, due to less availability for chromium to dissolve into the matrix, superseded by the aluminium. Increased aluminium content also reduces solidus and liquidus temperatures of the alloys, further promoting greater carbide formation.
- Slower solidification rates of the alloy coupled with adequate availability of chromium and carbon result in chromium carbides precipitating in a Chinese-scrip style morphology through growth in the interdendritic regions of the matrix.
- Increased chromium carbide volume fraction results in reduced niobium carbide volume fraction. This reduction in niobium carbides negatively effects the oxidation behaviour of the alloy, as niobium carbides at grain boundaries act as barriers to diffusion of elements such as nickel and iron, therefore inhibiting their impact on surface oxidation products.
- The Base alloy forms an outwardly growing chromium oxide layer, which is fuelled by the dissolved chromium in the matrix and by dissolving near surface chromium carbides. A manganese chromite ($MnCr_2O_4$) layer forms atop the chromium oxide layer.
- The manganese chromite layer displays poor bonding to the chromium oxide layer, when compared to that of the chromium oxide layer to the substrate surface.
- The Base alloy displayed a two-stage oxidation process, which appeared to be caused by the exhaustion of the manganese, allowing chromium oxide to form without competition. This occurred after 21 hours at 1100°C.

- Addition of aluminium to the alloy does not guarantee the formation of surface aluminium oxide in favour of chromium oxide. The chromium dissolved in the matrix, as a function of the chromium carbide production, has a significant effect. If there is enough matrix-dissolved chromium acting by the third element effect, and precipitated niobium carbides inhibiting elemental diffusion, an aluminium oxide layer can form on the alloy.
- An aluminium oxide layer is formed as a significantly thinner oxide than chromium oxide, on the surface of the invesigated alloys. This is particularly beneficial due to the importance of the maintenance of the oxide layer, which is impacted by the thermal coefficient of expansion differences between the alloy and the oxide layer, with a thicker oxide layer exacerbating these differences.
- Low partial pressure of oxygen oxidation treatments can be used to elicit a continuous aluminium oxide layer on aluminium containing alloys which otherwise do not display this behaviour when oxidised in air. Internal oxidation is also supressed due to the limited oxygen availability. This treatment is not necessary for the Optim-Al alloy however, due to its ability to form an aluminium oxide layer in air oxidation.
- An $NiAl_2O_4$ spinel phase was found to form atop the aluminium oxide layer after extended oxidation at high temperatures. This phase has been used as a catalyst in hydrocarbon reforming in other work.
- Oxide growth rates increase with increasing temperatures for both chromium oxide forming and aluminium oxide forming alloys, however higher temperatures resulted in greater spallation of the oxide layer for all alloys investigated, but particularly the chromium oxide forming Base alloy.
- Spallation of the oxide layer was much more widespread, and seen at lower temperatures, for the chromium oxide layer of the Base alloy when compared to the aluminium oxide layer of the Optim-Al alloy. All spallation observed appeared to initiate around surface

machining marks. A mechanism for this behaviour has been suggested. Suggested improvements to the surface finish of the substrate to remove the machining marks is hypothesized to reduce spallation or inhibit it completely.

- Adhesion of the aluminium oxide layer was significantly greater than that of the chromium oxide layer, particularly on the Optim-Al alloy.
- The adherent and fully covering thin aluminium oxide layer produced on the Optim-Al alloy after air oxidation represents a significant improvement for anti-coking behaviour over the currently used Base alloy.

6.2 Future Work

Examination of the effects of surface treatments to the oxidation behaviour of Optim-Al alloy must be explored further, to fully understand the ideal oxidation conditions of the alloy. Furthermore, the repassivation characteristics of the alloy should be explored, to determine the extent to which the Optim-Al alloy is able to lose and reform the aluminium oxide layer before exhaustion of aluminium depletion. The mechanical properties of the alloy in such conditions should also be examined to evaluate any potential degradation in necessary properties.

In-situ coking testing must be completed to validate the conclusions of the improvement in coking resistance of the Optim-Al alloy. Such research was unable to be completed in this body of work due to the complexities of creating an accurate rig to test the alloys.

The long-term creep properties of this alloy should be assessed to confirm its superiority to the other alloys currently used in industry from both an anti-coking and mechanical performance point of view.

7 List of References

1. Geyer R, Jambeck JR, Law KL. Production, use, and fate of all plastics ever made. Sci Adv. 2017;3(July):25–9.

2. Federation BP. Oil Consumption [Internet]. 2019 [cited 2019 Sep 21]. Available from: https://www.bpf.co.uk/press/oil_consumption.aspx

3. icis.com. Ethylene Uses and Market Data [Internet]. 2010 [cited 2019 Sep 21]. Available from: https://www.icis.com/explore/resources/news/2007/11/05/9075777/ethylene-uses-and-market-data

4. Ceresana. Market Study : Ethylene 2nd Edition [Internet]. 2014. Available from: https://www.ceresana.com/en/market-studies/chemicals/ethylene/ethylene-market-share-capacity-demand-supply-forecast-innovation-application-growth-production-size-industry.html

5. Reporter P. The Ethylene Technology Report 2016 [Internet]. 2016. Available from: https://www.researchandmarkets.com/research/2xl4dr/the_ethylene

6. Markit I. Chemical Economics Handbook - Ethylene [Internet]. 2019. Available from: https://ihsmarkit.com/products/ethylene-chemical-economics-handbook.html

7. Alshammari A, Kalevaru VN, Bagabas AA. Petrochemical Catalyst Materials , Processes , and Emerging Technologies. 2016.

8. Geyer R, Jambeck JR, Law KL. Supplementary Materials for Production, use, and fate of all plastics ever made. 2017;1700782(July):19–24.

9. Olah GA, Molnár Á. Hydrocarbon Chemistry [Internet]. Second. Hoboken, NJ, USA: John Wiley & Sons, Inc.; Available from:

https://books.google.co.uk/books?hl=en&lr=&id=KSrTF6ZmkrwC&oi=fnd&pg=PR5&dq=olah+and+molnar&ots=EsrGHuwgLf&sig=U7Wuy9i7pcdhmmqewFHDhM93VUs#v=onepage&q=olah and molnar&f=false

10. Abghari S. Investigation of Coke Formation in Steam Cracking of Atmospheric Gasoil. J Pet Sci Res. 2013;2(2):82–91.

11. Otegui JL, Bona J De, Fazzini PG. Effect of coking in massive failure of tubes in an ethylene cracking furnace. Eng Fail Anal [Internet]. 2015 Feb [cited 2016 Jan 8];48:201–9. Available from: http://www.sciencedirect.com/science/article/pii/S1350630714003380

12. Kosmac A. Stainless Steels at High Temperatures. Vol. 18. 2012. 36 p.

13. Klueh RL, Harries DR. Development of High 7-12% Chromium Martensitic Steels. High-chromium Ferritic Martensitic Steels Nucl Appl. 2001;5–29.

14. Sims CT. A History of Superalloy Metallurgy for Superalloy Metallurgists. Superalloys 1984. 1984;399–419.

15. Bullock E, Brunetaud R, Conde JF, Keown S., Pugh SF. Research and Development of High Temperature Materials for Industry [Internet]. London and New York: Elsevier Science Publishers Ltd; 1989. 680 p. Available from: https://books.google.co.uk/books?id=iTTwCAAAQBAJ&printsec=frontcover&dq=Research+and+Development+of+High+Temperature+Materials+for+Industry&hl=en&sa=X&ved=0ahUKEwiF-Lql7c3kAhXSnFwKHVZxAR8Q6AEIKjAA#v=onepage&q=Research and Development of High Temperature M

16. Meetham GW, Van de Voorde MH. Materials for High Temperature Engineering Applications. Illustrate. Springer Science & Business Media; 2012.

17. Simcoe CR. The History of Alloy Steels : Part I. 2014;(July):34–5.

18. De Almeida LH, Ribeiro AF, Le May I. Microstructural characterization of modified 25Cr-35Ni centrifugally cast steel furnace tubes. Mater Charact. 2002;49(3):219–29.

19. Garbiak M, Jasi W, Piekarski B. Materials for Reformer Furnace Tubes . History of evolution. 2011;11(2):47–52.

20. Kolmetz K, Kivlen J, Gray J, Sim CP, Soyza CA. Advances in Cracking Furnace Technology. In: Refining Technology Conference. Dubai; 2002.

21. Li CS, Yang YS. A glass based coating for enhancing anti-coking and anti-carburizing abilities of heat-resistant steel HP. Surf Coatings Technol. 2004;185(1):68–73.

22. Ma L, Lv WJ, Yang Q, Fan Y. Study of SiO_2 coat preparation and its anti-coking behaviour. Mater Res Innov [Internet]. 2014;18(S2):S2-527-S2-531. Available from: http://www.maneyonline.com/doi/abs/10.1179/1432891714Z.000000000483

23. Muñoz Gandarillas AE, Van Geem KM, Reyniers M-F, Marin GB, Gandarillas EM, Geem KM Van. Influence of the Reactor Material Composition on Coke Formation during Ethane Steam Cracking. Ind Eng Chem Res [Internet]. 2014 Apr 16 [cited 2016 Jan 8];53(15):6358–71. Available from: http://dx.doi.org/10.1021/ie500391b

24. Song R, Wu S. Microstructure evolution and residual life assessment of service exposed Cr35Ni45 radiant tube alloy. Eng Fail Anal [Internet]. 2018;88(September 2016):63–72. Available from: https://doi.org/10.1016/j.engfailanal.2018.01.002

25. Masuyama F. History of Power Plants and Progress in Heat Resistant Steels. 2001;41(6):612–25.

26. Wang F, Northwood DO. The Effect of Carbon Content on the Microstructure of an Experimental Heat-Resistant Steel. 1993;10:3–10.

27. Bonaccorsi L, Guglielmino E, Pino R, Servetto C, Sili A. Damage analysis in Fe – Cr – Ni centrifugally cast alloy tubes for reforming furnaces. Eng Fail Anal [Internet]. 2014;36:65–74. Available from: http://dx.doi.org/10.1016/j.engfailanal.2013.09.020

28. Zhi X, Xing J, Fu H, Xiao B. Effect of niobium on the as-cast microstructure of hypereutectic high chromium cast iron. Mater Lett [Internet]. 2008;62(6–7):857–60. Available from: http://linkinghub.elsevier.com/retrieve/pii/S0167577X07006945

29. Jones DRH, Ashby M. Engineering materials. 1993.

30. Alnegren P. Oxidation behavior of selected FeCr alloys in environments relevant for solid oxide electrolysis applications. Chalmers University of Technology; 2012.

31. Freche JC. Progress in superalloys. 1964;(October).

32. Appleby W, Gibson J, Good G. Coke formation in catalytic cracking. Ind Eng … [Internet]. 1962;102–10. Available from: http://pubs.acs.org/doi/abs/10.1021/i260002a006

33. Nunes FC, Almeida LH De, Dille J, Delplancke J, May I Le. Microstructural changes caused by yttrium addition to NbTi-modified centrifugally cast HP-type stainless steels Microstructural changes caused by yttrium addition to NbTi-modified centrifugally cast HP-type stainless steels. 2007;(February).

34. Golightly FA, Stott FH, Wood GC. The influence of yttrium additions on the oxide-scale adhesion to an iron-chromium-aluminum alloy. Oxid Met. 1976;10(3):163–87.

35. Stott FH, Wei FI, Enahoro CA. The influence of manganese on the high-temperature oxidation of iron-chromium alloys. Werkstoffe und Korrosion. 1989;40:198–205.

36. Wilson PR, Chen Z. The effect of manganese and chromium on surface oxidation products formed during batch annealing of low carbon steel strip. Corros Sci. 2007;49:1305–20.

37. Smialek JL. Maintaining Adhesion of Protective Al 2 O 3 Scales. 2000;

38. Goswami A, Kumar S. Failure of pyrolysis coils coated with anit-coking film in an ethylene cracking plant. Eng Fail Anal [Internet]. 2014 Apr [cited 2015 Dec 4];39:181–7. Available from: http://dx.doi.org/10.1016/j.engfailanal.2014.01.019

39. Bjärbo A, Hättestrand M. Complex carbide growth, dissolution, and coarsening in a modified 12 pct chromium steel—an experimental and theoretical study. Metall Mater Trans A [Internet]. 2001;32(1):19–27. Available from: http://link.springer.com/10.1007/s11661-001-0247-y

40. Venkatraman M, Neumann JP. The C-Cr (Carbon-Chromium) System. 1990;11(2):152–3.

41. Reihani A, Haghighi RD. Failure analysis and weld ability improvement of 35 % Cr – 45 % Ni heat resistant alloy. Eng Fail Anal [Internet]. 2015;52:97–108. Available from: http://dx.doi.org/10.1016/j.engfailanal.2015.03.005

42. Sabol GP, Stickler R. Microstructure of Nickel-Based Superalloys. Phys status solidi [Internet]. 1969 [cited 2015 Nov 22];35(1):11–52. Available from: http://doi.wiley.com/10.1002/pssb.19690350102

43. Lagneborg R, Bergman B. The stress creep rate behaviour of precipitation hardened alloys. Met Sci. 1976;20.

44. Powell GLF, Laird II G. Structure , nucleation , growth and morphology of secondary carbides in high chromium and Cr-Ni white cast irons. 1992;27:29–35.

45. Monobe LS, Schön CG. Microstructural and fractographic investigation of a centrifugally cast 20Cr32Ni + Nb alloy tube in the “as cast” and aged states. J Mater Res Technol. 2013;

46. Babakr AM, Al-Ahmari A, Al-Jumayiah K, Habiby F. Sigma Phase Formation and

Embrittlement of Cast Iron-Chromium-Nickel (Fe-Cr-Ni) Alloys. J Miner Mater Charact Eng [Internet]. 2008;07(02):127–45. Available from: http://www.scirp.org/journal/PaperDownload.aspx?DOI=10.4236/jmmce.2008.72011

47. Donachie MJ, Donachie S. Superalloys - A Technical Guide (2nd Edition) [Internet]. 2nd Editio. ASM International; 2002. Available from: https://app.knovel.com/web/toc.v/cid:kpSATGE003/viewerType:toc/root_slug:superalloys-technical/url_slug:kt008GQS51

48. Manufacturing TL of. True Centrifugal Casting [Internet]. [cited 2015 Aug 30]. Available from: http://thelibraryofmanufacturing.com/true_centrifugal_casting.html

49. Trejo E. Centrifugal Casting of an Aluminium Alloy. University of Birmingham; 2011.

50. Kapranos P, Carney C, Pola A, Jolly M. Investment casting, centrifugal casting, squeze casting, metal spinning and batch casting. In: Advanced Casting Methods. 2014. p. 39–67.

51. Seifzadeh Haghighi S, Rahimpour MR, Raeissi S, Dehghani O. Investigation of ethylene production in naphtha thermal cracking plant in presence of steam and carbon dioxide. Chem Eng J [Internet]. 2013;228:1158–67. Available from: http://dx.doi.org/10.1016/j.cej.2013.05.048

52. Jakobi D, Gommans R. Typical failures in pyrolysis coils for ethylene cracking. Mater Corros. 2003;54(11):881–6.

53. Alselaa RAM, Elfghi FM. Reduction of Coke Accumulation and Energy Resources by Adding Steam and Carbon Dioxide in Naphtha Based Ethylene Production [Internet]. Vol. 28, Chemical and Process Engineering Research. 2014 [cited 2016 Jan 8]. p. 21–31. Available from: http://iiste.org/Journals/index.php/CPER/article/view/17090

54. Kopinke F, Zimmermann G. Relative rates of coke formation from hydrocarbons in steam

cracking of naphtha. 2. Paraffins, naphthenes, mono-, di-, and cycloolefins, and acetylenes. Ind … [Internet]. 1993;32:56–61. Available from: http://pubs.acs.org/doi/abs/10.1021/ie00013a009

55. Reyniers GC, Froment GF, Kopinke F-D, Zimmermann G. Coke Formation in the Thermal Cracking of Hydrocarbons. 4. Modeling of Coke Formation in Naphtha Cracking. Ind Eng Chem Res [Internet]. 1994 Nov [cited 2016 Jan 8];33(11):2584–90. Available from: http://pubs.acs.org/doi/abs/10.1021/ie00035a009

56. Kopinke FD, Zimmermann G, Nowak S. On the mechanism of coke formation in steam cracking—conclusions from results obtained by tracer experiments. Carbon N Y. 1988;26(2):117–24.

57. Rostrup-Nielsen JR. Industrial relevance of coking. Catal Today. 1997;37(3):225–32.

58. Rostrup-Nielsen, Jens R. ; Trimm DL. Mechanisms of carbon formation on nickel-containing catalysts. J Catal [Internet]. 1977;48(1–3):155–65. Available from: http://www.sciencedirect.com/science/article/pii/0021951777900872

59. Wu XQ, Jing HM, Zheng YG, Yao ZM, Ke W. Coking of HP tubes in ethylene steam cracking plant and its mitigation. Br Corros J [Internet]. 2001 Feb 18 [cited 2015 Dec 4];36(2):121–6. Available from: http://www.maneyonline.com/doi/abs/10.1179/000705901101501541

60. Sundaram KM, Van Damme PS, Froment GF. Coke Deposition in the Thermal Cracking of Ethane. 1981;27(6):946–51.

61. Manafzadeh H, Sadrameli SM, Towfighi J. Coke deposition by physical condensation of poly-cyclic hydrocarbons in the transfer line exchanger (TLX) of olefin plant. Appl Therm Eng. 2003;23(11):1347–58.

62. Mohamadalizadeh A, Towfighi J, Karimzadeh R. Modeling of catalytic coke formation in

thermal cracking reactors. J Anal Appl Pyrolysis. 2008;82(1):134–9.

63. Towfighi J, Sadrameli M, Niaei A. Coke formation mechanisms and coke inhibiting methods in pyrolysis furnaces. J Chem Eng Japan. 2002;35(10):923–37.

64. Marin GB, Gandarillas EM, Geem KM Van. Coking Resistance of Specialized Coil Materials during Steam Cracking of Sulfur-Free Naphtha Andre s. 2014;

65. Cai H, Krzywicki a., Oballa MC. Coke formation in steam crackers for ethylene production. Chem Eng Process. 2002;41(3):199–214.

66. Bonnet F, Ropital F, Berthier Y, Marcus P. Filamentous carbon formation caused by catalytic metal particles from iron oxide. Mater Corros. 2003;54(11):870–80.

67. Chan GKY, Inal F, Senkan S. Suppression of Coke Formation in the Steam Cracking of Alkanes: Ethane and Propane. Ind Eng Chem Res [Internet]. 1998;37(3):901–7. Available from: http://dx.doi.org/10.1021/ie9704511

68. Trimm DL. Control of coking. Chem Eng Process Process Intensif. 1984;18(3):137–48.

69. Grabke HJ, Krajak R, Nava Paz JC. On the mechanism of catastrophic carburization: “metal dusting.” Corros Sci. 1993;35(5–8).

70. Albright LF, McConnell CF, Welther K. Types of Coke Formed During the Pyrolysis of Light Hydrocarbons. In: Oblad AG, Davis HG, Eddinger RT, editors. Thermal Hydrocarbon Chemistry. American Chemical Society; 1979. p. 175–91.

71. Bach G, Zimmermann G, Kopinke FD, Barendregt S, Van Den Oosterkamp P, Woerde H. Transfer-line heat exchanger fouling during pyrolysis of hydrocarbons. 1. Deposits from dry cracked gases. Ind Eng Chem Res [Internet]. 1995;34:1132–9. Available from: http://www.scopus.com/inward/record.url?eid=2-s2.0-

0029278414&partnerID=40&md5=7f1125ef5da41cb5ea8edd40ef08fc41

72. Albright LF, Marek JC. Coke formation during pyrolysis: roles of residence time, reactor geometry, and time of operation. Ind Eng Chem Res [Internet]. 1988;27(5):743–51. Available from: http://dx.doi.org/10.1021/ie00077a004

73. Albright LF, Marek JC. Mechanistic model for formation of coke in pyrolysis units producing ethylene. Ind Eng Chem Res [Internet]. 1988;27(5):755–9. Available from: http://pubs.acs.org/doi/abs/10.1021/ie00077a006

74. Shubo F, Liming S, Qiangkun L. A study on coke deposition and coking inhibitors during AGO pyrolysis in pulsed micro-reactor system. J Anal Appl Pyrolysis. 2002;65(2):301–12.

75. Baker R. Nucleation and growth of carbon deposits from the nickel catalyzed decomposition of acetylene. J Catal [Internet]. 1972;26(1):51–62. Available from: http://www.sciencedirect.com/science/article/pii/0021951772900322

76. Zhou J, Xu H, Liu J, Qi X, Zhang L, Jiang Z. Study of anti-coking property of SiO2/S composite coatings deposited by atmospheric pressure chemical vapor deposition. Mater Lett. 2007;61(29):5087–90.

77. Jiménez-González C, Boukha Z, de Rivas B, González-Velasco JR, Gutiérrez-Ortiz JI, López-Fonseca R. Behaviour of nickel–alumina spinel (NiAl2O4) catalysts for isooctane steam reforming. Int J Hydrogen Energy. 2015;40(15):5281–8.

78. Millward GR, Evans HE, Aindow M, Mowforth CW. The Influence of Oxide Layers on the Initiation of Carbon Deposition on Stainless Steel. Oxid Met. 2001;56(3/4):231–50.

79. Oberlin A, Endo M, Koyama T. Filamentous growth of carbon through benzene decomposition. J Cryst Growth. 1976;32(3):335–49.

80. Tari V, Najafizadeh a., Aghaei MH, Mazloumi M a. Failure Analysis of Ethylene Cracking Tube. J Fail Anal Prev. 2009;9(4):316–22.

81. Khodamorad SH, Haghshenas Fatmehsari D, Rezaie H, Sadeghipour a. Analysis of ethylene cracking furnace tubes. Eng Fail Anal [Internet]. 2012;21:1–8. Available from: http://dx.doi.org/10.1016/j.engfailanal.2011.11.018

82. Bozzano G, Dente M, Faravelli T, Ranzi E. Fouling phenomena in pyrolysis and combustion processes. Appl Therm Eng. 2002;22(8):919–27.

83. Wauters S, Marin GB. Kinetic Modeling of Coke Formation during Steam Cracking. Ind Eng Chem Res [Internet]. 2002;41(10):2379–91. Available from: http://dx.doi.org/10.1021/ie010822k

84. Glasier GF, Pacey PD. Formation of pyrolytic carbon during the pyrolysis of ethane at high conversions. Carbon N Y. 2001;39(1):15–23.

85. Lahaye J, Badie P, Ducret J. Mechanism of carbon formation during steamcracking of hydrocarbons. Carbon N Y. 1977;15(2):87–93.

86. Graff MJ, Albright LF. Coke Deposition From Acetylene, Butadiene and Benzene Decompositions at 500-900C On Solid Surfaces. 1981;20(4):319–30.

87. Guan K, Wang Q. Analysis of failed electron beam welds in ethylene cracking tubes. Eng Fail Anal. 2011;18(5):1366–74.

88. Bao B, Liu J, Xu H, Wan S, Zhang W. Effect of selective oxidation and sulphur/phosphorus-containing compounds on coking behaviour during light naphtha thermal cracking. Can J Chem Eng. 2017;95(8):1480–8.

89. Bao B, Liu J, Xu H, Liu B, Zhang W. Inhibitory effect of $MnCr_2O_4$ spinel coating on coke

formation during light naphtha thermal cracking. RSC Adv [Internet]. 2016 [cited 2016 Sep 27];6(73):68934–41. Available from: http://xlink.rsc.org/?DOI=C6RA13009G

90. Bao B, Wang Z, Xu H, Liu J. Anti-coking Effect of MnCr 2 O 4 Spinel Coating during Light Naphtha Thermal Cracking. Energy Procedia [Internet]. 2017;105:4808–13. Available from: http://linkinghub.elsevier.com/retrieve/pii/S1876610217310548

91. Cruchley S, Taylor MP, Ding R, Evans HE, Child DJ, Hardy MC. Comparison of Chromia Growth Kinetics in a Ni-based Superalloy, with and without Shot-peening. Corros Sci [Internet]. 2015;100:242–52. Available from: http://dx.doi.org/10.1016/j.corsci.2015.07.033

92. Chen JH, Rogers PM, Little JA. Oxidation Behavior of Several Chromia-Forming Commercial Nickel-Base Superalloys. 1997;47.

93. Schmucker E, Petitjean C, Martinelli L, Panteix PJ, Ben Lagha S, Vilasi M. Oxidation of Ni-Cr alloy at intermediate oxygen pressures. II. Towards the lifetime prediction of alloys. Corros Sci [Internet]. 2016;111:474–85. Available from: http://dx.doi.org/10.1016/j.corsci.2016.05.024

94. Evans HE, Hilton DA, Holm RA, Webster SJ. Influence of silicon additions on the oxidation resistance of a stainless steel. Oxid Met. 1983;19(1–2):1–18.

95. Durham RN, Gleeson B, Young DJ. Factors affecting chromium carbide precipitate dissolution during alloy oxidation. FE, Ferr Alloy. 1998;50(1–2):139–65.

96. Gheno T, Monceau D, Young DJ. Mechanism of breakaway oxidation of Fe-Cr and Fe-Cr-Ni alloys in dry and wet carbon dioxide. Corros Sci [Internet]. 2012;64:222–33. Available from: http://dx.doi.org/10.1016/j.corsci.2012.07.024

97. Wood GC, Hodgkiess T, Whittle DP. A comparison of the scaling behaviour of pure iron-

chromium and nickel-chromium alloys in oxygen. Corros Sci [Internet]. 1966 Jan [cited 2016 Mar 9];6(3–4):129–47. Available from: http://www.sciencedirect.com/science/article/pii/S0010938X66800045

98. Sahlaoui H, Sidhom H, Philibert J. Prediction of chromium depleted-zone evolution during aging of Ni-Cr-Fe alloys. Acta Mater. 2002;50(6):1383–92.

99. Li H, Zheng Y, Benum LW, Oballa M, Chen W. Carburization behaviour of Mn – Cr – O spinel in high temperature hydrocarbon cracking environment. Corros Sci [Internet]. 2009;51(10):2336–41. Available from: http://dx.doi.org/10.1016/j.corsci.2009.06.006

100. Li H, Chen W. High temperature carburization behaviour of Mn – Cr – O spinel oxides with varied concentrations of manganese. Corros Sci [Internet]. 2011;53(6):2097–105. Available from: http://dx.doi.org/10.1016/j.corsci.2011.02.021

101. Zurek J, Young DJ, Essuman E, Hänsel M, Penkalla HJ, Niewolak L, et al. Growth and adherence of chromia based surface scales on Ni-base alloys in high- and low-pO2 gases. Mater Sci Eng A. 2008;477(1–2):259–70.

102. Li H, Chen W. Stability of MnCr 2 O 4 spinel and Cr 2 O 3 in high temperature carbonaceous environments with varied oxygen partial pressures. Corros Sci [Internet]. 2010;52(7):2481–8. Available from: http://dx.doi.org/10.1016/j.corsci.2010.02.040

103. Evans HE. Spallation models and their relevance to steam-grown oxides. Mater High Temp. 2005;22(1–2):155–66.

104. Sun Z, Liebscher CH, Huang S, Teng Z, Song G, Wang G, et al. New design aspects of creep-resistant NiAl-strengthened ferritic alloys. Scr Mater [Internet]. 2013;68(6):384–8. Available from: http://dx.doi.org/10.1016/j.scriptamat.2012.10.040

105. Brady MP, Yamamoto Y, Santella ML, Maziasz PJ, Pint BA, Liu CT, et al. The Development of

Alumina-Forming Austenitic Stainless Steels for High-Temperature Structural Use *. JOM. 2008;July:71–7.

106. Deodeshmukh VP, Matthews SJ, Klarstrom DL. High-temperature oxidation performance of a new alumina-forming Ni-Fe-Cr-Al alloy in flowing air. In: International Journal of Hydrogen Energy. 2011.

107. Stott FH. The protective action of oxide scales in gaseous environments at high temperature. Reports Prog Phys [Internet]. 1987;50(7):861. Available from: http://stacks.iop.org/0034-4885/50/i=7/a=002

108. Jeurgens LPH, Sloof WG, Tichelaar FD, Mittemeijer EJ. Growth kinetics and mechanisms of aluminum-oxide films formed by thermal oxidation of aluminum. J Appl Phys. 2002;92(3):1649–56.

109. Hindam H, Whittle DP. Microstructure, adhesion and growth kinetics of protective scales on metals and alloys. Oxid Met. 1982;18(5–6):245–84.

110. Giggins CS, Pettit FS. Oxidation of Ni-Cr-Al Alloys Between 1000° and 1200°C. J Electrochem Soc [Internet]. 1971;118(11):1782. Available from: http://jes.ecsdl.org/cgi/doi/10.1149/1.2407837

111. Chyrkin A, Pillai R, Galiullin T, Wessel E, Grüner D, Quadakkers WJ. External α -Al 2 O 3 scale on Ni-base alloy 602 CA . – Part I : Formation and long-term stability. Corros Sci [Internet]. 2017;124(December 2016):138–49. Available from: http://dx.doi.org/10.1016/j.corsci.2017.05.017

112. Marin GB, Gandarillas EM, Geem KM Van, Muñoz Gandarillas AE, Van Geem KM, Reyniers M-F, et al. Coking Resistance of Specialized Coil Materials during Steam Cracking of Sulfur-Free Naphtha Andre s. Ind Eng Chem Res [Internet]. 2014 Sep 3 [cited 2016 Jan

8];53(35):13644–55. Available from: http://dx.doi.org/10.1021/ie502277e

113. Schietekat CM, Sarris SA, Reyniers PA, Kool LB, Peng W, Lucas P, et al. Catalytic Coating for Reduced Coke Formation in Steam Cracking Reactors. Ind Eng Chem Res [Internet]. 2015 Oct 7 [cited 2016 Jan 8];54(39):9525–35. Available from: http://dx.doi.org/10.1021/acs.iecr.5b02263

114. Wang Z, Xu H, Zhou J, Luan X. Simulation of SiO2/S coating deposition in a pilot plant set-up for coking inhibition. Chem Eng Res Des [Internet]. 2013;91(1):120–33. Available from: http://dx.doi.org/10.1016/j.cherd.2012.07.006

115. Zhou J, Xu H, Luan X, Ling X. Influence of the SiO 2/S coating and sulfur/phosphorus-containing coking inhibitor on coke formation during thermal cracking of light naphtha. Fuel Process Technol. 2012;104:198–203.

116. Zhou J, Wang Z, Luan X, Xu H. Anti-coking property of the SiO2/S coating during light naphtha steam cracking in a pilot plant setup. J Anal Appl Pyrolysis [Internet]. 2011;90(1):7–12. Available from: http://dx.doi.org/10.1016/j.jaap.2010.09.011

117. Zychlinski W, Wynns KA, Ganser B. Characterization of material samples for coking behavior of HP40 material both coated and uncoated using naphtha and ethane feedstock. Mater Corros. 2002;53(1):30–6.

118. Rahimi N, Karimzadeh R, Jazayeri SM, Nia KD. An empirical investigation of the influence of sulfur additives on the catalytic rate of coke deposition and CO formation in the steam cracking of LPG over Incoloy 600 and stainless steel. Chem Eng J [Internet]. 2014;238:210–8. Available from: http://linkinghub.elsevier.com/retrieve/pii/S1385894713013284

119. Fedorova E, Monceau D, Oquab D. Quantification of growth kinetics and adherence of oxide scales formed on Ni-based superalloys at high temperature. Corros Sci [Internet].

2010;52(12):3932–42. Available from: http://dx.doi.org/10.1016/j.corsci.2010.08.013

120. Reinking L. Examples of Image Analysis Using ImageJ [Internet]. Millersville, PA; 2007. Available from: https://imagej.nih.gov/ij/docs/pdfs/examples.pdf

121. Li J, Beres W. Scratch test for coating/substrate systems - A literature review. Can Metall Q. 2007;46(2):155–74.

122. Newbury DE, Ritchie NWM. Is Scanning Electron Microscopy / Energy Dispersive X-ray Spectrometry (SEM / EDS) Quantitative ? Scanning. 2013;35:141–68.

123. Saunders N, Guo Z, Li X, Miodownik AP, Schillé J. Using JMatPro to Model Materials Properties and Behavior. JOM. 2003;December:60–5.

124. Diekmann U. CALCULATION OF STEEL DATA USING JMATPRO Uwe Diekmann. In: Comat. 2012.

125. Han Z biao, Liu J hua, He Y, Li K wei, Ji Y long, Liu J. Determination of the liquidus and solidus temperatures of FeCrAl stainless steel. Int J Miner Metall Mater. 2015;22(11):1141–8.

126. Cieslak MJ, Headley TJ, Kollie T, Romig AD. Melting and solidification study of Alloy 625. Metall Trans A, Phys Metall Mater Sci. 1988;19 A(9):2319–31.

127. Buytoz S. Microstructural properties of M 7 C 3 eutectic carbides in a Fe – Cr – C alloy. 2006;60:605–8.

128. Li S, Xi X, Luo Y, Mao M, Shi X, Guo J, et al. Carbide Precipitation during Tempering and Its Effect. Materials (Basel). 2018;11.

129. Thorpe WR, Chicco B. The Fe-Rich Corner of the Metastable C-Cr-Fe Liquidus Surface. 1985;16(September):1541–9.

130. Mougin J, Galerie A, Dupeux M, Rosman N, Lucazeau G, Huntz A-M, et al. In-situ determination of growth and thermal stresses in chromia scales formed on a ferritic stainless steel *. 2002;490:486–90.

131. Wang K, Liu Y, Fergus JW. Interactions Between SOFC Interconnect Coating Materials and Chromia. 2011;4495:4490–5.

132. Huntz AM, Maréchal L, Lesage B, Molins R. Thermal expansion coefficient of alumina films developed by oxidation of a FeCrAl alloy determined by a deflection technique. Appl Surf Sci. 2006;252:7781–7.

133. Stallybrass C, Schneider A, Sauthoff G. The strengthening effect of (Ni,Fe)Al precipitates on the mechanical properties at high temperatures of ferritic Fe-Al-Ni-Cr alloys. In: Intermetallics [Internet]. Elsevier; 2005 [cited 2017 Nov 22]. p. 1263–8. Available from: http://www.sciencedirect.com/science/article/pii/S0966979505000701

134. Stott FH, Wood GC, Hobby MG. A Comparison of the Oxidation Behavior of Fe-Cr-AI, Ni-Cr-AI, and Co-Cr-Al Alloys. Oxid Met. 1971;3(2):103–13.

135. Bull SJ. Failure mode maps in the thin film scratch adhesion test. Tribol Int. 1997;30(7):491–8.

136. Bull SJ, G.-Berasetegui E. Chapter 7 An overview of the potential of quantitative coating adhesion measurement by scratch testing. Tribol Interface Eng Ser. 2006;51:136–65.

137. Xu CH, Gao W. Pilling-Bedworth ratio for oxidation of alloys. 2000;(March).

138. Jena AK, Chaturvedi MC. The Role of Alloying Elements in the Design of Nickel-base Superalloys. J Mater Sci. 1984;19(10):3121–39.

139. Tripathi A, Bagchi S, Singh J. Effect of Firing Temperature at the Porcelain-Metal Alloy

Interface in Porcelain-Fused-to-Metal Restorations . A SEM / EDS Study. 2017;355–60.

140. Pretorius R, Theron CC, Vantomme A, Mayer JW, Pretorius R, Theron CC, et al. Compound Phase Formation in Thin Film Structures Compound Phase Formation in Thin Film Structures. Vol. 8436. 2010.

141. Hicks M. Metals and alloys. Hume-Rothery rules. [Internet]. Shenyen National Laboratory for Materials Science. [cited 2019 Aug 30]. Available from: http://www.synl.ac.cn/org/non/zu1/knowledge/Hume-Rothery-rules.pdf

142. Kiani-Rashid AR. The bainite transformation and the carbide precipitation of 4 . 88 % aluminium austempered ductile iron investigated using electron microscopy. J Alloys Compd. 2009;474:490–8.

143. Delagnes D, Pettinari-sturmel F, Mathon MH, Danoix R, Bellot C, Lamesle P, et al. Cementite-free martensitic steels : A new route to develop high strength / high toughness grades by modifying the conventional precipitation sequence during tempering. Acta Mater. 2012;60(16):587–5888.

144. Jena AK, Chaturvedi MC. The Role of Alloying Elements in the Design of Nickel-base Superalloys. J Mater Sci [Internet]. 1984 Oct [cited 2015 Dec 14];19(10):3121–39. Available from: http://link.springer.com/10.1007/BF00549796

145. Fernandez R, Kattamis TZ, Introduction I, Matdriaux C. Effect of Solidification Parameters on the Growth Geometry of MC Carbide in IN-100 Dendritic Monocrystals. 1978;9(October):1381–6.

146. Xu YX, Lu JT, Li WY, Yang XW. Oxidation behaviour of Nb-rich Ni-Cr-Fe alloys: Role and effect of carbides precipitates. Corros Sci. 2018;140(May):252–9.

147. Berthod P, Aranda L. Thermal Expansion Behaviour of Ternary Nickel-Based , Cobalt-Based

, and Iron-Based Alloys Containing Very High Fractions of Carbides. ISRN Metall. 2012;2012:9.

148. Hidnert P. Thermal expansion of some nickel alloys. J Res Natl Bereau Stand. 1957;58(2):89–92.

149. Coble RL, Kingery WD. Effect of Porosity on Physical Properties of Sintered Alumina. J Am Ceram Soc. 1954;39(11):377–85.

150. Yan J, Gao Y, Liang L, Ye Z, Li Y, Chen W, et al. Effect of yttrium on the cyclic oxidation behaviour of HP40 heat-resistant steel at 1373 K. Corros Sci [Internet]. 2011;53(1):329–37. Available from: http://dx.doi.org/10.1016/j.corsci.2010.09.039

151. Brady MP, Yamamoto Y, Santella ML, Walker LR. Composition, microstructure, and water vapor effects on internal/external oxidation of alumina-forming austenitic stainless steels. Oxid Met. 2009;72(5–6):311–33.

152. Berthod P, Vébert C, Aranda L, Podor R, Rapin C. Study of carbide transformations during high-temperature oxidation of nickel-base superalloys. Oxid Met. 2005;63(1–2):57–72.

153. Holcomb GR, Alman DE. The effect of manganese additions on the reactive evaporation of chromium in Ni-Cr alloys. Scr Mater. 2006;54(10):1821–5.

154. Hammer JE, Laney SJ, Jackson RW, Coyne K, Pettit FS, Meier GH. The oxidation of ferritic stainless steels in simulated solid-oxide fuel-cell atmospheres. Oxid Met. 2007;67(1–2):1–38.

155. Lobnig RE, Schmidt HP, Hennesen K, Grabke HJ. Diffusion of Cations in Chromia Layers Grown on Iron-Base Alloys. Oxid Met. 1992;37(1/2):81–93.

156. Yan J, Gao Y, Shen Y, Yang F, Yi D, Ye Z, et al. Effect of yttrium on the oxide scale adherence

of pre-oxidized silicon-containing heat-resistant alloy. Corros Sci [Internet]. 2011;53(11):3588–95. Available from: http://dx.doi.org/10.1016/j.corsci.2011.07.002

157. Lei Q. Kinetics of internal oxidation of FeAlCr alloys at low oxygen partial pressures. Delft University of Technology; 2016.

158. Capell BM, Was GS. Selective internal oxidation as a mechanism for intergranular stress corrosion cracking of Ni-Cr-Fe alloys. Metall Mater Trans A Phys Metall Mater Sci. 2007;38(6):1244–59.

159. Xu YX, Lu JT, Li WY, Yang XW. Oxidation behaviour of Nb-rich Ni-Cr-Fe alloys: Role and effect of carbides precipitates. Corros Sci. 2018;

160. Niu Y, Zhang XJ. The third-element effect in the oxidation of in 1 atm O 2 at 900 – 1000 ° C. 2006;48:4020–36.

161. Stott FH, Wood GC, Stringert J. The Influence of Alloying Elements on the Development and Maintenance of Protective Scales. 1995;44.

162. Essuman E, Meier GH, Zurek J, Hänsel M, Norby T, Singheiser L, et al. Protective and non-protective scale formation of NiCr alloys in water vapour containing high- and low-pO2 gases. Corros Sci. 2008;50(6):1753–60.

163. Sabioni ACS, Huntz AM, Salgado MF, Pardini A, Rossi EH, Paniago RM, et al. Materials at High Temperatures Atmosphere dependence of oxidation kinetics of unstabilized and Nb-stabilized AISI 430 ferritic stainless steels in the temperature range 850 – 950 ° C Atmosphere dependence of oxidation kinetics of unstabilized and Nb-stabi. 2014;3409.

164. Liu S, Shen J, Wu XF, Li H, Niu Y. The effect of sulphur on the carburization of three Fe-19Ni-13Cr alloys with various Al additions at 900 °C in oxygen-contaminated CH 4 -H 2 -H 2 S atmospheres. Corros Sci [Internet]. 2016;112:94–109. Available from:

http://linkinghub.elsevier.com/retrieve/pii/S0010938X16303171

165. Brady MP, Yamamoto Y, Santella ML, Pint BA. Effects of minor alloy additions and oxidation temperature on protective alumina scale formation in creep-resistant austenitic stainless steels. 2007;57:1117–20.

166. Wen DH, Li Z, Jiang BB, Wang Q, Chen GQ, Tang R, et al. Materials Characterization E ff ects of Nb / Ti / V / Ta on phase precipitation and oxidation resistance at 1073 K in alumina-forming austenitic stainless steels. 2018;144(July):86–98.

167. Han S, Young DJ. Simultaneous Internal Oxidation and Nitridation of Ni – Cr – Al Alloys. 2001;55(1):223–42.

168. Smallman RE, Ngan AHW. Oxidation, Corrosion and Surface Engineering. Mod Phys Metall. 2013;617–57.

169. Badini CU, Laurella F. Oxidation of FeCrAl alloy : influence of temperature and atmosphere on scale growth rate and mechanism. 2001;291–8.